Krishna Jonnalagadda
Alankar Alankar
Nagamani Jaya Balila
Tanmay Bhandakkar   *Editors*

Advances in Structural Integrity

Structural Integrity Over Multiple
Length Scales

Springer

Lecture Notes in Mechanical Engineering

Series Editors

Francisco Cavas-Martínez , Departamento de Estructuras, Universidad Politécnica de Cartagena, Cartagena, Murcia, Spain

Fakher Chaari, National School of Engineers, University of Sfax, Sfax, Tunisia

Francesca di Mare, Institute of Energy Technology, Ruhr-Universität Bochum, Bochum, Nordrhein-Westfalen, Germany

Francesco Gherardini , Dipartimento di Ingegneria, Università di Modena e Reggio Emilia, Modena, Italy

Mohamed Haddar, National School of Engineers of Sfax (ENIS), Sfax, Tunisia

Vitalii Ivanov, Department of Manufacturing Engineering, Machines and Tools, Sumy State University, Sumy, Ukraine

Young W. Kwon, Department of Manufacturing Engineering and Aerospace Engineering, Graduate School of Engineering and Applied Science, Monterey, CA, USA

Justyna Trojanowska, Poznan University of Technology, Poznan, Poland

Krishna Jonnalagadda · Alankar Alankar ·
Nagamani Jaya Balila · Tanmay Bhandakkar
Editors

Advances in Structural Integrity

Structural Integrity Over Multiple Length Scales

Editors
Krishna Jonnalagadda
Department of Mechanical Engineering
Indian Institute of Technology Bombay
Bombay, Maharashtra, India

Alankar Alankar
Department of Mechanical Engineering
Indian Institute of Technology Bombay
Bombay, Maharashtra, India

Nagamani Jaya Balila
Department of Metallurgical Engineering
and Materials Science
Indian Institute of Technology Bombay
Bombay, Maharashtra, India

Tanmay Bhandakkar
Department of Mechanical Engineering
Indian Institute of Technology Bombay
Bombay, Maharashtra, India

Proceedings of the 3rd Structural Integrity Conference and Exhibition—SICE2020

Structural Integrity at Multiple Length Scales

Editors

Krishna Jonnalagadda, Mechanical Engineering, Indian Institute of Technology Bombay
Alankar Alankar, Mechanical Engineering, Indian Institute of Technology Bombay
Tanmay K. Bhandakkar, Mechanical Engineering, Indian Institute of Technology Bombay
Nagamani Jaya Balila, Metallurgical Engineering and Materials Science, Indian Institute of Technology Bombay

Associate Editors

Dheepa Srinivasan, Pratt and Whitney Research Center, Bengaluru
Srikanth Gollapudi, Materials Science, Indian Institute of Technology Bhubaneshwar
Ravishankar Kottada, Metallurgical Engineering, Indian Institute of Technology Madras
Viswanath Chinthapenta, Mechanical and Aerospace Engineering, Indian Institute of Technology Hyderabad
Naresh Varma Datla, Mechanical Engineering, Indian Institute of Technology Delhi
Prakash Nanthagopalan, Civil Engineering, Indian Institute of Technology Bombay
Manish Kumar, Civil Engineering, Indian Institute of Technology Bombay
Zafir Alam, Defence Metallurgical Research Laboratory, Hyderabad
Eswar Korimilli, Materials Science and Engineering, Indian Institute of Technology Bombay
Gaurav Tiwari, Mechanical Engineering, National Institute of Technology Nagpur

Pritam Chakraborthy, Metallurgical Engineering, Indian Institute of Technology Kanpur
Anup Keshri, Metallurgical Engineering, Indian Institute of Technology Patna
Abhay Kumar Kuthe, Mechanical Engineering, National Institute of Technology Nagpur
Amber Srivastava, Mechanical Engineering, Indian Institute of Technology Bombay
Anirban Patra, Metallurgical Engineering and Materials Science, Indian Institute of Technology Bombay
Chandra Sekhar Yerramalli, Aerospace Engineering, Indian Institute of Technology Bombay

Reviewers

Aayush Kant, University of Pennsylvania, USA
Amber Shrivastava, IIT Bombay, India
Amit Singh, IIT Bombay, India
Amuthan Ramabathiran, IIT Bombay, India
Anirban Patra, IIT Bombay, India
Anup Keshri, IIT Patna, India
Chandra Sekher Yerramalli, IIT Bombay, India
Debashis Das, University of Illinois, USA
Eswar Prasad, IIT Indore, India
Gaurav Singh, University of Southampton, UK
Gurusideswar S., SRM Institute of Science and Technology, India
Hirshikesh Hirshikesh, IIT Bombay, India
Ilaksh Adlakha, IIT Madras, India
Jay Ghosh, IIT Bombay, India
K. Sridhar, Naval Metallurgical Research Laboratory, India
K. V. N. Surendra, IIT Pallakad, India
Lakshminarayanan Ramasubramanian, IIT Delhi, India
M. P. Gururajan, IIT Bombay, India
Mahendra K. Samal, BARC, India
Manish Kumar, IIT Bombay, India
Maya Kini, MPIE Duesseldorf, Germany
Mayank Chouksey, IIT Kanpur, India
MJNV Prasad, IIT Bombay, India
Moirangthem Dinachandra, IIT Bombay, India
Murshid Imam, IIT Patna, India
Narasimhan Swaminathan, IIT Madras, India
Naresh Datla, IIT Delhi, India
Niloy Khutia, IIT Kanpur, India
Nipal Deka, Rutgers University, India
P. J. Guruprasad, IIT Bombay, India

Parag Tandaiya, IIT Bombay, India
Pavan Kolluru, Texas A&M University, USA
Prakash Nanthagopalan, IIT Bombay, India
Prita Pant, IIT Bombay, India
Pritam Chakraborty, IIT Kanpur, India
R. Sunder, BISS-ITW, Bangalore, India
Rajesh Korla, IIT Hyderabad, India
Ratna Kumar Annabattula, IIT Madras, India
Sachin Singh Gautam, IIT Guwahati, India
Salil S. Kulkarni, IIT Bombay, India
Sarthak S. Singh, IIT Kanpur, India
Shailesh I. Kundalwal, IIT Indore, India
Srikanth Gollapudi, IIT Bhubaneswar, India
Srikanth Korla, NIT Warangal, India
Subhobroto Koley, IIT Kanpur, India
Sujith Kumar, IIT Bombay, India
Suprtaik Mukhopadhyay, IIT Kanpur, India
Sushil Mishra IIT Bombay, India
Susmita Naskar, IIT Bombay, India
Tanmoy Mukhopadhyay, IIT Kanpur, India
Tejas Prakash Gotkhindi, IIT Dharwad, India
Vikram Jayaram, IISc Bangalore, India
Vinod Pare, SGSITS, Indore, India
Viswanath Chintapenta, IIT Hyderabad, India

Editors' Preface

The proceedings of the 3rd Structural Integrity Conference and Exhibition—SICE2020 were yet another opportunity for us in showcasing the efforts of the structural integrity community in India. It was an occasion where we had an opportunity to review work done across various disciplines binded by the common theme of *structural integrity*. We thank all the organisers, reviewers, and, more importantly, the authors for presenting and submitting their contributions to these proceedings.

SICE is a biannual conference organised under the aegis of the Indian Structural Integrity Society (InSIS). The third edition was held online between 11–13 and 18–20 December 2020. The earlier editions of the conference attracted a large number of Indian and foreign researchers and practitioners to share their work and network. The year 2020 has a special place in our minds, with the COVID-19 pandemic affecting almost every country on the planet. The regular offline conference, supposed to be held in the second week of December 2020, was suspended, and the online avatar was introduced just six months before the original conference dates. With unwavering support from the InSIS board, distinguished plenary and keynote speakers, symposium organisers, sponsors, and local committee at IIT Bombay, we were able to announce and conduct the online version of the SICE2020 conference over two long weekends in December 2020. We thank all the speakers for accepting our request at a short notice and participating over the weekend.

The conference consisted of 6 plenary, 16 keynote, and 8 industry presentations delivered by distinguished Engineers and Scientists across the world. In addition, we had 44 invited presentations across various symposium tracks and more than 50 contributory presentations by authors of these proceedings. We appreciate the knowledge and insight shared by all the speakers over the online platform that is new to everyone and required acclimatization. The conventional poster presentations were replaced by video poster presentations made available for online viewing throughout the conference duration with the option of online feedback. The freedom to watch the videos anytime and on any device was very much appreciated by the participants.

The proceedings consist of 43 full-length peer-reviewed manuscripts from various disciplines related to structural integrity. We once again thank the authors for investing their time and effort to present their work and submit it in writing. We

are also thankful to all our reviewers, who helped us to critique the submitted work and bring it to the stage that you see through these proceedings.

On a parting note, we firmly believe that this book, consisting of technological advances in the area of structural integrity, will help the readers in increasing their knowledge and encourage discussion and further advancement in their respective research areas.

Bombay, India   Krishna Jonnalagadda
                                                                                  Alankar Alankar
                                                                              Tanmay Bhandakkar
                                                                            Nagamani Jaya Balila

Contents

About the Editors

Prof. Krishna Jonnalagadda is an Associate Professor of Mechanical Engineering at Indian Institute of Technology (IIT) Bombay. His research interests are in the areas of experimental mechanics, fracture mechanics and plasticity. He has published several papers, which includes two best paper awards and the prestigious M. Hetenyi award from Society for Experimental Mechanics. Currently, he is on the editorial board of Experimental Mechanics Journal. He has also been a reviewer for several journals in the area of experimental solid mechanics and mechanical behavior of materials. He has guided several Ph.D. and Master's theses, and currently leads a group of research students on dynamic deformation and in situ mechanics of materials.

Prof. Alankar Alankar is currently an Associate Professor at the Department of Mechanical Engineering, Indian Institute of Technology (IIT) Bombay. He is an expert on crystal plasticity, multiscale computational mechanics of crystalline materials. His current research interests span application of AL and ML for scientific problems. He has co-authored several international research publications and technical reports. Prof. Alankar serves on the editorial board of Materials Theory (Springer Nature) and is an active reviewer for several reputed journals in the broad area of mechanics of materials. He leads the ICME and Materials Genome (IMaGen) Group at the Department of Mechanical Engineering IIT Bombay where he is mentoring several Ph.D., masters and undergraduate students.

Prof. Nagamani Jaya Balila is an Associate Professor at the Department of Metallurgical Engineering and Materials Science, Indian Institute of Technology (IIT) Bombay. She completed her Ph.D. in Materials Engineering from the Indian Institute of Science, Bangalore and her post-doctoral research at the Department of Structure and Nano-/Micro-mechanics of Materials, Max Planck Institut für Eisenforschung, Duesseldorf. Her current areas of research are in fracture mechanics at multiple length scales and design of materials with improved damage tolerance. She has published more than 22 journal articles and 3 reviews in the field of microscale deformation and fracture behavior of materials. She is a reviewer of several international journals

in the field of mechanics and materials engineering. She is currently leading a group of 5 Ph.D. students, 3 Master's students, 2 Bachelor's students while having guided more than 8 Master's students and 6 Bachelor's students in their thesis.

Prof. Tanmay Bhandakkar is an Associate Professor, Department of Mechanical Engineering, Indian Institute of Technology (IIT) Bombay. His area of interest is mathematical modelling of contact, fracture and elasticity. He has more than 20 international publications and is a regular reviewer of several journals dedicated to solid mechanics. He has guided 4 Ph.D. students and over 40 Master's student towards their thesis.

Performance-Driven Fan Case Design for Durability Evaluation in a Blade Impact Event

Ashutosh Bhat, Sandeep Sharma, and Lavya Sharma

Abstract The present work's objective focuses on identifying the containment capability of a hybrid fan case that uses an impact-absorbing (periodic) corrugated lattice structure core (LSC) sandwiched between the inner ring and outer cover. Bi-directional corrugated lattices have distinct impact resistance owing to excellent strength to stiffness ratio at a low relative density which makes it ideal for design against impact. Four cases with different (LSC) configurations: general (a), refined general (b), twill (c) and inverted twill (d) patterns that have similar relative density are investigated under a single fan blade out (FBO) condition. For identical packaging, the geometrical topology of a lattice is controlled by varying it's unit cell parameters. Durability of casing under highly non-linear interactions with blade is numerically resolved using LS-DYNA simulations and cases 1–4 are evaluated by comparing the plastic damage, energy absorption, blade momentum and crack propagation. Essentially, having sufficient inner ring stiffness is vital to resist the abrupt impact forces while maintaining structural integrity, for which a suitable thickness of 1mm is estimated after performing explicit tests between a range of 0.6–2mm shell thicknesses. Results of complete hybrid casing exhibits severe damage for cases 1, 2, and 3 as the lattice fragments and also debonds at various locations due to local buckling caused by high tension forces. However, responses for case 4 are found to be reassuring as it maintains enough interferential strength to counter shear and absorbs 44.5% of total energy, which is 5–16% higher than other cases. The stiffness of inverted twill is considered accountable here, which resists the casing tear with smallest recorded circumferential crack length. The performance test cycle is limited to 6ms which includes the prominent effect of three critical events: initial perforation, successive tear, and root impact occurring at discrete time intervals. Also, the gouge occurring on the outer cover for case 2 and 4 is 87 and 71% larger relative to case 3, whereas case 1 remains undamaged. Lastly, the paper demonstrates that the   performance of inverted twill bi-directional corrugated lattice as a potential structural core is found superior relative to other (LSC) arrangements as it not only satisfies the containment criteria effectively but also showcases excellent impact resistance characteristics.

A. Bhat (✉) · S. Sharma · L. Sharma
Aerosphere Solutions Pvt.Ltd, Chandigarh 160036, India

1   Introduction

Failure of aero-engine due to blade loss from a turbofan rotor leads to dangerous effects making airworthiness a major flight safety concern in commercial aviation. This event also recognized as Fan Blade-Out (FBO) may occur due to a number of reasons including heavy strike from birds or drones, blade detachment due to fatigue, overheating and manufacturing defects [1]. Thus, a high energy liberated blade if not contained can lead to catastrophic outcome due to initial and subsequent damage caused to critically important units such as fluid line, control hardware, and also airframe in close proximity. International regulatory bodies such as Federal Aviation Administration (US) and Ministry of Defense (UK) [2, 3] address this concern, wherein turbofan engine manufactures have to successfully demonstrate fan case capability to maintain adequate structural integrity in a dynamic event of such high intensity. Large dynamic loads occurring during impact and further during spool down induce large deformations, material plastic damage, and high-speed contact interactions, which makes it an extremely complex non-linear case of structural dynamics [2]. Therefore, series of early investigation becomes necessary and comprises of: coupon test for material selection [3], subscale ballistic test [4] to understand failure response and full-scale rig test [5] for design validation before being commercially available. According to literature by Sarkar and Atluri [6], a great deal of casing thickness is required in a setup having complete array of blades to limit damage and contain released blade fragment. Whereas, enhancing thrust to weight ratio of a jet engine requires lightweight solutions. In past few decades, composite fabric has proven to be the material of choice in aerospace and is accepted in numerous applications. Haijun Xuan et al. [7] in their study propose that Kevlar's ability to contain broken blade is 52% higher exclusive of inner shell but to maintain structural reliability inner ring must have adequate stiffness. Researchers [6, 7] conclusive of validation between numerical method and experiment report similar findings. Pingchao et al. [8] in their previous work have demonstrated the effect of non-linear excitations caused by a FBO event where sudden unbalance, asymmetric blade disc, and blade case rubbing were analytically presented. In the aftermath of blade loss, the fan–disk rotating system starts moving off-center in the heavier side of the disk due to sudden large imbalance introduced on the rotor shaft. This eccentric rotor no longer remains symmetric about its center of rotation, and the spinning of the asymmetric rotor introduces another set of non-linearities. The inertial asymmetry and effect of rubbing between k-th blade and casing schematic are represented in Fig. 1 for reference. After losing a fan blade, rotor becomes unbalanced due to sudden change in eccentricity e from an initial zero and subsequently. The lost blade destroys the symmetry of the bladed disk. Then the polar moment of inertia about the rotating axis O changes to $J'_p \frac{1}{4} J_p m_{loss} R^2$, where J_p is the polar moment

Fig. 1 FBO condition
illustration
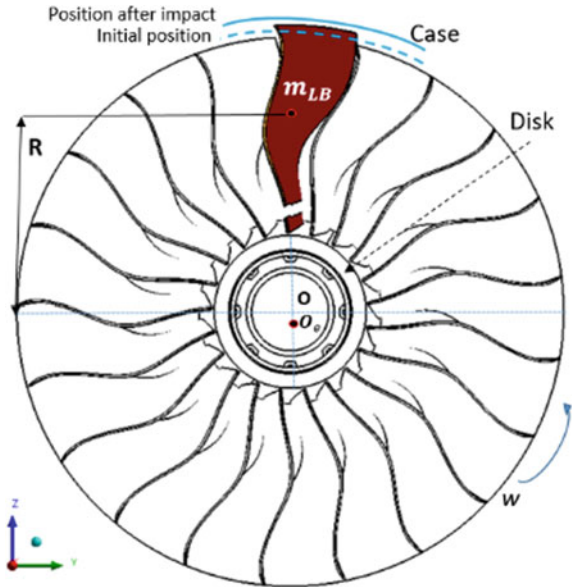
of inertia before blade off, mloss is the mass of the lost blade, and R is the distance
between mass centroid of the lost blade and rotating axis O. The diametric moments
of inertia about the axis x and y become Jx ¼ Jp = 2 mlossR2 and Jy ¼Jp = 2,
respectively. Lagrange method is used to compute numerical solution in such case
and governing equations can be found in author's previous work [9].

Corrugation technique provides innovative means of developing lightweight struc-
ture with intriguing possibilities, and likewise various indigenous anisotropy in
combination with advanced materials, in recent years, have come to light. Dayyani
et al. [10] in their literature has nicely summarized the mechanics of corrugated struc-
tures along with suitable perspective on mechanical properties, buckling, vibration,
fatigue, and impact characteristics. In context with current research, it is impor-
tant to highlight previous work done by Semenyuk and Neskhodovskaya [11], in
which important analytical relations are derived to estimate buckling behavior for
corrugated shells. Such methodology allows design control, and desired stability for
shells can be estimated. However, for a non-linear case, the buckling behavior is
rather complex and often requires numerical solutions to predict large deformations.

2   Containment Case Design

A containment case for a jet-engine radially encloses fan blades and disk in close
proximity, which is typically cylindrical or frustoconical in form. The stationary
case extends longitudinally about its central axis and is adjoined with wing through

pylon at its rear outer boundary. During operation, the case must satisfy its ability in regards with safety and should have sufficient resistance to prevent any perforation. Considering a FBO event that is unusual, the expelled blade at such high speed first makes contact with the casing and if not contained can cause unpredictable damage to other components in its trajectory. To prevent any such possibility, two widely accepted approaches for containment design that are in common use can be categorized into hard wall and soft wall method [2, 3]. The choice of method is subjected to weight penalty, which increases exponentially relative to case diameter. It is noted that a soft wall case uses multiple layers of low-density high strength synthetic fibers (mostly Kevlar or Zylon) wrapped around a rigid cylinder (usually aluminum) for construction whereas a hard wall case only comprises of a thick hollow cylinder. Released blade can be found to quickly penetrate the primary layer and later contained by secondary layer (with high energy absorbing capability) in case of soft wall, however, in hard wall case, blade is deflected back into the system where subsequent high-speed interactions persist. Major disadvantage of using hard wall case type is its inability to maintain structural integrity. On impact, high axial forces develop a burst of shear energy in outward direction leading to abrupt geometrical changes, which, in turn, imposes extreme tension stresses at connection points, further shown in section [5]. On the contrary, it provides better scope for designers to achieve smaller circumscribed space with hard wall case since no "dead" room is required for containment process. Emphasizing on lightweight construction, Zekan et al. [12] recently reported validation study on performance of soft wall casing and also highlighted the use of triaxial braided carbon composites being used in GEnx engines.

3   Defining Design

The focus of the current study is on conceptualizing the introduction of lattice-core structure as a sandwich layer between primary and secondary face plates in limited perimeter subjected to dynamic impact loading. This formation, also termed as Lattice-core sandwich cylinder (LSC) [13], offers excellent strength to stiffness ratio at low specific density, which depends on selection of lattice type and other factors such as: size and shape, series and parallel repetition, connectivity, and parent material. At a critical thickness if blade is allowed to penetrate, the first layer elastic stretching of metal ring can be controlled and remaining K.E can be converted into large plastic deformation in the central core. Thus, a hybrid sandwich casing has been devised to test in a FBO scenario numerically. The casing is substructured into three distinct layers: the inside layer is a thin-walled cylinder followed by a bi-directional corrugated lattice core, which is wrapped around circumference and lastly covered using hat like shell. Norman et al. [14] first reported the concept of sinusoidal corrugation in curved orientation, which can significantly adapt to elastic shape variations with much local stretching of the surface. Further, the effect of blade-case rubbing contact can lead to severe damage on the inner casing, in which

case bi-directional interlocking in (Y,Z) direction provides enough stiffness to ensure structural reliability. Wanxin Li et al. [15] demonstrated novel octagonal corrugated trusses developed using carbon fiber for estimating mechanical characteristics when wrapped around a cylinder. Also, the compression stiffness and strength are exponentially higher compared to unidirectional isogrid structures, which can be commonly found in technique provides effective means of such application. Higher interfacial strength (shear) is achieved due to enough contact between skin and core in comparison to traditionally used lattices such as micro lattice, pyramidal truss, iso truss, and also octet truss, which presents wide opportunities to optimize deterministic parameters. Moreover, the faceplate thickness can be minimized by some factor relative to use of honeycomb and foam cores due to smaller buckling load.

Textile industry, in particular, is known to utilize corrugation methods in order to produce various patterns, which can be broadly classified into 2-D and 3-D formations as follows: Weaves, Braids, Knits, and Non-crimps. Further classification of these patterns is carried based on their interlock orientation, and some frequently used types are the twill weave, the satin weave, the triaxial weave, the biaxial braid, the warp knit, the orthogonal interlock weave, through thickness angle interlock, 3-D braided T-stiffener, and the multi-axial warp knit etc. Yang et al. [16] have previously investigated the influence of such weaving architecture under ballistic impact and demonstrated better retention capability offered by the plain-weave anatomy. Figure 2 represents a hybrid casing schematic where a curved bi-directional corrugated lattice core serves as an insert between the inner ring and outer cover. Four cases (1, 2, 3, and 4), as shown in Fig. 3, incorporate the use of distinct Corrugated LSC's described as follows: general, refined general, twill, and inverted twill. A detailed

Fig. 2 Hybrid case with LSC sandwiched
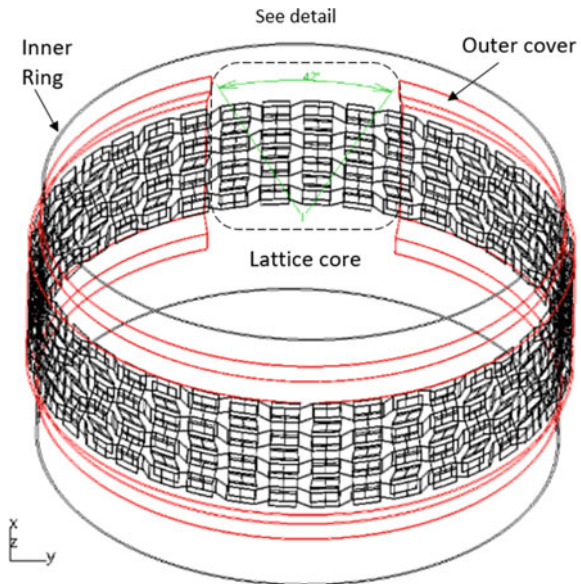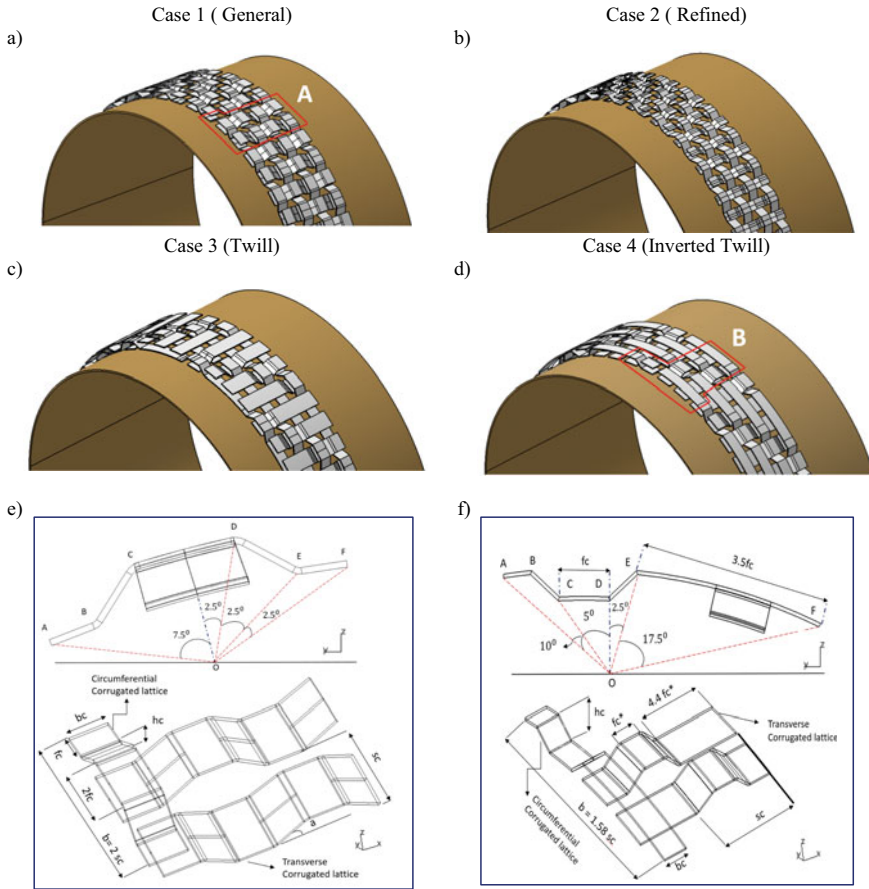
Fig. 3 Schematic of different lattice configurations: **a** General, **b** Refined general, **c** Twill, and **d** Inverted twill along with modeling parameters for general (**e**) and Twill (**f**)

cut section view further showcases the periodical configuration of circumferential and transverse trusses for general and twill type with defined parameters in Fig. 3e, f. 2D Unit cell topological constituents are expressed in terms of *(sc, fc, bc, hc, tc and a)* where, *(sc)* determines equidistant spacing, *(fc)* is face length, *(bc)* is width, hc is cell height, *(tc)* is rib thickness and *(a)* being the inclination angle. Arc length for one unit cell can be estimated using: $\int_{fc}^{b} ds$; where a, b are constants and ds is in polar form; however, it can be parameterized in constant length b = 2*sc and b = 1.58*sc for general and twill type. To develop a uniform model, constant curve length *'b'* was set to 15, 10, 30, and 30 from the neutral axis having a total number of 96, 144, 48, 48 cells positioned circumferentially (yz) for general, refined general, twill, and inverted twill. Similarly, a total count of 40, 60, 48, and 48 instances was modeled in transverse (x) direction. Inclination angle *(a)* is defined as equivalent to

arc tan $\left(\frac{(hc)-(tc)}{(sc)-n(fc)} \right)$, where 'n' is the factor on which face width depends for different truss anatomies. Relative density structure, ρ, is given as:

$\rho = \frac{2\,bc\,tc(c+fc\sin(a))}{hc\sin(a)\,(d)^2}$, where d = $hc\cot(a) + fc$, which is the cell dimension.

4 Numerical Modeling

Numerical simulations are preferred mainly for design validation studies, but off-late have contributed extensively toward optimization solutions and new product development. With shorter lead times and high capital costs for a case such as FBO, organizations prefer a deterministic design approach to test and weigh multiple design cases. In this article, a highly non-linear transient event involving uncertain blade–case interaction is studied with the aid of an explicit time integration scheme.

4.1 Material Modeling

Because of the high strain rates that occur in an FBO event, strain rate-dependent material properties were necessary for these simulations. The Johnson–Cook (J-C) material model has been rigorously studied found suitable to account for strain rate-dependent plasticity and failure estimations. Plasticity and failure data for each of the materials were referred from previously evaluated tests available in the open literature [17]. Further, a prior experimentation and numerical investigation demonstrated by Lawrence Livermore National Laboratory (LLNL) [5] to determine failure parameters of Ti-6Al-4 V and Al 2024-T3 are used to predict damage behavior during fan–case interaction as shown in Table 1. The model equation represents individual effects of strain hardening, strain-rate and thermal softening and is expressed as:

Table 1 Plasticity and J-C parameters for Ti 6Al-4 V and Al 2024-T3

Material	E (Gpa)	V	ρ (kg/m3)	$T_{m\ (K)}$	Tr (K)	Cρ (J/kg/K)
Al 2024-T3	181	0.4	7.85×10^3	1587	293	468
Ti-6Al-4 V	205	0.26	8.24×10^3	1563	293	481
Material	Johnson–Cook constitutive relation constant					
	$\dot{\varepsilon}0\ (^{s}-^{1})$	A (MPa)	B (MPa)	n	C	m
Al 2024-T3	1	755	1893	1	0	10
Ti-6Al-4 V	1	1350	1139	0.6522	0.0134	1
Material	Johnson–Cook Damage criterion constant					
	D1		D2	D3	D4	D5
Al 2024-T3	0.112		0.123	1.5	0.007	0
Ti-6Al-4 V	0.09		0.27	0.48	0.014	3.87
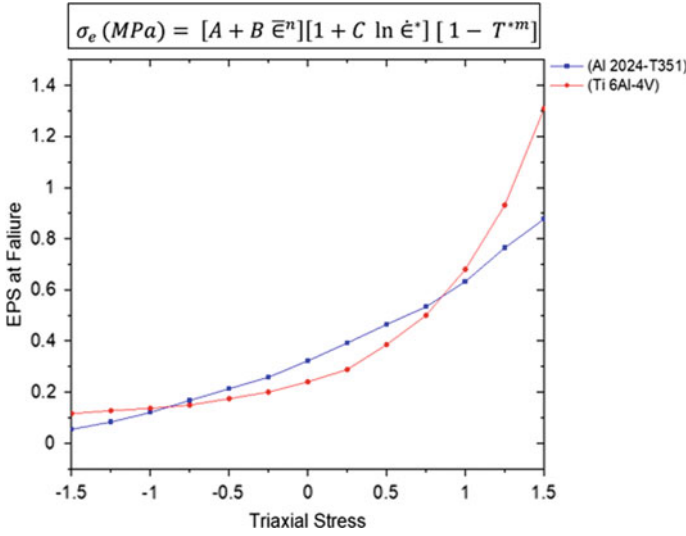
$$\sigma_e\,(MPa) = [A + B\,\overline{\in}^n][1 + C\,\ln\dot{\in}^*]\,[1 - T^{*m}]$$

Fig. 4 Fracture locus of Ti-6Al-4v and Al 2024-T351 at nominal strain rate of 1/s

$$\sigma_e(MPa) = \left[A + B\overline{\in}^n\right]\left[1 + C\ln\dot{\in}^*\right]\left[1 - T^{*m}\right],$$

where σ_e is equivalent plastic stress; $\overline{\in}$ is the effective plastic strain; $\dot{\in}^*\left(s^{-1}\right)$ is ratio of effective plastic strain rate to reference equivalent plastic strain rate; $T^*(°C) = (T - T_r)/(T_m - T_r)$ is the temperature relation assumed as adiabatic where T is the absolute temperature, T_r is the room temperature and T_m is the material melting temperature, respectively. *A, B, C, n, and m* are material constants determined from experimental tests. The damage locus at a nominal strain rate of 1/s for Ti-6Al-4 V and 2024-T3/T351 can be seen in Fig. 4.

4.2   Finite Element Model

To accurately conduct the blade–case impact problem, a complete finite element model was scaled on the premise of a specific type of real turbofan engine casing. In reference [4], reliable numerical solutions have been established for blade containment studies using ANSYS/LS-Dyna suite and were chosen for current work. A total of 21 wide chord curved blades with diametric profile of 7.13″ were modeled and attached to rotor (rigid body) positioned at absolute zero. The hybrid casing is formed by enclosing a 0.19″ bi-directional corrugated lattice core between inner case and outer cover having thickness of 1 and 0.8 mm, respectively. Schematic representation of geometrical dimensions and discretization for entire model is shown in Fig. 5. Connection of lattice on inner and outer sides is defined using surface_to_surface
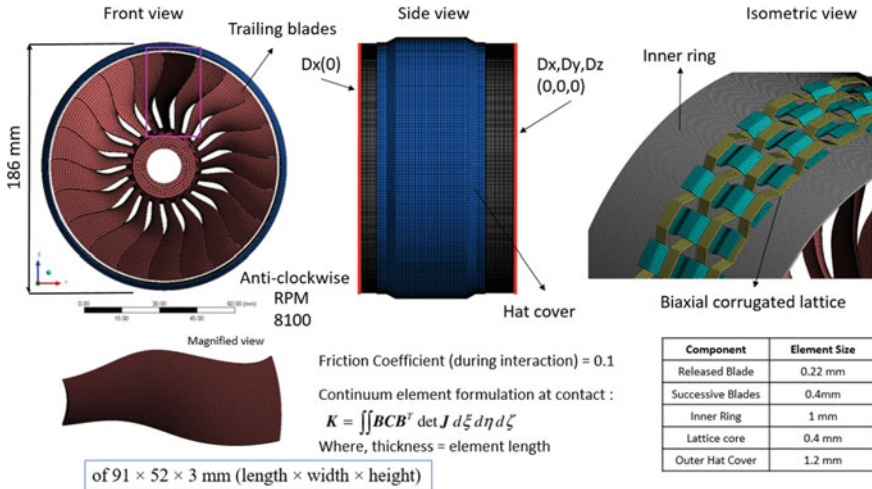
Fig. 5 Full rig geometrical representation with details of discretization and boundary conditions

contact because of non-uniform offset between nodes of individual components. Any overlapping contact pair between lattices is suppressed to predict real-time behavior. Interaction between blade and case components is governed via body_to_body erosion contact with a static frictional value of 0.1. Hence, the resistance offered by friction will not allow sliding, and the blade will tend to curl as desired. This type of contact retains and constantly updates the inertia of eroded material with changing location and allows secondary contact with new surfaces. Hughes [5], in their prior work, has analyzed the effect of varying friction coefficient on blades kinetic energy and realized a net change of 40% on increasing friction by a factor of 0.1. Material failure for blade due to self or foreign contact is set to automatic erosion type which reiterates the inertia of eroded material after each time step. Al20204 with J-C damage parameters are exclusively used for the entire casing whereas Ti-6Al-4 V (J-C) is selected for blade material. It must be emphasized that material characteristics have immense contribution on structure's ability to resist and absorb loads, so with strength mainly coming from the skins, selected material should showcase desired results. Further, the fan case is isolated from the fan rotor, so zero displacement constraints were applied in the axial direction (Dx) to the node set on the front surface of the casing. Whereas, the rear face nodes were constrained in vertical and horizontal displacements (Dy and Dz) as the coupled response with lugs is not considered in this study to avoid any discrepancy during interactions. The dynamic impact study was performed for a total time of 6 ms after initializing the rotor at an angular velocity of 8100 RPM about its global coordinate's center.

Meshing is prudently addressed to optimize the computational expense by assessing suitable element quality and consequently the solution time. To effectively capture the damage response in this highly non-linear dynamic event, uniform brick
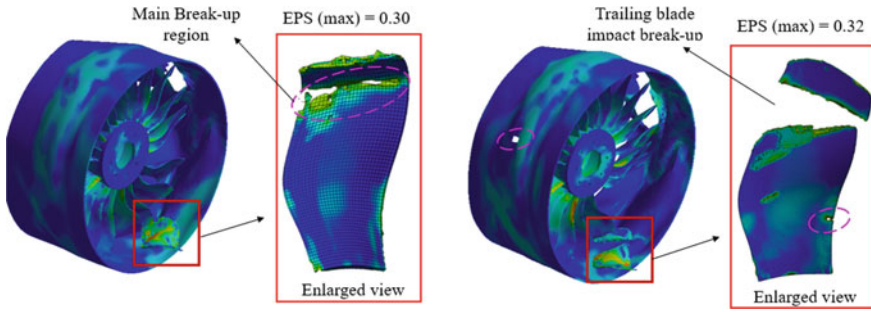
Fig. 6 Effect of element size on blade breakup and case perforation at e: 1.2, 0.4 mm and e: 1, 0.22 mm

modeling (hexahedral elements) with reduced integration is used, as tests with tetra-hedral and tetra-hex mix failed to produce reasonable results. A full rig test including trailing blades with plain hard wall case is conducted to address mesh and convergence sensitivity as shown in Fig. 6. With an element size (e) of 1.2 and 0.4 mm for case and blade that blade fragmentation appears to partially develop but does not fail as desired due to lower aspect quality and no secondary perforation occurs on the case. However, failure at top 1/3 part of blade during interaction with trailing blades is evident on increasing the mesh density at 'e' equivalent to 0.22 mm, and moreover, a small gouge on the case is also recorded as a result of rubbing by blades. Also, a small crack further initiates at around 1/6 part of blade after plastic strain reaches 0.15, and results appear to be in great harmony with the tests performed by FAA [5]. Hence, 'e' of 0.22 and 1 mm for blade and casing having four and one element through thickness are considered enough for this study based on convergence results achieved for plastic strain and velocity, as shown in Fig. 7. Similarly, the values of 0.4 and 1.2 mm were determined for corrugated lattice core and outer hat cover for final tests.

5 Results and Discussion

5.1 Containment Casing Thickness

Containment casing thickness is a significant consideration that determines containment and structural integrity based on blade release speed and mass of the blade. In order to identify suitable case thickness, without changing the internal diameter, shell thicknesses ranging from 0.6 to 2 mm are evaluated under the single blade impact, which can later be used along bi-direction corrugated (LSC). Figure 8 represents the effect of selected thicknesses on containment against internal energy, where points A, B, C determine the uncontained situation and D, E, and F determine the
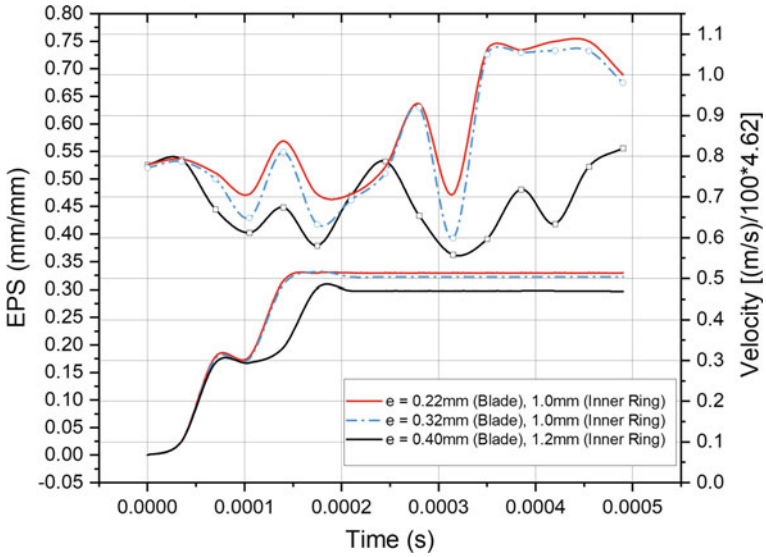
Fig. 7 Solution convergence plot for various mesh values
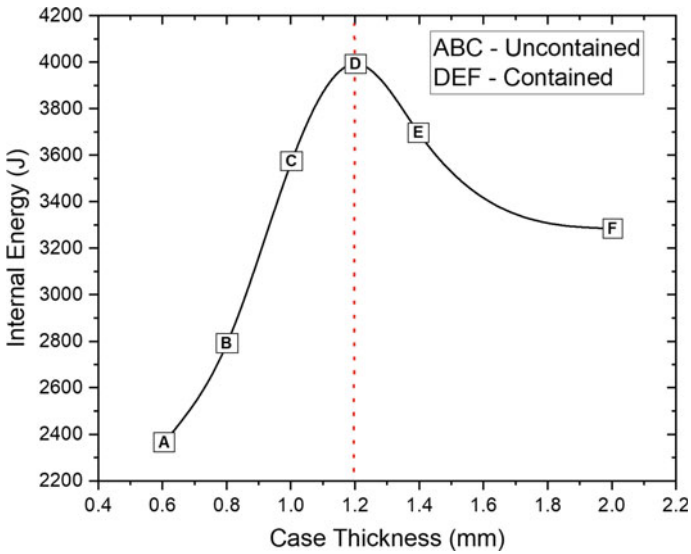
Fig. 8 Energy absorbed by case at different thickness values
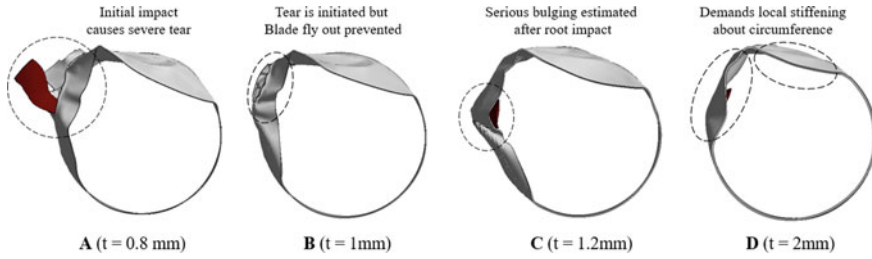
Fig. 9 Effect of inner ring thickness on containment and structural integrity

contained state. The graph's inflection point is evident at location D, having a value of 1.2 mm, which is the critical containment thickness. Figure 9 presents the casing damage and failure for four cases having thickness (t) values of 0.8, 1, 1.2, and 2 mm. As the blade release speed exceeds the case's critical containment speed, the metal ring demonstrates extremely poor stiffness for cases A, B and C. The blade quickly develops a circumferential crack and flies out, which is highly undesirable. Zekan He et al. [12], in their previous work, also emphasized the importance of perfect thickness for a metal ring in a soft wall design, as even when the blade is contained, the fabric loses support if the case is broken. Cases (D, E, and F) seem to showcase better stiffness where the blade is successfully contained, and visible large elastic deformations are noted. So, the trade-off from a design point of view aims to reduce the overall structural weight and the inner metal ring being the primary contributor should be as light as possible. Hence, use of both lightweight material and small wall thickness tend to govern the effectiveness during design phase. For the present study, a casing thickness of 1 mm is selected as it allows us to understand better the performance variation for different lattice configurations toward maintain structural integrity.

5.2 Impact Analysis

Figure 10 shows the blade impact process on casing, and the total time of impact test is about 6 ms. Critical stages during interaction are evaluated, and details are represented at different time histories against all four cases, which were separately performed. For better assessment, the entire process is bifurcated into three typical events: initial perforation, successive tear, and root impact (Fig. 11).

During Event 1, the tip strikes to make its first contact with the case at 0.36 ms and can be circumferentially located at around 15–16.5° from its reference position at 0. After that first puncture on the case is observed at 0.51 ms and is common for cases 1–4. On the contrary, the energy dissipation due to friction induced by the variable contact area of corrugated (LSC) and its stiffness mainly governs the elongation of tear. Event 2 recorded at 2.16 ms up till which severe tear is formed on the inner

Case 1 – General Bi-directional Corrugated Lattice Core sandwiched casing.

t = 0.51 ms   t = 2.16 ms   t = 3.46 ms   t = 6 ms

Case 2 – Refined General Bi-directional Corrugated Lattice Core sandwiched casing.

t = 0.51 ms   t = 2.16 ms   t = 3.46 ms   t = 6 ms

Case 3 – Twill Bi-directional Corrugated Lattice Core sandwiched casing

t = 0.51 ms   t = 2.16 ms   t = 3.46 ms   t = 6 ms

Case 4 – Inverted Twill Bi-directional Corrugated Lattice Core sandwiched casing

t = 0.51 ms   t = 2.16 ms   t = 3.46 ms   t = 6 ms

Fig. 10 Representation of impact sequence at different time intervals for cases 1, 2, 3, and 4

case in the radial direction as the blade glides. In comparison, maximum tear length is observed for Case 1, which extends up to 38°, whereas minimum tear happens in case 4 at 24°. For cases 3 and 4, estimated tear is found to be 30 and 34°, respectively. At the present time interval, perforation is also observed at the outer cover for cases 2 and 4, which is a result of higher stiffness offered by refined general and inverted
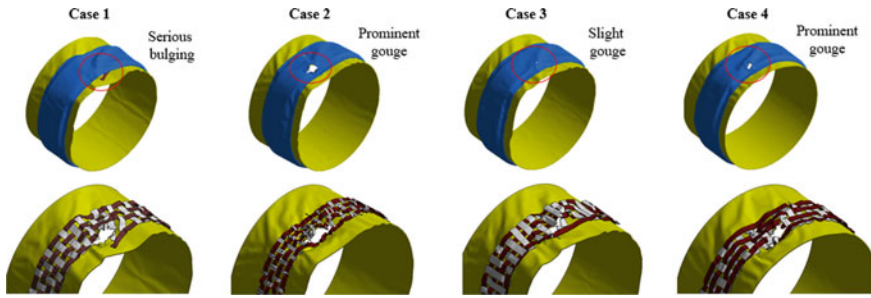
Fig. 11 Perforation and bulging responses for outer cover and lattice core for cases 1–4 at 6 ms

twill corrugation. However, for cases 1 and 3, which uses general and twill type corrugation core, serious bulging and progressive wrinkling due to tension forces can be seen. After losing approximately 60–65% K.E due to the case's resistance, minor blade fragmentation occurs near the tip. Resultant momentum at the bottom of the blade further changes its trajectory leading to subsequent root impact referred to as Event 3.

5.2.1 Effect of Lattice Core and Energy Analysis

The lattice core aims to offer resistance against impact by absorbing blades kinetic energy and maintaining sufficient structural integrity. While the blade shears radially, the lattice core is fragmented, and the case stretches outwards. The casing absorbs approximately 55.5–63% energy till 2.35 ms, and the contribution of the core is found to be 37, 42.5, 37.6, and 44.5% for cases 1–4, respectively, shown in Fig. 12. In the process, the lattice core fragments while the blade makes contact with it during shearing. The remaining stiffness is then responsible for the bulging that occurs on the inner case due to secondary root impact. Local buckling of the lattice is further seen, which leads to deboning at various locations and is found to be minimum for cases 2 and 4. Inverted twill corrugation pattern used in case 4 showcases superior buckling resistance as it makes maximum circumferential contact with the outer cover, whereas transverse cells take most of the impact loads. Also, the blades internal energy accounted for 15.7, 12.8, 17.1, and 11.4% caused due to reaction forces and plastic deformation. Figure 12 also shows the history of contact forces between blade and casing. For cases 1–3, similar behavior of contact forces is realized, where the first peak force equivalent to 3.1, 3.8, and 3.5 kN is recorded at about 0.9 ms when the blade initiates penetration. The second peak follows at 2.3, 2.1, and 2.7 kN during the crack transition at a time interval of 1.46 ms. Contact forces reach the highest peak of 4.5, 4.9, and 4.27 kN at 2.5 ms when the bottom root of the blade impacts and deforms the casing. However, for case 4, only one peak of 3.27 kN is observed, followed by a linear transition until the peak reaches up to 5.29 kN. Hence, the intensity of contact forces is directly proportional to the damage caused to the casing.
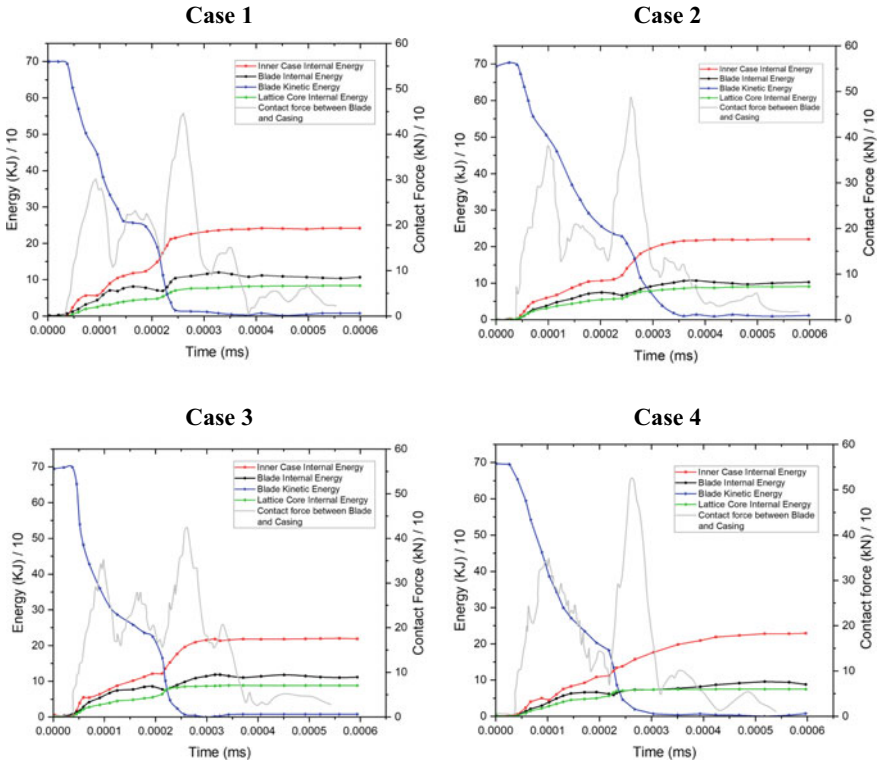
Fig. 12 Energy variation and contact force–time histories between blade and casing

In the present study, bi-directional corrugated LSC in inverted twill fashion demonstrates suitable characteristics of efficient energy absorption and minimum case damage. It seems to have excellent stiffness compared to other lattice types, due to which it is safe to consider it as a promising design solution.

5.2.2 Case Damage Overview

In this paper, damage on fan–case due to blade impact for various models with separate lattice configurations is studied. At a time interval of 5.6 ms, effective plastic strain (EPS) and velocity are compared. Minor plastic deformation is observed at 0.51 ms shortly after the blade first makes contact with the inner case, followed by tremendous damage due to successive events of tearing and root impact at 2.16 and 2.53 ms, respectively. Numerical predictions demonstrate two main damage zones, mainly located at an inner case and outer cover, as shown in Fig. 13. Regions A, B, and C provide detailed insight into the severity of the damage. Although the blade is contained for all configurations, gouge (region A) on the outer cover is

Case 1 – General Bi-directional Corrugated Lattice Core sandwiched casing
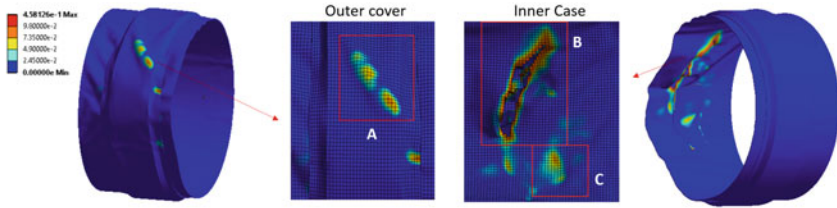
Case 2 – Refined General Bi-directional Corrugated Lattice Core sandwiched casing
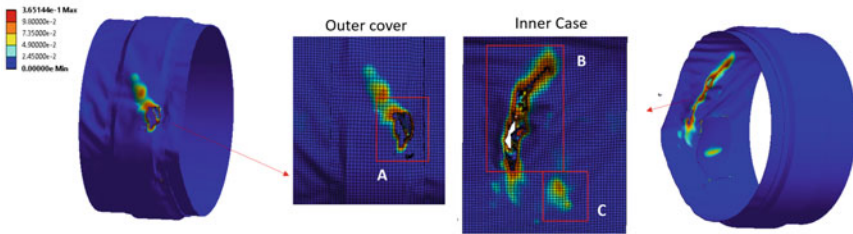
Case 3 – Twill Bi-directional Corrugated Lattice Core sandwiched casing
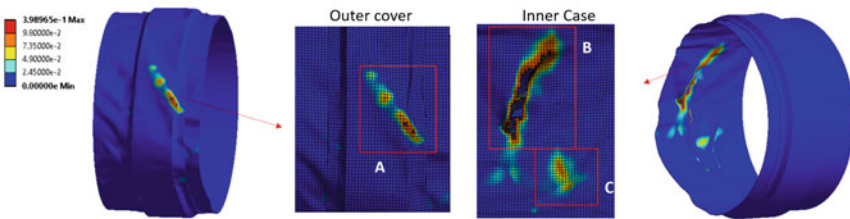
Case 4 – Inverted Twill Bi-directional Corrugated Lattice Core sandwiched casing
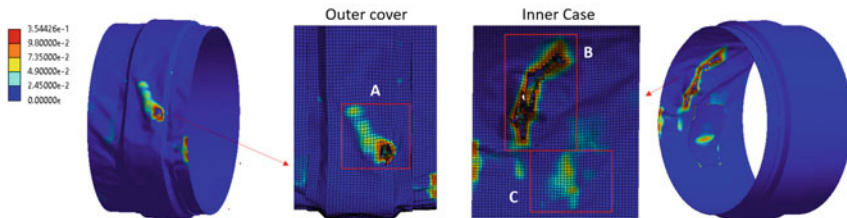
Fig. 13 Damage zones on inner case and outer cover for cases 1–4 at 6 ms
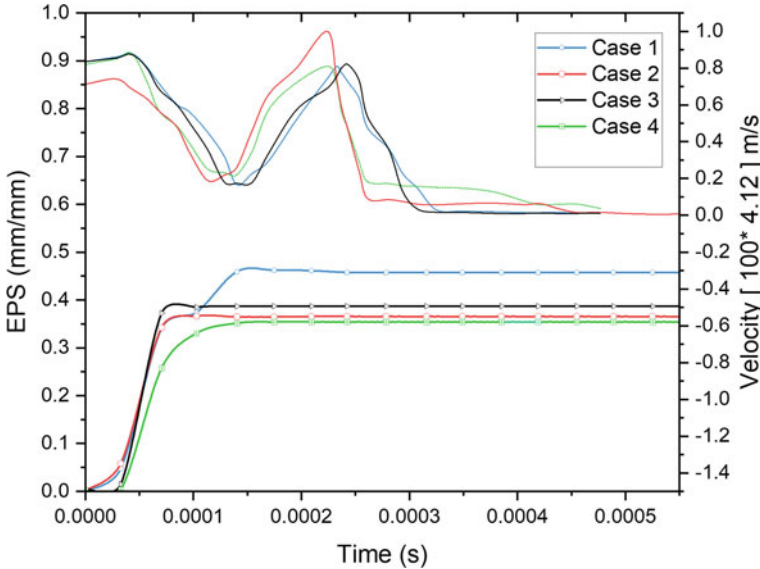
Fig. 14 EPS and velocity estimations for cases 1–4

approximately 87 and 71% larger for cases 2 and 4 than case 3 when calibrated at a similar resolution, whereas nothing is observed for case 1. Region B demonstrates the material loss/element failure due to radial crack and is maximum for case 2. Around the crack's vicinity, a state of biaxial tension bulges the case with significant wrinkling between constraint locations. It is vital to consider the effects of geometrical topology for various corrugated (LSC's) on the sensitivity of radial crack for which crack length is plotted on a scale of 0–0.8, as shown in Fig. 15. Region C is the outcome of plastic dent developed during root impact, which occurs at a minimum yaw angle. Peak resultant strain is estimated for case 3, which can be correlated with blade velocity, reaching a value of 4.17e + 05 mm/s at 2.24 ms, i.e. 10% higher (see Fig. 14). Predicted damage profiles are in great co-relation with existing literature previously carried for bird strikes and full-rig tests [5, 18].

6   Conclusion

In this paper, durability of a hybrid fan–case under a typical blade impact event is evaluated numerically for four cases having different core inserts: general, refined general, twill, and inverted twill bi-directional corrugated lattice. Performance assessment of casing is carried using qualitative comparison of results achieved from explicit finite element study, and some conclusions are presented as follows:
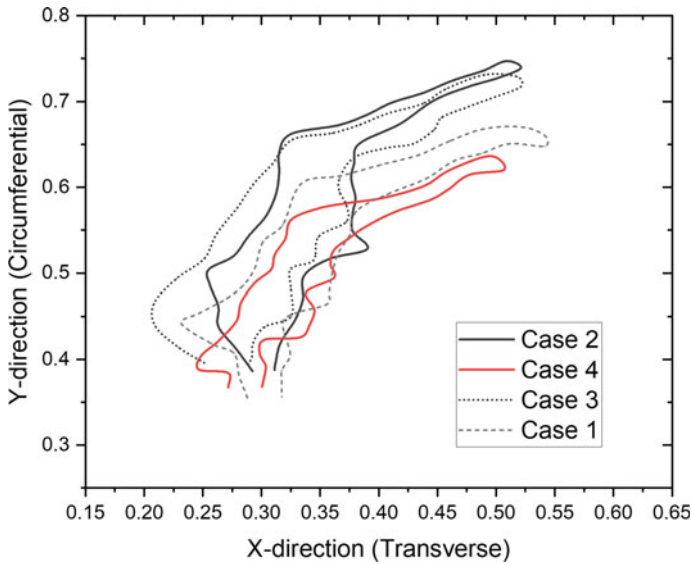
Fig. 15 Crack length for cases 1–4

(1) The stiffness of inner case is a prime consideration from the perspective of structural integrity and thickness value of 1 mm is selected to be optimal based on series of tests carried between ranges of 0.6–2 mm. The overall containment ability largely depends on the geometric topology of the lattice and is better explained by bifurcating the impact process in an orderly sequence of events defined as Initial perforation, successive tear and root impact. During the events, a radial tear of 38, 30, 34, and 24° is predicted for cases 1–4, which happens during shearing resulting in 37–44.5% of total blade energy. While the lattice fractures locally, severe buckling and deboning at various locations are predominating for cases 1 and 2, followed by case 3. On the contrary, case 4 represents superior resistance with minimum damage in the vicinity of impact without deboning anywhere. Further, the root impact takes place and based on different yaw angles caused during a shift of trajectory, the magnitude of contact force between blade and case determines the bulge depth. Surprisingly, with forces reaching a highest of 5.29 kN for case 4, least outward deformation is observed compared to other cases. Ability of Inverted twill is more superior compared to other cases from energy and force analysis as internal energy linearly increases with no signs of secondary spike for contact forces. Moreover, it is clearer from the bulge's size, which is approximately 48% smaller than other cases. Hence, case 4 showcases encouraging energy-absorbing characteristics along with maintaining structural integrity.

(2) Damage at three locations categorized into A, B, and C zones are investigated separately to understand the correlation between crack length and root impact. It is evident that the casing tear is governed by the interferential strength of

lattice case contact. However, outcome in case 4 is least damaged with a plastic strain of 0.35. Impact is effectively propagated via lattice toward outer cover where the surface contact is maximum and is punctured. Even with the smallest crack length and maximum root impact force, damage is within controlled limits, which is only possible as the lattice neither buckles nor loses the contact circumferentially. It is concluded that the inverted twill bi-directional corrugation is the safest choice of core configuration for hybrid casing under an allowed damage limitation of 1/7.5 times the case diameter.

References

1. Sinha SK, Dorbala S (2009) Dynamic loads in the fan containment structure of a turbofan engine. J Aerosp Eng 22(3):260–269
2. He Q, Xie Z, Xuan H, Liu L, Hong W (2016) Multi-blade effects on aero-engine blade containment. Aerosp Sci Technol 49:101–111
3. Murakami T, Morita H, Oikawa K (2013) Development of composite fan system. J IHI Technol 53(4):63–67
4. Stahlecker Z, Mobasher B, Rajan SD, Pereira JM (2009) Development of reliable modeling methodologies for engine fan blade out containment analysis. Part II: finite element analysis. Int J Impact Eng 36(3):447–459
5. Model, Full-Fan Rig (2015) Development of a generic gas turbine engine fan blade-out
6. Sarkar S, Atluri SN (1996) Effects of multiple blade interaction on the containment of blade fragments during a rotor failure. Finite Elem Anal Des 23(2–4):211–223
7. Xuan H, Hu Y, Wu Y, He Z (2018) Containment ability of Kevlar 49 composite case under spinning impact. J Aerosp Eng 31(2):04017096
8. Yu P, Zhang D, Ma Y, Hong J (2018) Dynamic modeling and vibration characteristics analysis of the aero-engine dual-rotor system with fan blade out. Mech Syst Signal Process 106:158–175
9. Sarkar S, Atluri SN (1996) Effects of multiple blade interaction on the containment of blade fragments during a rotor failure. Finite Elem Anal Des 23(2–4):211–223. https://doi.org/10.1016/S0168-874X(96)80008-4
10. Dayyani I, Shaw AD, Saavedra Flores EI, Friswell MI (2015) The mechanics of composite corrugated structures: A review with applications in morphing aircraft. Compos Struct 133:358–380. https://doi.org/10.1016/j.compstruct.2015.07.099
11. Semenyuk NP, Neskhodovskaya NA (2002) On design models in stability problems for corrugated cylindrical shells. Int Appl Mech 38(10):1245–1252
12. He Z, Xuan H, Bai C, Song M, Zhu Z (2019) Containment of soft wall casing wrapped with Kevlar fabric. Chin J Aeronaut 32(4):954–966. https://doi.org/10.1016/j.cja.2019.01.008
13. Li Z, Chen W, Hao H (2018) Numerical study of sandwich panel with a new bi-directional Load-Self-Cancelling (LSC) core under blast loading. Thin-Walled Struct 127:90–101. https://doi.org/10.1016/j.tws.2018.02.003
14. Norman AD, Seffen KA, Guest SD (2009) Morphing of curved corrugated shells. Int J Solids Struct 46(7–8):1624–1633. https://doi.org/10.1016/j.ijsolstr.2008.12.009
15. Li W, Sun F, Wang P, Fan H, Fang D (2016) A novel carbon fiber reinforced lattice truss sandwich cylinder: fabrication and experiments. Compos Part A: Appl Sci Manuf 81:313–322
16. Yang CC, Ngo T, Tran P (2015) Influences of weaving architectures on the impact resistance of multi-layer fabrics. Mater Des 85:282–295
17. Carney KS, Pereira JM, Revilock DM, Matheny P (2009) Jet engine fan blade containment using an alternate geometry. Int J Impact Eng 36(5):720–728

18. Hou N, Li Y, Liu J (2019) Numerical simulation of bird impact on hollow blades of titanium fan assembly. J Aerosp Eng 32(4):04019044

Molecular Dynamics Simulations of Dislocation Nucleation from a Pristine and Damaged Grain Boundary in Nickel and Quantification of Associated Activation Energy Parameters

S. Chandra, M. K. Samal, and V. M. Chavan

Abstract Grain boundaries are important microstructural features in polycrystalline materials that impact their deformation and failure behavior at the macroscopic scale. Thus, we perform atomistic simulations at the nanoscale along with nudged elastic band calculations to quantify activation parameters for dislocation nucleation from a grain boundary. Since $\sum 3$ grain boundaries are most common in polycrystalline metals and alloys of face-cantered cubic structure, we choose $\sum 3$ twin boundary in bicrystal Ni as a model system for this purpose. We also introduce a pre-existing defect (a void) at the grain boundary and contrast the activation parameters for partial dislocation nucleation from pristine as well as damaged grain boundary in the material. We find that the activation energy as well as kinetic parameters for dislocation nucleation are different for pristine and damaged grain boundary. This highlights a change in the underlying kinetics of the deformation process when a damaged grain boundary is present in the material. Consequently, this approach can be generalized to determine kinetic parameters for other thermally activated grain boundary-dominated deformation or failure processes in metallic polycrystals like grain boundary sliding at a higher temperature, intergranular crack growth, etc. It can, therefore, provide direct numerical inputs to the flow rules of phenomenological crystal plasticity-based finite element models that explicitly take into account the grain boundary effects on plasticity and damage behavior of the material at the continuum scale.

Keywords Molecular dynamics · Plasticity · Grain boundary · Damage

S. Chandra (✉)
Homi Bhabha National Institute, Mumbai 400 084, India
e-mail: sagarc@barc.gov.in

M. K. Samal
Reactor Safety Division, Bhabha Atomic Research Centre, Mumbai 400 085, India

V. M. Chavan
Refueling Technology Division, Bhabha Atomic Research Centre, Mumbai 400 085, India

1   Introduction

Increasing global demand for safer, energy-efficient and safety applications requires the development of new polycrystalline aggregates with tuned interface structures. Since grain boundaries (GBs) are the dominant microstructural features in governing the deformation and failure behavior of polycrystalline materials, a nanoscale understanding of the structure-property relationship is indispensable. This fact has motivated ever-lasting efforts geared toward unraveling the underlying GB physics, which has shown that both the macroscopic degrees of freedom and microscopic local structure affect the physical properties of GBs and hence the constituent mechanical behavior of the material [1, 2].

The macroscopic behavior of polycrystalline materials is also influenced by the presence of defects at GBs, which cause a local variation in the properties [3, 4]. For such explorations, atomistic simulation methods are widely used to study the local GB structures and processes, which may or may not be thermally activated [4]. Thermally activated GB processes like dislocation nucleation are one of the basic deformation mechanisms in crystalline materials [4]. This has motivated previous studies to quantify the kinetic parameters for dislocation nucleation from GB [2] using atomistic techniques like nudged elastic band (NEB) method [3]. The quantified activation parameters can also serve as input to the flow rules of crystal plasticity (CP)-based finite element models at the mesoscale [4].

Thus far, these kinetic activation parameters for plasticity evolution from a GB have been quantified for perfect GBs (without considering any GB defect) [1, 2]. However, it is well known that the presence of volumetric defects like voids at GBs can influence the dislocation nucleation and consequent deformation behavior of metals [5]. This urges us to quantify the activation parameters for nucleation of partial dislocations from a GB containing a void using molecular dynamics (MD) and NEB calculations. This information is crucial for predicting the flow behavior of crystalline materials at much higher length scales, like CP.

2   Computational Methodology

LAMMPS (Large-scale Atomic/Molecular Massively Parallel Simulator) [6] code is used to perform molecular dynamics (MD) simulations using the Foiles et al. [7] embedded-atom method potential for Ni. The simulation cell consists of two crystals of Ni oriented to form a $\sum 3$ coherent twin boundary. The bottom grain (Fig. 1) has its x-, y- and z-axis along $[1\bar{1}0]$, $[\bar{1}\bar{1}1]$ and $[\bar{1}\bar{1}\bar{2}]$ directions, respectively. To create the $\sum 3$ interface, the top grain is rotated by 60^0 about y-axis. It may be noted that the frequent observation of this particular interface in polycrystals is the reason behind its investigation in this work [8]. Periodic boundary conditions are applied along the orthogonal directions. The GB energy obtained after static minimization is 78.42 mJ/m^2, which is consistent with previous studies [5].

Fig. 1 Ni bicrystal containing a voided $\sum 3$ GB at the center. Only atoms in non-centrosymmetric (as per color-bar) (defective) environment are shown and perfect face-centered cubic atoms are removed for clarity
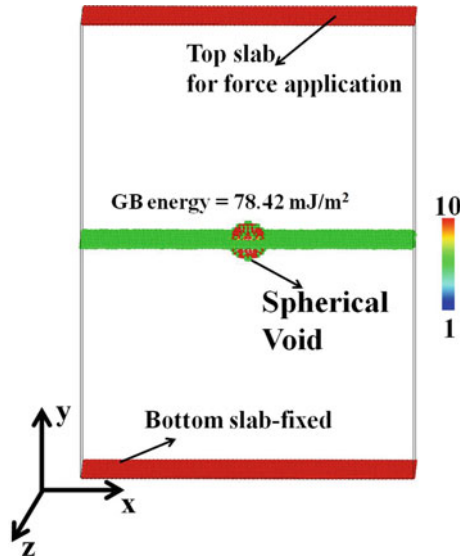
After relaxation, a spherical void of radius equal to 2.86 nm and 3.60 nm is inserted at the GB (Fig. 1). This corresponds, respectively, to an overall void volume fraction (vvf) of 0.35% and 0.70%. To counter the size effects that may arise, simulation cell dimensions are kept equal to 34.85 nm, 51.82 nm and 15.52 nm along x-, y- and z-axis. This results in $\cong 2,500,000$ atoms in the simulation domain.

After equilibrating the system at the temperature of 300 K using the micro-canonical NVE ensemble for 50,000 timesteps, uniaxial tension is applied along the y-axis perpendicular to the interface. During loading, the bottom slab of atoms is constrained to move and the top slab is given a uniform positive displacement (0.05% per load step) along y-direction to simulate tensile loading. During loading, dynamic equilibration is performed using the NVE (N- No. of atoms, V- system Volume, E- system Energy) ensemble for another 2000 steps so that force equilibrium between the slabs is achieved. The timestep used is 1.0 femtoseconds, as is customary in such MD simulations.

Following the standard procedure given in Ref. [2], NEB calculations are then performed. Several states are taken from the deformation trajectory at set stresses to form initial states for NEB computations. Similarly, several atomic configurations are extracted once the dislocation is nucleated from GB to give final configurations for use in NEB calculations. The defected configurations (with dislocation nucleation from GB) are rescaled to match the initial state bicrystals. After this, energy minimization at a tolerance of 10^{-6} eV using the conjugate-gradient method is performed. Subsequently, the systems are quenched slowly to 0 K under the NVE ensemble by enabling the atomic velocities to zero. After that, the system is again relaxed using the fast inertial relaxation engine (FIRE) [9] algorithm and by using the same energy tolerance. A total of 28 replicas are employed for NEB simulations.

It may be noted that the minimum energy path (MEP) for any thermally activated process may have one or more minimas (intermediate stable configurations) and maximas (saddle points). This MEP is then used to quantify the activation energy for the process, which is determined by the highest maxima (saddle point). In order to have a good enough shape of the MEP, it is desirable to have at least 4–20 replicas of the system being examined. In our work, 28 replicas were found to be sufficient to adequately represent the MEP. In addition, the convergence criteria were the energy tolerance of 10^{-6} eV, which provided a converged energy solution while also balancing the computational cost. Performing NEB calculations using an energy tolerance of 10^{-9} eV resulted in the difference of only 0.6% in the energy barrier but required more than 200% longer simulation time. Therefore, the parameters for NEB are chosen based on the balance between computational cost and the accuracy of desired results.

3   Results and Discussion

During loading, an initial straight stress-strain curve (elastic regime) appears followed by a sudden drop in stress, which implies dislocation nucleation. Such observations are common in MD simulations of crystalline materials containing GBs [5]. The activation energy for the process is ΔG, which can be written as [4]:

$$\Delta G = \Delta F \left[1 - \left(\frac{\sigma}{\sigma_0} \right)^p \right]^q \tag{1}$$

where ΔF is the kinetic activation energy required to nucleate the partial dislocation from GB in the absence of applied stress (σ) and σ_0 is the critical athermal stress above which the dislocation nucleation event switches to a pure mechanical process from a thermally activated process; p and q are profiling exponents. It should be noted that the aforementioned equation is common in materials science to rationalize various thermally activated processes occurring in crystalline materials [2]. A representative minimum energy path is displayed in Fig. 2 and the results of NEB calculations are presented in Fig. 3 for the perfect as well as damaged GB in Ni. The data points are simulation results and solid lines in Fig. 3 are fit to the aforementioned equation. During fitting, the dimensionless parameters p and q are varied to obtain the best possible fit to the data. It can be seen that kinetic activation parameters are sensitive to the nature of GB (whether the boundary is perfect or contains some defect). The figure also depicts that for the same magnitude of thermal activation energy, less mechanical work is required if the GB contains a defect. This implies that at any given value of activation energy (say, 40 eV), more amount of mechanical work in the form of applied stress (x-axis) is required for pristine GB in comparison to damaged GB. Moreover, an increase in amount of defects at the GB (here, void volume fraction) further decreases the amount of mechanical stress required to activate the thermally activated phenomena (here, dislocation nucleation) (Fig. 3).
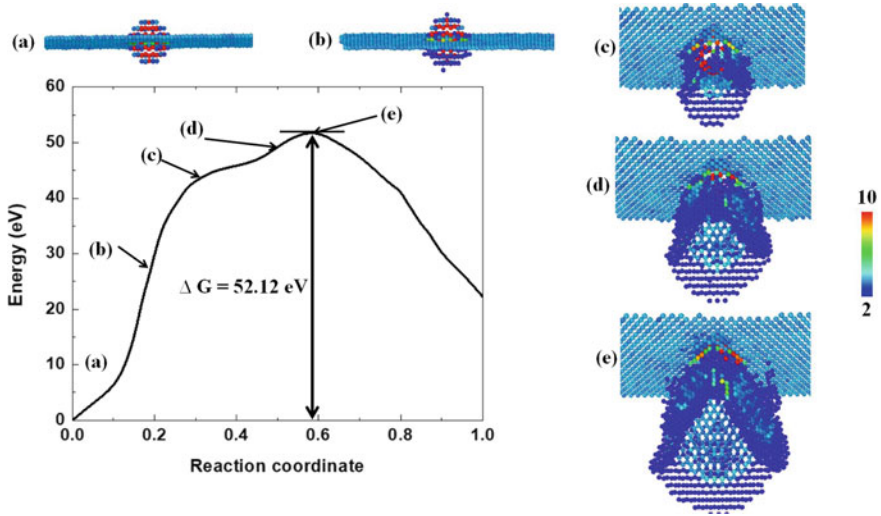
Fig. 2 A representative minimum energy path (3.0 GPa stress) of partial dislocation nucleation from voided GB in Ni. Atoms in atomic configurations are colored according to their centrosymmetric parameter

Fig. 3 Results of NEB calculation showing activation energy as a function of applied stress in Ni bicrystal containing perfect and damaged (0.35% and 0.7%) $\sum 3$ boundary. Points are simulation results and solid lines are fit to the data as mentioned in the text
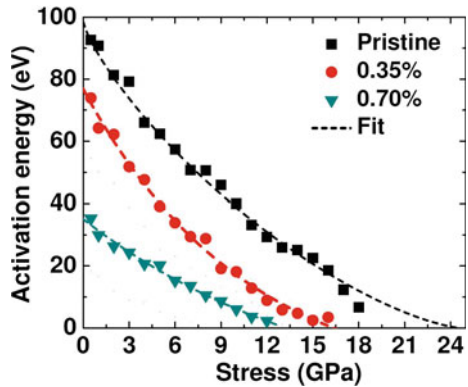
Another observation that is worth noting is that the profiling parameters p and q are different for perfect ($p = 0.798$ and $q = 1.397$) and damaged GB ($p = 0.962$ and $q = 1.715$) (Table 1) and that these parameters remain unchanged with increase in overall vvf. This clearly highlights a change in the deformation kinetics of partial dislocation nucleation under uniaxial loading when a defect (void here) is present at a GB in comparison to a perfect interface.

The activation energy at zero stress, ΔF, is an important parameter that directly goes in CP simulations at higher length scales. This parameter can be extracted by extrapolating the $\Delta G - \sigma$ curve and obtaining the intercept on the y-axis (Fig. 3). As

Table 1 Activation metrics for pristine and damaged GB obtained in this study

vvf (%)	Radius, r (nm)	ΔF (eV)	σ_0 (GPa)	p	q
0	0	98.38	24.63	0.798	1.397
0.35	2.86	76.18	17.02	0.962	1.715
0.70	3.60	36.30	14.17	0.962	1.715

can be seen, ΔF is also sensitive to the change in defect content at the GB. This can cause appreciable deviations in the predicted response using CP simulations from the laboratory experiments if the wrong value of ΔF is employed in such calculations.

4　Conclusions

The activation parameters for dislocation nucleation from the $\sum 3$ grain boundary in Ni are quantified using lower length scale atomistic simulations and NEB calculations. The activation energy as well as dimensionless profiling parameters are quite distinct for pristine as well as damaged GB. To the belief of authors, these findings can benefit the materials community by serving as direct input to CP-based finite element models at the mesoscale.

References

1. Burbery NJ, Das R, Ferguson WG (2016) Transitional grain boundary structures and the influence on thermal, mechanical and energy properties from molecular dynamics simulations. Acta Mater 108:355–366
2. McPhie MG, Berbenni S, Cherkaoui M (2012) Comput Mater Sci 62:169–174
3. Henkelman G, Uberuaga BP, Jnsson H (2000) A climbing image nudged elastic band method for finding saddle points and minimum energy paths. J Chem Phys 113:9901–9904
4. Kocks UF, Argon AS, Ashby MF (1975) Thermodynamics and kinetics of slip. Prog Mater Sci 19:1–281
5. Chandra S, Samal MK, Chavan VM (2019) Dislocation nucleation from damaged grain boundaries in face centered cubic metals—an atomistic study. Materialia 8:100497
6. Plimpton S (1995) Fast parallel algorithms for short-range molecular dynamics. J Comput Phys 117:1–19
7. Foiles SM, Hoyt JJ (2006) Computation of grain boundary stiffness and mobility from boundary fluctuations. Acta Mater 54:3351–3357
8. Saylor DM, Dasher BSE, Rollett AD, Rohrer GS (2004) Distribution of gain boundaries in aluminium as a function of five macroscopic parameters. Acta Mater 52:3649–3655
9. Bitzek E, Koskinen P, Franz G, Moseler M, Gumbsch P (2006) Structural relaxation made simple. Phys Rev Lett 97:170201

Viscoplastic Constitutive Parameters for Inconel Alloy-625 at 843 K

S. C. S. P. Kumar Krovvidi, Sunil Goyal, J. Veerababu, A. Nagesha, and A. K. Bhaduri

Abstract Inconel alloy-625 is one of the candidate materials for high-temperature bellows in sodium-cooled fast reactor (SFR) systems. Typical temperature in SFR systems is around 843 K at which failure modes such as creep and creep–fatigue interaction are significant. Viscoplastic analysis gives the combined strains due to fatigue including stress relaxation during hold time. This paper presents the estimation and validation of the parameters of Inconel alloy-625 for Chaboche and Rousselier viscoplastic constitutive model at 843 K. A set of low cycle fatigue and creep–fatigue interaction tests were carried out. The parameters defining the isotropic and kinematic hardening of the material were estimated from the LCF tests. The viscous parameters were estimated from the stress relaxation data obtained from the CFI tests. Validation of the parameters of the viscoplastic constitutive parameters was carried out by successfully predicting the hysteresis loops, and the stress relaxation behavior exhibited by the alloy.

Keywords Inconel alloy-625 · SFR systems · Viscoplastic · Isotropic hardening · Kinematic hardening · Finite element analysis

Abbreviations

E	Young's modulus
υ	Poisson's ratio
f	Yield function
σ'	Deviatoric stress tensor

S. C. S. P. K. Krovvidi (✉) · J. Veerababu · A. Nagesha · A. K. Bhaduri
Indira Gandhi Centre for Atomic Research, Kalpakkam 603102, India
e-mail: krovvidi@igcar.gov.in

S. C. S. P. K. Krovvidi · A. K. Bhaduri
Homi Bhabha National Institute, Kalpakkam 603102, India

S. Goyal
Nuclear Fuel Complex, Kota Project, Rawatbhata 323003, India

x'	Deviatoric back stress tensor
r	Isotropic drag stress tensor
σ_y	Yield stress tensor
ε_p	Plastic strain
$\dot{\varepsilon}_p$:	Plastic strain rate
p	Cumulative or equivalent plastic strain
C & γ	Kinematic hardening parameters of the Chaboche and Rousselier viscoplastic constitutive model
Q & B	Isotropic hardening parameters of the Chaboche and Rousselier viscoplastic constitutive model
C_1 & n	Viscous parameters of the Chaboche and Rousselier viscoplastic constitutive model

1 Introduction

Inconel alloy-625 is one of the candidate materials for high-temperature applications in sodium-cooled fast reactor (SFR) systems due to its superior mechanical properties and excellent corrosion resistance. Typical application of Inconel alloy-625 in SFR systems includes its use as bellows [1] in bellow-sealed sodium valves. Typical operating temperature in SFR systems ranges from 823 K to 843 K wherein the failure modes such as fatigue, creep and creep–fatigue interaction (CFI) are significant [2]. High temperature design of SFR components for cyclic loading requires estimation of the total inelastic strain (elasto-plastic and creep strains). Viscoplastic analysis is one of the unified approaches in which the total inelastic strains due to both time-dependent and the time-independent strains (including the effect of stress relaxation) [3, 4] are estimated. This paper discusses the generation and validation of the viscoplastic constitutive parameters for Inconel alloy-625 at 843 K, which will be used for the inelastic analysis of SFR components subjected to cyclic loading.

Methodology and estimation of the Chaboche and Rousselier viscoplastic constitutive parameters for nickel-based superalloys at 923 K were discussed by Tong et al. [5]. The parameters defining the isotropic hardening and kinematic hardening were estimated from a set of low cycle fatigue (LCF) tests, and the viscous parameters were estimated by creep–fatigue interaction (CFI) tests. Veerababu et al. [6] presented the estimation of the material constants of Modified 9Cr-1Mo steel at 823 K [6] in which two back stress components were considered while modeling the kinematic hardening of the material. Estimation of the material parameters of the unified viscoplastic constitutive model for SS316 based on a series of LCF and CFI experiments at 873 K was presented by Gong et al. [7]. This paper presents the generation and validation of the material parameters defining the Chaboche- Rousselier unified viscoplastic constitutive model [3] for Inconel alloy-625 at 843 K. The data generated in this investigation can be used for creep–fatigue design of Inconel-625 components operating at 570 °C.

2 Experimental

The chemical composition of Inconel alloy-625 material was measured using optical emission spectroscopy. For carbon content measurement, wet chemical analysis was carried out. The material, which was obtained in the form of 16 mm thick plate, was annealed as per ASTM B443 [8] that involved heating the material to a temperature of 1223 K followed by air quenching. Metallography specimens were extracted from the material and polished up to 1 micron diamond finish followed by swab etching in Glyceregia. Specimens with a gauge length of 15 mm and a gauge diameter of 6 mm (Fig. 1) were machined from the annealed plate, as per the standard, ASTM E606/606 M [9]. A series of LCF and CFI tests were carried out at various total strain amplitudes in the range, ±0.25–±0.8% at a fixed temperature of 843 K on a 100 kN DARTEC servo-hydraulic fatigue testing machine, equipped with a resistance heating furnace (Fig. 2). A peak tensile hold time of 1 min was used for the CFI
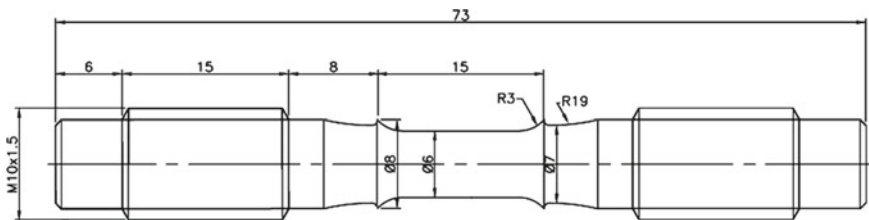
Fig. 1 Geometry of LCF and CFI test specimen (dimensions in mm)

Fig. 2 Servo-hydraulic fatigue testing machine
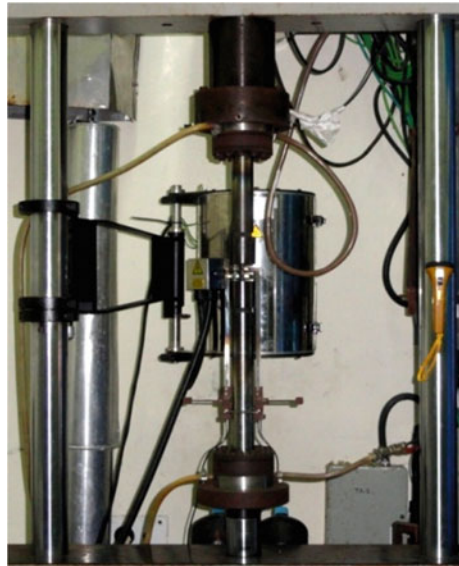
testing for ±0.4% and ±0.6% strain amplitudes. The data on stress relaxation were generated by carrying out CFI tests till stable hysteresis loops are obtained, at the strain amplitudes of ±0.4% and ±0.6%.

3   Results

The chemical composition of the material (weight %) is given in Table 1. The chemical composition of the material was found to be conforming to ASTM B443 [8]. The material reveals a polycrystalline structure as shown in Fig. 3.

The cyclic stress response, strain–life relationships and cyclic stress–strain curve obtained on the material were presented by Krovvidi et al. [10]. The fatigue lives exhibited by the alloy as a function of strain amplitude are given in Table 2. The hysteresis loops corresponding to the first cycle and half-life cycles are presented in Fig. 4. The stable hysteresis loops with stress relaxation resulted under the CFI tests at the strain amplitudes of ±0.4% and ±0.6% are given in Figs. 5 and 6, respectively.

Table 1 Nominal and measured chemical composition of Inconel alloy-625, wt. %

Element	Ni	Cr	Mo	Si	Fe	Nb + Ta	Al	Ti	Co	C	Mn
Nominal value	> 58	20–23	8–10	<0.5	<5	3.1–4.2	<0.4	<0.4	<1	<0.1	<0.5
Measured value	60.5	21.3	9.29	0.4	3.98	3.2	0.14	0.24	0.1	0.04	0.2

Fig. 3 The prior microstructure of Inconel alloy-625
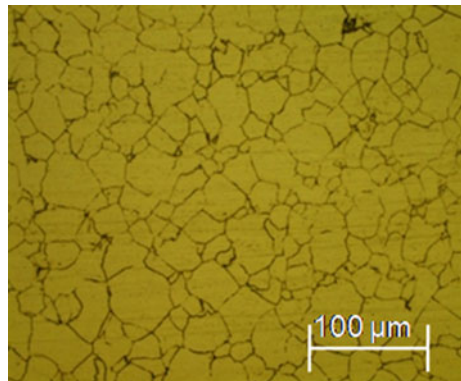
Table 2 Variation of fatigue life with strain amplitude

Total strain amplitude, %	±0.25	±0.4	±0.5	±0.6	±0.7	±0.8
Fatigue life at 843 K	41,712	7511	2449	923	725	322
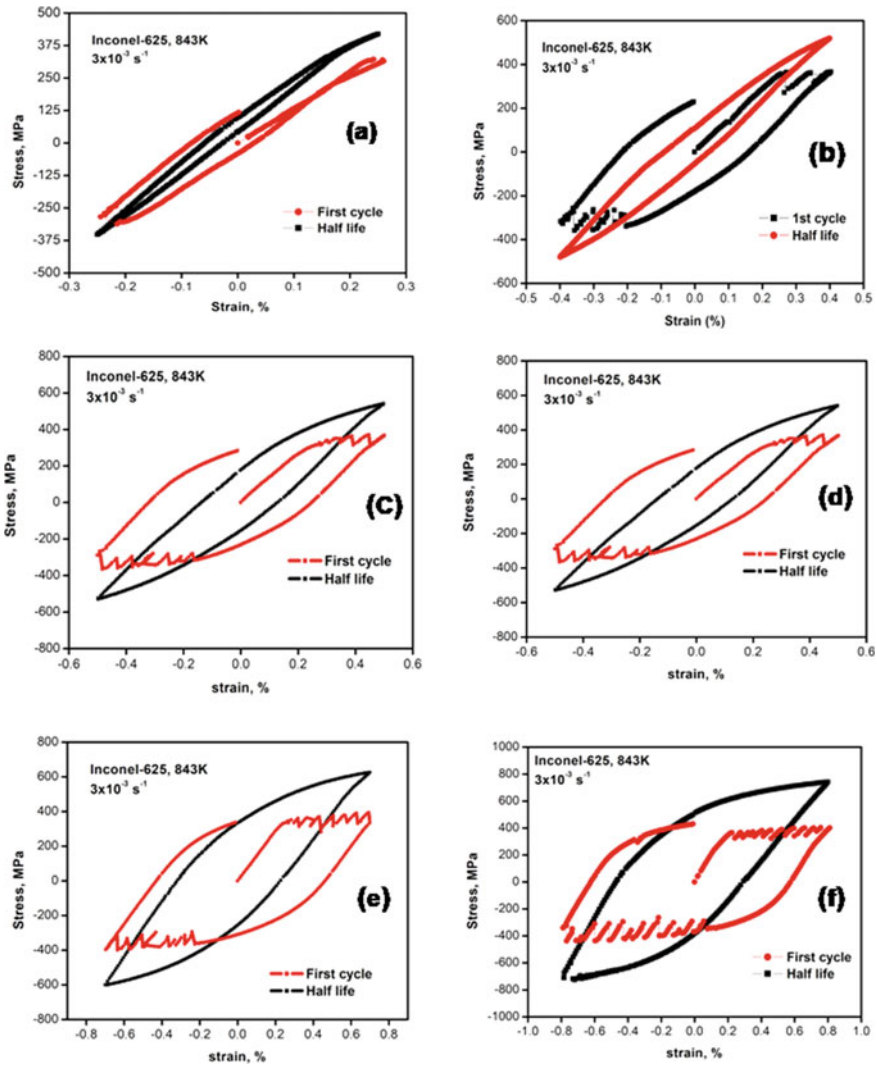
Fig. 4 Hysteresis loops obtained at the strain amplitudes of **a** ±0.25%, **b** ±0.4%, **c** ±0.5%, **d** ±0.6%, **e** ± 0.7% and **f** ±0.8%

CFI tests were discontinued after obtaining the stable hysteresis loops (after 3500 and 450 cycles at ±0.4% and ±0.6% strain amplitudes, respectively). From the hysteresis loops (Fig. 4a–f)), the increase in the peak stress and the reduction in the width of the hysteresis loops indicate that the material is cyclically hardening. Krovvidi et al. [14] also reported that the material was cyclically hardening. The stress relaxation at ±0.4% and ±0.6% strain amplitudes is 7 MPa and 8 MPa, respectively. The material showed less stress relaxation compared to other materials used in FBR
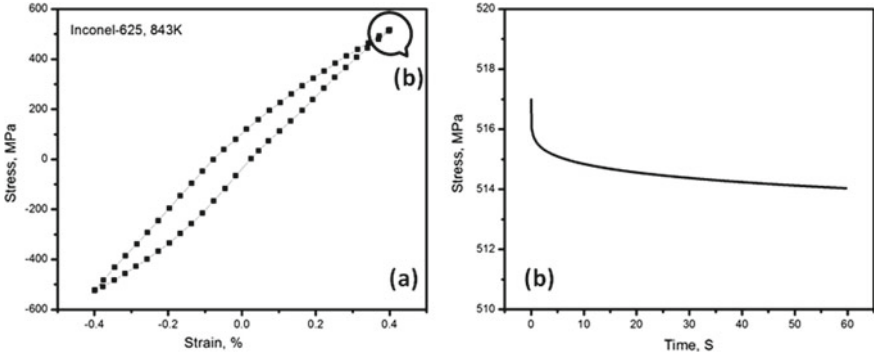
Fig. 5 Stable hysteresis loop and stress relaxation observed in 1 min hold time during CFI testing at the strain amplitude of ±0.4%
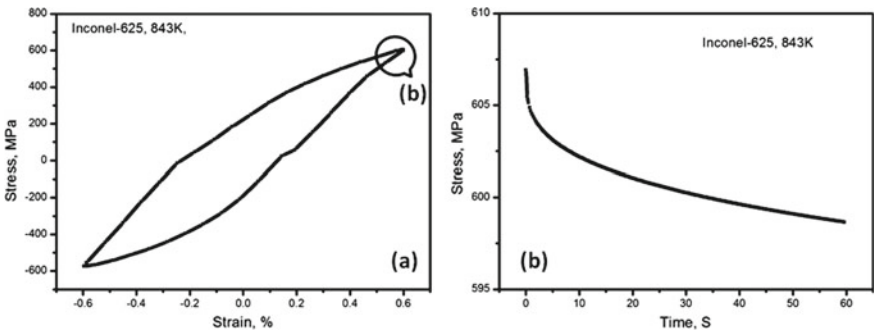
Fig. 6 Stable hysteresis loop and stress relaxation observed in 1 min hold time during CFI testing at the strain amplitude of ±0.6%

systems such as austenitic stainless steels [11, 12] and modified 9Cr-1Mo [6] and other nickel-based super alloys such as Alloy 617 M [13] in this temperature range.

4 Viscoplastic Constitutive Model

Chaboche and Rousselier viscoplastic constitutive model was considered in this analysis.

The constitutive model is represented mathematically with the von-Mises yield function, isotropic and kinematic hardening functions. The von-Mises yield function (f), which gives the behavior of the material under elasto-plastic deformation, can be defined as:

$$f = \left(\frac{3}{2}(\sigma' - x') : (\sigma' - x') \right)^{1/2} - r - \sigma_y = 0 \qquad (1)$$

where σ', x', r and σ_y are the deviatoric stress tensor, deviatoric back stress tensor, isotropic hardening function and yield stress of the material respectively [3, 4].

In case of nonlinear kinematic hardening, the back stress is defined by the following equation:

$$\dot{x} = \frac{2}{3}c\dot{\varepsilon}^p - \gamma x \dot{p} \qquad (2)$$

where, $\dot{x}$ is the rate of change of back stress, $\dot{\varepsilon}^p$ and $\dot{p}$ are the plastic strain rate and accumulated plastic strain rate. C and γ are the constants defining the kinematic hardening material.

The isotropic hardening function is defined by the equation:

$$\dot{r} = B(Q - r)\dot{p} \qquad (3)$$

Here, B and Q are material constants, which give an exponential shape to the stress–strain response leading to saturation with increasing plastic strain. The nonlinear isotropic kinematic hardening model given in ABAQUS uses the material constants C, γ, B and Q. The constants are computed from the experimental LCF data for the strain amplitude of $\pm 0.4\%$. From the hysteresis loop of the first cycle during the LCF testing at $\pm 0.4\%$, the back stress value was found to be 218 MPa (Fig. 7). The accumulation of the plastic strain (ε_p) with the number of cycles (N) was estimated as:

Fig. 7 Estimation of back stress from hysteresis loop of first cycle
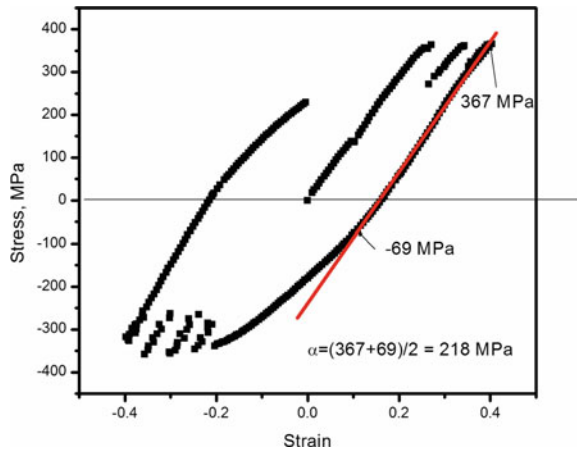
$$p = \frac{1}{2}(4N - 3)\varepsilon_p \tag{4}$$

The variation of the isotropic hardening parameter (defined as the difference between the peak tensile stress and the back stress) with the accumulated plastic strain was plotted as shown in Fig. 8. From curve fitting, the parameters B and Q were found to be 61.9 MPa and 0.78, respectively.

The kinematic hardening constants were estimated by plotting the variation of the back stress with the plastic strain during the first 1/4th cycle of the LCF loading, as shown in Fig. 9. From curve fitting, the parameters C and γ were found to be 76,689.6 MPa and 450.4, respectively.

The time-dependent creep deformation was also considered in this unified model by estimating the viscoplastic strain. According to this model, the rate dependency

Fig. 8 The variation of the isotropic hardening parameter with equivalent plastic strain
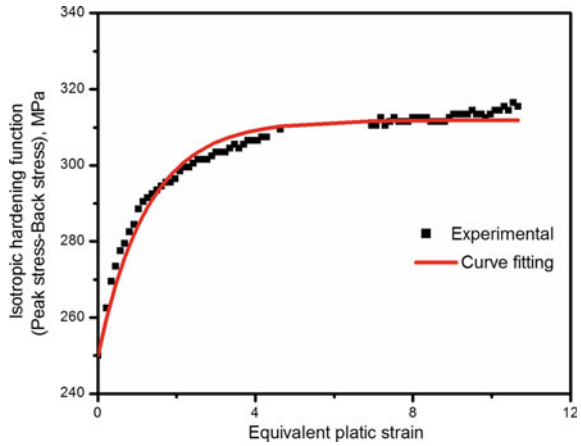
Fig. 9 Variation of back stress with plastic strain
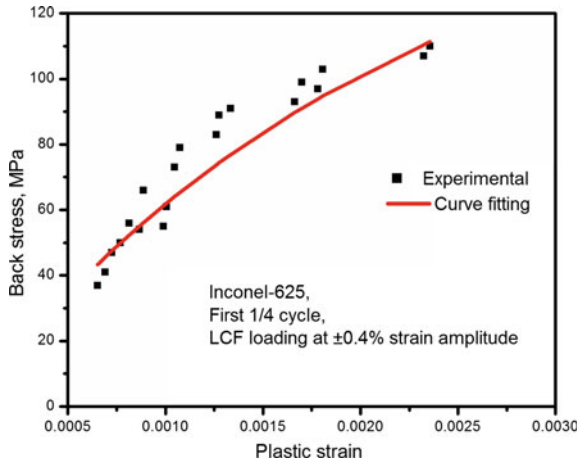
Fig. 10 Variation of the viscous stress with strain rate
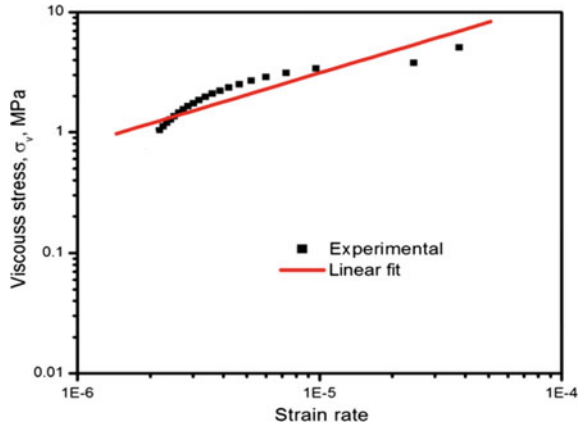
of viscous stress σ_v can be defined by the power law as:

$$\sigma_v = Z_1 \dot{p}^{1/n} \tag{5}$$

where, Z_1 and n are constants defining the stress relaxation during hold time. The parameter n controls the initial stress relaxation rate. Increase in n and decrease in Z_1 increases the stress relaxation. Rewriting the above equation in the form:

$$\dot{\varepsilon}_p = C_1 \sigma^n; \ C_1 = \left(1/Z_1\right)^n \tag{6}$$

The total stress can be decomposed into initial yield stress, drag stress, back stress and viscous stress in the following form:

$$\sigma = \alpha + (R + k + \sigma_v)\mathrm{sgn}(\sigma - \alpha) = E(\varepsilon - \varepsilon_p)$$

From the stress relaxation data during the CFI tests, the variation of the viscous stress with the strain rate is plotted as shown in Fig. 10. From the linear fit in log–log scale, the parameters C_1 and n were obtained as 1×10^{-39} and 20 respectively.

5 FE Analysis and Validation

5.1 FE Model

The parameters of the unified viscoplastic model were validated by numerical prediction of the stable hysteresis loops during LCF loading and stress relaxation during the CFI loading and comparing with the finite element (FE) analysis in ABAQUS

Fig. 11 FE model of specimen
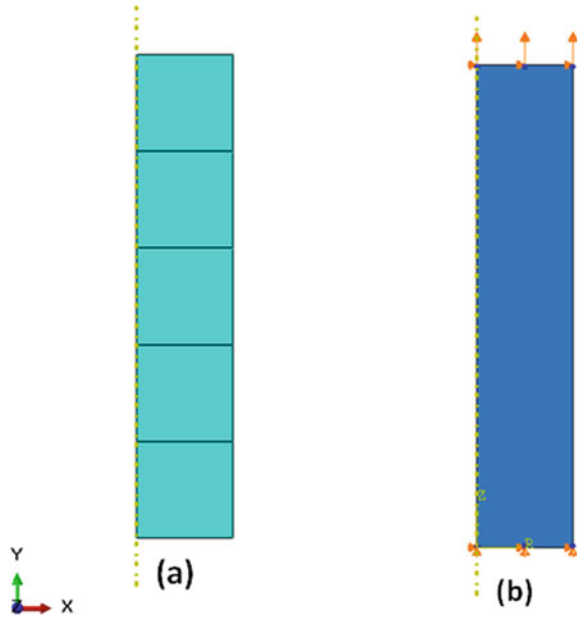
[14]. The Chaboche and Rousselier unified viscoplastic model is one of the in-built constitutive models available in ABAQUS.

The geometry, loading and the boundary conditions of the LCF and CFI test specimen are given in Fig. 11. The width and length of the axisymmetric model considered in this analysis are 3 mm (6 mm gauge diameter) and 15 mm, respectively. One of the edge (at bottom), the rotation (θ) and the axial displacement (U2) were constrained and at the other edge, U2 was imposed corresponding to the strain amplitude (± 0.06 mm for $\pm 0.4\%$ amplitude). The waveform defined for LCF and CFI loading at $\pm 0.4\%$ amplitude is given in Fig. 12a, b, respectively. The parameters estimated as given in the previous section were defined in ABAQUS as material model in the plastic range. The geometry was modeled with axisymmetric shell elements (CAX4R). The element global size is 3 mm. The material properties used for inelastic analysis are provided in Table 3.

5.2 FE Results

The predicted and the experimental hysteresis loops of the specimens during the LCF loading at the strain amplitudes of $\pm 0.4\%$ and $\pm 0.6\%$ are given in Figs. 13 and 14, respectively. The numerically predicted and the experimental hysteresis loops are found to be in close agreement. The stress relaxation during the hold time, predicted using the viscoplastic analysis, was also found to compare well with the experimental

Fig. 12 The waveform applied during FE analysis for ± 0.4% amplitude
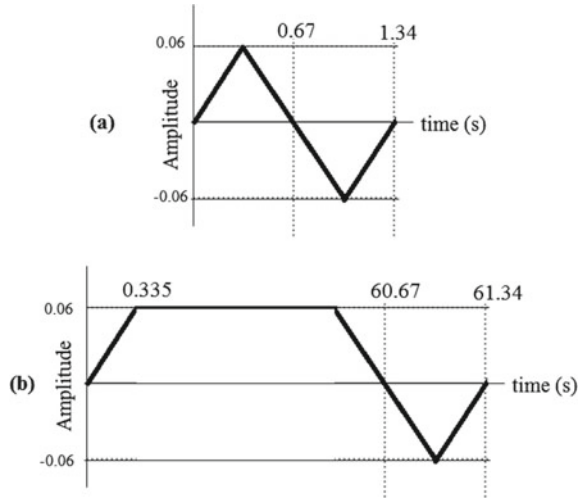
Table 3 Viscoplastic material constants of Inconel-625 at 843 K

E GPa	υ	Kinematic hardening parameters		Isotropic hardening parameters		Viscous parameters	
		C (MPa)	γ	Q (MPa)	B	C_1	n
175	0.3	76,689.6	450.4	61.9	0.78	1×10^{-39}	20

Fig. 13 Predicted and experimental hysteresis loops at 843 K and ± 0.5% strain amplitude
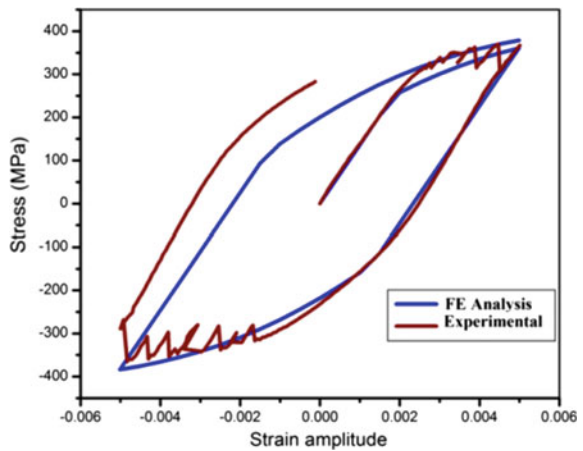
results as shown in Fig. 15, effectively validating the approach used viscoplastic in the present investigation.

Fig. 14 Predicted and experimental hysteresis loops at 843 K and ± 0.6% strain amplitude
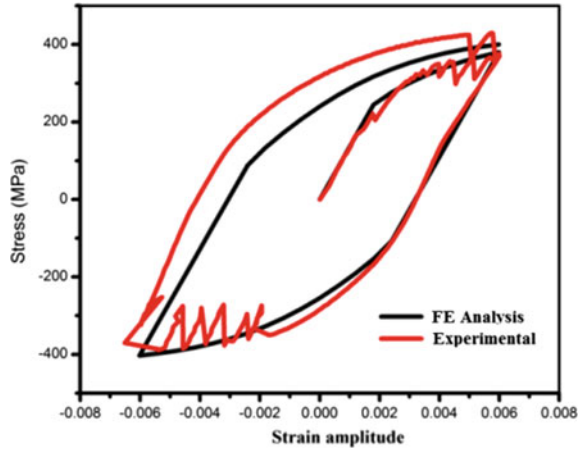
Fig. 15 Experimental and analytically estimated stress relaxation
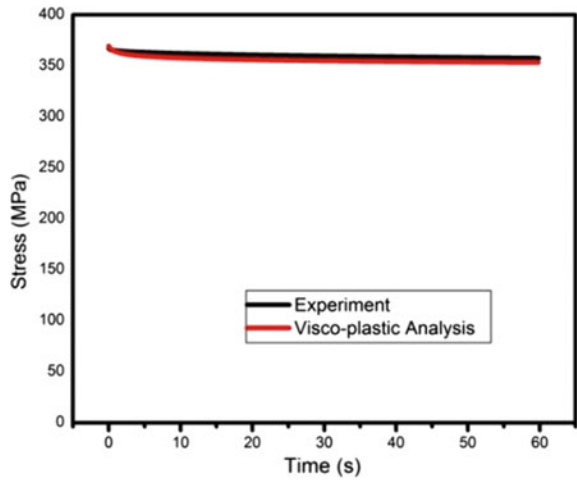
6   Conclusions

The following conclusions were derived from the present investigation.

- The Chaboche and Rousselier unified viscoplastic constitutive model can be used to find total permanent strain including time-independent plasticity and time-dependent stress relaxation. Hence, this model can be effectively used for estimating the total strain when the creep–fatigue loading is present.
- Cyclic hardening taking place in the material manifested itself in the form of reduction in the cyclic plastic strain.
- The results of the investigation established the applicability of both isotropic and kinematic models for Inconel 625. Furthermore, a close agreement between

the numerically predicted and the experimentally obtained hysteresis loops was observed under LCF loading. This validates the combined nonlinear isotropic and kinematic hardening model considered for the analysis.

- The stress relaxation during CFI test at 843 K was found to be small. A close agreement was observed between the predicted and the experimentally observed stress relaxation behavior. This validates the viscous parameters of the constitutive model.
- The data in the present investigation can be used for designing Inconel-625 components operating under creep–fatigue loading.

References

1. Kumar Krovvidi SCSP, Padmakumar G, Bhaduri AK (2017) Experience of various materials for design and manufacture of bellows for nuclear industry. J Adv Mater Proceed, VBRI press, 2(3):156–161
2. Bhoje SB, Chellapandi P (1996) Creep fatigue design of FBR components, Proceedings of IAEA conference on 'Creep-fatigue damage rules for advanced fast reactor design', IAEA-TECDOC-933, Manchester, UK
3. Chaboche JL, Rousselier G (1983) On the plastic and viscoplastic constitutive equations—part 1: rules developed with internal variable concept. J Pressure Vessel Technol, Trans ASME 105(2)
4. Chaboche JL, Rousselier G (1983) On the plastic and viscoplastic constitutive equations—part 2: rules developed with internal variable concept. J Pressure Vessel Technol, Trans ASME 105(2)
5. Tong J, Zhan BV (2004) Modelling of cyclic plasticity and viscoplasticity of a nickel-based alloy using Chaboche constitutive equations. Int J Fatigue 26:829–837
6. Veerababu J, Goyal S, Sandhya R (2018) Cyclic viscoplastic analysis for steam generator material of Indian fast breeder reactor. Fatigue Fracture Eng Mater Struct 1–14
7. Gong YP, Hyde CJ, Sun W, Hyde TH (2009) Determination of material properties in the Chaboche unified viscoplasticity model. Proceed Inst Mech Eng, Part L: J Mater Design Appl 224:19–29
8. ASTM B443–00(2014) Standard specification for Nickel chromium Molybdenum-Columbium Alloy (UNS N06625) and Nickel-Chromium-Molybdenum-Silicon Alloy (UNS N06219) Plate, Sheet and Strip; ASTM International, West Conshohocken, Pennsylvania
9. ASTM E606/ 606M (2019) Standard Test Method for Strain-Controlled Fatigue Testing; ASTM International, West Conshohocken, Pennsylvania
10. Kumar Krovvidi SCSP, Goyal S, Ranjan Das C, Bhaduri AK (2020) Tensile and Low Cycle Fatigue Behavior of Inconel alloy-625 and its weld joints. Submitted to J Mater Sci Eng-A
11. Krovvidi SCSP, Goyal S, Bhaduri AK (2019) Low cycle fatigue and creep-fatigue response of the 316Ti stainless steel. Frattura ed Integrità Strutturale 13(48):577–584. https://doi.org/10.3221/IGF-ESIS.48.56
12. Prasad Reddy GV, Sandhya R, Mathew MD, Sankaran S (2013) The effect of nitrogen alloying on the low cycle fatigue and creep-fatigue interaction behavior of 316LN stainless steel. Adv Mater Res 794 (September 2013):441–48
13. Sunil Goyal K, Mariappan VS, Sandhya R, Laha K, Bhaduri AK (2018) Studies on creep-fatigue interaction behaviour of Alloy 617M. Mater Sci Eng-A, A 730:16–23
14. ABAQUS/Standard User's Manual, Version 6.9 (2009), Simulia, Providence, RI

Design of Shock Absorber for Radioactive Coolant Tube Transportation Cask and Impact Analysis of Cask with Shock Absorber

J. V. Mane, Ravindra Pal, Lokendra Kumar, and V. M. Chavan

Abstract Radioactive coolant tube transportation cask has been designed for in-house storing of full-length pressure tube of 220 MWe PHWR. The existing configuration of cask is not type approved and will not qualify for regulatory accident condition tests. In order to meet compliance with the regulatory requirements of IAEA/AERB such as 9 m drop on unyielding target and 800 °C thermal test, an external shock absorber along with thermal shield should be designed and used. Therefore, a suitable shock absorber is conceptualized and designed without modifications in the cask, which will meet the regulatory requirements of accident condition transport. Thermal shield in the form of sandwiched ceramic board is mounted inside shock absorber cage, which will meet the qualifying requirement under thermal test. Through number of FE simulations, configuration of shock absorber is finalized. The performance of cask with shock absorber is evaluated in all possible most damaging orientations under 9 m drop on rigid target. It is observed that cask components meet the structural integrity requirements. Also, delicate thermal shield is protected without any damage. Thermal analysis of cask with thermal shield for regulatory accident condition is also carried out. The detailed shock absorber design along with thermal shield and compliance with regulatory requirements using FE and CFD simulations are presented in the paper.

Keywords Cask · Impact · Shock absorber

1 Introduction

Radioactive coolant tube transportation cask has been designed for in-house storing of full-length pressure tube of 220 MWe Pressurized Heavy Water Reactor (PHWR). The cask is long cylindrical in shape, and Lead is used as radiation shielding material.

J. V. Mane (✉) · L. Kumar · V. M. Chavan
Refuelling Technology Division, Bhabha Atomic Research Centre, Mumbai 400085, India
e-mail: jvmane@barc.gov.in

R. Pal
Remote Tooling Systems, Nuclear Power Corporation of India Ltd, Mumbai 400094, India

It consists of outer shell, inner shell, and ends are provided with end closures. Outer shell outer diameter is 435 mm with thickness of 12 mm and made up of IS2062 Gr-A material. Inner shell inner diameter is 128 mm with thickness of 6.65 mm made up of IS2062 Gr-A material. Overall length of cask is 5750 mm. The annular space between outer shell and inner shell is filled with Lead material. The cask is supported on two saddle supports. Two lifting trunnions with removable eye bolts are provided near ends of cask for handling purposes. The cask cavity is closed by Lead filled end closures with bolting arrangement. Gross mass of cask is 8.2 ton. The construction details of cask are shown in Fig. 1. The cask during transportation and handling has to be used in horizontal configuration.

It is required to transport full-length pressure tube from reactor site for post-irradiation examination. The transportation of cask with coolant tube is feasible only if it is qualified for at least Type B(M) requirement of AERB/IAEA regulation [1, 2]. Therefore, cask needs to demonstrate compliance with the regulatory requirement of normal and accident conditions of transport. The existing configuration of cask is not type approved. The cask is Lead shielded, long structure with structurally weak closures with bolted arrangements and cask does not have any impact limiting structure on outer periphery. This type of existing design will not meet the structural integrity requirement under 9 m regulatory drop tests and may not meet the thermal test requirement considering issues related to Lead melting and solidification. In order to meet compliance with the regulatory accident condition requirements, shock-absorbing structure is inevitable for 9 m drop tests requirements and will require thermal shield to protect cask against 800 °C thermal tests. Therefore, a suitable shock absorber is conceptualized in such a way that it will meet structural requirements, and it is suitable for mounting thermal shield also without any modification in the existing cask, which will meet the regulatory requirements of accident condition drop. The detailed shock absorber design along with thermal shield and compliance with regulatory requirement using explicit Finite Element (FE) and Computational Fluid Dynamics (CFD) simulations is presented in the paper.
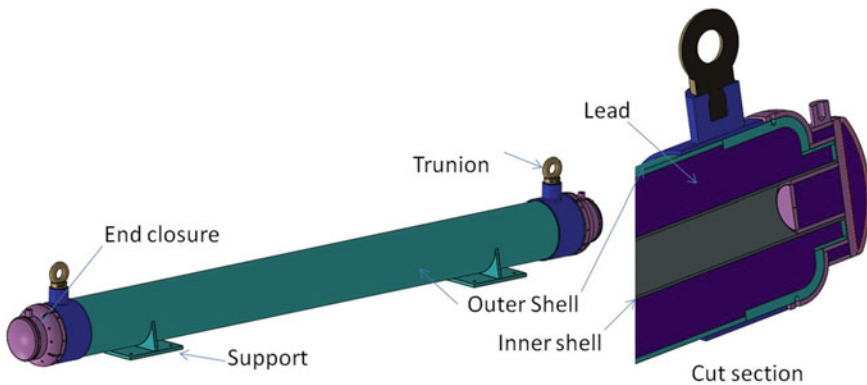
Fig. 1 Coolant tube transportation cask

2   Description of Shock Absorber Cage of Cask

Different concepts of shock absorber are thought for this cask and evaluated its performance in different drop orientations through explicit FE simulations with the number of modifications based on the results of simulations. Final configuration of shock absorber for this cask is decided based of FE results. It consists of structurally strong base made up of two C-channels (ISMC 250) running throughout the length and stiffened by C-channels (ISMC150) at different locations. Support plate is provided on the base for mounting cask with the help of cask saddle support. At six locations, saddle-type supports are provided on cage base for mounting cask. This arrangement of strong base and support a number of locations will avoid bending of cask during different drop orientations. Top structure of shock absorber is made up of pipe mesh of size 3" Sch.40 in rectangular shape, which will protect cask in inverted horizontal drop orientations. Top pipe structure is made in four parts for handling purpose. Ends parts of top structure are provided with double layer of pipe mesh considering corner and end drop. At six locations, support plates are provided and made integral with top structure at corresponding locations of six base saddle support for the cask. This will firmly fix the cask into the cage. Six support plates in top structure will help in inverted horizontal drop, side horizontal drop and long edge drop orientations by arresting movements of cask inside cage. Top structure is connected with base with the help of strong pins of size 50 mm at 12 locations. The pins are designed in such a way that these will avoid separation of top structure from base in any drop orientation. Bolting is also provided to firmly fix top structure with base without any play. The cask with this shock absorber arrangement is mounted on truck chassis with bolting and transported in horizontal orientations. Material of construction of shock absorber is IS2062 Gr A.

Different types of insulating materials, viz., different types of wool, polyurethane foam and ceramic board are considered for protection against regulatory thermal tests. However, ceramic board sandwiched between steel plates is found suitable considering geometry of cask. Thickness of ceramic board is decided based on number of thermal analyses. It is found that 25 mm ceramic board will limit outer shell temperature of cask well below Lead melting point of 327 °C and hence, Lead melting, solidification and related issues are avoided. Thermal analysis with final results is presented in Sect. 5 of this paper. The sandwiched 25 mm thick ceramic board in 2.5 mm thick steel plates is mounted firmly on inside surface of top structure of shock absorber cage. Ceramic board can be firmly fixed between two C-channels at bottom of base structure as single piece or at top of base structure in pieces. The construction details of shock absorber are shown in Figs. 2 and 3.
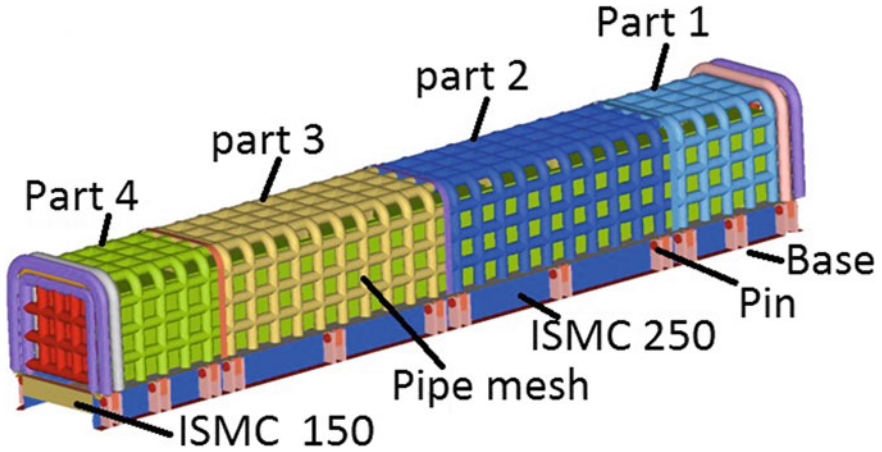
Fig. 2 Cask shock absorber cage
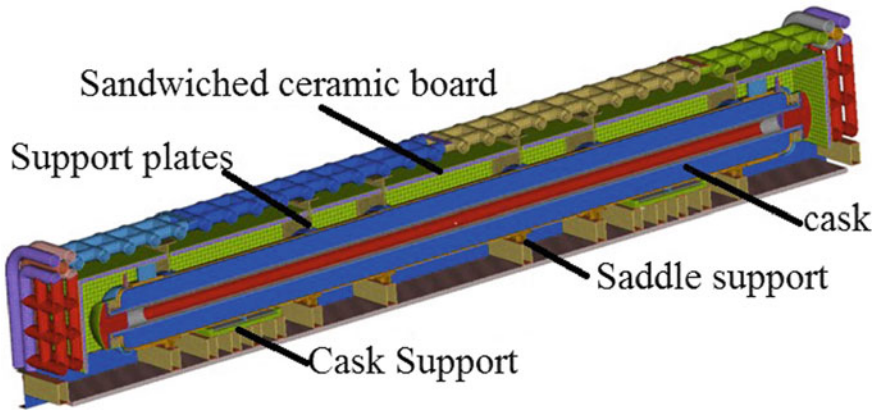
Fig. 3 Cask with shock absorber cage

3 Finite Element Modeling

FE meshing of cask component with shock absorber cage is carried out using FE software Visual-Environment v7.5. Components of cask and shock absorber are discretized using shell, solid, beam and rigid elements. Outer shell, inner shell, pipe structures and relatively thin plates used for construction of cask and shock absorber cage are modeled using Belytchko-Tsay shell elements. Lead and thick components are modeled using eight noded hexahedral solid elements. Bolts are modeled with beam elements and rigid links. FE model is shown in Figs. 2 and 3. Total number of nodes is 451,551, and total number of elements is 358,426. FE mass of cask is 8164 kg and that of shock absorber cage is 3891 kg. Initial velocity of 13.41 m/s

Table 1 Material properties

Properties	IS2062 Gr-A	Lead	SA193GrB	Ceramic
Density (Kg/m^3)	7800	11,350	7800	320.0
Young modulus (GPa)	200	16.2	200	215
Poisson's ratio	0.3	0.45	0.3	0.2
Yield strength (MPa)	240	3.2	727	69.0
Ultimate tensile strength (MPa)	410	10.8	860	–
Elongation (%)	20	50	16	–
Tangent modulus (MPa)	782.6	15.3	869.0	~69.0

corresponding to 9 m drop height is defined to all nodes of structure. Rigid wall is defined as perfectly infinite plane with frictionless surface on which cask will drop under different orientations. Type of contact used is frictionless self-impacting with edge treatment. The bilinear elastic–plastic material properties are assumed at room temperature. Strength of weld is considered equivalent to parent material. Weld is not modeled explicitly. Bolts materials are modeled with failure at 1% plastic strain to visualize bolt failure effects on cask components, which will be useful in design improvement of cask [3]. Material properties without strain rate effect used in FE simulations are given in Table 1.

4   FE Simulation Results and Discussion

FE simulations are carried out using PAM-Crash v2011 explicit FE software, which is validated for cask-impact simulations [3]. Performance of cask with different cage concepts is evaluated using FE simulations under most damaging orientations, and cage design is finalized. Results of FE simulation of cask with final cage design are presented in this paper. Seven drop orientations, viz., end drop, side horizontal drop, base horizontal drop, inverted horizontal drop, top long edge drop, corner drop and slap down drop are considered for FE simulations thought to be most damaging. All the simulations are carried out for first impact, and subsequent impacts on rebound are ignored. However, results of end drop, inverted horizontal drop and slap down drop are presented, and results of other drop orientation are similar. In end drop orientations, i.e. drop on closure side, point of contact and center of gravity of cask are perpendicular to rigid wall. In case of slap down drop, line joining point of contact and center of gravity inclined at 15^0 to rigid wall normal and gravity is defined in FE model. Cask will first strike to rigid wall, rotate and other end of cask strikes the rigid wall with velocity greater than initial velocity. In inverted horizontal drop orientation, cask will fall on side opposite to base support on rigid wall. Final deformation of cask under 9 m end drop, slap down drop and inverted horizontal drop are shown in Figs. 4, 6 and 7. It is observed in all drop orientation that cage successfully protects
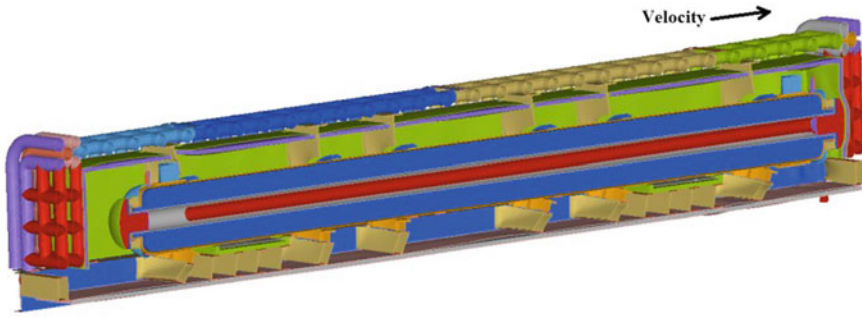
Fig. 4 Final deformation of cask with cage under 9 m end drop (sectional view)

the cask and delicates thermal shield. Plastic strain obtained in cage and cask components under end drop orientation are shown in Fig. 5. Similar plastic strain results are obtained in other drop orientations. Conversation of energy and cask overall deceleration during impact duration are given in Figs. 8 and 9 for inverted horizontal drop only. Results such as maximum 'g' loadings (deceleration), Lead slump, impact duration and rebound velocity maximum plastic strain observed in different cask components are obtained. The plastic strains obtained in FE simulations are very localized and will cause local denting only. Except minor local denting, rest of cask body remains in elastic condition and meets structural integrity requirements, which can be verified graphically. In all drop orientations, thermal shield remains in its position with local dents and slight deformation, which will not result in increase in temperature of cask under thermal test. Closure bolts remain in elastic condition. Lead slump is observed only in end and corner drop, which will not result increase in radiation level. It is found that inverted horizontal drop is worst orientation considering cask movement inside shock absorber cage and end drop as worst orientation considering Lead slump.
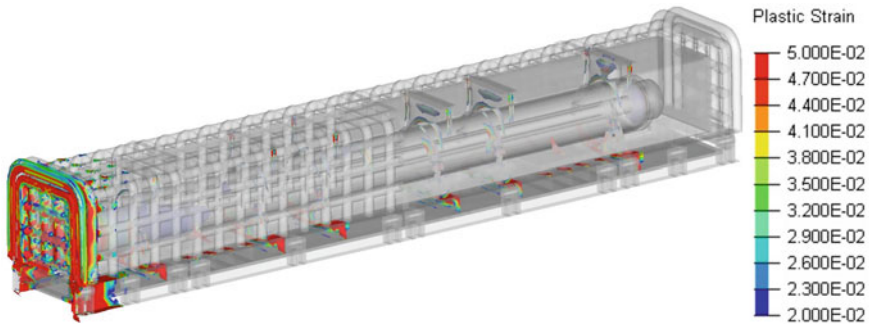
Fig. 5 Plastic strain in cask components under 9 m end drop (transparent view)
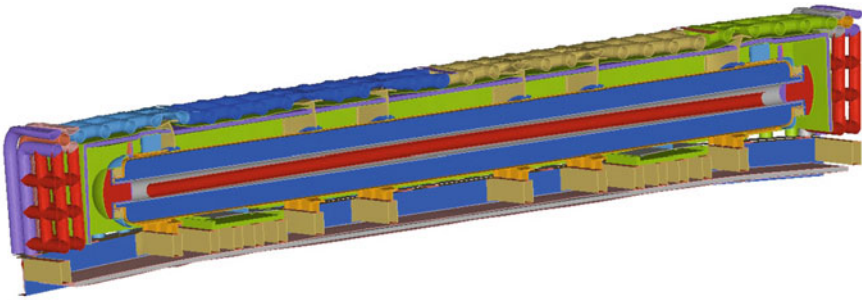
Fig. 6 Final deformation of cask with cage under 9 m inverted horizontal drop
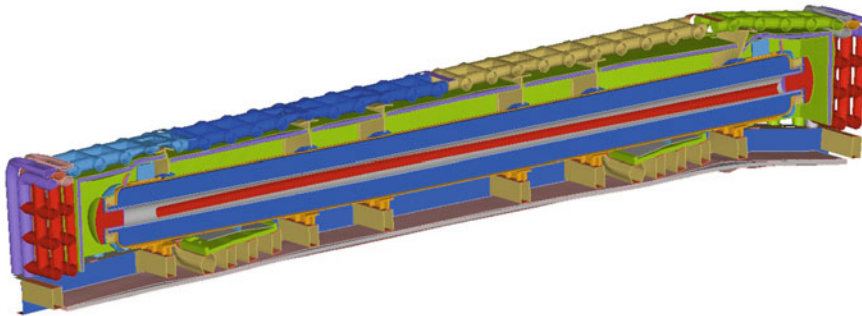
Fig. 7 Final deformation of cask with cage under 9 m slap down drop

Fig. 8 Energy plot
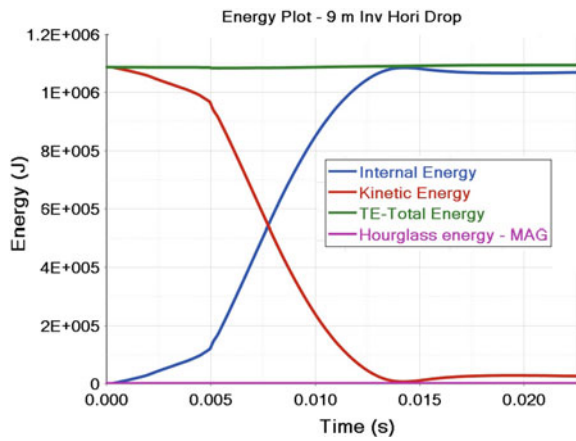
Fig. 9 Deceleration plot
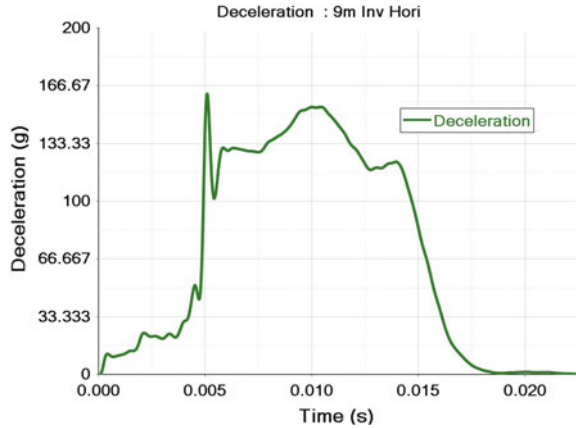
5 Thermal Analysis of Cask

Thermal analysis of cask with thermal shield of different thicknesses has been carried out for regulatory normal condition and accident condition. Two different environments for regulatory thermal accident conditions are average flame temperature of 800 °C and fully engulfing pool fire (temperature of 1151 °C). 2D Thermal analysis is carried out as cask has high length to width ratio and schematic cross-section at mid plane is shown in Fig. 10. The thermo-physical properties and boundary conditions are given in Tables 1 and 2, respectively. Based on the analysis, it is found that

Fig. 10 Schematic of cross-sectional view at midplane
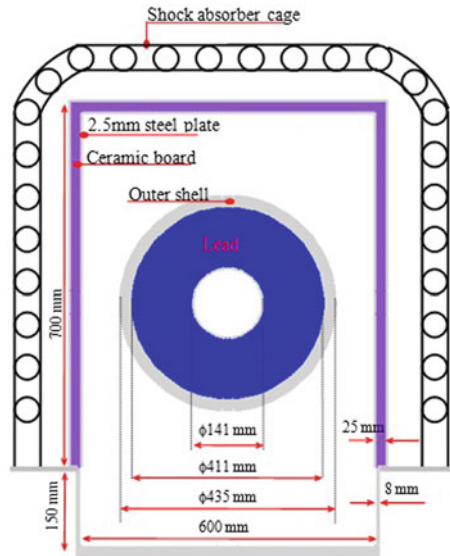
Table 2 Thermo-physical properties of materials

Property	Ceramic board	Carbon steel	Lead
Density (kg/m^3)	240	8030	11,340
Thermal conductivity (W/m–K)	0.11	55	33.9
Specific heat (J/kg-K)	1100	502.48	132

Table 3 Boundary condition for different cases

Normal conditions		Accidental conditions	
Ambient temperature	38 °C	Initial condition	Solar insolation
Convection coefficient (h)	5 W/m^2/K	Fire temperature	800 °C and 1151 °C
Surface emissivity	0.3	Fire emissivity	1
Decay heat	4.4 W	Surface absorptivity	1
Solar insolation	Heat flux as per regulation	Convection coefficient (h)	10 W/m^{2}K

25 mm thick ceramic board is sufficient to keep cask temperature well below Lead melting point (Table 3).

In normal conditions with 25 mm thick ceramic board, cask outer surface temperature is below 50 °C, and temperature of outer Lead surface reaches up to 139 °C for adiabatic surface temperature of 1151 °C (most severe condition). Hence, there is sufficient margin to avoid Lead melting (Fig. 11).
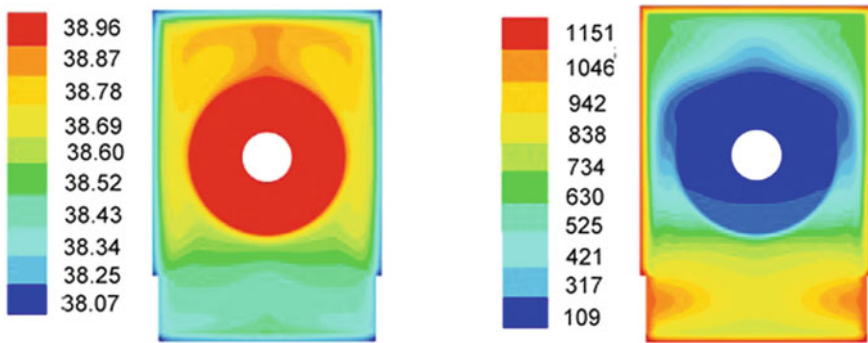
Fig. 11 Temperature (°C) contour for normal and accidental condition

6   Conclusion

The existing coolant tube transportation cask is not meeting the structural integrity requirement. Therefore, shock absorber cage along with thermal shield for coolant tube transportation cask is conceptualized, designed without any modification in the existing cask using FE simulations to meet the regulatory requirement under accident condition transport viz., 9 m drop on unyielding target and 800 °C thermal test. Its performance is evaluated using FE simulations under most damaging orientations and its design is finalized. The performance of cask with shock absorber is evaluated in all possible most damaging orientations, viz., end drop, side horizontal drop, base horizontal drop, inverted horizontal drop, top long edge drop, corner drop and slap down drop on unyielding rigid wall. It is observed that cask components are in elastic conditions with localized dents and meet the structural integrity requirements. It is found that inverted horizontal drop is worst orientation considering cask movement inside shock absorber cage and end drop as worst orientation considering Lead slump. Thermal analysis is carried out under two different thermal environments of equivalent to average flame temperature of 800 °C and fully engulfing pool fire condition, Lead outer surface reaches up to 139 °C. There is sufficient margin for Lead melting. Thus, cask with shock absorber cage meets the regulatory requirement of accident condition drop and thermal tests.

References

1. AERB Safety Code No. AERB/NRF-TS/SC-1, ' Safe Transport of Radioactive Material'
2. IAEA, 'Regulation for the safe transport of radioactive material' Safety Guide TS-R-1
3. Mane JV, Sharma S, Chavan VM, Kar DC, Agrawal RG (2011) Cage design, impact analysis and experimental testing of teletherapy source transportation flask. Transactions, SMiRT 21, 2011, New Delhi, India', Div-V: Paper ID 315

Design, Impact and Thermo-Mechanical Analysis of Radioactive Surveillance Specimen Transportation Cask

J. V. Mane, S. Sharma, H. Ali, and V. M. Chavan

Abstract One of the important issues in designing radioactive material transportation cask is shielding material. Lead is widely available and used as a radiation shielding material. However, Lead is having a low melting point and upon melting, it expands. Melting and subsequent solidification will generate a void in shielding. Therefore, surveillance specimen transportation cask without Lead is conceptualized and designed as a Type B(M) package. Considering the availability of material and its form, the present cask is designed as welded plates structure. Steel plates are used effectively both for shielding as well as as a structural material. As welded steel plate cask will act as a monolithic solid piece, a shock absorber is needed to meet the structural integrity criteria under regulatory 9 m drop on rigid target. Therefore, the shock absorber is conceptualized and designed. FE simulations under 9 m drop on unyielding target are carried out with shock absorber and finalized cask configuration so as to meet the structural integrity requirement. Coupled transient thermo-mechanical FE simulation of the cask has been carried out to evaluate performance and assess the structural integrity of cask design under regulatory thermal test. The cask design with shock absorber and demonstration of compliance to the regulatory requirement are presented in the paper.

Keywords Cask · Impact · Shock absorber

1 Introduction

Transportation of radioactive material through the public domain is one of the important activities in the nuclear industry. Radioactive substances in the various physical, chemical and geometrical forms are transported for a wide variety of applications ranging from power generation to uses in medicine, industry, agriculture, etc. The transportation of radioactive material is carried out through specially designed and

J. V. Mane (✉) · S. Sharma · H. Ali · V. M. Chavan
Refuelling Technology Division, Bhabha Atomic Research Centre, Mumbai 400085, India
e-mail: jvmane@barc.gov.in

Type approved packages called as casks or flasks so as to control radiation, criticality and thermal hazards to an acceptable level. Cask designed needs to meet the compliance of the tests specified by AERB/IAEA [1, 2] regulatory requirements under different conditions of transport.

One of the important issues in the designing of cask is radiation shielding material. The widely available and used shielding material is Lead due to its ease of manufacturing and better shielding property. However, Lead is having a low melting point and upon melting, it expands. Melting and subsequent solidification will generate a void in shielding which will lead to direct streaming of radiation. Also, it is difficult to meet the structural integrity requirement under molten Lead conditions. This leads to a difficulty in the design of casks. Therefore, Lead is avoided as shielding material for cask even if it has better shielding properties, and steel as one of the candidate materials is chosen. However, steel will require higher thickness as compared to Lead for the same gamma source [3]. The concept, design and compliance to regulatory requirements using FE simulations are explained in subsequent paragraphs.

2   Design of Cask and Shock Absorber

Considering the availability of in-house material and its form, the present cask is designed using steel plates. The basic design selected for the manufacturing of the cask is welded stack of plates to form a cylinder with removable end closures on both ends. Steel plates of thickness 40 mm and 50 mm made up of IS2060 Gr-B material are used efficiently both for shielding as well as as a structural material as shown in Figs. 1 and 2. The plates are welded along the length as well as to the end plates which are provided on both ends (Fig. 3). Staggered shear pins are provided to adjacent plates at different locations along the length of the cask and are shown in Fig. 4. Shear pins along with welds and end plates resist shear load under impact loading. Two lifting trunnions are provided on the cask main body for cask handling operation. These can be used for tie-down arrangements on transportation trailers.

Fig. 1 Cask
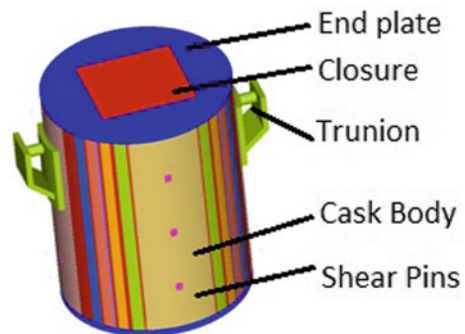
Fig. 2 Cask Body
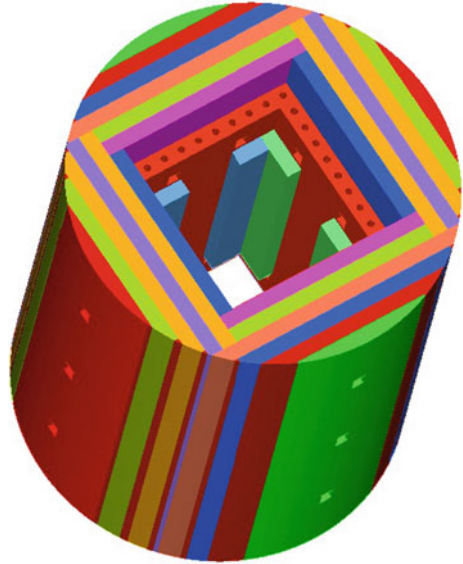
Fig. 3 Cask end closure
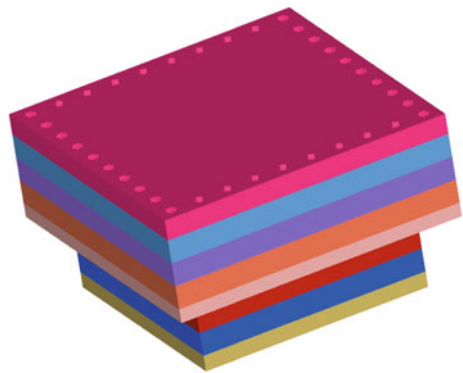
The construction details of the cask are shown in Figs. 1, 2, 3 and 4. The cask during transportation and handling has to be used in a vertical configuration.

The cask is designed as a type B(M) package, as per the regulatory standard of AERB/IAEA [1, 2]. Therefore, it should demonstrate compliance to regulatory accident condition mechanical tests, i.e. 9 m drop on rigid target in most damaging orientation and thermal test, i.e. 800 °C engulfing pool fire test for 30 min. The steel plate cask will act as a monolithic solid piece which requires an external shock absorber to meet the structural integrity requirement under regulatory 9 m drop on a rigid wall. Therefore, a shock absorber is conceptualized and designed in such a way that it will reduce the number of worst orientation drops to this cask. The shock absorber is provided on both ends of cask and bolted to the cask main body. The shock

Fig. 4 Cask shear pin top
view
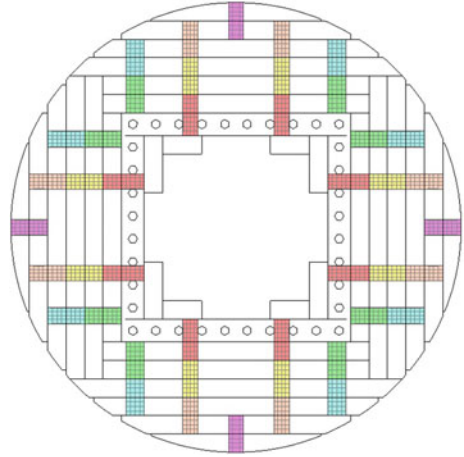
absorber is in the form of a short closed cylinder which is sufficient to absorb energy
in all possible drop orientations. The shock absorber consists of a cylindrical outer
shell and inner shell. The ends of cylinders are closed by plates. The annular space
is filled with the number of bend pipes held together by tube sheet type circular plate
and spot welded. The central space is filled with fins. A number of Finite Element
(FE) simulations of the cask with shock absorber under 9 m drop on unyielding target
are carried out to decide the number of bend pipes and its size, thickness, material
of construction and locations of pipes. Shock absorber components are made up of
IS2062 Gr-B material. The construction details of the cask and shock absorber are
shown in Figs. 5, 6 and 7 which is one of the optimized outcomes of FE simulations
to meet the structural integrity requirement [2].

3 Finite Element Model for Impact Analysis

FE meshing and simulations are carried out using PAM-Crash v 2011 explicit FE
software which is validated for cask-impact simulations [4, 5]. FE meshing of cask
structure along with shock absorber is carried out using shell, solid, beam and rigid
elements. Plates used for construction of cask and its closure are meshed using 8
noded hexahedral solid elements. Shock absorber components are meshed using
Belytchko–Tsay [4] shell elements since these are relatively thin structures. Bolts
are meshed with beam elements and rigid links. FE model is shown in Fig. 5. The
total number of nodes is 1,720,504 and the total number of elements is 1,424,595. FE
mass of cask is 6653 kg and that of the shock absorber is 1541 kg. The initial velocity
of 13.41 m/s corresponding to 9 m drop height is defined to all nodes of the structure.
Rigid wall, i.e. target is defined as an infinite plane on which cask will drop under
different orientations. The type of contact used is frictionless self-impacting with

Fig. 5 Cask with shock
absorber

Inner Shell

Outer Shell
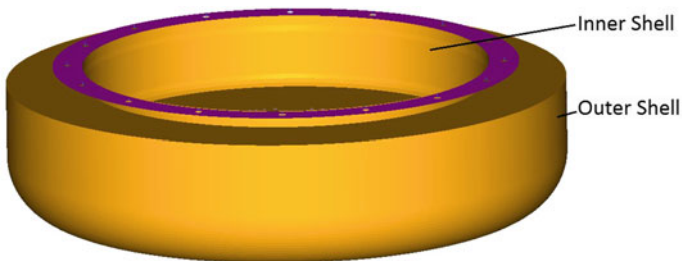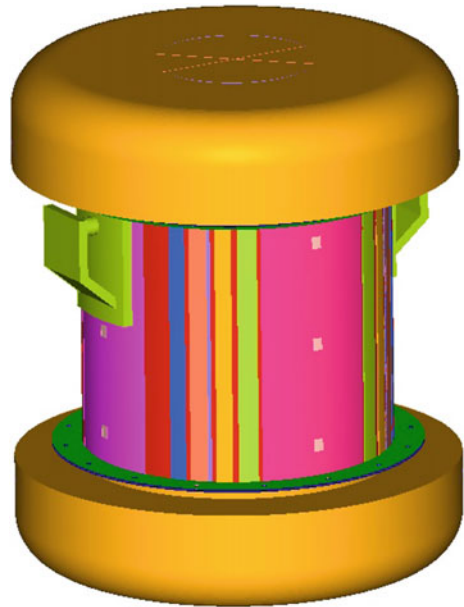
Fig. 6 Shock absorber of cask

edge treatment. Three drop orientations (viz., end drop, horizontal drop and inverted corner drop) are considered for FE simulations, thought to be most damaging to cask. The strength of the weld is considered equivalent to the parent material. Weld is not modelled explicitly. The bilinear elastic–plastic material properties are assumed at room temperature. Bolts material SA193Gr-B is modelled with failure at 1% plastic strain. Material properties without strain rate effect used in FE simulations are given in Table 1.
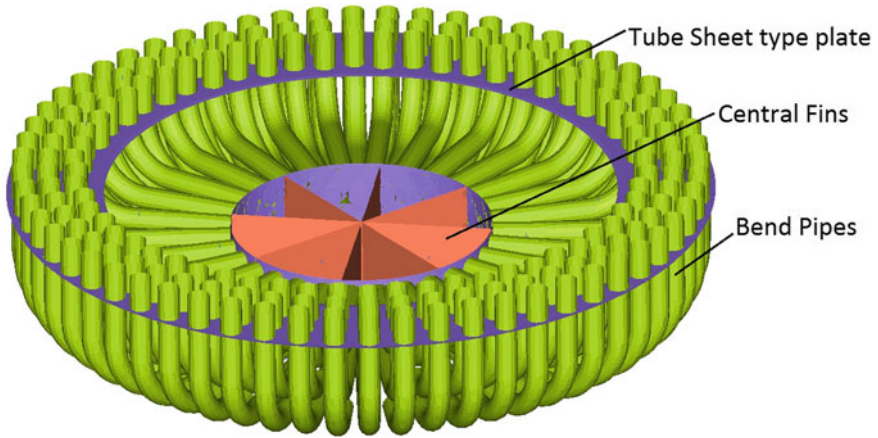
Fig. 7 Pipes and internal structure of shock absorber

Table 1 Material properties

Properties	IS2062 Gr-B	SA193Gr-B
Density(Kg/m3)	7800	7800
Young's Modulus(GPa)	200	200
Poisson's Ratio	0.3	0.3
Yield Strength (MPa)	240	727
Ultimate Tensile Strength (MPa)	410	860
Elongation (%)	20	16
Tangent Modulus (MPa)	782.6	869.0
Reference Temperature (°K)	311	–
Thermal Expansion Coefficient (m/m °C)	11.7E-6	–
Thermal Conductivity (W/m °K)	41	–
Specific Heat (J/kg °K)	434	–
Heat transfer coefficient for mild steel to mild steel contact (W/m^2 °K) [6]	11,000	–

4 FE Simulation Results and Discussion

FE simulations of cask under different drop orientations viz., end drop, horizontal drop and inverted corner drop on the unyielding rigid wall are carried out. All the simulations are carried out for the first impact, and subsequent impacts on the rebound are ignored. The conservation of energy can be checked with the plot of total, kinetic and internal energies with time. The final deformation of the cask with shock absorber is shown in Figs. 8, 10 and 12. The maximum plastic strain observed is also shown in Figs. 9, 11 and 13. In the case of end and corner drop, the maximum plastic strain
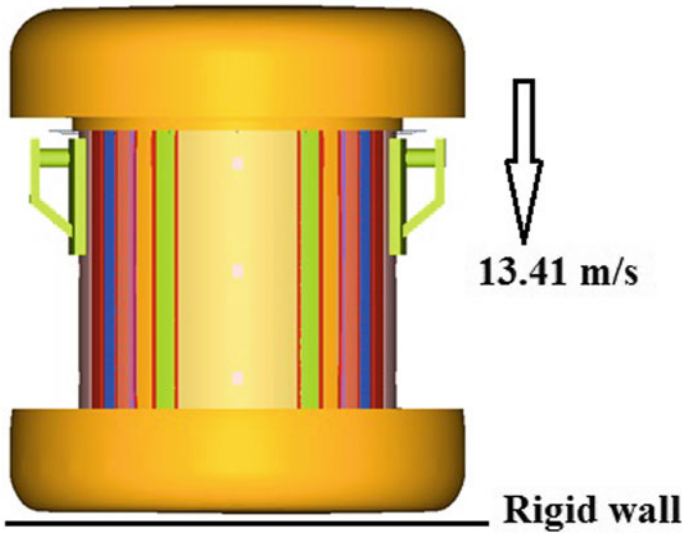
Fig. 8 Final deformation of the cask with a shock absorber (9 m End drop)

is observed in end plate of the cask. In the case of a horizontal drop, the maximum plastic strain is observed in the trunnion. The higher plastic strain is very localized and will lead to local dents in the non-containment location of the cask and the rest of the cask body remains in the elastic condition including the sealing area. These local dents will not reduce shielding thickness. Stresses in all bolts are within the elastic limit. Therefore, regulatory requirements of cask to prevent loss or dispersal of the radioactive contents and increase in radiation level based on reduction of thickness are satisfied [2]. It is observed in all drop orientations that the shock absorber protects the monolithic cask design. Results such as maximum 'g' loadings (deceleration), impact duration and rebound velocity can be obtained for detailed study under impact events. It is found that inverted corner drop is the worst orientation for this cask based on plastic strain and local dents observed in the cask end plate.

5 Thermo-Mechanical FE Analysis

During the thermal test of 800 °C engulfing pool fire for 30 min, the cask will be subjected to transient non-uniform temperature distribution in the cask body. Due to this, cask steel plates will expand non-uniformly and will try to separate from each other if not constrained properly. To constrain the plates under thermal test, staggered shear pins are provided between plates as shown in Fig. 4. As plates are constrained by staggered pins and end plates, free expansions of cask plates are arrested and this will lead to develop stresses in the cask body. Therefore, thermo-mechanical
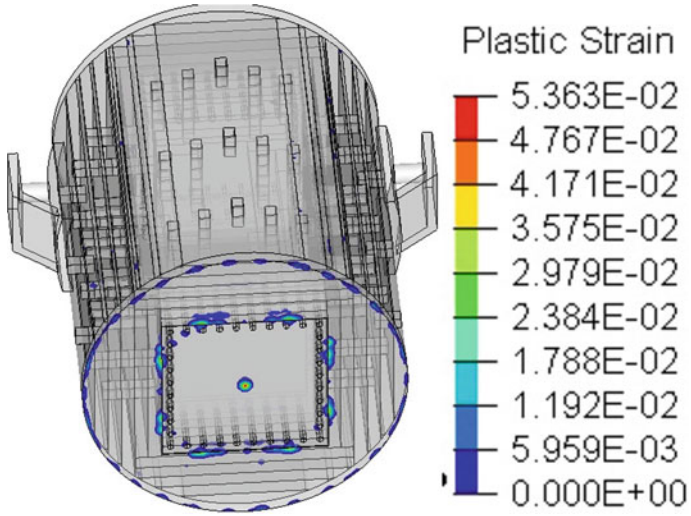
Fig. 9 Plastic strain in cask components (9 m End drop)

Fig. 10 Final deformation
of the cask with a shock
absorber (9 m Horizontal
drop)
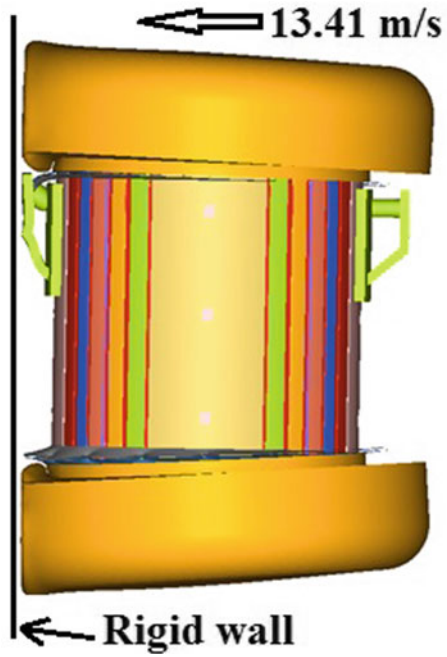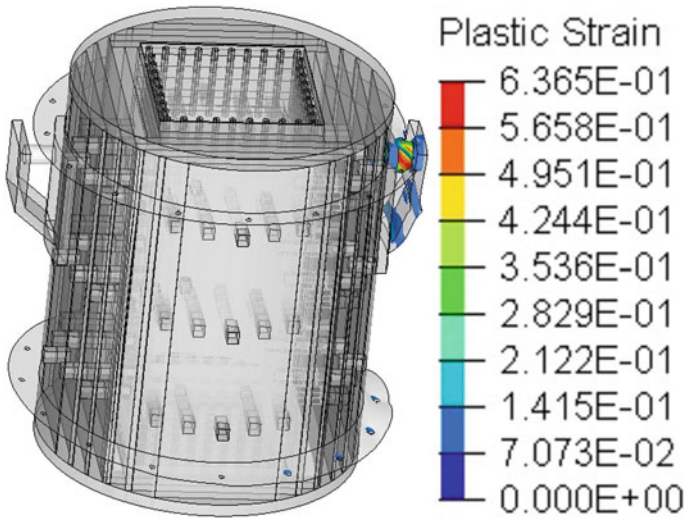
Fig. 11 Plastic strain in cask components (9 m Horizontal drop)

Fig. 12 Final deformation
of the cask with a shock
absorber (9 m Corner drop)
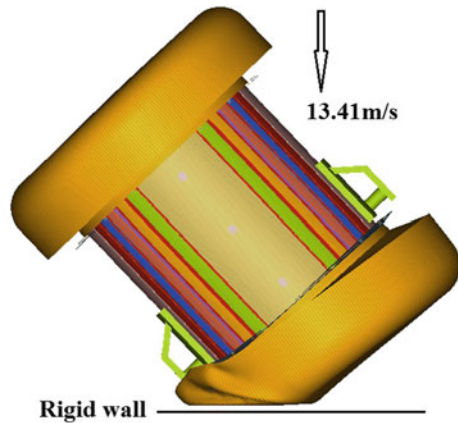
simulations are carried out to evaluate structural integrity under regulatory thermal
tests. Thermo-mechanical simulation methodology and results are explained in the
subsequent paragraph.

The regulatory thermal test for this cask is a transient coupled thermo-mechanical
problem. To simulate this, implicit FE simulation methodology is used. FE simula-
tion is carried out in two subsequent load steps. The first load step is the thermal
simulation and the second load step is mechanical/structural simulation. FE meshing
of cask structures viz., steel plates of cask body, steel plates of cask closure, staggered
shear pins, bolts and fillet welds is carried out using only solid elements. All plates
are modelled separately without merging and with gap. The shock absorber is not
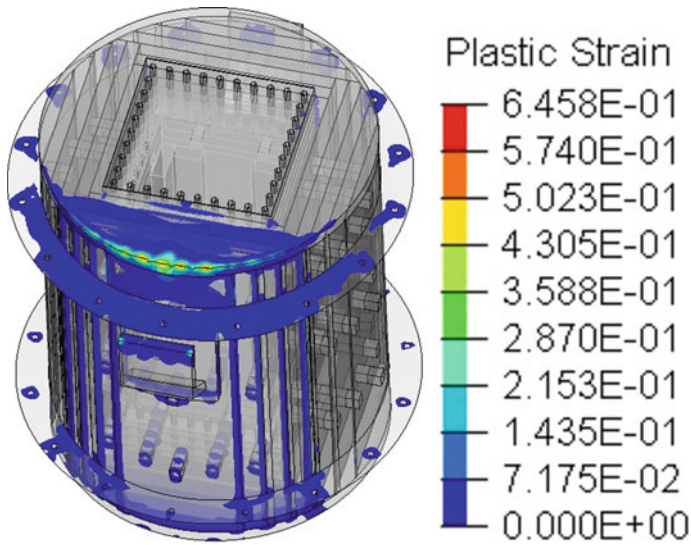
Fig. 13 Plastic strain in cask components (9 m Corner drop)

considered for simulations. 1/8th symmetry is assumed for simulations. The number of nodes is 169,982 and the number of elements is 132,681 in the FE model. Bilinear elastic–plastic material properties are assumed at room temperature and given in Table 1.

5.1 Load Step 1: Thermal Simulation, Boundary Condition and Assumptions

In the first load step, cask body, closure, staggered shear pins, bolts and fillet weld are considered and shock absorber is not considered. The presence of a shock absorber in actual conditions will lower the fire temperature on the cask. However, for FE simulation, a uniform temperature of 800 °C is applied on all outer surfaces of the cask in the first thermal load step for 30 min. This is a conservative assumption as in the case of actual engulfing pool fire, the temperature of the outer surface is lower because of the convection and radiation phenomenon of fire. Subsequent cooling is not considered in simulation as thermal gradient will be high during the initial phase and the cask does not have any burning material. This assumption will reduce computation time. An initial temperature of 38 °C is assumed. On the inner surface of the cask, zero thermal flux is assumed, i.e. insulated condition so that temperature is allowed to increase. Inside air is not modelled as it is not absorbing much heat energy. Adjacent plates are in close proximity with each other and will have some air gaps. Therefore, heat transfer between adjacent plates is due to conduction across

the actual contact area and radiation across the gaps. The total resistance to heat transfer due to the contact interface is called thermal contact resistance. The inverse of contact resistance can be expressed in terms of interfacial heat transfer coefficient (hc) and its value is determined experimentally. In FE simulations, close contact is defined between all contact pairs of adjacent plates, and the value of hc is taken as 11,000 W/m^2 °K [6]. This is equivalent to mild steel to mild steel contact pair. 1/8th symmetry is assumed for simulations, and on the symmetry plane, zero heat flux is assumed, i.e. insulating boundary condition, i.e. temperature gradient is zero. As discussed above, appropriate boundary conditions, i.e. transient temperature load with respect to time and thermal flux with respect to time are defined to FE mesh. Appropriate element type and material properties are defined. One-to-one contact is defined for all contact pairs with required contact property, i.e. interfacial heat transfer coefficient. Transient heat transfer analysis is carried out for 1800 s with implicit time step increment of 30 s. The grid temperature with respect to time is obtained for all grid nodes. This result will be input for subsequent mechanical/ structural simulation to obtain stresses developed in the cask due to constrained thermal expansion.

5.2   Load Step 2: Mechanical/structural Simulation, Boundary Condition and Assumptions

The same FE model consisting of all solid elements as used for thermal simulation is used in this load step of the structural simulation. In the structural load step, stresses developed due to constrained expansion of cask components are obtained. 1/8th symmetry is assumed for simulations with structural symmetry boundary conditions. Temperature with respect to time obtained at all grid node locations in the thermal step is used as input temperature load. Non-linear quasi-static implicit simulation is carried out for 1800 s with implicit time step increment of 30 s. The stresses, plastic strains and displacements results are obtained in this load step.

5.3   Thermo-Mechanical Simulation Results and Discussion

Temperature with respect to time on the cask outer surface, cask inside temperature and closure inside surface temperature are shown in Fig. 14. The graphical contour result of temperature distribution with respect to time for thermal load step, displacements equivalent stresses and plastic strains for structural load step is obtained with respect to time. However, the results of the last step, i.e. at the end of 30 min are given in Figs. 15 and 16 only for temperature and plastic strain. The maximum temperature reached in the inner cavity of the cask after 1800 s is 615 °K and 388 °K at the middle of the body and closure on the inner surface, respectively. It is seen in structural simulations that almost in all parts of the cask, plastic strain is less
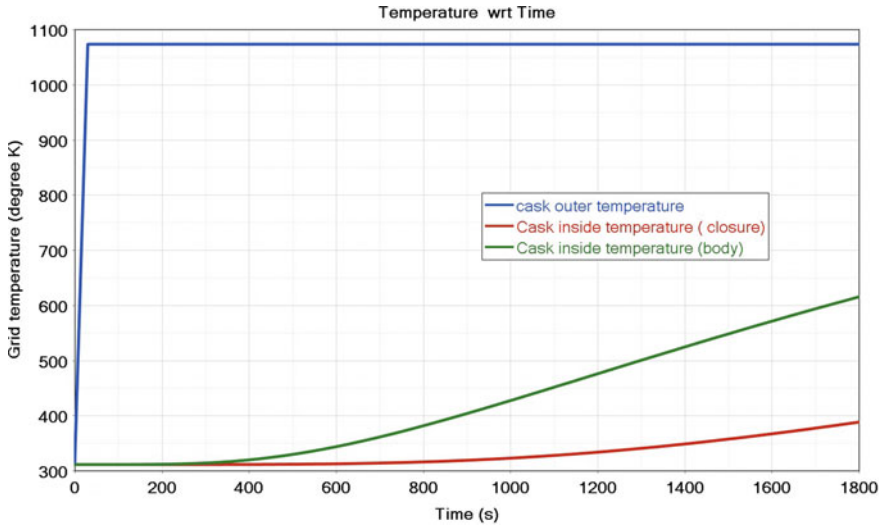
Fig. 14 Temperature with respect to time at three locations in cask during thermal simulation
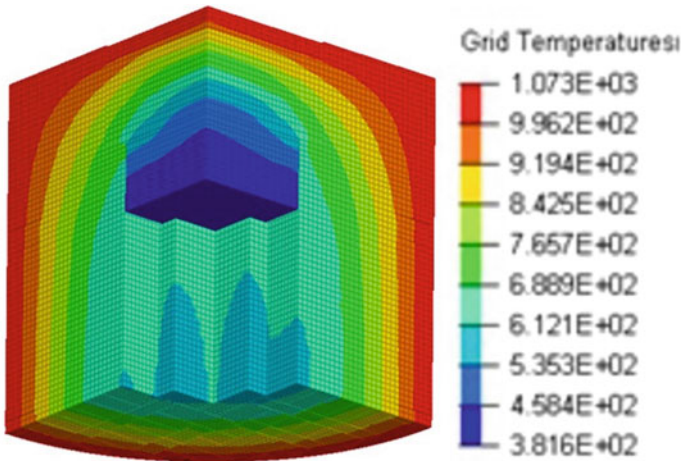
Fig. 15 Temperature contour (°K) at time 1800 s

than 1.5%. At some very localized points, plastic strain is 13%. These locations are shear pin edges. In actual cases, staggered pins are cylindrical in shape; however, for simplicity of modelling, these are modelled as parallelepiped. Cylindrical pins will reduce plastic strain.
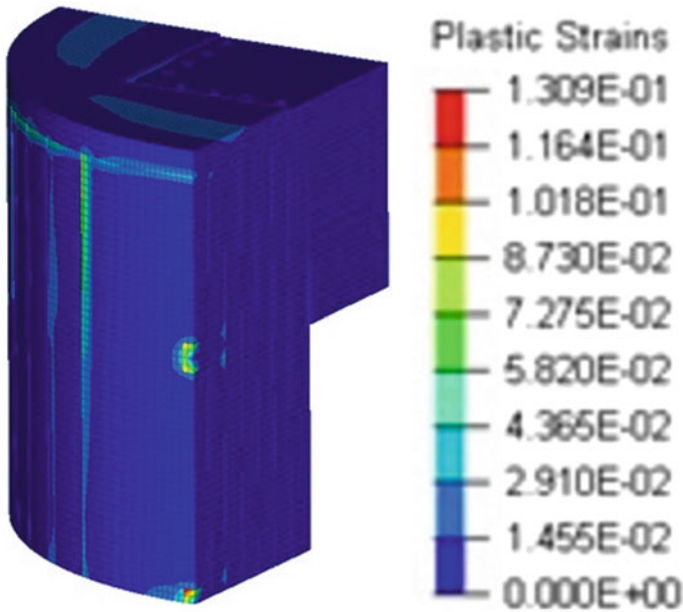
Fig. 16 Equivalent plastic strain at time 1800 s

6 Conclusion

Surveillance specimen transportation cask is conceptualized and designed as a type B(M) package made up of steel plates without Lead as radiation shielding material owing to its issues related to melting and solidifications. Compliance of cask to regulatory requirements is demonstrated using FE simulations. The structural and shielding materials for this cask are solid steel plates. Hence, the shock absorber is needed to meet the structural integrity criteria under regulatory 9 m drop on the rigid wall. Therefore, the shock absorber is conceptualized and designed in such a way that it will reduce the number of worst orientation drops to this cask. FE simulations of the drop of the cask with shock absorber in different orientations on unyielding target are carried out. It is observed that cask components are in elastic conditions with localized dents of plastic deformations. Also, there is no reduction in shielding thickness.

Coupled transient thermo-mechanical simulation has been carried out to evaluate performance and assess the structural integrity of cask design under regulatory thermal test using finite element analysis. Transient temperature, equivalent stresses and plastic strain developed during 800 °C engulfing pool fire test are obtained. It is seen in thermo-mechanical simulations that almost in all parts of the cask, plastic strain is less than 1.5% except very localized high plastic strain region which would not lead to failure. It is concluded that the cask with a shock absorber meets structural integrity requirements [2] under the regulatory accident condition test.

References

1. AERB Safety code No. AERB/NRF-TS/SC-1, 'Safe Transport of Radioactive Material'
2. IAEA Regulation for the safe transport of radioactive material' Safety Guide TS-R-1
3. McAlister DR (2018) Gamma ray attenuation properties of common shielding materials, PG Research Foundation, Inc. 1955 University Lane Lisle, IL 60532, USA
4. "PAM CRASH TM" Explicit finite element software, ESI Group
5. Mane JV, Sharma S,Chavan VM, Kar DC, Agrawal RG (2011) Cage design, impact analysis and experimental testing of teletherapy source transportation flask. Transactions, SMiRT 21, 2011, New Delhi, India', Div-V: Paper ID 315
6. Babu KN (2015) Thermal contact resistance experiments and simulation, Master's thesis. Chalmers University of Technology, Sweden, Dept of App Mech

Modified Cowper-Symonds Model for Predicting the Stress–Strain Behavior of SA516 Gr. 70 Carbon Steel

S. Sharma, M. K. Samal, and V. M. Chavan

Abstract The flow behavior of SA516 Gr.70 carbon steel under dynamic loading conditions was studied experimentally using the split-Hopkinson pressure bar (SHPB). These tests were performed at room temperature at strain rates ranging from 450/s to 3500/s. Quasi-static tensile tests were performed for comparison with high strain rate test results. The strain rate sensitivity at these dynamic rates was found to be positive. The experimental data were fit to the Cowper-Symonds (CS) model. As the CS model did not fit the high strain rate data satisfactorily, the Cowper-Symonds model was modified. This modified Cowper-Symonds model gave the best fit to the experimental data.

Keywords High strain rate · Split Hopkinson bar · Strain rate sensitivity

1 Introduction

Material properties under dynamic loading conditions are important for design, safety and structural integrity assessment of structures subjected to high rate of loading. A few examples of such applications are design of armor systems, vehicle crashworthiness tests in automobile industry, impact analysis, drop test of radioactive material shipping cask and high speed machining. Materials respond differently under static and dynamic conditions of loading. The flow behavior of a material is a function of strain rate and varies with change in strain rate. Also, as the strain rate of the test is

S. Sharma (✉)
Homi Bhabha National Institute, Mumbai 400094, India
e-mail: sudhansh@barc.gov.in

M. K. Samal
Reactor Safety Division, Bhabha Atomic Research Centre, Mumbai 400085, India
e-mail: mksamal@barc.gov.in

Division of Engineering Sciences, Homi Bhabha National Institute, Mumbai 400094, India

V. M. Chavan
Refueling Technology Division, Bhabha Atomic Research Centre, Mumbai 400085, India

increased from quasi-static to dynamic, conditions change from isothermal to adiabatic. High strain rate tests are, thus, necessary to understand the material response under such loading conditions.

SA516 Gr.70 carbon steel, the material of interest in this paper, is a pressure vessel steel and has ferritic–pearlitic microstructure. As a pressure vessel and reactor-grade steel used in nuclear piping system, the fracture properties of this alloy have been studied at different conditions, from quasi-static to high strain rate, and from sub-room temperature to elevated temperature. The effect of loading conditions, notch root radius, radiation and geometry of sample on fracture toughness has been studied [1–3]. These studies show that the fracture properties of the material are significantly influenced by the loading rate and temperature. It was stated that serrations are observed in quasi-static flow stress data, and DSA is found to deteriorate the fracture properties. However, to the best of our knowledge, the flow behavior of SA516 Gr.70 at high strain rates and the corresponding constitutive material model for the prediction of the flow stress of this steel at high strain rate are very rare in literature.

This paper presents the high strain rate compression flow behavior of SA516 Gr.70 pressure vessel steel using the SHPB. A comparison of stress–strain curves at different strain rates has been made, and a constitutive equation to predict the flow behavior at high strain rates is also presented.

2   Experimental Procedure

The present study was carried out on SA516 Gr. 70 carbon steel plate material with the chemical composition as given in Table 1. The rest is that of Fe in the Table 1 for chemical composition of the material. The material was obtained as rolled and normalized in the form of a block of size 310 mm × 120 mm × 90 mm. Cylindrical sample of 5 mm diameter and 5 mm length was used for compression tests. The high strain rate tests were done at strain rates ranging from 450/s to 3500/s at room temperature. Molybdenum disulfide grease was used as lubricant to reduce friction at the bar–specimen interfaces. These high strain rate tests were carried out using the Split-Hopkinson Pressure Bar (SHPB) test set-up [4–6].

The output of a high strain rate SHPB test is the elastic strain generated in incident and transmission bar, as shown Fig. 1, measured by strain gauges in volts. The volt signal is converted to equivalent strain using the gauge factor and excitation voltage values. These elastic strains, namely, the reflected strain and transmitted strain are used to calculate the stress and strain in the test specimen. The expression given below provides the relation between the elastic strain generated in SHPB and specimen

Table 1 Composition of A516 Gr.70 Carbon steel (wt %)

C	Mn	Si	P	S	Ni	Cr	Cu
0.24	1.14	0.2	0.016	0.022	47 ppm	30 ppm	180 ppm
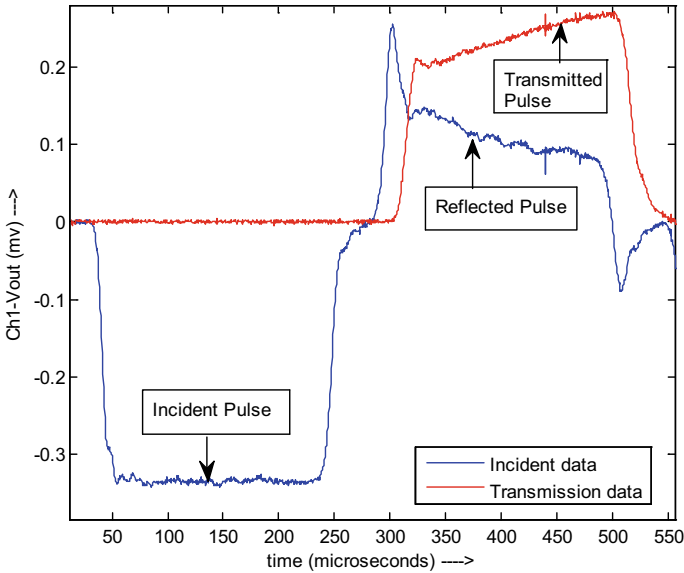
Fig. 1 Raw data output from SHPB test showing the incident and transmitted signal in volts

stress, strain and strain rate.

$$\text{Stress, } \sigma_s = \frac{A_0 E \varepsilon_t}{A_s} \tag{1}$$

$$\text{Strain, } \varepsilon_s = \frac{-2C_0}{L_s} \int_0^t \varepsilon_r dt \tag{2}$$

$$\text{Strain rate, } \dot{\varepsilon}_s = \frac{-2\varepsilon_r C_0}{L_s} \tag{3}$$

where A_o and A_s are the cross-section area of bar and specimen, C_0 is stress wave velocity for a wave of infinite wavelength, E is young's modulus of bar, L_s is length of specimen, σ_s, ε_s and $\acute{\varepsilon}_s$ are specimen stress, strain and strain rate, respectively. ε_r is the reflected strain in incident bar and ε_t is the transmitted strain in transmission bar.

3 Results and Discussion

The test data were processed using the equations mentioned in the previous section. The stress–strain curves obtained at different strain rates are presented in Fig. 2. The
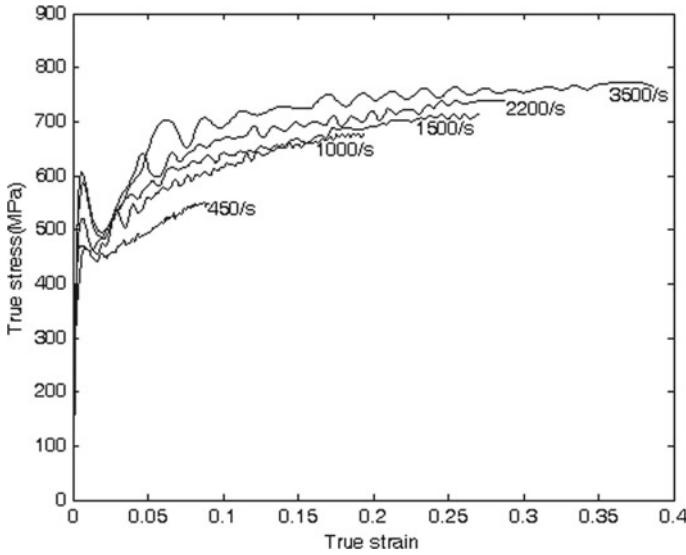
Fig. 2 Plot of adiabatic true stress versus true strain curves at room temperature. Nominal strain rate during the test are shown

flow stress of SA516 Gr.70, at high strain rates, increases with increasing strain rate. As the strain rate increases, the strain also increases. This is typical in compression SHPB. The oscillations seen in the curves are due to wave dispersion effects and not due to material property. All high strain rate tests are adiabatic in nature, i.e. the heat generated during high strain rate deformation does not have sufficient time to dissipate. This increases the specimen temperature.

To determine the isothermal stress–strain, the heat generated during the test has to be calculated and adjusted in terms of stress. The increase in specimen temperature is calculated as,

$$T = T_0 + \frac{\beta}{\rho C_p} \int_0^\varepsilon \sigma \, \partial\varepsilon, \tag{4}$$

Or

$$\Delta T = T - T_0 = \frac{\beta}{\rho C_p} \int_0^\varepsilon \sigma \, \partial\varepsilon, \tag{5}$$

where, T_0 is the initial temperature of the test, ΔT is rise in the specimen temperature due to adiabatic nature of the test, β is the fraction of heat dissipation due to plastic deformation assumed as 1 [7], ρ is the density of the material and Cp is the specific
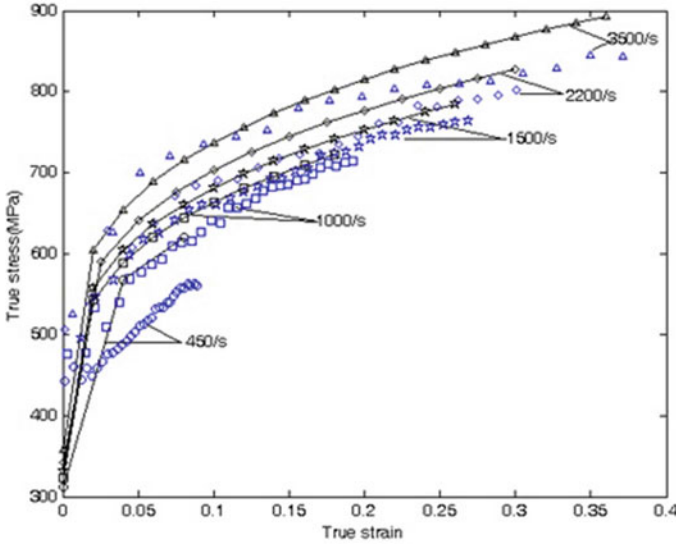
Fig. 3 CS material model fit to the isothermal stress–strain curves. Solid lines with marker are the constitutive model fit to experimental data represented by markers

heat at constant pressure. For SA516 Gr.70, the value of Cp is 490 J/kg.K and ρ is 7800 kg/m^3. The isothermal stress σ_{iso} is estimated from the adiabatic stress σ_{adbt} as,

$$\sigma_{iso} = \sigma_{adbt} - \frac{\partial\sigma}{\partial T}\Delta T, \tag{6}$$

where, the later term on RHS is the temperature sensitivity of stress as determined from the high strain rate experimental data of σ versus T. The experimental isothermal flow stress as determined from Eq. 6 of the high strain rate tests is shown in Fig. 3 onwards, in markers. The flow curves at different strain rates appear parallel to each other only being shifted vertically.

3.1 Fit to Constitutive Model

The use of a constitutive equation for material deformation is essential during FEM calculations in the plastic domain. There are numerous constitutive equations used to describe the flow behavior in both high and low strain rate regimes. The simplest are the ones at constant temperature and strain rates, where the only variation of flow stress is with strain. These are usually described using either power laws or an exponential relation. The strain rate effect on flow stress is also usually described using a power law and in some cases a logarithmic form. The effect of temperature

Table 2 Constants of CS model

A'	B'	p	D	q
295	580	0.27	35,000/s	1.5

on the flow stress of the material is either clubbed together with the strain rate term in models based on thermally activated deformation, or treated separately as a power law. A combination of the effect of strain, strain rate and temperature on the flow stress when represented as one equation is referred to as the constitutive model for plastic deformation of that material. The present high strain rate data were fit to the Cowper-Symonds (CS) [8, 9] model and a modified form of the Cowper-Symonds model. Quasi-static tension test data at room temperature were used to determine some of the constants in the equation.

3.2 Cowper-Symonds Model

The CS model is similar to the JC model in that the strain and strain rate terms are multiplicative; however, the effect of temperature is not included in this. The general form of CS model is,

$$\sigma = \left(A' + B' \varepsilon^p \right) \left(1 + \left(\frac{\dot{\varepsilon}}{D} \right)^{\frac{1}{q}} \right), \tag{7}$$

where, the first bracket is the static flow stress of the material as a function of plastic strain, and the second bracket is the effect of strain rate hardening on flow stress. The first term (work hardening) is of the power law type. This second term, referred as the dynamic hardening factor, is a function of power of strain rate rather than a logarithm term. The procedure for the determination of the parameters A', B', and p of Eq. 7 is similar to the one used in Ref. [6]. The constants A' is the yield stress of the material experimentally determined along with B' and p from quasi-static data. Using these constants and the high strain rate test data, constants D and q were calculated. The high strain rate data were fit to Eq. 7 (Fig. 3) using the constants as listed in Table 2. The fit of the data to the CS model was not satisfactory.

3.3 Modified Cowper-Symonds Model

As the Cowper-Symonds models did not fit the high strain rate data well, a modification to the dynamic hardening factor of the Cowper-Symonds model was made and used to fit high strain rate test data. A simple modification of removing the power

Table 3 Constants of modified CS model

A'	B'	p	C'	r
295	580	0.30	1900/s	0.20

from the strain rate to a power to the full strain rate term was used as the modified Cowper-Symonds equation,

$$\sigma = \left(A' + B' \varepsilon^{p} \right) \left(1 + \frac{\dot{\varepsilon}}{C'} \right)^{r},$$
(8)

where, A', B', p, r and C' are the constants to be calculated. A' is the yield stress of the material experimentally determined along with B' and p from quasi-static data. The constants C' and r are determined using high strain rate test data. The high strain rate data were fit to Eq. 8 using the constants as listed in Table 3 (Fig. 4). It is observed that the high strain rate data fit the modified Cowper-Symonds model better than the Cowper-Symonds model.
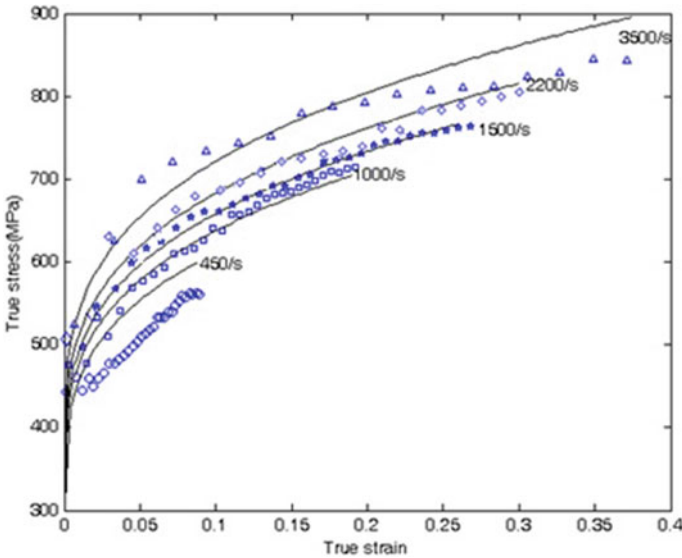
Fig. 4 Modified CS material model fit to the isothermal stress–strain curves. Solid lines are the constitutive model fit to experimental data represented by markers

4　Conclusion

The study of flow behavior of SA516 Gr.70 carbon steel material under dynamic loading conditions (strain rate range from 450/s to 3500/s) was carried out using SHPB at room temperature. The material is showing positive rate sensitivity in the strain rate range of the tests. Material constants for Cowper-Symonds and modified Cowper-Symonds model were determined. It was observed that the modified Cowper-Symonds model fitted the high strain rate experimental data better than the Cowper-Symonds model.

References

1. Yoon JH, Lee BS, Hong JH (1999) Effects of loading rate and temperature on J–R fracture resistance of an SA516-Gr.70 steel for nuclear piping. Int J Press Vessels Pip 76:663–670
2. Seok CS, Murty KL (1999) Effect of dynamic strain aging on mechanical and fracture properties of A516 Gr. 70 steel. Int J Press Vessels Pip 76:945–953
3. Seok CS, Kim SY (2002) Effect of specimen configurations on the fracture resistance curve. Nucl Eng Des 214:47–56
4. Bazle AG, Lopatnikov SL, Gillespie JW (2004) Hopkinson bar experimental technique: a critical review. Appl Mech Rev 57:223–250
5. Nemat-Nasser S (2000) Mechanical testing & evaluation. ASM Handbook, Ohio 8:427–436
6. Qianab X, Pengc X, Songc Y, Huanga J (2020) Dynamic constitutive relationship of CuCrZr alloy based on Johnson-Cook model. Nuclear Mater Energy 24
7. Kapoor R, Nemat-Nasser S (2000) Comparison between high and low strain-rate deformation of tantalum. Metall Mater Trans A 31:815–823
8. Jiang B, Wangb Z, Wang M, Yamb MCH, Ding F (2020) Effects of loading mode on mechanical properties of high strength steel Q690 and their application in coupon test. Constr Build Mater 253
9. Mahallea G, Kotkundea N, Gupta AK, Singh SK (2019) Cowper-Symonds strain hardening model for flow behaviour of inconel 718 Alloy. Mater Today: Proceed 18:2796–2801

Synthesis and Comparative Characterization of Electroless Ni–P, Ni–P-nano-Al$_2$O$_3$ and Duplex Ni–P/ Ni–P-nano-Al$_2$O$_3$ Coatings on Aerospace-Graded AA2024 alloy

Rajsekhar Chakrabarti, Souvik Brahma Hota, and Pradipta Basu Mandal

Abstract The essence of electroless coatings is realized by the scientists since last decade, which makes them a vital player in material coating industry. Incorporation of a second phase micro or nanoelement into the Ni–P matrix widens the area of applications for these types of coatings. Researchers are showing their interest to develop more innovative electroless coatings where they are deploying different types of second phase material to enhance their physical, mechanical and chemical properties. Duplex coatings have shown promising capabilities by providing excess hardness, wear and corrosion resistance, which can be attributed to the resultant effect of two consecutive layers of coating. In our research, three different types of electroless nickel phosphorous (EN) coatings were applied on the aerospace-graded AA2O24 alloy substrate. The first type was plain Ni–P coating, the second one was a composite coating where nanoalumina was incorporated into the electroless Ni–P matrix, and the third coating was a duplex coating with the inner layer having Ni–P and the outer layer consisting of a Ni–P layer incorporated with nanoalumina particles. Characterization of the deposits by scanning electron microscopy (SEM) along with energy dispersive X-ray spectroscopy (EDS) confirms the production of flawless, adherent coatings onto the substrate. Maintaining the surface roughness at an acceptable level, a great increase in nanohardness was observed that was further enhanced by incorporation of nano-Al$_2$O$_3$ particles and provision of one additional external layer in duplex coating. Excellent wear resistance was also evaluated by the nanoscratch test. On the basis of results obtained, this study suggested the superiority of the electroless duplex coating onto AA2024 substrates especially used in aerospace and defence industries.

Keywords Duplex coatings · Nanohardness · Nanoscratch test · Aerospace and defence industries

R. Chakrabarti · P. B. Mandal
Department of Mechanical Engineering, Techno India University, EM-4, Sector V, Salt Lake City, Kolkata, West Bengal 700091, India

S. B. Hota (✉)
Faculty, Department of Mechanical Engineering, Techno India University, EM-4, Sector V, Salt Lake City, Kolkata, West Bengal 700091, India
e-mail: souvik.h@technoindiaeducation.com

1   Introduction

Over the years, the lifespan of manufactured goods over the globe has played a great role in its sales. The fact that a product is indestructible could eventually be the new trend. Looking into the possibilities of a substance being damaged over a period of time can vastly depend on a few factors such as corrosion, lack of strength and thermal resistance. Eventually, finding a solid body with all of the qualities was proved to be hypothetical, and creation of solid alloys to work as a material replacement was expensive, and hence, coating of surfaces with alloys became a solution.

Substances with a great anticorrosive nature were vastly known by those of Ni and its alloys were known to do the job. With the property to be able to be coated around any surface irrespective of its texture and materials, Ni alloys were even more accepted. However, it is not as well reputed with magnesium, being very highly electrochemically active. Ni could only prove a coating, which could fail in case of physical erosion, and the results would be catastrophic.

In electroless duplex coating, two different layers are superimposed to yield a resultant coating, which exhibits drastic increment in hardness, wear resistance and frictional property due to the combined effect of both contributory layers. Introducing the second phase nanoalumina (Al_2O_3) into the Ni–P matrix of outer layer of the duplex coating will enhance further improvement of the coating qualities. Studies had been made and combinations were revealed for different surfaces, such as Duplex Ni–P/Ni–W–P coatings on AZ31B magnesium alloy [1], duplex electroless NiP/NiB coatings, with Nickel–phosphorous as the internal layer on 2024 aluminium alloys [2] and mild steel [3], Duplex Ni–P-ZrO_2/Ni–P coating on stainless steel [4] and of Duplex Ni–P-TiO_2/Ni–P nanocomposite coating onto brass substrates [5] etc. to name a few.

In this study, basically, three types of electroless coatings have been produced by using hypophosphite reduced bath, and nanosized alumina (Al_2O_3) is used as the second phase dispersed particle due to its high elastic modulus, great wear resistance and high stability at elevated temperature. An optimum concentration of alumina (Al_2O_3) has to be maintained in the electroless coating bath to achieve the desired level of mechanical and allied properties [6]. The reasons behind choosing AA2024 alloy as the substrate for our experiment are an enormous amount of strength and fatigue resistance, which has widened its application in aircraft structural parts, especially wing and fuselage structures under tension. In spite of having those lucrative properties AA2024 shows poor resistance to corrosion, which drives us to develop these coatings over it. To achieve excellent corrosion resistance, high phosphorus Ni–P coating was prepared as the inner layer, while low phosphorus outer layer that is sol-enhanced Ni–P–Al_2O_3 coating was deposited to strengthen the mechanical property. Varying percentage of phosphorus in the inner and outer layers was simply achieved by changing the phosphoric acid (H_3PO_4) content in the bath. Morphology, composition, mechanical properties of all the coatings were systematically investigated in this paper.

Table 1 Chemical composition of AA2024 alloy substrate

Chemical composition [wt.%]						
Cu	Mn	Mg	Si	Fe	Zn	Ti
4.1	0.6	1.4	0.5	0.5	0.25	0.15

2 Experimental Details

2.1 Surface Preparation

The AA2024 alloy sheet of 2 mm thickness that is basically used for flap material is procured from Air India maintenance section and cut into 20 × 20 mm of pieces, which is suitable for our electroless coating arrangement. The chemical composition of the substrate is presented in Table 1. One corner side of the square-shaped sample was drilled to make small hole for hanging the sample during coating process. The surface of the substrate was ground and polished with 320, 800, 1200, 2000 grit SiC (emery) paper to maintain the roughness of the surface nearly 0.2 µm [7].

Final polishing with diamond abrasion paper is carried out after all consecutive grinding and polishing were performed. This made a smoother substrate surface with negligible amount of unevenness needed for the coating.

2.2 Pretreatment and Activation

Pretreatment process includes keeping the sample in soap water at 40 °C for 5 min, which is followed by acetone cleaning for removing dust and dirt from the surface. After a thorough cleaning, the sample is subjected to acid pickling for getting oil and grease-free surface with 10% HCl. Finally, samples are required to be activated before putting into the electroless bath. Generally, there are some recommendations to use Ni striking [1] or $PdCl_2$ solution [8] activation technique in various researches; here we use a combination of $PdCl_2$ and $SnCl_2$ solution with proper proportion of the constituents to make a activator solution for our experiment. Although we tried with our very own two-step acid activation technique to minimize the cost but results are not satisfying as it leads to corrosion of AA2024 substrate. After completion of the combination of $PdCl_2$ and $SnCl_2$ solution activation, samples are readily dipped into the electroless solution, which already attains an initial temperature of 80 °C and pH of 5.5.

2.3 Bath Preparation

Electroless bath for each type of coating comprises some basic constituents like a source of nickel ion, a reducing agent, a stabilizer, a complexing agent and the buffer, which are more or less same for all the three types of electroless coating solution for our experiment. A surfactant is the additional chemical needed for increasing the wettability of the second phase nanoalumina (Al_2O_3) particle to have a better inclusion in Ni–P matrix to develop good nanocomposite and duplex nanocomposite coating. The details of bath compositions of electroless Ni–P, Ni–P-nano-Al_2O_3 composite and duplex Ni–P/Ni–P-nano-Al_2O_3 composite coatings are shown in Table 2.

The bath composition for duplex coating shown in Table 2 is for the second bath, which is used to get outer coating of Ni–P-nano-Al_2O_3. Inner Ni–P coating will be developed by the bath composition used for plain Ni–P coating as shown in the Table 2. All the constituents of the bath need to mix with required amount of distilled water solution and stirred well in a Borosil beaker with the help of a magnetic stirrer (Tarsons Spinot). A mercury in-glass thermometer (Erose, Maximum range: 360 °C) is placed inside the bath to measure temperature and a universal pH indicator (Merck) is used to get the pH of the bath.

Table 2 Chemical composition of the bath

Constituents	Ni–P	Ni–P-nano-Al_2O_3	Duplex-P/Ni–P-nano-Al_2O_3
Metal ions	Nickel Sulphate 35 g/l	Nickel Sulphate 35 g/l	Nickel Sulphate 35 g/l
Reducing agents	Sodium Hypophosphite 15 g/l	Sodium Hypophosphite 15 g/l	Sodium Hypophosphite 15 g/l
Complexant	Sodium Succinate 12 g/l	Sodium Succinate 12 g/l Sodium Acetate 5 g/l	Sodium Succinate 10 g/l Sodium Acetate 5 g/l Sodium Citrate 5 g/l
Stabilizers	_	Lead Acetate 1 mg/l	Lead Acetate 2 mg/l
Surfactant	_	Sodium Dodecyl Sulphate 0.2 g/l	Sodium Dodecyl Sulphate 0.2–0.4 g/l
Second phase particle	_	Nano-Al_2O_3 (APS:20-30 nm) 5 g/l	Nano-Al_2O_3 (APS:20-30 nm) 5 g/l
	_	H_3PO_4	H_3PO_4
Temperature	80–90 °C	85–90 °C	82–90 °C
pH	5–6	4.5–5.5	4.5–5.5
Time	2 h	2.5 h	3 h

2.4 Nanoalumina Sol Preparation

Nanoalumina (Al_2O_3) powder is collected from Sisco Research Laboratories (SRL) with average particle size of 20–30 nm. Sol of 5 g/l nano-Al_2O_3 powder is prepared by mixing it with 15 ml of distilled water by ultrasonic agitator (LABMAN) for 15 min. For the electroless Ni–P-nano-Al_2O_3 composite coating, the sol is to be added after the first hour of coating. In case of duplex coating, this has to be added to the second solution for the outer layer of the coating only after 30 min of coating. The dispersion of second phase nanoalumina particle is maintained by proper stirring done by a magnetic stirrer cum heater (TarsonsSpinot) used for our experiment.

2.5 Sample Characterization

The surface morphology of electroless Ni–P, Ni–P-nano-Al_2O_3 composite and duplex Ni–P/Ni–P-nano-Al_2O_3 composite coating is assessed by Scanning Electron Microscope (HITACHI S-3400 N). HORIBA EMAX Si (Li)-Liquid nitrogen cooling type x-ray detector, which is integrated with the SEM, is used for composition analysis of these coatings. Nanoindentation test is performed to evaluate the individual hardness of the coating and also to justify the purpose of nanoalumina inclusion along with the duplex coating. A CSM NHTX S/N: 55-0019 nanohardness tester (NHT) calibrated on pure silica and aluminium and used for this purpose. A triangular pyramidal diamond indenter (Berkovichtip, B-I 93) with a tip radius of 0.2 μm under a constant load of10 mN and the pause time was 2 s. The loading rate was 20 mN/min, and unloading rate was also kept at.20 mN/min with a data acquisition rate of 10 Hz. The hardness was calculated using the Oliver-Pharr analysis method [9–11], which could be executed from the software provided by CSEM Instruments. Instrumented elastic moduli (EIT) were estimated from the initial gradient of the unloading curves using the Oliver and Pharr [12] model. Nanoscratch test was performed using CSM NST: 50–133 nanoscratch tester under a normal load of 5 mN with a scratching speed of 1.2 mN/min, and the length of the scratch was ~5 mm to measure the wear rate of the coatings. A typical single scratch test has been carried out on the coating with a loading rate of 10 mN/min. The Sphero-conical diamond indenter's (SB-A63) tip radius was 2 μm.

3 Results and Discussions

3.1 Surface Morphology and Composition

SEM micrographs of Ni–P-nano-Al_2O_3 composite coating with concentrations of 5 g/L of alumina (Al_2O_3) are shown in Fig. 1b. In Ni–P-nano-Al_2O_3 coating, second
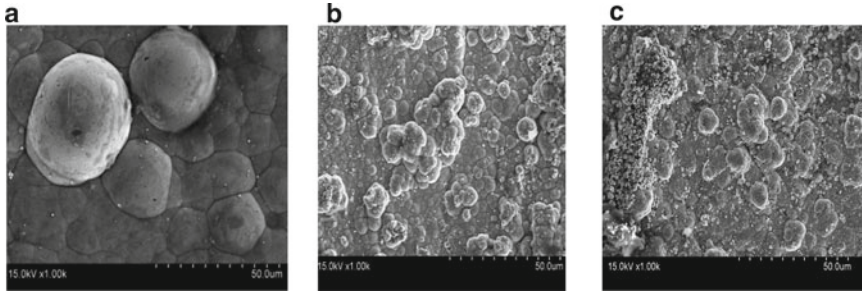
Fig. 1 SEM micrograph of various electroless coatings. **a** Ni–P coating, **b** Ni–P-nano-Al_2O_3 composite coating, **c** Duplex Ni–P-nano-Al_2O_3/Ni–P composite coating
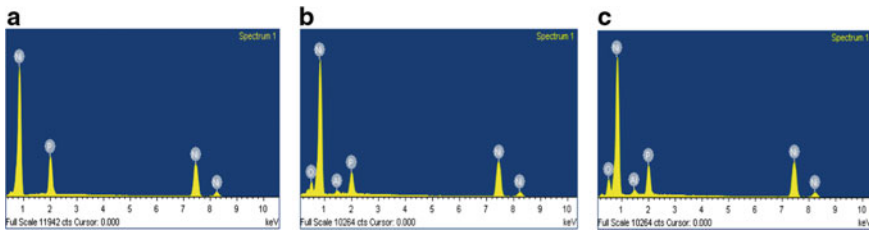
Fig. 2 Composition of various electroless coatings. **a** Ni–P coating, **b** Ni–P-nano-Al_2O_3 composite coating, **c** Duplex Ni–P-nano-Al_2O_3/Ni–P composite coati**ng**

phase white nanoalumina particles are successfully co-deposited and uniformly distributed throughout the Ni–P matrix. The alumina particles take their place in Ni–P matrix. The co-deposition of nano-Al_2O_3 particles increases the catalytic actives sites and, thus, increases the reduction of nickel ions. The randomly adsorbed nano-Al_2O_3 particles on the surface were covered by nickel due to further reduction reaction, which leads to dim surface of the coating compared to plain Ni–P coating. No superficial surface damage is found, and the coating appears to be dense.

The EDX analyses of coated samples are shown in Fig. 2a–c. The peaks shown in Fig. 2a of nickel and phosphorous are quite specific with respect to the obtained parameters in this experiment. Figure 2b, c shows additional peaks of aluminium and oxygen, which confirms the inclusion of second phase nanoalumina particles in Ni–P matrix for the last two cases where we suppose to prepare electroless Ni–P-nano-Al_2O_3 composite coating and duplex Ni–P-nano-Al_2O_3/Ni–P composite coating.

3.2 Hardness

Figure 3 shows the typical load versus depth of indentation curve of Ni–P, Ni–P-nano-Al_2O_3 composite and duplex Ni–P/Ni–P-nano-Al_2O_3 composite coatings, in
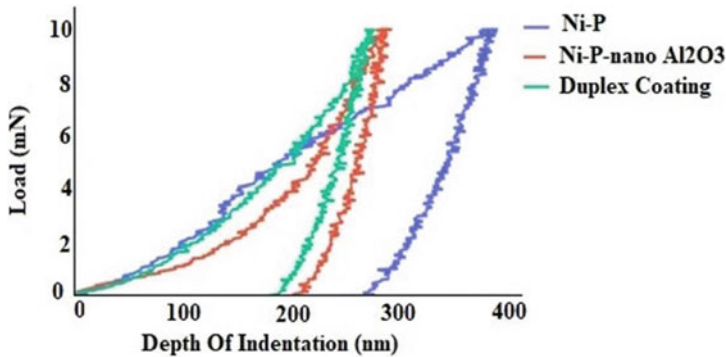
Fig. 3 Load–displacement curves for Ni–P, Ni–P-nano-Al$_2$O$_3$ composite and duplex Ni–P/Ni–P-nano-Al$_2$O$_3$ composite coatings during nanoindentation test

which residual depth (h$_r$), maximum depth (h$_{max}$) have been shown. Ni–P coating exhibits h$_r$ value of 313.83 nm while the value is 232.99 nm for Ni–P-nano-Al$_2$O$_3$ composite coating, and for duplex Ni–P-nano-Al$_2$O$_3$ coating, the value is 216.77 nm. Hence, ~25.75% reduction in residual depth of Ni–P-nano-Al$_2$O$_3$ composite coating was observed, and for duplex Ni–P-nano-Al$_2$O$_3$/Ni–P composite coating there is a reduction of ~6.96% in residual depth, indicating the increase in hardness of the Ni–P-nano-Al$_2$O$_3$ and duplex Ni–P-nano-Al$_2$O$_3$/Ni–P composite coatings. The average hardness value for Ni–P coating was 278.02 Hv. It gets increased to 654.62 Hv in case of Ni–P-nano-Al$_2$O$_3$ composite coating. Further increase in hardness is found in case of duplex Ni–P-nano-Al$_2$O$_3$/Ni–P composite coating up to 828.67 Hv. Improvement in hardness nanocomposite coating could be attributed to the incorporation of the hard Al$_2$O$_3$ particles in the coating. The duplex Ni–P-nano-Al$_2$O$_3$/Ni–P composite coating achieved higher hardness due to two consecutive factors; (a) development of dual layer and (b) incorporation of nano-Al$_2$O$_3$ particles in the outer layer.

3.3 Elastic Modulus

Instrumented elastic modulus (E$_{IT}$) for electroless Ni–P coating is found to be 60.957 GPa, for Ni–P-nano-Al$_2$O$_3$ composite coating the value of instrumented elastic modulus is increased to 145.09 GPa with a drastic improvement of 138%. This shows the inclusion of nano-Al$_2$O$_3$ particles in the Ni–P matrix makes the coating capable enough to resist deformation. Duplex Ni–P/Ni–P-nano-Al$_2$O$_3$ composite coating shows further improvement in elastic modulus up to 150.94 GPa (4.03% increment). This attributes the fact of additional outer layer of duplex coating gives some percentages of additional resistance to deformation. These increments of elastic modulus establish the fact of increased hardness for nanocomposite and duplex coatings.
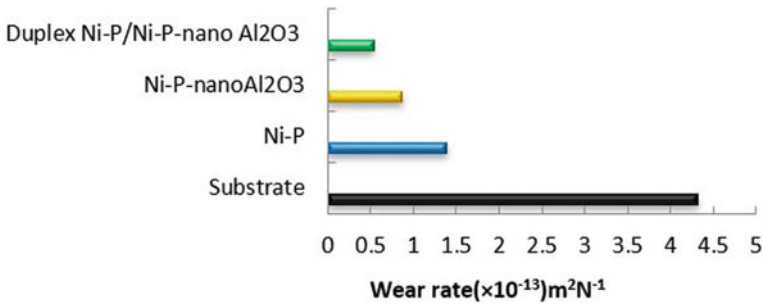
Fig. 4 Wear rate for different coatings and substrate as per nanoscratch test

3.4 Wear Resistance

At a constant load of 5 mN, the wear rate of the scratch of electroless Ni–P coating was found to be $1.39 \times 10^{-13} \mathrm{m}^2 \mathrm{~N}^{-1}$ while the wear rate of the scratch of Ni–P-nano-Al_2O_3 coating was observed to be $0.87 \times 10^{-13} \mathrm{m}^2 \mathrm{~N}^{-1}$, and for duplex Ni–P-nano-Al_2O_3/Ni-Pcomposite coating, it was much reduced to $0.54 \times 10^{-13} \mathrm{m}^2 \mathrm{~N}^{-1}$. The wear rate for different coatings is shown in Fig. 4. The weight loss during the nanoscratch test for AA2024 substrate is highest under the applied load. Lesser weight loss in case of the coated samples shows their better wear resistance than that of AA2024 substrate. Incorporation of nanosized alumina is observed to increase the wear resistance of the coating in last two cases. Additional improvement in wear resistance for duplex Ni–P-nano-Al_2O_3/Ni–P composite coating can be attributed to the combined effort of dual layer of this coating.

4 Conclusions

Co-deposition of alumina particles in Ni–P electroless coating changes surface morphology of deposits with alumina in Ni–P-nano-Al_2O_3 composite coating and duplex Ni–P-nano-Al_2O_3/Ni–P composite coating. Cauliflower-type spherical shapes are formed for Ni–P coating, which are basically having 30–40 μm of diameter. These spheres are nickel and smaller nodular structure represents phosphorous. Nanoalumina (Al_2O_3) when included with Ni–P matrix produces nanocomposite coating, and the whitish and blackish small particles in SEM image are nothing but the included alumina particles in the composite coating. Same particle inclusion also takes place in the outer layer of duplex coating, which is confirmed in composition analysis. Ni–P coating shows 278.02 Hv of hardness value, which increased about 135% in case of Ni–P-nano-Al_2O_3 coating, which is mainly attributed to the inclusion of hard alumina particles into the Ni–P matrix. Along with this particle inclusion effect, it is observed that there is an increment of 26.58% in hardness value (828.67 Hv) in case of the duplex composite coating. This additional hardness increment is

the resultant effect of inner and outer layer of the coating. Wear resistance is also improved for electroless nanoalumina composite and duplex composite coating, and this can be attributed to the improving hardness value. Therefore, it is revealed from the present experiment that duplex Ni–P-nano-Al$_2$O$_3$/Ni–P composite coating is an excellent protective coating for AA2024 alloy. Electrochemical Impedance Spectroscopy (EIS) is a powerful tool to study the corrosion resistance of coatings, which can be used in the further investigation of the corrosion properties of these coatings.

References

1. Selvi VE, Chatterji P, Subramanian S, Balaraju JN (2014) Autocatalytic duplex Ni–P/Ni–W–P coatings on AZ31B magnesium alloy. Surf Coat Technol 240:103–109
2. Vitry V, Sens A, Kanta AF, Delaunois F (2012) Wear and corrosion resistance of heat treated and as-plated Duplex NiP/NiB coatingson 2024 aluminum alloys. Surf Coat Technol 206
3. Sankara Narayanan TSN, Krishnaveni K, SeshadriSK (2003) Electroless Ni–P/Ni–B duplex coatings: preparation and evaluation of microhardness, wear and corrosion resistance. Mater Chem Phys 82: 771–779
4. Wang YX, Shu X, Wei SH, Liu CM, Gao W, Shakoor RA et al (2015) Duplex Ni-P-ZrO2/Ni-P electroless coating on stainless steel. J Alloy Compd 630:189–194
5. Zhang W, Cao D, Qiao Y, He Z, Wang Y, Li X, Gao W (2019) Microstructure and properties of duplex Ni-P-TiO2/Ni-P nanocomposite coatings. Mater Res 22(Suppl. 2): e20180748. Epub
6. Alirezaei S, Monirvaghefi SM, Salehi M, Saatchi A (2004) Surf Coat Technol 184:170
7. Karthikeyan S, Vijayaraghavan L (2016) Influence of Nano Al$_2$O$_3$ particles on the adhesion, hardness and wear resistance of electroless NiP coatings. Int J Mater Mech Manuf 4(2):106–110
8. Gadhari P, Sahoo P (2014) Study of tribological properties of electroless Ni–P–Al$_2$O$_3$ composite coatings. IOSR J Mech Civil Eng: 34–37
9. Carrasco CA, Vergara V, Benavente R, Mingolo N, Ríos JC (2002) The relationship between residual stress and process parameters in TiN coatings on copper alloy substrates. Mater Charact 48:81–88
10. Oliver WC, Pharr GM (2004) Measurement of hardness and elastic modulus by instrumented indentation: advances in understanding and refinements to methodology. J Mater Res 19(1):3–20
11. Fischer-Cripps AC (2006) Critical review of analysis and interpretation of nanoindentation test data. Surf Coat Technol 200(14–15):4153–4165
12. Oliver WC, Pharr GM (1992) Improved technique for determining hardness and elastic modulus using load and displacement sensing indentation experiments. J Mater Res 7(6):1564–1580

Clamped Beam Bending for Mixed Mode Fracture Toughness Measurements

Ashwini Kumar Mishra, Neha Kumari, and Balila Nagamani Jaya

Abstract Clamped beam bending geometry has been successfully used for evaluation of mode-I fracture toughness on micro and macro specimen (Jaya B, N., Jayaram, V. & Biswas, S. K.: A new method for fracture toughness determination of graded (Pt,Ni)Al bond coats by microbeam bend tests. Philos. Mag. 92, 3326–3345 (2012).; Mishra, A. K., Lambai, A., Jayaram, V. & Jaya, B. N.: The edge-notched clamped beam bend specimen as a fracture toughness test geometry. Theor. Appl. Fract. Mech. 105, 102,409 (2020) [1, 2]. The present study explores the utility of clamped beam bending for studying mixed mode fracture. Mode-I and mode-II stress intensity factor solutions are obtained by changing the position of the loading point with respect to the notch (offset), and of angular notches with respect to the loading axis. Mode-II stress intensity factor is computed as a function of the loading offset and relative crack length using the finite element method (FEM). FEM results show that clamped beam with offset loading point is able to provide pure mode I, pure mode II and any mixed mode loading condition for L/W = 4 with a/W = 0.5 to 0.7. Clamped beam with angled crack shows pure mode I and mixed mode but can't provide pure mode II. Using this information, mixed mode fracture trajectory is predicted, which is relevant for the evaluation of fracture behavior of multilayered and composite structures.

Keywords Mixed mode · Clamped beam bending · FEM

1 Introduction

Cracks or flaws generate in engineering components during manufacturing or loading during service eventually lead to failure of the component. These components are subjected to complex loading conditions during their service life, which leads to mixed mode failure, i.e. a combination of mode-I and mode-II. It is well known that

A. K. Mishra (✉) · N. Kumari · B. N. Jaya
Department of Metallurgical Engineering and Materials Science, Indian Institute of Technology Bombay, Mumbai 400076, India

the fracture resistance of a material is dependent on mode mixity [3]. Therefore, it becomes important to analyze mixed mode failure.

Some geometries that have been suggested in the literature for the analysis of mixed mode brittle fracture are described here. Rectangular plate with inclined crack and subjected to tension is one of the oldest geometries used to study mixed mode failure [4]. Asymmetrically loaded three or four point bend geometry [5, 6], Brazilian disk geometry [7, 8], semi-circular bend geometry [9–11] and compact tension-shear geometry [12, 13] have all been used for mixed mode failure studies of various engineering materials. Edge notch disc bending geometry [14–16] and diagonally loaded square plate containing center crack [17] are recent geometries for mixed mode failure analysis.

In the recent past, clamped beam bending geometry [1, 2, 18] has emerged as a technique for the evaluation of mode-I fracture toughness at both micro and macro scales. This geometry is suitable for fracture testing because of easy sample preparation and easy loading fixtures and due to the intrinsic stability during crack propagation. Therefore, modified clamped beam bending is proposed for mixed mode failure analysis in this paper. Mode mixity is varied by a) changing the position of the loading point with respect to crack (offset) and b) by creating angular cracks with respect to the loading axis. Various aspects of mode mixity are analyzed using finite element method (FEM), and the results are presented below.

2 Simulation Procedure

The clamped beam bending geometry with offset loading is shown in Fig. 1a. Loading point was offset with respect to crack by distance L_o. The state of mode mixity was introduced by varying this offset distance (L_o). When L_o is zero, loading condition is symmetric with crack line and specimen is subjected to pure mode I. But with increasing L_o, mode II begins to appear. Stress intensity factor for mode-I and mode-II was determined by FEM.
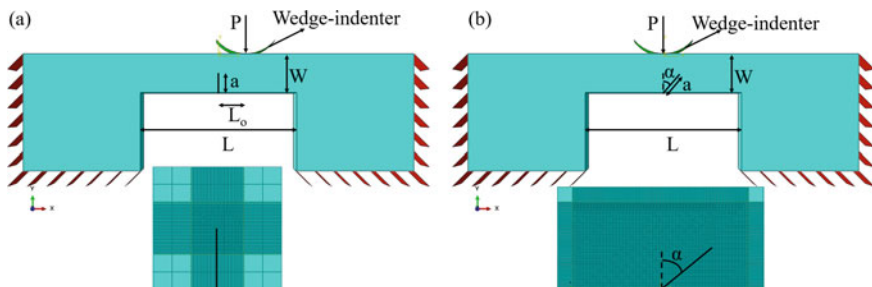
Fig. 1 Finite element model of a clamped beam bending with **a)** offset loading point and **b)** angular crack

The beam was modeled as three-dimensional (3-D) deformable body of dimensions: length (L) × Width (W) × Thickness (B). Three lengths were chosen—40 mm, 80 mm and 160 mm, while keeping W constant at 10 mm, to obtain L/W ratios of 4, 8 and 16. The thickness (B) was also maintained constant at 6 mm. Crack length (a) was varied to obtain five a/W ratios ranging from 0.3 to 0.7 at intervals of 0.1. Offset distance of loading point (L_o) was varied to obtain eleven L_o/L ratios ranging from 0 to 0.475 at intervals of 0.05 up to 0.45. Linear elastic fracture mechanics (LEFM) formulation was used for the simulations. Encastered boundary condition was applied to the two sides and bottom of clamped beam legs. A wedge indenter of 10 mm tip radius was used to load the beam. Loads of 250 N, 125 N and 62.5 N were applied on beams of L/W ratios of 4, 8 and 16, respectively, to maintain a constant stress of 16.67 MPa, as given by:

$$\sigma = \frac{PL}{BW^2} \tag{1}$$

The indenter was restricted to move only along the y-direction. A fine mesh was used in a partitioned domain around the crack (Fig. 1a) as well as close to loading point. C3D8R (8-node bilinear brick element) type of elements were used in the three-dimensional (3-D) model. A total of ~93,724 elements were used for the simulation.

The clamped beam bending geometry with an angular crack is shown in Fig. 1b. The state of mode mixity was introduced by changing the angle 'α' of the crack with respect to the vertical while maintaining the loading position at $L_o = 0$. The crack was rotated by fixing the bottom edge position and the angle α is varied from 0 to 80° at intervals of 10°. Stress intensity factors for mode-I and mode-II was again determined using FEM. A constant L/W ratio of 4 was used with 250 N applied load.

3 Results and Discussion

3.1 Clamped Beam Bending with Offset Loading Point

The stress intensity factor (K) of the clamped beam bending geometry for a given L/W and loading point offset can be written as

$$K_I = \frac{PL}{BW^2} \sqrt{\pi a} Y_I \left(\frac{a}{W}, \frac{L_o}{L} \right) \tag{2}$$

$$K_{II} = \frac{PL}{BW^2} \sqrt{\pi a} Y_{II} \left(\frac{a}{W}, \frac{L_o}{L} \right) \tag{3}$$

where P, W, B, L, L_o and a are applied load, specimen width, thickness, length, offset distance and crack length, respectively. Y_I and Y_{II} are the geometric factors

(normalized stress intensity factors) in mode I and mode II, respectively, as a function of relative crack length (a/W) and relative offset (L_o/L).

Figure 2 shows the normalized K_I and K_{II} as a function of L_o/L for various a/W ratios for the three L/W ratios of 4, 8 and 16. Only the magnitudes of normalized K_I and K_{II} are shown here. In all cases, the specimen is subjected to pure mode-I condition at L_o/L = 0. As L_o/L increases, normalized K_I decreases gradually, while normalized K_{II} increases rapidly initially and then decreases gradually. The normalized K_I
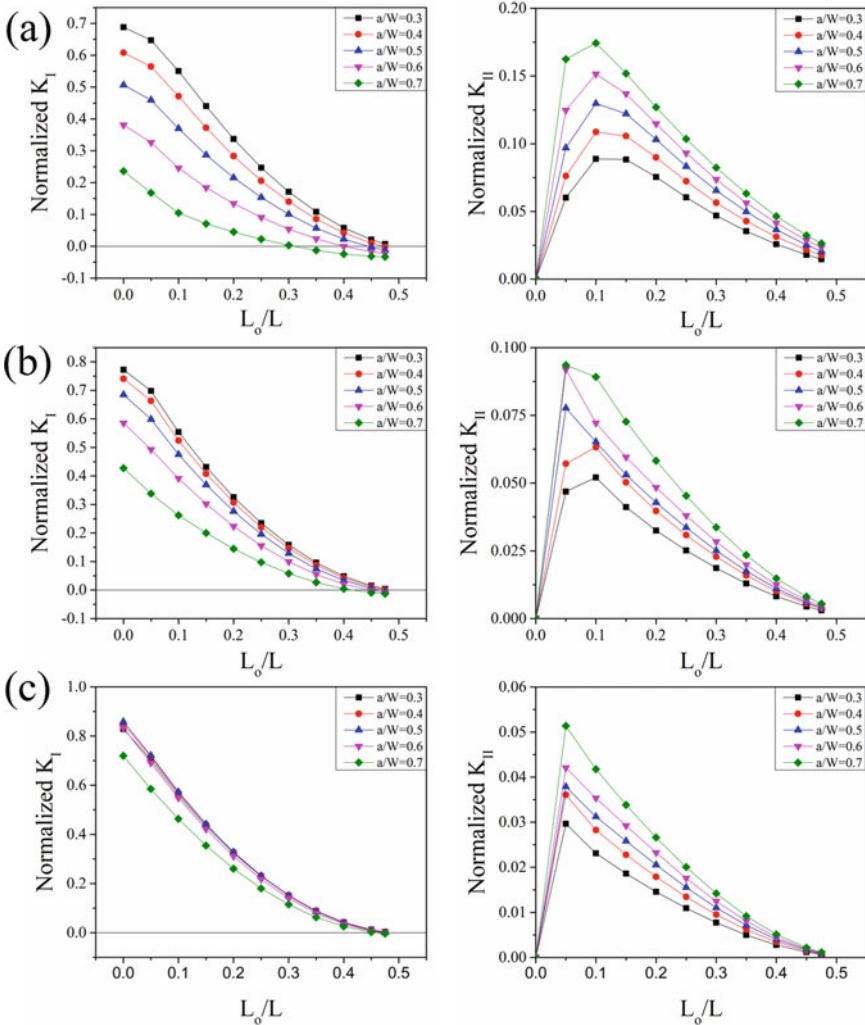
Fig. 2 Variation of Normalized K_I and Normalized K_{II} with L_o/L for L/W ratios of: **a)** 4, **b)** 8 and **c)** 16 in a clamped beam bending with offset loading point

became zero at increasingly higher L_o/L at higher a/W ratios for the three L/W ratios. On the other hand, the normalized K_{II} remained nonzero at all a/W ratios but decreased to values increasingly closer to zero with an increase in the L/W ratios.

Normalized K_I never reaches zero for low a/W ratios of 0.3. For higher L/W ratios, as normalized K_I reaches zero, normalized K_{II} also decreases (Fig. 2b, c). Figure 3a shows the L_o/L corresponding to pure mode-II condition for various a/W and L/W ratios. Considering all these factors, pure mode-II condition is best achieved in a specimen of L/W = 4 for a/W = 0.6 at a L_o/L = 0.4 (Fig. 2a). This offset distance is neither too close to the clamped boundary nor to the center position. For the same beam dimensions, the maximum mode-II occurs at a L_o/L = 0.1 where K_{II}/K_I = 0.62. A ratio of K_{II}/K_I = 1 is achieved at L_o/L = 0.24, for a/W = 0.6, L/W = 4 (Fig. 3b). In case of higher L/W ratios, it leads to increasing offset before K_{II}/K_I = 1 is achieved. Since an L/W ratio of 4 with low a/W ratio of ~ 0.37 is already recommended to achieve stable crack growth in pure mode-I [2], this outcome is beneficial for experimental measurements. Thus, the clamped beam bending can be used to achieve both pure mode-I and pure mode-II loading conditions by changing the loading offset, and enabling the same specimen to be used for mode-I, mode-II and mixed mode fracture toughness measurements. However, it is important to note that the absolute value of normalized K_{II} is significantly lower than normalized K_I requiring much higher load for fracture to occur under mode-II and mixed mode conditions.

The maximum principal stress (MAXPS) contours for clamped beams bending with L/W = 4 and a/W = 0.6 in the three different modes: pure mode-I (K_{II} = 0), mixed mode loading (K_{II}/K_I = 1) and pure mode-II (K_I = 0) are shown in Fig. 4. The stress contours are symmetric relative to crack plane in pure mode-I and asymmetric for mixed mode loading. It can be observed that shape of the stress contours at crack the tip is affected by mode mixity. These maximum principal stress (MAXPS) contours can be used as a first approximation to predict the crack trajectories under
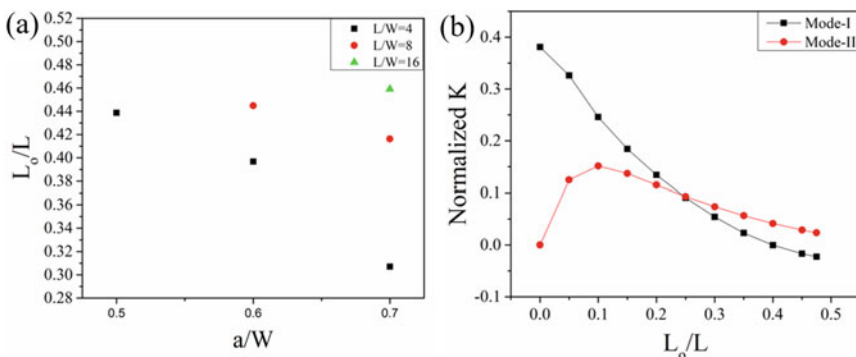
Fig. 3 a) L_o/L corresponding to pure mode-II condition in clamped beam bending with offset loading point geometry and for different values of a/W and L/W b) Normalized K for mode-I and mode-II with L_o/L for L/W = 4 and a/W = 0.6
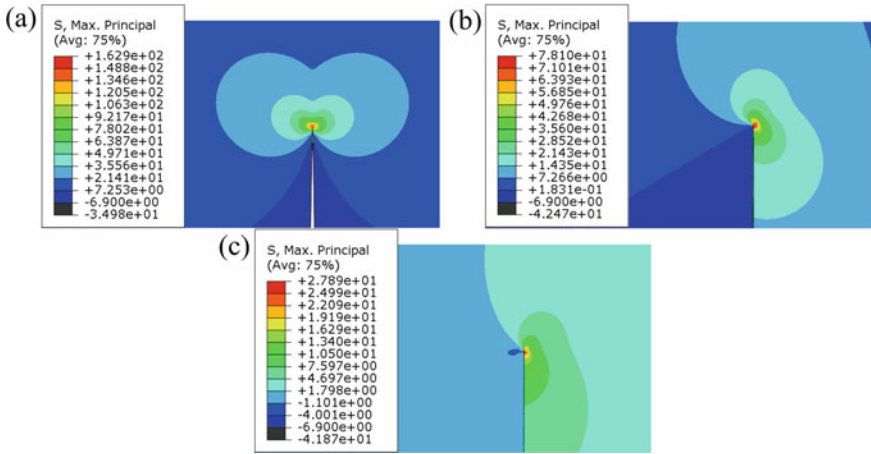
Fig. 4 Maximum principal stress contours in front of the crack tip for clamped beam bending with offset loading point (L/W = 4, a/W = 0.6) for **a)** pure mode-I, **b)** mixed mode ($K_I = K_{II}$) and **c)** pure mode-II

these various loading conditions following the Maximum tangential stress (MTS) criteria. The angle of crack growth is predicted with respect to initial crack plane and considered + ve clockwise. Accordingly, the crack will propagate at angles of 0°, 66.6° and 75.6° for pure mode-I, mixed mode and pure mode-II, respectively.

3.2 Clamped Beam Bending with Angular Crack

The stress intensity factor of clamped beam bending geometry with an angled crack for a given L/W ratio can be expressed as:

$$K_I = \frac{PL}{BW^2}\sqrt{\pi a}Y_I\left(\frac{a}{W}, \alpha\right) \tag{4}$$

$$K_{II} = \frac{PL}{BW^2}\sqrt{\pi a}Y_{II}\left(\frac{a}{W}, \alpha\right) \tag{5}$$

where, P, W, B, L, α and a are applied load, width, thickness, length, crack angle and crack length, respectively. Y_I and Y_{II} are normalized stress intensity factors of mode-I and mode-II, respectively, as stated earlier. Figure 5 shows normalized K_I and K_{II} as a function of α for various a/W ratios. In all cases, specimen is subjected to pure mode-I condition at α = 0. As α increases, normalized K_I decreases gradually, normalized K_{II} increases initially, reaches a maxima and then decreases. In particular, the point of maximum of normalized K_{II} shifts to higher α values with decreasing a/W ratios. The magnitude of normalized K_{II} at the maximum decreases with increasing a/W
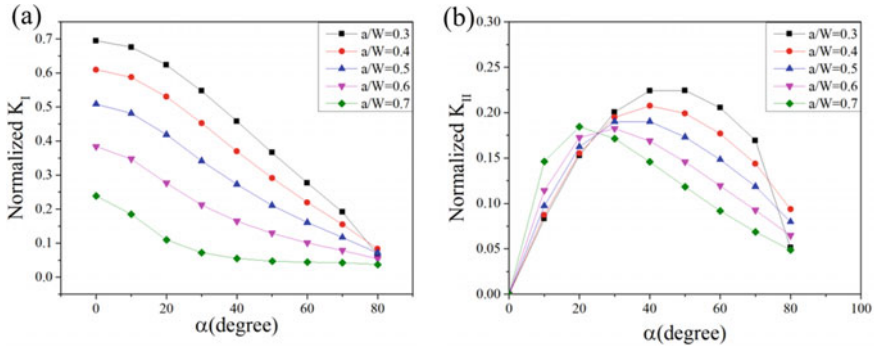
Fig. 5 Variation of **a)** Normalized K_I with α for different a/W ratios and **b)** Normalized K_{II} with α for different a/W ratios for a clamped beam bending with angular crack

ratios. An exception was observed at a/W ratio $= 0.7$, where the maximum is higher than the one at 0.6. Nevertheless, since normalized K_{II} decreases at high α values, mixed mode loading condition will occur. Normalized K_I never becomes zero in this condition, so pure mode-II condition will not be achieved in a clamped beam bending with angular crack. The maximum value of $K_{II}/K_I = 2.64$ can be achieved for an L/W $= 4$, a/W $= 0.7$ and $\alpha = 39.16°$. Hence, in case of angled cracks, longer cracks are preferable for achieving higher mode mixity.

Figure 6 shows the MAXPS contours of the clamped beam bending (L/W $= 4$, a/W $= 0.6$) with crack angle 0° (pure mode-I), 15° (mixed mode) and 38.7° (mixed
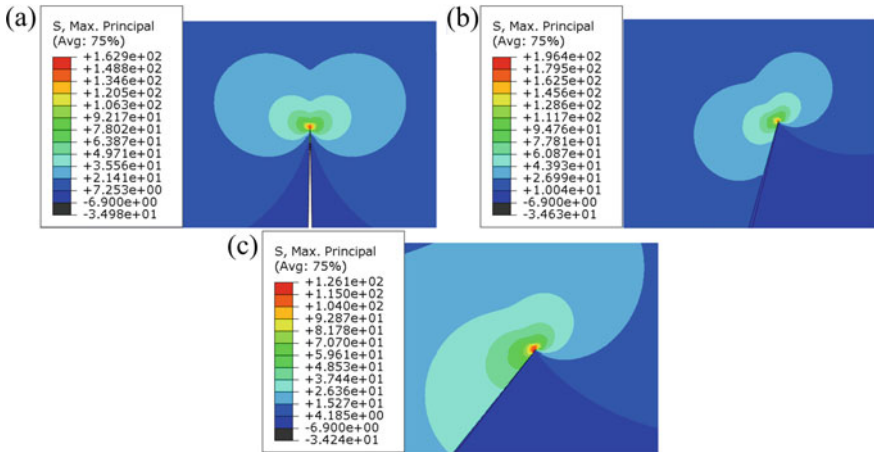
Fig. 6 Maximum principal stress contours in front of the crack tip for a clamped beam bending with angular crack (L/W $= 4$, a/W $= 0.6$) for **a)** pure mode-I ($\alpha = 0°$), **b)** mixed mode ($\alpha = 15°$) and **c)** mixed mode, $K_I = K_{II}$ ($\alpha = 38.7°$)

mode, $K_I = K_{II}$), predicting crack trajectories at angle of $0°$, $-28.4°$ and $-55.5°$ with respect to initial crack plane, respectively.

4 Conclusion

Mixed mode loading was studied for a clamped beam bending with offset loading and angular crack using finite element modeling. Clamped beam bending with offset loading is a simple and practical geometry to achieve not only pure mode-I and mode-II but also an entire range of mixed mode loading conditions. A beam with L/W = 4 and a/W = 0.6 with varying offset was found to be optimal for studying and testing mixed mode fracture behavior of brittle materials. Also, a clamped beam with an angular crack provides mixed mode loading as well, but it does not include the pure mode-II condition. The extent of mode mixity ratio K_{II}/K_I that it can achieve is highest at a crack angle $39.16°$ for a/W = 0.7.

References

1. Jaya BN, Jayaram V, Biswas SK (2012) A new method for fracture toughness determination of graded (Pt,Ni)Al bond coats by microbeam bend tests. Philos Mag 92:3326–3345
2. Mishra AK, Lambai A, Jayaram V, Jaya BN (2020) The edge-notched clamped beam bend specimen as a fracture toughness test geometry. Theor Appl Fract Mech 105:102409
3. Shi Z (2009) Crack analysis in structural concrete: theory and applications. Butterworth-Heinemann
4. Erdogan F, Sih GC (1963) On the crack extension in plates under plane loading and transverse shear. J Basic Engng Trans ASME 85(4):519–525
5. Fett T, Gerteisen G, Hahnenberger S, Martin G, Munz D (1995) Fracture tests for ceramics under mode-I, mode-II and mixed-mode loading. J Eur Ceram Soc 15:307–312
6. Xeidakis GS, Samaras IS, Zacharopoulos DA, Papakaliatakis GE (1996) Crack growth in a mixed-mode loading on marble beams under three point bending. Int J Fract 79:197–208
7. Awaji H, Sato S (1978) Combined mode fracture toughness measurement by the disk test. ASME. J. Eng. Mater. Technol. 100(2):175–182
8. Shetty DK, Rosenfield AR, Duckworth WH (1987) Mixed-mode fracture in biaxial stress state: application of the diametral-compression (Brazilian disk) test. Eng Fract Mech 26:825–840
9. Lim IL, Johnston IW, Choi SK, Boland JN (1994) Fracture testing of a soft rock with semi-circular specimens under three-point bending. Part 2—mixed-mode. Int J Rock Mech Min Sci Geomech Abstr 31:199–212
10. Krishnan GR, Zhao XL, Zaman M, Roegiers J-C (1998) Fracture toughness of a soft sandstone. Int J Rock Mech Min Sci 35:695–710
11. Ayatollahi MR, Aliha MRM, Saghafi H (2011) An improved semi-circular bend specimen for investigating mixed mode brittle fracture. Eng Fract Mech 78:110–123

12. Mahajan RV, Ravi-Chandar K (1989) An experimental investigation of mixed-mode fracture. Int J Fract 41:235–252
13. Richard HA, Benitz K (1983) A loading device for the creation of mixed mode in fracture mechanics. Int J Fract 22:R55–R58
14. Bahmani A, Aliha MRM, Jebalbarezi Sarbijan M, Mousavi SS (2020) An extended edge-notched disc bend (ENDB) specimen for mixed-mode I+II fracture assessments. Int J Solids Struct 193–194:239–250
15. Aliha MRM, Bahmani A, Akhondi S (2015) Determination of mode III fracture toughness for different materials using a new designed test configuration. Mater Des 86:863–871
16. Aliha MRM, Bahmani A (2017) Rock fracture toughness study under mixed mode I/III loading. Rock Mech Rock Eng 50:1739–1751
17. Ayatollahi MR, Aliha MRM (2009) Analysis of a new specimen for mixed mode fracture tests on brittle materials. Eng Fract Mech 76:1563–1573
18. Jaya BN, Jayaram V (2014) Crack stability in edge-notched clamped beam specimens: Modeling and experiments. Int J Fract 188:213–228

Homogenization of Transformed β Colony of a Titanium Alloy Using CPFEM

S. Mustafa Kazim [ID]**, Kartik Prasad** [ID]**, and Pritam Chakraborty** [ID]

Abstract The microstructure of Timetal 834 (Titanium alloy) consists of primary α grains and transformed β colonies. The colonies contain consecutive lamellae of alpha (HCP) and beta (BCC) phases. Depending on the Burgers Orientation Relation (BOR), the common slip systems between the two phases govern the transmission or hindrance of the mobile dislocations across the phase boundaries. These interactions dictate the elasto-plastic, fracture and fatigue response of the alloy and need consideration in the Crystal Plasticity (CP) models of the alloy. Though crucial, it is computationally not viable to include both the lath structure of the colony and the primary α grains in the CP Finite Element Method (FEM) simulations of this alloy owing to the disparate length scales of these microstructural features. Thus, two different types of equivalent models of the colony have been proposed in the literature to incorporate the effect of lath in CPFEM simulations. However, a detailed study to understand the accuracy of the models under different deformation histories is absent in the literature. In this work, a Representative Volume Element (RVE) of the lath structure has been developed and simulated using CPFEM. The macroscopic responses from the RVE simulations have been obtained using asymptotic expansion-based homogenization and compared with the equivalent models to identify their accuracy and adequacy for Timetal 834.

Keywords Homogenization · Crystal plasticity finite element method · Titanium alloys · Representative volume element analysis

S. M. Kazim · P. Chakraborty (✉)
Department of Aerospace Engineering, Indian Institute of Technology Kanpur, Kanpur, India
e-mail: cpritam@iitk.ac.in

S. M. Kazim
e-mail: mustafa@iitk.ac.in

K. Prasad
Defence Metallurgical Research Laboratory, DRDO, Hyderabad, India

1 Introduction

Timetal 834 is a near–α Titanium alloy which is widely used in the aero-engine due to its high specific strength, good creep and fatigue resistance at elevated temperatures [1]. The microstructure of this alloy consists of transformed β colonies and primary α grains. In the transformed β colony, the α (HCP phase) and β (BCC phase) are arranged in a lath structure. The interaction between the two phases significantly influences the deformation behaviour of the colonies and the matrix itself [2]. Therefore, the modelling of β lamellae is crucial to capture the mechanics of deformation of this alloy accurately. At the lath interface, the aligned slip systems between the two phases result in easy transmission of dislocations and such systems are termed as soft. On the contrary, dislocation motion is inhibited on the misaligned slip systems across the interface, resulting in significant lath size-dependent resistance to slip in the individual phases. These slip systems are termed as hard [3]. The Burgers Orientation Relation (BOR) determines the alignment of the soft slip systems between the phases and results in distinct anisotropic deformation behaviour of different colonies [4]. The BOR, $(101)_\beta || (0001)_\alpha$, $\left[1\overline{1}\overline{1}\right]_\beta || [2\overline{1}\overline{1}0]_\alpha$, given in Suri et al. [4] is used in the present study.

The length scale of the two phases in the transformed β colony of Timetal 834 differs widely with the average thickness of $\alpha \sim 2\mu$m and that of $\beta \sim 50$nm [5]. In CPFEM analyses, if the colony is meshed alike for both the phases, to maintain a healthy aspect ratio and comparable sized elements, the number of degrees of freedom can be humongous for a single colony and even more for the whole polycrystalline microstructure having primary α grains additionally. This easily renders the computations intractable even for a small polycrystalline microstructure. Thus, homogenization of the colony becomes crucial to perform an efficient simulation. Two different equivalent models have been proposed in the literature to address this issue. In the first model (called M1 hereafter), both the phases in the colony are considered separately at a material point with the assumption that they experience the same deformation gradient but has separate evolution of state. The stress at any material point is obtained from a mixture rule (Venkataramani et al. [3], Deka et al. [6]). In the second model (called M2 hereafter), a virtual homogenized crystal with both the BCC and HCP slip systems has been proposed (Mayeur and McDowell [7], Zhang et al. [8]).

Both the models have their limitations. In M1, the material response is dominated by the volume fraction of the individual phases within the colony, while in M2, the material response is driven by the soft slip modes. Moreover, for both the models, a thorough evaluation of their accuracy under general multi-axial loading has not been performed. For M1, a comparative study only under uniaxial tension and without incorporating size effect has been performed by Deka et al. [6]. A similar analysis under uniaxial tension but with size effect was performed by Zhang et al. [8]. In the present study, responses from these two equivalent models (M1 and M2) are compared with the volume averaged response from Representative Volume Element (RVE) simulations under mixed loading scenarios. The size effect due to dislocation

pileup at the lath interface has been captured using the Hall–Petch relation. The Crystal Plasticity (CP) model parameters are calibrated using the experimental results from Prasad et al. [9] and have been used in all the simulations. Periodic boundary conditions and asymptotic expansion-based homogenization have been applied to obtain the macroscopic stress–strain response.

2 Crystal Plasticity Constitutive Model

The CP model detailed in [10] has been used in this study. In the model, a multiplicative decomposition of the deformation gradient, $\underline{F}$, into elastic ($\underline{F}^e$) and plastic parts ($\underline{F}^p$) has been used. The plastic velocity gradient is then obtained by summing the slip rates on individual (αth) slip systems. The Schmid tensor ($\underline{S}^\alpha_o$) is used to get the resolved shear stress (τ^α) on the individual slip systems as well as to define the plastic velocity gradient in the virtual intermediate configuration. The slip rate, $\dot{\gamma}^\alpha$ for the αth slip system is a function of τ^α, drag stress, g^α and the back stress, χ^α. The threshold stress κ^α is used to capture the long-range effects and is assumed to evolve as a function of $\dot{\gamma}^\alpha$. The size effect in the individual phases of the colony is captured using the Hall–Petch relation, which is applied to the threshold stress and is given by

$$\kappa^\alpha_{cons} = \overset{\sim}{\kappa}^\alpha_{cons} + \frac{K}{\sqrt{l^\alpha}} \tag{1}$$

Where is the initial threshold stress value before the application of the Hall-Petch relation, l^α is the characteristic length for the αth system and K is a constant (unit: MPa$\sqrt{\mu m}$). The average size of the various microstructural features in the colony is taken from Prasad et al. [5] as shown in Table 1. Depending on the BOR, the dislocation motion along the soft slips will be able to reach the colony boundary unobstructed, thus for these slip systems, the average size of the colony is used to determine the Hall–Petch factor. For hard slip systems, the lamellae thickness of the individual phases serves as the characteristic length.

The orientations of colonies are given in terms of the Euler angles of the α phase. Thus, to determine the orientation of β phase with respect to the global axis system, an additional transformation matrix relating the β phase to the α phase is required.

Table 1 Characteristic lengths of microstructural features [5]

Characteristic length	Thickness
l_1 (average thickness of alpha lamellae within colony)	~2 μm
l_2 (average thickness of beta lamellae within colony)	~50 nm
l_3 (average size of colony)	~18 μm

This matrix is obtained from the BOR and is

$$[T_1] = \begin{bmatrix} 0.5774 & -0.5774 & -0.5774 \\ 0.4082 & 0.8165 & -0.4082 \\ 0.7071 & 0 & 0.7071 \end{bmatrix}.$$

Based on the observations made in the literature [3, 6–8], the following slip systems have been chosen as soft:

(i) α phase—basal slip systems $(0001)[2\bar{1}\bar{1}0]$ and $(0001)[\bar{1}\bar{1}20]$, and prismatic slip system $(0\bar{1}10)[2\bar{1}\bar{1}0]$.
(ii) β phase—$(101)[1\bar{1}\bar{1}]$ and $(101)[11\bar{1}]$.

In M1, the equivalent Cauchy stress at any material point ($\underline{\underline{\sigma}}^{hom}$) is obtained using the rule of mixture [6]

$$\underline{\underline{\sigma}}^{hom} = V_f^{hcp} \underline{\underline{\sigma}}^{hcp} + V_f^{bcc} \underline{\underline{\sigma}}^{bcc} \tag{2}$$

where $\underline{\underline{\sigma}}^{hcp}$ and $\underline{\underline{\sigma}}^{bcc}$ are the Cauchy stresses in HCP and BCC phases, respectively, and, V_f^{hcp} and V_f^{bcc} are the volume fractions of HCP and BCC phases in the colony, respectively. In M2, the slips of both the phases are appended to get the homogenized response. The plastic velocity gradient in the intermediate configuration for M2 can then be given by

$$\underline{\underline{\dot{F}}}^P \underline{\underline{F}}^{P-1} = \sum_{\alpha+\beta} \dot{\gamma}^\alpha \underline{\underline{S}}_o^\alpha \tag{3}$$

where $\sum_{\alpha+\beta}$ implies summation over all the slip systems in the α and β phases. The constitutive models are implemented as user material (UMAT) subroutines in the commercial FEM software ABAQUS, following the procedure outlined in [11].

3   Representative Volume Element Simulation

For the purpose of creating the RVE, the colony microstructure (Fig. 1a) is idealized as a periodic repetition of alternating α and β lamellae, as can be seen from Fig. 1b. The periodic arrangement allows isolating a sub-region from the colony to construct the RVE shown in Fig. 1c. A cubic RVE with dimension of $205 \, X \, 10^{-2} \, \mu m$ is selected based on the distance between consecutive β lamellae as shown in Fig. 1c. The RVE domain is meshed with 64 elements and is shown in Fig. 1d.

In this study, the accuracy of the two models (M1 and M2) is evaluated by comparing their responses with the RVE results, which is based on asymptotic expansion-based homogenization. Thus, experimentally fitted values of the CP model
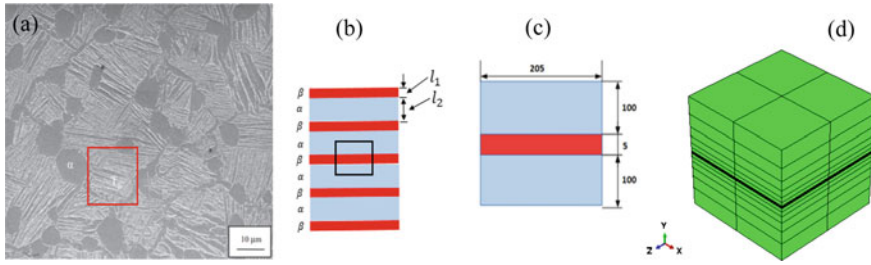
Fig. 1 **a** Microstructure of Timetal 834 (near $-\alpha$ Ti alloy) showing the transformed β colonies along with equiaxed primary α grains [5]. **b** Idealized representation of the region shown in red box in (**a**). **c** RVE with dimensions (magnified view of black box in (**b**)). **d** Meshed cubic RVE

parameters are not required as long as the same set of parameters is used in all the three models (RVE, M1, M2). However, in order to ensure that the parameters provide a yield strength close to 800–1000 MPa for isochoric strain history, which is typical of Ti alloys in uniaxial tension, an iterative procedure has been followed to arrive at these parameters. In this procedure, the initial set of CP model parameters is considered from Deka et al. [6], and then the g_o values are increased iteratively while maintaining the ratios between g_o values of various slip systems as given in [6]. The final set of parameters is shown in Table 2 and is used in all subsequent simulations.

Asymptotic expansion-based homogenization assumes periodicity of micro-response, and hence Periodic Boundary Conditions (PBC) must be applied to the RVE. Additional displacement boundary conditions are applied based on the far-field macroscopic deformation gradient [12]. For all the loading cases, the macroscopic stress and strain components are obtained by volume averaging over the RVE.

Table 2 CP model calibrated parameters for Timetal-834

Parameter	Calibrated value
μ	1
g_o for HCP basal (MPa)	450
g_o for HCP prismatic (MPa)	350
g_o for HCP pyramidal (MPa)	646
g_o for all BCC slip systems (MPa)	250
m	0.02
c	1000
d	50
$\dot{\gamma}_0^\alpha (s^{-1})$	0.0023
$\overset{\sim}{\kappa}{}_{cons}^\alpha$ for all HCP slip systems (MPa)	25
$\overset{\sim}{\kappa}{}_{cons}^\alpha$ for all BCC slip systems (MPa)	25
K for HCP phase (MPa $\sqrt{\mu m}$)	0.2
K for BCC phase (MPa $\sqrt{\mu m}$)	0.2

4 Results and Discussion

The responses from M1 and M2 are compared against the volume averaged results obtained from the RVE for six different applied macroscopic deformation gradients, $\overline{\underline{F}}$, to estimate their accuracy. The following six cases are considered:

Case 1: Isochoric deformation similar to uniaxial tensile loading along y-direction. The non-zero components of $\overline{\underline{F}}$ are: $\overline{F}_{22} = 1+a*t; \overline{F}_{11} = \overline{F}_{33} = 1-0.5*(a*t-1)$.

Case 2: Plane strain biaxial pull in x–y plane. The non-zero components of $\overline{\underline{F}}$ are: $\overline{F}_{11} = 1 + a * t; \overline{F}_{22} = 1 + a * t; \overline{F}_{33} = 1$.

Case 3: Pure sear loading in a plane perpendicular to the lath. The non-zero components of $\overline{\underline{F}}$ are: $\overline{F}_{12} = a * t; \overline{F}_{21} = a * t; \overline{F}_{11} = \overline{F}_{22} = \overline{F}_{33} = 1$.

Case 4: Plane strain biaxial pull in addition to a pure shear in $x - y$ plane. The non-zero components of $\overline{\underline{F}}$ are: $\overline{F}_{11} = 1 + a * t; \overline{F}_{22} = 1 + a * t; \overline{F}_{33} = 1; \overline{F}_{12} = a * t; \overline{F}_{21} = a * t$.

Case 5: Isochoric deformation similar to uniaxial tensile loading along z-direction. The non-zero components of $\overline{\underline{F}}$ are: $\overline{F}_{33} = 1+a*t; \overline{F}_{11} = \overline{F}_{22} = 1-0.5*(a*t-1)$.

Case 6: Pure sear loading in the $x - z$ plane, i.e. in the plane of the lath. The non-zero components of $\overline{\underline{F}}$ are: $\overline{F}_{13} = a * t; \overline{F}_{31} = a * t; \overline{F}_{11} = \overline{F}_{22} = \overline{F}_{33} = 1$.

In all the cases $a = 6.67 \times 10^{-4} s^{-1}$ and a total time of 75 s is used to maintain a quasi-static loading rate. From the simulation results (Figs. 2, 3 and 4), it can be seen that, in most of the cases, M1 response is slightly higher than that of M2 response, this can be the result of the extra stress contribution from BCC phase scaled by its volume fraction, as given in Eq. (2). A similar behaviour can be seen for Case 1
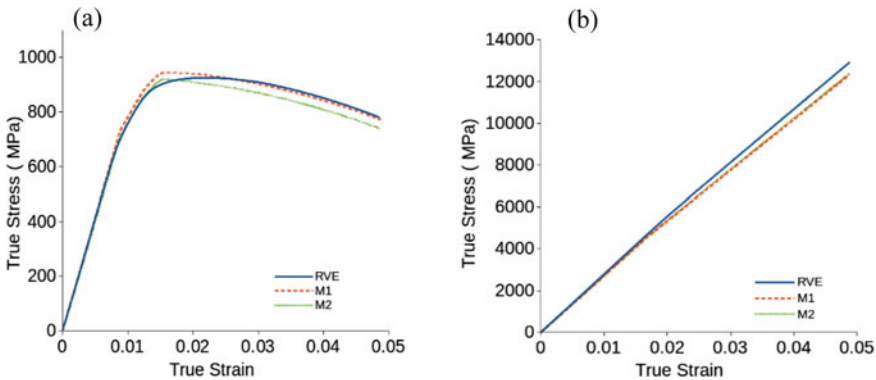
Fig. 2 True stress–strain for **a** Case 1 in the loading y-direction ($\sigma_{22} vs \varepsilon_{22}$). **b** Case 2 in the x-direction ($\sigma_{11} vs \varepsilon_{11}$)

(Fig. 2a). Both M1 and M2 match well with the RVE results for this case. In CPFEM simulations, the soft HCP prismatic slip shows the maximum activation.

For the Case 2, M1 and M2 results nearly overlap with each other. In this loading case, one of the directions (z-direction) is constrained and cannot relax freely while the other two directions are pulled resulting in a state of biaxial plane strain loading. In this case, the material experiences an overall high volumetric stress causing nearly zero plastic deformation and dominantly elastic response. Thus, the average stresses are significantly high and shows a nearly linear elastic behaviour as is reflected in Fig. 2b. At around $\varepsilon_{22} \sim 2\%$ pyramidal slip is activated resulting in deviation from the linear behaviour and can be observed as a kink in Fig. 2b.

For the Case 3, M1 response is again higher than the M2 response; this can again be attributed to the extra stress contribution from BCC phase scaled by its volume fraction, as given in Eq. (2). It is observed in the CPFEM simulations that the prismatic slip systems accumulate the most plastic deformation. For this case of shear loading, M2 gives a better match to the RVE results than M1 as can be seen from Fig. 3a. Since Case 4 is a combination of Case 2 and Case 3, M1 and M2, respond in a similar fashion as that of the previous cases, as can also be seen from Fig. 3b. The constraint in z direction gives rise to high volumetric stresses in the x and y directions. The shear response shows a higher hardening behaviour than Case 3, this can be attributed to the observation that, for this case, the harder prismatic slip also gets activated.

In Case 5, the loading is done along the c-axis of the HCP crystal, along with the incompressibility constraint $\det(\underline{F}) = 1$ being enforced to it. For both the models in this case (Fig. 4a), the yielding starts at a higher value than that of Case 1 (Fig. 2a), this behaviour can be explained based on the fact that the resolved shear stress in the basal and prismatic slips is zero for loading along c-axis, and thus all the load is resolved to the Pyramidal slip systems, which has a higher CRSS, and thus leads to higher yielding stress. In this case also, the response from M2 is lower than that from the M1 model. In Case 6, the RVE and the models are loaded under shear, in the
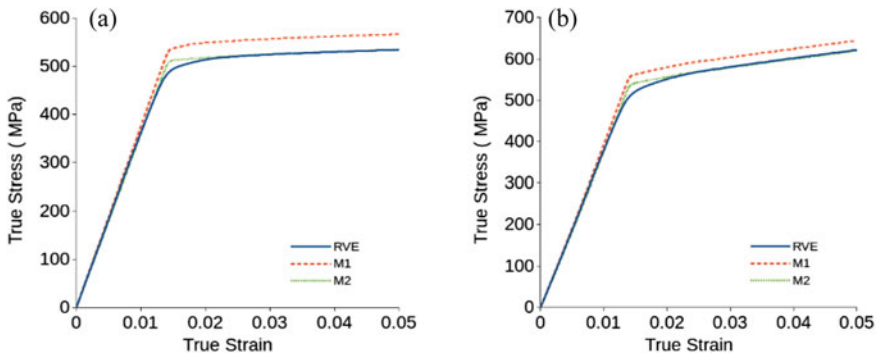
Fig. 3 True stress–strain for **a** Case 3 in the xy-plane ($\sigma_{12} vs \varepsilon_{12}$). **b** Case 4 in the xy-plane ($\sigma_{12} vs \varepsilon_{12}$)
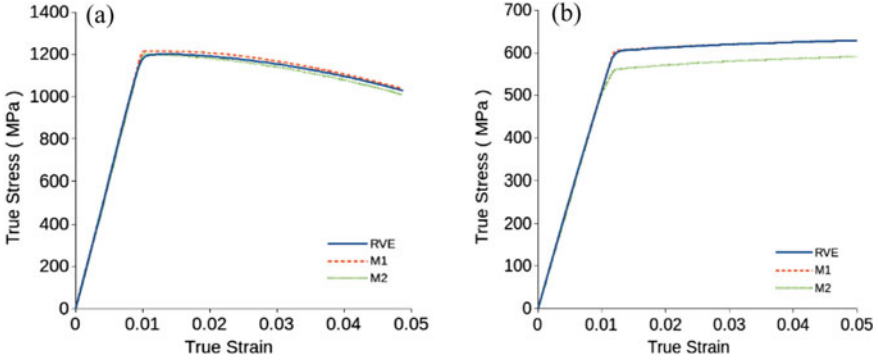
Fig. 4 True stress–strain for **a** Case 5 in the z-direction ($\sigma_{33}\, vs\, \varepsilon_{33}$). **b** Case 6 in the x–z plane ($\sigma_{13}\, vs\, \varepsilon_{13}$)

plane of the lath interface. The M1 scheme matches well with the CPFEM simulation results of the RVE, while on the contrary, the M2 model is not able to capture the lath response properly, as is evident from Fig. 4b. For this case, the soft BCC slips accumulate most of the plastic deformation.

The percentage error for each case can be calculated as

$$Error(\%) = \left| \frac{\tilde{\underline{\underline{\sigma}}}_{model} - \tilde{\underline{\underline{\sigma}}}_{RVE}}{\tilde{\underline{\underline{\sigma}}}_{RVE}} \right| \tag{4}$$

where $\tilde{\underline{\underline{\sigma}}}_{model}$ is the volume-averaged macroscopic stress from the respective models M1 and M2, and $\tilde{\underline{\underline{\sigma}}}_{RVE}$ is the volume-averaged macroscopic stress from the RVE. The error is calculated at two strain values, one near to the yield point ($\varepsilon \sim 2\%$, where non-linearity sets in) and the other near the end of the loading ($\varepsilon \sim 5\%$), these values are presented in Table 3. The error estimates show that M1 performs reasonably well for the cases: Case 1, Case 5 and Case 6, while M2 gives a closer match to that of the RVE response for cases: Case 3 and Case 4. For Case 2, the response from both the models (M1 and M2) nearly overlaps each other (Fig. 2b) as is also reflected from error values.

5 Summary

In the present study, different equivalent modes have been compared under complex loadings in order to assess their candidature for homogenizing the transformed β colony in Timetal 834. For this purpose, a cubic RVE with sandwiched lath configuration is modelled and loaded under various cases from a set of possible deformation gradient space. From the simulated results (Figs. 2, 3 and 4) and the error analysis

Table 3 Percentage error in M1 and M2 models with respect to the RVE results

Cases	Model	Error (%) at $\varepsilon \sim 2\%$	Error (%) at $\varepsilon \sim 5\%$
Case 1	M1	1.70	0.87
	M2	1.60	5.19
Case 2	M1	3.51	3.96
	M2	3.51	3.91
Case 3	M1	6.77	6.05
	M2	0.73	0.04
Case 4	M1	5.12	3.62
	M2	0.92	0.36
Case 5	M1	1.37	0.78
	M2	0.75	1.98
Case 6	M1	0.08	0.04
	M2	6.75	6.07

(Table 3), it can be inferred that both the models M1 and M2 perform adequately well for the volumetric loading scenarios whereas for the shear loading in the plane of the lath, results from M1 compared more accurately against the RVE results. The M1 model assumption considers the individual existence of the lath (thus both the phases), which is typically closer to the actual physical microstructure. Moreover, M1 is able to capture the equivalent response of the colony more accurately for loading cases in which there is a major interaction between the HCP and BCC slip systems (i.e. in Case 6). It can be concluded that M1 is more representative of the colony behaviour and can be considered in polycrystalline simulations using CPFEM.

References

1. Lütjering G, Williams JC (2013) Titanium. Springer, Berlin Heidelberg
2. Suri S, Viswanathan GB, Neeraj T, Hou DH, Mills MJ (1999) Room temperature deformation and mechanisms of slip transmission in oriented single-colony crystals of an α/β titanium alloy. Acta Mater 47:1019–1034. https://doi.org/10.1016/S1359-6454(98)00364-4
3. Venkataramani G, Kirane K, Ghosh S (2008) Microstructural parameters affecting creep induced load shedding in Ti-6242 by a size dependent crystal plasticity FE model. Int. J. Plast. 24, 428–454 (2008). https://doi.org/10.1016/j.ijplas.2007.05.001
4. Suri S, Neeraj T, Daehn GS, Hou DH, Scott JM, Hayes RW, Mills MJ (1997) Mechanisms of primary creep in α/β titanium alloys at lower temperatures. Mater Sci Eng A 234–236:996–999. https://doi.org/10.1016/S0921-5093(97)00322-5
5. Prasad K, Karamched PS, Bhattacharjee A, Kumar V, Bhanu Sankara Rao K, Sundararaman M (2015) Electron back scattered diffraction characterization of thermomechanical fatigue crack

propagation of a near α titanium alloy Timetal 834. Mater. Des 65:297–311. https://doi.org/10.1016/j.matdes.2014.09.006

6. Deka D, Joseph DS, Ghosh S, Mills MJ (2006) Crystal plasticity modeling of deformation and creep in polycrystalline Ti-6242. Metall Mater Trans A 37:1371–1388

7. Mayeur JR, McDowell DL (2007) A three-dimensional crystal plasticity model for duplex Ti–6Al–4V. Int J Plast 23:1457–1485. https://doi.org/10.1016/j.ijplas.2006.11.006

8. Zhang M, Zhang J, McDowell DL (2007) Microstructure-based crystal plasticity modeling of cyclic deformation of Ti–6Al–4V. Int J Plast 23:1328–1348. https://doi.org/10.1016/j.ijplas.2006.11.009

9. Prasad K, Sarkar R, Ghosal P, Satyanarayana DVV, Kamat SV, Nandy TK (2011) Tensile and creep properties of thermomechanically processed boron modified Timetal 834 titanium alloy. Mater Sci Eng A 528:6733–6741. https://doi.org/10.1016/j.msea.2011.05.069

10. Gupta R, Kazim SM, Prasad K, Chakraborty P (2021) Crystal plasticity modeling of a titanium alloy under thermo-mechanical fatigue. Mech Res Commun 111:103647. https://doi.org/10.1016/j.mechrescom.2020.103647

11. Balasubramanian S (1998) Polycrystalline plasticity: application to deformation processing of lightweight metals

12. Segurado J, Llorca J, González C (2002) On the accuracy of mean-field approaches to simulate the plastic deformation of composites. Scr Mater 46:525–529. https://doi.org/10.1016/S1359-6462(02)00027-1

Through-Thickness High Strain Rate Compressive Response of Glass/Epoxy-Laminated Composites Embedded with Randomly Oriented Discontinuous Carbon Fibers

Shubham, Chandra Sekher Yerramalli, Rajesh Kumar Prusty, and Bankim Chandra Ray

Abstract In the last few decades, fiber-reinforced polymer (FRP) composites have gained much attention because of their outstanding strength-to-weight ratio, superior corrosion resistance, and excellent thermo-mechanical properties. This study presents the high strain rate (HSR) compressive behavior of woven E-glass fiber-reinforced epoxy embedded with randomly oriented discontinuous carbon fibers (RODCF). For the compressive testing of samples at HSR along the through-thickness direction, a compressive split Hopkinson pressure bar (SHPB) setup was used. Samples of cylindrical shape were used for SHPB testing, having a length to diameter ratio (L/D) of 0.75. All the samples were tested at a constant propelling gas pressure of 30 PSI and the strain rate range of 1977–2214 s^{-1}. The amount of RODCF dispersion in the sample tested was 0.25% and 0.5% by weight of epoxy. It was observed that the mean compressive strength of the glass/epoxy (GE) sample increases up by 7.4% and 5.8% with RODCF addition of 0.25% and 0.5% by weight of epoxy, respectively. The signals obtained from the incident bar strain gauge and the transmitter bar strain gauge were used to obtain force versus time plots. The neat GE sample showed better stress equilibrium in the elastic regime as compared to GE samples containing RODCF. Dynamic plots of compressive strain rate versus time, true stress versus true strain as well as forces versus time were obtained for each type of sample and discussed.

Keywords Fiber-reinforced polymer · High strain rate · Split Hopkinson pressure bar · Glass/epoxy · Discontinuous carbon fibers

Shubham (✉) · R. K. Prusty · B. C. Ray
FRP Composites Laboratory, Department of Metallurgical and Materials Engineering, National Institute of Technology, Rourkela 769008, India

C. S. Yerramalli
Department of Aerospace Engineering, Indian Institute of Technology Bombay, Mumbai 400076, India

1   Introduction

The FRP composites are gradually becoming a material of significant importance in the last few decades. A wide variety of fibers and polymers are available for composite designing, be it for any application, conventional, or high technology. High specific strength, energy absorption, corrosive resistance, high specific stiffness, enhanced dimensional stability, as well as relatively low cost are some of the parameters that are generally considered during the selection of a material system for typical applications. Taking into account the different loading conditions to which the FRP composites are subjected during their service life, having more than one reinforcing material has proven to be more promising [1, 2]. In general, a high modulus and costly fiber are present in a hybrid composite material, with another fiber, which usually has lower mechanical properties and relatively cheaper cost. In such types of FRP composites, the fiber having a high modulus gives stiffness and load-bearing qualities. In contrast, damage tolerance is imparted by the low-modulus fiber, which keeps the total material system cost relatively lower [3]. Fibers such as boron and carbon, due to their high specific modulus, are extensively used in aerospace applications. However, the addition of low-modulus fibers like E-glass fibers in some percentage to the FRP composite containing high-modulus fiber can improve the impact properties effectively.

The compressive SHPB apparatus is an extensively used methodology for finding the composite response under HSR loading conditions. SHPB derives its principle from one-dimensional (1-D) wave propagation theory in elastic bars. Hopkinson first gave this concept of dynamic load testing of materials as he experimentally determined the pressure produced by an explosive with iron wires stress wave experiments. About four decades later, to determine the dynamic compressive stress–strain behavior of materials, the concept of split bars, along with data analysis and experimental procedure of one-dimensional pressure bar, was given by Kolsky. It was then that the split bar technique became popular and started to be used widely for the testing of materials at high strain rates [4]. Studies show that the loading pulse having a larger rise time when compared with the lesser rise time of loading pulse generates better stress uniformity [5]. Under compressive loading, various studies [6–9] were carried out on SHPB for determining the high strain rate (HSR) behavior of unidirectional, cross-ply composites as well as woven fabric-reinforced polymer composites [10, 11]. Wei Dong et al. [12], using several techniques, studied the fracture toughness and thermal stability of the short carbon fibers (SCF)/epoxy composites. The thermal stability of SCF/epoxy composites was reported to be similar to that of neat epoxy resin. In contrast, there was a significant improvement in the composites' fracture toughness relative to the neat resin. Their findings showed that the composite's toughness could be enhanced without risking the resin's mechanical integrity.

In this study, our approach is to enhance the HSR compressive strength in the GE composite's through-thickness direction. For this, RODCFs are embedded in the GE composite system and are then tested on the compressive SHPB setup at a constant propelling gas pressure of 30 PSI. All the samples were tested at room temperature.

The incident and transmitter bar's strain gauges are used to obtain the incident (I), reflected (R), and transmitted (T) pulse, which is further used to plot the true stress–true strain, strain rate versus time, and the forces versus time graphs for the GE as well as RODCF embedded GE samples.

2 Experimental Details

A compressive SHPB setup was used for testing the samples. Figure 1 shows the schematic of the SHPB apparatus used. The striker bar, propelling mechanism, incident and transmitter bar, and support stand are the major components of the compressive SHPB setup. The incident bar and transmitter bar's diameter is 12 mm, its length is 1400 mm, and a 250 mm long striker bar was used. The bars were made up of martensitic stainless steel of density 7800 kg/m^3, having Young's modulus of 203 GPa. The design and development details regarding SHPB compressive apparatus, testing procedures, and safety precautions are given in [4, 10].

Based on the concept of particle motion in a longitudinal direction, i.e., one-dimensional (1-D) propagation of the wave in elastic bars, the SHPB is designed. In an ideal 1-D system, its length can be considered to be infinite and diameter to be negligible. Since it is not possible practically, certain assumption has been taken while adopting the theory.

$$\text{The strain rate, } \dot{\varepsilon}(t) = \frac{C_0}{L_s}(\varepsilon_I - \varepsilon_R - \varepsilon_T) \tag{1}$$

$$\text{Stress, } \sigma(t) = \frac{E}{2}\frac{A_B}{A_S}(\varepsilon_I + \varepsilon_R + \varepsilon_T) \tag{2}$$

$$\text{The strain, } \varepsilon(t) = \left(\frac{C_0}{l_s}\right)\int_0^t (\varepsilon_I - \varepsilon_R - \varepsilon_T)dt \tag{3}$$
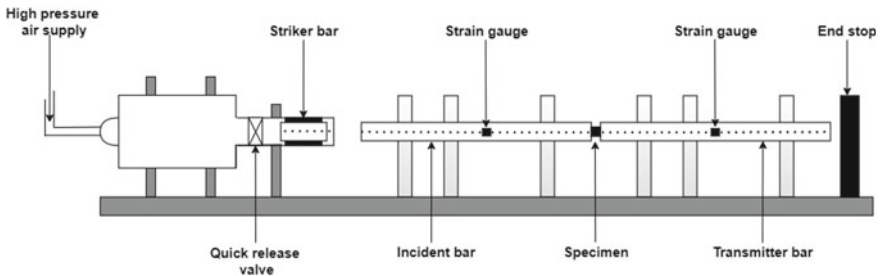
Fig. 1 Schematic arrangement of compressive split Hopkinson pressure bar (SHPB) apparatus

Here, $C_0 = \sqrt{\frac{E}{\rho}}$ represents the elastic wave velocity in the bars, the gauge length of the specimen is denoted by L_s, the cross-sectional area of bars and specimen are denoted by A_B and A_S, respectively. Young's modulus of the bars is denoted by E. ε_I, ε_R, and ε_T represent the incident strain pulse, reflected strain pulse, and transmitted strain pulse, respectively. ρ is the density of the bar, and t is the time duration. In this study, the engineering values of stress and strain were converted to true values by using equations (iv) and (v), taking the compressive stress and compressive strain to be positive values. The compressive strain rates were also taken as positive values:

$$\sigma_{true}(t) = \sigma(t)[1 - \varepsilon(t)] \tag{4}$$

and true strain as $\varepsilon_{true}(t) = -ln[1 - \varepsilon(t)]$ $\qquad$ (5)

3 Materials and Methods

3.1 Materials

Diglycidyl ether bisphenol A type epoxy resin was used, and triethylenetetramine was used as the curing agent which was supplied by Atul Industries Ltd, India. L-12 and K-6 are the trade names of the epoxy resin and hardener obtained. Plain weave type E-glass fiber of 360 GSM was used, which was obtained from Owens Corning, India. The filament diameter of E-glass fiber was about 15 μm. Carbon fibers (tensile strength ~3500 MPa, modulus ~230 GPa, and strain to failure ~1.5%) were made available from Toray Industries and were chopped to 9 mm in length.

3.2 Fabrication of Samples

A total of 20 layers of woven fiber fabric were used to prepare the laminate of neat GE using the hand lay-up technique. The ratio of epoxy resin and hardener was kept as 10:1 (weight) as per the instruction provided by the manufacturer. It was followed by compression in hot press at 60 °C temperature at a pressure of 10 kg/cm^2 for 20 min. The laminates were then kept at room temperature for 24 h. After that, the samples were cut out of the laminate and polished to the required dimension with an accuracy of $\pm$ 0.1 mm. The polished samples were then kept at 140 °C for 6 h for post-curing in the oven and allowed to cool inside the oven itself [13]. The fiber volume fraction (FVF) of the GE sample was found to be about 0.44. For the fabrication of the GE laminate containing RODCFs, the epoxy resin before the addition of hardener was mixed with the required amount of RODCFs for 30 min using a magnetic stirrer at

Table 1 Sample code for different sample configurations tested on compressive SHPB

Sample configuration	Sample code
Glass Epoxy	GE
Glass Epoxy + RODCF (0.25 wt% of epoxy)	GE-RODCF1
Glass Epoxy + RODCF (0.5 wt% of epoxy)	GE-RODCF2

400 RPM and temperature of 120 °C. The rest of the procedure was the same as followed for the fabrication of neat GE laminate. Table 1 shows the configuration of the samples prepared and the respective sample code. One reason for not choosing a RODCF content of more than 0.5 wt% of epoxy was the difficulty of applying the RODCF embedded epoxy resin on the woven glass fiber during the hand lay-up fabrication process due to the increase in viscosity of the resin.

The design of the specimen is one of the essential parameters considered during the SHPB testing. Within the specimen, to attain dynamic stress equilibrium, its geometry and length to depth L/D ratio are significant. Further, the strain rate generated in the specimen is also controlled by it. It has been observed from the literature that specimens of cylindrical geometry are considered suitable when the length (L) to diameter (D) ratio is in the range of 0.5–2.0 for SHPB compressive testing of FRP composites [14]. The samples tested had an L/D ratio of 0.75, with a diameter of 8 mm, and the depth or thickness of the specimen was 6 mm.

4   Results and Discussions

The study was executed experimentally on the HSR behavior of GE, GE-RODCF1, and GE-RODCF2 composite using compressive SHPB apparatus along the through-thickness direction. The pressure of the propelling cylinder was kept constant at 30 PSI which generated a strain rate in the range of about 1977–2214 s^{-1}. Five samples of each configuration were tested. Figure 2 shows the incidence (I) pulse, reflected (R) pulse, and transmitted (T) pulse signals obtained from the strain gauges of the incident rod and transmitter rod.

Figure 3a, b shows the absolute value of the compressive strain rate versus time plot and absolute mean strain rate values, respectively, for the GE, GE-RODCF1, and GE-RODCF2 composite samples. Figure 4a, b shows the true stress versus true strain plot and mean peak compressive stress, respectively. Strain gauge signals and equations (i)–(v) were used to obtain these plots. It should be taken into consideration that the sample fails in the time duration corresponding to peak stress in the graph. The reference strain rate is taken as strain rate at the first peak of strain rate versus time graph. The true strain-true stress plot can be divided into two regions, in which the behavior of the material until the peak compressive stress is reached can be one region. In contrast, another region, i.e., after the peak stress is reached, can be considered the material's post-failure behavior.
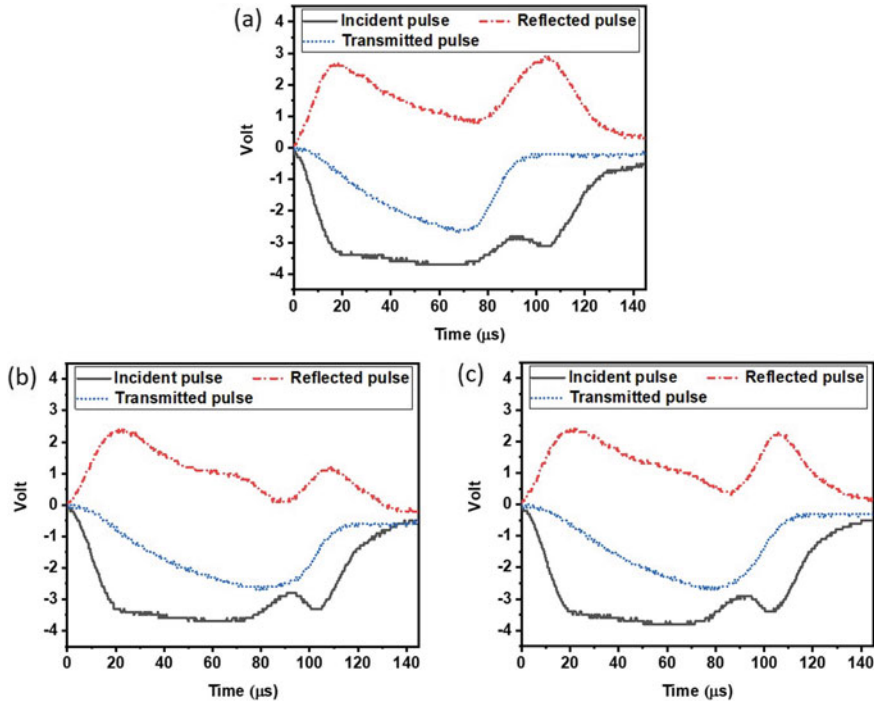
Fig. 2 Output signal of HSR compressive SHPB test along thickness of **a** GE sample, strain rate = 2135 s^{-1} **b** GE-RODCF1 sample, strain rate = 1977s^{-1} **c** GE-RODCF2 sample, strain rate = 2056s^{-1}
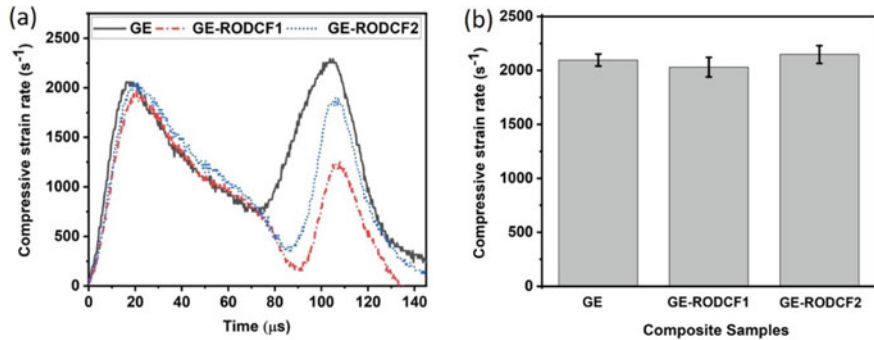
Fig. 3 HSR compressive SHPB tested samples along thickness direction **a** absolute strain rate vs time plot **b** absolute mean strain rate
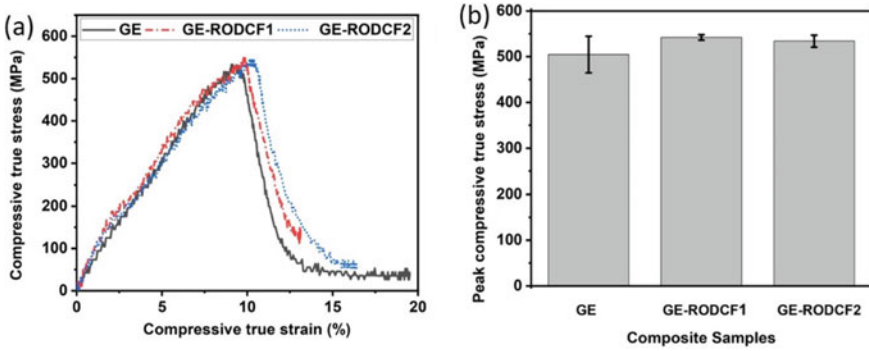
Fig. 4 HSR compressive SHPB tested samples along the thickness direction **a** true stress versus true strain plot **b** mean peak compressive stress
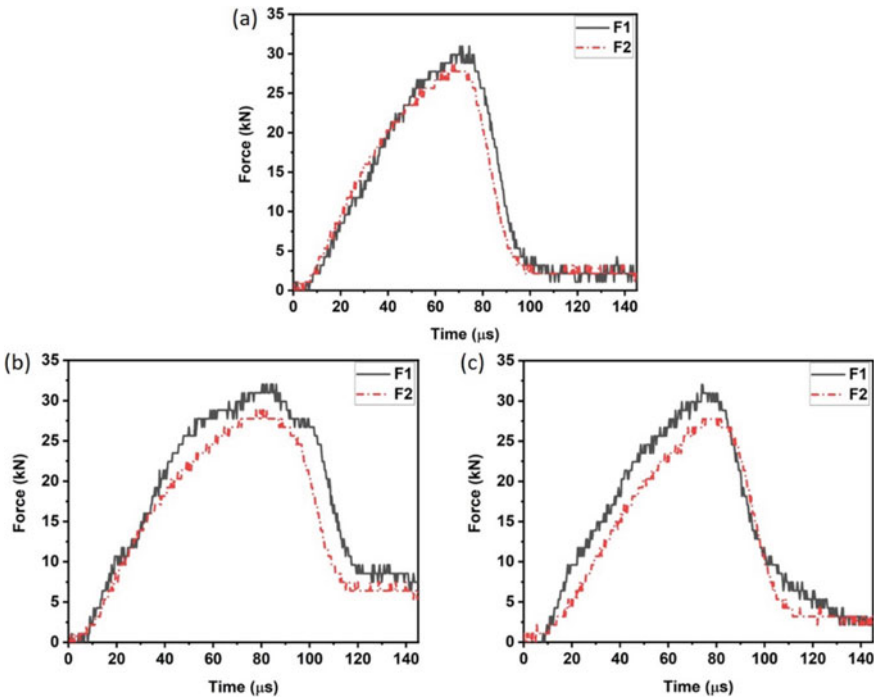
Fig. 5 Force versus time plot of HSR compressive test along thickness results of **a** GE sample, strain rate $= 2135\ s^{-1}$ **b** GE-RODCF1 sample, strain rate $= 1977\ s^{-1}$ **c** GE-RODCF2 sample, strain rate $= 2056\ s^{-1}$

In Fig. 5, F1 is termed as the force versus time plot obtained from the I + R signal. Similarly, F2 was obtained from the T signal. Force F1 acts on the interface between the specimen and the incident bar, whereas force F2 acts on the interface between the specimen and transmitter bar. Likewise, the true stress–true strain curve, the force versus time curve, is also considered to have two regions. The first region can be considered until the peak force is reached and after the peak force is reached, i.e., after the specimen has failed, the behavior is indicated by the second region. It becomes quite evident that F1 and F2 will not be the same after the peak is achieved. Even in region one, it was observed that the forces F1 and F2 are having some differences. Figure 5 shows the force versus time plots that were obtained from the strain gauge signals for the GE, GE-RODCF1, and GE-RODCF2 samples tested at $2135\,s^{-1}$, $1977\,s^{-1}$, and $2056\,s^{-1}$. The stress equilibrium was comparatively better in the elastic region of the GE sample's stress–strain behavior but was disturbed in the GE-RODCF1 and GE-RODCF2 samples. One of the major causes of this can be the stress wave attenuation caused due to the impedance mismatch between epoxy and RODCF along with the stress wave attenuation that would have taken place during damage evaluation.

5   Conclusions

The compressive properties under HSR loading condition in the through-thickness direction of GE composite, along with GE composite embedded with RODCFs (0.25% wt. of epoxy) as well as GE composite embedded with RODCFs (0.5% wt. of epoxy) are stated here. A constant propelling gas pressure of 30 PSI was kept for testing of all the samples resulting in a strain rate range of 1977–$2214\,s^{-1}$. The following points can be concluded from the study done.

1. An enhancement of 7.2% and 5.4% in the mean compressive strength of the GE composite samples was observed with the addition of RODCFs 0.25% and 0.5% wt. of epoxy, respectively.
2. The peak force F1 was observed to be higher than the peak force F2 in GE and GE-RODCF1 and GE-RODCF2 samples, which can be attributed to the stress wave attenuation in the woven composites. The stress equilibrium was seen to exist better in the neat GE sample's elastic regime than in the GE samples containing RODCF, which can be due to the additional stress wave attenuation because of impedance mismatch between epoxy and RODCF.

References

1. Woo S-C, Kim T-W (2016) High strain-rate failure in carbon/Kevlar hybrid woven composites via a novel SHPB-AE coupled test. Compos B Eng 15(97):317–328
2. Shubham, Rajesh Kumar Prusty, Chandra Ray B (2020) Mechanical modelling and experimental validation of woven composites. Mater Today Proc 1(27):2640–2644
3. Daryadel SS, Mantena PR, Kim K, Stoddard D, Rajendran AM (2016) Dynamic response of glass under low-velocity impact and high strain-rate SHPB compression loading. J Non-Cryst Solids 15(432):432–439
4. Naik NK, Ch V, Kavala VR (2008) Hybrid composites under high strain rate compressive loading. Mater Sci Eng A 498(1):87–99
5. Yang LM, Shim VPW (2005) An analysis of stress uniformity in split Hopkinson bar test specimens. Int J Impact Eng 31(2):129–150
6. Hsiao HM, Daniel IM (1998) Strain rate behavior of composite materials. Compos B Eng 29(5):521–533
7. Li Z, Lambros J (1999) Determination of the dynamic response of brittle composites by the use of the split Hopkinson pressure bar. Compos Sci Technol 59(7):1097–1107
8. Jenq ST, Sheu SL (1993) High strain rate compressional behavior of stitched and unstitched composite laminates with radial constraint. Compos Struct 25(1–4):427–438
9. Vural M, Ravichandran G (2004) Transverse failure in thick S2-glass/epoxy fiber-reinforced composites. J Compos Mater 38(7):609–623
10. Naik NK, Kavala VR (2008) High strain rate behavior of woven fabric composites under compressive loading. Mater Sci Eng A 474(1–2):301–311
11. Harding J (1993 Jun 1) Effect of strain rate and specimen geometry on the compressive strength of woven glass-reinforced epoxy laminates. Composites 24(4):323–332
12. Dong W, Liu H-C, Park S-J, Jin F-L (2014) Fracture toughness improvement of epoxy resins with short carbon fibers. J Ind Eng Chem 20(4):1220–1222
13. Kumar DS, Shukla MJ, Mahato KK, Rathore DK, Prusty RK, Ray BC (2015) Effect of post-curing on thermal and mechanical behavior of GFRP composites. IOP Conf Ser Mater Sci Eng 75:012012
14. Woldesenbet E, Vinson JR (1999) Specimen geometry effects on high-strain-rate testing of graphite/epoxy composites. AIAA J 37(9):1102–1106

Effect of Tungsten Addition on Shock Loading Behavior in Ta–W System: A Molecular Dynamics Study

A. Kedharnath [ID]**, Rajeev Kapoor, and Apu Sarkar**

Abstract The effect of tungsten addition to tantalum on spall strength is studied using the molecular dynamics technique. The single crystal configurations with piston plane lying on $(\bar{1}01)$, and $(1\bar{1}1)$ are modeled. The atoms within the piston region are frozen and do not move. The configurations with two tungsten contents of 0 and 10 weight percent tungsten are added as a solvent and equilibrated. The piston velocity is fixed as 1000 m/s and the initial temperature is 0 K. The piston is displaced till 4 nm and stopped which produces a square shock wave moving along $[\bar{1}01]$ and $[1\bar{1}1]$. The configurations are allowed to evolve dynamically using a microcanonical ensemble. The velocity of free surface and spall strength are analyzed for various crystallographic orientations of the single crystal with various tungsten contents. The addition of tungsten to tantalum increased the spall strength due to increased lattice friction provided by the tungsten atoms. Alpha (BCC) to Omega (HCP) phase transformation was observed in $[\bar{1}01]$ oriented single crystal. The addition of tungsten to tantalum resisted this phase transformation.

Keywords Molecular dynamics · Tantalum · Shock loading · Spall strength · Ta–W

1 Introduction

Tantalum and its alloys have profound corrosion resistance properties at high temperatures [1–3]. Tungsten addition to tantalum increases the value of the elastic constants, flow stress, and rate of work hardening [4–7]. Ta–W alloys are proposed alloys for high-temperature reactors and are already been used in containing molten plutonium. Ta–W alloys are used in ballistics and defense materials for their excellent spall strength during shock and high strain rate loading conditions [2, 3, 8]. They also have potential space applications as a coating on base materials and intricate parts to withstand micrometeoroids and debris. Spallation is a ductile fracture

A. Kedharnath (✉) · R. Kapoor · A. Sarkar
Mechanical Metallurgy Division, Bhabha Atomic Research Centre, Mumbai, India

Division of Engineering Sciences, Homi Bhabha National Institute, Mumbai, India

113

due to the formation and growth of voids which are formed due to the shock wave moving through the metals [9]. Spall strength depends on shock velocity (strain rate), temperature, alloying content, dislocation density, grain boundary types, and grain size [10–12]. Hsiung and Lassila [13] were the first to report phase transformation in BCC tantalum during shock loading deformation. Burakovsky et al. [14] and Haskins et al. [15] used ab initio simulations to explore phases at high pressure and temperature in tantalum. Molecular dynamics (MD) simulations of shock loading on differently oriented tantalum single crystals at various strain rates have been carried out in the last decades [9, 16–19]. Remington et al. [9] performed shock loading simulations on tantalum nanocrystalline configurations and showed that the failure occurred at the interface. The effect of tungsten addition to tantalum on the shock loading behavior of the alloy at various loading orientations is still an active area of research. In this work, the spall strength of pure tantalum and Ta-10 wt.% W oriented along $\left[\bar{1}01\right]$ and $\left[1\bar{1}1\right]$ directions were studied. The effect of tungsten addition to tantalum was analyzed.

2 Methodology

MD technique is a versatile tool for studying the dynamic evolution of many-body systems and their behavior at the nanoscale level [20, 31]. MD technique can be used for studying mechanical behavior with atomistic defect features such as Frenkel pairs, dislocations, grain boundaries, clusters, segregations, and precipitates [21–24]. MD technique involves solving Newton's equations and updating the atomic positions and velocities ($\boldsymbol{v}$) based on the interatomic potential (E_i) (Eqs. 1–3) [20, 31]. For metallic systems, embedded atom model (EAM) is used for calculating the pairwise part ($\phi(\boldsymbol{r})$) and electronic part ($U \wedge \rho(\boldsymbol{r})$).

$$\boldsymbol{F} = m\boldsymbol{a} = m\frac{d\boldsymbol{v}}{dt} = m\frac{d^2\boldsymbol{r}}{dt^2} \tag{1}$$

$$\boldsymbol{F} = -\nabla E_i \tag{2}$$

$$E_i = U\left(\sum_{j \neq i} \rho(\boldsymbol{r}_{ij})\right) + \frac{1}{2}\sum_{j \neq i} \phi(\boldsymbol{r}_{ij}) \tag{3}$$

$\boldsymbol{F}$ is the force between the atoms of mass m separated by a distance $\boldsymbol{r}_{ij}$. U is the embedding energy for an atom in the electron cloud with the electron transfer function $\rho(\boldsymbol{r})$. Classical MD code implemented through Large-scale Atomic/Molecular Massively Parallel Simulator (LAMMPS) [25] was used and Open Visualization Tool (OVITO) [26] was used for visualization.
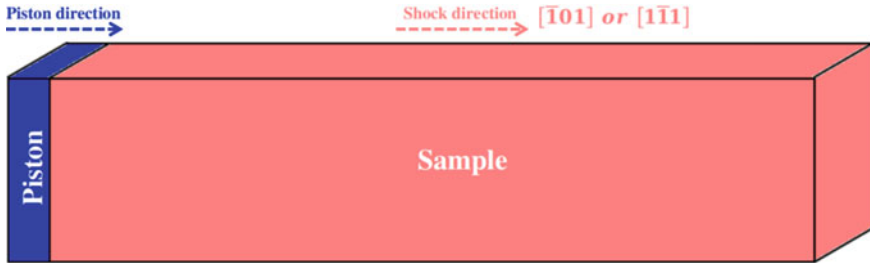
Fig. 1 Schematic of the simulation cell. Piston and its displacement direction are shown in blue color and the sample and the shock wave direction through the sample are shown in red color

Single crystals of tantalum with orientations $[\bar{1}01]$ and $[1\bar{1}1]$ along Z direction were modeled using Atomsk [27] and the schematic of the configuration is shown in Fig. 1. The third direction in both the single crystal configurations was $\langle 112 \rangle$. The box dimension of $25 \times 25 \times 100\,\text{nm}^3$ with 3.5 million atoms was chosen. One set of simulations were done on tantalum and the others were done on Ta-10 wt.% W. Ta atoms were randomly replaced/substituted by 10 wt.% (9.858 at.%) tungsten atoms and equilibrated to minimum energy configuration. The configurations were named as per the tungsten content and their orientation, for example, Ta_ $[\bar{1}01]$ refer to pure tantalum with $[\bar{1}01]$ along the Z direction and Ta-10W_ $[1\bar{1}1]$ refer to Ta-10 wt.% tungsten with $[1\bar{1}1]$ along the Z direction. The piston method of shock loading was used with a constant piston velocity of 1000 m/s. In the piston method, a group of rigid atoms (blue-colored in Fig. 1) is moved at constant velocity to create a perfect square shock wave that travels through the sample (red-colored in Fig. 1). The piston was displaced for 4 picoseconds (ps) moving 4 nm along the Z direction and then stopped. The microcanonical ensemble was used throughout the simulation. The initial temperature of the simulations was maintained near 0 K. The timestep of 0.002 femtoseconds (fs) was used. Periodic boundary conditions were used in X and Y directions and shrink-wrapped in the Z direction. The stress distribution along the Z direction and velocity of the atoms near the free surface was calculated to visualize the attenuation of the wave. The configurations were analyzed using common neighbor analysis (CNA), dislocation extraction algorithm (DXA), and velocity profile. The atoms were colored green for atoms that do not have any structure (other atoms) and brown for HCP atoms; the BCC atoms were removed after CNA. Using DXA, the atoms were removed to visualize dislocations and defect mesh surface generated using voids and defect atoms.

3 Results and Discussion

The stress (σ_{zz}) distribution along Z direction at various timesteps for Ta_ $\left[\overline{1}01\right]$ configuration is shown in Fig. 2a. The velocity of the free surface of various configurations is shown in Fig. 2b. The maximum velocity achieved by the free surface is highest in pure tantalum. Tungsten addition increases the lattice friction force which is the reason for the decrease in the peak velocity achieved by the free surface during the shock loading simulation.

Figure 3 gives the spall strength of various configurations. The spall strength is the difference between the minimum and maximum stress experienced by the sample during shock loading simulation. The addition of 10 wt.% tungsten to tantalum
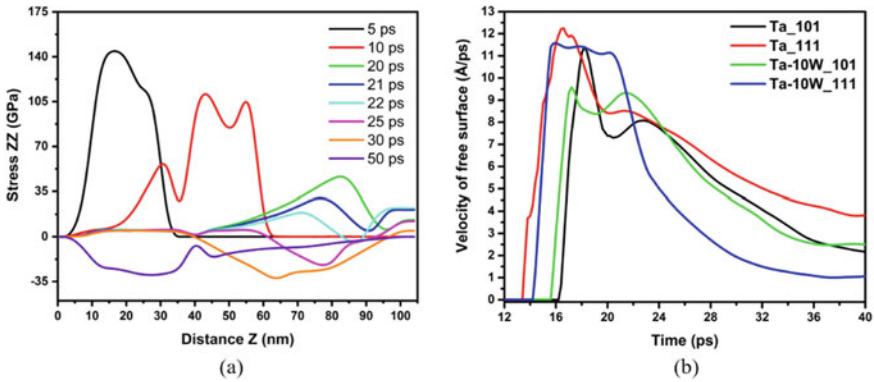
Fig. 2 **a** Stress (σ_{zz}) at various timesteps for Ta_ $\left[\overline{1}01\right]$ configuration. **b** The velocity of the free surface of various configurations

Fig. 3 Spall strength for pure tantalum and Ta-10 W for $\left[\overline{1}01\right]$ and $\left[1\overline{1}1\right]$ orientations. The colors are used to differentiate the data points
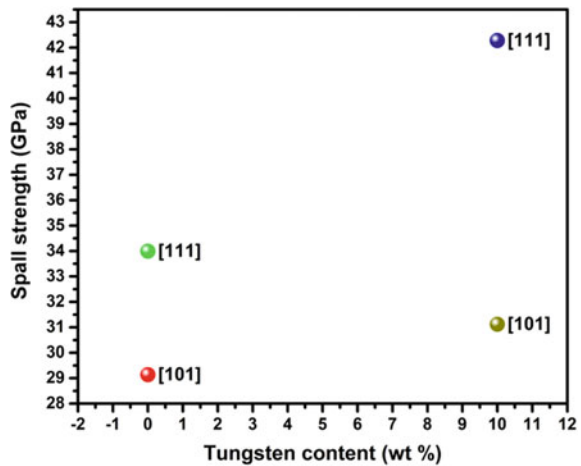
increases the spall strength from 29 to 31 GPa in $\left[\bar{1}01\right]$ orientation and from 34 to 42 GPa in $\left[1\bar{1}1\right]$ orientation.

The spallation events of various configurations are visualized in Fig. 4. The primary spallation was observed near the piston region due to void growth and coalescence caused by the overlap of tensile (returning wave) and compressive waves. The velocity profile showed the velocity of the compression and tensile waves. CNA results showed a phase transformation from BCC (α phase) to HCP (ω phase). DXA results showed the increased dislocation drag in Ta-10 W configurations due to increased lattice Peierls stress by the tungsten atoms. At 104 ps, the dislocations reached the free surface in pure Ta configurations while in Ta-10 W configurations they couldn't and this can be attributed to the dislocations dragging by the tungsten atoms.

Figure 5 shows the phase transformation from BCC → HCP in $\left[\bar{1}01\right]$ oriented single crystals. The phase transformation from BCC (α phase) to HCP (ω phase) takes place due to dynamic shear deformation along $\langle 111 \rangle$ direction causing changes in stacking sequence in {112} planes [28]. The stacking sequence in {112} BCC planes are ***ABCDEF*** which transform to form omega sequence ***ABED*** [29]. The dissociation of two $\frac{1}{2}\langle 111 \rangle$ dislocations into two $\frac{1}{12}\langle 111 \rangle$ and one $\frac{1}{3}\langle 111 \rangle$ in {112} planes to form the omega phase is energetically favorable as seen in Eq. (4) [30].

$$b^2 > b_1^2 + b_2^2 + b_3^2 \tag{4}$$

The orientation relation between BCC and HCP phases is given by two possible models [13, 30]:

Collapse model: {111}∥{0001} $\langle 110 \rangle$∥$\langle 11\bar{2}0 \rangle$

New model: {112}∥{1$\bar{1}$00} $\langle 111 \rangle$∥$\langle 0001 \rangle$ and $\langle 110 \rangle$∥$\langle 11\bar{2}0 \rangle$

According to the collapse model, one pair of {111} planes in the BCC phase collapse to form {0001} in HCP phase [13, 29, 30]. In the current $\left[\bar{1}01\right]$ oriented single crystal simulation, the {110}$_{bcc}$ planes are parallel to {0001}$_{hcp}$ and the $\langle 111 \rangle$ directions are parallel to $\langle 11\bar{2}0 \rangle$ direction. The new model [13, 30] takes into consideration the stacking sequence in {112} planes and shear in $\langle 111 \rangle$ directions. Hsiung et al. [13] showed that Ta-10 W alloy had a higher fraction of HCP phase (transformed from bcc) as compared to pure Ta, but did not explain this. However, the current MD results showed that Ta-10 W had a lower number of atoms in the HCP phase as compared to that of pure Ta. This result could be explained by the increase in the lattice friction with the addition of W to Ta, as the shear modulus of Ta is 69 GPa and that of tungsten is 130 GPa. An increase in lattice friction results in a higher resistance to shear deformation. The fraction of the HCP phase (obtained as fraction of hcp atoms to total number of atoms) are 3.9% for pure Ta and 3.2% for Ta-10 W at 14 ps (snapshot in Fig. 5). At 14 ps, the atomic fractions within the FCC phase are 2.2% for pure Ta and 1.6% for Ta-10 W.
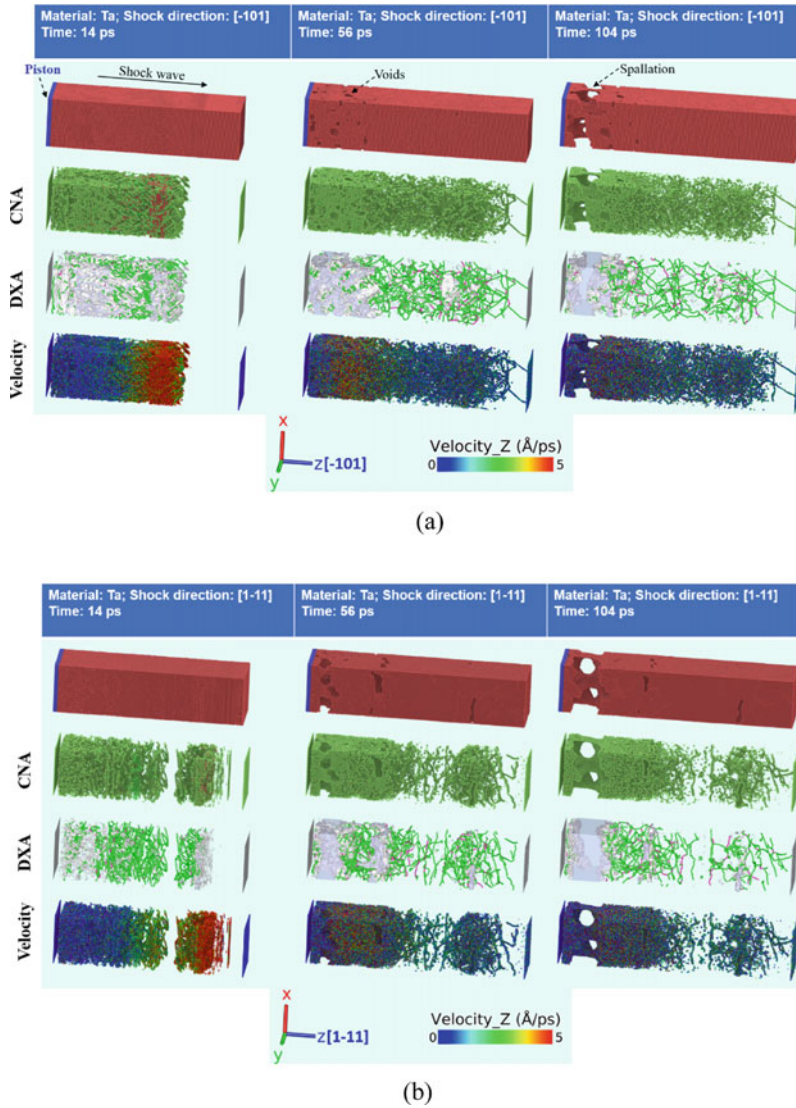
Fig. 4 Analysis and visualization of various configurations **a** Ta_ $\left[\bar{1}01\right]$, **b** Ta_ $\left[1\bar{1}1\right]$, **c** Ta-10W_ $\left[\bar{1}01\right]$, and **d** Ta-10W_ $\left[1\bar{1}1\right]$. The material, shock direction, and timestep are shown at the top, the coordinate axis and velocity scale are shown at the bottom of the figure. In each figure, configurations after piston modeling, CNA, DXA, and velocity profiling along the Z direction are visualized. In the piston model, the blue-colored atoms are modeled as the piston, the brown-colored atoms are tantalum and the yellow-colored atoms are tungsten. After CNA, the BCC atoms are removed, HCP atoms are brown colored and other atoms are green colored. After DXA, the atoms are removed to visualize dislocations and surface mesh. The green-colored dislocations are perfect dislocation and the red-colored dislocations are partial dislocations. After removing the BCC atoms after CNA, the atoms are colored according to the velocity scale
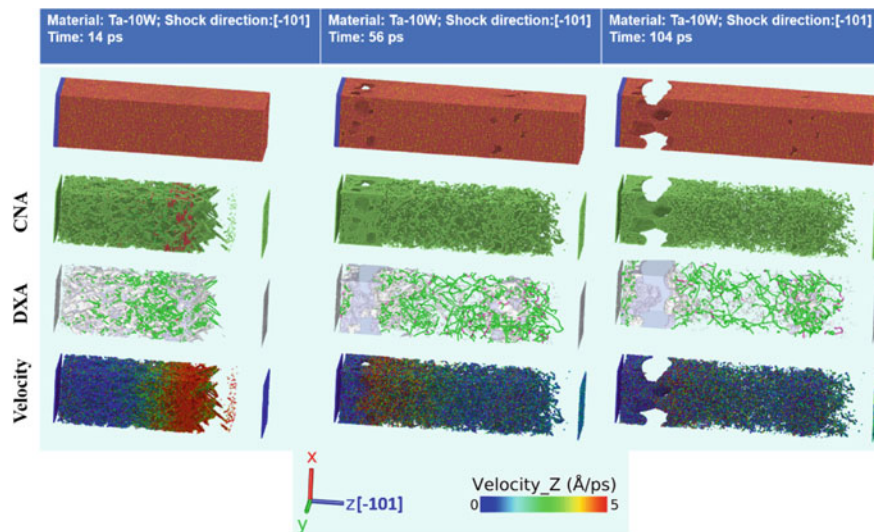
(c)
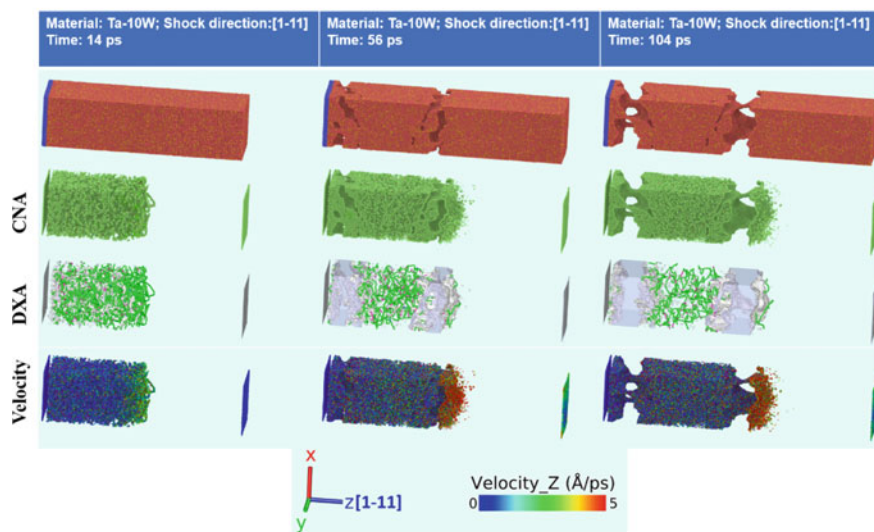
(d)

Fig. 4 (continued)
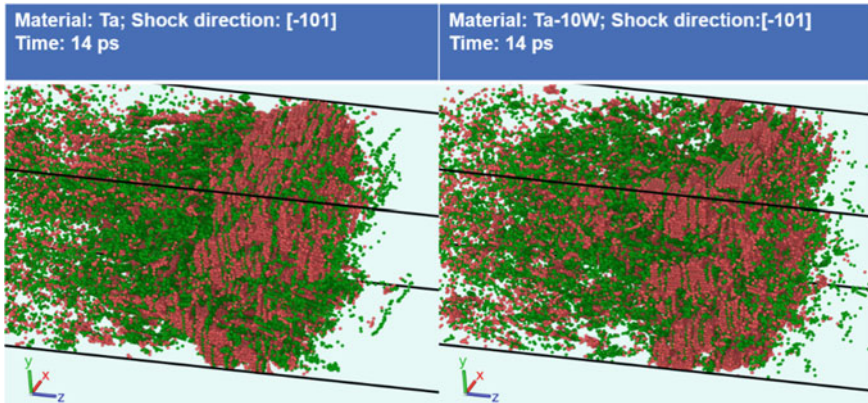
Fig. 5 Phase transformation observed in $\left[\bar{1}01\right]$ orientations of Ta and Ta-10 W configurations after CNA. The green-colored atoms are FCC atoms, the brown-colored atoms are HCP atoms and BCC atoms are removed

4 Conclusion

The current MD results and observations on the effect of tungsten addition to tantalum are listed below:

- The spallation event occurred due to the overlap of tensile and compressive waves leading to void formation, growth, and coalescence, and finally ductile fracture.
- Dislocation activity due to the compressive wave got hindered in Ta-10 W due to the increased drag force on the dislocations provided by tungsten atoms.
- Ta-10 W alloy showed a significant increase in spall strength as compared to pure Ta.
- BCC (α phase) $\rightarrow$ HCP (ω phase) transformation was observed for $\left[\bar{1}01\right]$ oriented single crystal, but not for the $\left[1\bar{1}1\right]$ oriented single crystal. The addition of tungsten reduced the ω phase formation, which was attributed to an increase in lattice friction.

References

1. Köck W, Paschen P (1989) Tantalum-processing, properties and applications. Jom 41:33–39. https://doi.org/10.1007/BF03220360
2. Cardonne SM, Kumar P, Michaluk CA, Schwartz HD (1995) Tantalum and its alloys. Int J Refract Met Hard Mater 13:187–194. https://doi.org/10.1016/0263-4368(95)94023-R
3. Buckman RW Jr (2000) New applications for tantalum and tantalum alloys. JOM 52:40–41
4. Arsenault RJ (1966) An investigation of the mechanism of thermally activated deformation in tantalum and tantalum-base alloys. Acta Metall 14:831–838. https://doi.org/10.1016/0001-6160(66)90003-4

5. Mitchell TE, Raffo PL (1967) Mechanical properties of some tantalum alloys. Can J Phys 45:1047–1062. https://doi.org/10.1139/p67-077

6. Smialek RL, Mitchell TE (1970) Interstitial solution hardening in tantalum single crystals. Philos Mag 22:1105–1127. https://doi.org/10.1080/14786437008226921

7. Anderson CE, Brotzen FR (1982) Elastic constants of tantalum-tungsten alloys. J Appl Phys 53:292–297. https://doi.org/10.1063/1.329929

8. Kothari M, Anand L (1998) Elasto-viscoplastic constitutive equations for polycrystalline metals: Application to tantalum. J Mech Phys Solids 46:51–67. https://doi.org/10.1016/S0022-5096(97)00037-9

9. Remington TP, Hahn EN, Zhao S, Flanagan R, Mertens JCE, Sabbaghianrad S, Langdon TG, Wehrenberg CE, Maddox BR, Swift DC, Remington BA, Chawla N, Meyers MA (2018) Spall strength dependence on grain size and strain rate in tantalum. Acta Mater 158:313–329. https://doi.org/10.1016/j.actamat.2018.07.048

10. Agarwal G, Dongare AM (2017) Atomistic study of shock hugoniot of single crystal Mg. AIP Conf Proc 1793. https://doi.org/10.1063/1.4971592

11. Agarwal G, Dongare AM (2016) Shock wave propagation and spall failure in single crystal Mg at atomic scales. J Appl Phys 119. https://doi.org/10.1063/1.4944942

12. Xiang M, Hu H, Chen J (2013) Spalling and melting in nanocrystalline Pb under shock loading: Molecular dynamics studies. J Appl Phys 113. https://doi.org/10.1063/1.4799388

13. Hsiung L, Lassila D (1998) Shock-induced displacive transformations in Ta and Ta-W alloys. Scr Mater 39:603–609. https://doi.org/10.1016/S1359-6462(98)00203-6

14. Burakovsky L, Chen SP, Preston DL, Belonoshko AB, Rosengren A, Mikhaylushkin AS, Simak SI, Moriarty JA (2010) High-pressure-high-temperature polymorphism in Ta: Resolving an ongoing experimental controversy. Phys Rev Lett 104:1–4. https://doi.org/10.1103/PhysRevLett.104.255702

15. Haskins JB, Moriarty JA, Hood RQ (2012) Polymorphism and melt in high-pressure tantalum. Phys Rev B - Condens Matter Mater Phys 86:18–22. https://doi.org/10.1103/PhysRevB.86.224104

16. An Q, Ravelo R, Germann TC, Han WZ, Luo SN, Tonks DL, Goddard WA (2012) Shock compression and spallation of single crystal tantalum. AIP Conf Proc 1426:1259–1262. https://doi.org/10.1063/1.3686509

17. Hahn EN, Fensin SJ, Germann TC, Gray GT (2018) Orientation dependent spall strength of tantalum single crystals. Acta Mater 159:241–248. https://doi.org/10.1016/j.actamat.2018.07.073

18. Hahn EN, Germann TC, Ravelo R, Hammerberg JE, Meyers MA (2017) On the ultimate tensile strength of tantalum. Acta Mater 126:313–328. https://doi.org/10.1016/j.actamat.2016.12.033

19. Hahn EN, Germann TC, Ravelo RJ, Hammerberg JE, Meyers MA (2017) Non-equilibrium molecular dynamics simulations of spall in single crystal tantalum. AIP Conf Proc 1793. https://doi.org/10.1063/1.4971594

20. Frenkel D, Smit B (2002) Understanding Molecular Simulation From Algorithms to Applications, Vol. 2. Academic Press

21. Kedharnath A, Kapoor R, Sarkar A (2019) Atomistic simulation of interaction of collision cascade with different types of grain boundaries in α-Fe. J Nucl Mater 523:444–457 . https://doi.org/10.1016/j.jnucmat.2019.06.021

22. Kedharnath A, Panwar AS, Kapoor R (2017) Molecular dynamics simulation of the interaction of a nano-scale crack with grain boundaries in α-Fe. Comput Mater Sci 137:85–99. https://doi.org/10.1016/j.commatsci.2017.05.026

23. Singh D, Parashar A, Kedharnath A, Kapoor R, Sarkar A (2019) Molecular dynamics-based simulations to study crack tip interaction with symmetrical and asymmetrical tilt grain boundaries in Zr. J Nucl Mater 526. https://doi.org/10.1016/j.jnucmat.2019.151739

24. Singh D, Parashar A, Kedharnath A, Kapoor R, Sarkar A (2019) Effect of symmetrical and asymmetrical tilt grain boundaries on the tensile deformation of zirconium bicrystals: a MD-based study. J Mater Sci 54:3082–3095. https://doi.org/10.1007/s10853-018-3032-7

25. Plimpton S (1995) Fast parallel algorithms for short-range molecular dynamics. J Comput Phys 117:1–19. https://doi.org/10.1006/jcph.1995.1039

26. Stukowski A (2010) Visualization and analysis of atomistic simulation data with OVITO-the Open Visualization Tool. Model Simul Mater Sci Eng 18. https://doi.org/10.1088/0965-0393/18/1/015012

27. Hirel P (2015) Atomsk: A tool for manipulating and converting atomic data files. Comput Phys Commun 197:212–219. https://doi.org/10.1016/j.cpc.2015.07.012

28. Lu CH, Hahn EN, Remington BA, Maddox BR, Bringa EM, Meyers MA (2015) Phase Transformation in Tantalum under Extreme Laser Deformation. Sci Rep 5:1–8. https://doi.org/10.1038/srep15064

29. Hsiung LM, Lassila DH (2000) Shock-induced deformation twinning and omega transformation in tantalum and tantalum-tungsten alloys. Acta Mater 48:4851–4865. https://doi.org/10.1016/S1359-6454(00)00287-1

30. Hsiung LL (2010) Shock-induced phase transformation in tantalum. J Phys Condens Matter 22. https://doi.org/10.1088/0953-8984/22/38/385702

31. Kedharnath A, Kapoor R, Sarkar A (2021) Classical molecular dynamics simulations of the deformation of metals under uniaxial monotonic loading: a review. Comput Struct 254:106614. https://doi.org/10.1016/j.compstruc.2021.106614

Coupling of Mechanical Deformation and Electrophysiology of Brain Neuron Cell

Rahul Jangid and Krishnendu Haldar

Abstract Traumatic brain injury (TBI), due to a vicious head impact in motor or space vehicle accidents, falls, and sports injuries, causes severe tissue deformation. The impact forces make the brain tissue distorted, twisted, and injured. Due to the impact, the stress inhomogeneity creates highly nonuniform strains and deforms the axons in the white matter. For more than half a century, electrophysiology of brain neurons was considered pure electrical phenomenon. However, recent experimental studies show that mechanical deformation plays a vital role in brain neuron's electrophysiology. In this work, we model the finite deformation-based coupling of mechanical deformation with the Hodgkin-Huxley (H-H) model of neuron electrophysiology. The sensitivity of stretching on the membrane potential and the generated electrical field is demonstrated.

Keywords Traumatic brain injury · Electrophysiology · Hodgkin-Huxley (H-H) model

1 Introduction

Brain deformation due to sudden trauma, blow, or jolt to the head leads to neuron cell deformation. This neuron cell deformation affects the cognitive functions or the signal flow in neurons (Electrophysiology). The loss of cognitive function due to the brain's deformation is called traumatic brain injury (TBI). Every year 70 million people suffer from TBI, and approximately 1.2 million people die worldwide [1].

The cerebrum is the largest part of the brain, which contains two cerebral hemispheres. The cerebrum consists of the frontal lobe, parietal lobe, occipital lobe, temporal lobe, and pituitary gland. Each part of the brain is responsible for different cognitive functions of the human [2]. The cerebral cortex is a layer of gray matter covering the white matter. White matter contains neuron cells in the form of fibers, which transmit electrical signals. There are three functional parts of a neuron, the

R. Jangid · K. Haldar (✉)
Aerospace Engineering, Indian Institute of Technology, Bombay, India
e-mail: krishnendu@aero.iitb.ac.in

cell body, dendrite, and axon. All the input signals are gathered and processed by the cell body, while dendrites collect the inputs from the other neurons, and the axon sends signals to the other neurons.

Mechanical behavior characterization of the brain is an essential step. Since 1960, many studies are done to understand brain deformation caused by traumatic brain injury [3–5], and many constitutive models are developed [6, 7]. For more than half a century, electrophysiology of the brain is considered pure electrical phenomenon. Recent studies on guinea pig spinal cord white matter under different loads showed that mechanical loads affect the electrical activity of neurons [8–10]. Computational models of the brain's electrophysiology for mechanical deformation of axon and tissue could be found in [11–13]. Most of the work reported on neuron cell deformation is small strain-based and predicts change in electrophysiology (signal flow) with damage model. However, in general, the large deformation leads to TBI [14]. So, there is a need for finite deformation-based coupling of neuron cell deformation to electrophysiology.

This work presents the coupling of the Hodgkin and Huxley model, a well-established model for the electrophysiology of neuron cell [15], and finite deformation due to the mechanical loading. We simulate coupled HH model, calculate the propagation of membrane potential along the length of the neuron axon, and demonstrate the effect of mechanical stretching on the membrane potential. We also calculate the electric field generated due to the change in membrane potential and geometry.

2 Hodgkin–Huxley Model

One major aspect of the computational modeling of neurons in neuroscience is understanding their electrical functionality and properties. The space inside the neurons is called intracellular space, and the space outside the neuron is called extracellular space. The potential difference between the intracellular(V_i) and the extracellular(V_e) space is called the membrane potential (V_m). The equilibrium membrane potential is known as the resting potential, which is around -65mV. The extracellular potential(V_e) remains fixed, whereas intracellular potential (V_i) changes. The change in intracellular potential (V_i) or membrane potential leads to electric current flow along the length of neurons cell and current flow between intracellular space and extracellular space through the membrane (Fig. 1). The intracellular medium and the extracellular medium contain differing concentrations of various ions. Some essential inorganic ions are positively charged cations, including sodium (Na^+), potassium (K^+), calcium (Ca^{2+}), magnesium (Mg^{2+}), and negatively charged anions such as chloride (Cl^-). The charges carried by anions and cations are usually almost balanced within and outside the cell. A typical neuron membrane contains a sodium channel, a potassium channel, and a leak channel. Sodium and potassium channels only allow the flow of sodium and potassium ions, respectively, where the sodium-potassium
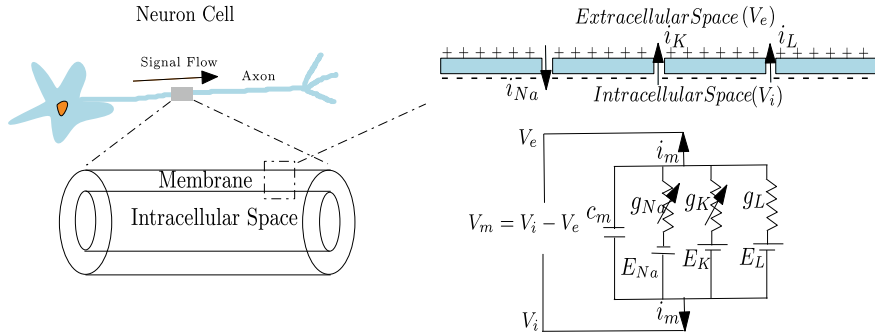
Fig. 1 HH model and neuron cell

ionic pump enables the flow of sodium-potassium ions. Hodgkin and Huxley performed experiments to measure the conductivity of potassium and sodium channels. They found that the conductivity of channels is dependent on potential and time. To represent in mathematical form, they consider four gating particles for the potassium channel and define the probability of opening and closing of gating particles by a function n. For sodium channel conductivity, they consider four gating particles, three gating particles having the probability of opening and closing as a function m and one as a function h. They finally represented the neurons as an electrical circuit, as shown in Fig 1, and derived the total membrane current (i_m) equation as [15]

$$i_m = c_m \frac{dV_m}{dt} + \bar{g}_{Na} m^3 h (V_m - E_{Na}) + \bar{g}_K n^4 (V_m - E_k) + g_L (V_m - E_L) \quad (1)$$

where,

$$g_{Na} = \bar{g}_{Na} m^3 h, \quad g_K = \bar{g}_K n^4$$

$$\frac{dn}{dt} = (1-n)\alpha_n - n\beta_n, \quad \frac{dm}{dt} = (1-m)\alpha_m - m\beta_m, \quad \frac{dh}{dt} = (1-h)\alpha_h - h\beta_h$$

$$\alpha_m = 0.1 \frac{V_m + 40}{1 - exp(-\frac{V_m+40}{10})}, \quad \alpha_n = 0.01 \frac{V_m + 55}{1 - exp(-\frac{V_m+55}{10})}, \quad \alpha_h = 0.07 \left(exp \left(-\frac{V_m + 65}{20} \right) \right)$$

$$\beta_m = 4 \left(exp \left(-\frac{V_m + 65}{18} \right) \right), \quad \beta_n = 0.125 \left(exp \left(-\frac{V_m + 65}{80} \right) \right), \quad \beta_h = \frac{1}{1 + exp(-\frac{V_m+35}{10})}.$$

Here, c_m, $\bar{g}_{Na}$, $\bar{g}_K$, and g_L are the capacitance per unit length, the conductivity of sodium channel per unit length, the conductivity of potassium channel per unit length, and the conductivity of leak channel per unit length, respectively. All these are the fundamental properties of the neuron membrane.

3   Cable Equation

A mathematical equation derived from an electric circuit, as shown in Fig. 2, for modeling the membrane, intracellular, and extracellular space to provide a quantitative description of current flow and membrane potential change is called cable equation. The cable equation derived from the equivalent electric circuit, shown in Fig. 2, is written as

$$\frac{d}{4R_i}\frac{\partial^2 V_m(x,t)}{\partial x^2} = C_m\frac{\partial V_m(x,t)}{\partial t} + G_{Na}m(x,t)^3h(x,t)(V_m(x,t) - E_{Na}) \tag{2}$$
$$+ G_Kn(x,t)^4(V_m(x,t) - E_k) + G_L(V_m(x,t) - E_L)$$

where,

$$\frac{\partial n(x,t)}{\partial t} = (1 - n(x,t))\alpha_n(x,t) - n(x,t)\beta_n(x,t)$$

$$\frac{\partial m(x,t)}{\partial t} = (1 - m(x,t))\alpha_m(x,t) - m(x,t)\beta_m(x,t)$$

$$\frac{\partial h(x,t)}{\partial t} = (1 - h(x,t))\alpha_h(x,t) - h(x,t)\beta_h(x,t).$$
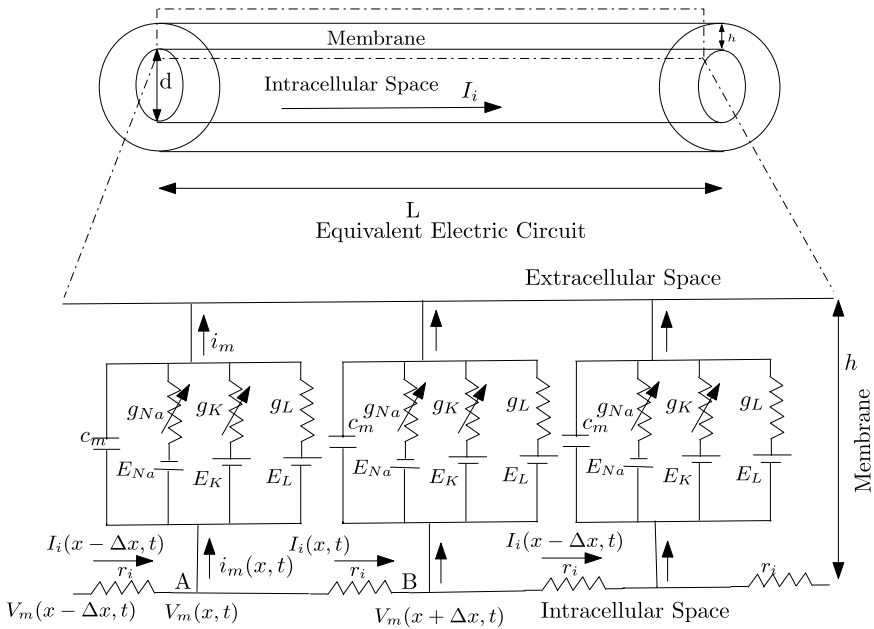
Fig. 2   Idealized neuron structure and electric circuit

Here, $C_m = \frac{c_m}{\pi d}$, $G_{Na} = \frac{\bar{g}_{Na}}{\pi d}$, $G_K = \frac{\bar{g}_K}{\pi d}$, $G_L = \frac{\bar{g}_L}{\pi d}$, $R_i = \frac{r_i \pi d^2}{4}$. Moreover, d, $I_i = -\frac{1}{r_i} \frac{\partial V_m}{\partial x}$, and r_i are the diameter of the axon of the neuron, axial current in intracellular space, and resistance per unit length of intracellular space.

4 Mechanical Deformation and Coupling

The deformation of a cylinder with torsion and extension can be written as

$$r = \bar{r}(R), \ \theta = \Theta + D\Theta, \ x = \lambda X$$

where (R, Θ, X) and (r, θ, x) are the cylindrical coordinates of a typical a point in the reference configuration and in the current configuration, respectively. X or x is in the direction of cylindrical ends, and The amount of axial stretch is denoted by $\lambda > 0$. D denotes the twist per unit undeformed length.

We consider that the dominant mode of deformation for neuron cells is an incompressible axial stretch. We write deformation,

$$r = \lambda^{-1} R, \ \theta = \Theta, \ x = \lambda X.$$

4.1 Coupling of Mechanical Deformation and Cable Equation

In the HH model and cable equation (Eqs. 1 and 2), R_i, $\bar{g}_{Na}$, $\bar{g}_K$, c_m, and g_L are the fundamental properties and only depend on axon composition. However, the capacitance and conductivity in Eq. 2 are geometry dependent. For example

$$C_m = \frac{c_m}{\pi d} = \frac{c_m}{\pi \lambda^{-1} d_0} = \lambda C_m^0.$$

Similarly

$$G_{Na} = \lambda G_{Na}^0, \ \ G_K = \lambda G_K^0, \ \ G_L = \lambda G_L^0, \ \ \frac{\partial^2 V_m(x, t)}{\partial x^2} = \lambda^{-2} \frac{\partial^2 V_m(X, t)}{\partial X^2}.$$

Then final Cable equation can be written in the reference configuration as

$$\lambda^{-4} \frac{d_0}{4R_i} \frac{\partial^2 V_m(X, t)}{\partial X^2} = C_m^0 \frac{\partial V_m(X, t)}{\partial t} + G_{Na}^0 m(X, t)^3 h(X, t)(V_m(X, t) - E_{Na})$$
$$+ G_K^0 n(X, t)^4 (V_m(X, t) - E_k) + G_L^0 (V_m(X, t) - E_L).$$

$$(3)$$

5 Coupled Solutions of Cable Equation with Stretch

We use the semi-finite difference approach for the simulation of the cable equation. We divide the length of neurons axon in N-1 number of elements (N number of nodes) with grid size δX, and the cable equation (Eq. 3) for ith node of neuron axon is written as follows

$$\lambda^{-4}\frac{d_0}{4R_i}\frac{d^2V_m^i}{dX^2} = C_m^0\frac{dV_m^i}{dt} + G_{Na}^0 m^{i3}h^i(V_m^i - E_{Na}) + G_K^0 n^{i4}(V_m^i - E_k) + G_L^0(V_m^i - E_L).$$
(4)

From central difference formula,

$$\frac{d^2V_m^i}{dX^2} = \frac{V_m^{i+1} - 2V_m^i + V_m^{i-1}}{\delta X^2}.$$

We further write

$$\begin{aligned} C_m^0\frac{dV_m^i}{dt} =& \lambda^{-4}\frac{d_0}{4R_i}\frac{V_m^{i+1} - 2V_m^i + V_m^{i-1}}{\delta X^2} - G_{Na}^0 m^{i3}h^i(V_m^i - E_{Na}) \\ & - G_K^0 n^{i4}(V_m^i - E_k) - G_L^0(V_m^i - E_L), \end{aligned}$$
(5)

where,

$$\frac{dn^i}{dt} = (1 - n^i)\alpha_n^i - n^i\beta_n^i, \frac{dm^i}{dt} = (1 - m^i)\alpha_m^i - m^i\beta_m^i, \frac{dh^i}{dt} = (1 - h^i)\alpha_h^i - h^i\beta_h^i$$

$$\alpha_m^i = 0.1\frac{V_m^i + 40}{1 - exp(-\frac{V_m^i + 40}{10})}, \alpha_n^i = 0.01\frac{V_m^i + 55}{1 - exp(-\frac{V_m^i + 55}{10})}, \alpha_h^i = 0.07\left(exp\left(-\frac{V_m^i + 65}{20}\right)\right)$$

$$\beta_m^i = 4\left(exp\left(-\frac{V_m^i + 65}{18}\right)\right), \beta_n^i = 0.125\left(exp\left(-\frac{V_m^i + 65}{80}\right)\right), \beta_h^i = \frac{1}{1 + exp(-\frac{V_m^i + 35}{10})}.$$

The given coupled ODEs have been solved using python's SciPy module, and the properties of the used materials are provided in Table 1 [15]. We consider a sealed end boundary condition, i.e., no current flow from both ends. Initially, one end of the axon is kept at 0 mV, and the rest of the axon is kept at equilibrium membrane potential(-65 mV). This initial condition leads to current flow along the length and current flow between intracellular space and extracellular space through the membrane.

Table 1 Material Properties

R_i	$1.87\ \Omega m$
d_0	$4\ \mu m$
C_m^0	$1\ \mu F cm^{-2}$
$\bar{G}_{Na}^0$	$120\ m Scm^{-2}$
$\bar{G}_K^0$	$136\ m Scm^{-2}$
$\bar{G}_L^0$	$10.3\ m Scm^{-2}$
E_{Na}	$50\ mV$
E_K	$-77\ mV$
E_L	$-54.4\ mV$
Equilibrium V_m	$-65\ mV$
Length of axon (L)	8 mm
Thickness of membrane (h_0)	4 nm

Boundary conditions:

$$\frac{\partial V_m(0, t)}{\partial X} = \frac{\partial V_m(L, t)}{\partial X} = 0$$

Initial condition:

$$V_m(X, 0) = \begin{cases} 0\ mV & x = 0 \\ -65\ mV & x > 0 \end{cases}$$

.

Fig. 3a shows the membrane potential along the length of a neuron at different time instances, whereas Fig. 3b shows the membrane potential along the length of axon for different values of axial stretch (λ). The propagation of membrane potential gets delayed with increasing axial stretch value (λ) as shown in Fig. 3b.

5.1   Radial Electric Field in Membrane

The voltage difference between the extracellular medium and intracellular medium leads to a radial electric field. We have calculated the radial electric field for different axial stretch values (λ) by using Eq. 6.

$$E_r^m = \frac{V_m}{h} = \lambda \frac{V_m}{h_0}. \tag{6}$$

The response is shown in Fig. 4a. The propagation of the radial electric field is getting delayed, and the maximum value of the radial electric field increases as axial stretch (λ) increases, where h_0 is the initial thickness of the membrane.

(a) Potential of neuron for no stretch   (b) Potential of neuron with axial stretch
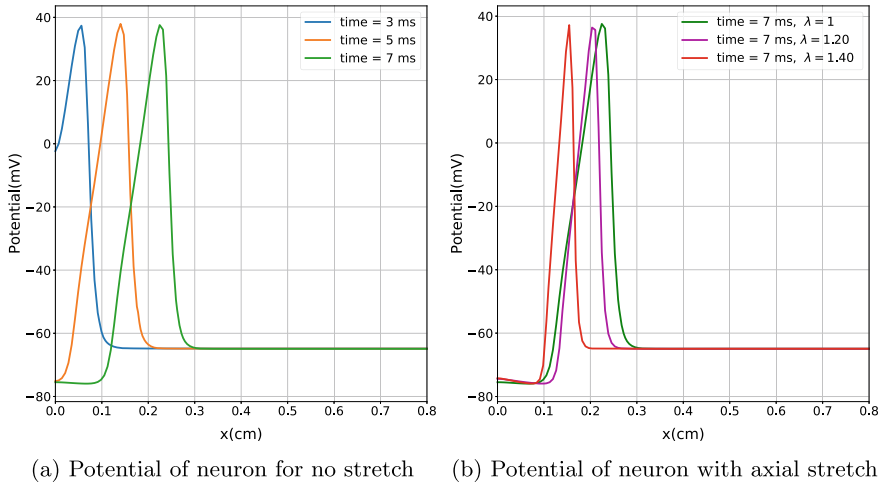
Fig. 3 Membrane potential of neuron

(a) Radial electric field in membrane   (b) Axial electric field in intracellular space
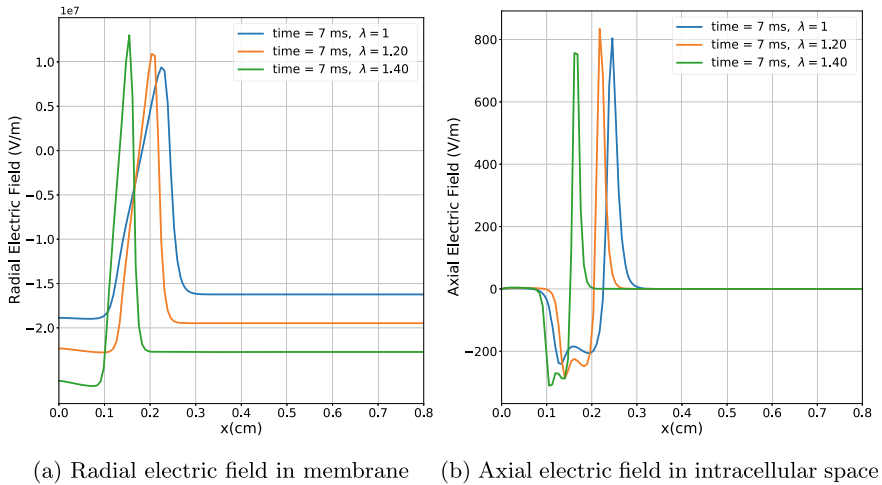
Fig. 4 Electric field in neuron

5.2 *Axial Electric Field in Intracellular Spcae*

There is also a voltage difference along the length of the neuron in the intracellular space. We have calculated the axial electric field for different axial stretch values (λ) by using Eq. 7.

$$E_x^i = -\frac{dV_i}{dx} = -\frac{dV_m}{dx} = -\lambda^{-1}\frac{dV_m}{dX}. \tag{7}$$

The response is shown in Fig. 4b. The propagation of the axial electric field is getting delayed as axial stretch (λ) increases.

6 Conclusion

In this work, we captured the natural coupling of the HH model with the deformation. We presented coupled cable equation with different axial stretches to show the changes in the membrane potentials along the axon length. We found a delay in the traveling membrane potential along the axon as the axial stretch increases (Fig.3b). This can eventually lead to a delay in cognitive functions. Based on the HH model solution, we derive the electric field in a neuron cell. We found a significant radial electric field in the membrane compared to the intracellular space axial electric field.

References

1. Dewan MC, Rattani A, Gupta S, Baticulon RE, Hung YC, Punchak M,Agrawal A, Adeleye AO, Shrime MG, Rubiano AM, Rosenfeld JV, Park KB (2018) Estimating the global incidence of traumatic brain injury. J Neurosurg JNS 130(4)
2. Carter R (2019) The brain book: an illustrated guide to its structure, functions, and disorders
3. Budday S, Sommer G, Birkl CR, Langkammer C, Haybaeck J, Kohnert JD, Bauer M, Paulsen F, Steinmann P, Kuhl E, Holzapfel GA (2017) Mechanical characterization of human brain tissue. Acta Biomater 48:319–340
4. Zhao H, Yin Z, Li K, Liao Z, Xiang H, Zhu F (2016) Mechanical characterization of immature porcine brainstem in tension at dynamic strain rates. Med Sci Monit Basic Res
5. Prange MT, Margulies SS (2002) Regional, directional, and age-dependent properties of the brain undergoing large deformation. J Biomech Eng 124(2):244–252
6. Haldar K, Pal C (2018) Rate dependent anisotropic constitutive modeling of brain tissue undergoing large deformation. J Mech Behav Biomed Mater 81:178–194
7. Velardi F, Fraternali F, Angelillo M (2006) Anisotropic constitutive equations and experimental tensile behavior of brain tissue. Biomech Model Mechanobiol 5(1):53–61
8. Shi R, Whitebone J (2006) Conduction deficits and membrane disruption of spinal cord axons as a function of magnitude and rate of strain. J Neurophysiol
9. Ouyang H, Galle B, Li J, Nauman E, RJ S (2008) Biomechanics of spinal cord injury: a multimodal investigation using ex vivo guinea pig spinal cord white matter. J Neurotrauma
10. Connell S, Ouyang H, Shi R (2011) Modeling blast induced neurotrauma in isolated spinal cord white matter. J Med Syst
11. Chen H, Garcia-Gonzalez D, Jérusalem A (2019) Computational model of the mechanoelectrophysiological coupling in axons with application to neuromodulation. Phys Rev E 99:032406
12. Jérusalem A, García-Grajales J, Merchán-Pérez A (2014) A computational model coupling mechanics and electrophysiology in spinal cord injury. Biomech Model Mechanobiol 13

13. Garcia-Gonzalez D, Jerusalem A (2019) Energy based mechano-electrophysiological model of cns damage at the tissue scale. J Mech Phys Solids 125:22–37
14. Atsumi N, Nakahira Y, Iwamoto M, Hirabayashi S, Tanaka E (2016) Constitutive modeling of brain parenchyma taking account of strain rate dependency with anisotropy and application to brain injury analyses. SAE Tech Pap
15. Hodgkin AL, Huxley AF (1952) A quantitative description of membrane current and its application to conduction and excitation in nerve. J Physiol

Nonlocal Diffused Approach to Model Delamination in Composites

Dhaladhuli Pranavi and Amirtham Rajagopal

Abstract Delamination is a critical failure mode in composites as its constituents get separated due to the weakening of the interface between the layers of such composites. Manufacturing defects, sites of stress concentrations, free edge effects are causes for delamination. Upon loading of such composites the delamination can grow and also mitigate between layers, finally leading to the structural failure. In order to assess structural integrity, the material parameters that govern the delamination growth should be determined. In the present work, a nonlocal diffused approach is proposed to model the delamination. Nonlocal approaches help in understanding the complex mechanisms of delamination growth and mitigation and operates at a material length scale. The performance of the proposed formulation is illustrated through representative numerical example. Parametric studies are conducted to understand the role of fiber orientation and the material properties leading to anisotropy.

Keywords Delamination · Composite · Nonlocal approach · Anisotropy

1 Introduction

Two or more components are combined structurally to form composite materials to enhance stiffness, thermal properties, strength and produce light weight materials. Fiber-reinforced composites consisting of fiber and matrix phases are widely applied in aerospace industry. Lamina with unidirectional fibers or woven fibers are stacked together in a sequence to acquire a laminated fiber-reinforced composite. The mechanical behavior of such composites depends on orientation of the fiber, properties and volume fractions of the matrix and fiber constituents. The interface between the two components in a lamina and also between the different laminae plays a key role in the structural stability of the composite. Due to the definite inhomogeneity and presence of varied interfaces, understanding fracture in composites

D. Pranavi (✉) · A. Rajagopal
Indian Institute of Technology, Hyderabad, India
e-mail: ce18m20p000001@iith.ac.in

is much more complex when compared to homogeneous, isotropic materials such as steel.

Crack initiation and crack propagation for a material can be explained by two criteria: (i) strength criteria and (ii) energy criteria. In the case of strength criteria, failure occurs when the stresses reaches a critical value in a laminate. The failure mechanism in composites is studied using this approach in [1]. The transverse cracking effect cannot be explained accurately using this criteria. On the other hand, energy criteria states that the crack propagates only when the energy release rate exceeds the critical energy release rate which is a material property [2].

Numerical methods can be employed to model the complex crack phenomena in composites. Stress intensity factors can be evaluated using FEM analysis [3]. Cohesive zone modeling is used to understand both the Mode I and Mode II failures in laminated composites in [4]. There are other methods like extended finite element method XFEM [5], Peridynamics [6] which can model composite fracture/failure. Smeared crack models are widely applied in solving complex problems involving crack initiation, crack branching and multiple cracking phenomena [7]. It considers regularization of the crack represented by a decreasing exponential function. The approach can also be applied to model brittle fracture [8], ductile fracture [9], dynamic fracture [10] and cohesive fracture [11]. This approach is further extended to anisotropic materials [13] to model directional fracture [14], intralaminar and translaminar fracture [15]. It can also be applied to nanocomposites [16], composites with varied stiffness [17] and hyper elastic materials [18].

Delamination under mode I loading is shown in Fig. 1. It ruptures the structure and also deteriorate the compressive strength of the laminate leading to excessive buckling. Delamination grows from pre-existent discontinuities such as notches, stress concentrations. For the complete structural assessment, knowledge on delamination initiation, propagation and the material parameters that impact these events is inevitable.

(a)   (b)
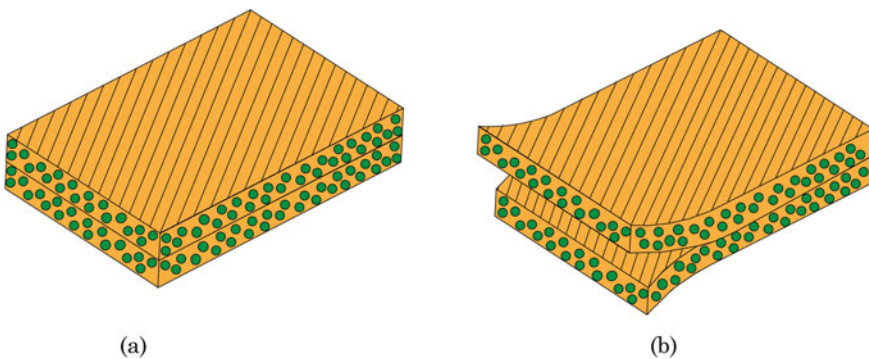
Fig. 1 Unidirectional fiber-reinforced composite lamina in **a** Undeformed state and **b** Deformed state after delamination under Mode I loading

In the present work, anisotropic crack density functional having a structural tensor corresponding to the fiber orientations of the composite is considered which is proposed and implemented in [14, 19, 20]. The anisotropic model is adopted to analyze the delamination in unidirectional fiber-reinforced composite. The crack driving force has two components corresponding to the matrix and fiber phases which determine the crack propagation. The effect of the interface between the fiber and matrix is not considered in the present analysis as at a macroscopic level, the properties of the composite are mostly influenced by the individual phases (matrix and fiber) than the interface (matrix-fiber interface). The main aim of this paper is to understand the influence of fiber orientation and anisotropy parameter α on the crack propagation and the mechanical response of the whole system.

2 Methodology

A solid body Ω with a sharp crack Γ_c is considered as shown in Fig. 2. The global energy functional can be written as (body forces and surface tractions are neglected).

$$E = \int_\Omega \psi(\boldsymbol{\varepsilon}(\boldsymbol{u}))d\Omega + \int_\Omega G_c dA \tag{1}$$

ψ is the energy storage functional, G_c is the critical energy release rate and $\gamma(s, \nabla s)$ is the crack density function. The sharp crack Γ_c is now diffused to Γ_s which is defined as

$$\Gamma_s = \int_a \gamma(s, \nabla s)d\Omega, \text{ where } \gamma(s, \nabla s) = \frac{1}{2l_s}s^2 + \frac{l_s}{2}(\nabla s \cdot \boldsymbol{A}\nabla s) \tag{2}$$
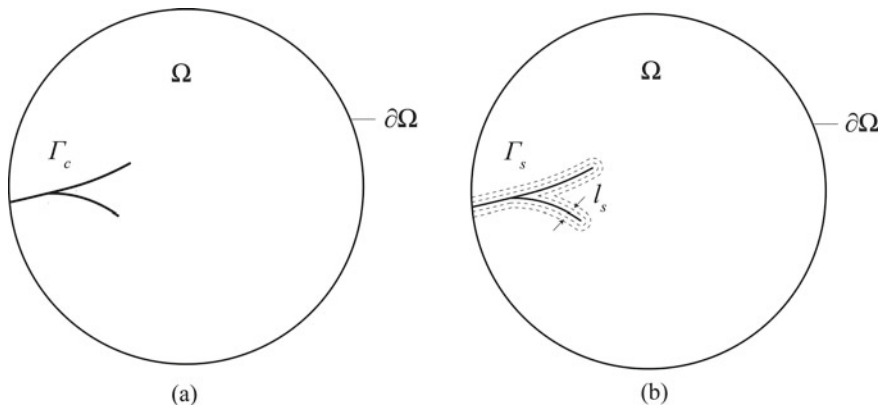
Fig. 2 Solid domain Ω having **a** sharp crack Γ_c and **b** the smeared crack Γ_s

where s represents the phase field variable whose value ranges between 0 and 1 and l_s represents the smeared width of the crack. $\boldsymbol{A}$ is the second order anisotropic structural tensor which is defined as

$$\boldsymbol{A} = \boldsymbol{I} + \alpha \boldsymbol{f} \otimes \boldsymbol{f} \tag{3}$$

$\boldsymbol{I}$ is the second order identity tensor, α is the anisotropy parameter and $\boldsymbol{f}$ is the unit vector corresponding to the fiber orientation in the composite. Equation (1) can be written in terms of the crack density function $\gamma(s, \nabla s)$ defined in Eq. (2) as

$$E = \int_\Omega \psi(\boldsymbol{\varepsilon}(\boldsymbol{u})) d\Omega + \int_\Omega G_c \gamma(s, \nabla s) d\Omega \tag{4}$$

The crack driving force can be written as

$$H = \frac{\psi^f}{G_f} + \frac{\psi^{mI}}{G_{mI}} + \frac{\psi^{mII}}{G_{mII}} \tag{5}$$

where ψ^f, ψ^{mI} and ψ^{mII} are the energy storage functional corresponding to fiber and matrix failure mechanisms.

Delamination Test
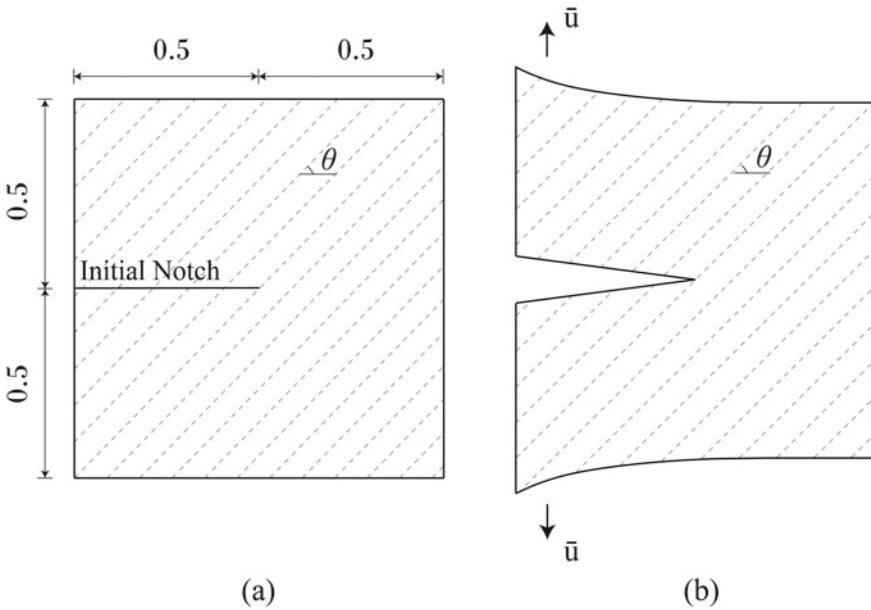
Fig. 3 **a** Geometry and **b** boundary conditions for the single edge notched specimen

	θ	α
M1-A	0°	0
M1-D	0°	20
M2-A	30°	0
M2-B	30°	10
M2-C	30°	15
M2-D	30°	20

Table 1 Combinations considered for the analysis

Consider a single edge notched (SEN) specimen of size 1×1 as depicted in Fig. 3a. The notch extends to the center of the specimen. An element size $h = 0.01$ mm and internal length scale $l_s = 2h$ is adopted. The load is applied in terms of displacement at top and bottom ends as shown in Fig. 3b and θ corresponds to the orientation of the fibers. Two models, M1, M2 corresponding to $\theta = 0°$ and $\theta = 30°$ and four cases, A, B, C, D corresponding to $\alpha = 0$, $\alpha = 10$, $\alpha = 15$ and $\alpha = 20$ are considered for the analysis. The combinations are given in Table 1.

Remark The unidirectional composite is considered to be orthotropic. The constitutive matrix can be written as.

$$\boldsymbol{C} = \boldsymbol{R}^T \boldsymbol{Q} \boldsymbol{R}, \boldsymbol{R} = \begin{bmatrix} \cos\theta & \sin\theta & 0 \\ -\sin\theta & \cos\theta & 0 \\ 0 & 0 & 1 \end{bmatrix}, \boldsymbol{Q} = \begin{bmatrix} Q_{11} & Q_{12} & 0 \\ Q_{12} & Q_{22} & 0 \\ 0 & 0 & Q_{66} \end{bmatrix} \tag{6}$$

$$Q_{11} = \frac{E_{11}}{1 - v_{12}v_{21}}, Q_{22} = \frac{E_{22}}{1 - v_{12}v_{21}}, Q_{12} = \frac{v_{12}E_{22}}{1 - v_{12}v_{21}}, Q_{66} = G_{12}$$

The longitudinal stiffness, transverse stiffness and shear stiffness of the lamina are taken as $E_{11} = 114.8$ GPa, $E_{22} = 11.7$ GPa and $G_{12} = 9.66$ GPa, respectively. Poisson's ratio, $v_{12} = 0.21$. The critical energy release rates are taken as $G_f = 106.3 \times 10^{-3}$ kN/mm, $G_{mI} = 0.2774 \times 10^{-3}$ kN/mm, $G_{mII} = 0.2774 \times 10^{-3}$ kN/mm (refer [19]).

3 Results

From Fig. 4, it is evident that the crack propagation is straight for M1-A and M2-A as the anisotropy parameter $\alpha = 0$ indicates isotropic case. For the anisotropy parameter, $\alpha = 20$, the crack propagation is along the fiber orientation θ which is 0° for M1-D and 30° for M2-D. The crack path for different values of anisotropy parameter for $\theta = 30°$ is plotted in Fig. 4c–f. It can be observed that as the anisotropy parameter α increases, the crack path is tending toward 30° and the difference is less
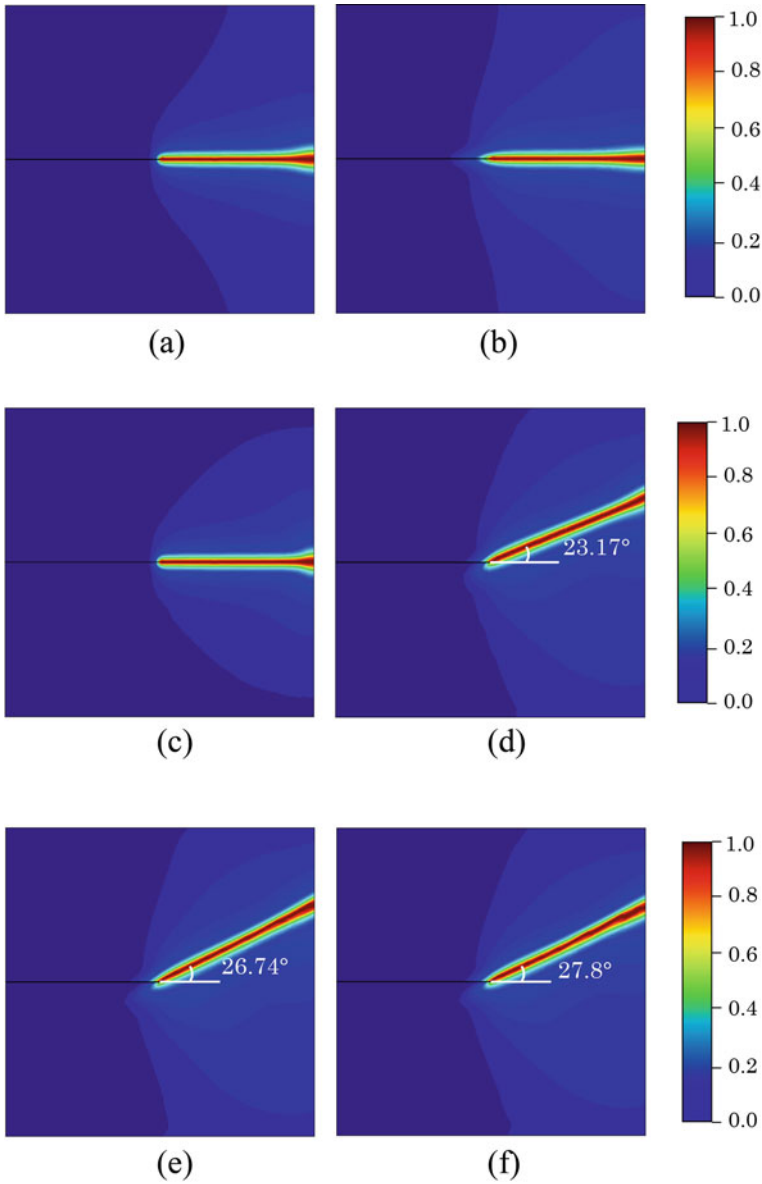
Fig. 4 Evolution of the crack phase field for **a** M1-A at $\bar{u} = 0.00989$ mm **b** M1-D at $\bar{u} = 0.0113$ mm **c** M2-A at $\bar{u} = 0.00663$ mm **d** M2-B at $\bar{u} = 0.00725$ mm **e** M2-C at $\bar{u} = 0.00736$ mm and **f** M2-D at $\bar{u} = 0.00744$ mm where $\bar{u}$ is the failure displacement. The contour plot of the phase field variable s varying from 0 to 1 is shown on the right side of each row.
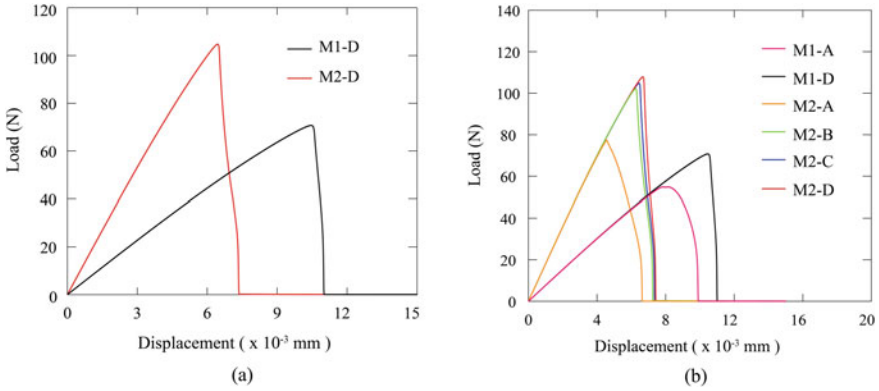
Fig. 5 Load–displacement plots for **a** M1-D and M2-D **b** M1-A, M1-D, M1-C3, M2-A, M2-B, M2-C and M2-D

between $\alpha = 15$ and $\alpha = 20$ when compared to other values of α. The load–displacement curves are plotted for (a) M1-D and M2-D in Fig. 5a, b M1-A, M1-D, M2-A, M2-B, M2-C and M2-D in Fig. 5b.

From Fig. 5a, it is evident that as the fiber orientation (θ) increases, the failure load increases. It can be observed from Fig. 5b that as the anisotropy parameter (α) increases the failure load increases and the rise is very high for anisotropic cases ($\alpha = 10, 15, 20$) when compared to the isotropic case ($\alpha = 0$).

4 Conclusions

From the results in Sect. 3, it can be inferred that the crack propagates along the fiber direction for the anisotropic case, $\alpha > 0$, because the fracture toughness of the fiber is high compared to the matrix, and the fiber failure is not possible. For the isotropic case, the crack propagates straight irrespective of fiber orientation as the crack propagation is not direction-dependent. From load–displacement plots, it can be observed that the failure load is very high for the anisotropic case and also failure load increases with an increase in fiber orientation and anisotropy parameter.

References

1. Puck A, Schürmann H (1998) Failure analysis of FRP laminates by means of physically based phenomenological models. Compos Sci Technol 58:1045–1067. https://doi.org/10.1016/B978-008044475-8/50028-7.
2. Griffith AA (1921) The phenomena of rupture and flow in solids. Philos Trans R Soc A 221:163–197. https://doi.org/10.1098/rsta.1921.0006

3. Barsoum RS (1976) On the use of isoparametric finite elements in linear fracture mechanics. Int J Numer Methods Eng 10:25–37. https://doi.org/10.1002/nme.1620100103
4. Zhao L, Gong Y, Zhang J, Chen Y, Fei B (2016) Simulation of delamination growth in multi-directional laminates under mode I and mixed mode I/II loadings using cohesive elements. Compos Struct 116:509–522. https://doi.org/10.1016/j.compstruct.2014.05.042
5. Yazdani S, Rust WJH, Wriggers P (2016) An XFEM approach for modelling delamination in composite laminates. Compos Struct 135:353–364. https://doi.org/10.1016/j.compstruct.2015.09.035
6. Ren H, Zhuang X, Rabczuk T (2017) Dual-horizon peridynamics: a stable solution to varying horizons. Comput Methods Appl Mech Eng 318:762–782. https://doi.org/10.1016/j.cma.2016.12.031
7. Francfort GA, Marigo JJ (1998) Revisiting brittle fracture as an energy minimization problem. J Mech Phys Solids 46:1319–1342. https://doi.org/10.1016/S0022-5096(98)00034-9
8. Miehe C, Welschinger F, Hofacker M (2010) Thermodynamically consistent phase-field models of fracture: variational principles and multi-field FE implementations. Int J Numer Methods Eng 83:1273–1311. https://doi.org/10.1002/nme.2861
9. Ambati M, Gerasimov T, De Lorenzis L (2015) Phase-field modeling of ductile fracture. Comput Mech 55:1017–1040. https://doi.org/10.1007/s00466-015-1151-4
10. Borden MJ, Verhoosel CV, Scott MA, Hughes TJ, Landis CM (2012) A phasefield description of dynamic brittle fracture. Comput Methods Appl Mech 217:77–95. https://doi.org/10.1016/j.cma.2012.01.008
11. Verhoosel CV, De Borst R (2013) A phase-field model for cohesive fracture. Int J Numer Methods Eng 96:43–62. https://doi.org/10.1002/nme.4553
12. Nguyen TT, Yvonnet J, Zhu QZ, Bornert M, Chateau C (2016) A phase-field method for computational modeling of interfacial damage interacting with crack propagation in realistic microstructures obtained by microtomography. Comput Methods Appl Mech Eng 312:567–595. https://doi.org/10.1016/j.cma.2015.10.007
13. Gültekin O, Dal H, Holzapfel GA (2016) A phase-field approach to model fracture of arterial walls: theory and finite element analysis. Comput Methods Appl Mech Eng 312:542–566. https://doi.org/10.1016/j.cma.2016.04.007
14. Clayton JD, Knap J (2015) Phase field modeling of directional fracture in anisotropic polycrystals. Comput Mater Sci 98:158–169. https://doi.org/10.1016/j.commatsci.2014.11.009
15. Quintanas-Corominas A, Reinoso J, Casoni E, Turon A, Mayugo JA (2019) A phase field approach to simulate intralaminar and translaminar fracture in long fiber composite materials. Compos Struct 220:899–911. https://doi.org/10.1016/j.compstruct.2019.02.007
16. Msekh MA, Cuong NH, Zi G, Areias P, Zhuang X, Rabczuk T (2018) Fracture properties prediction of clay/epoxy nanocomposites with interphase zones using a phase field model. Eng Fract Mech 188:287–299. https://doi.org/10.1016/j.engfracmech.2017.08.002
17. Natarajan S, Annabattula RK (2019) Modeling crack propagation in variable stiffness composite laminates using the phase field method. Compos Struct 209:424–433. https://doi.org/10.1016/j.compstruct.2018.10.083
18. Mandal TK, Nguyen VP, Wu JY (2020) A length scale insensitive anisotropic phase field fracture model for hyperelastic composites. Int J Mech Sci 188. https://doi.org/10.1016/j.ijmecsci.2020.105941
19. Zhang P, Hu X, Bui TQ, Yao W (2019) Phase field modeling of fracture in fiber reinforced composite laminate. Int J Mech Sci 161–162. https://doi.org/10.1016/j.ijmecsci.2019.07.007
20. Nguyen TT, Réthoré J, Baietto MC (2017) Phase field modelling of anisotropic crack propagation. Eur J Mech A Solids 65:279–288. https://doi.org/10.1016/j.euromechsol.2017.05.002

Numerical Analysis of Delamination Tolerance in Hybrid Composite Laminates

Savitha N. Nambisan and B. Dattaguru

Abstract Weight savings and better damage tolerance are the key drivers for the emergence and deployment of new materials in the Aerospace Industry. The development of hybrid composite laminates is a promising strategy to enhance tolerance to delamination type of defects in laminates considering the synergistic effect of different fibers. This paper presents a numerical study to develop a new carbon–glass hybrid laminate with minimum loss in stiffness and simultaneously delay or prevent delamination growth. Geometrical non-linear finite element analysis is carried out on three-dimensional models of delaminated non-hybrid and hybrid composite laminates. The mode 1 Strain Energy Release Rate (SERR) is calculated using Modified Virtual Crack Closure Integral (MVCCI). The mode 1SERR is compared for the hybrid and non-hybrid laminates. The hybridization leads to much smaller strain energy release rates at all levels of loading. Hybridizing CFRP laminate with GFRP lamina on the third interface is found to be an efficient way to improve delamination tolerance without reducing laminate resistance to flexural and impact loads.

Keywords Laminated composites · Delaminations tolerance · Hybridization

1   Introduction

Various industries like Aerospace, wind energy and Automotive desire designs of structures with materials possessing a high strength/weight ratio. Laminated composites are significantly used in the weight-sensitive industrial structures due to their excellent specific stiffness and specific strength properties. In spite of these advantages, there are important issues regarding damages in these multi-layer constructions, which need attention. One of the important damage of concern for designers is delamination between layers. During the operational phase, delamination might grow and fully delaminate a few layers and this will cause loss of buckling strength of the laminate. Intuitively one of the methods stated is to hybridize the laminate with different fibers which will prevent or delay the delamination growth.

S. N. Nambisan (✉) · B. Dattaguru
School of Aerospace Engineering, Jain (Deemed to be University), Bangalore, India

One more aspect in this connection is that delamination lies buried between the layers and may not be identified during the non-destructive inspection. For this purpose, "Barely Visible Impact Damage" (BVID) is identified for laminates. BVID, caused by low-velocity impact events such as dropped tools and impact of small runway debris leave surface indentations which are too small to be seen on routine aircraft inspections. Delaminations of sizes smaller than BVID are dangerous since they could be missed by the inspecting technician and they could grow during the operational life of the composite. Under compressive fatigue loading, such damage can propagate and it can cause further loss of overall buckling strength. Hence, delamination tolerance which is the ability of a composite structure to withstand or tolerate this damage and limit its propagation under service loading until the next scheduled inspection is of high significance.

Fiber hybridization is one of the ways to toughen the composite structures. Compared to laminated composites in which all the layers are of the same material, hybrid composites offer several advantages by combining two or more fiber types. For instance, replacing some of the carbon fibers in the middle of a laminate with cheaper glass fibers can significantly reduce the cost, while the flexural properties remain almost unaffected [1]. Andrew et al. [2] demonstrated that the structural efficiency for impact loading for laminate increases when Glass fiber reinforced polymer (GFRP) layers are added to Carbon fiber reinforced polymer layers (CFRP). Also, GFRP plies have a considerable cost advantage over CFRP plies. Further, GFRP plies may offer improved damage resistance. Hence, GFRP is considered as a better choice of hybridization material along with carbon fibers. Though the development of hybrid composites has been motivated by aerospace and marine industries to improve mechanical properties [6] and to lower operating costs, it can also be used to effectively deal with the growth of delaminations.

This paper presents a study to develop Carbon–Glass hybrid laminates with minimum loss in stiffness and simultaneously prevent delamination growth and consequently reduce the ill effects of delaminations. A 24-layer all CFRP layer composite of $(+45/-45/0/90)_{3\,s}$ layup is considered for analysis. This laminate was considered earlier in literature [3] for delamination tolerance analysis. The all CFRP layer composite laminate is hybridized using GFRP lamina(s) at suitable positions. The effect of GFRP layers on delamination tolerance is studied through their introduction at various through thickness positions.

2 Description of the Problem

A laminated composite panel of 92 mm × 74 mm (W × H) with 3 mm thickness is considered for the analysis. A 24-layer non-hybrid CFRP composite of $(+45/-45/0/90)_{3\,s}$ is selected as the baseline model, the thickness of each CFRP lamina being 0.125 mm [3]. The GFRP laminas are inserted at suitable positions to form different configurations. The thickness of each GFRP lamina is 0.25 mm. The CFRP and GFRP material properties are given in Table 1. The concept in the

Table 1 Material properties of CFRP and GFRP

Material	E_1 (GPa)	E_2 (GPa)	E_3 (GPa)	G_{12} (GPa)	G_{23} (GPa)	G_{31} (GPa)	v_{12}	v_{23}	v_{31}
CFRP	140.0	10.0	10.0	5.70	3.60	5.70	0.31	0.48	0.0221
GFRP	43.9	15.4	15.4	4.29	3.20	4.29	0.28	0.28	0.0221

Table 2 The configurations used in the present study

Configuration	Stacking sequence	Thickness (mm)	GFRP layers (%)
Config.1	$(+45_c/-45_c/0_c/90_c)_{3\ s}$	3	0
Config.2	$(0_g/(+45_c/-45_c/0_c/90_c)_3)_s$	3.5	7.69
Config.3	$(+45_c/-45_c/0_g/0_c/90_c/(+45_c/-45_c/0_c/90_c)_2)_s$	3.5	7.69

work is that the delaminations which are likely to occur in the top or bottom layers and which might grow during fatigue loading can be arrested or their growth can be delayed with hybrid construction.

The configurations considered in the present study are given in Table 2. The subscripts "c" and "g" denote CFRP or GFRP plies, respectively.

Three-dimensional finite element analysis is conducted using PATRAN for modeling and NASTRAN software package for structural analysis. Static displacements such as delamination opening and Strain Energy Release Rates (SERR) are compared for all the configurations.

3 Finite Element Modeling

The panel is analyzed with a circular delamination of size, $2a = 30$ mm at the interface between $(+45/-45)$ and the next layer. Hexa 20 iso-parametric brick elements with layered [3] elements (3 or 6 layers in each element) are used in the analysis. A typical layup sequence used for Config.3 is shown in Fig. 1.

The finite element model is prepared considering the quarter of the model, imposing symmetric boundary conditions on the edges. The boundary conditions are given as follows:

$$At\ x = 0,\ u = 0,\ F_y = 0.$$

Fig. 1 The Layup sequence used for Config.3
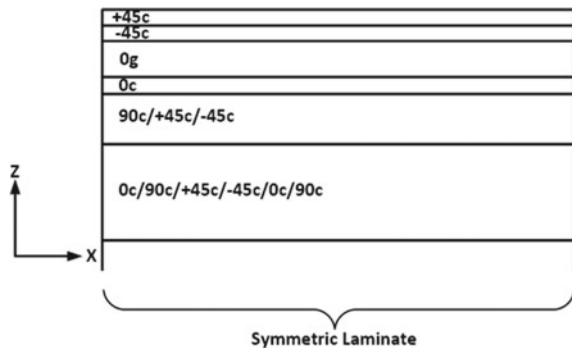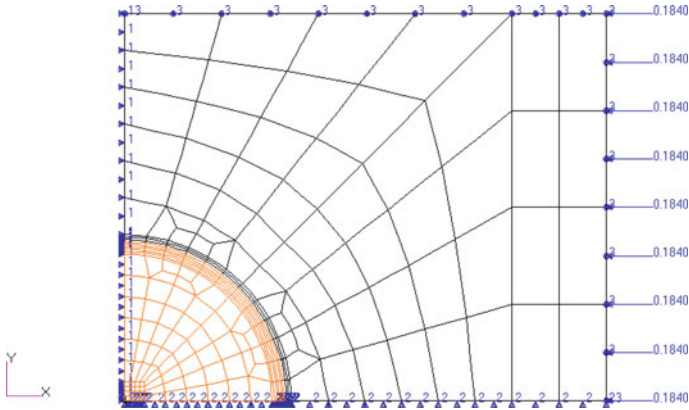
Fig. 2 The finite element mesh with applied boundary conditions, loads and delaminated area highlighted

$$\text{At } y \; = \; 0, \; v \; = \; 0, \; F_x \; = \; 0.$$

$$\text{At } x \; = \; W/2 \text{ and at } y \; = \; H/2 (\text{along the edges}), \; w \; = \; 0.$$

Uni-axial compressive strain (ε_x) is applied as constant displacement ($u_0 = \varepsilon_x H/2$) at x = W/2. The finite element mesh in the plane of the delamination is shown in Fig. 2. The quarter circular delaminated area is highlighted.

Contact constraints are given on the delamination region, so that interpenetration between the layers is avoided. Implicit non-linear analysis using NASTRAN solution sequence 400 is carried out. Maximum Strain Energy Release Rate happens at θ = 90° which is calculated using the Modified Virtual Crack Closure Integral (MVCCI) technique [4].

4 Modified Virtual Crack Closure Integral (MVCCI) for 20 Node Elements

The Modified Virtual Crack Closure Integral (MVCCI) is used for the estimation of strain energy release rates, G in individual and mixed-mode configurations in linear elastic fracture mechanics problems [5]. It is based on Irwin's Crack Closure Integral concept. For a virtual crack extension Δa from a crack length of a, the forces ahead of the crack tip and displacements behind the crack tip are used to calculate the work required to close the crack to its original length. For a straight delamination front, the strain energy release rate for Mode 1 [5] is derived as (Fig. 3)

Fig. 3 The finite element
nodes and areas used in GI
calculation for Hexa 20
elements
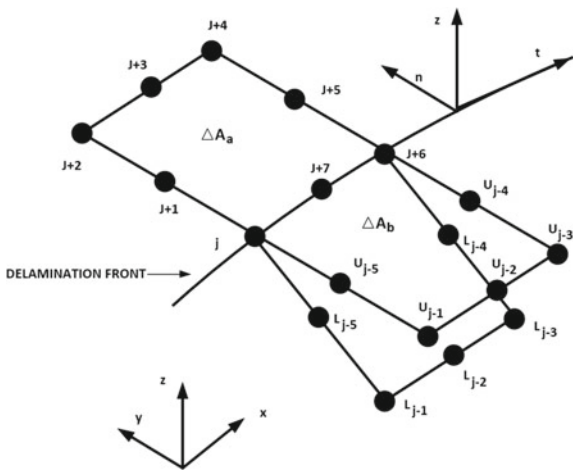
$$G_I = \frac{1}{2\Delta A_k}\left[\begin{array}{l} F_{z,j}\left(w_{Uj-1} - w_{Lj-1}\right) + F_{z,j+1}\left(w_{Uj-5} - w_{Lj-5}\right) \\ +F_{z,j+7}\left(w_{Uj-2} - w_{Lj-2}\right) + F_{z,j+6}\left(w_{Uj-3} - w_{Lj-3}\right) \\ +F_{z,j+5}\left(w_{Uj-4} - w_{Lj-4}\right) \end{array}\right], \quad (1)$$

where F_z is the nodal forces in z-direction at various nodes ahead of the crack tip
which is estimated as forces exerted by the structure below the crack plane, and "w"
is the displacement on the crack face. For example, $\left(w_{Uj-5} - w_{Lj-5}\right)$ is the crack
opening displacement at node j-5.

$$\Delta A_k = \frac{\Delta A_a + \Delta A_b}{2},$$

where k refers to the kth element along the delamination front.

By using Eq. 1, the maximum mode 1 strain energy release rate GI is calculated
for various uni-axial compressive strain values.

5 Results and Discussions

Singh et al. [3] provided parametric studies using geometric non-linear analysis for an
embedded delamination in non-hybrid CFRP laminate under uni-axial compression.
The same FE model is used as a baseline for the current work and their results are
used for comparison with the current FEM analysis with Hexa 20 elements. The
variation of mode 1 strain energy release rate with respect to varying compressive
strains from Singh et al. [3] and the current analysis is given in Fig. 4. Both the results
match well, with minor deviation at certain points.

Fig. 4 Max GI versus compressive strain comparison with Ref. [1] for delamination between $(+45/-45)_c$ and 0_c

Max GI Vs Compressive Strain
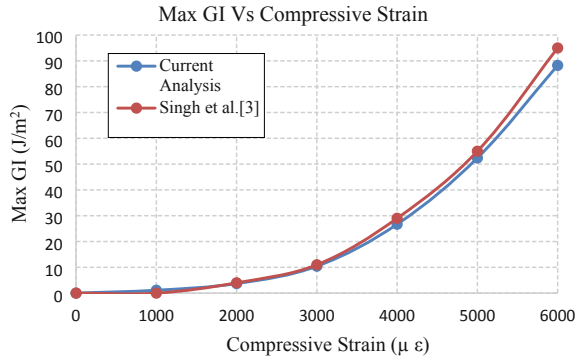
The variation of Maximum GI with applied compressive strain ($\mu\varepsilon$) for a delamination ($2a = 30$ mm) along the interface between $(+45/-45)_c$ and 0_c for the Config. 1 and 2 and between $(+45/-45)_c$ and 0_g for Config. 3 is shown in Fig. 5. With the increase in compressive strain, the delamination opens up with an increase in Mode 1 strain energy release rate. For non-hybrid CFRP laminate (Config.1), the delamination opens up at 2000 $\mu\varepsilon$. In Config.2, where the laminate is hybridized with GFRP lamina (0_g) on the top and bottom, the delamination growth happens only at 3000 $\mu\varepsilon$. A GFRP lamina(0_g) is inserted at the third layer in Config.3. In this case, a further delay can be observed for delamination opening. The delamination opens only at a higher applied compressive strain of 5000 $\mu\varepsilon$. Hence, Config. 3 provides the best among the three hybridized model propositions considered in delaying the delamination growth. The longitudinal stiffness of Config.1 is 54.672 GPa and that of Config. 2 and Config. 3 is 53.685 GPa. The reduction in longitudinal stiffness as a result of hybridization is 1.81%, which can be considered as small.

For operational service (fatigue) loading, the delamination tolerance is assessed as follows. The intersection of GI threshold ($=35$ J/m^2) with operational strain of 6000 $\mu\varepsilon$ is shown in Fig. 5. It is seen that for the first two configurations, the GI is above the threshold and delamination is likely to grow. For delamination in Config.3,

Fig. 5 Max GI versus compressive strain for three configurations

Max GI vs Compressive Strain
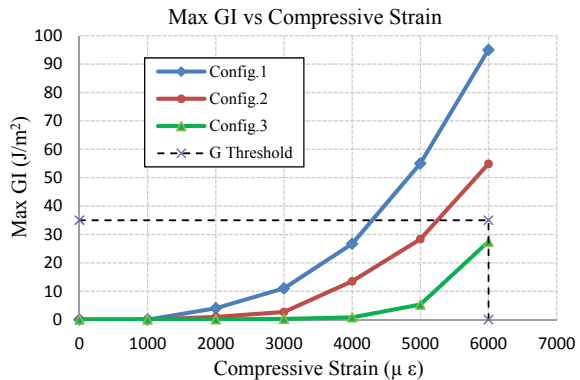
GI is below the threshold and delamination does not grow under fatigue loading. At 5000με, for both Config.2 and 3, delamination does not grow since GI is below the fatigue threshold.

6 Conclusions

A CFRP laminate is hybridized with a uni-directional GFRP lamina in two different configurations to study the impact of hybridization on the delamination growth. Three-dimensional finite element analysis is performed on the delaminated composite laminates of all the configurations. The mode I strain energy release rate is calculated using MVCCI. Both the hybridized configurations exhibited a considerable delay in delamination growth compared to non-hybrid CFRP laminate which can be explained by the fact that less stiff layers are at the top and bottom of the layup. Hybridizing CFRP laminate with GFRP lamina in the third layer is found to be better way to delay delamination growth and to improve delamination tolerance without compromising the flexural strength.

References

1. Swolfs Y, Gorbatikh L, Verpoest I (2014) Fibre hybridisation in polymer composites: a review. Composites Part A: Appl Sci Manuf 67:181–200
2. Andrew Head TR, Hua S, Butler R (2015) Damage resistance and damage tolerance of hybrid carbon-glass laminates. Composites: Part A 76 :224–232. www.elsevier.com/locate/compositesa
3. Singh KL, Dattaguru B, Ramamurthy TS (2006) Fracture analysis of delaminated composite panels in compression using numerically integrated MVCCI. Mech Adv Mater Struct 13(4):303–315
4. Badarinarayana K, Dattaguru B, Ramamurthy TS, Vijayakumar K (1994) A general procedure for modified crack closure integral in 3-D problems with cracks. Eng Fract Mech 48(2):167–176
5. Narayana KB, Geroge S, Dattaguru B, Ramamurthy TS, Vijayakumar K (1994) Modified Crack Closure Integral (MCCI) for 3-d problems using 20-noded brick elements. Fatigue Fract Eng Mater Struct 17(2):145–157
6. Cocchieri Botelho EI, Almeida Silva R, Cláudio Pardini L, Cerqueira Rezende M (2006) A review on the development and properties of continuous fiber/epoxy/aluminum hybrid composites for aircraft structures. Mater Res 9(3):247–256

Dynamic Creep Response of MWCNT-COOH-PP Nanocomposites

Vivek Khare and Sudhir Kamle

Abstract Viscoplastic deformation in multi-walled carbon nanotubes reinforced polypropylene nanocomposite films is investigated in the nonlinear creep regime. Isothermal creep and recovery strain experiments are conducted at a constant intermediate stress level of 10 MPa. The unrecovered strains at end of the recovery period are compared with those predicted from Schapery and Zapas–Crissman's nonlinear viscoelastic–viscoplastic solid model and the effect of nonlinear functions characterizing deformation is studied. The prediction of permanent deformation was found comparable with the evidence from the dynamic mechanical thermal analysis. 2% and 1% nanocomposite samples were found with lower viscoplastic deformation at 25 °C and 50 °C respectively.

Keywords Nanocomposites · Permanent deformation · Creep modelling

1 Introduction

Polypropylene (PP) is a widely used thermoplastic polymer in aerospace applications due to its strength, low cost, low weight, ease of formability and fatigue resistant properties. Its semi-crystalline state provides both strength and flexibility [1, 2]. Studies showed that thermoplastic matrix when reinforced with these high strength nanotubes increases the deformation resistance of the materials, provided the nanofillers are well dispersed in base matrix [3, 4]. However, at higher MWCNT concentrations, MWCNTs are self-assembled in form of agglomeration due to high Van der Waals attraction which hinders stress transfer efficiency from matrix to fibre [5, 6]. Functionalized multi-walled carbon nanotubes (MWCNT) significantly enhance mechanical properties of PP nanocomposites and make them potential candidate for aerospace applications such as flexible flapping wings in micro air vehicles [7, 8] and low temperature proton exchange membrane fuel cells [9–11].

V. Khare (✉) · S. Kamle
Department of Aerospace Engineering, Indian Institute of Technology Kanpur,
Kanpur 208002, Uttar Pradesh, India
e-mail: vivekkh@iitk.ac.in; vivekconcept@gmail.com
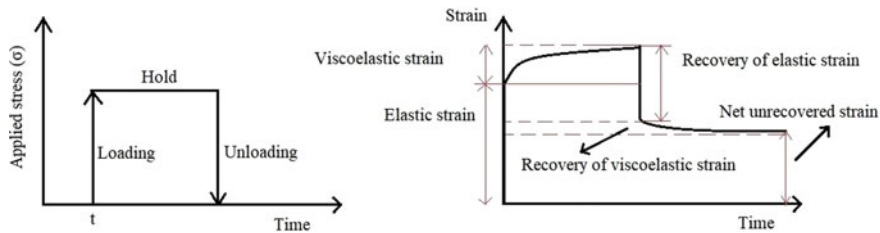
Fig. 1 Stress input and strain output response in creep test

In bioinspired flapping wing applications, the damping caused by the viscoelastic stresses can reduce the amplitude of oscillations [12]. Flapping wings simulation studies also suggest that the biomimicked wing skin should be modelled using nonlinear constitutive relations since the elastic properties would be inadequate [13]. To study the viscoelastic behaviour in nanocomposites, the creep and relaxation-based experiments are most preferred. The samples are loaded with constant stresses and strains and allowed to recover for longer times as shown in Fig. 1. Material nonlinearity in MWCNT reinforced polymers encourages the investigation of deformation under variable stress and temperature loading through experiments and nonlinear viscoelastic modelling. Jia et al. [14] studied the creep and recovery behaviour of MWCNT-PP composites at low stress levels in the linear viscoelastic region and found a reduction in creep strain and unrecovered strain in MWCNT reinforced samples. Schapery modelled the creep behaviour in polymers using a nonlinear viscoelastic formulation based on the law of irreversible thermodynamics [15–17]. The strains in creep and recovery were expressed using the integral form of prony series including the nonlinear terms. Estimation of permanent deformation in form of unrecovered strains has been reported in a few studies [18–21] which indicate that the permanent deformation is significantly attributed to the applied stress, loading time and temperature and was evaluated in terms of long-term compliance [22]. In our earlier studies, nanocomposites were observed with low creep strain and lower viscoplastic strains at the end of recovery [23]. However, the analysis of permanent deformation is further substantial at high stress loading since the viscoplastic strains exist with the viscoelastic strains once the elastic strains are fully developed [18]. Although the unrecovered strains at the end of experiments could be initially assumed as viscoplastic strains, the nonlinear functions affecting permanent deformation should also be analysed. Furthermore, there is a paucity of information on the creep and recovery behaviour of -COOH functionalized MWCNT-PP nanocomposites.

The present investigation elucidates the effect of functionalized carbon nanotubes (MWCNT-COOH) and temperature on dynamic creep and recovery strain in nanocomposites through experiments and nonlinear viscoelastic modelling. The solution casting method is used for the development of thin nanocomposite films using PP in pellet form and –COOH functionalized multi-walled carbon nanotubes with varying MWCNT concentrations. Temperature-controlled dynamic creep and recovery experiments were performed at a constant 10 MPa creep stress in a dynamic

mechanical analyser (DMA). Experiments reveal that the temperature-activated deformation is controlled by incorporating MWCNTs up to 1% volume fraction. Schapery's nonlinear viscoelastic model coupled with Zapas–Crissman's viscoplastic model is incorporated to study the development of unrecoverable viscoplastic strains predicted in experiments. The model prediction agrees with experimental findings. The present study recommends 1% MWCNT-COOH-PP nanocomposites for biomimicking of flapping wings in MAVs and NAVs.

2 Modelling for Permanent Strain in Nanocomposites

2.1 Nonlinear Viscoelastic–Viscoplastic Model

Nonlinear viscoelasticity in polymers and nanocomposite materials was initially modelled by Schapery based on creep and recovery observations. Time-dependent strains developed due to constant stress loading were modelled separately for creep and recovery steps. Total creep strain developed in materials includes elastic, viscoelastic and viscoplastic strains as shown in Eqs. 1 and 2 [15–17, 24]. The recoverable instantaneous strains are represented in the first term of Eq. 1 and are the functions of applied stress and instantaneous compliance. The second term represents the viscoelastic strains and is modelled using Prony series with a transient component of creep compliance.

$$\epsilon_c(t) = D_0 g_0 \sigma_0 + g_1 g_2 \sigma \sum_i D_i \left[1 - exp\left(\frac{-t}{a_\sigma \tau_i} \right) \right] + \epsilon_{vp}(t, \sigma) \tag{1}$$

$$\epsilon_r(t) = g_2 \sigma \sum_i D_i \left[(1 - exp\left(\frac{-t}{a_\sigma \tau_i} \right)) \left(exp\left(\frac{-(t - t_1)}{\tau_i} \right) \right) \right] + \epsilon_{vp}(t, \sigma) \tag{2}$$

where ϵ_c is the creep strain, ϵ_r is the recovery strain, D_i is the transient creep compliance, σ is the constant applied stress, a_σ is the stress-dependent horizontal shift factor, t_1 is the creep loading time and $\epsilon_{vp}(t, \sigma)$ is the viscoplastic strain developed during creep loading.

The nonlinear stress-based functions g_0, g_1, g_2 and a_σ are introduced in strain formulation. These functions represent the extent of elastic and viscoelastic behaviour of the material in form of instantaneous and transient creep compliance. At high stress loading, the transient compliance is investigated since the induced deformations are due to the loading in the nonlinear regime. The effect of transient compliance on deformation is expressed by g_2 term. The strain expressions are later coupled with Zapas–Crissman's viscoplastic term shown in Eq. 3 for the long-term creep loading and order of magnitude higher recovery periods.

$$\epsilon_{vp}(t) = C \left(\frac{1}{\tau_0^n} \right) \left(\int\limits_0^t \left(\frac{\sigma(\tau)}{\sigma_0} \right)^M d\tau \right)^n \qquad (3)$$

The viscoplastic strain is represented in a nonlinear functional form. The expression is normalized for unit retardation time τ and constant stress loading. The parameter n is obtained from linear creep data while C and M are evaluated from nonlinear least square fitting [25].

2.2 Estimation of Stress-Dependent Functions

The Levenberg–Marquardt nonlinear least square curve fitting algorithm was implemented to obtain the nonlinear functions from viscoelastic and viscoplastic model [26]. Root mean square error was considered as the objective function to be minimized. Prony series parameters obtained from the linear creep data were used to evaluate g_2, a_σ from recovery data and g_0, g_1 from creep data consecutively.

3 Experimental

3.1 Nanocomposite Films

We adopted the conventional solvent casting method and modified it for functionalized fillers in our earlier studies [4]. Isotactic polypropylene procured from Otto chemicals Pvt. Ltd. and -COOH functionalized MWCNTs from Nanoshel Pvt. Ltd. were processed for nanocomposite film development. 0.5%, 1% and 2% volume fraction of functionalized carbon nanotubes were sonicated with xylene solvent in an ice bath environment using ultrasonicator. The idea behind ultrasonication was to uniformly disperse nanotubes in the organic solvent. Later on, the polypropylene pellets were added to the sonicated solution by a heat treatment process in a condensation atmosphere. The solution was heated up to 23 min with simultaneous stirring. The solution was then poured in a preheated petri-dish kept in an environmental chamber at 180 °C for 2 h followed by a secondary heat treatment stage at 140 °C for one hour. The developed nanocomposite film was peeled off from the petri-dish. Our film development procedure was slightly different from the procedure adopted in our earlier studies where the functionalized fillers and matrix were processed separately with the xylene solvent before heating [23].

3.2   Isothermal Creep Loading

Figure 2 shows the loading of samples in dynamic mechanical analyser (MetraVib 100+). Neat PP and the nanocomposite samples were creep loaded at a constant stress of 10 MPa and at 25 °C and 50 °C. The loading stress was approximately half of the strength of the nanocomposites as reported in our earlier studies [4]. The loading was applied for 300 s followed by a recovery period of half an hour. The samples were allowed to recover up to six times more than the loading time. The idea behind the long recovery time was to investigate the traces of permanent creep deformation in form of viscoplastic strains in nanocomposites.

3.3   Estimation of Viscoplastic Strains

The unrecovered strains at the end of experiments were assumed as an initial guess of permanent deformation in the nanocomposites. To further investigate the existence of viscoplastic strains, the nonlinear viscoelastic–viscoplastic model was fitted to

Fig. 2 Creep testing in dynamic mechanical analyser

the experimental observations by implementing a nonlinear least square curve fitting algorithm developed in MATLAB. The viscoplastic strains were predicted from the model and compared with experimental findings. The nonlinearity parameters both from the viscoelastic and viscoplastic models were obtained.

4   Results and Discussions

4.1   Temperature Effects

Figure 3 represents the experimental creep and recovery stages for neat PP and nanocomposite samples at 25 °C and 50 °C. It is evident that MWCNT reinforced samples develop lower creep strain than the neat sample up to 1% concentration. At 25 °C, 1% samples were observed with 45.2% reduction in creep strain. Reinforcing effectiveness of MWCNTs was significantly observed at 50 °C with 9.85% and 47.86% reduction in creep strain for 0.5% and 1% sample. Though MWCNT reinforced samples are observed in reducing the creep strain, 2% sample showed a rise in creep strain than other considered samples. It represented 8.39% and 3.73% increase in strain than the neat sample.

In spite of the efficient reduction in creep strains due to MWCNT loading, the samples were observed with a higher increase in creep strain at 50 °C. High creep strains induce permanent deformation in material and hence estimation of viscoplastic strains is essential. The unrecovered strain from experiments was reported lowest for 2% sample at 25 °C. This could possibly be due to the presence of MWCNT clusters due to improper dispersion [23]. However, at 50 °C, these aggregates could have lowered the deformation resistance than the well-dispersed MWCNTs in 1%
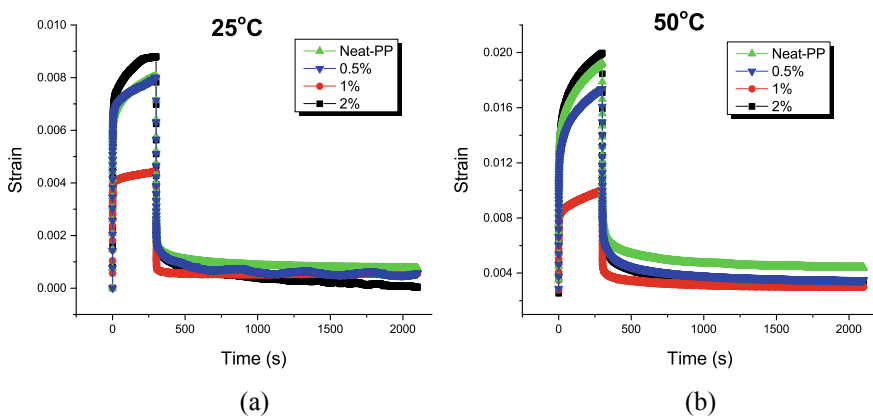
Fig. 3   Experimental Creep and recovery stages **a** 25 °C and **b** 50 °C

sample, and hence the unrecovered strain was found minimum for 1% sample. These unrecovered strains could be assumed as permanent deformation in samples due to high stress creep and temperature loading.

4.2 Model Predictions

The experimental observations are further fitted with a nonlinear model with the viscoplastic strain term. We found experimental observations to be in good agreement with the model prediction by adding ϵ_{vp} term. Figure 4 represents the model predictions for creep and recovery stages in nanocomposites. At 25 °C, when the unrecovered strains are smaller, we observed disagreement between experimental data and model prediction for 0.5% sample. This could be influenced by the presence of random small MWCNT aggregates which could have increased the interface strength between aggregates and the PP matrix. Although this effect was completely vanished at 50 °C. This indicates temperature-induced decrements in deformation resistance of samples and could have increased the unrecovered strains. The nonlinear model functions mentioned in Table 1 showed that nonlinear term g_2 was significantly larger than the other nonlinear terms. This represents that the deformation is more likely influenced by the transient compliance. However, g_2 in 1% sample was observed minimum which indicates temperature-induced structural stability in 1% sample than the neat PP and other nanocomposites.

The evolution of g_0, g_1, g_2 and a_σ is shown in Table 1. g_0 indicates effect of stress and temperature on elastic compliance whereas g_1, g_2 and a_σ correspond to the effect on transient compliance [23]. It is evident that g_0 was comparatively lower than other nonlinear terms which indicate the presence of viscoelastic strains. These increments in these nonlinear terms at 50 °C indicate the dominance of viscoelastic and viscoplastic strains.
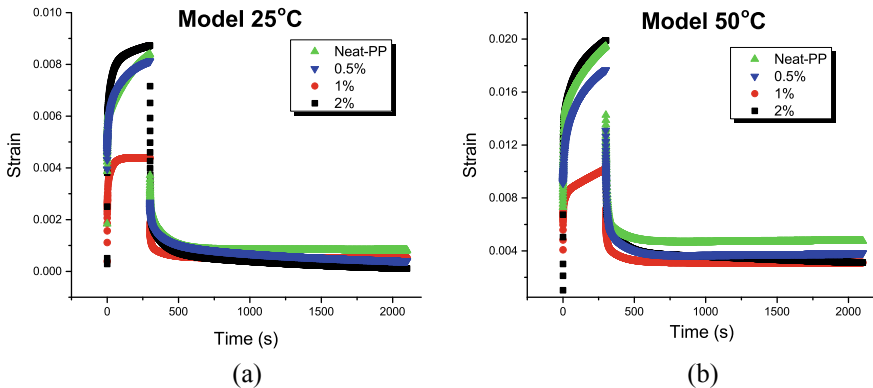
Fig. 4 Creep and recovery stages from model **a** 25 °C and **b** 50 °C

Table 1 Nonlinear functions from viscoelastic model

Sample (%)	25 °C				50 °C			
	g_0	g_1	g_2	a_{sigma}	g_0	g_1	g_2	a_{sigma}
0	0.091765	1.29	2.538	0.02142	0.721	2.219	5.599	3.784
0.5	0.3569	1.127	2.209	0.1422	0.2373	0.8021	19.12	10.71
1	0.6254	2.636	0.1891	0.2968	0.1827	0.9907	0.5444	0.1707
2	0.6461	1.357	0.8893	0.294	0.3626	1.085	2.065	0.6347

4.3 Permanent Strain

The prediction of permanent strains from the model and those obtained from experimental data is shown in Fig. 5. The viscoplastic strains are assumed to be developed during the creep stage. Therefore, the creep data was fitted to the viscoplastic model separately to obtain model functions. Table 2 indicates the functions produced. The model predictions agree well with experimental findings. The negative strain from the model prediction in 0.5% sample is very less (0.15%) compared to the stiffness of nanocomposite samples reported in our previous work [23]. This could be attributed to the small variation in strain near the end of the recovery period in 0.5% sample. This variation could be due to the dynamic displacement given during sinusoidal loading in experiments. Hence, more number of prony series terms can be considered in the nonlinear model fitting.

Fig. 5 Permanent strain from experiments and model
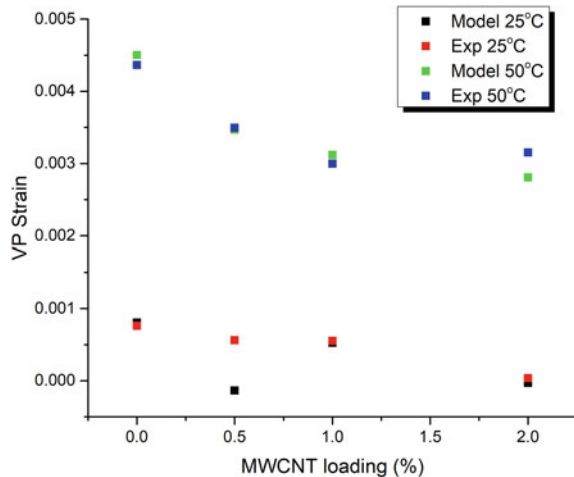
Table 2 Nonlinear functions from viscoplastic model

Sample (%)	n	25 °C		50 °C	
		C	N	C	N
0	0.1064	0.005985	0.5899	0.01308	0.5446
0.5	0.0512	0.002149	0.711	0.004606	0.7862
1	0.01913	0.006749	0.7655	0.01525	0.4253
2	0.02921	0.006345	0.09621	0.01299	0.4788

5 Conclusion

MWCNT-PP nanocomposites were characterized for their creep and recovery behaviour at 10 MPa stress which was 50% of the strength of nanocomposites. Temperature-induced deformation was first observed from experimental observations in form of creep strain at the end of the creep stage and uncovered strain at the end of the recovery period. The strains were later predicted from the nonlinear viscoelastic–viscoplastic model. 1% MWCNT reinforced sample was found with up to 45.2% and 47.86% reduction in creep strain at 25 °C and 50 °C, respectively. Viscoplastic strains which were first assumed as unrecovered strain in experiments match well with model findings at both the test temperatures. 2% and 1% samples indicate lower viscoplastic strains at 25 °C and 50 °C, respectively, and the same observations were predicted by fitting the viscoplastic model with experimental creep data.

References

1. Bikiaris D (2010) Microstructure and properties of polypropylene carbon nanotube nanocomposites. Materials 3:2884–2946
2. Szpieg M, Giannadakis K, Varna J (2011) Time dependent nonlinear behavior of recycled polypropylene in high tensile stress loading. J Thermoplast Compos Mater 24:625–652
3. Li C, Pang XJ, Qu MJ, Jhang QT, Wang B, Zhang BL (2005) Fabrication and characterization of polycarbonate/carbon nanotubes composites. Composite Part A 37:1485–1489
4. Khare V, Srivastava S, Kamle S, Kamath GM (2019) Effect of filler functionalization on the thermomechanical behavior of polypropylene nanocomposites. Procedia Struct Integr 14:215–225
5. Chanteli A, Tserpes KI (2015) Finite element modeling of carbon nanotube agglomerates in polymers. Compos Struct 132
6. Pegel S, Potschke P, Villmow T, Stoyan D, Heinrich G (2009) Spatial statistics of carbon nanotube polymer composites. Polymer 5:2123–2132
7. Khare V, Kumar D, Kamle S (2020) Structural damage assessment of MAV flapping wings using DIC-wavelet technique. In: SPIE 2020, Anaheim, California, USA, April

8. Kumar D, Shandilya S, Khare V, Kamle S, Chiang CH (2020) Insect-inspired micro air vehicle with nanocomposite flapping wings and flexure joints. In: SPIE 2020, Anaheim, California, USA, April

9. Porzare K, Mansourpanah Y, Farhadi S (2016) Advanced nanocomposite membranes for fuel cell applications, a comprehensive review. Biofuel Res J 12:496–513

10. Ijeri V, Cappelletto L, Bianco S, Tortello M, Spinelli P, Tresso E (2010) Nafion and carbon nanotube nanocomposites for mixed proton and electron conduction. J Membr Sci 363:265–270

11. Thomassin JM, Colar J, Caldarella G, Germain A, Jerome R, Detrembleur C (2007) Beneficial effect of carbon nanotubes on the performances of nafion membranes in fuel cell applications. J Membr Sci 303:252–257

12. Buoso S, Palacios R (2016) Viscoelastic effects in the aeromechanics of actuated elastomeric membrane wings. J Fluids Struct

13. Lin T, Xia W, Hu S (2021) Effect of chordwise deformation on propulsive performance of flapping wings in forward flight. Aeronaut J. In: International symposium on smart aircraft 2019 collection

14. Jia Y, Peng K, Gong XL, Zhang Z (2011) Creep and recovery of polypropylene/carbon nanotube composites. Int J Plast 27:1239–1251

15. Schapery RA (2000) Nonlinear viscoelastic solids. Int J Solids Struct 37:359–366

16. Schapery RA (1966) A theory of nonlinear thermoviscoelasticity based on irreversible thermodynamics. In: 5th national congress of applied mechanics

17. Schapery RA (1969) On the characterization of nonlinear viscoelastic materials. Polym Eng Sci 295

18. Zapas LJ, Crissman JM (1984) Creep and recovery behavior of ultra high molecular weight polyethylene in the region of small uniaxial deformations. Polymer 25(1):57–62

19. Roylance D (2001) Engineering viscoelasticity. Mechanics of materials course, MIT3 11F99 visco

20. Christensen RM (1982) Theory of viscoelasticity, 2nd edn. Academic, New York

21. Papanicolaou GC, Zaoutsos SP (2011) Viscoelastic constitutive modeling of creep and stress relaxation in polymers and polymer matrix composites. Woodhead, Sawston

22. Tuttle ME, Brinson HF (1985) Prediction of the long term creep compliance of general composite laminates. Exp Mech

23. Khare V, Kamle S (2020) Effect of temperature and filler volume fraction on the creep and recovery behaviour of MWCNT-COOH-reinforced polypropylene films. Arch Appl Mech (In press)

24. Schapery RA (1966) An engineering theory of nonlinear viscoelasticity with applications. Int J Solid Struct 2:407

25. Pasricha A, Dillard DA, Tuttle ME (1997) Effect of physical aging and variable stress history on the strain response of polymeric composites. Compos Sci Technol 57(9–10):1271–1279

26. Lourakis M (2008) Levenberg-Marquardt nonlinear least squares algorithms in c/c++. Technical report, http://users.ics.forth.gr/lourakis/levmar/

Coupled Thermomechanical Analysis of SMA Structures

Chenna Sai Krishna Chaithanya, Animesh Kundu, and Atanu Banerjee

Abstract Of late, shape memory alloys (SMA) are found in a wide variety of applications in the field of aerospace, robotics, biomedical, etc., due to their well-known behaviors called *shape memory effect* and *superelasticity*. To simulate the behavior of these alloys several constitutive models are proposed over the past four decades. To the best of authors' knowledge, in most constitutive models, temperature is considered as an input variable. However, in practice, it evolves as a state variable, depending on applied thermal and mechanical loads and material properties. Moreover, the martensitic transformation processes exhibit endothermic and exothermic effects, significantly affecting temperature and the response. Hence, a fully coupled thermomechanical finite element-based analysis tool is required to simulate the behavior of these materials. The objective of this work is to develop a coupled thermomechanical analysis tool to predict the response of SMA structures under practical thermomechanical loading conditions in ABAQUS. The thermodynamic-based constitutive model, as proposed by Lagoudas and coworker, is implemented in UMAT, a user material subroutine of ABAQUS, to analyze the response of SMA-based components, considering the effect of material level coupling terms, i.e., the latent heat of transformation and thermoelastic heating effects. The results emphasize a significant difference in the transient response of SMA structures while thermal coupling terms are considered, illustrating the importance of the coupled analysis of these materials. Finally, the response of SMA biomedical staple, used for idiopathic scoliosis treatment of the vertebral body, is simulated using the developed FE tool, considering the practical thermomechanical loading conditions.

Keywords Shape memory alloy · Coupled thermomechanical analysis · Material nonlinearity · Latent heat

C. S. K. Chaithanya · A. Kundu (✉) · A. Banerjee
Department of Mechanical Engineering, Indian Institute of Technology Guwahati, Guwahati, India
e-mail: animesh.kundu@iitg.ac.in

1 Introduction

Shape memory alloys (SMA) are active materials with the ability to show large deformations when loaded and recover their shape with the increase in temperature from the deformed shape, known as *shape memory effect (SME)*. In another phenomenon, named *pseudoelasticity (PE)* or *superelasticity (SE)*, it undergoes a large deformation with increment in load and subsequently recovers the same upon unloading. They have high actuation energy densities, which are exploited in a wide variety of applications in the field of aerospace, robotics, biomedical, etc. [1].

The necessity of understanding and modeling the thermomechanical response of SMAs led to the proposal of several constitutive models in the past four decades. In one class of approaches, such as Brinson [2], Tanaka [3], Liang and Rogers [4], the phase evolution is empirically derived from experiments, offering simplicity required for real-time applications; however, they have limited functionality toward modeling under practical thermomechanical loading cases. However, another class of approaches, such as Lagoudas [1], derives the phase evolution based on thermodynamic principles and requires many material parameters. It has been found that for the analyses of practical problems in 2D and 3D, under simultaneous variation of thermomechanical loading, the latter approaches are more suitable.

A vast majority of reported constitutive model considers the phase evolution, derived based on thermodynamic principles, taking temperature as an input variable. However, in reality, temperature is a state variable that depends on applied thermomechanical loads, boundary conditions and internal material properties. Besides, the endothermic and exothermic nature of the phase transformation affects the SMA's temperature and thus renders thermomechanical coupling essential. To effectively predict the response of SMA structures in non-isothermal conditions, a coupled analysis considering the effect of the latent heat and associated heat transfer conditions is necessary. To the best of authors' knowledge, a limited number of studies have been reported on fully coupled thermomechanical analysis by researchers in commercial finite element software.

Yang and Xu [5] incorporated the constitutive model of Seelecke and Muller [6], along with the heat conservation equation to simulate an SMA beam response under a tip force loading in COMSOL Multiphysics FE package. The thermomechanical response of an SMA wire was reported by Alipour et al. [7], under different loading conditions. The one-dimensional constitutive model of Brinson [2] was implemented in ABAQUS UMAT to solve the force and thermal energy conservation equations simultaneously. However, the effect of material level coupling during phase transformation was not considered in this formulation. Sengupta et al. [8] developed a thermomechanically coupled model for SMAs considering large deformation. It was incorporated in FEA package to simulate the response of SMA thin wall tube. Thiebaud et al. [9] implemented the SMA constitutive model of Raniecki and Lexcellent [10] in the COMSOL Multiphysics FE package. The SMA response of a plate in biaxial-tension and in-plane bending is simulated under the isothermal condition and validated using experimental data. Lagoudas et al. [11] proposed a

constitutive model by generalizing the concept of the critical thermodynamic forces for transformation, depending on the applied stress magnitude and the direction of transformation. Smooth hardening function is proposed along with the formation of favored martensitic variants, by applied stress magnitude without specifically accounting for martensitic reorientation. Tabesh et al. [12] reported the influence of latent heat and terms related to thermomechanical coupling on the response of SMA actuator undergoing thermomechanical load, based on the constitutive model of Qidwai and Lagoudas [13]. In 2014, Solomou et al. [14] proposed a 2D beam finite element, following Lagoudas et al. [11], for the coupled thermomechanical analysis of shape memory alloy actuators. First-order shear deformation theory (FSDT) was used, assuming the temperature distribution along the thickness direction as cubic and six-order [15] polynomial.

To design SMA-based components under non-isothermal condition, a thorough apprehension of the effect of the coupling terms, i.e., latent heat, thermoelastic heat and associated heat transfer conditions, is necessary. This article reports a fully coupled thermomechanical analysis of SMA-based structures considering all material level coupling terms. The thermodynamical constitutive model of Boyd and Lagoudas [16], along with numerical implementation scheme, as proposed by Qidwai and Lagoudas [13], is implemented in an incremental-based nonlinear finite element framework. Both the mechanical and thermal equilibrium equations are solved simultaneously, considering latent heat and thermoelastic heat, using Newton–Raphson (NR) iterative scheme. The introduction of heat equation with coupling terms is essential to bring the time scale in the system's transient response. The proposed formulation to predict the response under arbitrary thermomechanical loading is implemented in ABAQUS, through user material subroutine (UMAT).

The organization of the current paper is as follows: First, the constitutive modeling of SMA is discussed briefly in Sect. 2, followed by a coupled finite element formulation. Section 4 illustrates the implementation of the mentioned formulation in the case of the SMA wire and a biomedical staple. It is found that the latent heat, during both forward and backward transformations, impedes the time response of the SMA components. Finally, some concluding remarks are given in Sect. 5.

2 SMA Constitutive Model

In this section, the thermodynamic-based constitutive model is presented for polycrystalline shape memory alloys, as proposed by Boyd and Lagoudas [16]. The Gibbs free energy (G) function is depicted in terms of Cauchy stress (σ_{ij}), temperature (T) and other internal state parameters like martensitic volume fraction (ξ) and transformation strain (ε_{ij}^t). The explicit form of Gibbs free energy is written as

$$G(\sigma_{ij}, T, \xi, \varepsilon_{ij}^t) = -\frac{1}{2\rho}\sigma_{ij}\mathbb{S}_{ijkl}\sigma_{kl} - \frac{1}{\rho}\sigma_{ij}[\alpha_{ij}(T - T_0) + \varepsilon_{ij}^t]$$
$$+ c\left[(T - T_0) - T\ln\left(\frac{T}{T_0}\right)\right] - s_0 T + u_0 + \frac{1}{\rho}f(\xi) \quad (1)$$

Here, T_0 is the reference temperature. The material parameters, $\mathbb{S}_{ijkl}$ depicts the fourth-order effective compliance tensor, α_{ij} signifies the second-order effective thermal expansion tensor, and c denotes the effective specific heat. s_0 and u_0 are the effective specific entropy and effective specific internal energy, respectively, at the reference state. The transformation hardening function is denoted by $f(\xi)$. The effective material properties can be determined by the following expressions:

$$\chi(\xi) = (1 - \xi)\chi_A + \xi\chi_M \quad (2)$$

where $()_M$ and $()_A$ represent SMA properties at pure martensite and austenite phase, respectively. The constitutive relation, to relate stress with strain and temperature using internal material parameters from first and second law of thermodynamics, can be obtained as

$$\varepsilon_{ij} = -\rho\frac{\partial G}{\partial \sigma_{ij}} = \mathbb{S}_{ijkl}\sigma_{ij} + \alpha_{ij}(T - T_0) + \varepsilon_{ij}^t \quad (3)$$

In addition, during phase transformation, the evolution of transformation strain tensor with the formation of martensitic volume fraction, is written as

$$\dot{\varepsilon}_{ij}^t = \Lambda_{ij}\dot{\xi} \quad (4)$$

where Λ_{ij} is the transformation tensor, determining the transformation strain considering the flow direction and is assumed to have the following form:

$$\Lambda_{ij} = \begin{cases} \frac{3}{2}H\frac{\sigma_{ij}'}{\bar{\sigma}} & ; \text{(Forward transformation, } \dot{\xi} > 0) \\ H\frac{\varepsilon_{ij}^{t-r}}{\bar{\varepsilon}^{t-r}} & ; \text{(Backward transformation, } \dot{\xi} < 0) \end{cases} \quad (5)$$

Here, H denotes the maximum uniaxial transformation strain, ε_{ij}^{t-r} is the transformation strain at the reversal of phase transformation. The other terms are expressed as

$$\bar{\sigma} = \sqrt{\frac{3}{2}\sigma_{ij}'\sigma_{ij}'}, \quad \sigma_{ij}' = \sigma_{ij} - \frac{1}{3}(\text{tr}(\sigma_{ij}))I_{ij}, \quad \bar{\varepsilon}_{ij}^{t-r} = \sqrt{\frac{2}{3}\varepsilon_{ij}^{t-r}\varepsilon_{ij}^{t-r}} \quad (6)$$

This is implemented using *return mapping algorithm* following *elastic predictor-transformation corrector* method in a finite element framework, as given by Qidwai and Lagoudas [13].

3 Coupled Thermomechanical Modeling

The governing differential equations include the stress equilibrium and thermal energy balance equation. The stress equilibrium equation takes the following form:

$$\sigma_{ij,j} + f_i = 0_i \tag{7}$$

The heat energy conservation equation following Lagoudas et al. [11] is written as

$$q_{i,i} + \rho c \dot{T} - q_s - q_L - q_t = 0 \tag{8}$$

and

$$\boldsymbol{q} = \begin{Bmatrix} q_x \\ q_y \\ q_z \end{Bmatrix} = - \begin{bmatrix} k_x & 0 & 0 \\ 0 & k_y & 0 \\ 0 & 0 & k_z \end{bmatrix} \begin{Bmatrix} T_{,x} \\ T_{,y} \\ T_{,z} \end{Bmatrix} = -\boldsymbol{k}\nabla T \tag{9}$$

where $\boldsymbol{q} = \{q_x, q_y, q_z\}$ depicts the heat flux vector (defined in Eq. (9)) related to gradient of temperature by k_x, k_y and k_z, heat conduction coefficients in x, y and z directions, respectively. ρ signifies the density of the material, c is the specific heat and $\dot{T}$ is the time derivative of the material temperature. q_s, q_L and q_t represent the distributed heat sources per unit volume, latent heat absorption or release per unit volume due to phase transformations and the energy release or absorption per unit volume due to the thermoelastic effect, respectively. q_L and q_t are related to stress σ_{ij} and other material parameters, following Lagoudas et al. [11]

$$q_L(\sigma_{ij}, T, \xi) = \left(\pi - \frac{\partial \pi}{\partial T} T\right)\dot{\xi}, \quad q_t(\sigma_{ij}, T, \xi) = -\alpha_{ij}\dot{\sigma}_{ij} T \tag{10}$$

Here, π is the thermodynamic force obtained from Gibbs-free energy. Replacing the thermomechanical coupling terms, one obtains

$$q_L + q_t = \left(\sigma_{ij}\Lambda_{ij} + \frac{1}{2}\sigma_{ij}\Delta\mathbb{S}_{ijkl}\sigma_{ij} - \sigma_{ij}\Delta\alpha_{ij}T_0 \right.$$
$$\left. +\rho\Delta c(T - T_0) - \rho\Delta u_0 - \frac{\partial f}{d\xi}\right)\dot{\xi} - \alpha_{ij}\dot{\sigma}_{ij}T \tag{11}$$

Using standard time discretization procedure [17], Eq. (8) can be written as

$$\rho C \left(\frac{T^{n+1} - T^n}{\Delta t_n}\right) = \theta\psi^{n+1} + (1 - \theta)\psi^n \tag{12}$$

where $\psi = [\boldsymbol{k}(\nabla.(\nabla T)) + q_s + q_{L} + q_{t}]$. The superscript n indicates function evaluations at time t_n (similarly for $n + 1$) and $\Delta t_n = t_{n+1} - t_n$ is the time step size and $\theta \in [0, 1]$. q_{L} and q_{t} (Eq. (10)) are nonlinear terms depending on stress and temperature. After linearization with respect to stress and temperature at nth step, one gets

$$(q_{L} + q_{t})^{n+1} = (q_{L} + q_{t})^{n} + \mathcal{X}_{ij}^{n} \,_{n}\Delta\sigma_{ij} + \mathcal{Y}^{n} \,_{n}\Delta T \tag{13}$$

where $_{n}\Delta\sigma_{ij}$ and $_{n}\Delta T$ are the increment in Cauchy stress and temperature, respectively, at nth step. $\mathcal{X}_{ij}{}^{n}$ and $\mathcal{Y}^{n}$ can be obtained as

$$\mathcal{X}_{ij}^{n} = \frac{\partial}{\partial\sigma_{ij}}(q_{L} + q_{t})^{n}; \quad \mathcal{Y}^{n} = \frac{\partial}{\partial T}(q_{L} + q_{t})^{n}$$

Expressing, $_{n}\Delta\varepsilon$ and $_{n}\Delta T$ in terms of increment in nodal displacement (ΔU) and nodal temperature (ΔT) degrees of freedom, respectively, using finite element discretization, the system of equations can be represented as

$$\underbrace{\begin{bmatrix} \boldsymbol{K}_{UU} & \boldsymbol{K}_{UT} \\ \boldsymbol{K}_{TU} & \boldsymbol{K}_{TT} \end{bmatrix}_{n}}_{\text{Tangent Stiffness Matrix}} \quad \underbrace{\left\{ \begin{matrix} \Delta U \\ \Delta T \end{matrix} \right\}_{n+1}}_{\text{Incremental DOFs}} = \underbrace{\left\{ \begin{matrix} \Delta F_U \\ \Delta F_T \end{matrix} \right\}_{n+1}}_{\text{Residue}} \tag{14}$$

Equation (14) has to be solved iteratively at each time step following Newton–Raphson method (Fig. 1), till the residual of mechanical and thermal load vectors are driven to zero.

4 Result and Discussion

In this section, two representative problems are simulated, demonstrating the capability of the developed FE formulation. Initially, in Sect. 4.1, the thermomechanical response of a pre-strain SMA wire subjected to thermal load at one of its ends is simulated. The same problem has been simulated considering both with and without latent heat and thermoelastic heat terms, to apprehend the effect of coupling terms in the response of SMA wire actuators. In Sect. 4.2, the response of a biomedical staple, used in orthopedic scoliosis treatment, is analyzed to understand the importance of coupling under practical thermomechanical loading. In the discussion, the responses obtained from the developed FE that considers the material level coupling terms (Eq. (10)) are called coupled responses, otherwise referred to as uncoupled responses.
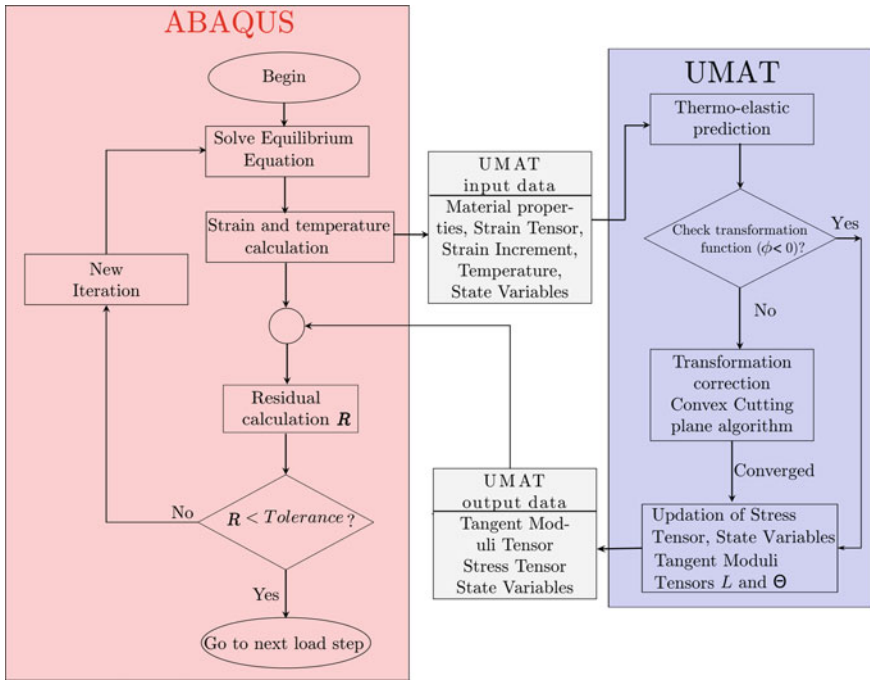
Fig. 1 Flowchart for ABAQUS analysis process for a time step at an integration point of an element

4.1 SMA Wire Heated at One End

An axially pre-strained SMA wire, as shown in Fig. 2a, is initially at the equilibrium state in fully martensitic phase ($\xi = 1$), at the ambient temperature of 310 K. The imparted strain is equal to maximum transformation strain. The wire has a square cross-section of 0.8 mm $\times$ 0.8 mm, length of 200 mm and is modeled using a uniform mesh of 20 coupled temperature displacements elements, C3D8T (eight-node thermally coupled brick, trilinear displacement and temperature). The material properties used in this simulation are listed in Table 1. Adiabatic boundary conditions are considered at all faces. Temperature is applied at the free end B, increasing linearly from the environmental temperature of 310 K up to 360 K in 100 s and then remains constant, as shown in Fig. 2a. As the temperature of the heat source is raised, the determination of the wire temperature and end displacement is of primary interest. The simulation is continued until a steady-state condition is reached, that is, the temperature of all nodes is stabilized to a constant value. The results are compared with that presented by Solomou et al. [14] and a good agreement is observed between them.

Figure 2b depicts the evolution of temperature with time under adiabatic condition. As the temperature increases, the endothermic nature of backward transformation
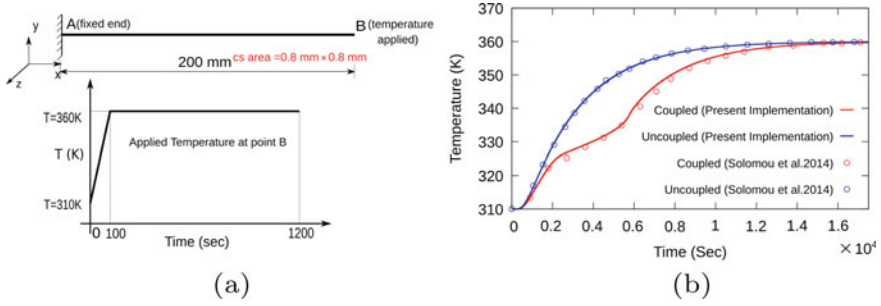
Fig. 2 **a** Schematic diagram of SMA wire fixed at left end A, heated at end B and **b** Evolution of temperature at the fixed end (A)

Table 1 Shape memory alloy material parameters [14]

Material parameter	Symbol	Value
Elastic modulus, Austenite	E^A	66.2 GPa
Elastic modulus, Martensite	E^M	25.6 GPa
Martensite finish temperature	M_f	280 K
Martensite start temperature	M_s	303 K
Austenite start temperature	A_s	325 K
Austenite finish temperature	A_f	338 K
Thermal expansion coefficient, Austenite,	α^A	29×10^{-6}
Thermal expansion coefficient, Martensite,	α^M	29×10^{-6}
Maximum transformation strain,	H	0.031
Stress influence coefficient, Austenite,	C^A	10.4 MPaK^{-1}
Stress influence coefficient, Martensite,	C^M	7.3 MPaK^{-1}
Thermal conductivity,	k	18 W/Km
Poisson's ratio	ν	0.33
Density	ρ	6500 kgm^{-3}

strongly affects the temperature response. There is a change in the slope of temperature response at $t \approx 2000$ s, making the initiation of reverse phase transformation from austenite to martensite. The transformation continues till $t \approx 8000$ s. This is also exhibited through the delayed displacement response (shown in Fig. 3a). Displacement distribution is plotted along the length for different time instants in Fig. 3b. The corresponding temperature and martensite volume fraction distribution along the length are depicted in Fig. 4. However, the temperature distribution is uniform through-thickness of the cross-section. As the heat convection coefficient increases, different portion settles down to different temperature because of heat energy loss to the surroundings and the effect of latent heat diminishes; as a result, the difference in response vanishes.
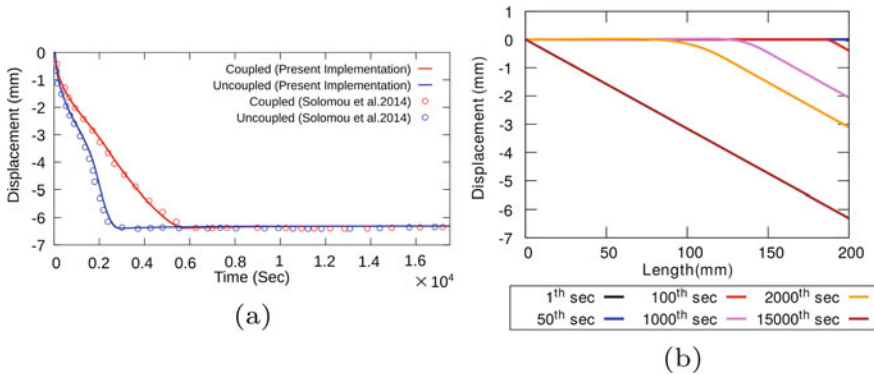
Fig. 3 **a** Difference in displacement response at the free end (B) for uncoupled and coupled analysis, **b** Displacement distribution along the length at different time instants for coupled analysis
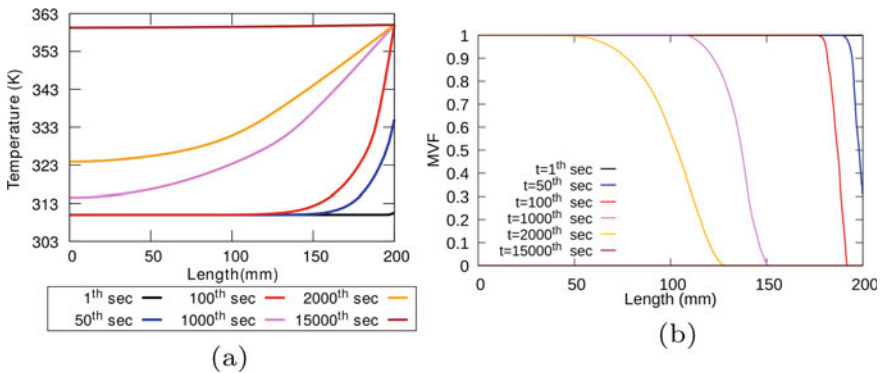
Fig. 4 Predicted distribution of **a** temperature and **b** martensite volume fraction distribution along the length for coupled model at different time instants

4.2 Coupled Thermomechanical Analysis of Biomedical Staple

A NiTi-based biomedical staple is used for hand and foot bone fragments osteotomy fixation and joint arthrodesis, one of the practical applications of SMA. In this problem, the coupled thermomechanical response of a biomedical staple subjected to a practical loading scenario is simulated using the developed FE tool. Following the work of Jaber et al. [18], the staple dimension is shown in Fig. 5, with a rectangular cross-section area of width 2 mm and thickness 2.5 mm. The staple is initially in austenite phase ($\xi = 0$) at a temperature of 288 K. It is loaded with a concentrated force of F = 28 N at each end of the two prongs for 0.9 s and subsequently unloaded in the next 0.1 s. It is then heated to a temperature of 310 K (human body temperature) linearly as shown in applied thermomechanical loading history diagram. The
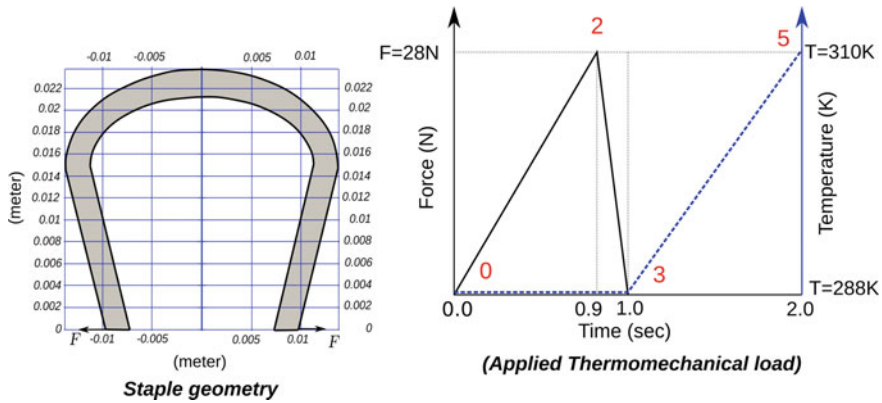
Fig. 5 Schematic of a biomedical staple used for idiopathic scoliosis treatment and applied thermomechanical loading

Table 2 Shape memory alloy material parameters [18]

Material parameter	Symbol	Value
Elastic modulus, Austenite	E^A	70 GPa
Elastic modulus, Martensite	E^M	70 GPa
Martensite finish temperature	M_f	273 K
Martensite start temperature	M_s	283 K
Austenite start temperature	A_s	293 K
Austenite finish temperature	A_f	303 K
Maximum transformation strain,	H	0.06
Stress influence coefficient, Austenite,	C^A	5 MPaK^{-1}
Stress influence coefficient, Martensite,	C^M	5 MPaK^{-1}
Poisson's ratio	ν	0.3
Density	ρ	6500 kgm^{-3}

model is meshed with C3D20T (coupled temperature displacement) elements, to obtain accurate stress distribution and free-end deflection during bending. Adiabatic condition is taken during mechanical loading and during thermal loading temperature boundary condition is used. The material parameters used for the simulation are listed in Table 2. The thermal properties used in this simulation are the same as the ones used in the previous example.

Figure 6 shows the difference in the displacement response for coupled and uncoupled models. As the load increases, initially the response is linear due to elastic loading up to 0.4 s. Further loading leads to starting of forward transformation, resulting in the formation of martensite. This in turn leads to the release of latent heat and thermoelastic heat. As a result, the temperature increases in the zone of higher stresses, which leads to a stiffer model in the presence of coupling terms. On the other hand,
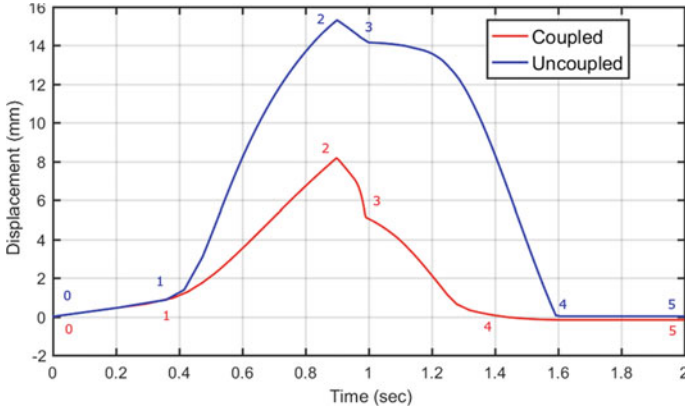
Fig. 6 Displacement response in the direction of F at the point of loading
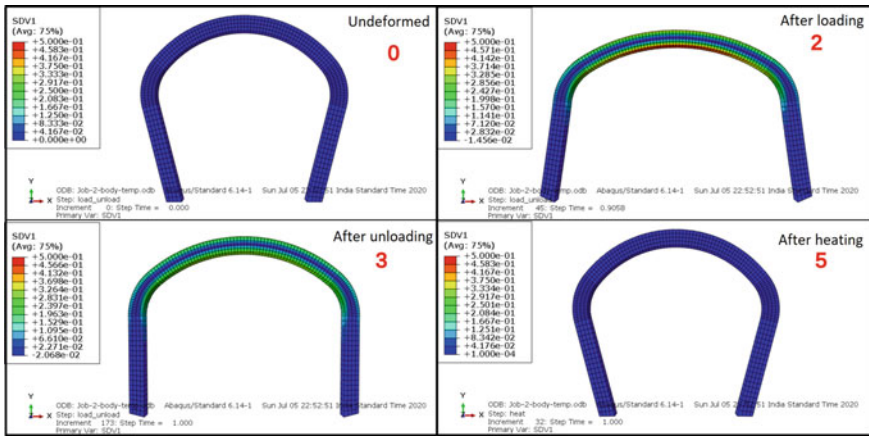
Fig. 7 Martensite volume fraction distribution in the staple for coupled analysis at different time instant

the uncoupled analysis could not capture this phenomenon, as the effects of latent heat and thermoelastic heat are ignored. The corresponding distribution of marten-sitic volume fraction at different instants is shown in Fig. 7. During unloading from point 2 to point 3 the strain recovery is small as the transformation strain is not recov-ered. Further, as the temperature increased to 310 K, martensite gets transformed to austenite, bringing the staple back to initial shape.

5   Summary and Conclusion

In this work, a thermomechanically coupled formulation for SMA structures is developed and implemented in a nonlinear finite element framework. The effects of the coupling terms, i.e., latent heat of transformation and thermoelastic heat due to phase transformation, are explored in this formulation. Consideration of mechanical loading applied heat source and boundary conditions significantly alters the performance of the system. To effectively predict the response of SMA-based components, the effect of latent heat is essential to capture the effect of the exothermic or endothermic nature of transformation, especially during phase transformation. Finally, the developed FE is used to find the response of a biomedical staple under practical thermomechanical loading cases. It is found that the coupled analysis is required to effectively predict the thermomechanical response, which cannot be captured using uncoupled analysis. This formulation can be extended for other 2D and 3D applications, such as SMA stents, origami structures, considering geometric nonlinearity, which will be explored in the future.

References

1. Lagoudas DC (2008) Shape memory alloys, modelling and engineering applications. Springer, New York
2. Brinson LC (1993) One-dimensional constitutive behavior of shape memory alloys: thermomechanical derivation with non-constant material functions and redefined martensite internal variable. J Intell Mater Syst Struct 4:229–242
3. Tanaka K (1986) A thermomechanical sketch of shape memory effect; one dimensional tensile behavior. Int J Numer Methods Eng 18:251–263
4. Liang C, Rogers CA (1990) One-dimensional thermomechanical constitutive relations for shape memory materials. J Intell Mater Syst Struct 2:207–234
5. Yang SB, Xu M (2011) Finite element analysis of 2d SMA beam bending. Acta Mech Sin 27(5):738
6. Seelecke S, Muller I (2004) Shape memory alloy actuators in smart structures: modeling and simulation. Appl Mech Rev 57(1):23–46
7. Alipour A, Kadkhodaei M, Ghaei A (2015) Finite element simulation of shape memory alloy wires using a user material subroutine: parametric study on heating rate, conductivity, and heat convection. J Intell Mater Syst Struct 26(5):554–572
8. Sengupta A, Papadopoulos P, Kueck A, Pelton AR (2011) On phase transformation models for thermo-mechanically coupled response of nitinol. Comput Mech 48(2):213–227
9. Thiebaud F, Collet M, Foltete E, Lexcellent C (2007) Implementation of a multi-axial pseudoelastic model to predict the dynamic behavior of shape memory alloys. Smart Mater Struct 16(4):935
10. Raniecki B, Lexcellent C (1998) Thermodynamics of isotropic pseudoelasticity in shape memory alloys. Eur J Mech-A/Solids 17(2):185–205

11. Lagoudas D, Hartl D, Chemisky Y, Machado L, Popov P (2012) Constitutive model for the numerical analysis of phase transformation in polycrystalline shape memory alloys. Int J Plast 32:155–183
12. Tabesh M, Lester B, Hartl D, Lagoudas D (2012) Influence of the latent heat of transformation and thermomechanical coupling on the performance of shape memory alloy actuators. In: Smart materials, adaptive structures and intelligent systems, vol 45103, pp 237–248. American Society of Mechanical Engineers
13. Qidwai M, Lagoudas D (2000) Numerical implementation of a shape memory alloy thermo-mechanical constitutive model using return mapping algorithms. Int J Numer Methods Eng 47:1123–1168
14. Solomou AG, Machairas TT, Saravanos DA (2014) A coupled thermomechanical beam finite element for the simulation of shape memory alloy actuators. J Intell Mater Syst Struct 25(7):890–907
15. Solomou AG, Machairas TT, Saravanos DA, Hartl DJ, Lagoudas DC (2016) A coupled layered thermomechanical shape memory alloy beam element with enhanced higher order temperature field approximations. J Intell Mater Syst Struct 27(17):2359–2384
16. Boyd J, Lagoudas DC (1996) A thermodynamical constitutive model for shape memory materials. Int J Plast 12:805–842
17. Crank J, Nicolson P (1947) A practical method for numerical evaluation of solutions of partial differential equations of the heat-conduction type. In: Mathematical proceedings of the Cambridge philosophical society, vol 43, pp 50–67. Cambridge University Press
18. Jaber MB, Smaoui H, Terriault P (2008) Finite element analysis of a shape memory alloy three-dimensional beam based on a finite strain description. Smart Mater Struct 17(4):045005

Multiaxial Fatigue Behavior of Near Alpha Titanium Alloy for Aeroengine Applications

Adya Charan Arohi, Vikas Kumar, N. Chitti Babu, and N. Narasaiah

Abstract Titanium alloys are considered as an attractive material for aerospace applications owing to their unique characteristics such as high specific strength, good ductility, and better corrosion resistance. IMI 834 alloy is a near α Ti alloy that is used in the compressor discs and blades of turbine engines. These components rotate at very high rotational speed and often experience the combined effect of axial and centrifugal stress. It has been noticed that the failure of these components occurs due to the cyclic load during its normal operation. Hence, the aim of the present study is to evaluate the tensile and multiaxial fatigue behavior of IMI 834 alloy at room temperature. Tensile tests are performed at a strain rate of 6.67×10^{-4} s^{-1}. Fully reversed pure axial, pure torsion, and combined axial-torsion fatigue experiments are conducted on the tubular specimen in in-phase load conditions at a frequency of 0.3 Hz. Hysteresis loops are determined for all the fatigue tests at half of the fatigue life. Cyclic stress response curves are generated and noted that the alloy tends to show neither cyclic hardening nor cyclic softening during the pure axial fatigue. On the other hand, it shows cyclic softening for the case of pure torsion and combined axial-torsion fatigue. Subsequently, the fatigue life is correlated to Von-Mises equivalent stress and strain under various load combinations. The alloy exhibits the lowest fatigue life under combined axial-torsion load and the highest life under pure torsion fatigue. It is noteworthy to observe that the effect of axial fatigue is more dominant under the combined axial-torsion fatigue. Pure torsion fatigue specimens are noted to fracture at 45° whereas pure axial fatigue specimens fracture at 90° to the specimen axis.

Keywords IMI 834 · Axial · Torsion · Multiaxial fatigue · Tubular

A. C. Arohi (✉)
Department of Metallurgical and Materials Engineering, Indian Institute of Technology, Kharagpur, India

V. Kumar · N. C. Babu
Defence Metallurgical Research Laboratory, Hyderabad, India

N. Narasaiah
Department of Metallurgical and Materials Engineering, National Institute of Technology, Warangal, India

1 Introduction

Titanium (Ti) alloys are commercially important in many industries [1]. High strength, low density, better ductility, and good corrosion resistance are the main properties of Ti alloys [2]. These unique properties make Ti alloys attractive for various applications in the aerospace, biomedical, and chemical industries [3]. Pure Ti shows an allotropic phase transformation from body-centered cubic β to hexagonal closed packed α phase at 882 °C. They are classified as α, (α + β) and β Ti alloys depending on the presence of alloying elements. Furthermore, they are subdivided into near α and metastable β alloy categories. Among all the Ti alloys, Ti-6Al-4 V is the most common and widely used alloy and accounts for 60% production of overall Ti alloys. However, Ti-6Al-4 V is limited up to a service temperature of 300 °C due to its poor creep and oxidation properties at higher temperatures [4]. Therefore, there is a great demand for such alloys which can be used at higher temperatures without degradation in the mechanical and corrosion properties.

Increasing demand for high-temperature alloys leads to the development of IMI 834 alloy [2]. It can be used up to 600 °C and is considered as a suitable candidate to replace Ni-based superalloy for aero-engine components. This alloy finds applications for high-pressure compressor disc and turbine blades [5]. These components rotate at very high rotational speed during the service condition. Therefore, they are subjected to a high axial as well as centrifugal stress throughout the components. Most of the time, it is observed that their failure occurs due to periodic cyclic loading. These fatigue failures have no prior intimation and hence they are still complex to the industry. So, many researchers have contributed their time in evaluating the microstructural analysis, tensile and low cycle fatigue properties of IMI 834 alloy at room as well as at high temperatures. Lutjering and William's study shows that a wide range of microstructures can be generated by tailoring the thermomechanical processing routes [2]. Amit et. al. have evaluated the tensile properties of IMI 834 alloy with varying primary alpha (α_p) phase fractions. It is noteworthy from the literature that the maximum tensile strength of 1087 MPa is achieved for the specimen with a 14.4% α_p volume fraction [6]. IMI 834 alloys having bimodal microstructure show better tensile strength and fatigue resistance than the lamellar microstructure. Various literature are available on the cyclic deformation of IMI 834 alloy. Kartik et. al. have found that IMI 834 alloy shows cyclic softening during the initial cycle and followed by cyclic hardening behavior till fracture [7].

All the studies described above are investigated by considering the uniaxial stress only. But in reality, the aerospace components experience multiaxial stresses i.e., a combination of axial and shear stress throughout the structure [8, 9]. Hence, it is extremely important to investigate the multiaxial fatigue behavior of an alloy system. Zhi-Rong et. al. have studied the axial-torsion fatigue behavior of TC4 alloy by varying the phase angle between axial and shear strain. They found that TC4 alloy exhibits additional cyclic hardening during the non-proportional loading [10]. In another study, Von-Mises equivalent stress and strain models are used to determine

Table 1 Nominal chemical composition of IMI 834 alloy (in wt. %)

Al	Sn	Zr	Nb	Mo	Si	C	Ti
5.8	4.0	3.5	0.7	0.5	0.35	0.06	Balance

the fatigue life for Ti-6Al-4 V alloy [11]. However, the data on multiaxial fatigue for IMI 834 alloy is very limited.

The present study focuses on evaluating the tensile and multiaxial fatigue behavior of near alpha titanium alloy IMI 834. This includes the pure axial, pure torsion, and in-phase combined axial-torsion fatigue load conditions. This study provides a scope to determine the fatigue life and to generate the hysteresis loops at half of the fatigue life under different load conditions. It also focuses on understanding the cyclic hardening and softening behavior of materials. Von-Mises equivalent stress criterion is used to analyze the stress-life curve. Failure analysis is also carried out to develop a deeper understanding of the crack orientation.

2 Material and Experimental Details

2.1 Material

IMI 834 alloy is received in the form of a ring having an outer and inner diameter of 450 mm and 350 mm, respectively. The height of the ring is measured to be 47 mm. The nominal chemical composition of the present alloy is given in Table 1. The thermal heat treatment history of the as-received material is as follows: (1) initially forged below the β-transus temperature (2) subsequently recrystallization and aging treatment in the (α + β) regime. These heat treatments are performed to achieve the bimodal microstructure which is suitable for fatigue-prone applications.

2.2 Microstructural Characterization

Prior to the microstructural examination, the specimen of 5 mm × 5 mm × 5 mm is cut using the diamond slow speed cutter to avoid any surface damage. The specimen is polished using different grades of emery paper varying from P100 to P2000. This is followed by cloth polishing using the diamond paste of particle size of 3 μm and 1 μm respectively. Subsequently, the specimen is etched using a solution containing 4% HF, 8% HNO_3 and 88% distilled water called Kroll's reagent for around 10–12 s. The microstructure is observed using the optical Olympus DSX510 series and scanning electron microscope Zeiss EVO 18.
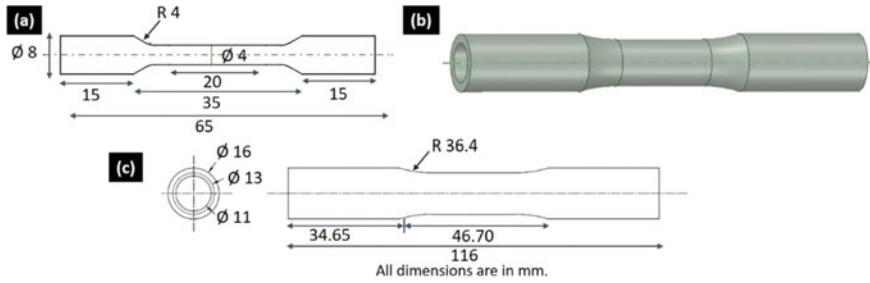
Fig. 1 **a** Tensile test specimen geometry, **b** 3-D view of a multiaxial fatigue test specimen, and **c** Multiaxial fatigue specimen geometry

2.3 Tensile Tests

The conventional dog-bone-shaped tensile specimens of 8 mm diameter and 65 mm length are prepared according to ASTM standard E-8 [12]. Monotonic tests are performed using a Walter + Bai AG servo-hydraulic universal test machine having a load capacity of 100 kN. All the tensile tests are done at a constant strain rate of 6.67×10^{-4} s^{-1}. A contact-type extensometer of 12.5 mm gauge length is mounted on the specimen surface to record the strain. The specimen geometry is shown in Fig. 1a.

2.4 Multiaxial Fatigue Specimen Preparation

Tubular specimens with 1.5 mm wall thickness and 116 mm length are used for conducting all three different categories of fatigue tests. The external and internal diameter of the specimen is 16 mm and 11 mm, respectively. The three-dimensional tubular specimens as shown in Fig. 1b are prepared according to the ASTM standard E-2207 [13]. The dimensions of the tubular specimen are given in Fig. 1c. This unique specimen geometry is recommended for carrying multiaxial fatigue tests because they possess a high surface-to-volume ratio without appreciable shear strain gradient throughout the gauge length.

Fabricating thin-walled tubular specimens of any titanium alloy is quite a challenging problem. The main problems associated with Ti alloys during machining are their low thermal conductivity and long chip formation [14]. Hence, they are machined using carbide tools with a proper coolant supply. Figure 2 shows the specimen preparation technique in a sequential manner. The as-received ring is first cut into seven equal segments using an electric discharge machine (EDM) wire cutting. Subsequently, the cylindrical bar of 17.5 mm is extracted from the segment of the ring. Turning operation is carried out to decrease the diameter of the cylindrical bar. Rimmer of different diameters 5 mm, 7 mm, 8 mm, 10 mm, and 10.8 mm are used
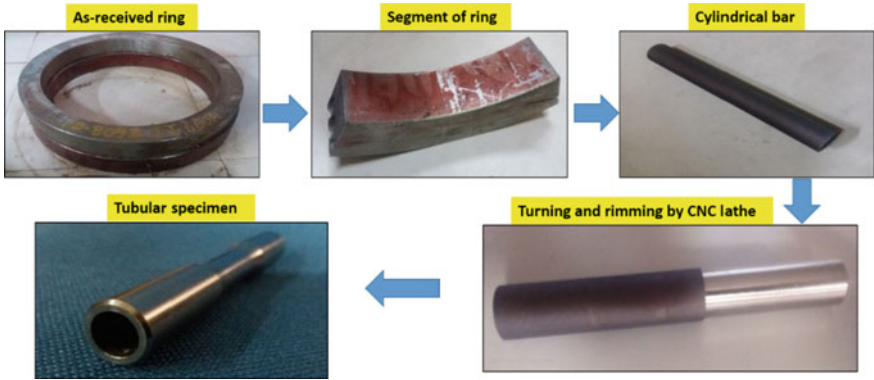
Fig. 2 Specimen preparation technique for thin-walled tubular specimen

to make it tubular. Mechanical Polishing using emery paper is done to achieve the minimum surface roughness on the outer and inner sections of the specimen.

2.5 Multiaxial Fatigue Test Equipment and Procedures

Figure 3 represents the servo-hydraulic test set up for conducting multiaxial fatigue experiments. This dynamic triaxial testing equipment Walter + Bai AG LFV is

Fig. 3 Multiaxial fatigue test equipment

capable of performing tension–torsion fatigue tests in in-phase and out-of-phase mode up to a combination of the maximum load of 100 kN and torque 1000 Nm. It also has a provision of attaching a contact type axial-torsion extensometer to monitor the axial as well as shear strain.

The present study focuses on three categories termed pure axial, pure torsion, and in-phase combined axial-torsion fatigue. All the fatigue tests are carried out under fully reversed triangular waveforms with a frequency of 0.3. The stroke and angle control mode is selected for axial and torsion fatigue respectively. Pure axial fatigue tests are carried out at different stroke amplitudes of $\pm$ 0.35 mm, $\pm$ 0.45 mm, and $\pm$ 0.55 mm respectively. Whereas for pure torsion fatigue tests, the angle amplitude is varied as $\pm$ 4°, $\pm$ 5°, and $\pm$ 6° respectively. Three combinations of stroke and angle amplitude i.e. ($\pm$ 0.35 mm and $\pm$ 4°), ($\pm$ 0.45 mm and $\pm$ 5°) and ($\pm$ 0.55 mm and $\pm$ 4°) are selected to perform the combined axial-torsion fatigue tests. All the tests are done till the failure of the specimen. A 20% load drop criterion is considered to be the failure of a specimen. The axial load and torque corresponding to the stroke and angle are recorded and used to calculate the axial and shear stress amplitude respectively. Following are the two equations used to calculate the axial (σ_a) and shear (τ_a) stress amplitude:

$$\sigma_a = \frac{\Delta\sigma}{2} = \frac{\Delta P}{2A} \tag{1}$$

$$\tau_a = \frac{\Delta\tau}{2} = \frac{\Delta T}{2r_m A} \tag{2}$$

where $\frac{\Delta P}{2}$ and $\frac{\Delta T}{2A}$ are axial load and torque amplitude, r_m is the mid-section radius and A is the cross-section area of the specimen.

3   Results and Discussions

3.1   Microstructural Analysis

Representative optical and scanning electron micrographs (SEM) of as-received IMI 834 alloy are shown in Fig. 4. It is evident from the optical micrograph (see Fig. 4a), that one phase looks brighter and appears to be globular and equiaxed. This phase is retained after the heat treatment and is hereafter referred to as the primary alpha (α_p) phase. The average size and volume fraction of the globular α_p phase is measured to be 10.5 $\pm$ 3 μm and 18 $\pm$ 2.5%, respectively. Figure 4b is an SEM image that represents the typical bimodal microstructure of the alloy as it contains two different kinds of α phases which are crystallographically similar but different in origin and morphology. The microstructure consists of α_p and lamellae of α and β phases inside the prior β grain. This lamellar α forms during the cooling and is referred to as the
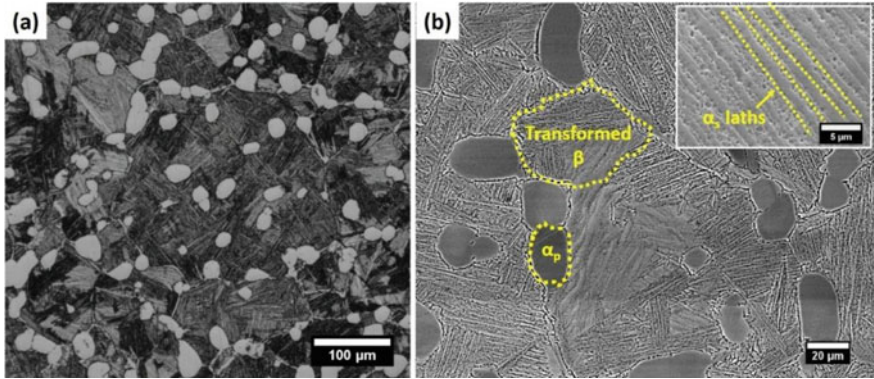
Fig. 4 a Optical and **b** SEM image of as-received IMI 834 alloy

Table 2 Tensile properties of IMI 834 alloy at room temperature

YS (MPa)	UTS (MPa)	Elongation (%)	Strain hardening exponent (n)	UTS/YS ratio
1003 ± 27	1084 ± 26	13.5 ± 0.5	0.03	1.08

secondary alpha (α_s) phase. The prior β grain and lath spacing between α lamellae is measured to be 85 ± 12 µm and 1.27 ± 0.27 µm respectively.

3.2 Tensile Properties

Table 2 shows the tensile properties of IMI 834 alloy at room temperature. The yield strength (YS) and ultimate tensile strength (UTS) are measured to be 1003 ± 27 and 1084 ± 26 MPa respectively. The material has quite a good amount of ductility and elongation to failure under tension test which is noted to be 13.5 ± 0.5%. High strength and excellent ductility can be related to its microstructure. The microstructure consists of a high volume fraction of α_p phase which enhances the strength to a great extent. Similar values of strength and ductility are well reported in the literature [6]. It is interesting to note that the alloy has a UTS to YS ratio of 1.08. The UTS to YS ratio below 1.20 tends to show cyclic softening during the cyclic test.

3.3 Pure Axial Fatigue (PAF) Analysis

Axial stress amplitude, axial strain amplitude, plastic strain amplitude, and elastic strain amplitude is denoted by σ_a, ε_a, ε_p and ε_e, respectively. Stress amplitude is

calculated using Eq. 3 where σ_{max} and σ_{min} are the maximum and minimum stress developed in the hysteresis loops corresponding to the half of fatigue life. The plastic strain is measured from the hysteresis loop by considering the strain which is not recovered after unloading. The half of width of the hysteresis loop represents the plastic strain amplitude. Elastic strain amplitude is calculated by subtracting the plastic strain amplitude from total strain amplitude and is given in Eq. 4.

$$\sigma_a = \frac{\Delta\sigma}{2} = \frac{\sigma_{max} - \sigma_{min}}{2} \tag{3}$$

$$\varepsilon_e = \varepsilon_t - \varepsilon_p \tag{4}$$

3.3.1 Hysteresis Loops for Pure Axial Fatigue

Pure axial fatigue tests are conducted at a stroke amplitude of ± 0.35 mm, ± 0.45 mm and ± 0.54 mm respectively. The representative stabilized hysteresis loops are plotted at their respective half of the fatigue life and shown in Fig. 5a, b, c. The corresponding
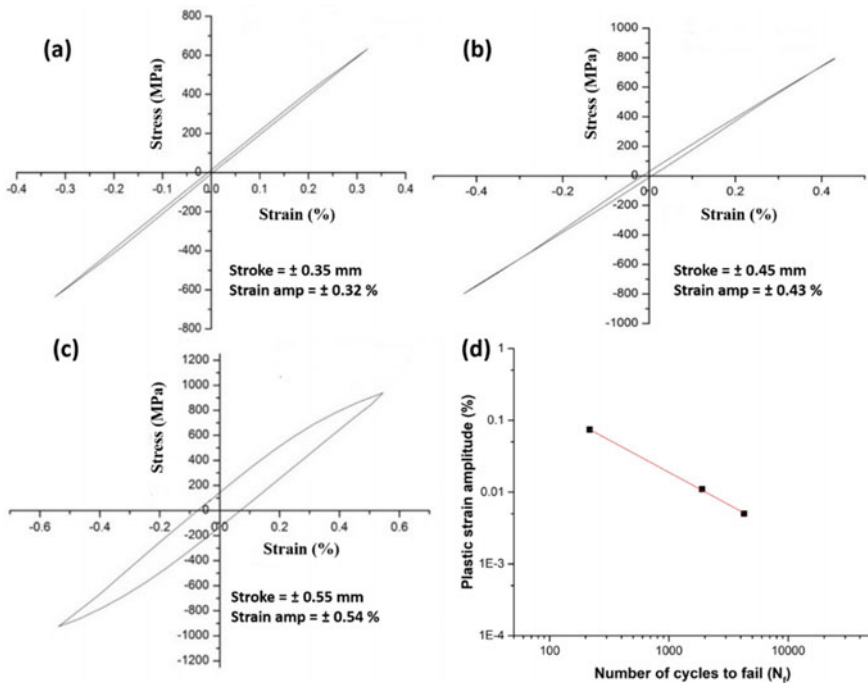
Fig. 5 Pure axial fatigue hysteresis loops developed at strain amplitude of **a** 0.32%, **b** 0.43% and **c** 0.54% and **d** strain-life curve for pure axial fatigue tests

Table 3 Different parameters observed from pure axial fatigue tests

Specimen ID	Stroke (mm)	ε_t (%)	ε_e (%)	ε_p (%)	σ_a (MPa)	N_f
PAF_01	± 0.35	± 0.32	0.314	0.006	631	4268
PAF_02	± 0.45	± 0.43	0.420	0.010	797	1895
PAF_03	± 0.55	± 0.54	0.466	0.074	932	216

strain amplitude is estimated to be ± 0.32%, ± 0.43%, and ± 0.54% respectively. The width of the hysteresis loops is directly related to the plastic strain associated with the specimen. It is evident from Fig. 5a that there is a negligible amount of plastic deformation at low strain amplitude of ± 0.32%. Plastic strain amplitude is noted to increase with an increase in the stroke and strain amplitude. The specimens tested at a strain amplitude of 0.54% exhibit the lowest life among all. All the parameters such as elastic strain amplitude, plastic strain amplitude, stress amplitude, and the number of cycles to fail are given in Table 3.

3.3.2 Strain-Life Curve for Pure Axial Fatigue

Earlier research shows that the plastic strain amplitude parameter is mainly responsible for the low cycle fatigue failure [15, 16]. Therefore, the half-life plastic strain-life curve is plotted using the Coffin–Mansion relationship and shown in Fig. 5d. The C–M equation is as follows:

$$\frac{\Delta \varepsilon_p}{2} = \varepsilon'_f \left(N_f\right)^c \tag{5}$$

where ε'_f the strain ductility coefficient and c is the strain ductility exponent. It is evident from Fig. 5d that the specimen exhibits higher life at low plastic strain amplitude. The intercept ε'_f and slope c of the linear fit are measured as 0.96 and -0.67, respectively. Zhi-Rong et al. have found the ε'_f and c as 0.58 and -0.68 respectively for TC-4 Ti alloy [10]. The value for ε'_f appears to be slightly higher as compared to the reported value in the literature. The reason can be attributed to the higher yield strength of IMI 834 alloy as compared to TC-4 alloy.

3.3.3 Cyclic Stress Response Curve for Pure Axial Fatigue

Variation in cyclic stress amplitude with an elapsed cycle for all the specimens are evaluated and shown in Fig. 6. Cyclic stress variation with elapsed cycle represents the cyclic hardening and softening behavior of any material. An increase in the stress amplitude with respect to the elapsed cycle signifies the cyclic hardening, whereas the reverse phenomenon is considered as the cyclic softening behavior. However, it is
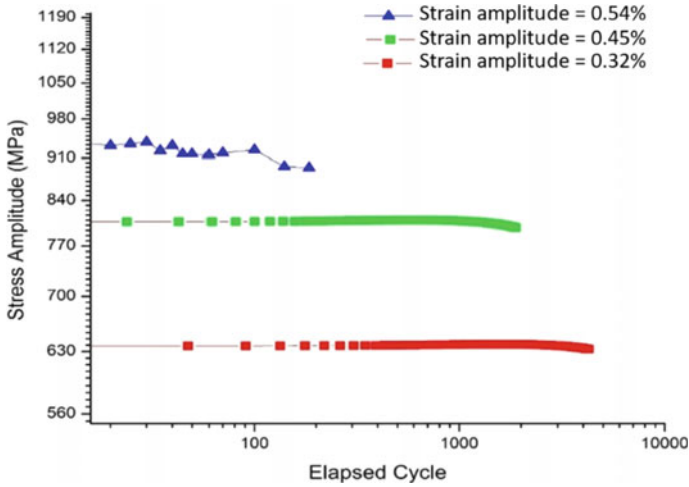
Fig. 6 Cyclic stress response curve for pure axial fatigue tests

apparent from Fig. 6 that the material does not show any cyclic hardening/softening behavior. Instead, the material exhibits the cyclic saturation behavior till the fracture. The reasons can be attributed to the applied strain amplitude. At low strain amplitudes, the material exhibits restricted plastic deformation. Hence, the softer phase present in the material experiences the plastic deformation whereas the harder phase is still in elastic domain. Similar cyclic saturation behavior for titanium alloy is also reported in the literature [17].

3.4 Pure Torsion Fatigue (PTF) Analysis

Shear stress amplitude, shear strain amplitude, plastic shear strain amplitude, and elastic shear strain amplitude is denoted by τ_a, γ_a, γ_p and γ_e, respectively. Shear stress amplitude is calculated using Eq. 6 where τ_{max} and τ_{min} are the maximum and minimum shear stress in the hysteresis loops. Similar to the different axial fatigue parameters, elastic and plastic shear strain amplitude are calculated from the hysteresis loops by following the same theory. Elastic shear strain amplitude is calculated using Eq. 7.

$$\tau_a = \frac{\Delta\tau}{2} = \frac{\tau_{max} - \tau_{min}}{2} \tag{6}$$

$$\gamma_e = \gamma_a - \gamma_p \tag{7}$$
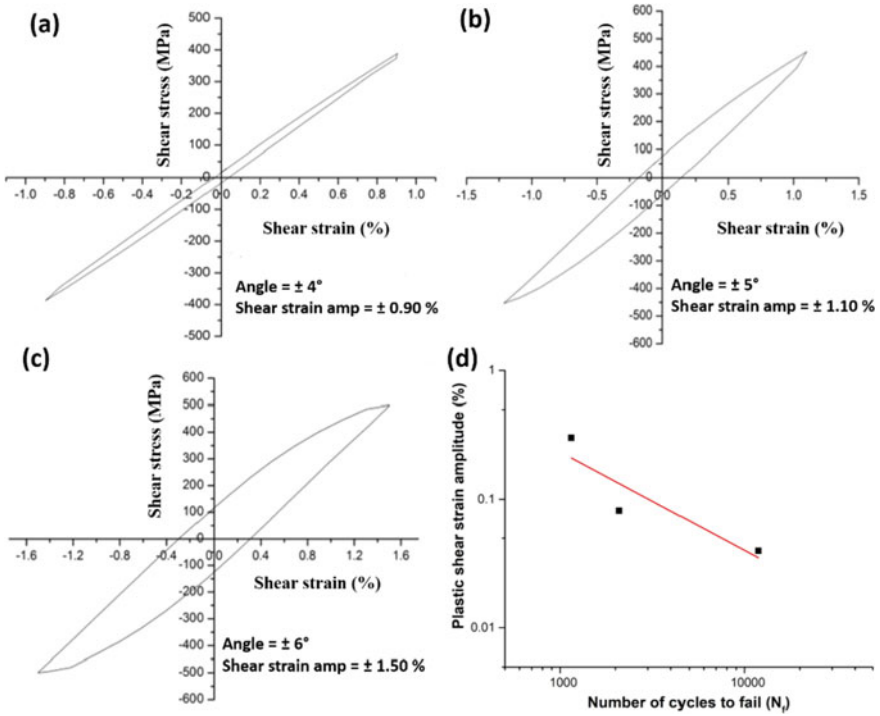
Fig. 7 Pure torsion fatigue hysteresis loops developed at strain amplitude of **a** 0.90%, **b** 1.10% and **c** 1.50% and **d** shear strain-life curve for pure torsion fatigue tests

3.4.1 Hysteresis Loops for Pure Torsion Fatigue

Pure torsion fatigue tests are conducted at an angle amplitude of $\pm 4°$, $\pm 5°$ and $\pm 6°$ respectively. Figure 7a, b, c show the typical shear stress–strain loops of the present alloy at three different conditions. These loops are plotted at half of their respective fatigue life. It is noted from the Fig. 7 that shear stress and shear strain increases with the increase in angle amplitude. The corresponding shear stress and shear strain are measured for each category. It is observed that the width of the hysteresis loop i.e. the plastic shear strain range increases with an increase in the angle amplitude. All the parameters such as elastic and plastic shear strain amplitude, shear stress amplitude and the number of cycles to fail are also listed in Table 4.

3.4.2 Shear Strain-Life Curve for Pure Torsion Fatigue

Figure 7d shows the plastic shear strain-life curve for pure torsion fatigue tests conducted at three different load conditions. This curve is plotted using similar Coffin–Mansion equation and is given in Eq. 8.

Table 4 Different parameters observed for pure torsion fatigue tests

Specimen ID	Angle (°)	γ_t (%)	γ_e (%)	γ_p (%)	τ_a (MPa)	N_f
PTF_01	± 4°	± 0.90	0.86	0.04	385	11,892
PTF_02	± 5°	± 1.10	1.02	0.08	448	2092
PTF_03	± 6°	± 1.50	1.20	0.30	499	1152

$$\frac{\Delta\gamma_p}{2} = \gamma_f'\left(N_f\right)^{c'} \tag{8}$$

where γ_f' is the shear strain ductility coefficient and c' is the shear strain ductility exponent. It is evident from the Fig. 7d that the specimen exhibits the highest life at low plastic shear strain amplitude. The intercept γ_f' and slope c' of the linear fit are measured as 1.67 and −0.77 respectively. W. John Evans et al. have reported similar values of intercept and slope by conducting torsion fatigue in near alpha and alpha–beta titanium alloys [8, 18].

3.4.3 Cyclic Shear Stress Response Curve

The variation of shear stress amplitude with elapsed cycles for different specimens is shown in Fig. 8. It is observed that shear stress amplitude decreases with an increase in the number of cycles for the specimens corresponding to high strain amplitude of 1.10% and 1.50% only. This behavior exhibits the extensive cyclic softening of IMI 834 alloy under pure torsion fatigue load. The softening phenomenon is
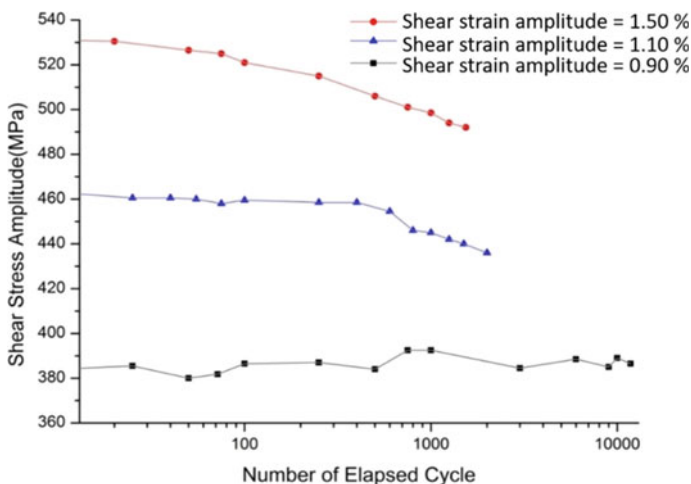
Fig. 8 The Cyclic stress response curve for pure torsion fatigue tests

dominant at higher shear strain amplitude. Cyclic softening behavior is attributed to the thermo-mechanical treatment which is pursued to the alloy. Hot forging leads to the generation of dislocations inside the material. During the fatigue tests, these dislocations rearrange themselves and annihilation occurs by releasing the stress and leading to softening. It is also supported with the observed value of work hardening exponent n < 0.15 which tends to show the cyclic softening behavior. On the other hand, dislocation activity may not be prominent for the specimen tested at low strain amplitude i.e., at 0.90% and hence do not show softening behavior.

3.5 Combined Axial-Torsion Fatigue (CATF) Analysis

3.5.1 Hysteresis Loops for Combined Axial-Torsion Fatigue

Subsequent to the pure axial and pure torsion fatigue tests, the present investigation is extended further to the in-phase combined axial-torsion fatigue tests (CATF). Typical axial and shear stress–strain hysteresis loops are plotted for CATF_01, CATF_02 and CATF_03 specimens in Fig. 9a, b, c respectively. Since all the tests are done in in-phase conditions, the maximum and minimum axial and shear stress occur at the same point in time. The axial stress is noted to be higher than the shear stress for each condition.

Since the specimens are subjected to both axial as well as shear strain, it is better to calculate the equivalent stress and strain parameter. Hence, the Von-Mises equivalent stress–strain criterion is used and described below. Von-Mises equivalent stress ($\underline{\sigma}_a$) is calculated using Eq. 9.

$$\underline{\sigma}_a = \sqrt{\sigma_a{}^2 + 3\tau_a{}^2} \tag{9}$$

Where σ_a and τ_a are the axial and shear stress amplitude, respectively.

Von-Mises total equivalent strain amplitude ($\underline{\varepsilon}_{t,a}$) is the sum of equivalent elastic strain amplitude ($\underline{\varepsilon}_{e,a}$) and equivalent plastic strain amplitude ($\underline{\varepsilon}_{p,a}$) and represented in Eq. 10. The equations for equivalent elastic and plastic strain amplitude is given in Eqs. 11 and 12, respectively.

$$\underline{\varepsilon}_{t,a} = \underline{\varepsilon}_{e,a} + \underline{\varepsilon}_{p,a} \tag{10}$$

$$\underline{\varepsilon}_{e,a} = \frac{1}{\sqrt{2(1 + \vartheta_e)}} \sqrt{2\varepsilon_{e,a}{}^2(1 + \vartheta_e)^2 + \frac{3}{2}\gamma_{e,a}{}^2} \tag{11}$$

$$\underline{\varepsilon}_{p,a} = \sqrt{\varepsilon_{p,a}{}^2 + \frac{1}{3}\gamma_{p,a}{}^2} \tag{12}$$
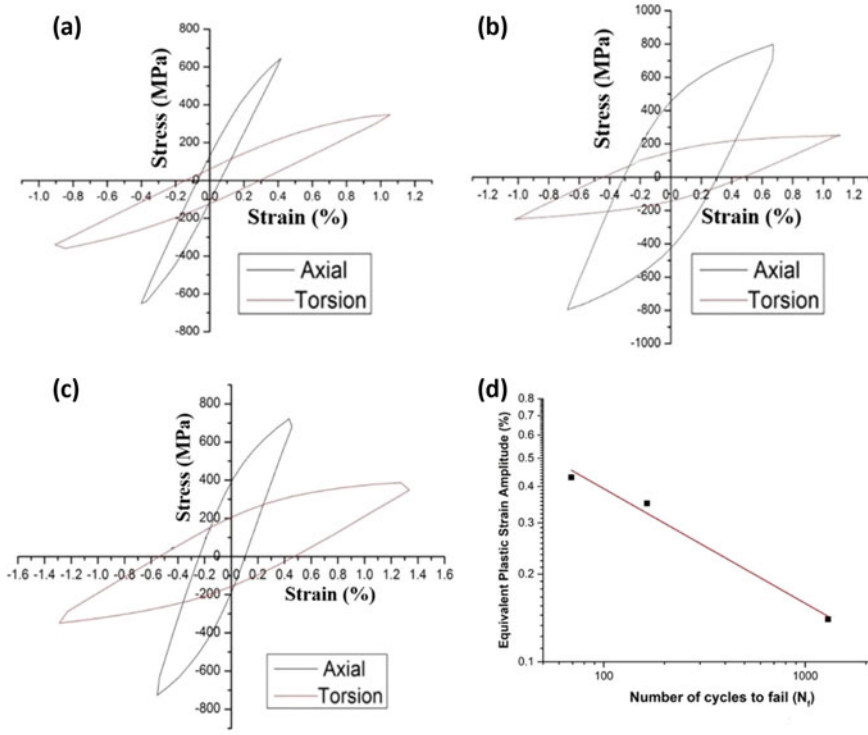
Fig. 9 Combined axial-torsion fatigue hysteresis loops developed for **a** CATF_01, **b** CATF_02 and **c** CATF_03 specimens and **d** equivalent strain-life curve for combined axial-torsion fatigue tests

where $\varepsilon_{e,a}$ and $\varepsilon_{p,a}$ are axial elastic and plastic strain, respectively, $\gamma_{e,a}$ and $\gamma_{p,a}$ are shear elastic and plastic strain respectively and ϑ_e is elastic Poisson's ratio. The ϑ_e for IMI 834 alloy is assumed as 0.3. All the parameters such as axial and shear stress, equivalent stress and strain amplitude are mentioned in Table 5.

Table 5 Different parameters observed for combined axial-torsion fatigue tests

Specimen ID	Stroke (mm)	Angle (°)	ε_a (%)	γ_a (%)	$\varepsilon_{t,a}$(%)	σ_a(MPa)	N_f
CATF_01	± 0.35	± 4°	0.40	0.97	0.763	854	1297
CATF_02	± 0.55	± 4°	0.66	1.04	0.980	902	164
CATF_03	± 0.45	± 5°	0.54	1.33	1.01	941	69

3.5.2 Equivalent Strain-Life Curve for Combined Axial-Torsion Fatigue

Equivalent plastic strain amplitude is calculated using the above-mentioned Eq. 12. The typical equivalent plastic strain-life curve for the combined axial-torsion fatigue tests is shown in Fig. 9d. It is clearly visible that there exists a linear relationship between the plastic strain amplitude at half-life and the number of cycles to fail in the logarithmic scale. The intercept and slope of the linear fit are found to be 0.38 and − 0.39 respectively. The specimen corresponding to the low plastic strain exhibits the maximum fatigue life.

3.5.3 Cyclic Equivalent Stress Response Curve

Similar to the pure axial and pure torsion cyclic stress response curve, the variation of equivalent stress amplitude with elapsed cycles is plotted in Fig. 10. It is noteworthy from the figure that the specimen at lower equivalent strain amplitude shows a low amount of cyclic softening as compared to the specimens which are tested at higher strain amplitude. Earlier research also shows cyclically stable behavior at lower strain amplitude. It is reported that localized plastic deformation is not prominent at the low strain amplitude to shear the Ti_3Al precipitates [19]. On the other hand, the heavily deformed IMI 834 alloy shows the rearrangement of dislocations leading to cyclic softening at higher strain amplitude.
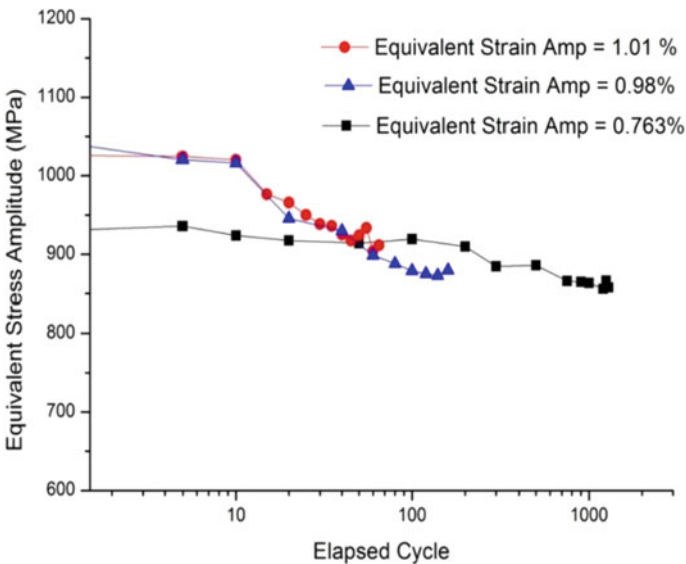
Fig. 10 Cyclic equivalent stress response curve for combined axial-torsion fatigue tests

Fig. 11 Von-Mises
equivalent stress-life curve
for all the specimens
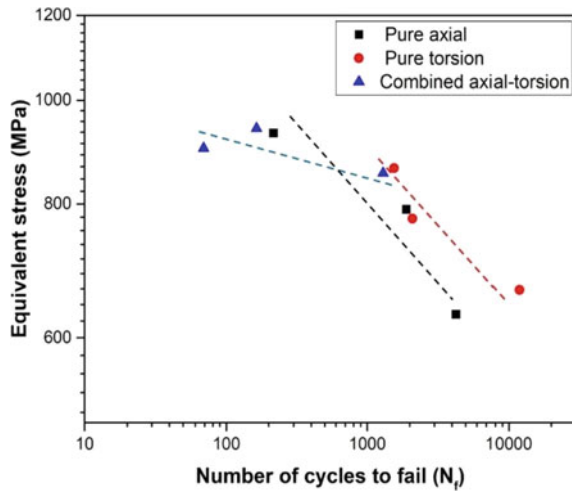
3.6 Comparison of Pure Axial, Torsion, and Combined Axial-Torsion Fatigue Life

Figure 11 shows the Von-Mises equivalent stress-life curve for pure axial, pure torsion as well as combined axial-torsion fatigue tests. Von-Mises equivalent stress for all the categories of tests is calculated using Eq. 9. It is clearly noted from Fig. 11 that the specimens which are subjected to both axial and torsion load have the highest equivalent stress. This results in a high amount of plastic deformation in the specimens. Subsequently, they exhibit the lowest fatigue life as compared to the other conditions. Some of the combined axial-torsion specimens have equal or little lower equivalent stress than pure axial and pure torsion fatigue specimens. But they show lower fatigue life than pure axial and pure torsion fatigue specimens. The reason can be attributed to the hysteresis loops which are generated during the combined axial-torsion fatigue tests. The combined axial as well as shear hysteresis loops result in a high loop area. This loop area is nothing but the strain energy absorbed in the specimen. Higher absorption of strain energy in the specimens during fatigue tests leads to reducing the fatigue life significantly. It is also noted that the specimens that are subjected to the pure torsion fatigue load exhibit the highest fatigue life. One major observation in Fig. 11 is that the pure axial, pure torsion, and combined axial-torsion follow a different linear fit curve.

3.7 Mode of Failure

Failure analysis is considered an important parameter in fatigue study. Complicated fracture mode exists for multiaxial fatigue failure due to a combination of tension

Fig. 12 Different modes of failure for **a** pure axial, **b** pure torsion and **c** combined axial-torsion fatigue tests

and torsion load. Figure 12 shows the three different modes of failure for pure axial, pure torsion, and combined axial-torsion fatigue tests, respectively. It is noteworthy from Fig. 12 that all the specimens have fractured within the gauge section. The specimens subjected to pure axial fatigue load fail at a perpendicular (90°) to the specimen axis as shown in Fig. 12a. However, the specimens which experience the pure torsional fatigue load fail at an angle of 45° to the specimen axis as shown in Fig. 12b. The reason is attributed to the maximum tensile principal stress developed during torsion fatigue. According to the Von-Mises theory, the maximum principal stress exists at an angle of 45°. For the case of combined axial-torsion fatigue tests, the fracture of the specimen takes place at a helical angle to the axis as shown in Fig. 12c. This type of fracture is called the mixed mode of fracture. The orientation of the crack path and fracture mode is dependent on the degree of multiaxiality.

3.8 Fractography of Fatigue Tested Specimen

Subsequent to the fracture mode analysis, the study is further extended to understand the fracture micro-mechanism using a scanning electron microscope. Fatigue fracture consists of three stages: (1) crack initiation zone, (2) crack propagation zone, and (3) final catastrophic failure. Cracks generally initiate from the high-stress concentration region and they propagate radially from the initiation sites. Figure 13 shows the SEM
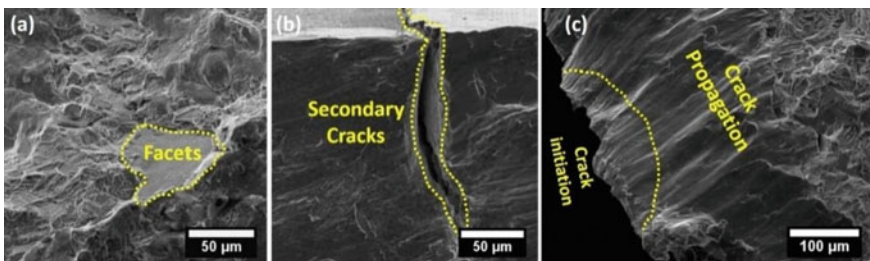
Fig. 13 SEM fractographs of **a** pure axial, **b** pure torsion, and **c** combined axial-torsion fatigue specimens

images of the fractured surface of the pure axial, pure torsion, and combined axial-torsion fatigue-tested specimens, respectively. It is observed that the fatigue crack has initiated near the facets for the case of pure axial (Fig. 13a) fatigue loading condition. However, the crack initiation sites for the specimen subjected to pure torsion fatigue are not clearly visible. Some secondary cracks are noted for the pure torsion fatigue specimens as shown in Fig. 13b. Crack initiation and propagation zones are observed for the specimen subjected to the combined axial-torsion fatigue load as shown in Fig. 13c.

4   Conclusions

In this present investigation, the tensile and multiaxial fatigue behavior of IMI 834 alloy is studied thoroughly. Particularly, the hysteresis loop, strain-life curve, equivalent stress-life curve, cyclic stress response, different modes of failure are analyzed. The following conclusions are drawn from this study:

- IMI 834 alloys having bimodal microstructure exhibits good yield and ultimate tensile strength of 1003 ± 27 and 1084 ± 26 MPa respectively. Also, it shows an excellent elongation to failure of $13.5 \pm 0.5\%$ under the tension test.
- This study proves that combined axial-torsion fatigue load is more detrimental than pure axial as well as pure torsion fatigue load. The specimens which are subjected to the combined axial-torsion load exhibit the lowest fatigue life among all category.
- Von-Mises equivalent stress is also maximum for the combined axial-torsion fatigue load conditions. The higher stress induces more plastic deformation and higher strain energy in the specimen leading to short fatigue life.
- Pure axial fatigue specimens do not show cyclic softening/hardening behavior. However, the specimens subjected to the pure torsion fatigue and combined axial-torsion fatigue show extensive cyclic softening behavior.
- Different modes of failure are observed for each load condition. Pure axial fatigue specimens fracture at $90°$ to the specimen axis whereas the pure torsion fatigue specimens fracture at $45°$ to the specimen axis. Combined axial-torsion fatigue specimens fracture at a helical angle and the mode of failure depends on the degree of multiaxiality.

References

1. Boyer RR (1996) An overview on the use of titanium in the aerospace industry 213:103–114
2. Lutjering G, Williams JC (2007) Titanium, 2nd edn. Springer, New York
3. Kolli RP, Devaraj A (2018) A Review of Metastable Beta Titanium Alloys. Metals (Basel). 8:1–41. https://doi.org/10.3390/met8070506
4. Eylon D, Fujishiro S, Froes FH (1984) Titanium Alloys for High Temperature Applications—A Review. High Temp Mater Process 6:81–91. https://doi.org/10.1515/HTMP.1984.6.1-2.81
5. Singh N, Singh GV (2006) Low cycle fatigue Behaviour of Ti alloy Timetal 834 at 873 K. Int J.Fatigue 29
6. Singh A, Balasundar I, Gautam JP, Raghu T (2019) Effect of primary α phase fraction on tensile behavior of IMI 834 alloy. Procedia Struct. Integr. 14:78–88. https://doi.org/10.1016/j.prostr.2019.05.011
7. Prasad K, Sarkar R, Ghosal P, Varma VK (2008) The influence of dynamic strain aging on the low cycle fatigue behavior of near alpha titanium alloy IMI 834. Mater Sci Eng A 494:227–231. https://doi.org/10.1016/j.msea.2008.04.025
8. Bache MR, Evans WJ (1992) Tension and torsion fatigue testing of a near-alpha titanium alloy 5:331–337
9. Joseph J, Bonnen F (1998) Multiaxial fatigue response of normalized 1045 steel subjected to periodic overloads: experiments and analysis I * m
10. Wu Z, Hu X-T, Song YD (2014) Multiaxial fatigue life prediction for titanium alloy TC4 under proportional and non-proprtional loading. Int J Fatigue 59:170–175
11. Renzo DA, Sgambitterra E, Magarò P, Maletta C, Biffi CA (2020) Multiaxial fatigue behavior of additively manufactured Ti6Al4V alloy: axial—torsional proportional loads. 1–10. https://doi.org/10.1002/mdp2.190
12. ASTM E8 (2010) ASTM E8/E8M standard test methods for tension testing of metallic materials 1, Annu B ASTM Stand 4(02):1–27. https://doi.org/10.1520/E0008
13. Standard Practice for Strain-Controlled Axial-Torsional Fatigue Testing with Thin-Walled Tubular Specimens, Annual Book (2008) 1–8. doi:https://doi.org/10.1520/E2207-08.2.
14. Gao Y, Wang G, Liu B (2016) Chip formation characteristics in the machining of titanium alloys: a review. Int J Mach Mach Mater 18:155–184. https://doi.org/10.1504/IJMMM.2016.075467
15. Wagn RF, Li YT, An HP (2013) Low cycle fatigue life prediction of Ti-6Al-4V titanium alloy under multi-axial non proportional cyclic loading. 668:814–817. https://doi.org/10.4028/www.scientific.net/AMR.668.814
16. Wu J, Lin C (2005) Effect of strain rate on high-temperature low-cycle fatigue of 17–4 PH stainless steels. 390:291–298. https://doi.org/10.1016/j.msea.2004.08.063
17. Zhang S, Zhang H, Hao J, Liu J, Sun J, Chen L (2020) Cyclic stress response behavior of near β titanium alloy and deformation mechanism associated with precipitataed phase. Metals 10:1482
18. Evans WJ, Whittaker MT, Jones JP (2007) Torsion fatigue in near alpha and alpha-beta titanium alloys. Japan Inst Met 1333–1336
19. Rao KS, Prasad K, Varma VK, Singh V (2008) Influence of hold time on low cycle fatigue behaviour of near alpha titanium alloy IMI 834 At 873K. Trans Indian Inst Met 61:407–414

Magnetic Shape Memory Alloys: Phenomenological Constitutive Modeling and Analysis

Avinash Kumar and **Krishnendu Haldar**

Abstract Increasing demand for a lighter and more durable material with sensing and actuation functionality, Magnetic Shape Memory Alloys (MSMA) are promising members, among many other smart materials. This study investigates the Magneto-Thermo-Mechanical (MTM) behavior of MSMA through a 3D phenomenological constitutive modeling thermodynamically consistent way. A specific Helmholtz free energy function is considered after identifying the external and internal state variables. The evolution equations of the internal state variables are defined by proposing a transformation function. The model parameters are calibrated through different MTM loading conditions. Selective model simulations demonstrate the magnetic field coupling with the actuation strain.

1 Introduction

Magnetic shape memory alloys (MSMA) are one of the most emerging classes of multi-functional materials which respond to the magnetic field, temperature, and external load [1–4]. It has the potential to produce large Magnetic-Field-Induced Strain (MFIS) through microstructural changes at least one order of higher magnitude than those of available magnetostrictive materials [5–9]. MSMAs also exhibit conventional pseudo-elastic and shape memory behavior. However, MSMAs have advantages on actuation frequency (1KHz) over conventional SMAs due to the availability of high frequency applied magnetic field [10].

A. Kumar (✉) · K. Haldar
Department of Aerospace Engineering, Indian Institute of Technology Bombay,
Mumbai 400076, India
e-mail: krishnendu@aero.iitb.ac.in

The macroscopic responses of MSMAs are the manifestations of four fundamental microscopic mechanisms: the motion of magnetic domain walls, the rotation of magnetization vector, field-induced variant reorientation, and field induced phase transformation [11, 12]. Ni-Mn-Ga alloys are the most widely investigated MSMAs for variant reorientation. Martensitic transformation in Ni_2MnGa alloys was firstly reported by Webster et al. [13]. The detailed studies on the crystal structure of MSMAs were done by Zasimchuk et al. [14]. Ullako et al. [15] reported the first magnetic controlled shape memory effect in MSMAs. They observed 0.2% magnetic-field-induced strain (MFIS) in a stress-free experiment. NiCoMnIn alloys also exhibit MFIS under applied magnetic field. Such type of MFIS is caused by Field Induced Phase Transformation (FIPT) [16–18].

In this work, we develop a coupled constitutive equation of MSMAs for FIPT. The microstructure dependence is approximated phenomenologically by the evolution equations of the selected internal state variables. The model parameters are calibrated from the experimental data. Finally, MTM responses are simulated for FIPT.

2 Mechanism of Field-Induced Phase Transformation

FIPT mechanism is similar to the temperature-induced phase transformation in conventional Shape Memory Alloys (SMAs). The *Zeeman Energy* (ZE)[1], which depends on the difference between saturation magnetizations of austenitic and martensitic phase, is converted to mechanical energy through FIPT [19–21]. The higher symmetric austenitic phase is ferromagnetic [22–24]. The anti-ferromagnetic martensitic phase has three possible variants of the tetragonal crystalline structure, which is depicted in Fig.1. The specimen is in the austenitic phase at room temperature and at a high magnetic field. After removing the applied field, the phase is transformed into the martensitic phase.

3 Constitutive Modeling

A *multiplicative decomposition* of deformation gradient $\boldsymbol{F}$ into *lattice* $\boldsymbol{F}_l$ and *inelastic* part $\boldsymbol{F}_\iota$ is considered [25, 26] such that

$$\boldsymbol{F} = \boldsymbol{F}_l \boldsymbol{F}_\iota.$$

The selection of an appropriate free energy function is one of the significant challenges for modeling multi-functional material. The function should be proposed in such a way so that the constitutive responses should be able to capture all the significant features of MSMA like phase transformation, and its temperature dependence.

---

[1] Energy of magnetized body in an external applied magnetic field
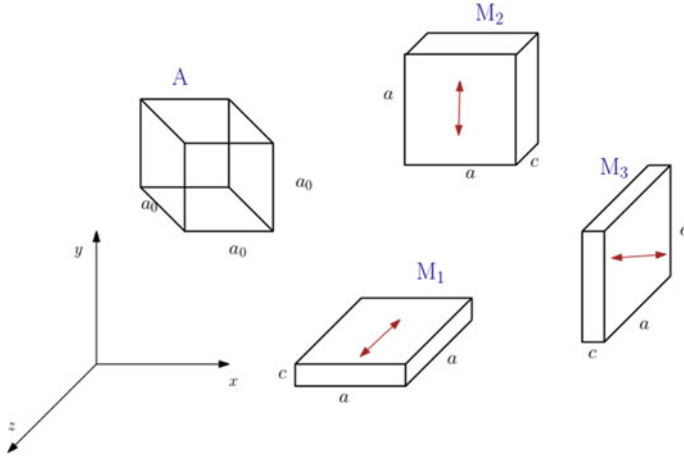
Fig. 1 Crystalline structure of austenitic phase (A) and martensitic phase (M). M_1 is variant-1, M_2 is variant-2, and M_3 is variant-3

We propose a Helmholtz free energy density $\tilde{\psi}$ per reference volume, containing a lattice energy $\tilde{\psi}_l$, an inelastic energy $\tilde{\psi}_\iota$, and a mixing energy $\tilde{\psi}_{mix}$ as [27–30]

$$\tilde{\psi}(\boldsymbol{C}_l, \boldsymbol{C}_\iota, \boldsymbol{H}, \xi, \theta) = \tilde{\psi}_l(\boldsymbol{C}_l, \boldsymbol{H}, \theta, \xi) + \tilde{\psi}_\iota(\boldsymbol{C}_\iota) + \tilde{\psi}_{mix}(\xi) \qquad (1)$$

and we obtain the constitutive equations using Coleman-Noll [31] procedure :

$$\boldsymbol{S} = 2\rho_0 \boldsymbol{F}_\iota^{-1} \frac{\partial \tilde{\psi}_l}{\partial \boldsymbol{C}_l} \boldsymbol{F}_\iota^{-T}, \quad \eta = -\frac{\partial \tilde{\psi}_l}{\partial \theta}, \quad \mu_0 \boldsymbol{M} = -\rho_0 \frac{\partial \tilde{\psi}_l}{\partial \boldsymbol{H}}, \quad -\rho_0 \frac{\partial \tilde{\psi}}{\partial \xi} \cdot \dot{\xi} \geq 0.$$

The lattice right Cauchy green tensor $\boldsymbol{C}_l = \boldsymbol{F}_l^T \boldsymbol{F}_l$, magnetic field strength $\boldsymbol{H}$, and temperature θ are the physical or external state variables for the constitutive equations. Further, $\boldsymbol{C}_\iota$ and the martensitic volume fraction ξ are the internal state variables. Moreover, $\boldsymbol{S}$ is the Second Piola-Kirchhoff stress, η is the entropy, and $\boldsymbol{M}$ is the magnetization.

4 Numerical Implementation and Model Calibration

For the small strain assumption, multiplicative decomposition becomes additive decomposition of strain with a lattice and an inelastic part

$$E = \varepsilon := \frac{1}{2}\left(C - I\right)$$

$$= \frac{1}{2}\left(F^T F - I\right)$$

$$= \frac{1}{2}\left((F_l F_\iota)^T (F_l F_\iota) - I\right)$$

$$= \frac{1}{2}\left((I + \nabla u_\iota^T + \nabla u_l^T)(I + \nabla u_\iota + \nabla u_l) - I\right)$$

$$= \frac{1}{2}\left(\nabla u_l + \nabla u_l^T\right) + \frac{1}{2}\left(\nabla u_\iota + \nabla u_\iota^T\right) + h.o.t$$

$$= \varepsilon_l + \varepsilon_\iota. \tag{2}$$

The lattice strain could further be decomposed into an elastic and a thermal strain, i.e., $\varepsilon_l = \varepsilon_e + \varepsilon_\theta$. We discard the thermal expansion and write $\varepsilon_l = \varepsilon_e$. Moreover, for FIPT, the inelastic strain becomes transformation strain, i.e., $\varepsilon_\iota = \varepsilon_t$. After identifying the internal state variable (ξ, ε_t) and external state variables $(\varepsilon_e, \theta, \boldsymbol{H})$, the explicit form of Helmholtz free energy function [32] is given by

$$\psi\left(\varepsilon_e, \theta, \boldsymbol{H}, \varepsilon_t, \xi\right) = -\frac{1}{2\rho}\varepsilon_e : \boldsymbol{L} : \varepsilon_e - \boldsymbol{\sigma} : \varepsilon_t + u_0 - \frac{\mu_0}{\rho}\boldsymbol{H} \cdot \boldsymbol{M} - \theta\eta_0 + \frac{1}{\rho}f\left(\xi\right), \tag{3}$$

where, $\boldsymbol{L}$, u_0, η_0, c, and $\boldsymbol{M}$ are the stiffness tensor, internal energy, entropy, specific heat, and saturation magnetization, respectively. The effective material properties are determined by using the rule of mixture. $f\left(\xi\right)$ is the hardening function during forward and reverse phase transformation. We used the polynomial type hardening function [33],

$$f\left(\xi\right) = \begin{cases} \frac{1}{2}A\left(\xi + \frac{\xi^{n_1+1}}{n_1+1} + \frac{(1-\xi)^{n_2+1}}{n_2+1}\right) + C\xi; \ \dot{\xi} > 0 \\ \frac{1}{2}B\left(\xi + \frac{\xi^{n_3+1}}{n_3+1} + \frac{(1-\xi)^{n_4+1}}{n_4+1}\right) + D\xi; \ \dot{\xi} < 0 \end{cases}. \tag{4}$$

where A, B, C, D represent model parameters. Moreover, n_1, n_2, n_3 and n_4 are hardening exponents for phase transformation. Considering the explicit form of (3), we write by using Coleman-Noll procedure

$$\left(\boldsymbol{\sigma} - \rho\frac{\partial\psi}{\partial\varepsilon_e}\right) : \dot{\varepsilon}_e - \rho\left(\frac{\partial\psi}{\partial\theta} + \eta\right)\dot{\theta} + \left(\mu_0\boldsymbol{M} + \rho\frac{\partial\psi}{\partial\boldsymbol{H}}\right) \cdot \dot{\boldsymbol{H}} + \boldsymbol{\sigma} : \dot{\varepsilon}_t - \rho\frac{\partial\psi}{\partial\xi}\dot{\xi} \geq 0.$$

The constitutive equations then take the following forms:

$$\boldsymbol{\sigma} = \rho\frac{\partial\psi}{\partial\varepsilon_e} = \boldsymbol{L} : \varepsilon_e \quad \eta = -\frac{\partial\psi}{\partial\theta}, \quad \mu_0\boldsymbol{M} = -\rho\frac{\partial\psi}{\partial\boldsymbol{H}},$$

and the residual inequality reads

$$\boldsymbol{\sigma} : \dot{\varepsilon}_t - \rho \frac{\partial \psi}{\partial \xi} \dot{\xi} \geq 0. \tag{5}$$

We further consider the flow rule of the transformation strain

$$\dot{\varepsilon}_t = \boldsymbol{\Lambda} \dot{\xi}. \tag{6}$$

Expanding the entropy inequality equation (5), we finally obtain

$$\pi \dot{\xi} \geq 0 \tag{7}$$

where, $\pi = \boldsymbol{\sigma} : \boldsymbol{\Lambda} - \rho \frac{\partial \psi}{\partial \xi} \dot{\xi} \geq 0$ is the thermodynamics driving force.

4.1   1-D Reduction of the Model

We represent the 1-D result by assuming the uniaxial loading in a prismatic bar along its longitudinal axis. The stress tensor has only one non-zero component, that is

$$\sigma_{11} = \sigma \neq 0.$$

The one dimensional form of thermodynamic driving force reduces to

$$\pi = E_{max}|\sigma| + \frac{1}{2} L^{-1} \sigma \cdot \Delta L \cdot L^{-1} \sigma + \rho \Delta \eta_0 \theta + \mu_0 \Delta M \cdot H - \rho \Delta u - \frac{\partial f}{\partial \xi}. \tag{8}$$

We now introduce the following transformation function

$$\phi := \begin{cases} \pi - Y, & \dot{\xi} > 0 \\ \pi + Y, & \dot{\xi} < 0 \end{cases},$$

where Y is a positive scalar associated with the internal dissipation during the microstructure evolution [33]. The constraint on the evolution of the martensitic volume fraction can be expressed in terms of so-called Kuhn-Tucker conditions for both forward and reverse phase transformations as [34]

$$\phi \leq 0, \quad \phi \dot{\xi} = 0. \tag{9}$$

The material parameters required for model calibration can be found out directly from the experiments, and the values are given in Table 1. The hardening parameters, $A, B, C, D,$ and Y are calibrated from the following end conditions

Table 1 Material parameters for smooth transformation hardening model [20]

$E^A = 12 \times 10^9 \, Pa$	$E^M = 25 \times 10^9 \, Pa$
$\rho \cdot \Delta \eta_0 = -11.45 \times 10^4 \, \frac{J}{m^3 K}$	$E_{max} = 0.032$
$\mu_0 H_{As} = 7.2T$	$\mu_0 H_{Af} = 11.4T$
$\mu_0 H_{Ms} = 8.4T$	$\mu_0 H_{Mf} = 4T$
$\Delta u = 0$	$\theta_0 = 200K$
$n_1 = 0.2$	$n_2 = 0.23$
$n_3 = 0.3$	$n_4 = 0.4$
$M_A = 115$ emu/g	$M_M = 15$ emu/g
$M_s at = 115$ emu/g	$\mu_0 = 1.2566e - 6$
$\nu_A = 0.33$	$\nu_M = .33$

$$\pi (\boldsymbol{\sigma}, \boldsymbol{H}_{Ms}) = Y \implies \dot{\xi} > 0; \quad \xi = 0$$
$$\pi (\boldsymbol{\sigma}, \boldsymbol{H}_{Mf}) = Y \implies \dot{\xi} > 0; \quad \xi = 1$$
$$\pi (\boldsymbol{\sigma}, \boldsymbol{H}_{As}) = -Y \implies \dot{\xi} < 0; \xi = 1$$
$$\pi (\boldsymbol{\sigma}, \boldsymbol{H}_{Af}) = -Y \implies \dot{\xi} < 0; \xi = 0$$
$$f (\xi = 1) \big|_{\dot{\xi}>0} = f (\xi = 1) \big|_{\dot{\xi}<0}.$$

Figure 2a represents the phase transformation between stress and magnetic field plane at a specified temperature. The red curve demonstrates the forward phase transformation, and the blue curve is for the reverse phase transformation. The transformation magnetic field increases with an increase in applied load. With a uniaxial tensile load at stress level ($\sigma = 100$ MPa), the new transformation magnetic fields are represented as M_{Hf}, M_{Hs}, A_{Hs}, and A_{Hf} as the martensitic finish, martensitic start, austenitic start, and austenitic finish magnetic field, respectively. On the other hand, Fig. 2b represents the phase transformation in the stress and temperature field plane at the specified magnetic field.

Figure 3a represents the model simulation of the magnetic field induced strain at constant stress ($\sigma = -1$ MPa) in an isothermal environment. The material is initially in the martensitic phase. The initial strain and magnetic field are zero. When we increase the magnetic field up to A_{Hs}, there is negligible change in the strain. As the magnetic field increases from A_{Hs} to A_{Hf}, strain increases due to the magnetic-field-induced phase transformation. The anti-ferromagnetic martensite is transformed into the ferromagnetic austenite in this regime. Similarly, the austenite transforms to martensite during the unloading process. The phase transformation starts at magnetic flux M_{Hs} and ends when it reaches M_{Hf}. The hysteresis effects are captured both in mechanical as well as magnetization constitutive response. Figure 3b represents the model prediction of magnetization response at constant stress ($\sigma = -1$ MPa).
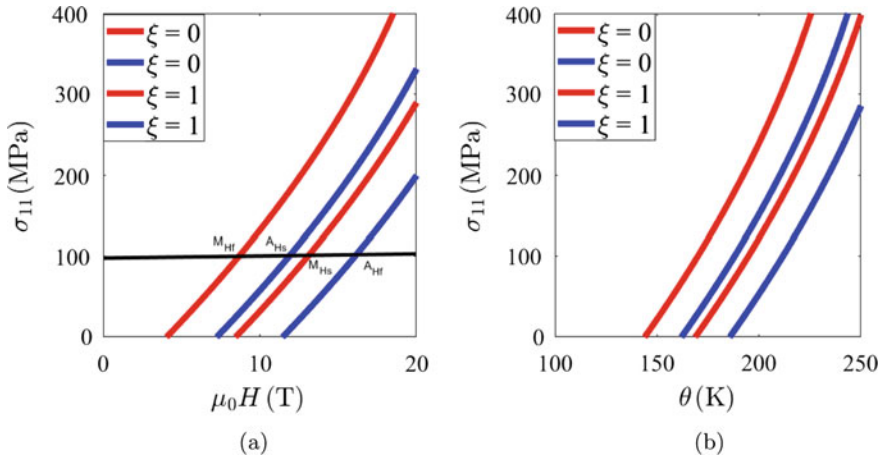
Fig. 2 **a** Phase transformation diagram in $\sigma_{11} - \mu_0 H$ plane at $(\theta = 200$ K). **b** Phase Transformation diagram in the $\sigma_{11} - \theta$ plane at $(\mu_0 H = 13$ T)
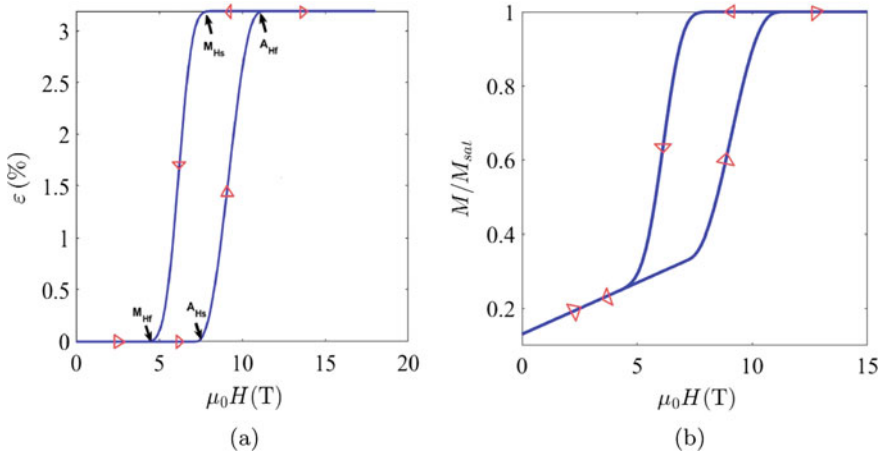
Fig. 3 **a** Model response for strain-field response at $(\sigma = -1$ MPa). **b** Model prediction of magnetization response at $(\sigma = -1$ MPa)

5 Conclusion

This work proposes the magneto-thermo-mechanical coupled model for MSMAs. The magneto-thermo-mechanical constitutive equations are derived from a proposed Helmholtz free energy function in a consistent thermodynamic way. The hysteretic behaviors of such materials are taking into account through evolution equations of internal variables. We did not verify our results to any experimental data yet.

However, our main objective is to capture qualitatively memory effect of such material system. Model predictions capture the hysteresis effects, both for the mechanical and magnetic responses.

References

1. Hobza A, Patrick CL, Ullakko K, Rafla N, Lindquist P, Müllner P (2018) Sensing strain with Ni-Mn-Ga. Sens Actuators A, Phys 269:137–144. https://doi.org/10.1109/ACCESS.2020.3020647
2. Heczko O, Straka L, Ullakko K (2003) Relation between structure, magnetization process and magnetic shape memory effect of various martensites occurring in Ni-Mn-Ga alloys. In: Journal de Physique IV (Proceedings), vol 112, EDP sciences, pp 959-962
3. O'Handley RC, Murray SJ, Marioni M, Nembach H, Allen SM (2000) Phenomenology of giant magnetic-field-induced strain in ferromagnetic shapememory materials (invited). J Appl Phys 87(2):4712-4717
4. Murray SJ, Marioni M, Tello PG, Allen SM, O'Handley RC (2001) Giant magnetic-field-induced strain in Ni-Mn-Ga crystals: experimental results and modeling. J Magn Magn Mater 226:945–947
5. Yamamoto T, Taya M, Sutou Y, Liang Y, Wada T, Sorensen L (2004) Magnetic field-induced reversible variant rearrangement in Fe–Pd single crystals. 52(17):5083–5091. https://doi.org/10.1016/0022-2836(81)90087-5
6. Müllner P, Murray SJ, et al (2001) Giant magnetic-field-induced strain in Ni–Mn–Ga crystals: experimental results and modeling. J Magn Magn Mater 226:945-947
7. Shield TW (2003) Magnetomechanical testing machine for ferromagnetic shape-memory alloys. Rev Sci Instrum 74(9):4077–4088
8. Likhachev AA, Sozinov A, Ullakko K (2004) Different modeling concepts of magnetic shape memory and their comparison with some experimental results obtained in Ni-Mn-Ga. Mater Sci Eng: A 378(1–2):513–518
9. Ullakko K, Huang JK, Kantner C, O'Handley RC (1966) Large magnetic-field-induced strains in Ni2MnGa single crystals. Appl Phys Lett 69:1966. https://doi.org/10.1063/1.117637
10. Tellinen J, Suorsa I, Jääskeläinen A, Aaltio I, Ullakko K (2002) Basic properties of magnetic shape memory actuators. In: 8th International conference ACTUATOR. pp 566–569
11. Kittel C, McEuen P, McEuen P (1996) Introduction to solid state physics (vol 8, pp 105-130). New York: Wiley
12. Faraji M, Yamini Y, Rezaee M (2010) Magnetic nanoparticles: synthesis, stabilization, functionalization, characterization, and applications. J Iran Chem Soc 7(1):1–37
13. Webster PJ, Ziebeck KR, Town SL, Peak MS (1984) Magnetic order and phase transformation in Ni2MnGa. Phil Mag B 49(3):295–310
14. Zasimchuk IK, Kokorin VV, Martynov VV, Tkachenko AV, Chernenko VA (1990) Crystal structure of martensite in Heusler alloy Ni2MnGa. Phys Met Metall 69(6):104–108
15. Ullakko K, Huang JK, Kantner C, O'handley RC, Kokorin VV (1996) Large magnetic-field-induced strains in Ni2MnGa single crystals. Appl Phys Lett 23 69(13):1966-1968
16. Sarawate N, Dapino M (2006) Experimental characterization of the sensor effect in ferromagnetic shape memory Ni-Mn-Ga. Appl Phys Lett 88(12):121923
17. Spaldin NA (2010) Magnetic materials: fundamentals and applications. Cambridge university press

18. Kainuma R, Imano Y, Ito W, Sutou Y, Morito H, Okamoto S, Kitakami O, Oikawa K, Fujita A, Kanomata T, Ishida K (2006) Magnetic-field-induced shape recovery by reverse phase transformation. Nature 439(7079):957–960
19. Kiefer B, Karaca HE, Lagoudas DC, Karaman I (2007) Characterization and modeling of the magnetic field-induced strain and work output in Ni2MnGa magnetic shape memory alloys. J Magn Magn Mater 312(1):164–175
20. Haldar K, Lagoudas DC, Karaman I (2014) Magnetic field-induced martensitic phase transformation in magnetic shape memory alloys: modeling and experiments. J Mech Phys Solids 1(69):33–66
21. Haldar K, Chatzigeorgiou G, Lagoudas DC (2015) Single crystal anisotropy and coupled stability analysis for variant reorientation in Magnetic Shape Memory Alloys. Eur J Mech A/Solids 1(54):53–73
22. Karaca HE, Karaman I, Basaran B, Ren Y, Chumlyakov YI, Maier HJ (2009) Magnetic field-induced phase transformation in NiMnCoIn magnetic shape-memory alloys-a new actuation mechanism with large work output. Adv Funct Mater 19(7):983–998
23. Karaca HE, Karaman I, Basaran B, Lagoudas DC, Chumlyakov YI, Maier HJ (2007) On the stress-assisted magnetic-field-induced phase transformation in Ni2MnGa ferromagnetic shape memory alloys. Acta Materialia 55(13):4253–4269
24. Karaca HE, Karaman I, Basaran B, Chumlyakov YI, Maier HJ (2006) Magnetic field and stress induced martensite reorientation in NiMnGa ferromagnetic shape memory alloy single crystals. Acta Materialia 54(1):233–245
25. Lee EH, Liu DT (1967) Finite-strain elastic-plastic theory with application to plane-wave analysis. J Appl Phys 38(1):19–27
26. Mandel J (1973) Thermodynamics and plasticity. In: Foundations of continuum thermodynamics. (pp 283-304). Palgrave, London
27. Lagoudas DC, Haldar K, Basaran B, Karaman I (2009) Constitutive modeling of magnetic field-induced phase transformation in NiMnCoIn magnetic shape memory alloys. In: Smart Materials, Adaptive Structures and Intelligent Systems. (vol 48968, pp 317-324)
28. Qidwai MA, Lagoudas DC (2000) Numerical implementation of a shape memory alloy thermomechanical constitutive model using return mapping algorithms. Int J Numer Methods Eng 47(6):1123–1168
29. Kiefer B, Lagoudas DC (2009) Modeling the coupled strain and magnetization response of magnetic shape memory alloys under magnetomechanical loading. J Intell Mater Syst Struct 20(2):143–170
30. Hirsinger L, Lexcellent C (2003) Modelling detwinning of martensite platelets under magnetic and (or) stress actions on Ni-Mn-Ga alloys. J Magn Magn Mater 1(254):275–277
31. Hütter G (2020) Coleman-Noll procedure for classical and generalized continuum theories. Encycl Continuum Mech 2020:316-323
32. Leclercq S, Lexcellent C (1996) A general macroscopic description of the thermomechanical behavior of shape memory alloys. J Mech Phys Solids 44(6):953–980
33. Boyd JG, Lagoudas DC (1996) A thermodynamical constitutive model for shape memory materials. Part I. The monolithic shape memory alloy. Int J Plast 12(6):805-842
34. Hanson MA (1981) On sufficiency of the Kuhn-Tucker conditions. J Math Anal Appl 80(2):545-550

Remaining Life of Fastener Joints Under Bearing and Bypass Fatigue Loading

I. Syed, B. Dattaguru, and A. R. Upadhya

Abstract Fastener joints are the desired joining techniques in many engineering applications since they make a rapid method to assemble and disassemble large structures. However, these joints are often susceptible to stress concentrations at critical locations due to their geometry with discontinuities. With further usage under fatigue loading, damage initiates and grows to a critical value at these locations affecting the integrity of the structure. Numerical analysis is carried out to study the stress variations in the plate-hole boundary of lap joint with fasteners accounting for different bearing and bypass loads ratios. The damage severity is studied under different R-ratios when subjected to FALSTAFF loading where the four-point rainflow cycle counting is used to extract the number of cycles. Damage growth is assessed by Paris' law with Elber correction factor wherein the fracture parameters are computed using MVCCI formulation. This approach helps in estimating the remaining life of the joint at any given operational conditions which in turn assists in the development of a computational model to build a digital twin for structural joints.

Keywords Fasteners · Bearing and bypass load · MVCCI

List of symbols

a	Material constants in Paris' law
C and m	Crack length
$G_{I:}$ Mode I	strain energy release rate (SERR)
K_{IC}	Mode I fracture toughness
σ_a	Applied load in the form of UDL
e	Distance to the centre of hole from right support
P_f	Bypass load
U_0	Imposed displacement at right end
R_P	Load ratio $= \frac{P_{\min}}{P_{\max}}$

I. Syed (✉) · B. Dattaguru · A. R. Upadhya
School of Aerospace Engineering, Jain (Deemed-To-Be University), Bengaluru, India

$\sigma_{\theta\theta}$	Tangential stress
a' and b'	Material constants in Elber's crack growth model
E and v	Young's modulus and Poisson's ratio
K_I	Mode I stress intensity factor (SIF)
N	Number of cycles
P_b	Bearing load at pin
P_a	Total applied load
$K_{\max}$ and $K_{\min}$	Maximum and minimum SIF
P_b/P_f	Bearing-bypass load ratio

1 Introduction

Fastener joints are widely used in aircrafts to connect different parts in primary and secondary structures. These create a non-permanent joint, unlike the case of welded or adhesive bonds and also allow easy assembly and dismantling [1]. However even though fastener joints provide easy access to inspect, they pose the problem of stress concentrations and are susceptible to damages such as cracks under operational conditions. Such cracks could grow to the critical sizes under aircraft flight loads during service life. It becomes necessary that such a fastener joint is analysed suitably to ensure safety. Research has been carried out both experimentally and numerically on fastener joints in both metallic as well as composite structures to estimate the strength of the joints under varying bearing to bypass loading ratios [2, 3, 13]. Considerable work has been done both metallic and composite joints before 2010. Whereas in the past decade most of the work is carried out on multi-fastener composites joints. Recent work involving a metallic joint under fatigue loading to predict remaining life is scanty. Prediction of joint strength using numerical methods has been carried out on multi-fastener composite joints [7] by considering effects of bypass load and the results are compared with existing experimental work. An experimental investigation on fatigue crack growth behaviour in composites has been carried out [14] by considering pin loading effects and bypass load and it was found that the pin loading dominates the crack growth in the vicinity of the pin hole. A numerical method is performed to assess fatigue life of multi-row riveted metallic lap joint using a global/local FE model coupling approach [5] using standard AFGROW. The present work on a single-fastener metallic joint configuration is aimed to contribute to the work on Digital Twin which is a current research topic.

Also work has been conducted on estimation of fatigue life of these joints based on S–N life extensively. However, there is limited work on evaluating the health of these joints considering damage (crack) growth under fatigue loading with different bearing to bypass load ratios. This paper attempts to address the issues in computing the remaining life of these joints under different loading conditions, viz: constant amplitude and variable amplitude loading, respectively.

Constant amplitude block may not be representative of actual flight conditions [11]. Fighter aircraft loading standard for fatigue (FALSTAFF) simulates the loading spectra from actual flight records of wing-root loads from different fighter aircrafts on various missions [8]. Block-type loading is constructed from one mission and repeated to define a new sequence of load. Negative loads are filtered, and the data is normalised. In the variable amplitude loading, the challenge is to account for the number of cycles which is done in this paper by using rainflow cycle counting which reduces the spectrum into an equivalent set of simple stress levels. This is achieved by the four-point method [12]. Crack like damages which initiate and grow at critical locations of these joints affect the strength of the joint to a greater extend which if not monitored may lead to fracture. Crack growth analysis under the conditions mentioned above is conducted using Paris' Law with Elber correction for crack closure [4] where the useful life of these joints is computed at any given instance of loading.

2 Problem Definition

The geometry and configuration of fastener joint is shown in Fig. 1. Here, the 'L' is the length of plate, 'd' is the diameter of hole, 'e' is the distance between hole centre and right support and 't' is the thickness. The left end of the plate is subjected to a uniformly distributed load (UDL), and the right end is subjected to a constant displacement. This results in a total load of P_a at the left end and the bearing load of P_b at the pin and a bypass load of P_f. Aluminium 2024-T3 is the material of the plate. The material properties used in the analysis are listed in Table 1. The material is homogeneous and isotropic. The analysis is conducted on linear elastic material.

Fig. 1 Fastener joint configuration
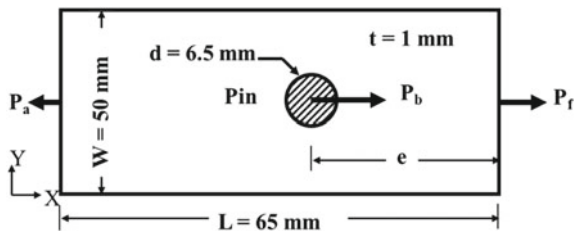
Table 1 Material properties of plate [6]

Properties	Plate (Al 2024-T3)
E	72 GPa
v	0.3
σ_{yield}	324 MPa
K_{1C}	790 MPa $\sqrt{mm}$

Fig. 2 Loads and boundary conditions in the model
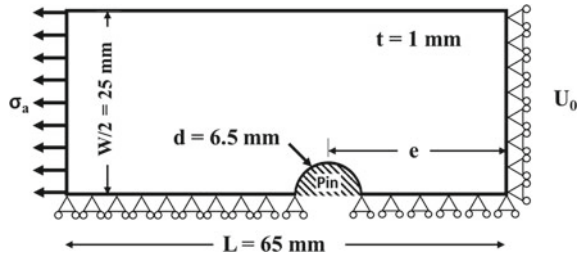
Fig. 3 FE model of the joint for configuration with e/L = 0.5

No. of elements = 4758
No. of nodes = 4932
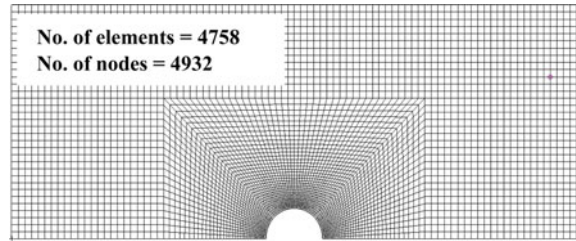
3 Methodology

3.1 FE Modelling

Numerical study of fastener joint is carried out using two-dimensional finite element analysis (FEA) with four-node quad elements using MSC NASTRAN [15] as the solver and post-processed in MSC PATRAN [16]. The boundary conditions of this configuration are shown in Fig. 2 along with the dimensions. The finite element mesh is arrived at after a convergence study with respect to bearing-bypass load ratio (Fig. 3). This mesh has 4758 elements and 4932 nodes. Since the model is symmetric about y-axis, a half-symmetry model is considered for analysis.

3.2 Damage Growth Study

Modified virtual crack closure integral (MVCCI) technique is used in estimating fracture parameters in crack growth studies and is shown pictorially in Fig. 4 and is given in Eqs. 1 and 2 [9, 10]. The elements near the crack tip are square elements. Crack growth life is estimated by Paris law with Elber correction [4] as given in Eq. 3. The constants in the equation are taken from literature [6].

$$G_I = \frac{1}{2\Delta A}[F_{xi}(U_x(i-1) - U_x(i-1)\prime)] \qquad (1)$$

Fig. 4 MVCCI technique for a four-node quad element
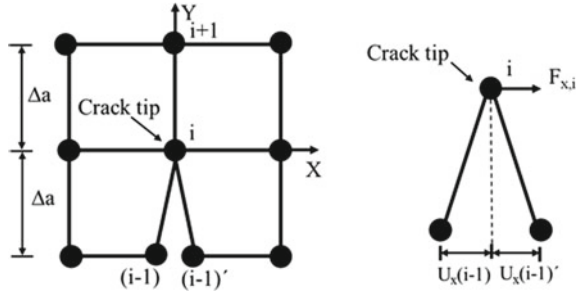
$$K_I = \sqrt{G_I * E} \tag{2}$$

where $\Delta A = \Delta a * b$, $\Delta a = \text{elementlengththatcrackfront}$, $b = \text{widthoftheelement}$

$$N_f = \int_{a_0}^{a_c} \frac{da}{C(\Delta K_{eff})^m} \tag{3}$$

where $K_{min} = (a' + b'R)K_{max}$, $K_{max} = \sigma_{max}\sqrt{\pi a_c}$, and $\Delta K_{eff} = K_{max} - K_{min}$
    Here, a' and b' are crack growth material constants.

4 Results and Discussions

4.1 Stress Distribution Around Hole

Linear elastic analysis is conducted and the typical stress distribution for $e/L = 0.5$, $P_b/P_f = 0.61$, around the hole boundary is shown in Fig. 5.

4.2 Effect of Location of Hole on SCF

Stress concentration changes with the change in location of the hole. A study is conducted to see how the stress concentration factor (SCF) varies with respect to various locations of hole (e/L). SCF is computed by dividing tangential stress at 90° with nominal stress (Eq. 5). The nominal stress is defined in Eq. 4. The values of P_b/P_f (bearing-bypass ratio) and SCF for various locations of e/L are listed in Table 2. The variation of P_b/P_f is seen to be linear (Fig. 6).

Fig. 5 Stress distribution around the hole
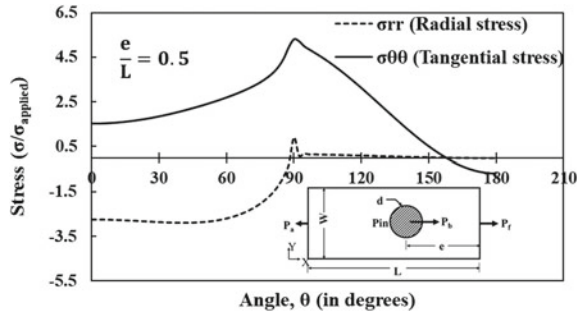
Fig. 6 Variation in bearing-bypass ratio with e/L
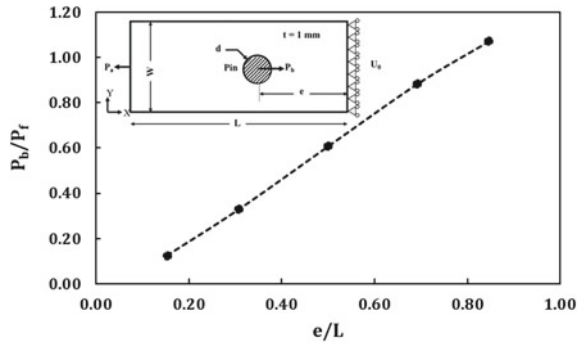
$$\sigma_{\text{nominal}} = \sigma_a \left(\frac{w}{w - d} \right) \tag{4}$$

$$\text{SCF} = \frac{\sigma_{\theta\theta}}{\sigma_{\text{nominal}}} \tag{5}$$

Table 2 Variation of P_b/P_f and SCF with e/L

e/L	P_b/P_f	SCF
0.15	0.12	2.88
0.31	0.33	3.81
0.50	0.61	4.61
0.69	0.88	5.11
0.85	1.07	5.10

4.3 Effect of Bearing-Bypass Ratio on SCF

Analysis is carried out by varying the P_b/P_f by varying the constant displacement imposed at the right end. The variation of SCF is plotted with respect to P_b/P_f and is compared with SCF from the previous section (Sect. 4.2) and is shown in Fig. 7. This shows that a bearing-bypass ratio can be chosen as an alternate in-place of location of hole (*e/L*) and gives similar stress distribution around the hole. Thus, the FEA due to change in the location of hole can be simulated by just varying the bearing-bypass ratio for affixed hole location. This reduces the need for separate finite element models for modelling fastener joint with holes at different locations. Three configurations have been considered as described in Table 3. Case 1 is considered to study when the entire load is bypassed to the right-side support. Case 2 is the typical configuration where some of the load is taken by the pin and rest is bypassed to the right support (Fig. 8). Case 3 is considered when all the load is taken by the pin and none of the load is bypassed. Any ratio of bearing-bypass load falls between those

Fig. 7 Variation of SCF with bearing-bypass ratio
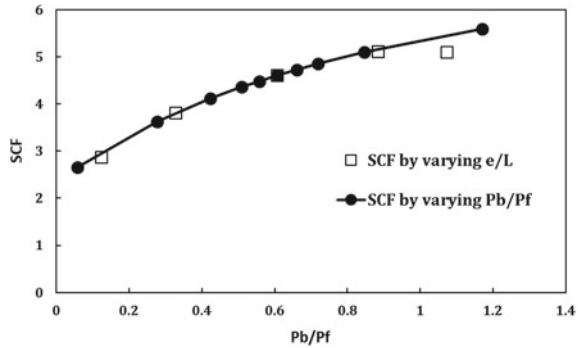
Table 3 Three cases considered for further study

Case No.	Boundary Condition
Case 1	Right support is present but the pin is removed
Case 2	Both pin and right support are present
Case 3	Pin is present and the right support is removed

Fig. 8 Loads and boundary conditions for case 2
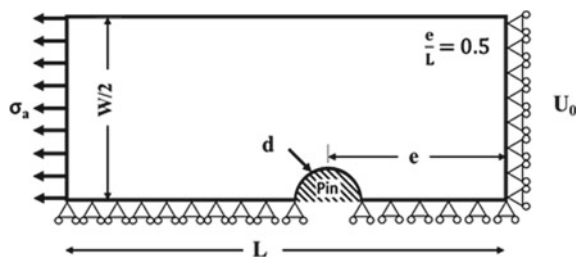
Table 4 SCF for two different configurations

	SCF	Tangential stress (MPa)
Case 2	4.61	338
Case 3	8.40	618

corresponding to case 1 and case 3. SCF for cases 2 and 3 are listed in Table 3 (Table 4).

4.4 Crack Growth Analysis

Crack growth analysis is conducted for various bearing-bypass ratios. The configuration of plate with crack is shown in Fig. 9. An initial crack of 1 mm is assumed to be present (following the damage tolerance procedure) at the critical location ($\theta = \pm 90°$) where the stress concentration is highest.

For the applied load (64 MPa), the stress intensity factor (SIF) for various crack sizes is plotted in Fig. 10 for two different bearing-bypass ratios. The configuration with higher bearing-bypass ratio has higher SIF. The difference between their SIF values narrows down as the crack grows farther from the hole. This is due to the
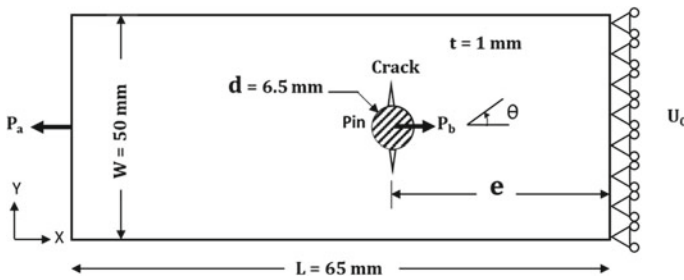
Fig. 9 Configuration of plate with crack

Fig. 10 SIF plots for two different bearing-bypass ratios
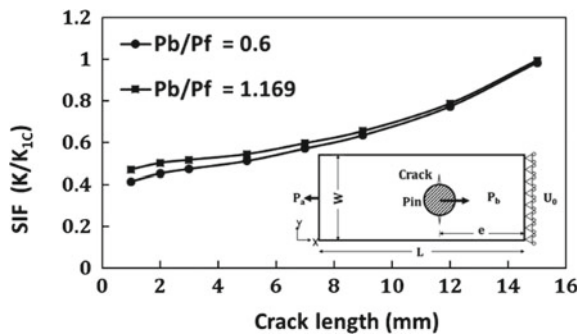
Fig. 11 SIF plots for three cases (Table 3)
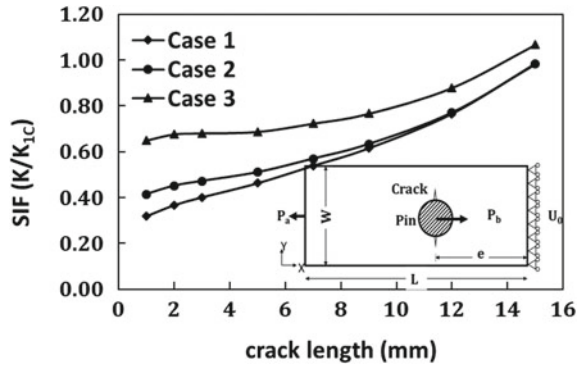
reduced effect of bearing load in the region away from hole. So, the regions away from hole are more influenced by bypass load than bearing load. To examine this, the crack is modelled and SIFs are compared for the three cases as listed in Table 3. It can be noted that the highest SIF is for the presence of crack in case 3 where all the load is taken by the pin (Fig. 9). The lowest SIF is for case 1 where the whole load is bypassed to the support. Case 2 which corresponds to sharing of the load between the pin (bearing) and the support (bypass) lies in between the two. This shows that a configuration with any positive bearing-bypass ratio lies in between configurations corresponding to case 1 and case 3 (Fig. 11).

Crack growth studies are also conducted for two different bearing-bypass ratios and the number of cycles to failure is computed and is plotted in Figs. 12 and 13. It can be seen that for the crack at same location, bearing-bypass ratios can have a significant effect on crack growth life (Fig. 12). Crack propagation for the three cases mentioned (Table 3) is also computed and plotted in Fig. 13. It can be seen that in case 3 where the load is completely reacted by the pin, the crack growth life is approximately one-sixth of that when the complete load is bypassed to the support (case 1). Case 2 lies in between cases 1 and 3 as expected. This shows that the crack growth life is significantly affected by the bearing stress at the hole boundary.

Fig. 12 Crack growth life for two ratios of bearing-bypass loading
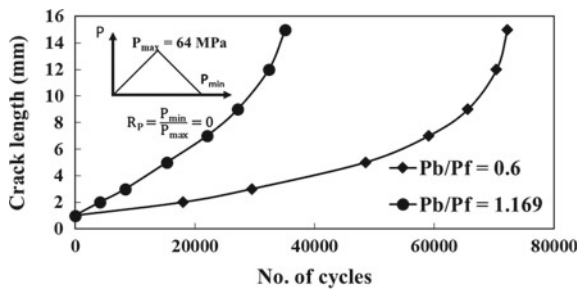
Fig. 13 Crack growth life
for three cases
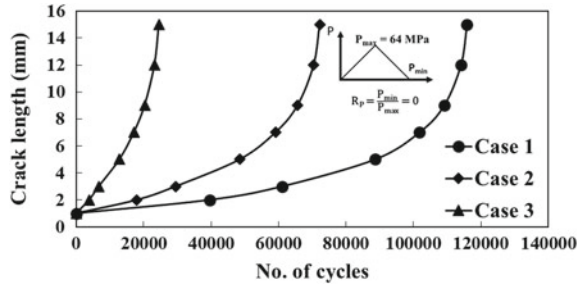
4.5 S–N Life

FF module (Fatigue and Fracture module) is a program that is developed in-house.
FF module is used to compute S–N life. This program is written in Fortran 77. An
algorithm is written for rainflow cycle counting. It uses the four-point rainflow cycle
counting method to extract the cycles from a variable amplitude loading. 350 data
points were taken from one mission profile from FALSTAFF load spectra and are
constructed to form a load sequence. This generates 165 cycles from the rainflow
cycle counting technique. This is applied as one block of loading (Fig. 14). The
program has the options to apply multiple blocks of loading. The fatigue loading
can be given as blocks of constant amplitude cycles, or multiple cycles of constant
amplitude of different magnitudes or as a variable amplitude (as in the current work).
The program computes the remaining life in blocks of loading till failure. Palmgren–
Miners's rule (Eq. 6) is used for predicting the failure due to fatigue. Failure occurs
when the Miner's index D reaches a value of 1.

$$D = \sum_{i=1}^{N} \frac{n_i}{N_i} \tag{6}$$

Fig. 14 One block of load
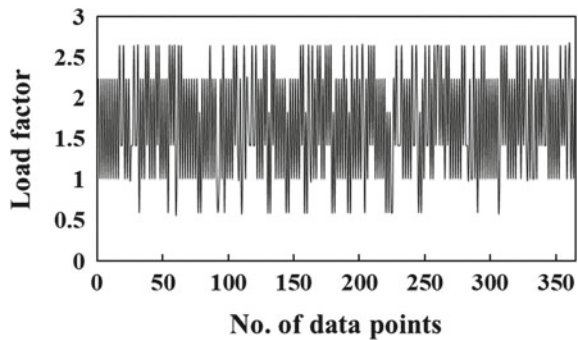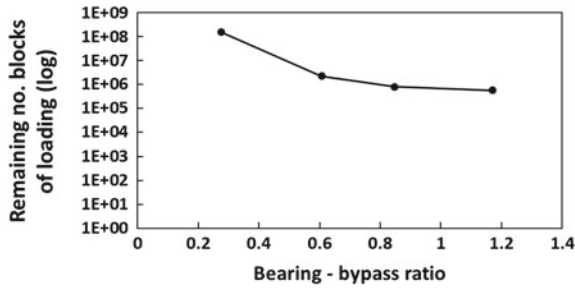
Fig. 15 Remaining life for various bearing-bypass ratios
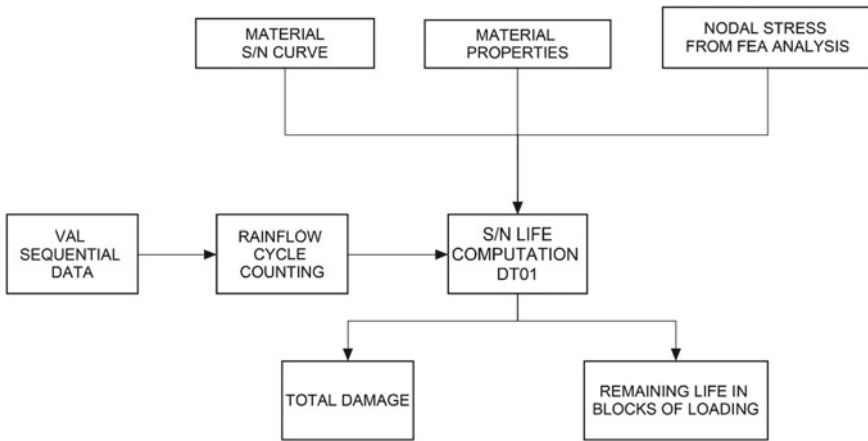
Fig. 16 Program flow chart showing the important steps

where n_i is the number of fatigue stress cycles of i type and N_i is the total number of cycles to failure of each of the i type fatigue cycles. A flowchart displaying the process of the program is shown in Fig. 15. Mean stress effects in fatigue are considered using Goodman relation. The remaining life for various bearing-bypass ratios is computed and shown in Fig. 15. It is seen that the remaining life of the joint varies significantly with respect to bearing-bypass load ratio. A flow chart depicting the important steps in the program is shown in Fig. 16.

5   Summary and Conclusions

- Two-dimensional, linear elastic finite element analysis of fastener joint is conducted using MSC PATRAN and MSC NASTRAN with four-node quad elements for different bearing-bypass load ratios.

- It is clearly seen that the effect of variation in stress due to position of hole can be simulated by varying the bearing-bypass load ratio in the finite element model with a fixed hole position, thus reducing the modelling and computational effort.
- Small allowable initial crack length is assumed at location of SCF, and the fracture parameters are computed by MVCCI. Cracks of smaller length are affected by the bearing stress near to the hole boundary compared to a longer crack.
- Crack growth life is estimated for various bearing-bypass load ratios. The remaining life is seen to decrease with increase in bearing-bypass load ratios.
- A computational program is used to compute the S–N life of the joint. An algorithm is written to extract the cycles from the variable amplitude load following the rainflow cycle counting method.
- There is a significant difference in S–N life for various bearing-bypass load ratios.

References

1. Broughton WR, Crocker LE, Grower MRL (2002) Design requirements for bonded and bolted composite structures. NPL Report MATC(A) 65
2. Crews JH, Jr, Naik RVA (1984) Failure analysis of a graphite/epoxy laminate subjected to bolt bearing loads. NASA Tech Memo 86297
3. Crews JH, Jr, Naik RVA (1986) Combined bearing and bypass loading on a graphite/epoxy laminate. NASA Tech Memo 87705
4. Elber W (1971) The significance of fatigue crack closure, In: damage tolerance in aircraft structure. ASTM, Phila (486):230–242
5. Li G, Renaud G, Liao M, Okada T, Machida S (2017) A methodology for assessing fatigue life of a countersunk riveted lap joint. Adv Aircr Spacecr Sci 4(1):1–19
6. Gomez MP, Ernst H, Vazquez H (1976) On the validity of Elber's results on fatigue crack closure for 2024-T3 aluminium. Int J Fract 12:178–180
7. Kabeel AM, Maimi P, Gonzalez EV, Gascons N (2015) Net-tension strength of double-lap joints under bearing-bypass loading conditions using the cohesive zone model, vol 119, pp 443–451
8. Manjunatha CM, Ranganath VR (2007) Prediction of optimum spectrum for full scale fatigue test. In: 15th national seminar on aerospace structures, Coimbatore, Tamil Nadu, India, pp 15–16
9. Ramamurthy TS, Krishnamurthy T, Badrinarayana K, Vijaykumar K, Dattaguru B (1986) Modified crack closure integral method with quarter point elements. Mech Res Commun 13(4):179–186
10. Rybicki EF, Kanninnen MF (1977) A finite element calculation of stress intensity factors by a modified crack closure integral. Eng Fract Mech 9(4):931–938
11. Ward-Close CM. (1983) Simulated flight (Falstaff) fatigue crack growth in titanium alloy Ti-4A1-4Mo-2Sn-0.5Si. RAE Technical Report No 83056
12. Lee Y-L, Rjhung T (2012) Rainflow cycle counting techniques, metal fatigue analysis handbook. In: Practical problem-solving techniques for computer-aided engineering, pp 89–114
13. Whitman ZL (2012) The effect of fatigue cracks on fastener flexibilty, load distribureation, and fatigue crack growth. Ph.D. thesis
14. Zhang Z, Wang W, Rans C, Benedictus R (2016) An experimental investigation into pin loading effects on fatigue crack growth in fiber metal laminates. In: Proceedia structural integrity 2, 21st European conference on fracture, ECF21, pp 3361–3368

15. The MSC NASTRAN documentation (2017) MSC Software Corporation, Macarthur Court, Newport Beach-CA, USA, 4675

Quantifying the Effect of Voids on the Response of a Viscoelastic Solid

Pullela Mythravaruni and **Parag Ravindran**

Abstract A thermodynamically consistent constitutive model is developed to capture the mechanical response of a solid that exhibits nonlinear viscoelastic response. Voids present in the solid have a significant effect on the viscoelastic response of the solid. In the present work, we develop a compressible constitutive model within a thermodynamical framework using two scalar potentials, namely, stored energy potential and the rate of dissipation. The model is used to study the viscoelastic response of the solid in the presence of voids when subjected to uniaxial tension. The effect of voids is studied by comparing the mechanical response of the solid in the presence of voids to the response in the absence of voids.

Keywords Viscoelastic solid · Voids · Constitutive model · Thermodynamical framework

1 Introduction

Voids are frequently occurring defects that affect the structural integrity. It is difficult to completely remove these undesirable voids from structures. So, it is important to study the effect of voids on the mechanical response of structures. Cowin [1] showed that a linear elastic material with voids subjected to quasi-static homogeneous deformation exhibits viscoelastic response of a standard linear solid. Shiraishi and Tabuchi [2] performed finite element analysis to derive the stress–strain relationship of a material with voids in the matrix.

P. Mythravaruni (✉) · P. Ravindran
IIT Kharagpur, Kharagpur, West Bengal 721302, India
e-mail: pmvaruni@rtc.iitkgp.ac.in

P. Ravindran
e-mail: paragr@iitm.ac.in

2 Constitutive Model Formulation

In this section, we develop a homogenized three-dimensional non-linear viscoelastic model within a thermodynamic framework [3] to study the effect of voids on the mechanical response of a viscoelastic solid. In the present work, we propose a new form for the specific stored energy potential.

2.1 Kinematics

The kinematics of the viscoelastic body is now briefly described.

Let κ_R denote the reference configuration and κ_t denote the current configuration of the viscoelastic solid. The motion is a mapping that assigns at every time t a position $\mathbf{x}$ in κ_t to every point $\mathbf{X}$ in κ_R

$$\mathbf{x} = \chi_{\kappa_R}(X, \mathrm{t}) \tag{1}$$

The deformation gradient from the reference to the current configuration is defined as

$$\mathbf{F}_{\kappa_R} = \frac{\partial \chi_{\kappa_R}}{\partial \mathbf{X}} \tag{2}$$

The left and right Cauchy–Green stretch tensors are defined using the deformation gradient as

$$\mathbf{B}_{\kappa_R} = \mathbf{F}_{\kappa_R}\mathbf{F}_{\kappa_R}^{\mathrm{T}}, \, \mathbf{C}_{\kappa_R} = \mathbf{F}_{\kappa_R}^{\mathrm{T}}\mathbf{F}_{\kappa_R}. \tag{3}$$

We assume that body has instantaneous elasticity due to which it goes instantaneously to a relaxed or natural (stress-free) configuration upon removal of applied loads from the current configuration. Let $\kappa_{p(t)}$ denote this natural configuration associated with the current configuration. The left and right Cauchy–Green stretch tensors associated with $\mathbf{F}_{\kappa_{p(t)}}$ may be defined through

$$\mathbf{B}_{\kappa_{p(t)}} = \mathbf{F}_{\kappa_{p(t)}}\mathbf{F}_{\kappa_{p(t)}}^{\mathrm{T}}, \, \mathbf{C}_{\kappa_{p(t)}} = \mathbf{F}_{\kappa_{p(t)}}^{\mathrm{T}}\mathbf{F}_{\kappa_{p(t)}}. \tag{4}$$

$\mathbf{F}_{\kappa_R}$ is decomposed as

$$\mathbf{F}_{\kappa_R} = \mathbf{F}_{\kappa_{p(t)}}\mathbf{G}, \tag{5}$$

where $\mathbf{G}$ is the mapping from the reference configuration to the current natural configuration $\kappa_{p(t)}$(please see Fig. 1). The velocity gradients are, $\mathbf{L} = \dot{\mathbf{F}}_{\kappa_R}\mathbf{F}_{\kappa_R}^{-1}$

Fig. 1 Various configurations associated with the body in the modelling framework
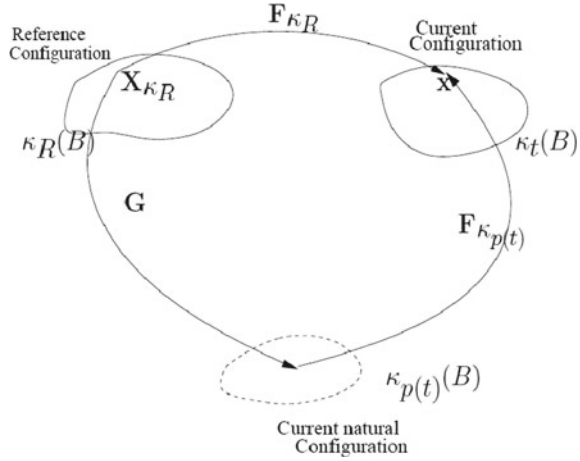
and $\mathbf{L}_{\kappa_{p(t)}} = \dot{\mathbf{G}}\mathbf{G}^{-1}$. The rates of deformation tensors are given by the symmetric parts of the velocity gradients as $\mathbf{D} = \frac{1}{2}(\mathbf{L} + \mathbf{L}^{\mathrm{T}})$ and $\mathbf{D}_{\kappa_{p(t)}} = \frac{1}{2}(\mathbf{L}_{\kappa_{p(t)}} + \mathbf{L}_{\kappa_{p(t)}}^{\mathrm{T}})$.

2.2 Conservation Laws

The balance of mass is written as

$$\dot{\rho}_{\kappa_t} + \rho_{\kappa_t}\mathrm{div}(\mathbf{v}) = 0 \tag{6}$$

where ρ_{κ_t} is the density of the body in the current configuration and $\mathbf{v}$ is the velocity. div denotes the divergence. The balance of linear momentum is written as

$$\mathrm{div}(\mathbf{T}^{\mathrm{T}}) + \rho_{\kappa_t}\mathbf{b} = \rho_{\kappa_t}\dot{\mathbf{v}} \tag{7}$$

where $\mathbf{T}$ is the Cauchy stress tensor, and $\mathbf{b}$ is the specific body force. The balance of energy is written as

$$\rho_{\kappa_t}\dot{\epsilon} = \mathbf{T} \cdot \mathbf{L} - \mathrm{div}\mathbf{q} + \rho_{\kappa_t}r \tag{8}$$

where ϵ is the internal energy, $\mathbf{q}$ is the heat flux vector, r is the specific radiant heating, and $\mathbf{L}$ is the velocity gradient. Balance of angular momentum requires that

$$\mathbf{T} = \mathbf{T}^{\mathrm{T}} \tag{9}$$

in the absence of internal body couples.

2.3 Thermodynamically Consistent Constitutive Model

The second law of thermodynamics,

$$\rho_{\kappa_t}\dot{\eta} - \rho_{\kappa_t}\frac{r}{\theta} + \text{div}\Big(\frac{\mathbf{q}}{\theta}\Big) \geq 0 \tag{10}$$

η is the specific entropy, and θ is the absolute temperature.

The second law of thermodynamics may also be written in the form introduced by [4] as

$$\rho_{\kappa_t}\dot{\eta} - \rho_{\kappa_t}\frac{r}{\theta} + \text{div}\Big(\frac{\mathbf{q}}{\theta}\Big) = \rho_{\kappa_t}\zeta \tag{11}$$

where ζ is total rate of entropy production per unit mass.

The specific radiant heating term is eliminated between Eq. (11) and the energy balance Eq. (8) to obtain

$$\mathbf{T}\cdot\mathbf{D} - \rho_{\kappa_t}\dot{\epsilon} + \rho_{\kappa_t}\dot{\eta}\theta - \frac{1}{\theta}\mathbf{q}\cdot\text{grad}(\theta) = \rho_{\kappa_t}\theta\zeta = \xi \tag{12}$$

where ξ is the rate of dissipation. From $\psi = \epsilon - \eta\theta$, (where ψ is the specific Helmholtz free energy), the reduced dissipation equation is obtained

$$\mathbf{T}\cdot\mathbf{D} - \rho_{\kappa_t}\dot{\psi} - \rho_{\kappa_t}\eta\dot{\theta} - \frac{1}{\theta}\mathbf{q}\cdot\text{grad}(\theta) = \xi \tag{13}$$

We assume the total rate of dissipation to be sum of contributions due to heat conduction and mechanical dissipation,

$$-\frac{1}{\theta}\mathbf{q}\cdot\text{grad}(\theta) = \xi_{\text{cond}} \geq 0 \tag{14}$$

Thus, Eq. (13) reduces to

$$\mathbf{T}\cdot\mathbf{D} - \rho_{\kappa_t}\dot{\psi} - \rho_{\kappa_t}\eta\dot{\theta} = \xi_{\text{diss}} \tag{15}$$

Further, assuming an isotropic compressible viscoelastic solid

$$\Big(\psi = \psi(\theta, \rho_{\kappa_{p(t)}}, I_{1_{\mathbf{c}_{\kappa_R}}}, I_{2_{\mathbf{c}_{\kappa_R}}}, I_{3_{\mathbf{c}_{\kappa_R}}}, I_{1_{\mathbf{c}_{\kappa_{p(t)}}}}, I_{2_{\mathbf{c}_{\kappa_{p(t)}}}}, I_{3_{\mathbf{c}_{\kappa_{p(t)}}}})\Big), \text{ we obtain}$$

$$
\mathbf{T} \cdot \mathbf{D} - \rho_{\kappa_t} \left(\frac{\partial \psi}{\partial \theta} \dot{\theta} + \frac{\partial \psi}{\partial \rho_{\kappa_{p(t)}}} \dot{\rho}_{\kappa_{p(t)}} + \frac{\partial \psi}{\partial I_{1 \mathbf{C}_{\kappa_R}}} \dot{I}_{1 \mathbf{C}_{\kappa_R}} + \frac{\partial \psi}{\partial I_{2 \mathbf{C}_{\kappa_R}}} \dot{I}_{2 \mathbf{C}_{\kappa_R}} \right.
$$

$$
+ \frac{\partial \psi}{\partial I_{3 \mathbf{C}_{\kappa_R}}} \dot{I}_{3 \mathbf{C}_R} + \frac{\partial \psi}{\partial I_{1 \mathbf{C}_{\kappa_{p(t)}}}} \dot{I}_{1 \mathbf{C}_{p(t)}} + \frac{\partial \psi}{\partial I_{2 \mathbf{C}_{\kappa_{p(t)}}}} \dot{I}_{2 \mathbf{C}_{\kappa_{p(t)}}} + + \frac{\partial \psi}{\partial I_{3 \mathbf{C}_{\kappa_{p(t)}}}} \tag{16}
$$

$$
\left. \dot{I}_{3 \mathbf{C}_{\kappa_{p(t)}}} \right) - \rho_{\kappa_t} \eta \dot{\theta} = \xi_{\mathrm{diss}} \geq 0
$$

where the specific form of the stored energy potential is chosen to be.

$$
\psi = \frac{c_1}{\rho_{\kappa_R}} \left(\bar{I}_{1 \mathbf{C}_{\kappa_R}} - 3 \right) + \frac{c_2}{\rho_{\kappa_R}} \left(\bar{I}_{2 \mathbf{C}_{\kappa_R}} - 3 \right) + \frac{K_1}{\rho_{\kappa_R}} \left(\sqrt{I_{3 \mathbf{C}_{\kappa_R}}} - 1 \right)^2
$$

$$
+ \frac{c_3}{\rho_{\kappa_{p(t)}}} \left(\bar{I}_{1 \mathbf{C}_{\kappa_{p(t)}}} - 3 \right) + \frac{K_2}{\rho_{\kappa_{p(t)}}} \left(\sqrt{I_{3 \mathbf{C}_{\kappa_{p(t)}}}} - 1 \right)^2 \tag{17}
$$

where ρ_{κ_R} is the density in the reference configuration, $\rho_{\kappa_{p(t)}}$ is the density in the current natural configuration, c_1, c_2, c_3, K_1 and K_2 are model parameters,

$$
\bar{I}_{1 \mathbf{C}_{\kappa_R}} = I_{3 \mathbf{C}_{\kappa_R}}^{-1/3} I_{1 \mathbf{C}_{\kappa_R}}, \; \bar{I}_{2 \mathbf{C}_{\kappa_R}} = I_{3 \mathbf{C}_{\kappa_R}}^{-2/3} I_{2 \mathbf{C}_{\kappa_R}}, \; \text{and } \bar{I}_{1 \mathbf{C}_{\kappa_{p(t)}}} = I_{3 \mathbf{C}_{\kappa_{p(t)}}}^{-1/3} I_{1 \mathbf{C}_{\kappa_{p(t)}}}
$$

From Eq. (16), after substituting for derivatives of the specific stored energy potential from Eq. (17), and by sufficiency, the constitutive relation is obtained as

$$
\mathbf{T} = \frac{2}{J} \left(c_1 \bar{\mathbf{B}}_{\kappa_R} + c_2 \left(\bar{I}_{1 \mathbf{C}_{\kappa_R}} \bar{\mathbf{B}}_{\kappa_R} - \bar{\mathbf{B}}_{\kappa_R}^2 \right) \right) + \left(\frac{-2}{3} \frac{c_1}{J} \bar{I}_{1 \mathbf{C}_{\kappa_R}} - \frac{4}{3} \frac{c_2}{J} \bar{I}_{2 \mathbf{C}_{\kappa_R}} + 2K_1 (J - 1) \right)
$$

$$
+ \frac{2}{J_{\kappa_p}} c_3 \bar{\mathbf{B}}_{\kappa_{p(t)}} + \left(\frac{-2}{3} \frac{c_3}{J_{\kappa_p}} \bar{I}_{1 \mathbf{C}_{\kappa_{p(t)}}} + 2K_2 (J_{\kappa_p} - 1) \right) \tag{18}
$$

$$
\text{where } J = \sqrt{I_{3 \mathbf{C}_{\kappa_R}}} \text{ and } J_{\kappa_p} = \sqrt{I_{3 \mathbf{C}_{\kappa_{p(t)}}}}.
$$

Also from Eq. (16), we have $\frac{\partial \psi}{\partial \theta} = -\eta$. The remaining part of Eq. (16) is

$$
\mathbf{T}^e \cdot \mathbf{D}_{\kappa_{p(t)}} = \xi_{\mathrm{diss}} \tag{19}
$$

where, the specific form of the rate of dissipation, following [5] is chosen as

$$
\xi_{\mathrm{diss}} = \eta_1 \left(\mathbf{D}_{\kappa_{p(t)}} \cdot \mathbf{B}_{\kappa_{p(t)}} \mathbf{D}_{\kappa_{p(t)}} \right)^\beta \tag{20}
$$

Here, η_1 and β are model parameters and

$$\mathbf{T}^e = 2\rho_{\kappa_t} \left(\frac{\partial \psi}{\partial I_{1\mathbf{C}_{\kappa_{p(t)}}}} \mathbf{B}_{\kappa_{p(t)}} + \frac{\partial \psi}{\partial I_{3\mathbf{C}_{\kappa_{p(t)}}}} I_{3\mathbf{C}_{\kappa_{p(t)}}} \mathbf{I} \right)$$
$$- \frac{\mathbf{I}}{J_{kp}} \left(c_3 \left(\overline{I}_{1\mathbf{C}_{\kappa_{p(t)}}} - 3 \right) + K_2 \left(J_{\kappa_p} - 1 \right)^2 \right)$$

Now, by maximizing the rate of dissipation ξ_{diss}, using Eq. (19) as constraint, we obtain the equation for evolution of natural configuration as

$$\overset{\nabla}{\mathbf{B}}_{\kappa_{p(t)}} = \frac{-2}{\eta_1^{\frac{1}{2\beta-1}}} (x)^{\frac{1-\beta}{2\beta-1}} \left(\phi_1 \mathbf{B}_{\kappa_{p(t)}} + \phi_2 \mathbf{I} \right) \tag{21}$$

where $\overset{\nabla}{\mathbf{B}}_{\kappa_{p(t)}}$ is the upper convected derivative of $\mathbf{B}_{\kappa_{p(t)}}$.

$x = \phi_1^2 \mathrm{tr}\left(\mathbf{B}_{\kappa_{p(t)}} \right) + 6\phi_1 \phi_2 + \phi_2^2 \mathrm{tr}\left(\mathbf{B}_{\kappa_{p(t)}}^{-1} \right)$. tr denotes trace.

$$\phi_1 = 2\rho_{\kappa_t} \frac{\partial \psi}{\partial I_{1\mathbf{C}_{\kappa_{p(t)}}}}$$
$$\phi_2 = 2\rho_{\kappa_t} \frac{\partial \psi}{\partial I_{3\mathbf{C}_{\kappa_{p(t)}}}} I_{3\mathbf{C}_{\kappa_{p(t)}}} - \frac{1}{J_{\kappa p}} \left(c_3 \left(\overline{I}_{1\mathbf{C}_{\kappa_{p(t)}}} - 3 \right) + K_2 \left(J_{\kappa_p} - 1 \right)^2 \right)$$

3 Application of the Model: Uniaxial Extension

In the case of uniaxial tension of a bar of square cross-section,

$$x_1 = \lambda_1 X_1; \ x_2 = \lambda_2 X_2; \ x_3 = \lambda_2 X_3 \tag{22}$$

where λ_1 is the stretch applied in the direction of tension. The deformation gradient and the left Cauchy stretch tensor from the definitions Eqs. (2) and (3) are

$$\mathbf{F}_{\kappa_R} = \mathrm{diag}(\lambda_1, \lambda_2, \lambda_2)$$
$$\mathbf{B}_{\kappa_R} = \mathrm{diag}(\lambda_1^2, \lambda_2^2, \lambda_2^2) \tag{23}$$

Accordingly, we choose the form of $\mathbf{B}_{\kappa_{p(t)}}$ to be

$$\mathbf{B}_{\kappa_{p(t)}} = \mathrm{diag}(B_1(t), B_2(t), B_2(t)) \tag{24}$$

Invariants of $\mathbf{B}_{\kappa_R}$

$$I_{1\mathbf{C}_{\kappa_R}} = \lambda_1^2(t) + 2\lambda_2^2(t)$$

$$I_{2\mathbf{C}_{\kappa_R}} = \lambda_2^4(t) + 2\lambda_1^2(t)\lambda_2^2(t) \tag{25}$$

$$I_{3_{C_{\kappa_R}}} = \lambda_1^2(t)\lambda_2^4(t)$$

Invariants of $\mathbf{B}_{\kappa_{p(t)}}$

$$I_{1_{C_{\kappa_{p(t)}}}} = B_1(t) + 2B_2(t)$$

$$I_{2_{C_{\kappa_{p(t)}}}} = B_2^2(t) + 2B_1(t)B_2(t) \tag{26}$$

$$I_{3_{C_{\kappa_{p(t)}}}} = B_1(t)B_2^2(t)$$

Substituting from Eqs. (23) to (24), and the invariants of $\mathbf{B}_{\kappa_R}$ and $\mathbf{B}_{\kappa_{p(t)}}$ from Eqs. (25) to (26) in Eq. (18), we get the stress components T_{11}, T_{22} and T_{33}.

$$
\begin{aligned}
T_{11} = {} & \tfrac{2}{J}\Big(J^{-2/3}c_1\lambda_1^2 + c_2 J^{-4/3}\big(\lambda_1^2(\lambda_1^2 + 2\lambda_2^2) - \lambda_1^4\big)\big) + \big(\tfrac{-2}{3}\tfrac{c_1}{J}J^{-2/3}(\lambda_1^2 + 2\lambda_2^2) \\
& - \tfrac{4}{3}\tfrac{c_2}{J}J^{-4/3}\big(\lambda_2^4 + 2\lambda_1^2\lambda_2^2\big) + 2K_1(J-1)\big) \\
& + \tfrac{2}{J_{\kappa_p}}c_3 J_{\kappa_p}^{-2/3}B_1 + \Big(\tfrac{-2}{3}\tfrac{c_3}{J_{\kappa_p}}J_{\kappa_p}^{-2/3}(B_1 + 2B_2) + 2K_2\big(J_{\kappa_p} - 1\big)\Big)
\end{aligned}
\tag{27}
$$

where $J = \lambda_1\lambda_2^2$, $J_{\kappa_p} = \sqrt{B_1}B_2$. Applying the boundary condition that the lateral surfaces are traction free, $T_{22} = 0$ and $T_{33} = 0$, we get

$$
\begin{aligned}
T_{22} = T_{33} = {} & \tfrac{2}{J}\big(J^{-2/3}c_1\lambda_2^2 + c_2 J^{-4/3}\big(\lambda_2^2(\lambda_1^2 + 2\lambda_2^2) - \lambda_2^4\big)\big) \\
& + \big(\tfrac{-2}{3}\tfrac{c_1}{J}J^{-2/3}(\lambda_1^2 + 2\lambda_2^2) - \tfrac{4}{3}\tfrac{c_2}{J}J^{-4/3}\big(\lambda_2^4 + 2\lambda_1^2\lambda_2^2\big) + 2K_1(J-1)\big) \\
& + \tfrac{2}{J_{\kappa_p}}c_3 J_{\kappa_p}^{-2/3}B_2 + \Big(\tfrac{-2}{3}\tfrac{c_3}{J_{\kappa_p}}J_{\kappa_p}^{-2/3}(B_1 + 2B_2) + 2K_2\big(J_{\kappa_p} - 1\big)\Big) = 0
\end{aligned}
\tag{28}
$$

Using Eq. (21) and the definition of upper convected derivative of $\mathbf{B}_{\kappa_{p(t)}}$, $\overset{\nabla}{\mathbf{B}}_{\kappa_{p(t)}} = \dot{\mathbf{B}}_{\kappa_{p(t)}} - \mathbf{L}\mathbf{B}_{\kappa_{p(t)}} - \mathbf{B}_{\kappa_{p(t)}}\mathbf{L}^{\mathrm{T}}$, we get two ODEs,

$$
\begin{aligned}
\frac{dB_1}{dt} &= 2B_1\frac{\dot{\lambda}_1}{\lambda_1} - \frac{2}{\eta_1^{\frac{1}{2\beta-1}}}(x)^{\frac{1-\beta}{2\beta-1}}(\phi_1 B_1 + \phi_2) \\
\frac{dB_2}{dt} &= 2B_2\frac{\dot{\lambda}_2}{\lambda_2} - \frac{2}{\eta_1^{\frac{1}{2\beta-1}}}(x)^{\frac{1-\beta}{2\beta-1}}(\phi_1 B_2 + \phi_2)
\end{aligned}
\tag{29}
$$

3.1 Results

In all the three cases, namely, specimen without void, with void of 5 mm size in the centre and with void of 9 mm size in the centre, we apply displacement to one end of

tensile specimen at a controlled rate of 50 mm/min (which corresponds to a strain rate of 0.0185/s) and simulate the uniaxial extension of the dog-bone specimen in commercial Finite Element package, ABAQUS, and the response is shown in Fig. 2b. Finite element simulations in ABAQUS are also performed at different displacement rates of 5, 50 and 500 mm/min on specimens without void and with void of 6 mm size in the centre and the responses are shown in Figs. 3a, b and 4a, b. The specimen with void in the centre is meshed with 17,208 8-node linear brick elements with reduced integration (C3D8R) and enhanced hourglass control. The mesh in the region around void is made fine, having an element size of 0.8 mm. The specimen without void is meshed with 2800 C3D8R elements with a uniform mesh size of 1.7 mm and enhanced hourglass control. In order to capture large deformations which involve very large mesh distortions, we use a fine mesh of reduced-integration C3D8R brick elements. In the absence of voids, for homogeneous deformation, we can also solve Eqs. (28) and (29) numerically in MATLAB for $\lambda_2(t)$, $B_1(t)$ and $B_2(t)$ with $\lambda_1(t)$ known from the applied displacement. Then we obtain the uniaxial stress T_{11} from
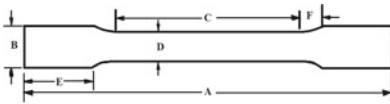
(a) A=180 mm, B=20 mm, C=90 mm,
D=10 mm, E=30 mm and F=15 mm
to get Fig. 2b.
A=135 mm, B=18 mm, C=54 mm, D=9 mm
E=15.3 mm and F=25.2 mm to get
Figs. 3a, 3b, 4a and 4b.
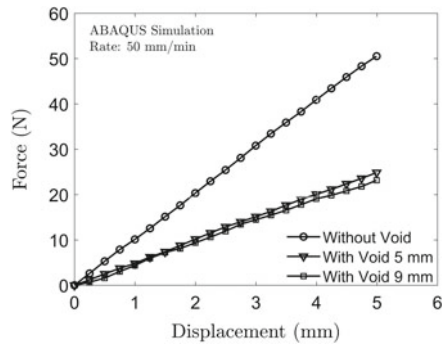
Fig. 2 **a** Tensile test dumbbell specimen. **b** Force versus displacement in uniaxial extension without void, and in the presence of voids of sizes 5 and 9 mm in the centre at 50 mm/min
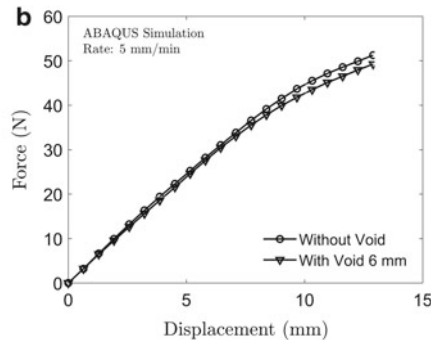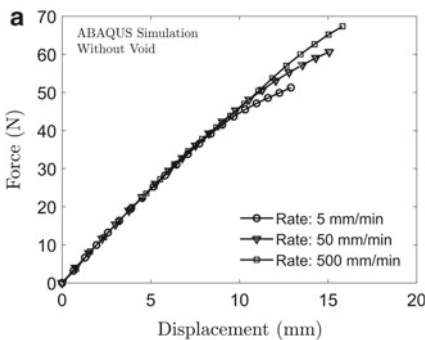
Fig. 3 Force versus displacement in uniaxial extension **a** without void at 5, 50, and 500 mm/min, **b** without void and with void of 6 mm in the centre at 5 mm/min
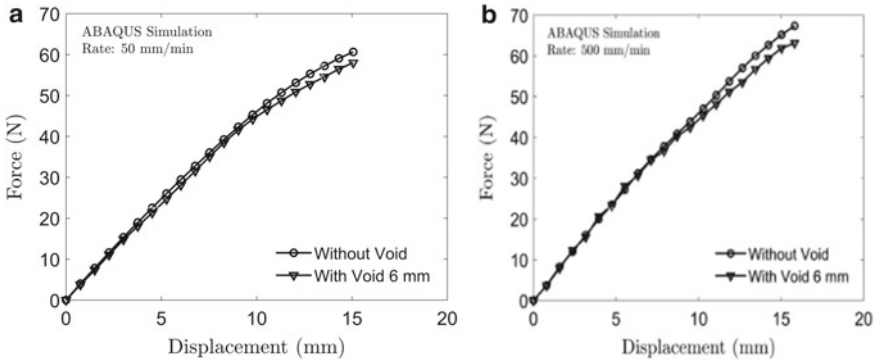
Fig. 4 Force versus displacement in uniaxial extension without void and with void of size 6 mm in the centre at **a** 50 mm/min, **b** 500 mm/min

Table 1 Model parameter values used in simulation

c_1	c_2	c_3	η_1	K_1	K_2	β
(MPa)	(MPa)	(MPa)	(MPa $-$ s)	(MPa)	(MPa)	
0.07	0.48	0.46	0.48	200	320	0.556

Eq. (27) and then integrate this stress over the cross-section to get the uniaxial force in the dog-bone specimen with gauge length of 45 mm. The model parameters used in the calculations are given in Table 1.

3.2 Discussion

In material with voids, the compressibility effects may become important particularly at large strains. The model developed herein allows for the material to undergo motions that may not preserve volume.

Figure 2b shows that as the void size increases the viscoelastic solid becomes less stiff. Figure 3a shows the viscoelastic response in the absence of void. From Figs. 3b to 4a, b, it can be seen that the samples with voids exhibit strain rate-dependent response. Further, these figures show that the response to strain rate is sensitive to the presence of voids.

The model developed shows expected trends and may now be calibrated and tested against experimental data.

4 Conclusions

Thus, it can be inferred from Fig. 2b that as the void size increases, the viscoelastic solid becomes less stiff which is the expected behaviour. Figure 3a shows the viscoelastic response in the absence of void. We can see from Figs. 3b and 4a, b that the solid without void exhibits more stiffness as expected. Figures 3b and 4a, b show that the response to strain rate is sensitive to the presence of voids. The model captures the mechanical response in a unified and consistent manner within a thermodynamic framework. The model may now be tested with experimental data for further refinement.

References

1. Cowin SC (1985) The viscoelastic behavior of linear elastic materials with voids. J Elast 15(3):185–191. https://doi.org/10.1007/BF00041992
2. Cowin SC (2000) Analysis of stress-strain relationship in materials containing voids by means of plastic finite element method. J Nucl Sci Technol 37(3):288–299. https://doi.org/10.1080/188 11248.2000.9714896
3. Rajagopal KR, Srinivasa AR (2000) A thermodynamic frame work for rate type fluid models. J Non-Newton Fluid Mech 88(3):207–227. https://doi.org/10.1016/s0377-0257(99)00023-3
4. Green AE, Naghdi PM (1977) On thermodynamics and nature of second law. Proc R Soc London Ser A 357:253270. https://doi.org/10.1098/rspa.1977.0166
5. Ramkumar A, Kannan K, Gnanamoorthy R (2010) Experimental and theoretical investigation of a polymer subjected to cyclic loading. Int J Eng Sci 48(2):101–110

Application of Direct Displacement-Based Design for Base Isolated Reinforced Concrete Framed Structures

Channabasaveshwar Chikmath [ID]**, Ankit Sodha, Prince Adani, and S. A. Vasanwala**

Abstract Direct displacement-based design is a nonlinear static procedure and has to check the suitability of the method against different types of ground motions, namely far field, near-field forward directivity and near-field fling step. The method is applied for the buildings supported on fixed base and hysteric isolation bearings. Seismic isolators are provided between the foundation and super structure to minimize the influence of ground motion on super structure. The method is applied for four, eight and twelve storeys reinforced concrete frame structures equipped with and without seismic isolators. Lead rubber bearing is used as seismic isolator. The results were validated with nonlinear time history analysis and were found to be in good agreement with the Direct displacement-based design methodology for far-field ground motions. The performance of the building was measured with respect to inter-story drift ratio, time period, acceleration of top floor, base shear, isolator displacement.

Keywords Direct displacement based design · Seismic isolators · Hysteretic damping · Lead rubber bearing · Far field · Forward directivity · Fling step

1 Introduction

Direct displacement-based design (DDBD) is a displacement-based design method developed by Priestly [1] on reinforced concrete frame buildings. The method introduces the use of two different deformed shapes for buildings less than or equal to four storey and for buildings greater than four storey, hysteretic damping in addition to viscous damping in the procedure and an expression for higher modes in tall structures was proposed. The results were validated using time history analysis of various earthquake intensity ranges. Two displacement-based methods namely direct displacement-based design and displacement-based seismic design method using

C. Chikmath (✉) · P. Adani · S. A. Vasanwala
Sardar Vallabhbhai National Institute of Technology, Surat, India

A. Sodha
Indus Institute of Technology & Engineering, Indus University, Ahmedabad, India

227
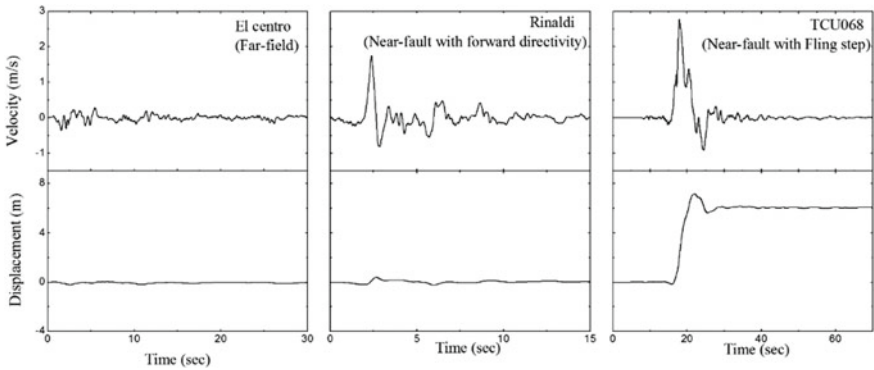
Fig. 1 Comparison of far field, forward directivity and fling step ground motions

damage control were applied on a twelve storeys plan irregular RC frame building [2]. The latter one gave better result but still needs to be validated to considering different configurations of the building.

Ground motion records are of two types, based on the distance of recording station from the fault site namely far field(>15 km) and near field(<15 km) [3]. Far-field ground motions have large amplitude in longer duration. Near-field earthquakes are associated with two paramount effects known as directivity effect and fling step effect. In forward directivity, rupture propagation is aligned to the site and fault rupture velocity is approximately equal to shear wave velocity of the site [4]. This results in large amplitude, long period and short duration. The permanent ground displacement due to tectonic deformations causes fling step effect. It produces large amplitude velocity pulse. Diagrammatic representation of far field, forward directivity and fling step is shown in Fig. 1.

Bhandari et al. [3] worked on ten storey base-isolated RC building frame subjected to far field, near-field forward directivity and near-field fling step ground motions of design base earthquake (DBE) and maximum considered earthquake (MCE) in terms of base shear, floor acceleration, interstorey drift, isolator displacement and the number of hinges formed. Lead rubber bearing was used as the isolator.

In this work, the direct displacement-based design procedure developed by Cardone et al. [5] is applied on fixed base (FB) and base isolated (BI) building of four, eight and twelve storeys RC frame buildings considered as low rise, medium rise and high rise buildings [1], respectively, located in Zone-V, medium soil of Indian seismic code [6] subjected to far field, near-field forward directivity and near-field fling step ground motions. Lead rubber bearing (LRB) is used as isolator. An equivalent damping ratio, derived from the particular characteristics of buildings supported on isolation bearings, is suggested.

2 Procedure

In this method, multi-degree of freedom system is represented into an equivalent single degree with effective mass m_e and effective height h_e as shown in Fig. 2. This system has secant stiffness K_e related to ultimate displacement shown in Fig. 3. The steps involved are as follows:
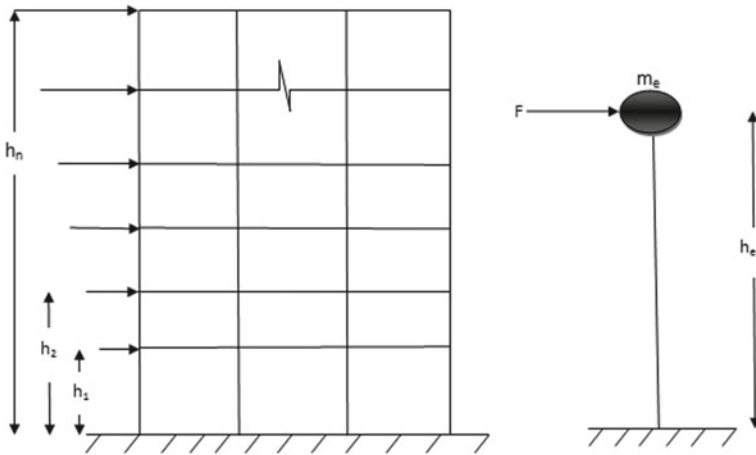
Fig. 2 Simulation of MDOF to SDOF

Fig. 3 Effective stiffness
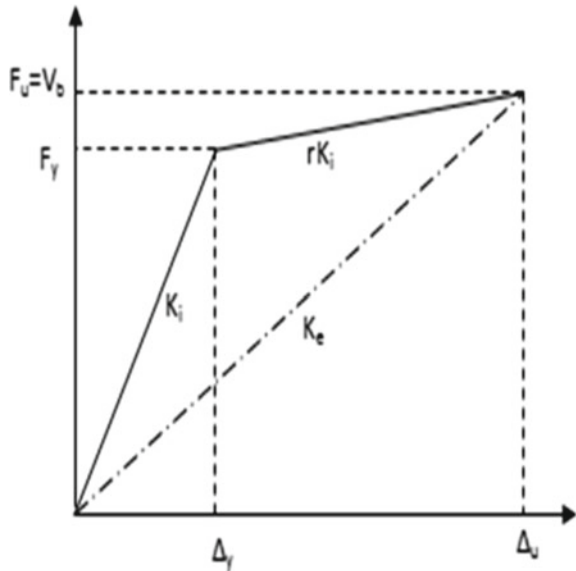
1. The first mode deformed shape is derived using the expression [5] given by

$$\Phi_i = \cos\left[\left(\frac{1}{I_r}\right).\left(1 - \frac{h_i}{h_n}\right).\frac{\pi}{2}\right] - \cos\left[\left(\frac{1}{I_r}\right).\frac{\pi}{2}\right] \tag{1}$$

where h_i = height of ith storey from base,

h_n = total height of the structure.

I_r is the ratio of effective period of vibration of seismically isolated structure to fundamental period of vibration of fixed building. For fixed supported building $I_r = 1$.

2. Select the appropriate base isolator with the isolator displacement D_d and maximum interstorey drift ratio θ_d. The critical storey is the storey where the maximum interstorey drift ratio is reached. The maximum interstorey drift ratio is reached in the first storey [2] and is assumed as

$$\theta_d = 100\frac{\Delta_c}{h_c} \tag{2}$$

3. The displacement profile [5] for the ith storey of the structure is given as

$$\Delta_i = D_d + \theta_d \cdot c_1 \cdot \Phi_i \tag{3}$$

$$c_1 = \frac{h_1}{100\Phi_1} \tag{4}$$

4. Design displacement Δ_d, effective mass m_e, effective height h_e of equivalent SDOF system are given by Eq. 5–7, respectively,

$$\Delta_d = \frac{\sum_{i=1}^{n} m_i \Delta_i^{\,2}}{\sum_{i=1}^{n} m_i \Delta_i} \tag{5}$$

$$m_e = \frac{\sum_{i=1}^{n} m_i \Delta_i}{\Delta_d} = \frac{\left[\sum_{i=1}^{n} m_i \Delta_i\right]^2}{\sum_{i=1}^{n} m_i \Delta_i^{\,2}} \tag{6}$$

$$h_e = \frac{\sum_{i=1}^{n} m_i \Delta_i h_i}{\sum_{i=1}^{n} m_i \Delta_i} \tag{7}$$

5. Since displacement, drift, ductility are the governing parameters in displacement-based design method, design ductility can be controlled as

$$\mu_d = \frac{\theta_d}{\theta_y} \tag{8}$$

Fig. 4 Design displacement spectrum for IS 1893–2016 for Zone-V
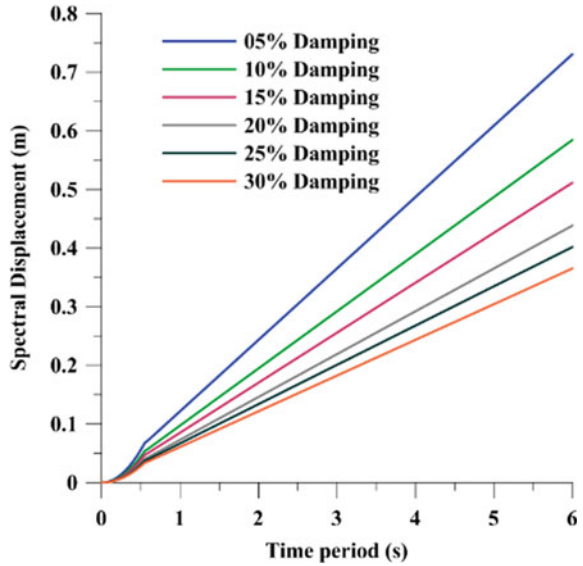
$$\theta_y = 0.5\varepsilon_y \frac{l_b}{h_b} \tag{9}$$

ε_y = yield strain in steel=0.2%

l_b = beam length and

h_b = beam depth

6. In addition to 5% elastic viscous damping, hysteretic damping is added to include energy dissipation by RC members during earthquake and is known as equivalent viscous damping of super structure [2].

$$\xi_S = (5 + \xi_{hyst})\%$$

$$\xi_S = 5 + 120 \left(\frac{1 - \mu_d^{-0.5}}{\pi} \right)\% \tag{10}$$

7. The equivalent damping ratio ξ_{eq} of base-isolated structure is the combination of damping ratios of super structure and base isolator at their corresponding displacements given as

$$\xi_{eq} = \frac{[\xi_{IS}.D_d + \xi_S \cdot (\Delta_D - D_d)]}{\Delta_D} \tag{11}$$

8. The effective time period T_{eq} is established by entering the displacement spectra set shown in Fig. 4 with the design displacement Δ_d and the equivalent viscous damping.

9. The equivalent stiffness K_{eq} for the design displacement of the equivalent SDOF system using

$$K_{eq} = 4\pi^2 \frac{m_e}{T_{eq}^2} \qquad (12)$$

10. This equivalent stiffness is multiplied by the design displacement, Δ_d, to obtain the design base shear as

$$V_{b(DDBD)} = K_{eq}\Delta_d \qquad (13)$$

11. Distribute the base shear along the height of the building using Eq. (14)

$$F_i = V_{b(DDBD)} \cdot \frac{m_i \Delta_i}{\sum_{i=1}^{n} m_i \Delta_i} \qquad (14)$$

12. The stiffness of the base isolator is given by

$$K_{IS} = \frac{V_{b(DDBD)}}{D_d} \qquad (15)$$

3   Characteristics of Lead Rubber Bearing

The typical hysteresis loop of a lead rubber bearing can be modelled as bilinear. The parameters d_1, F_1, d_2 and F_2 that define the bilinear curve are given by the manufacturers for each standard LRB [7]. The hysteretic behaviour of an LRB can also be modelled as linear, by means of the effective stiffness K_e and the equivalent viscous damping coefficient ξ_e, that depend on the maximum displacement d_2 and on the corresponding force F_2 to which they refer Fig. 5.

$$K_e = \frac{F_2}{d_2} \qquad (16)$$

$$\xi_{IS} = \frac{2}{\pi}\left[\frac{F_1}{F_2} - \frac{d_1}{d_2}\right] \qquad (17)$$

Fig. 5 Hysteresis loop for
LRB
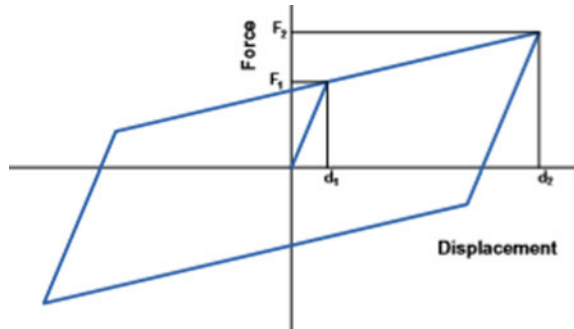
4   Characteristics of Ground Motions

Ground motion data of six sets each for far field, near-field forward directivity and
near-field fling step, respectively, have been selected [4]. The details of the ground
motions in terms of magnitude, recording station, PGA, fling step displacement are
shown in Table 1.

5   Building Details

The plan of a RC frame building with dimensions is shown in Fig. 6. The building is
located in medium soil for Bhuj area which falls under Zone-V considered extreme
zone according to Bureau of Indian Standards [6]. The design is carried out using
Bureau of Indian Standard code [8]. The drift is limited to 2% [9]. Nonlinear time
history analysis (NLTHA) is carried out to verify the inter-story drift ratio, time
period, acceleration of top floor, base shear, isolator displacement for six sets of each
earthquake ground motions of far field, near-field forward directivity and near-field
fling step, respectively, for FB and BI. The analysis and design were carried out in
MIDAS/GEN 2019 software. The live load is 3 kN/m². external wall of 230 mm
thick exists. Thickness of slab is 150 mm. characteristic strength of main steel and
secondary steel are 500 N/mm² and 415 N/mm², respectively. Secondary beams are
of 300 × 450 mm in dimension. The lead rubber bearing provided is manufactured
by *FIP INDUSTRIALE* [7]. Isolator properties are shown in Table 2. The width of the
beam is 300 mm. The depth was taken as 550 mm, 650 mm and 750 mm, respectively,
for four, eight and twelve storeys. The size of the column is 550 × 650 mm, 600 ×
650 mm and 600 × 750 mm, respectively.

Table 1 Ground motion records

Record label	Earthquake	Magnitude	Station	PGA (g)	Fling Disp. (cm)
Far-field ground motions					
FF 1	1999 Chamoli	6.4	Chamoli	0.359	–
FF 2	1940 Imperial Valley	6.95	El Centro	0.313	–
FF 3	1989 Loma Prieta	6.9	Capitola	0.420	–
FF 4	1994 Northridge	6.7	Northridge-Saticoy	0.529	–
FF 5	1994 Northridge	6.7	Canoga Park	0.477	–
FF 6	1987 Superstition Hills	6.7	El Centro Imp Co. Centre	0.512	
Near-fault ground motions with forward directivity					
NFD 1	1994 Northridge	6.7	Rinaldi	0.890	–
NFD 2	1994 Northridge	6.7	Sylmar	0.730	–
NFD 3	1994 Northridge	6.7	Newhall	0.720	–
NFD 4	1979 Imperial Valley	6.4	EL Centro Array 7	0.460	–
NFD 5	1992 Landers	7.3	Lucerne Valley	0.710	–
NFD 6	1979 Imperial Valley	6.7	EL Centro Array 5	0.370	
Near-fault ground motions with fling step					
NFS1	1999 Chi Chi	7.6	TCU129_NS	0.610	67.54
NFS 2	1999 Chi Chi	7.6	TCU084_NS	0.420	59.43
NFS 3	1999 Chi Chi	7.6	TCU074 EW	0.590	174.56
NFS4	1999 Chi Chi	7.6	TCU052_NS	0.440	697.12
NFS5	1999 Chi Chi	7.6	TCU068_EW	0.500	601.84
NFS 6	1999 Kocaeli	7.4	YPT	0.23	145.79

6 Discussion of the Results

The results of the analysis are tabulated in Table 3. The response parameters for 4-storey, 8-storey, 12-storey are shown in Tables 4, 5 and 6, respectively The following observations were made in the study:
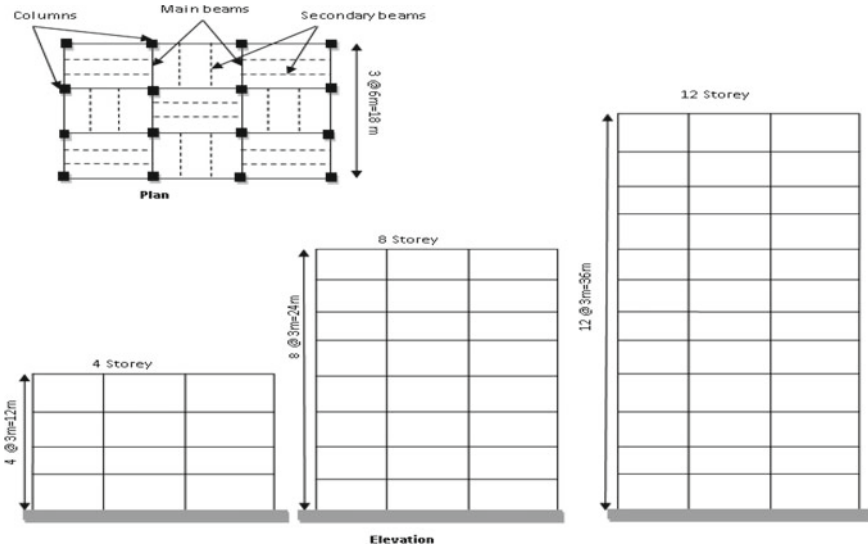
Fig. 6 Geometry of the building

Table 2 Isolator properties

	4 Storey	8 Storey	12 Storey
Name of the isolator	LRB-S 550/200-120	LRB-S 550/200-120	LRB-S 600/204-130
Isolator displacement D_d(m)	0.4	0.4	0.4
Effective stiffness $K_{(effkN/m)}$	810	810	950
Initial stiffness $K_{(1}$kN/m	7875	7875	9250
Effective damping $\xi_{IS(\%)}$	26.65	26.65	26.85
Post yield stiffness ratio γ	0.058	0.058	0.057
Yield force F_y(kN)	126	126	148
Vertical stiffness K_v (kN/m)	789,000	789,000	844,000

Table 3 Results of analysis

No of storeys	T_{eq} (s)	I_r	$\xi_{eq}(\%)$		$V_{b(DDBD)}$ (kN)	
			BI	FB	BI	FB
4	5.30	3.39	24.70	16.19	1237	3524
8	5.70	2.43	23.11	16.19	2621	3554
12	6.08	2.05	22.17	16.19	4116	4136

Table 4 Four storey response parameters

Earthquake	Roof accel (% reduction)	Max drift ratio (% reduction) (%)	Isolator disp (mm)
FF1	26.96	−98.15	16.7
FF2	48.03	−27.82	44.2
FF3	32.60	−20.00	15
FF4	53.61	−34.15	12.9
FF5	30.13	−29.21	19.7
FF6	41.64	−26.51	15
NFD1	20.63	−37.50	57.9
NFD2	38.27	26.02	41.3
NFD3	36.63	53.85	36.8
NFD4	10.81	−35.48	28.1
NFD5	26.47	26.09	31.8
NFD6	39.34	2.13	33.4
NFS1	27.44	−14.94	38.8
NFS2	29.07	−0.85	39.8
NFS3	41.70	12.31	24.5
NFS4	18.71	−13.04	22.4
NFS5	34.81	26.19	35.4
NFS6	40.55	9.33	25.3

1. V_b(NLTHA) for 4-storey building exceeds Vb(DDBD) up to 25% in near-field forward directivity (NFD 1, NFD 2, NFD 4, NFD 6) and up to 20% in case of near-field fling step (NFS 1, NFS 2) for the BI structure (Table 7). For 8-storey BI, V_b(NLTHA) exceeds V_b(DDBD) up to 19% in case of near-field forward directivity (NFD 1, NFD 2) (Table 8). For 12-storey BI, V_b(NLTHA) exceeds V_b(DDBD) up to 7% in case of near-field forward directivity (NFD 2) and 31% for near-field fling step (NFD 1, NFD 2) for FB structure (Table 9).
2. V_b(NLTHA) of BI structure is greater than V_b(NLTHA) of FB for 12-storey building as well as V_b(DDBD) for BI is nearly equal to V_b(DDBD) for FB (Table 9).

Table 5 Eight storey response parameters

Earthquake	Roof accel (% reduction)	Max drift ratio (% reduction) (%)	Isolator disp (mm)
FF1	26.15	32.71	40
FF2	51.61	29.60	69.3
FF3	25.24	10.00	39.2
FF4	25.99	28.33	35.2
FF5	31.18	21.28	46
FF6	28.32	40.38	31.2
NFD1	37.10	15.32	135.1
NFD2	20.62	14.29	177.8
NFD3	34.38	12.82	36.6
NFD4	32.25	25.75	64.5
NFD5	28.59	32.43	28.2
NFD6	40.63	37.58	62.9
NFS1	34.10	21.35	83.6
NFS2	31.39	21.08	74.2
NFS3	26.47	13.04	27.9
NFS4	30.87	33.82	44.5
NFS5	26.18	18.87	36.5

3. The base shear values of BI buildings in case of nonlinear time history analysis were less than the corresponding fixed support values for four storey (Fig. 7) and except one case in fling step, NFS 5 in eight storey (Fig. 8). But for 12-storey building exceeds the base shear values of FB (Fig. 9) for far field, near field forward directivity and near field fling step ground motions.
4. For the 4-storey building, the drift ratios of BI structure were higher in all the far field, 2 cases in forward directivity (NFD 1, NFD 4), 3 cases in fling step (NFS 1, NFS 2, NFS 4) ground motions (Table 4) when compared to FB which was higher in first storey.
5. There is a reduced top floor acceleration in BI buildings when compared to FB.

7 Conclusions

The Direct displacement-based design developed by Cardone et al. was applied to four, eight and twelve storey buildings regular in plan for fixed base and lead rubber bearing as isolator, subjected to far field, near-field directivity and near field fling step ground motions. The following conclusions were drawn from the study:

Table 6 Twelve storey response parameters

Earthquake	Roof accel (% reduction)	Max drift ratio (% reduction) (%)	Isolator disp (mm)
FF1	18.03	41.59	26.6
FF2	22.82	17.09	36.1
FF3	26.60	27.32	55.8
FF4	16.61	29.31	28.3
FF5	20.52	23.08	46.4
FF6	16.45	25.23	29.5
NFD1	41.79	37.38	223.1
NFD2	41.83	43.81	256.7
NFD3	22.00	20.73	50.8
NFD4	25.25	27.89	62.7
NFD5	29.40	25.00	33.9
NFD6	34.77	40.64	60.9
NFS1	8.79	40.48	108.2
NFS2	24.69	21.59	94.1
NFS3	19.19	22.29	37.5
NFS4	19.84	39.68	38.9
NFS5	6.23	26.32	30.2
NFS6	19.71	23.47	58.6

Table 7 Four storey base shear ratios V_b (NLTHA)/V_b (DDBD)

	$V_b^{(a)}$			Far field			Near-field forward directivity			Near-field fling step	
				$V_b^{(b)}$	(b)/(a)		$V_b^{(c)}$	(c)/(a)		$V_b^{(d)}$	(d)/(a)
BI DDBD	1237	BI time history	FF1	942	0.76	NFD1	1541	1.25	NFS1	1372	1.11
			FF2	1088	0.88	NFD2	1428	1.15	NFS2	1481	1.20
			FF3	941	0.76	NFD3	1016	0.82	NFS3	1037	0.84
			FF4	970	0.78	NFD4	1251	1.01	NFS4	1172	0.95
			FF5	885	0.72	NFD5	1173	0.95	NFS5	1198	0.97
			FF6	943	0.76	NFD6	1268	1.02	NFS6	1232	1.00
FB DDBD	3524	FB time history	FF1	1216	0.35	NFD1	1973	0.56	NFS1	1802	0.51
			FF2	1906	0.54	NFD2	1661	0.47	NFS2	1692	0.48
			FF3	1213	0.34	NFD3	1432	0.41	NFS3	1285	0.36
			FF4	1190	0.34	NFD4	1501	0.43	NFS4	1328	0.38
			FF5	1397	0.40	NFD5	1438	0.41	NFS5	1536	0.44
			FF6	1217	0.35	NFD6	1519	0.43	NFS6	1303	0.37

Table 8 Eight storey base shear ratios V_b (NLTHA)/V_b (DDBD)

	$V_b^{(a)}$			$V_b^{(b)}$	(b)/(a)		$V_b^{(c)}$	(c)/(a)		$V_b^{(d)}$	(d)/(a)
				Far field			Near field forward directivity			Near field fling step	
BI DDBD	2621	BI time history	FF1	1724	0.66	NFD1	2769	1.06	NFS1	2277	0.87
			FF2	1835	0.70	NFD2	3120	1.19	NFS2	2259	0.86
			FF3	1973	0.75	NFD3	1852	0.71	NFS3	1782	0.68
			FF4	1743	0.66	NFD4	2148	0.82	NFS4	1797	0.69
			FF5	1980	0.76	NFD5	1674	0.64	NFS5	1737	0.66
			FF6	1722	0.66	NFD6	1930	0.74	NFS6	1927	0.74
FB DDBD	3554	FB time history	FF1	1776	0.50	NFD1	2961	0.83	NFS1	2372	0.67
			FF2	2052	0.58	NFD2	3317	0.93	NFS2	2563	0.72
			FF3	2074	0.58	NFD3	2036	0.57	NFS3	1979	0.56
			FF4	2030	0.57	NFD4	2357	0.66	NFS4	2151	0.61
			FF5	2165	0.61	NFD5	1894	0.53	NFS5	1715	0.48
			FF6	1814	0.51	NFD6	2423	0.68	NFS6	2144	0.60

Table 9 Twelve storey base shear ratios V_b (NLTHA)/V_b (DDBD)

	$V_b^{(a)}$			$V_b^{(b)}$	(b)/(a)		$V_b^{(c)}$	(c)/(a)		$V_b^{(d)}$	(d)/(a)
				Far field			Near-field forward directivity			Near-field fling step	
BI DDBD	4095	BI time history	FF1	2053	0.50	NFD1	4114	1.00	NFS1	2937	0.72
			FF2	2025	0.49	NFD2	4397	1.07	NFS2	2986	0.73
			FF3	2636	0.64	NFD3	2493	0.61	NFS3	2432	0.59
			FF4	2015	0.49	NFD4	2670	0.65	NFS4	1997	0.49
			FF5	2405	0.59	NFD5	2181	0.53	NFS5	1934	0.47
			FF6	2094	0.51	NFD6	2444	0.60	NFS6	2691	0.66
			FF1	1712	0.41	NFD1	4767	1.15	NFS1	3329	0.81
			FF2	1980	0.48	NFD2	5406	1.31	NFS2	3224	0.78
FB DDBD	4136	FB time history	FF3	2705	0.65	NFD3	2327	0.56	NFS3	2395	0.58
			FF4	2186	0.53	NFD4	2649	0.64	NFS4	2190	0.53
			FF5	2420	0.59	NFD5	2501	0.60	NFS5	1671	0.40
			FF6	2045	0.49	NFD6	2809	0.68	NFS6	2606	0.63

1. The method proposed by Cardone et al. holds good for the far-field ground motions with fixed support as well as the base-isolated buildings frames.
2. The base shear demand was higher for near-field forward directivity and near-field fling step method as seen by nonlinear time history analysis.
3. There was a significant reduction in drift ratios in eight and twelve storey base-isolated buildings and the percentage increased for four storey although the
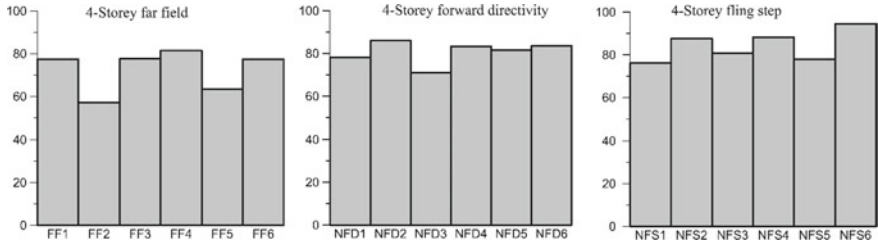
Fig. 7 Four storey base shear ratio of fixed base versus base-isolated structure of NLTHA
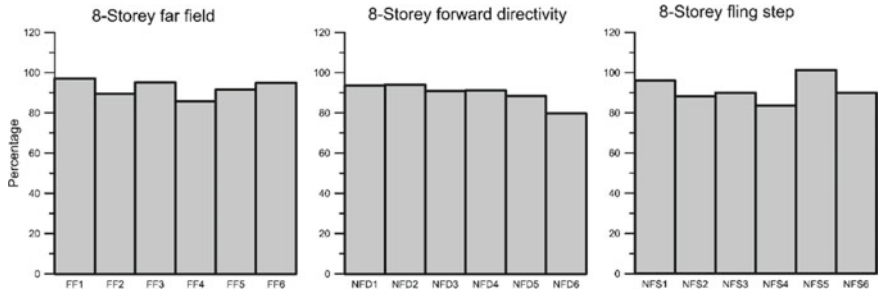
Fig. 8 Eight storey base shear ratio of fixed base versus base-isolated structure of NLTHA
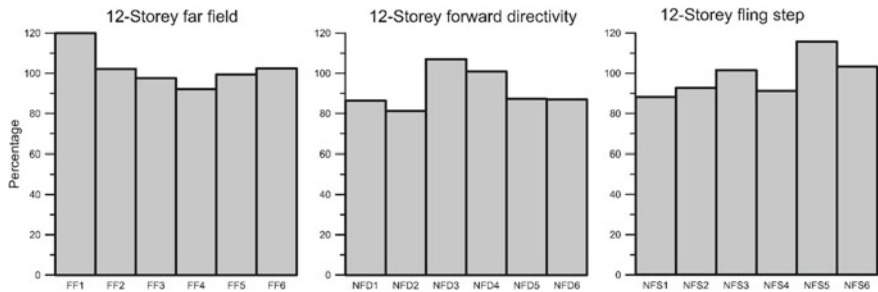
Fig. 9 Twelve storey base shear ratio of fixed base versus base-isolated structure of NLTHA

values are very much less than the design drift of 2%. The maximum drift was predominantly in first storey in four-storey structure.

4. The base shear of 12-storey frame building with base isolation was very near to the base shear value of fixed support. The same result was reflected in nonlinear time history analysis suggesting that only base isolation is not sufficient for high-rise frame building. Supplementary arrangements such as auxiliary dampers may be provided.

5. The reduced floor acceleration in base-isolated building indicate the safety and comfort for the occupants.

6. Although this study proves the applicability of the method to far-field ground motions, it suggests that still more earthquake ground motions be considered especially for near field directivity and near field fling step method to possibly find a modification factor.

References

1. Priestley MJN, Pettinga JD (2005) Dynamic behaviour of reinforced concrete frames designed with direct displacement-based design. J Earthq Eng 9:309–330
2. Ayala G, Castellanos H, Lopez S (2012) A displacement-based seismic design method with damage control for RC buildings. Earthq Struct 3:413–434. https://doi.org/10.12989/eas.2012.3.3_4.413
3. Bhandari M, Bharti SD, Shrimali MK, Datta TK (2018) The numerical study of base-isolated buildings under near-field and far-field earthquakes. J Earthq Eng 22:989–1007. https://doi.org/10.1080/13632469.2016.1269698
4. Kalkan E, Kunnath SK (2006) Effects of fling step and forward directivity on seismic response of buildings. Earthq Spectra 22:367–390. https://doi.org/10.1193/1.2192560
5. Cardone D, Palermo G, Dolce M (2010) Direct displacement-based design of buildings with different seismic isolation systems. J Earthq Eng 14:163–191. https://doi.org/10.1080/13632460903086036
6. IS-1893. Indian standard criteria for earthquake resistant design of structures-Part 1 general provisions and buildings (2016) Bureau of Indian Standards, New Delhi
7. FIP Industriale (2016) Lead rubber bearings Series LRB
8. IS-456 (2000) Indian standard code of practice for plain and reinforced concrete. Buereau of Indian Standards, New Delhi
9. SEAOC Blue Book (1999) Recommended lateral force requirements and commentary

Enhancing Dynamic Fracture Behavior of Laminated Composite by Short Fiber Reinforcement

Manoj K. Singh and **R. Kitey**

Abstract Continuous fiber reinforced laminated composites are mostly preferred in engineering applications where in-plane strength and modulus are key requirements. Although the composites' in-plane mechanical and failure behavior can be tailored to meet the end user requirements, their weaker out-of-plane characteristics often remain a cause of concern. Failure in such materials initiates either at fiber/matrix interfaces or from matrix-rich regions within the laminae or at the inter-laminar regions. Stiffening matrix-rich zones by using reinforcements is one of the methods which is employed to reduce the probability of failure. In this investigation, a short fiber reinforced matrix is used to enhance the failure characteristics of laminated composites under impact loading conditions. Sixteen layers of plain weave bidirectional Glass Fiber Reinforced Polymer (GFRP) composites are fabricated by hand layup technique. Neat epoxy and chopped fiber reinforced epoxy systems are used as matrix materials to prepare unreinforced and reinforced laminates. Impact tests are conducted at 5 and 20 J energy levels by following ASTM D7136M standards. At lower impact energy, nearly 50% reduction in visible damage area is observed in the case of reinforced laminates, whereas at higher impact, the damage areas differ only by 6.5%. While the force associated to failure initiation remains unaffected by short fiber reinforcement, it improves the laminate's response by inducing higher resistance to deformation. The laminate stiffness in general is observed to increase with increasing impact energy as well with the short fiber reinforcements. The data exhibits higher energy dissipation at higher impact energy with only a marginal influence of reinforcement. SEM images reveal transverse matrix cracking at lower impact energy in both unreinforced and short fiber reinforced cases with a few inter-laminar failures in the prior. On the contrary, when the laminates are subjected to higher impact energy, significant matrix cracking along with the delamination at several interfaces is observed.

Keywords GFRP · Impact energy · Fracture mechanisms

M. K. Singh (✉) · R. Kitey
Indian Institute of Technology Kanpur, Kanpur 208016, India
e-mail: manojmsk@iitk.ac.in

1 Introduction

The usage of continuous fiber composites in aviation, high-performance automobiles, and civil structures is continuously growing due to their high specific strength, high specific modulus, and corrosion resistance characteristics. The cost-effectiveness of glass fiber laminated composites makes them suitable not only for secondary parts of airplanes but also in the fabrication of load-bearing members in unmanned air vehicles and civil structures. The laminates are characteristically weaker in the out-of-plane direction. They are quite susceptible to impact damage which often remains obscured within the opaque laminae. Tool drop, hailstorm, and foreign particle hit are some of the events that subject the laminated structures to low velocity impact and induce complicated damage patterns owing to a combination of different failure mechanisms [1–3]. The load-carrying capacity of the damaged laminates drastically reduces which in turn poses challenges to the reliability and structural integrity of structures. There have been attempts to improve the out-of-plane failure characteristics of the laminates through stitching [4], reinforcements [5], and/or chemical treatments [6]. However, a unique solution is yet to evolve in the absence of a quantifiable damage evolution in the complex heterogeneous laminated structures.

Kim [4] suggested that by employing toughened matrix, woven fabric, interleaving, through thickness stitching, and hybrid fibers, various failure properties, such as interlaminar fracture toughness, energy absorbing capacity, and compression after impact strength can be improved. While weave structures in woven fabric greatly restrict the development of shear cracks and delamination propagation, the other strategies may have a deteriorating effect on mechanical properties. Incorporation of toughened matrix and interleaving reduces the stiffness and compressive strength, especially under hot wet conditions. Through thickness stitching may cause localized damage to the longitudinal fibers. Bull et al. [5] performed low velocity impact and indentation tests on carbon fiber composites where they used 4 to 30 μm diameter thermoplastic particles to toughen the matrix epoxy. They used impact energies between 25 and 50 J whereas the indentation depth was varied from 2 to 5 mm. They reported matrix cracking, delamination with bridging ligament, failure of bridging ligament, and fiber fracture as the key failure mechanisms. The fiber fracture was observed at the last stage of displacements. They suggested that the failure mechanism at micro-scale in the toughened epoxy system was sensitive to strain rate. Boumbimba et al. [6] reinforced bidirectional woven glass fibers in thermoplastic acrylic resin to fabricate the laminated composites. For enhancing the impact resistance of the laminates, they added acrylic tri-block copolymer into the matrix at three different weight percentages, 5, 10, and 15%. They subjected the specimens to 30, 40, and 50 J impact energies where the experiments were conducted at three different temperatures, 20, 80, and −80 °C. They suggested that the first loss in the laminate stiffness was due to matrix cracking. This was followed by damage propagation until the maximum load was observed at which the fibers fractured. They reported that the toughening reinforcements increased the damage resistance only at 20 and 80 °C test temperatures. They also concluded that the strengthening fillers reduced

the energy absorption capacity of the laminate at higher impact energies. Francesconi and Aymerich [7] investigated the effect of through thickness stitching on the impact response of carbon/epoxy laminated composites prepared with two different stacking sequences, $(0_3/90_3)_S$ and $(0/90)_{3S}$. They reported a significant increase in the delamination resistance in the stitched laminate cases when compared to the unstitched ones. However, they observed that the stitching reduced the in-plane properties of the laminates due to the inherent inclusion of defects, such as voids and resin-rich areas around the stitches [8]. Walker et al. [9] used interleaving and short fiber reinforcement techniques to enhance the impact resistance of carbon fiber epoxy composites. They randomly dispersed five different reinforcements in the interlaminar regions and subjected the laminates to low velocity impact. They suggested that the short fiber reinforced laminates absorbed the least incident energy, thus increasing its elastic energy storage capacity, when compared to the unreinforced or interleave cases. Although the smallest damage area was observed in the case of interleaved laminate, the intensity of damage was significantly larger when compared to the reinforced laminate case.

Sharma et al. [10] studied the effect of metal layer thickness and their distribution on the failure behavior of fiber metal laminated composites. They fabricated constant thickness composites by alternately stacking unidirectional glass fiber laminae and aluminum sheets of different thicknesses and subjected them to the impact energy up to 75 J. They observed crack initiation at lower impact energy when thinner aluminum layers were used at the top and bottom of the laminates. They also demonstrated that a greater number of thinner metal sheets in the laminates provided better energy absorption characteristics when compared to the laminates with thicker but a smaller number of aluminum layers. In the case of thinner sheets, the delamination distribution and its spread were more uniform when compared to the thicker metal layer case. Sun et al. [11] prepared woven basalt fiber, plain weave carbon, and unidirectional glass fiber laminates and impregnated them with hydrophilic silica nanoparticles and polyethylene glycol. They studied the response of composites at 30 J impact energy. They reported that impregnated laminates exhibited better impact performance for all three types of fiber laminates as compared to the unimpregnated laminate case. Among the three laminates, the glass fibers offered the maximum resistance against impact loading and showed better energy dissipation characteristics. Bull et al. [12] reinforced thermoplastic particles in the base resin and prepared $[45/0/45/90]_{3S}$ laminates. They subjected the laminates to the impact energies, from 25 to 50 J, and studied the effect of toughening particles on the impact response of the laminates. They reported improved damage resistance in the case of toughened epoxy laminate. The increase in the damage resistance was attributed to the bridging mechanism. Sarasini et al. [13] prepared multi-walled carbon nanotube (MWCNT) reinforced cross-ply unidirectional carbon/epoxy prepreg laminates. In between the laminae, they also laid two different electrospun nanofiber veils with 1.5 GSM and 4.5 GSM values. By subjecting the laminates to 5 and 7.5 J impact energies, they reported that the delamination was significantly reduced when the 4.5 GSM veils were symmetrically oriented through the laminate thickness. They suggested that MWCNT along with nanofiber interleaving worked synergistically in improving the

laminates' impact characteristics. Yesgat and Kitey [14] studied the effect of filler shape and volume fraction on the flexural and fracture properties of the reinforced matrix. They embedded 34 μm diameter spherical glass particles and 200 μm long milled fibers with 16 μm diameter into an epoxy system up to 10% volume fraction. They reported that the enhancement in the mechanical and failure properties of the matrix is significantly higher in the case of short fiber composites. Singh et al. [15] further extended the study and analyzed the quasi-static and dynamic response of the two composite systems. They suggested that the slender fillers provide more resistance to deformation and higher yield strength when compared to the spherical ones.

The literature review suggests that there are limited research articles on improving the impact resistance of the laminated composite. While most of those studies suggested that the enhancement of interlaminar characteristics was accompanied with deteriorated mechanical properties, these studies often remained limited to analyzing the macroscopic behavior of laminates, and less attention was paid to the evolution of damage at the microscopic level. In this investigation, chopped glass fibers are reinforced into glass fiber reinforced polymer (GFRP) laminate, and the effect of reinforcement on the impact-induced failure characteristics is quantified. Post-failure analysis is performed to reveal the failure mechanisms involved at the microscopic scale.

2 Material Preparation

GFRP composite laminates are prepared by stacking sixteen layers of epoxy smeared plain weave bidirectional glass fabric with an areal density of 0.045 gm/cm^2. The epoxy matrix was prepared by mixing diglycidyl ether of bisphenol-A (DGEBA) and methyl tetra hydrophthalic Anhydride (MTHPA) curing agent in a 1:1 ratio by weight. The stacked layers were vacuum bagged for 45 min and cured in a hot press at 3 bar pressure. The curing cycle consisted of 85 °C for 3 h, followed by 140 °C for 12 h. Another set of laminates is fabricated by using short fiber reinforced epoxy as the matrix material. For preparing reinforced matrix, 16 μm diameter chopped glass fibers with an average length of 6 mm were mixed in the epoxy resin at a 4% volume fraction. The mixture was degassed at a 25-inch Hg vacuum, mechanically stirred, and sonicated. The process was successively repeated until a uniform filler dispersion is attained. In both unreinforced and filler reinforced matrix cases, a small amount of accelerator, 2,4,5-tris[(dimethylamino)methyl]-Phenol, was used to increase the rate of curing. Here onwards, the unreinforced and short fiber reinforced laminates are abbreviated as URL and SRL, respectively.

3 Experimental Method and Measurements

The 4.5-mm-thick cured laminates are machined into the test specimens of dimension 150 mm × 100 mm as per ASTM D7136M standard [16]. A drop tower INSTRON CEAST 9340 with a free fall impactor mass of 3.132 kg is used for performing impact tests. As shown in Fig. 1a, the specimens are fixed over a specimen fixture with 125 mm × 75 mm rectangular cutout. For subjecting the test specimens to 5 J and 20 J impact energies, the free fall height of hemispherical tup is adjusted such that it strikes the specimens at 1.79 m/s and 3.55 m/s velocity, respectively. Representative force histories associated to 5 J impact energy are shown in Fig. 1b. The data is recorded by the instrumented tup at 100 kHz. The plots exhibit excellent experimental repeatability. The velocity history $v(t)$ and displacement history $\delta(t)$ of the tup, and the impact energy $E(t)$ absorbed by the specimen are determined by employing the following equations.

$$v(t) = v_0 + gt - \int_0^t \frac{F(t)}{m} dt \tag{1}$$

$$\delta(t) = \delta_0 + v_0 t + \frac{gt^2}{2} - \int_0^t \left(\int_0^t \frac{F(t)}{m} dt \right) dt \tag{2}$$

$$E(t) = \frac{1}{2} m v_0^2 - \frac{1}{2} m (v(t))^2 + mg\delta(t) \tag{3}$$

In the above equations, the initial values (associated to time $t = 0$) are subscripted with '0', which correspond to the instant when the tup first comes in contact with the specimen. The integral terms in the above equations are calculated by employing Simpson's 1/3rd integration scheme.
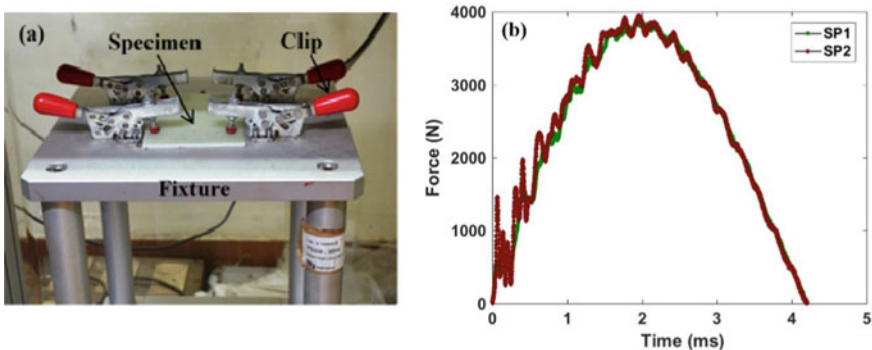
Fig. 1 **a** showing specimen mounted on a fixture and simply supported with four clips. **b** Force–time graph for 5 J impact energy, showing repeatability of the test

4 Results and Discussion

The force histories obtained by impacting URL and SRL specimens at 5 and 20 J energies are plotted in Fig. 2a. Plots show significant undulation in the rising (loading) part of the curves, whereas the unloading path is relatively smooth for all cases. The zigzag force histories indicate successive localized failures in the laminates. The damage initiation is inferred from the first drop observed in the increasing portion of force history [1, 6, 17]. Plots show that for a given impact energy (5 or 20 J), the dynamic force required to initiate the damage remains the same in URL and SRL cases. These threshold force magnitudes are tabulated in Table 1. The data for both URL and SRL cases exhibit higher force at damage initiation for 20 J impact energy. Upon closer observation of the force histories, it is noticed that the rate of increase of the force with respect to time remains nearly the same in between the first few localized peaks. In other words, the curves rise to the localized peaks (enumerated as '1', '2', and '3' in the plots) with nearly the same slope. The phenomenon indicates that during initial localized failures, the laminates retain their stiffness. It can also be observed from the plots that the localized peaks are lesser in numbers and smaller in magnitudes for 5 J impacted specimens when compared to the 20 J case (see,
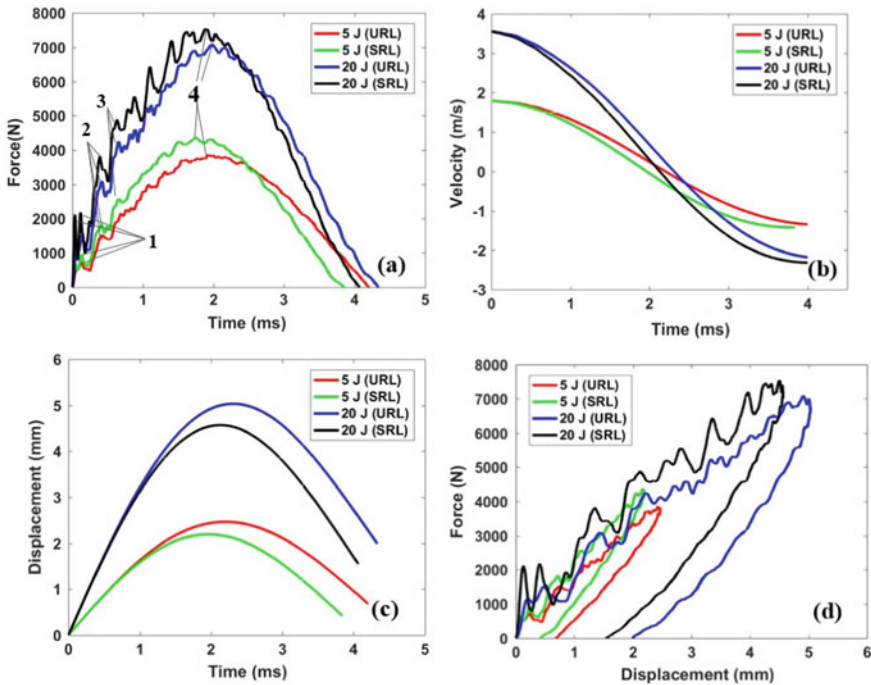
Fig. 2 Representative data obtained by performing impact tests at 5 and 20 J incident energy levels on URL and SRL composites. **a** Force histories, **b** velocity histories, **c** displacement histories, and **d** force versus displacement plots

Table 1 Effect of short fiber reinforcement on the performance parameters of laminates, subjected to impact loading

Type of laminate	Impact energy (J)	First damage force (F_1) (N)	Max. force (kN)	Dent depth (μm)	Dissipated energy (J)		Damage area at the rear surface (mm^2)
					From F- δ curves	From E − t curves	
URL	5	711	3.90 ± 0.04	35 ± 7	2.02 ± 0.16	2.0 ± 0.16	57 ± 11
	20	1492	6.99 ± 0.15	160 ± 2	12.30 ± 0.36	12.30 ± 0.26	321 ± 2
SRL	5	643	4.48 ± 0.14	40 ± 14	1.90 ± 0.04	1.89 ± 0.05	29 ± 1
	20	1407	7.45 ± 0.13	150 ± 21	11.64 ± 0.40	11.59 ± 0.39	300 ± 9

Fig. 2a). Following peak '3', multiple localized drops in the curve are accompanied with continually reduced slopes until the forces peak (shown by '4' in the plots). While the maximum force recorded by the tup (point '4') is higher for the 20 J impact, the curves exhibit that for both 5 and 20 J impact energies, the maximum force is consistently higher in the SRL case. This indicates increased resistance to deformation in the laminate due to short fiber reinforcements. The data in Table 1 suggests the maximum force experienced by the reinforced specimens is increased by 15% and 7% for the 5 J and 20 J impact energy cases, respectively. The plots also suggest that the loading tup remains in contact with the specimen for a lesser duration in the SRL case.

The velocity histories for the representative cases, obtained by employing Eq. (1), are plotted in Fig. 2b. The curves show a marginal but consistently higher velocity for the unreinforced matrix specimens. Also, the specimens which were impacted with higher energies experience higher maximum as well as higher rebound velocity. Next, the displacement data are evaluated by using Eq. (2). The representative displacement histories plotted in Fig. 2c exhibit that the URL specimens are subjected to higher maximum displacement when compared to the SRL cases, which suggests that the short fiber reinforcement has increased the resistance to deformation. Similar to the velocity data, higher displacement is observed at higher impact energy.

The force versus displacement data plotted in Fig. 2d show that the average slope of the loading part of the curve increases with increasing impact energy. The slopes are consistently higher for the SRL case, which again indicates increased laminate stiffness. Interestingly, the points of maximum displacement and maximum force do not coincide. The laminate attains maximum displacement somewhat later during the unloading part of the curve. The zero force during unloading indicates that the tup has lost contact with the specimen and completely rebounded. A lesser magnitude of the displacement associated to this point in the case of SRL specimens again indicates that the laminate with short fiber reinforcement provides better resistance to deformation. The dent made by the tup on the laminates is measured by a depth gage after 24 h of conducting the experiments. The data tabulated in Table 1 indicate that the short fiber reinforcement has a negligible effect on dent depth, while it increases with increasing impact energy.

Fig. 3 Variation of energy
in URL and SRL composites
obtained by conducting
impact tests at 5 and 20 J
incident energy levels
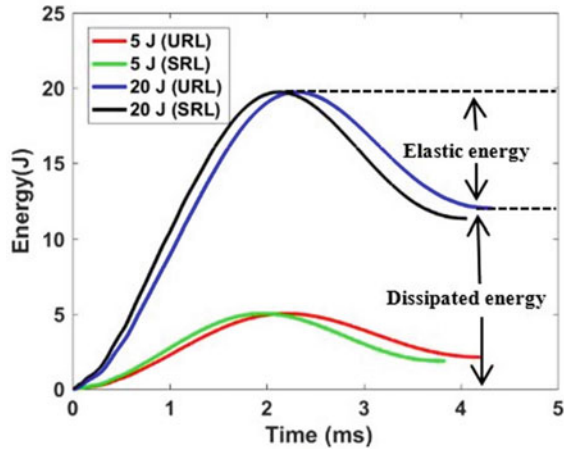
The variation of the absorbed energy with time for various test cases is calculated
by using Eq. (3) and plotted in Fig. 3. The peak value of the plotted curves nearly
matches the intended impact energy levels, which suggests that the frictional losses
during the experiments were negligible. Following peak values, which also corre-
spond to the maximum displacements, the energies decrease monotonically until a
non-zero plateau is attained. At these plateaus, the tup records zero force value which
indicates that unloading has been followed by a complete rebounding of the tup. The
energy associated to the plateau region indicates the energy dissipated in the failure
process. The magnitude of the dissipated energy for various test cases is tabulated
in Table 1. This energy can also be calculated from the area under the curve from
force versus displacement plots, shown in Fig. 2d. They are also tabulated in Table 1
for comparison. The data suggest that for a given impact energy level, lesser energy
has been dissipated in the SRL composites when compared to the URL cases. The
elastic energy, which is calculated by subtracting dissipated energy from the impact
energy, shows marginally but consistently higher values for the SRL cases.

4.1 Micrographic Analysis

The visible damage areas on the specimen surface, opposite to the impacted ones, are
illustrated in Fig. 4. The two images correspond to the URL (a) and SRL (b) specimens
when they were subjected to 5 J impact energy. The images show lesser damage in
the case of SRL composites. The damage areas are measured by digitizing the images
which are tabulated in Table 1. The data suggest that the short fiber reinforcement
has reduced the damage in the laminates by 48.5% and 6.5%, for the 5 J and 20 J
impact energies, respectively.
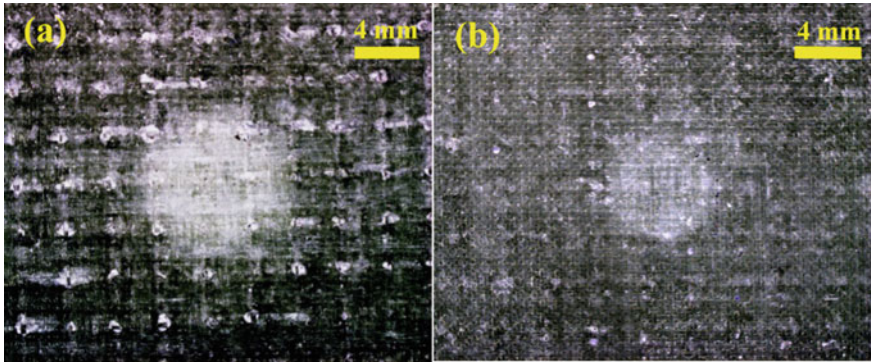
Fig. 4 The visible damage associated to 5 J impact energy. Images illustrated in (**a**) and (**b**) correspond to stress wave-induced visible damage at the back surface of the URL and SRL laminate, respectively

To get more insight into the failure evolution in the laminates, the damaged specimens are carefully sectioned across the damage zone and polished by using a 1 μm silica powder slurry. Through thickness cut surfaces are examined under the scanning electron microscope. Micrographs included in Fig. 5a, b correspond to the URL and SRL specimens subjected to 20 J impact energy, respectively. The arrow indicates the direction of impact. Interlaminar delamination and intralaminar cracks developed during the fracture process and their transition from one mode to the other are clearly visible from the micrographs. It appears that the SRL composites have comparatively lesser microscopic damage. Scanned electron microscopic images (SEM) reveal transverse matrix cracking at lower impact energy in both URL and SRL cases with a few interlaminar failures in the prior (not shown for brevity). On the contrary, when the laminates are subjected to higher impact energy, significant matrix cracking along with the delamination at several interfaces is observed (see, Fig. 5).
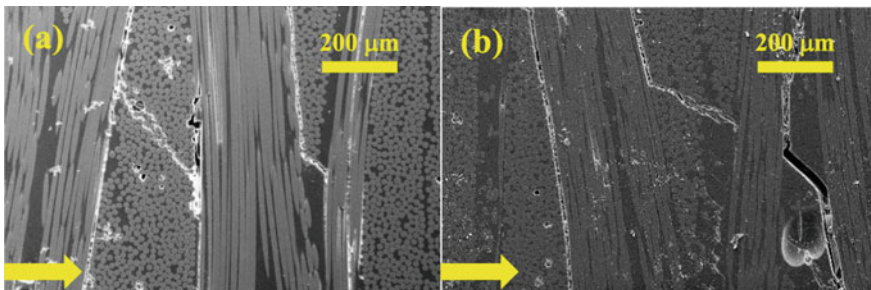
Fig. 5 Scanned electron microscopic images showing failure mechanisms in **a** URL and **b** SRL composites

5   Conclusion

The effect of matrix reinforcement on the impact behavior of Glass Fiber Reinforced Polymer (GFRP) composites is studied. Plain weave bidirectional fiber cloth and neat epoxy reinforced with chopped fibers are used to prepare the laminates. ASTM D7136M standard is followed to conduct the impact experiments. The test specimens are subjected to 5 and 20 J energy levels. Optical micrographs of visible damage at the rear surface of specimens exhibit that at lower impact energy, the short fiber reinforcement has reduced the damage area by 48.5%, whereas at higher impact energy, the associated reduction in the area is only 6.5%. The force histories suggest a successive localized failure in the laminates until a peak energy level is attained. While the laminates retain their stiffness during the first few localized failures, the laminate stiffness in general is observed to increase with increasing impact energy as well with the short fiber reinforcements. The maximum displacement as well as the dent depth are observed to be smaller in the case of reinforced laminates. The force versus displacement curves exhibit higher energy dissipation at higher impact energy. Only a marginal effect of reinforcement on the energy dissipation is evident from the data. SEM images reveal transverse matrix cracking at lower impact energy in both unreinforced and short fiber reinforced cases with a few interlaminar failures in the prior. On the contrary, when the laminates are subjected to higher impact energy, significant matrix cracking along with the delamination at several interfaces is observed.

References

1. Evci C, Gülgeç M (2012) An experimental investigation on the impact response of composite materials. Int J Impact Eng 43:40–51
2. Richardson MOW, Wisheart MJ (1996) Review of low-velocity impact properties of composite materials. Compos A Appl Sci Manuf 27(12):1123–1131
3. Cantwell WJ, Morton J (1991) The impact resistance of composite materials—A review. Composites 22(5): 347–362
4. Kim JK (1998) Methods for improving impact damage resistance of CFRPs. In: Key engineering materials, vol 141. Trans Tech Publications Ltd, pp 149–168
5. Bull DJ, Spearing SM, Sinclair I (2015) Investigation of the response to low velocity impact and quasi-static indentation loading of particle-toughened carbon-fibre composite materials. Compos A Appl Sci Manuf 74:38–46
6. Boumbimba RM, Coulibaly M, Khabouchi A, Kinvi-Dossou aG, Bonfoh N, Gerard P (2017) Glass fibres reinforced acrylic thermoplastic resin-based tri-block copolymers composites: Low velocity impact response at various temperatures. Compos Struct 160:939–951
7. Francesconi L, Aymerich F (2017) Numerical simulation of the effect of stitching on the delamination resistance of laminated composites subjected to low-velocity impact. Compos Struct 159:110–120
8. Shah SZH, Karuppanan S, Megat-Yusoff PSM, Sajid Z (2019)Impact resistance and damage tolerance of fiber reinforced composites: a review. Compos Struct 217:100–121
9. Walker L, Sohn M-S, Hu X-Z (2002)Improving impact resistance of carbon-fibre composites through interlaminar reinforcement. Compos Part A: Appl Sci Manuf 33(6):893–902

10. Sharma AP, Khan SH, Kitey R, Parameswaran V (2018) Effect of through thickness metal layer distribution on the low velocity impact response of fiber metal laminates. Polym Test 65:301–312
11. Sun L, Minghai W, Zhu J (2021) Low velocity impact performance of fiber-reinforced polymer impregnated with shear thickening fluid. Polymer Test 96:107095
12. Bull DJ, Scott AE, Spearing SM, Sinclair I (2014) The influence of toughening-particles in CFRPs on low velocity impact damage resistance performance. Compos A Appl Sci Manuf 58:47–55
13. Sarasini F, Tirillò J, Bavasso I, Bracciale MP, Sbardella F, Lampani L, Cicala G (2020) Effect of electrospun nanofibres and MWCNTs on the low velocity impact response of carbon fibre laminates. Compos Struct 234:111776
14. Yesgat AL, Kitey R (2016) Effect of filler geometry on fracture mechanisms in glass particle filled epoxy composites. Eng Fract Mech 160:22–41
15. Singh SS, Chakraborty P, Kitey R (2019) Deformation characteristics of glass-filled epoxy composite under compression: role of filler shape and volume fraction. Polym Compos 40(12):4726–4741
16. ASTM D (2001) 7136. Standard test method for measuring the damage resistance of a fiber-reinforced polymer matrix composite to a drop-weight impact event. ASTM Int
17. Belingardi G, Vadori R (2002) Low velocity impact tests of laminate glass-fiber-epoxy matrix composite material plates. Int J Impact Eng 27(2):213–229

Crystal Plasticity Modelling of Neutron Irradiation Effects on the Flow and Damage Behaviour of Zircaloy-4

Nevil Martin Jose, M. K. Samal, P. V. Durgaprasad, Alankar Alankar, and B. K. Dutta

Abstract Zircaloy-4 is an alloy of zirconium used to make the cladding of nuclear fuel tubes in reactors. The cladding is subjected to neutron irradiation during its service inside the nuclear reactor that leads to degradation of its mechanical properties. In this work, the irradiation hardening and softening of the polycrystalline Zircaloy-4 under various doses of neutron irradiation are simulated using a crystal plasticity finite element model (CPFEM). The crystal plasticity model is based on dislocation density and defect (produced during irradiation) density-based kinetics of plastic deformation in crystals. An increase in yield stress due to irradiation is modelled by considering the defect density produced by irradiation. The defect density evolution models the loss in ductility occurring to the irradiated materials due to the formation of defect-free channels with plastic straining. The model parameters are obtained by fitting the simulation against experimental data from the literature.

Keywords Zircaloy-4 · Crystal plasticity · Irradiation · Damage

1 Introduction

Zirconium alloys are used to manufacture various core components of a nuclear reactor. Their low neutron absorption cross section, excellent mechanical properties and corrosion resistance are the primary reasons for which they are selected for these applications [1]. The core components of a nuclear reactor are subjected to high temperature and pressure and neutron irradiation which degrades their mechanical properties. Zirconium alloys are susceptible to various degradation mechanisms dur-

N. M. Jose (✉) · M. K. Samal · P. V. Durgaprasad
Reactor Safety Division, Bhabha Atomic Research Centre, Trombay, Mumbai 400085, India
e-mail: nevil@barc.gov.in

N. M. Jose · B. K. Dutta
Homi Bhabha National Institute, Anushaktinagar, Mumbai 400094, India

A. Alankar
Department of Mechanical Engineering, IIT Bombay, Powai, Mumbai 400076, India

ing their operation in nuclear reactors like irradiation creep, irradiation hardening, loss of ductility, embrittlement due to hydrogen absorption, etc. [2]. In this work, the numerical modelling of irradiation hardening and loss in ductility of Zircaloy-4 used to make cladding of the nuclear fuel rods, subjected to different dpa (dpa stands for displacement per atom due to irradiation by energetic particles [3]) levels of irradiation, is carried out using CPFEM. CPFEM takes into account the characteristics of the material like crystallographic texture, crystal structure and the type of slip systems [4]. Neutron irradiation inside a nuclear reactor leads to the formation of defects in materials like voids, dislocation loops, etc., which change the resistance of slip systems to plastic deformation thereby altering its mechanical properties. Thus, the crystal plasticity-based models are suitable to model the effects of irradiation on the mechanical properties of materials.

In the literature, there are various studies carried out by various researchers to model the irradiation effects on mechanical properties using CPFEM. Arsenlis et al. [5] have carried out the CPFEM modelling of irradiated copper using a dislocation and defect density-based crystal plasticity model. Krishna et al. [6] have carried out a simulation of irradiated copper using CPFEM analysing the behaviour of the material before and after yield point. Crystal plasticity simulations of irradiated bcc materials have been carried out by Patra et al. [7] and Krishna et al. [8]. Modelling of irradiation hardening of irradiated zirconium alloys has been carried out by Onimus et al. [9]. In all these aforementioned works, the mechanism for material property degradation considered is that of irradiation damage. Nie et al. [10] have modelled the irradiation effect on steels using a crystal plasticity model coupled with a damage model. This damage model is used to capture the damage mechanisms occurring in materials which are not due to irradiation, like the ductile damage mechanisms occurring in unirradiated materials. In this work, we have used a dislocation and defect density-based crystal plasticity model coupled with a ductile damage model, which accounts for the material failure due to void growth and coalescence.

2 Model

2.1 Crystal Plasticity Formulation

The crystal plasticity model used in this analysis is based on the works of Taylor [11], Hill et al. [12–14], Rice [15, 16], Asaro et al. [17], Pierce et al. [18] and Huang [19]. In this model, the total deformation gradient applied to the body is assumed to consist of two parts viz., an elastic deformation gradient $\mathbf{F}^e$ and a plastic deformation gradient $\mathbf{F}^p$ as given by

$$\mathbf{F} = \mathbf{F}^e \mathbf{F}^p \tag{1}$$

The plastic deformation gradient is assumed to be solely due to the slip occurring in the crystal as given by

$$\mathbf{F}^p = \mathbf{I} + \sum_{\alpha} \gamma^{\alpha} \left(\mathbf{s}^{\alpha} \otimes \mathbf{m}^{\alpha} \right) \tag{2}$$

In Eq. 1, $\mathbf{I}$ is the second-order identity tensor, γ^{α} is the shear strain on slip system and $\mathbf{s}^{\alpha}$ and $\mathbf{m}^{\alpha}$ are the unit vectors along the slip direction and slip plane normal in the intermediate configuration where only plastic deformation is assumed to occur. The rate of shear strain occurring on a slip system is given by a rate-dependent flow rule [20] given by

$$\dot{\gamma} = \dot{\gamma}_0 exp \left(\frac{-\Delta F}{kT} \left(1 - \left(\frac{\tau^{\alpha} - g^{\alpha \alpha}}{S_t} \right)^p \right)^q \right); if \ |\tau^{\alpha}| > g^{\alpha}$$
$$= 0; otherwise \tag{3}$$

In Eq. 3, $\dot{\gamma}_0$ is the reference shear strain rate, ΔF is the activation energy, k is the Boltzmann constant, T is the absolute temperature, τ^{α} is the resolved shear stress due to applied loading, g^{α} is the critical resolved shear stress (slip resistance) due to local short-range barriers and p and q are shape parameters for the activation energy function. The resolved shear stress (in the final configuration, after both $\mathbf{F}^e$ and $\mathbf{F}^p$ have been applied) is given by [16]

$$\tau^{\alpha} = \mathbf{m}^{(e)\alpha} \frac{\rho_0}{\rho} \mathbf{s}^{(e)\alpha} \tag{4}$$

Here, $\boldsymbol{\sigma}$ is the Cauchy stress, ρ_0 is the reference density, ρ is the current density and $\mathbf{s}^{(e)\alpha}$ and $\mathbf{m}^{(e)\alpha}$ are the vectors along slip direction and plane normal in the final configuration. The elastic constitutive law is given by [14]

$$\overset{\nabla *}{\sigma} + \sigma(\mathbf{I} : \mathbf{D}^e) = \mathbf{E} : \mathbf{D}^e \tag{5}$$

where $\mathbf{E}$ is fourth-order elasticity tensor, $\mathbf{D}^e$ is the rate of elastic stretching and $\overset{\nabla *}{\sigma}$ is the Jaumann stress rate. The hardening of the slip system with applied loading is given by [7, 8]

$$g^{\alpha} = \tau^{\alpha} + \mu b \sqrt{\sum_{\alpha} \left(h_{\alpha\beta} \rho_d^{\beta} + l_{\alpha\beta} \rho_{def}^{\beta} \right)}$$
$$\rho_d^{\alpha} = \rho_M^{\alpha} + \rho_I^{\alpha}$$
$$\rho_{def} = N_{def} d_{def} \tag{6}$$

Here, τ_0^{α} refers to the threshold slip resistance, μ is the shear modulus, b is the magnitude of the Burgers vector, ρ_d^{α} is the dislocation density, ρ_{def} is the defect density due to irradiation, N_{def} is the number density per unit volume of the defects and d_{def} is the average diameter of the defects. The coefficients $h_{\alpha\beta}$ and $l_{\alpha\beta}$ are the coefficients matrix for self and latent hardening of dislocations and defects, respectively. The dislocation density is assumed to be composed of two parts viz.,

mobile (ρ_M^α) and immobile dislocations (ρ_I^α). The evolution of dislocation density is given by the evolution of mobile and immobile dislocation densities as given by [7]

$$\dot{\rho}_M^\alpha = \left(\frac{k_{mul}}{bl_d} - \frac{2Rc}{b}\rho_M^\alpha - \frac{1}{b\lambda^\alpha} \right) |\dot{\gamma}^\alpha|$$

$$l_d = \frac{1}{\sqrt{\sum_M^\alpha}}; \ \lambda^\alpha = \frac{1}{\beta_{rho}\sqrt{\rho_M^\alpha + \rho_I^\alpha}} \tag{7}$$

$$\dot{\rho}_I^\alpha = \left(\frac{\beta_\rho}{b\lambda^\alpha} - k_{dyn}\rho_I^{alpha} \right) |\dot{\gamma}^\alpha|$$

Here, k_{mul} is the coefficient for mobile dislocation multiplication, R_c is the capture radius for the annihilation of dislocation dipoles, β_ρ is the coefficient of the rate of change of immobile dislocations (which in turn affects mobile dislocation density evolution through Eq. 7) and k_{dyn} is the coefficient for the elimination of immobile dislocations. The evolution of defect density is given by [8]

$$\dot{\rho^{\alpha_{def}}} = - \left(\sum_\alpha \rho_d^\alpha \right) A_s \rho_{def}^\alpha \frac{d_{def}^\alpha}{b^\alpha} |\dot{\gamma}^\alpha| \tag{8}$$

where $A_s = 2d_s S + \pi d_s^2$; $S = k \left(\sum_\alpha \rho_d^\alpha \right)^{-1/2}$. d_s is the standoff distance below which irradiation produced defects are captured by mobile dislocations and k is a material constant.

2.2 Ductile Damage Based on Void Growth

Rice and Tracey [21] have derived a void evolution-based damage parameter for ductile (elastic–plastic) material having voids subjected to tensile stresses. The damage parameter is a function of the void growth parameter, f given by

$$\dot{f} = \frac{\delta V}{V} = 3 \left(0.283 exp \left(\frac{1.5\sigma_m}{\sigma_{eq}} \right) \dot{\epsilon}_{eq}^p \right) \text{ if } \sigma_m > 0$$

$$\dot{f} = 0 \text{ if } \sigma_m < 0 \tag{9}$$

The current value of f is obtained by integrating the instantaneous value of the increment of f corresponding to each time step. In Eq. 9, σ_m is the mean stress obtained after carrying out the stress update corresponding to the plastic strain increments and σ_{eq} is the von Mises equivalent stress and is the equivalent plastic strain which are also obtained after the stress update as mentioned earlier. The degradation of slip system strength is calculated using the damage factor, D:

$$D = C_1.f.cosh \left(\frac{3\sigma_m}{2\sigma_{eq}} \right) \tag{10}$$

In Eq. 10, C_1 stands for the damage coefficient. This value of D is then used to calculate the effective applied resolved shear stress, as given by

$$\tau_{eff}^{\alpha} = \frac{\alpha}{(1 - D)} \tag{11}$$

In the simulations with damage model, this modified value τ_{eff} was used in Eq. 3, in place of τ^{α}.

3 Simulations

In this work, the crystal plasticity model was used to simulate the tensile deformation of a body having material properties of Zircaloy-4. The specimens were modelled to be oriented along the axial direction of the clad tube. The crystallographic texture of the specimen used for the model is shown in Fig. 1. The experimental data used in this work is used from the work of Farrel et al. [22]. The analysis has been carried out to simulate the stress–strain data of the irradiated (0.001 dpa and 0.8 dpa) and unirradiated tensile specimens. To carry out these analyses, the constitutive equations as described in the previous section were modelled in the crystal plasticity subroutine of Huang [19].

A polycrystalline Zircaloy-4 specimen was modelled having length of 25 mm, width 4 mm and thickness of 1 mm. The model was meshed with 6400 elements (Fig. 2) using 8 node solid brick elements. The size of each element was 250 × 250 × 250 microns. Each element in the model corresponds to a single grain. The orientation of each element (and thus each grain) was assigned randomly based on the crystallographic texture shown in Fig. 1. The four sets of slip system used in this model are Basal, Prismatic, Pyramidal $< a >$ and Pyramidal$< c + a >$ type, which are the major operating slip systems of the Zircaloy-4 material which has a hexagonal crystal symmetry. In order to carry out uniaxial tensile tests, at the bottom face of the specimen, all the degrees of freedom of displacement were constrained. At the top
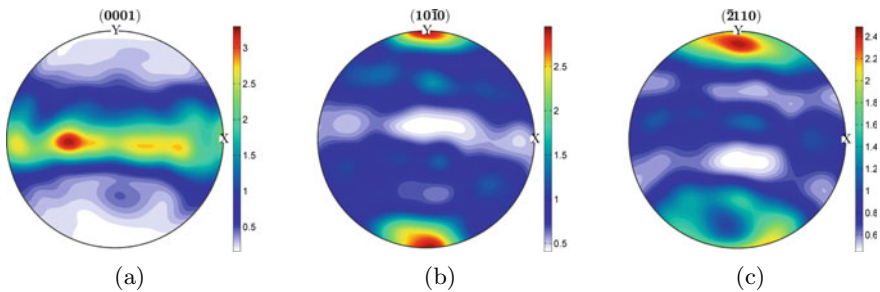
Fig. 1 Initial crystallographic texture of the specimens used for simulations

At the top face (Y=25 mm)
Uy=Applied Displacement
Ux=Uz=0

Y

Z   X

At the bottom face (Y=0)
Ux=Uy=Uz=0
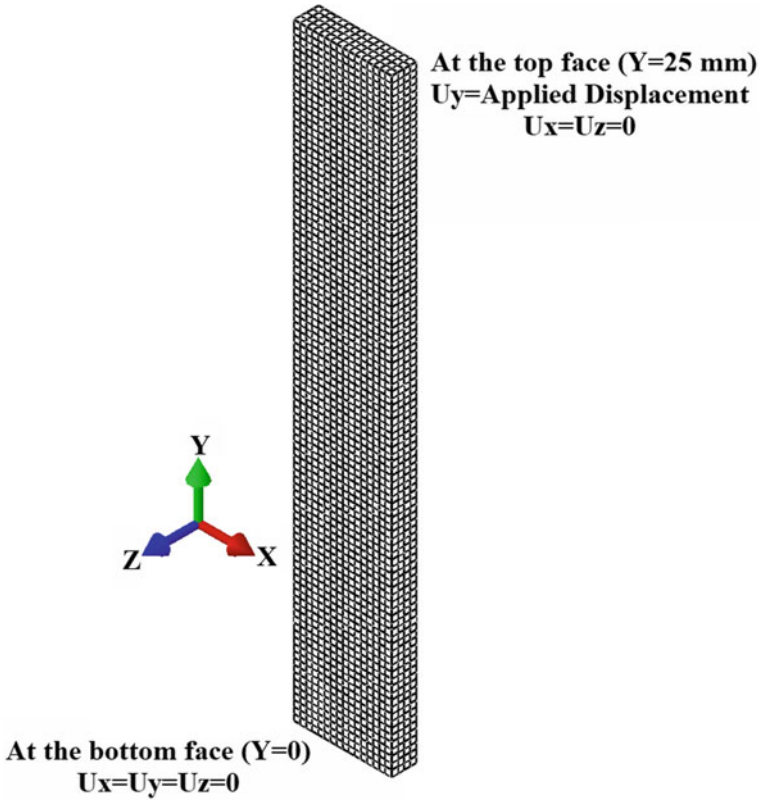
Fig. 2 Finite element mesh

face, displacement-controlled loading was applied along the axial direction of the specimen, while keeping the other two in plane, degrees of freedom of displacement were constrained. Since the side surfaces of a tensile specimen are traction-free surfaces, no constraints were applied on them.

As reported in the literature [22], the specimens were in the annealed state. So, the initial dislocation density of the mobile and immobile dislocations used in the analysis was 1.0e12 m^{-2}, which is typical of annealed Zircaloy-4 [23]. The value of the dislocation density was the same for all four sets of slip systems. For each set (modes) of the slip system, the dislocation density was divided by the no. of slip systems in that set. For example, for the basal slip system, each slip mode has a dislocation density of 1.0e12 m^{-2}/3, as the basal mode has three slip systems. The average defect density used for the simulation of irradiated specimens was taken from Farrel et al. [22]. The slip systems of all slip modes were assigned the same defect density. The value of the other parameters used in this analysis namely the flow rule parameters, dislocation density evolution parameters and defect density parameters, respectively, are reported in Tables 1, 2 and 3. The simulated yield strength depends

Table 1 Flow rule parameters

Dose (dpa)	$\dot{\gamma_0}$ (s^{-1})	τ_0 (MPa)				s (MPa)	F_0 ($\times \mu b^3$) (J)	T (K)	p	q
		Bas	Pri	Pyr $< a >$	Pyr $< c + a >$					
0	4.0e4	140.0	130.0	145.23	150.0	50.0	0.26	300	0.3	1.5
0.001	4.0e4	140.0	130.0	145.23	150.0	50.0	0.26	300	0.3	1.5
0.8	4.0e4	140.0	130.0	145.23	150.0	50.0	0.26	300	0.3	1.5

Table 2 Dislocation evolution parameters

Dose (dpa)	ρ_0 (m^{-2})	k_{mul}	k_{dyn}	R_c (m)[a]	R_c (m)[b]	β_i	
0	1.1e12	0.066	0.08	100.0	1.938e−9	3.64e−9	NA
0.001	1.1e12	0.09	0.08	100.0	1.938e−9	3.64e−9	0.1
0.8	1.1e12	0.09	0.08	100.0	1.938e−9	3.64e−9	0.1

[a] For bas, pris and pyr$< a >$
[b] For pyr$< c + a >$

Table 3 Defect evolution parameters

Dose (dpa)	N_{def} (m^{-3})	d_{def} (m)	d_s (m)
0	0	0	NA
0.001	1.2e22	1.2e−9	$1.5 \left(\dfrac{0.2}{\sqrt{\sum_\alpha \rho^\alpha}} \right)$
0.8	6.1e22	1.4e−9	$1.5 \left(\dfrac{0.2}{\sqrt{\sum_\alpha \rho^\alpha}} \right)$

on the threshold slip resistance (τ_0^α), dislocation densities and defect densities. The value of threshold slip resistance was adjusted in these simulations to match the experimental yield stress. To match the remaining part of the stress–strain data, the values of dislocation density evolution parameters were adjusted.

3.1 Behaviour of Unirradiated Zircaloy-4

The simulation results of unirradiated Zircaloy-4 are given in Fig. 3. The analysis was carried out with and without a damage model. The initial value of τ_0^α used was the smallest for the prismatic slip systems as the prismatic slip system was the most active slip system in the experiment [22]. It was found that in the simulation without the damage model, the fitted stress–strain curve matched only up to the ultimate stress. The Zircaloy-4 material has been reported to have a fracture surface consisting of voids [24] formed due to plastic instability. This type of fracture surface is typical for
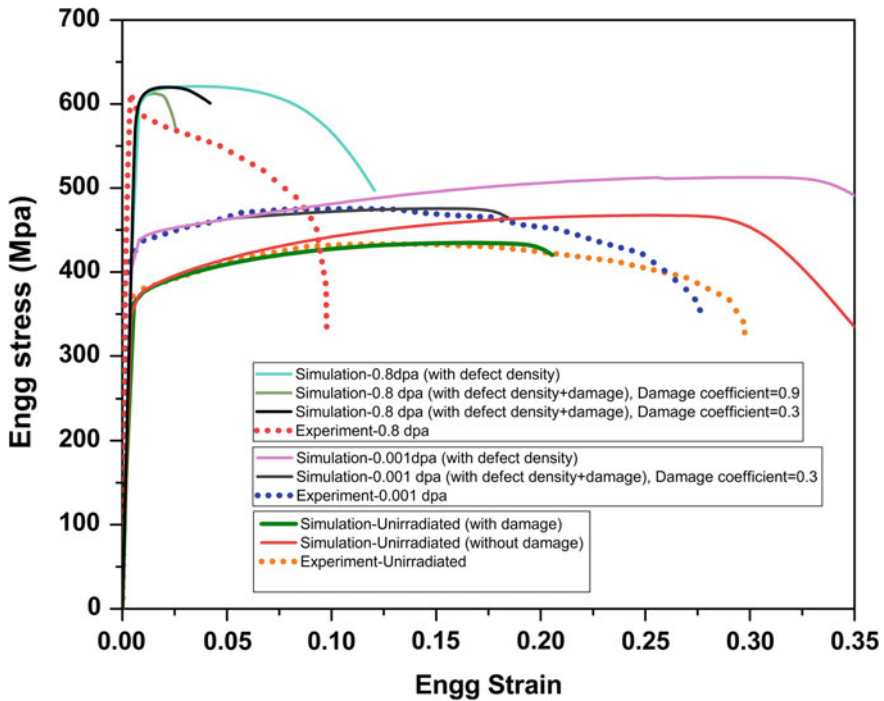
Fig. 3 Simulation results and comparison with experimental data

ductile materials [21]. To include this phenomenon in the material model, the damage model was included. With the damage model, it was found that the experimental stress–strain data could be simulated beyond the ultimate stress region as shown in Fig. 3.

3.2   Behaviour of Irradiated Zircaloy-4

The simulation of unirradiated zircaloy-4 was carried out for 0.001 dpa and 0.8 dpa. For carrying out the simulations, the defect density values given in Farrel et al. [22] were used. The initial dislocation densities were the same as for the unirradiated specimen. The defect density decreases with the applied loads, but its overall effect is the reduction in CRSS, as can be seen from Eq. 6. In the experiments [22], it was reported that in the irradiated specimens, the prismatic slip system was the most active slip system followed by a small amount of activity of pyramidal <a> slip system. Accordingly, defect density was allowed to evolve with plastic strain only for these two slip systems in the analysis. The analysis was carried with and

without a damage model as shown in Fig. 3. It was found that for the case of 0.001 dpa, without damage model, the simulation matched up to the ultimate stress only. This shows that the annihilation of defects was not sufficient for causing the drop in the stress–strain data after ultimate stress. With the use of a damage model in the simulation, the stress–strain data was matched beyond the ultimate stress. The analysis carried out for 0.8 dpa without a damage model did not simulate the sharp yield stress drop as seen in the experiments. This shows that the annihilation of defects was not sufficient to simulate the drop in stress–strain data at 0.8 dpa. The analysis was repeated with the damage model with a damage coefficient value of 0.3. But with this value of damage coefficient, the yield drop was not simulated. A high value of 0.9 for damage coefficient was used which simulated the sharp yield drop satisfactorily.

3.3 Evolution of Crystallographic Texture

The crystallographic texture of the specimens corresponding to axial strain at ultimate stress is given in the pole figures given in Figs. 4, 5 and 6. It was found from Figs. 4 and 5 that there was no appreciable difference in the crystallographic texture between the 0.001 dpa specimen and the unirradiated specimen. As evident from Fig. 6, the texture of specimen irradiated to 0.8 dpa, at ultimate tensile stress, is different from the texture of other two specimens given in Figs. 4 and 5. However, the initial texture given in Fig. 1 is almost unchanged in the case of the 0.8 dpa specimen. This must be due to the fact that the 0.8 dpa specimen failed without appreciable plastic strain (Table 4).
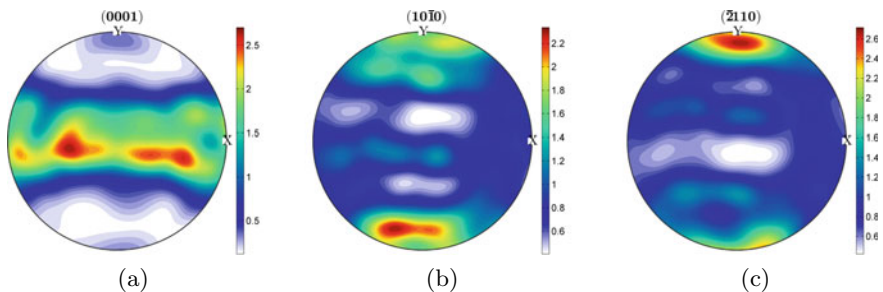
Fig. 4 Crystallographic texture of unirradiated specimens at axial strain of 0.16
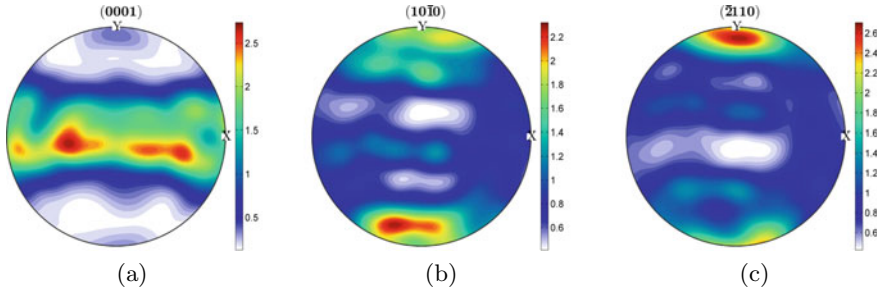
Fig. 5 Crystallographic texture of 0.001 dpa specimens at axial strain of 0.15
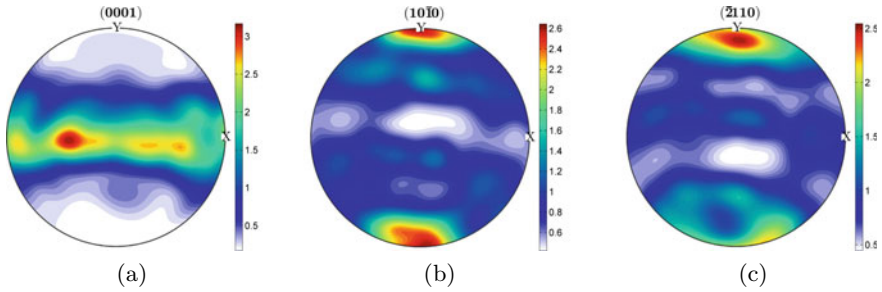
Fig. 6 Crystallographic texture of 0.8 dpa specimens at axial strain of 0.0405

Table 4 Hardening coefficients

Dislocation hardening coefficients	Defect interaction coefficients
$h_{\alpha\beta} = 0.13(\alpha = \beta); h_{\alpha\beta} = 0.026(\alpha \neq \beta)$	$l_{\alpha\beta} = 0.13(\alpha = \beta); l_{\alpha\beta} = 0.026(\alpha \neq \beta)$

4   Conclusions

It was found that the defect (produced due to irradiation) density evolution model alone was not sufficient to simulate the drop in the stress–strain data of the irradiated material. Thus, a damage model which can capture the damage mechanisms occurring due to plastic instability in the material was introduced. The change in texture observed was primarily dependent on applied strains. No appreciable change in texture was observed with irradiation.

References

1. Yau TL, Annamali VE (2016) Corrosion of zirconium and its alloys. Reference module in materials science and materials engineering. Elsevier, Amsterdam
2. Suri AK (2013) Material development for India's nuclear power program. Sadhana, Part 5 38: 859–895. Indian Academy of Sciences
3. Was GS (2016) Fundamentals of radiation material science, 2nd edn. Springer, Berlin
4. Montgomery R, Tomé C, Liu W, Alankar A, Subramanian G, Stanek, C (2017) Use of multiscale zirconium alloy deformation models in nuclear fuel behavior analysis. J Comput Phys 328(1):278–300
5. Arsenlis A, Wirth BD, Rhee M (2004) Dislocation density-based constitutive model for the mechanical behaviour of irradiated Cu. Philos Mag 84(34):3617–3635
6. Krishna S, Zamiri A, De S (2010) Dislocation and defect density-based micromechanical modeling of the mechanical behavior of fcc metals under neutron irradiation. Philos Mag 90(30):4013–4025
7. Patra A, McDowell DL (2012) Crystal plasticity-based constitutive modelling of irradiated bcc structures. Philos Mag 92:861–887
8. Krishna S, Zamiri A, De S (2011) A temperature and rate-dependent micromechanical model of molybdenum under neutron irradiation. Mech Mater 43:99–110
9. Onimus F, Bono M, Verhaeghe B, Soniak A, Pilvin P (2020) Pilvin: polycrystalline modeling of the behavior of neutron-irradiated recrystallized zirconium alloys during strain path change tests. Int J Plast 134:102835
10. Nie J, Liu Y, Xie Q, Liu Z (2019) Study on the irradiation effect of mechanical properties of RPV steels using crystal plasticity model. Nucl Eng Technol 51:501–509
11. Taylor GI (1938) Plastic strain in metals. J Inst Metals 62:307
12. Hill R (1966) Generalized constitutive relations for incremental deformation of metal crystals by multislip. J Mech Phys Solids 14:95
13. Hill R (1967) The essential structure of constitutive laws for metal composites and polycrystals. J Mech Phys Solids I5:79
14. Hill R, Rice JR (1972) Constitutive analysis of elastic-plastic crystals at arbitrary strain. J Mech Phys Solids 20:401
15. Rice JR (1970) On the structure of stress-strain relations for time-dependent plastic deformation in metals. J Appl Mech 37:728
16. Rice JR (1971) Inelastic constitutive relations for solids: an internal-variable theory and its application to metal plasticity. J Mech Phys Solids 19:433
17. Asaro RJ (1983) Crystal plasticity. J Appl Mech 5O:921
18. Peirce D, Shih CF, Needleman A (1984) A tangent modulus method for rate dependent solids. Comput Struct 18:875
19. Huang Y (1991) A user-material subroutine incorporating single crystal plasticity in the Abaqus finite element program. Division of Applied Sciences Harvard University Cambridge, Massachusetts
20. Kocks UF, Argon AS, Ashby MF (1975) Thermodynamics and kinetics of slip, vol 19. Progress in materials science. Pergamon Press, Oxford
21. Rice JR, Tracey DM (1969) On the ductile enlargement of voids in triaxial stress fields. J Mech Phys Solids 17(3):201–217
22. Farrell K, Byun TS, Hashimoto N (2004) Deformation mode maps for tensile deformation of neutron-irradiated structural alloys. J Nucl Mater 335:471–486
23. Thool K, Patra A, Fullwood D, Krishna KVM, Srivastava D, Samajdar I (2020) The role of crystallographic orientations on heterogeneous deformation in a zirconium alloy: a combined experimental and modeling study. Int J Plast
24. Cockeram BV, Chan KS (2009) In situ studies and modeling the fracture of Zircaloy-4. J Nucl Mater 393:387–408

Investigation into Hydrogen-Induced Blister Cracking and Mechanical Failure in Pipeline Steels

Vishal Singh, Kanwer Singh Arora, and Dhiraj K. Mahajan

Abstract This work aims to investigate the role of hydrogen-induced blisters on tensile and fatigue damage of pipeline steels (X65 and X80). The electrochemical method of hydrogen charging is employed to simulate hydrogen-induced blister formation. Similar hydrogen charging conditions resulted in different sizes, shapes, and numbers of blisters in both types of steels. DIC analysis coupled with in-situ tensile testing confirmed the blisters as potential stress concentration sites. Synergistic action of hydrogen and stress concentration around these blister-type notches intensified the overall mechanical damage of material under the hydrogen atmosphere. The size and relative position of blisters are significant factors to degrade the mechanical performance of investigated pipeline steels.

Keywords Hydrogen embrittlement · Blisters · Pipeline steels · Fatigue damage

1 Introduction

American Petroleum Institute (API 5L) graded pipeline steels are an efficient means for long-distance bulk transportation [1]. The electrochemical evolution of hydrogen atoms, a byproduct of cathodic over-protection and other corrosion processes, makes these pipeline steels prone to hydrogen-assisted degradation [2]. Hydrogen-induced cracking and blister formation based upon pressure theory (reported by Zapffe and Sims [3]) are abundantly reported as one of the major threats to the integrity of pipeline steels. Material imperfections like non-metallic inclusions, grain boundaries, dislocations, and hard phase constituents act as potential traps for hydrogen [4, 5]. Hydrogen trapped at these imperfections can recombine to hydrogen gas. This hydrogen gas of critical amount can lead to void creation (filled by dihydrogen

V. Singh · D. K. Mahajan (✉)
Ropar Mechanics of Materials Laboratory, Department of Mechanical Engineering, Indian Institute of Technology Ropar, Rupnagar, Punjab 140001, India
e-mail: dhiraj.mahajan@iitrpr.ac.in

K. S. Arora
Research and Development, TATA Steel, Jamshedpur 831001, India

gas), and, eventually, blister formation from subsurface cracks can take place. Blisters formation can be perceived if hydrogen pressure in the voids induces a stress in excess to yield strength of material [6]. The blistering phenomenon based upon superabundant vacancies that combine with hydrogen to generate hydrogen-vacancy clusters is well supported by various latest characterization techniques [7]. Other than hydrogen atmosphere, blistering gets influenced by microstructural and loading conditions [8]. These hydrogen (pre-charging by electrochemical method or by high-pressure hydrogen atmosphere) induced blisters can act as potential stress concentration sites and can alter the stress state locally. The role of these blisters on the structural integrity in terms of tensile and fatigue behavior of two API pipeline steel grades is discussed in the present paper.

2   Experimental Procedure

The chemical composition of investigated pipeline steel grade X65 and X80 is shown in Table 1. To simulate a hydrogen atmosphere, specimens were exposed to an electrolyte containing $1 \, N \, H_2SO_4$ solution (along with 1.4 g/L Thiourea as recombination poison) under a constant current density of 20 mA/cm^2 for a period of 4 h. Specimen as cathode and platinum mesh as anode were maintained during hydrogen charging. Specifications along with the preparation method of samples used for tensile and fatigue (with pre-induced notch sample for fatigue) testing are discussed elsewhere [9].

Optical, Scanning Electron Microscopy (SEM) and Energy Dispersive X-ray Spectroscopy (EDS) analysis were conducted to reveal microstructural convoluted details. All the tensile tests were conducted at a strain rate of $5 \times 10^{-5} \, s^{-1}$. Fatigue experiments were performed with R-ratio and frequency of 0.1 and 35 Hz, respectively, in both types of steels under hydrogen charged and uncharged conditions. Whereas stress ranges of 315 MPa and 400 MPa were used for X65 and X80 steel, respectively. Digital Image Correlation (DIC) coupled with in-situ tensile testing under SEM atmosphere was conducted to reveal the role of blisters on local stress/strain state in the observed material microstructure.

Table 1 Chemical composition (in wt. %) of X65 and X80 pipeline steels (balance is Fe)

Element	C	S	P	Mn	Si	Cr	Ni	Mo	Cu	Al	V	Nb
X65	0.054	0.001	0.012	1.5	0.23	–	–	0.086	–	0.029	0.035	0.057
X80	0.04	0.001	0.012	1.8	0.24	0.05	0.19	0.18	0.18	–	0.018	0.048

3 Results and Discussion

3.1 Effect of Electrochemical Hydrogen Charging on Blister Formation

Details regarding the starting microstructure of both types of steels can be obtained from [10]. Hydrogen charging resulted in blister formation in both types of steels (see Fig. 1a, b). Most of the blisters in both types of steels were accompanied by the cracks on their wall, termed as blister wall cracks (BWC). EDS analysis confirmed the presence of Al–Si–O-rich inclusions along the BWC in X65 steel (see Fig. 2). Similar types of inclusions were observed in X80 steel. Only a few discrete numbers of blisters nearly circular in shape with a maximum size of ~1500 um were observed in X80 steel (one such large size blister is shown in Fig. 1a). On the contrary, multiple oval-shaped blisters but comparatively small in size (max. size ~ 500 um) were observed in X65 steel (see Fig. 1b). Increased number of blisters in X65 (ferrite–pearlite) steel than in X80 (ferrite–bainite) steel can be attributed to easy blister nucleation in ferrite–pearlite than in ferrite–bainite microstructure as earlier reported by Hejazi et al. [11]. However, as high-strength steels are more susceptible to hydrogen embrittlement, once a blister nucleated, X80 steel microstructure favored the easy growth of blisters.
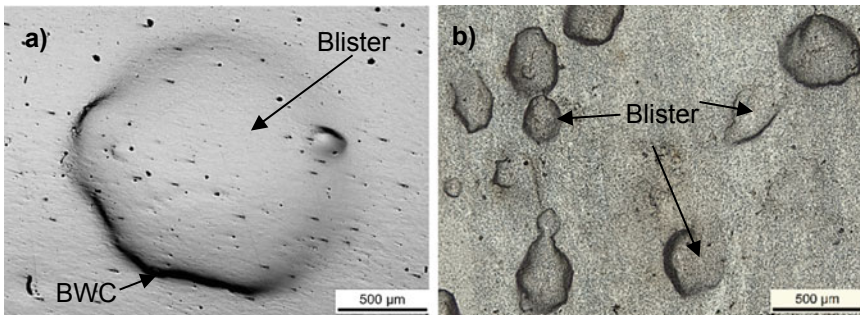

Fig. 1 Optical images of blisters formation after hydrogen charging in **a** X80 and **b** X65 steel. Crack at the wall of blister is marked as BWC
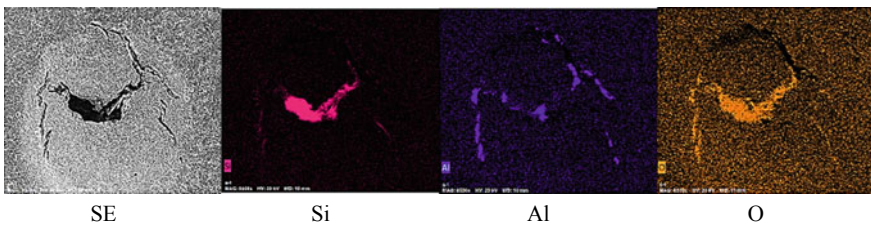

Fig. 2 EDS analysis of blister cracking along the Al–Si–O inclusions in X65 steel

3.2 Effect of Blisters on Tensile Behavior

Tensile curves for uncharged and hydrogen charged steel samples are presented in Fig. 3a. An increase in yield strength after hydrogen charging was observed in both types of steel specimens. Wu and Kim [12] reported similar behavior in low alloy steels due to the pinning effect of solute hydrogen to the dislocations and/or impediment of moving dislocations to cross slip. Nearly no significant effect of hydrogen on ultimate tensile strength was observed in both types of steel specimens.

In X65 steel, uniform elongation before and after hydrogen charging remained the same; however, a decrease in total elongation was observed. Meanwhile, both uniform and total elongation deteriorated significantly after hydrogen charging in X80 steels. Post-tensile fractographic analysis revealed a signature of ductile fracture in uncharged specimens of both types of steels (see Fig. 3b, d). Meanwhile, tensile fractographs of hydrogen charged specimens (Fig. 3c, e) revealed a decrease in an overall reduction in area (in comparison to uncharged specimen) in both types of steels, which is a typical signature of hydrogen-induced embrittlement [6]. Sites marked with arrows in Fig. 3c, e are showing the blisters decohesion from the material matrix during tensile loading. Only two such decohesion sites were present in X80 steel specimen (Fig. 3c), whereas multiple decohesion sites but comparatively small in size were observed in X65 steel (Fig. 3e). This was in agreement with the observed difference in size and blister density of both types of steels.

Hydrogen-induced damage in such types of steels has been discussed abundantly in literature and hydrogen concentration-dependent hydrogen embrittlement (HE) mechanisms primarily HELP (hydrogen-enhanced localized plasticity) under low hydrogen concentration and/or HEDE (hydrogen-enhanced decohesion) under high
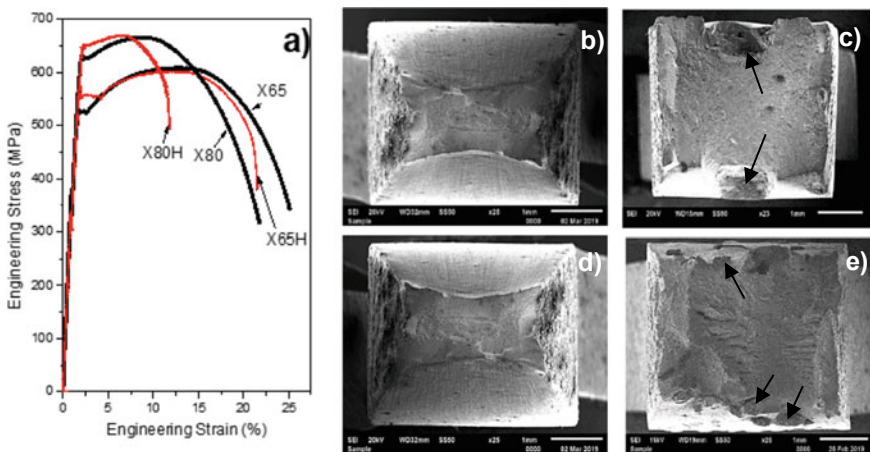

Fig. 3 **a** Tensile curves for X80, X80H, X65, and X65H; (**b**) and (**c**) are tensile fractographs of X80 and X80H, respectively; and (**d**) and (**e**) are tensile fractographs of X65 and X65H respectively. H: Hydrogen charged
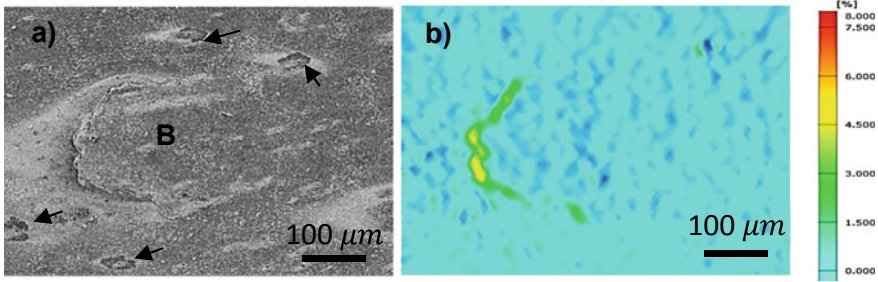
Fig. 4 DIC analysis of X65 steel specimen. **a** SEM image of blister used as a reference location for DIC analysis. **b** DIC image showing localized strain along blister wall (scale corresponds to strain values on DIC map). Arrows indicating small size blisters with no significant strain partitioning around them. B indicates blister causing significant strain partitioning

hydrogen concentration have been reported. The scope of the present work was to investigate the role of hydrogen pre-charging-induced blisters on the mechanical failure of pipeline steels. Hence, to get more insight into the role of blisters, DIC (coupled with the in-situ tensile under SEM) analysis was conducted. Results obtained from the DIC analysis revealed localized strain partitioning around these blister-type defects (see Fig. 4). Koyama et al. [13] reported for low alloy dual-phase steels that hydrogen does not affect the uniform elongation regime but causes the ductility to deteriorate mainly in the post-necking regime. This means that HE mechanisms get intensified due to localization of strain during necking, and microstructural feature causing strain localization plays a key role in hydrogen-induced degradation. As observed from DIC analysis, hydrogen blisters were preferential sites for strain localization and hence were concluded to affect the tensile properties under hydrogen atmosphere significantly.

Similar uniform elongation but a reduction in fracture elongation after hydrogen charging in X65 steels was consistent with the observations of Koyama et al. [13]. This also indicates no special role of small size blisters on the tensile behavior (can also be seen from Fig. 4). However, the size of the blisters in X80 was much larger than X65 steels, so the strain localization around the blisters in X80 steels was presumed to be more significant. Decohesion at the blister walls due to strain partitioning can reduce the incubation period for necking as well as for post-necking hydrogen caused degradation. This phenomenon was more significant in the X80 steel (due to large blister size) and hence, a substantial loss of uniform as well as total elongation after hydrogen charging was observed. A critical combination of stress concentration and hydrogen content intensifies the localized micro-plastic damage by hydrogen concentration-dependent activated HE mechanism [9]. Stress concentration around these blisters can attract more hydrogen during external loading (due to high hydrostatic stress) and hence can alter the HE-based degradation significantly.
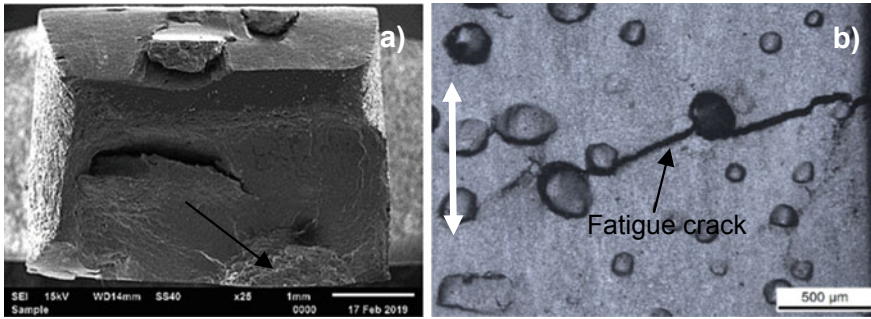
Fig. 5 **a** Fractograph showing fatigue crack initiated from blister (marked by black arrow) in X80 steel and **b** fatigue crack path deflected by blisters in X65 steel (white arrow showing loading direction)

3.3 Effect of Blisters on Fatigue Behavior

In our previous paper [9], short fatigue crack growth framework was used to highlight the role of blister wall cracks to accelerate fatigue crack growth. To keep a track on crack initiation and its propagation during fatigue loading cycles, samples used for fatigue analysis were containing a through-thickness notch of size ~50 um. In X65 steels, crack initiated always from the pre-notched area. On the contrary, crack initiation other than the notch area was observed frequently in X80 steels. This difference was due to the difference in the size of the blisters in both types of steel specimens. As blisters in X80 steel were large comparative to X65 steel, these large size blisters were acting as preferential sites for crack initiation in comparison to pre-induced notch. SEM analysis of one such specimen of X80 steel in which fatigue crack is initiated from a large blister (instead of notch area) is presented in Fig. 5a.

As reported previously [9], coalescence of propagating short fatigue crack with BWC results in a rapid increase in the crack length, i.e., reduces the number of cycles for crack propagation to the equivalent crack length. Apart from that, blisters were found to deflect the crack path significantly. Figure 5b is also an extension of the same work (X65 steels) and clearly indicates the role of blisters on fatigue crack path. The blisters act as potential stress concentration sites and hence can deflect the crack path by altering the localized stress state in materials. In X65 steels, the size of blisters was comparatively small but the blister density was high, and hence the proneness to the coalescence of crack with blisters was also high. The large size of blisters in X80 steel was dominating the crack initiation, whereas the density of randomly distributed small size blisters was having a prominent effect on the propagation behavior of fatigue crack in X65 steel. All the specimens tested for tensile and fatigue were tested immediately after hydrogen charging, and hence the effect of hydrogen as commonly known HE mechanisms such as HELP and/or HEDE mechanism was not excluded during investigating the role of blisters, which otherwise can be done by baking the samples after hydrogen charging. Research in

this direction along with using $\sqrt{\text{area}}$ parameter method on blister-type defects is in progress.

4 Conclusions

This study evaluated the role of hydrogen-induced blister cracking on tensile and fatigue behavior of X65 and X80 steels. Large size blisters but few in numbers were observed in X80 steel, whereas multiple but comparatively small size blisters were observed in X65 steel. Blisters are preferential sites for strain localization and can alter the local stress state considerably. Decohesion along the wall of large size blisters reduced the uniform and total elongation significantly in X80 steel. During fatigue loading also, large size blisters were found to be preferential sites for crack initiation (as observed in X80 steels). However, multiple randomly distributed small size blisters as observed in X65 steels affected the fatigue crack propagation behavior significantly. The size and relative position of blisters are significant factors to govern the overall mechanical performance of investigated pipeline steels.

References

1. Mariana C, De O, Rodrigo MF, Heloísa AA, Eduardo NC (2018) Corrosion behavior of API 5L X65 steel subject to plastic deformation. J Mater Res Technol 7:314–318
2. Ohaeri E, Eduok U, Szpunar J (2018) Hydrogen related degradation in pipeline steel: a review. Int J Hydrog Energy 43:14584–14617
3. Zapffe C, Sims C (1941) Hydrogen embrittlement, internal stress and defects in steel. TMS-AIME 145:225–232
4. Rajwinder S, Vishal S, Aman A, Dhiraj KM (2020) In-situ investigations of hydrogen influenced crack initiation and propagation under tensile and low cycle fatigue loadings in RPV steel. J Nucl Mater 529
5. Dhiraj KM, Randhir S, Yashpal S, Rajwinder S, Kanwar SA, Mahadev S, Gurmeet S (2017) Study of hydrogen embrittlement of API X65 & X80 pipeline steels using short fatigue cracks. CORCON 2017, Mumbai, India
6. Zhang L, Shen H, Lu K, Cao W, Sun Y, Fang Y, Xing Y, Du Y, Lu M (2017) Investigation of hydrogen concentration and hydrogen damage on API X80 steel surface under cathodic overprotection. Int J Hydrog Energy 42:29888–29896
7. Griesche A, Dabah E, Kannengiesser T, Kardjilov N, Hilger A, Manke I (2014) Three-dimensional imaging of hydrogen blister in iron with neutron tomography. Acta Mater 78:14–22
8. Ayadi S, Charles Y, Gaspérini M, Caron Lemaire I, Da Silva Botelho T (2017) Effect of loading mode on blistering in iron submitted to plastic prestrain before hydrogen cathodic charging. Int J Hydrog Energy 42:10555–10567
9. Vishal S, Rajwinder S, Kanwar SA, Dhiraj KM (2019) Hydrogen induced blister cracking and mechanical failure in X65 pipeline steels. Int J Hydrog Energy. https://doi.org/10.1016/j.ijhydene.2019.06.098
10. Vishal S, Rajwinder S, Amanjot S, Dhiraj KM (2018) Tracking hydrogen embrittlement using short fatigue crack behavior of metals. Procedia Struct Integr 13:1427–1432

11. Hejazi D, Saleh A, Haq A, Dunne D, Calka A, Gazder AA, Pereloma EV (2014) Role of microstructure in susceptibility to hydrogen embrittlement of X70 microalloyed steel. Mater Sci Forum 783–786:961–966
12. Wu XQ, Kim IS (2003) Effects of strain rate and temperature on tensile behavior of hydrogen-charged SA508 Cl.3 pressure vessel steel. Mater Sci Eng A 348:309–318
13. Koyama M, Tasan CC, Akiyama E, Tsuzaki K, Raabe D (2014) Hydrogen-assisted decohesion and localized plasticity in dual-phase steel. Acta Mater 70:174–187

Fracture Evaluation of a High-Pressure Gas Bottle by J-Integral Based Failure Assessment Diagram Using Ansys

A. K. Asraff, K. Anjali Raj, V. Viswanath, S. Vivek, and Aneena Babu

Abstract Metallic pressure vessels are used in launch vehicles in the form of propellant tanks, high-pressure gas bottles, etc. Different metals like Titanium alloys, Aluminium alloys, steels, etc. are used for the fabrication of these pressure vessels which may contain cracks, either inherently present in the base material or introduced during fabrication processes such as welding. These cracks have the potential to propagate rapidly under tensile stresses during pressure testing or during service condition loadings leading to its catastrophic failure. It is required to study the effect of these cracks in pressure vessels through the application of linear elastic as well as elastic-plastic fracture mechanics principles. The Failure Assessment Diagram (FAD) concept is used to evaluate whether a crack may cause structural failure. The FAD technique accounts for both brittle and ductile failure modes of the cracked structure using two ratios: Load ratio (L_r) and Brittle fracture ratio (K_r). In this work, the variation of fracture parameters such as stress intensity factors and J-integral values along the crack front in a high-pressure gas bottle containing part through crack used in an ISRO developed satellite launch vehicle has been studied using ANSYS/Workbench (18.1). The objective of this paper is to ensure the structural integrity of the above gas bottle using J-integral based FAD. Both elastic and elastic-plastic fracture analysis of the gas bottle has been done. The ultimate pressure carrying capacity of the structure in the presence of a specific crack has been calculated directly from the FAD. The mode of failure of the structure is also predicted from the above diagram.

Keywords Failure assessment diagram · Stress intensity factor · J integral · Part through crack

A. K. Asraff · S. Vivek
Mechanical Design and Analysis Entity, LPSC/ISRO, Valiamala, Thiruvananthapuram 695547, India

K. Anjali Raj (✉) · A. Babu
Mar Baselios College of Engineering and Technology, Thiruvananthapuram 695015, India

V. Viswanath
Structural Mechanics Division, Mechanical Design and Analysis Entity, LPSC/ISRO, Valiamala, Thiruvananthapuram 695547, India

1 Introduction

High pressure gas bottles are one of the major structural components of any launch vehicle system to carry helium at room temperature as well as cryogenic temperatures. These bottles are mainly designed for internal pressure loading. There may be crack or crack-like defects present in these structures which appear during various stages like fabricating, processing, and assembling processes. Due to application of repeated loads or due to a combination of loads and environmental attack, these cracks might grow with time and thus increases the stress concentration induced by it leading to crack initiation and propagation. Hence presence of defects results in reduction of strength of structures and catastrophic failure.

Fracture mechanics is the field of mechanics dealing with the study of the propagation of cracks in materials [15]. Fracture failures are generally dangerous and costly when encountered in pressure vessels used for aero-structures, missiles and launch vehicles, automobile chassis, railway bridges, ships, and pipelines. Fracture mechanics can be divided into Linear Elastic Fracture Mechanics (LEFM) and Elastic Plastic Fracture Mechanics (EPFM). LEFM gives excellent results for brittle-elastic materials like high-strength steel, glass, ice, concrete, etc., while EPFM is well suited for ductile materials like low carbon materials like steel, stainless steel, certain aluminium alloys, and polymers [16].

Newman and Raju [1] presented stress intensity factor coefficients for a wide range of semi-elliptical surface cracks at both the inner and outer surfaces of a cylinder. The crack surfaces were subjected to four stress distributions: uniform, linear, quadratic, and cubic. It was observed that the maximum influence of the coefficients, occurred at maximum depth points except for semi-circular surface crack in which maximum value was obtained at surface points. The configuration of surface crack is given in Fig. 1.

Kumar et al. [2] extended the analysis procedures already available for brittle-elastic materials to tough and ductile steels used in the construction of pressurized components. These new elastic-plastic methods describe more accurately the behavior of ductile materials.

Fig. 1 Plate with surface crack
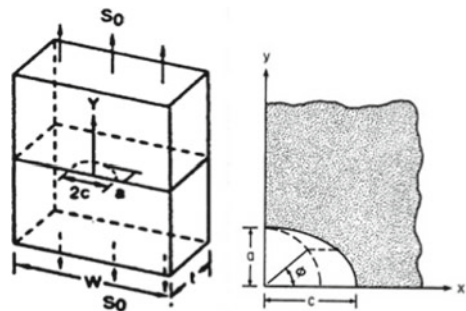
Failure Assessment Diagram (FAD) is an approach equally applicable for low, medium, and high ductile materials. This elegant concept can predict failure of a component due to brittle as well as ductile fracture. Dowling and Townley [3] first proposed a two parameter (limit analysis-fracture mechanics) based approach which combines both limiting cases of failure by brittle fracture on one hand and plastic collapse, if the plastic limit load is attained, on the other hand. The transition region between the fracture region and the limit load region was based on the strip-yield model of Bilby et al. [4]. Harrison et al. [5] developed the concept of FAD and this came to be known as the R6 [6] procedure. They introduced two parameters: toughness ratio, K_r (K/K_{mat}) and stress ratio or load ratio, S_r (F/Fy). The condition $K_r = 1$ denotes LEFM fracture. The J-integral based FAD was first introduced by Chell [7]. He proposed that the K_r ratio can be written in terms of $\sqrt{(J_{el}/J)}$. This criterion is dependent on material and component geometry. Since the J integral is one of the best parameters to describe elasto-plastic fracture mechanics, instead of K_{IC}, J based solutions are used. The detailed procedure for generation of the FAD is stated in API 579 [8] and BS 7910 [9]. Tonkovic et al. [10] performed nonlinear finite element analyses to obtain the plastic limit and collapse loads for external axial semi-elliptical cracks in steam generator tubes under internal pressure. It was shown that compared to existing solutions, the proposed analytical approximation of the limit and collapse pressures provides very useful tools for assessing pressurized tube integrity.

The FAD is used for the evaluation of crack-like flaws in components. The FAD approach was adopted because it provides a convenient, technically based method to provide a measure for the acceptability of a component with a crack-like flaw when the failure mechanism is measured by two distinct criteria: unstable fracture and plastic collapse. Unstable fracture usually controls failure for flaws in components when the material of construction is in a brittle state, i.e., low toughness, and plastic collapse typically controls failure for large flaws if the material of construction is in a ductile state, i.e., high toughness. In the analysis of crack-like flaws, the results from a stress analysis, stress intensity factor and reference stress solutions, the material strength, and fracture toughness are combined to calculate a toughness ratio, K_r, and load ratio, L_r. These two quantities represent the coordinates of a point that is plotted on a two-dimensional FAD to determine acceptability. Figure 2 shows the default FAD [11, 12]. The FAD curve's shape accounts for the interaction between brittle fracture and plastic collapse. L_r, K_r assessment points inside the FAD curve are predicted to be stable (green dots in Fig. 2). Points on the FAD curve are critical (yellow dot) and are on the verge of failure, which can be useful to determine predicted critical crack sizes. Points outside the FAD curve, above the FAD or to the right of L_{rmax}, are predicted to be unstable (red dots).

Ismail et al. [13] reviewed the use of ANSYS FE program in analyzing the engineering structures containing cracks. This code has a fracture mechanics module capable of modeling different crack geometries easily and efficiently. Two approaches are used to calculate the stress intensity factors (SIF)—the Displacement Extrapolation Method (DEM) and Interaction Integral Method (IIM). The Virtual Crack Closure Technique (VCCT) is used to calculate Energy Release Rate (ERR). Based
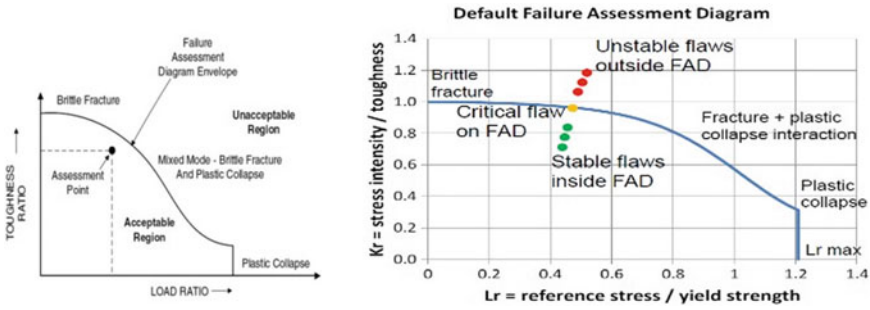
Fig. 2 Default FAD plot for evaluating cracks for failure

on the comparison, it is found that SIF evaluated through DEM, VCCT, and J-integral techniques have good comparison with the results obtained from open literature. Kumar et al. [14] studied the evaluation of SIF in plates containing part through crack using FE analysis in ANSYS software.

2 Methodology

2.1 Details of FE Model of Gas Bottle with Part Through Crack

The gas bottle investigated in this paper is used to store high-pressure helium gas that has an internal diameter of 608.2 mm and thickness of 11.2 mm. It is made of an aluminium alloy having tensile yield strength of 276 MPa, modulus of elasticity of 70,000 MPa, Poisson's ratio of 0.33, and plane strain fracture toughness of 900 MPa$\sqrt{}$mm. Only 40° sector of the gas bottle was modeled to reduce computation time. The gas bottle was fixed at one end and free elsewhere during pressure testing. Symmetric boundary conditions were provided on side faces. Both linear and nonlinear analyses were carried out using ANSYS/Mechanical Workbench (Version 18.1).

The maximum operating pressure inside the bottle is 10 MPa, proof test pressure is 15 MPa (a proof pressure test is done to check for the workmanship of the gas bottle, one of the design requirements being that at proof pressure the gas bottle should not exhibit detrimental yielding), and ultimate pressure is 20 MPa (the other design requirement is that at ultimate pressure the gas bottle should not fail). Internal pressure of 23 MPa was applied on the gas bottle. Figure 3 shows the solid model of the gas bottle used for the analysis. An internal semi-elliptical part through crack of size 3.5 × 3.5 mm (a × c) was introduced in the minimum thickness region of the gas bottle. Figure 4 shows the FE mesh details for the sector of gas bottle. The
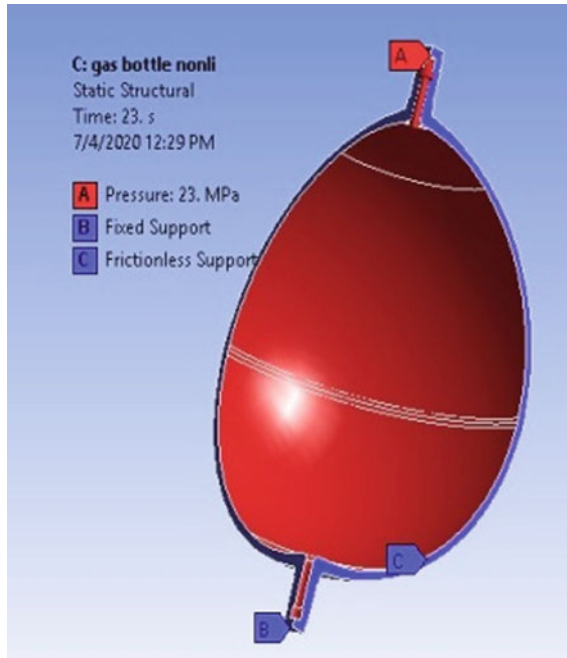
Fig. 3 Solid model of sector of gas bottle
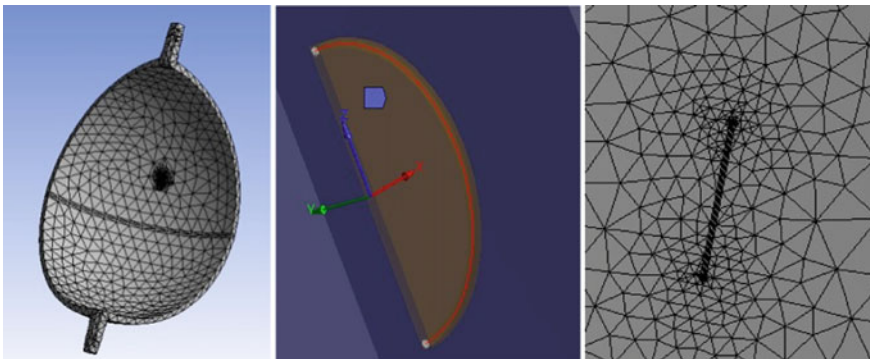
Fig. 4 FE mesh used for the sector of gas bottle

linear elastic and elasto-plastic fracture analysis of the gas bottle induced with semi-elliptical crack was carried out and different fracture parameters including SIF, J elastic, and J plastic were obtained. Also the J based FAD was constructed.

3   Results and Discussions

3.1   Linear Elastic Fracture Analysis

An internal pressure of 23 MPa was given which was found to be the last converged pressure and is termed as the collapse pressure. After introducing the semi-elliptical crack with the above said crack details, fracture analysis was done. SIF KI and J elastic (Jel) values were evaluated. Figures 5 and 6 show the variation of KI and J elastic along the crack front. Since the aspect ratio (a/c) of the crack chosen was equal to one, the maximum values for KI and Jel were observed at the surface points of the crack. The maximum value for KI and Jel obtained are 717.88 MPa$\sqrt{}$/mm and 6.4929 N/mm at 23 MPa pressure.
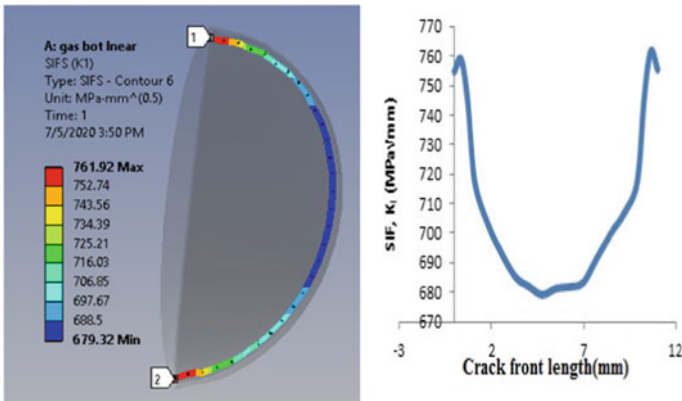
Fig. 5   Variation of K_I along crack front
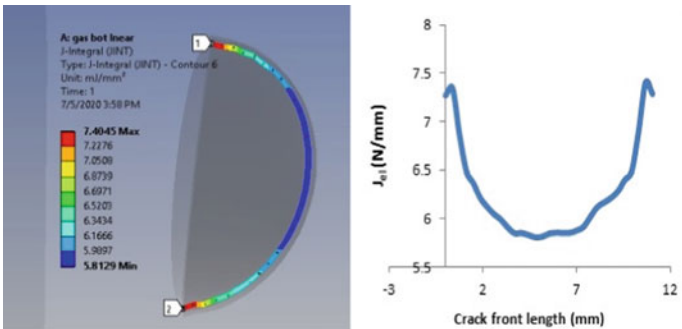
Fig. 6   Variation of J_{el} along crack front

3.2 Elasto Plastic Fracture Analysis

In the nonlinear fracture analysis, the stress-strain graph (Fig. 7) of aluminium alloy which is obtained from the previously conducted experimental results was taken. The number of substeps provided was 23 (from 0 to 23 MPa) and the nonlinear fracture analysis was done to obtain the total J (J_{tot}) against applied pressure. Therefore, J plastic (J_{pl}) is the difference between total J and elastic J which is obtained from nonlinear and linear fracture analysis, respectively. Figure 8 shows the variation of total J (J_{tot}) along the crack front.
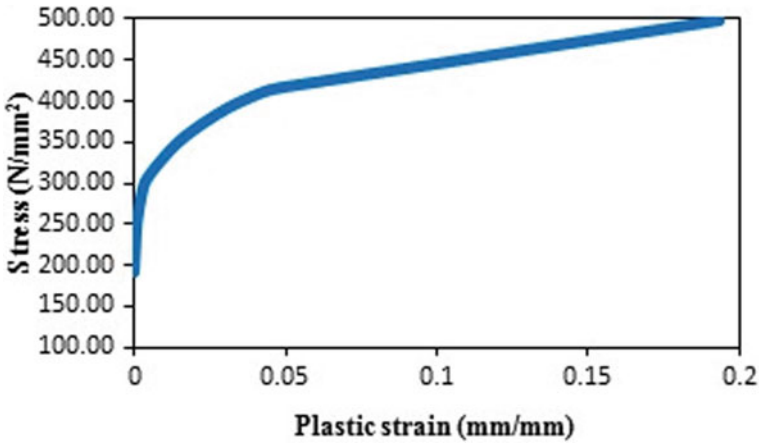
Fig. 7 Stress-strain graph of aluminium alloy
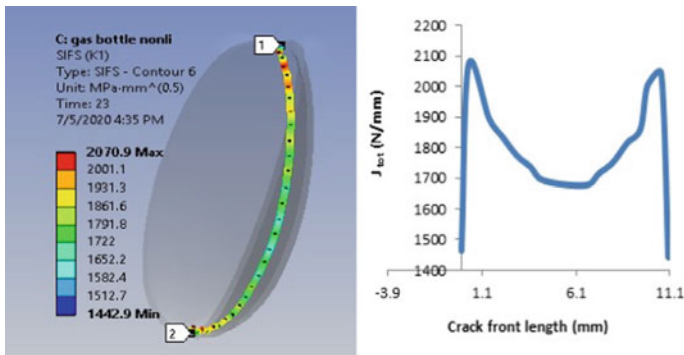
Fig. 8 Variation of J_{tot} along crack front
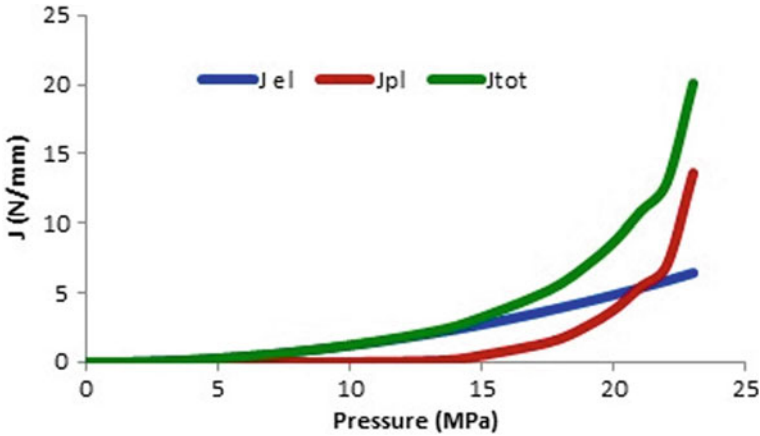
Fig. 9 Variation of J with loading

3.3 Construction of J-Integral Based FAD

The J_{el}, J_{pl}, and J_{tot} evaluated from the Finite Element Analysis (FEA) are plotted against applied pressure. Figure 9 shows the variation of J_{el}, J_{pl}, and J_{tot} with loading. From the graph, it is clear that for the initial applied pressure, there is no much increase in the J value. J value increases as the pressure increases to 23 MPa. The maximum value of J from the linear analysis (J elastic) was 6.49 N/mm whereas in nonlinear analysis (J plastic), the maximum values are around 20.143 N/mm, this is due to the yielding. The Failure Assessment Diagram (FAD) method provides evaluation of crack stability using two ratios: K_r and L_r. Here, pressure-based FAD is constructed.

The K_r value is computed using the elastic stress intensity factor, K, and the material toughness K_{mat} (Eq. 1) and also defined as the square root of the ratio of elastic J to the total J (Eq. 2). L_r is the ratio of applied pressure to collapse pressure (Eq. 3).

$$K_r = \frac{K}{K_{mat}} \tag{1}$$

$$K_r = \sqrt{J_r} = \sqrt{\frac{J_{el}}{J_{tot}}} \tag{2}$$

$$L_r = \frac{\text{Applied pressure}}{\text{Collapse pressure}} \tag{3}$$

The FAD curve's shape accounts for the interaction between brittle fracture and plastic collapse. The FAD curve K_r and L_r values are computed at every load increment. Figure 10 shows the FAD for gas bottle plotted from the obtained results.
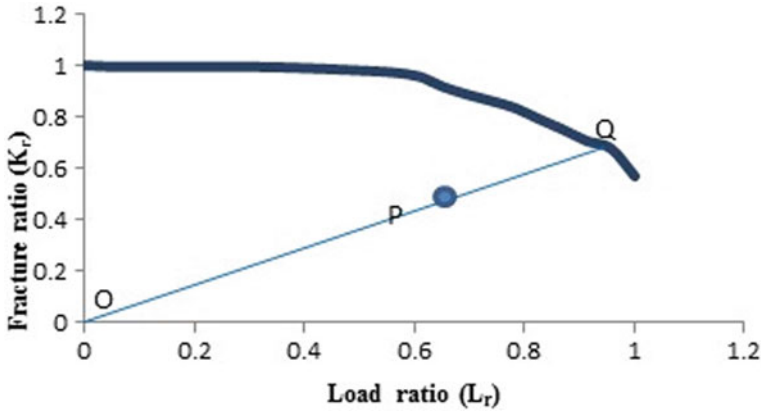
Fig. 10 FAD for gas bottle

Failure Assessment Point (FAP) was plotted from K based approach where K_r is the ratio of K and K_{mat}. The plain strain fracture toughness (K_{mat}) is 900 MPa$\sqrt{}$mm. L_r is the ratio of applied pressure and collapse pressure. The Failure Assessment Point was plotted for the proof pressure of 15 MPa. Therefore,

$L_r = 15/23 = 0.65$; $K = 468.18$ MPa$\sqrt{}$mm (from linear FEA at 15 MPa)

$K_{mat} = 900$ MPa$\sqrt{}$mm; $Kr = K/K_{mat} = 468.18/900 = 0.52$

In Fig. 10, P (L_r, K_r) is the FAP. A line is drawn from origin to FAP and is extended toward the Failure Assessment Curve (FAC). From FAD approach, the fracture point is $L_r = 0.92$ and $K_r = 0.65$. Therefore, the ultimate pressure carrying capacity is $= 0.92 \times 23 = 21.16$ MPa.

Factor of safety against fracture is also calculated as below:

$$FOS \text{ against fracture} = OQ/OP = 1.4;$$
$$\text{Margin of safety against fracture} = 1.4 - 1 = 0.4$$

Directly from the FE analysis, the ultimate pressure carrying capacity of the gas bottle is evaluated in a very short time span when compared with theoretical calculations. Thus, this method could be adopted for many other structures especially when closed form solutions are not available.

4   Conclusion

The structural integrity of a high-pressure gas bottle used in launch vehicle structures with part through crack has been evaluated by J-integral based FAD using ANSYS. The ultimate pressure carrying capacity of gas bottle is directly obtained from the FE

analysis and this method can be applied to a variety of other structures, especially where closed form solutions are not available. A positive margin of safety, against failure by fracture, is observed in presence of the minimum detectable crack size. It is concluded that the gas bottle structure would not experience a fully brittle or ductile failure, but a combination of both.

References

1. Newman JC, Raju IS (1982) Stress intensity factor influence coefficients for internal and external surface cracks in cylindrical vessels. J Press Vessel Technol 104:293–298
2. Kumar V, German DM, Shih FC (1981) An engineering approach for elastic-plastic fracture analysis, general electric company corporate research and development. River Road Schenectady, New York
3. Dowling AR, Townley CHA (1975) The effect of defects on structural failure : a two criteria approach. Int J Press Vess Piping 3:77–107
4. Bilby BA, Cottrell AH, Swinden KH (1963) The spread of plastic yield from a notch. Proc R Soc A272:304–314
5. Harrison RP, Loosemore K, Milne I (1976) Assessment of the integrity of structures containing defects. CEGB Report R/H/R6, Central Electricity Generating Board, The United Kingdom
6. R6 (2013) Assessment of the integrity of structures containing defects. Revision 4, Amendment 10, EDF Energy, Gloucester
7. Chell GG (1979) A procedure for incorporating thermal and residual stresses into the concept of a failure assessment diagram. In: Landes JD, Begley JA, Clarke GA (eds) Elastic-plastic fracture, ASTM STP 668. American Society for Testing and Materials, pp. 581–605
8. API 579-1/ASME FFS-1 (2005) Fitness-for-service, June 2016, Annex 9G, Section 9G.4, "FAD-Based Method for Non-Growing Cracks", and Section 9C.5.10 reference stress, The American Society of Mechanical Engineers and the American Petroleum Institute. API Publishing Services, 1220 L Street, N.W., Washington, D.C
9. BS 7910:2013, Guide to methods for assessing the acceptability of flaws in metallic structures, British Standards Institution, BSI Standards Limited, 2013, Section P.9.4
10. Tonkovic Z, Skozrit I, Alfievic I (2008) Influence of flow stress choice on the plastic collapse estimation of axially cracked steam generator tubes. Nucl Eng Des 238:1762–1770
11. Thorwald G, Garcia V, Kwon O (2018) Steam turbine critical crack evaluation and ranking cracks to prioritize inspection, quest integrity
12. Osage DA (2015) Fatigue assessment for in-service components—a new part for API 579–1/ASME FFS-1 fitness-for_service. Proc Eng 133:320–347
13. Ismail AE, Jamian S, Kamarudin K, Mohd Khir Mohd Nor, Mohd Norihan Ibrahim, Moch. Agus Choiron (2018) An overview of fracture mechanics with ANSYS. Int J Integr Eng 10(5):59–67
14. Kumar PS, Viswanath V, Asraff AK, Jayalekshmi R (2019) Evaluation of stress intensity factor in plates containing defects through finite element analysis. In: Proceedings of national conference on recent advances in civil engineering and technology, REACT'19, Vidya Academy of Science and Technology
15. Anderson TL (2017) Fracture mechanics fundamentals and applications, 4th edn. Taylor & Francis Group
16. Saxena A (1997) Non linear fracture mechanics for engineers. CRC Press, Boca Raton, Boston, London, New York

Hot-Wet Environmental Effects on In-Plane Shear Strength of IMA/M21E Aircraft Grade CFRP Composites

Kishora Shetty, C. M. Manjunatha, Suhasini Gururaja, and Shylaja Srihari

Abstract Effect of hot-wet environments by moisture absorption on properties of CFRP structures is a valuable factor to designers and application engineers in assessing the structural integrity of the parts. In this present study, using standard autoclave process QI (Quasi-Isotropic) composite laminates were manufactured from HexPly® M21E/34%/UD/194/IMA prepreg. In-plane shear (IPS) strength test specimens were prepared from these laminates. Conditioning of these specimens were done at three hot-wet environmental conditions: 45 °C/85% relative humidity (RH), 75 °C/85% RH, and 55 °C/100% RH, until achieving complete moisture absorption saturation in each case. IPS tests were carried out as per ASTM test standard ASTM D3518 specifications using a 100 kN servo-hydraulic test machine. The in-plane shear strength properties were determined for both conditioned and un-conditioned laminate specimens. Similar hot-wet conditions were maintained while conducting the IPS tests. From tests results it is seen that moisture absorption rate increases progressively and attains saturation at about 1.2 wt. % under these three hot-wet conditions. Increase in temperature and RH has shown increase in moisture absorption. IPS strength was reduced by about 8% due to presence of moisture. Tensile strengths were also measured while carrying out IPS tests.

Keywords Structures · Composite · Hot-wet · IPS

1 Introduction

Application of Carbon Fibre Reinforced Plastic (CFRP) composites in aerospace structures are increasing due to their high specific strength and stiffness [1–3]. During

K. Shetty (✉) · C. M. Manjunatha · S. Srihari
Academy of Scientific and Innovative Research (AcSIR), Ghaziabad 201002, India

C. M. Manjunatha · S. Srihari
CSIR-National Aerospace Laboratoires, Bangalore 560017, India

S. Gururaja
Indian Institute of Science, Bangalore 560017, India

their service, aircraft composite structures are usually exposed to a variety of environmental conditions including hot-wet, ultraviolet (UV) radiation, chemical environments, biological conditions, etc. These conditions make the composite structures to deteriorate mainly by making changes to polymer matrix and to matrix/reinforcement interface. The material degradation due to these environmental conditions leads to mainly chemical changes in the matrix material of the composite and de-bonding at the interface of fibre and matrix. Environmental conditions of hot-wet (also termed as hygrothermal), water get absorbed in the matrix or at the interface of fibre and at matrix. This would act as a plasticizer causing gaps in the polymer chains. This is expected to cause a substantial decrease in glass transition temperature and also results in relieving of internal stress built up through the absorption of moisture. These differences to FRP (Fibre Reinforced Plastic) composites affect properties and thus overall performance of composites like strength, stiffness, and damage tolerance [4–10]. So, it becomes very important to evaluate mechanical properties of CFRP composites under different hot-wet conditions [11, 12]. The absorbed moisture causes variation in chemical and physical properties and fibre/matrix interface properties. This feature becomes a crucial controlling factor for the reinforcement in these FRP composites [13–15]. Understanding the moisture absorption rate is an important factor. This helps in predicting the long-term performance of composite materials under hot-wet environmental conditions. As absorbed moisture effects matrix and fibre/matrix interface and thereby properties, the IPS test gives good indication of effect of absorbed moisture on the composite mechanical properties like in-plane shear strength and associated tensile strength.

CFRP composite materials used in aircraft applications are of different grades. The need for new composite materials with increased stiffness, toughness, resistance to environment, lightning strike protection, etc., is growing. The IMA/M21E CFRP composite used in this study is one such new material with higher toughness. The designation of this composite material is 'HexPly® M21E/34%/UD/194/IMA'. M21E resin content of 34% wt., with unidirectional IMA Carbon fibre of 194 gsm areal weight. The experiments are conducted to measure the absorption of the moisture and its effects on in-plane shear strength of its CFRP composite. M21E is an epoxy (polymer) resin with high performance, high toughness which is developed by Hexcel Composites. This composite is used in primary aircraft structures.

2 Experimental

2.1 Material and Specimens

HexPly® M21E/34%/UD/194/IMA composite system is studied here. The prepreg system is made up of Intermediate Modulus Aerospace (IMA) grade, unidirectional (UD) carbon fibre with 194 gsm areal weight and M21E resin with 34% by weight. The curing temperature of this M21E resin is 180 °C. Prepregs of this CFRP
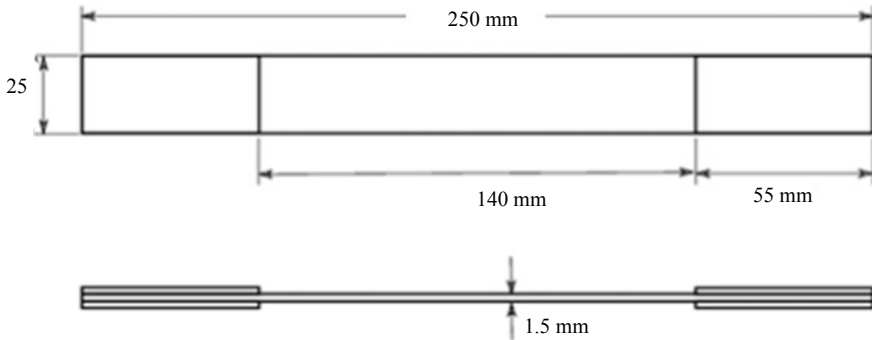
All dimensions are in mm

Fig. 1 Schematic diagram showing dimensions of IPS test specimens

composite were obtained from Hexcel Composites. QI (Quasi-Isotropic) laminates with stacking sequence [±45°] were prepared using these prepregs. The dimensions of the laminate were 600 mm wide and 600 mm long. About 1.5 mm thick laminate was prepared using eight layers of prepregs for IPS test specimens. Using standard autoclave method, curing under 7 bar pressure along with slow heating of 3 °C/min these laminates were prepared. Curing condition was 180 °C for 120 min and then the laminates were cooled at a rate of 5 °C/min.

As per ASTM D5529/D 5229 M-92 [16] standard weight gain specimens (traveler coupons) with dimensions 25 mm × 25 mm × 1.12 mm were prepared from composite laminates. ASTM D3518 [17] test method was followed for IPS test. Number of test specimens for weight gain measurements and IPS tests were five. These test specimens were conditioned at each hot-wet condition. All the test specimens were dried at 40 °C for 1 h in an oven to remove any moisture content prior to conditioning under different hot-wet environments. IPS test specimens diagram is shown in Fig. 1. Photo of IPS test specimen is shown in Fig. 2.

2.2 Hot-Wet Ageing

For studying effect of hot-wet aging on mechanical properties of this IMA/M21E CFRP composite, specimens were conditioned at different hot-wet conditions under different RH and temperatures. These media are expected to be encountered by aerospace components that provide moisture levels of different degrees. This influences the absorption characteristics of the composites. Edge coating of test specimens done with a resin before conditioning to ensure uniform moisture absorption from all the surfaces. Another requirement to do so is to avoid exposure of cut fibres of the composite specimens. Using a Sartorious balance with accuracy up to four decimals,

Fig. 2 IPS test specimens

initial weights of traveler coupons were taken. Conditioning is done by selecting the following hot-wet environments in temperature and humidity chambers. For water immersion at 55 °C, a constant temperature water bath is used.

i.   45 °C/85% RH
ii.   70 °C/85% RH
iii. 55 °C/100% RH (water immersion).

To find out the moisture absorption, weight gain was measured on traveler coupons at regular intervals of time. Weight gain in percentage was calculated till the specimens achieve saturation for each hot-wet condition. Weight measurements were done initially in short intervals of about 24–48 h and in about 1–2 weeks intervals later.

2.3   IPS Testing

IPS test was considered mainly to find out the effect of moisture absorption on matrix and fibre/matrix interface. Tests were conducted for both RT (un-conditioned or control) and hot-wet conditioned specimens. As per ASTM standard tests were done utilizing a servo-hydraulic Universal Testing Machine (UTM) of 100 kN capacity with a crosshead displacement rate of 2 mm/min. Respective hot-wet conditions were maintained while testing. The load to break the specimen (the maximum load on load indicating mechanism) was recorded. One of the test specimens in each conditioning was fitted with strain gauge to measure the IPS at 50,000 μm strain. Photograph of a IPS tested specimen is shown in Fig. 3.

Fig. 3 IPS tested specimen

Table 1 The maximum moisture absorption in various hot-wet conditions

Hot-wet condition	Maximum moisture absorption (wt. %)	Duration for saturation (months)
45 °C/85% RH	0.75	13
70 °C/85% RH	0.81	11
55 °C/100% RH	1.23	9

3 Results and Discussions

3.1 Moisture Absorption

Results of moisture absorption behavior of IMA/M21E CFRP composite for various hot-wet conditions with maximum moisture absorption are given in Table 1.

From the three hot-wet conditions, water immersion at 55 °C showed highest moisture absorption. Also, time taken for saturation is less when compared to other two conditions. Condition 45 °C/85% RH showed least moisture absorption and longest duration for saturation whereas 70 °C/85% RH exhibited intermediate behavior. Maximum absorbed moisture content at saturation is 1.23% for water immersion at 55 °C, 0.81% for 70 °C/85% RH, and 0.75% for 45 °C/85% RH, respectively. Studies conducted on similar type of CFRP composites by other researchers [18] also shown this trend. A comparison between this IMA/M21E CFRP and results reported by other researchers on similar CFRP composites, this composite has shown less amount of saturation moisture. For example, 0.82% saturation moisture (specimens in longitudinal tensile configurations) for Carbon fibre (C-160)/Epoxy (LY 5052) at 45 °C/85% RH [19] compared to 0.75% for the same condition in the CFRP is studied here.

3.2 In-Plane Shear Tests

IPS results are presented in Table 2. At each condition, total five specimens were tested and average test results are presented here. Table 2 also contains standard deviation in IPS strength results (Fig. 4).

Table 2 In-plane shear strength of IMA/M21E CFRP composite

Aging Condition	IPS (MPa) at 50,000 µm strain*	IPS Test—UTS (MPa)	% Reduction in IPS at 50,000 µm strain	% Reduction in IPS—UTS
Control (No conditioning)	70	235 ± 6.9	–	–
45 °C/85% RH	66	218 ± 5.1	6	7
70 °C/85% RH	66	213 ± 4.6	6	9
55 °C/100% RH	66	199 ± 5.5	6	15
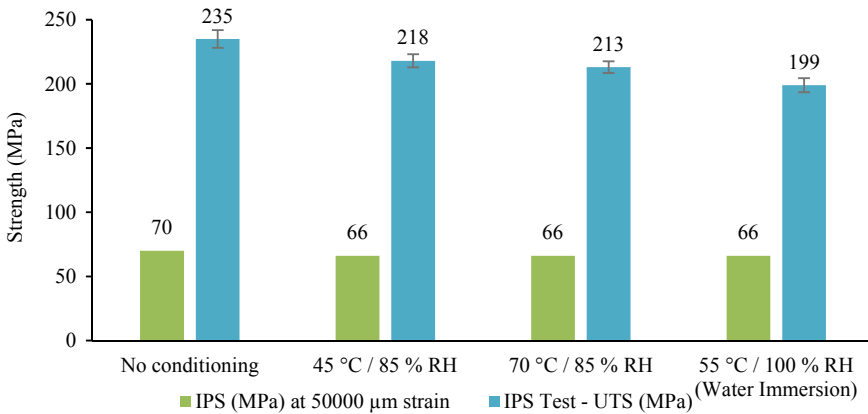
Fig. 4 Comparison of degradation in IPS after conditioning for IMA/M21E CFRP composite

From the results it is observed that IPS strength reduced moderately by about 6% (for 50,000 µm strain) due to moisture presence and about 15% for UTS-IPS. The reduced IPS strength of this composite due to hot-wet environments shows that material undergoes changes in properties in these environments. Aging carried out at all the three conditions has shown equal amount of reduction in IPS strength (for 50,000 µm strain) compared to un-conditioned specimens. This is as expected as presence of moisture aids the shear. Moisture presence makes the difference not the amount of moisture. IPS specimens conditioned at 55 °C/100% RH (water immersion) has shown highest reduction in IPS strength when measured in terms of UTS which is about 15% compared to control samples i.e., un-aged. It is observed that as the absorbed moisture amount increases, the degradation in IPS in terms of UTS increases. The severity of deterioration of IPS strength in terms of UTS depends on moisture absorption amount by the CFRP composite material. The order of extent of this deterioration is 45 °C/85% RH < 70 °C/85% RH < 55 °C/100% RH for IPS strength. Hot-wet environmental conditioning done on 977-2 HTS 12 K 34% carbon

prepreg [20] shown 22% reduction in IPS strength. This shows the IMA/M21E CFRP composite studied here is comparatively a better composite material.

4 Conclusions

The moisture absorption at various hot-wet environments and how it effects in decreasing IPS strength of IMA/M21E CFRP composite were studied here in this research work. From the results obtained, following conclusions are drawn:

- Temperature and amount of relative humidity in the environment together influences the quantity of moisture being absorbed by the carbon fibre reinforced epoxy composite. For the most severe condition i.e., water immersion at 55 °C the total maximum moisture absorption observed was 1.23%. Amount of moisture absorbed by IMA/M21E composite increases with increasing severity of the hot-wet conditioning. The mechanism of moisture absorption leading to saturation is as expected and reported by researchers for similar CFRP composites. Moisture absorption happens through matrix and also through the interface of matrix and fibre.
- In-Plane Shear strength gets deteriorated by hot-wet conditioning. The amount of decrease is 6% (for 50,000 μm strain) for all the conditions as presence of moisture makes the difference but not the amount here. For UTS measured in IPS test, the maximum deterioration is 15% for the most severe hot-wet condition. For UTS, both presence of moisture and amount of moisture in the CFRP composite brings in deterioration. This indicates how absorbed moisture effects the mechanical properties like IPS of CFRP composites.
- This CFRP Composite IMA/M21E looks to be more promising in the modern aircraft manufacturing when compared to the other CFRP composites at present.

References

1. Shetty K, Bojja R, Srihari S (2020) Effect of hygrothermal aging on the mechanical properties of IMA/M21E aircraft-grade CFRP composite. Adv Compos Lett
2. Shetty K, Srihari S, Manjunatha CM (2016) A survey on the environmental effects on aerospace fibre reinforced plastic composites. In Proceedings of 14th ISAMPE national conference on composites (INCCOM-14)
3. John KM, Thirumalai Kumaran S, Kurniawan R, Park KM, Byeon JH (2018) Review on the methodologies adopted to minimize the aterial damages in drilling of carbon fibre reinforced plastic composites. J Reinf Plast Composit 1–18
4. Dogan A, Arman Y, Ozdemir O (2018) Experimental investigation of transverse loading on composite panels coated with different gelcoat colors subjected to UV radiation and hygrothermal aging. Mater Res Expr 6(2):025301

5. Dogan A, Arman Y (2019) The effect of hygrothermal aging and UV radiation on the low-velocity impact behavior of the glass fiber-reinforced epoxy composites. Iran Polym J 28(3):193–201

6. Shetty K, Srihari S, Manjunatha CM (2019) Effect of hygrothermal aging on the interlaminar shear strength of a carbon fibre composite. Proc Struct Integr 14:849–854

7. Ogi K (2003) Influence of thermal history on transverse cracking in a carbon fiber reinforced epoxy composite. Adv Compos Mater 11(3):265–275

8. Sala G (2000) Composite degradation due to fluid absorption. Compos B 31(5):357–373

9. Tsenoglou CJ, Pavlidou S, Papaspyrides CD (2006) Evaluation of interfacial relaxation due to water absorption in fiber–polymer composites. Compos Sci Technol 66(15):2855–2864

10. Abdel- B, Ziaee S, Gass K (2005) M Schneider M: The combined effects of load, moisture and temperature on the properties of E-glass/epoxy composites. Compos Struct 71(3–4):320–326

11. Kellas S, Morton J, Curtis PT (1990) The effect of hygrothermal environments upon the tensile and compressive strengths of notched CFRP laminates. Part 2: Fatigue loading, Composites, vol 21, no 1

12. Behera A, Thawre MM, Ballal A (2020) Hygrothermal aging effect on physical and mechanical properties of carbon fiber/epoxy cross-ply composite laminate. Mater Today Proc

13. Liu X, Gu, Weimin, Liu Q, Lai X, Liu L (2018) Damage of hygrothermally conditioned carbon epoxy composites under high-velocity impact. Materials 11:2525

14. Zhong Y, Joshi SC (2015) Initiation of structural defects in carbon fiber reinforced polymer composites under hygrothermal environments. J Compos Mater 50(8)

15. Giurgiutiu V (2016) Structural health monitoring of aerospace composites. Elsevier, pp 1–23

16. ASTM D5529/D 5229M-92 (2004) Standard test method for moisture absorption properties and equilibrium conditioning of polymer matrix composite materials. ASTM International, West Conshohocken, PA

17. ASTM D3518/D3518M-18 (2018) Standard test method for in-plane shear response of polymer matrix composite materials by tensile Test of a ±45° Laminate. ASTM International, West Conshohocken, PA

18. Aoki Y, Yamada K, Ishikawa T (2008) Effect of hygrothermal condition on compression after impact strength of CFRP laminates. Compos Sci Technol 68:1376–1383

19. Srihari S, Rao RMVGK (1999) Hygrothermal characterisation and diffusion studies on carbon/epoxy composites. J Reinf Plast Compos 18(10):921–930

20. Ryan JM, Adams R, Brown SGR (2009) Moisture ingress effect on properties of CFRP. In: Proceedings of 17th international conference on composite materials, Edinburgh, UK

Residual Stress Analysis in Large Water Quenched Stainless Steels

S. Hossain and A. M. Shirahatti

Abstract Age-related degradation mechanisms in nuclear plant crucially rely on weld residual stress. Earlier residual stress measurements in thick section welded components revealed there is sufficient driving force for creating creep damage during high temperature operation. To understand how the presence of residual stress influences creep degradation a number of laboratory samples were quenched to generate well defined residual stress. The stresses were modelled in finite element analysis (FEA) with the aim to assess how these stresses act as a driving force for creating creep damage. To numerically predict creep damage using finite element analysis (FEA), it is required to accurately model the stress distribution and validate the stresses experimentally. The focus of this paper is on the quenched residual stress analysis. A time-of-flight method developed at ISIS facility at Rutherford Appleton Laboratory was used to measure residual stress distributions in type 316H stainless steel large as-quenched specimens. An excellent correlation existed between measurements and FEA simulations.

Keywords Quench residual stress · Finite element · Neutron diffraction

1 Introduction

Quenching is a common process of metal heat treatment which is rapid cooling of components to achieve desired mechanical properties [1]. While improving mechanical properties of metals such as hardening, quenching also introduces residual stresses. Severe temperature gradient induces thermal stresses resulting in plastic strain. The residual stress arises from the complex interaction of thermal stresses and phase transformation [1]. Predicting quench residual stresses has been of interest for a long time [2]. Residual stress measurement techniques [3] are experimental tools

S. Hossain (✉)
Department of Aeronautical Engineering, Military Technological College, Muscat, Sultanate of Oman

A. M. Shirahatti
Jain College of Engineering, Visvesvaraya Technological University, Belagavi, India

to evaluate residual stresses. Centre-hole drilling [4] and X-ray diffraction [1] can only measure the near-surface residual stresses. Neutron diffraction [5] can measure residual stress field through thickness of components but component size limitation and expensive procedure are the main drawbacks of the method for routine application. Analytical solutions to quench residual stress are limited to simple geometry [6]. Numerical analysis of quenching by finite element analysis are provided in [7].

Numerical tool is a cost-effective approach to simulate the quenching conditions and predict the residual stresses in different geometries. However, experimental and analytical approaches are required to validate the numerical results since there is a variety of influencing factors which contribute to quenching processes such as thermal boundary condition and thermo-physical properties. These factors cannot easily be simulated in numerical codes, especially when there is material transformation during quenching. Aksel et al. [8] investigated the quenching process of a long thin rectangular aluminium bar. The work was a good example of utilising all three approaches to predict residual stress fields during quenching.

In this study numerical and experimental studies of rapid spray water quenching of cylindrical bodies for the subsequent creep study were carried out. Large cylindrical bodies were used for the quenching tests compared to earlier studies [9]. Two cylinders of diameter 60 mm and length 160 mm were quenched by using rapid spray water quench [4]. In order to reduce the flight path lengths during neutron diffraction measurements, a series of holes were carefully drilled in one of the quenched cylinders. Figure 1 shows the schematic of these cylinders together with the overall dimensions. Results of finite element study and residual stress measurement using neutron diffraction are reported while the creep study is outside the scope.

2 Finite Element Analysis

In quenching stainless steels there is no phase transformation and the thermal gradient is the only cause of residual stress. Thermal analysis using finite element code was solved as an uncoupled problem. Temperature history acquired during quenching was used to solve the non-linear stress analysis, neglecting the heat generated in the uncoupled heat transfer analysis due to plastic deformation.

2.1 Material Model

The specimens were extracted from type 316H stainless steel ex-header. The material data included temperature-dependent mechanical and thermo-physical properties, i.e. stress strain curve, Poisson ratio, Young's modulus, conductivity, and thermal expansion as a function of temperature and defined in ABAQUS input deck [10].
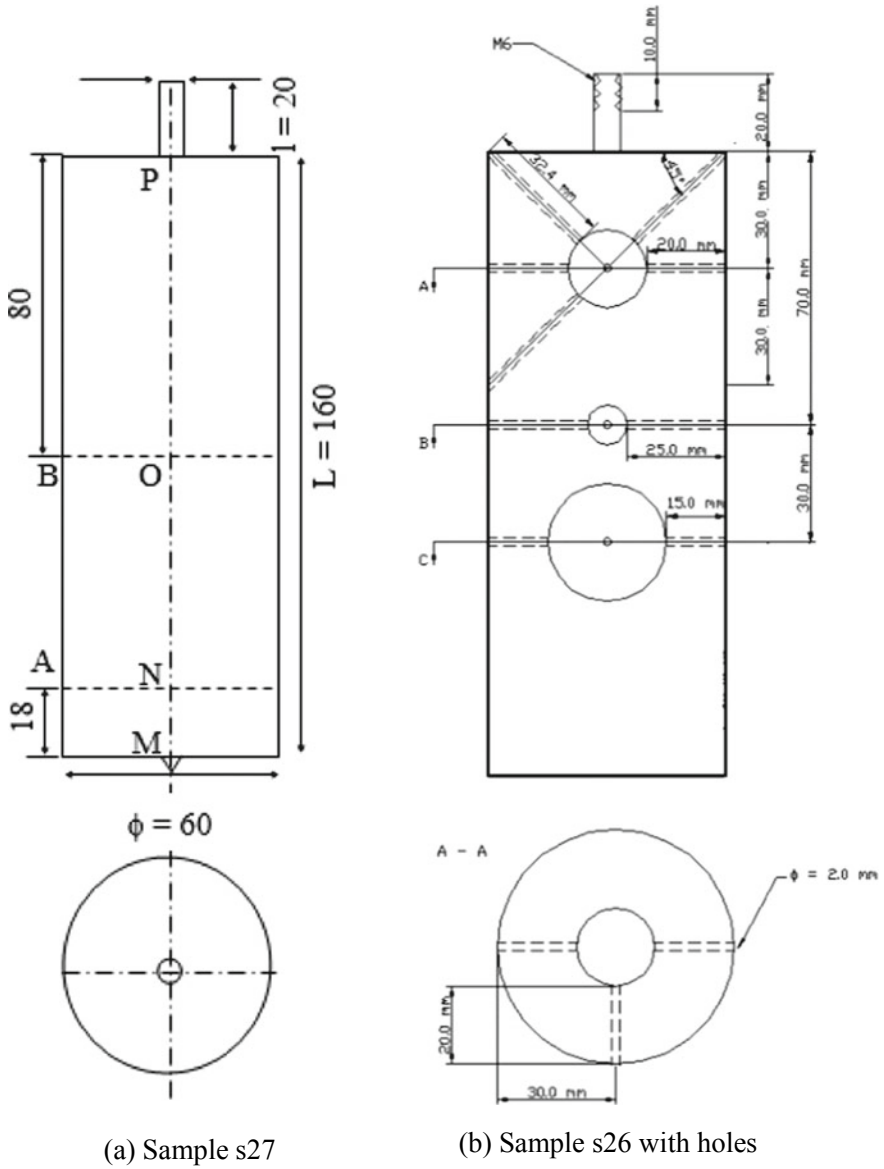
(a) Sample s27

(b) Sample s26 with holes

Fig. 1 Schematic of quenched 316H stainless steel cylinders *s27* and *s26*

2.2 FEA Models for Quenched Cylindrical Bodies

The numerical simulation of quenching carried out using the commercial ABAQUS FEA code [10] consisted of an uncoupled heat transfer analysis with a subsequent thermal stress analysis. Axi-symmetric models were employed with temperature gradients in both radial and axial directions. Because of symmetry, only a quarter of the specimen was modelled using 2400 elements (DCAX for heat transfer, CAX8R for stress analysis) and 7421 nodes. The boundary condition included convective heat transfer on the outer surface, and adiabatic condition on both the axial and radial axes. The quenching water temperature was 20 °C. The rapid spray water quench minimised film boiling effects in the analysis and the heat transfer coefficient was assumed independent of temperature [11]. The material was assumed elastic with strain hardening plasticity and with yield stress that decreased with increasing temperature. Transient stresses were sufficiently large to cause significant plastic flow and residual stresses remained after the specimens reached the coolant temperature.

Drilled Quenched Cylinder. A further FEA analysis was carried out to study feasibility of ND measurement using hole-drilled cylinder, with a purpose to reduce flight path length and time of flight. The analysis consisted of a three-dimensional FEA to model the effect of drilling holes on the initial residual stress field present within the quenched cylindrical body. Figure 2 shows the FEA mesh of the model. Due to the three symmetry planes, one-eighth model was constructed using 10,520 quadratic elements and 12,237 nodes. The hole drilling process was modelled in ABAQUS using "Model Change" keyword [10] by incrementally removing element set which defined the geometry of the hole.
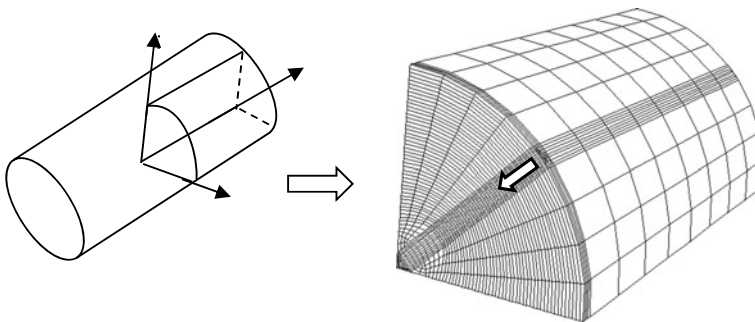

Fig. 2 FEA mesh of one-eighth model of a cylinder, *s26*, dia 60 mm, len 160 mm. The arrow on the mesh shows the element set defining the hole that was drilled and the direction of the drilling

2.3 FEA Results

Solid Quenched Cylinder. Figure 3 shows the predicted residual stress (radial, axial and hoop) along the longitudinal axis "PM" (Fig. 1.a) in s27. A constant heat transfer coefficient, $h = 7000 \ \mathrm{Wm^{-2} \ K^{-1}}$ [11] and an initial temperature of 850 °C with kinematic hardening model assumption was used in the FEA model. Previous studies [4] revealed a good correlation between measurements and FEA under kinematic hardening model. As expected, the axial stress was zero on outer surfaces at either ends of the bar, and was tensile throughout the remaining section away from the ends. Both radial and hoop stresses were identical along longitudinal axis. They were compressive (−300 MPa) close to outer surfaces and tensile (280 MPa) near the centre section. The axial stress was the principal stress component with a magnitude 580 MPa near the centre.

Drilled Quenched Cylinder. In order to reduce the flight path lengths during neutron diffraction measurements, a series of holes were drilled in the second cylinder as shown in Fig. 1b. The effect of drilling a hole on the residual stress distribution in a quenched cylindrical bar (s26) is shown in Fig. 4. The drilling was modelled by removing element sets successively every "mm" using the "Model Change" keyword in ABAQUS [10]. In order for a pronounced illustration, only the effect of drilling 15 mm and a maximum 25 mm hole depth on the as-quenched residual stress distribution is shown. Clearly the effect of drilling a depth of 25 mm (position "B" in
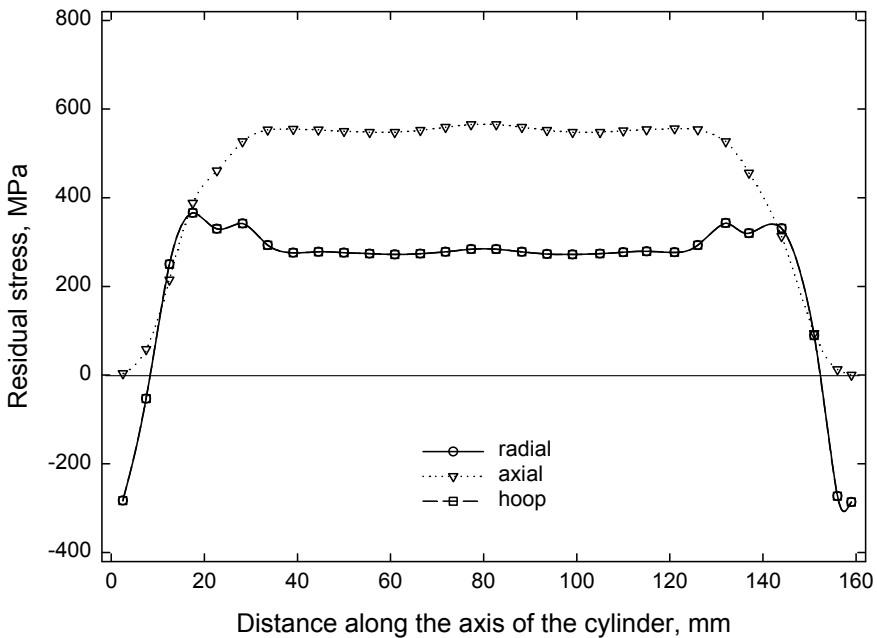
Fig. 3 Residual stresses in *s27* along longitudinal axis PM (see Fig. 1a)
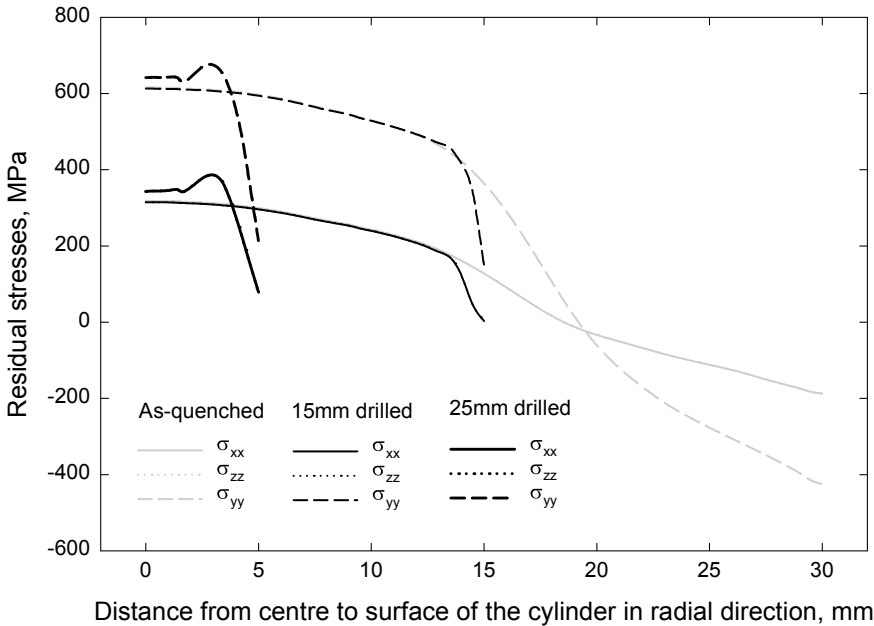
Fig. 4 Effect of drilling on FEA predicted stresses in *s26*. The residual stress distribution is radially across the bar, along drilling path shown in Fig. 2

Fig. 1b) was to redistribute the original as-quenched residual stresses at the centre of the cylinder by 25 MPa, ~ND measurement error. In contrast, the effect of drilling 15 mm depth (position C) on the initial as-quenched residual stress was practically negligible. The intention was to measure residual strains at the centre of each virtual spheres denoted by "A", "B" and "C" in Fig. 1 b.

3   Experimental Study

3.1   Neutron Diffraction Measurement Set-Up

The neutron diffraction (ND) technique was used to measure the internal strain distribution in the quenched specimens using time-of-flight method [12] developed at ISIS facility at Rutherford Appleton Laboratory. Three samples were studied using the purpose-built stress instrument ENGIN-X [12] on ENGIN-X beam line. To measure the strains the lattice parameter of strained material is compared with unstrained reference d0 comb sample [4]. As a time-of-flight facility, multiple diffraction peaks were acquired simultaneously. Strain was measured by analysing the full diffraction pattern using profile refinement techniques to produce an overall average [13].
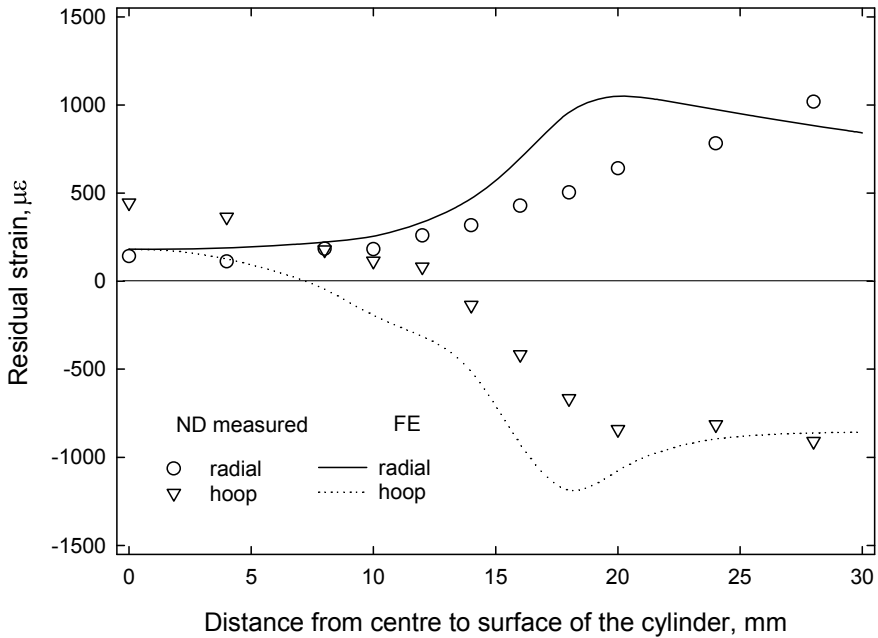
Fig. 5 Residual strains in s27 across OB (Fig. 1a)

3.2 Internal Residual Stress Distribution

The reference sample started as quenched sphere, diameter 30 mm that was later electric-discharge machined to produce comb with 7 fingers (cross-section 2×2 mm^2). The second sample was quenched cylinder *s27* for which a gauge volume of $4 \times 4 \times 5$ mm^3 was used. The third sample consisted of a quenched cylinder with drilled holes *s26* for which a gauge volume of $2 \times 2 \times 4$ mm^3 was used. Figure 5 summarises the ND measured residual radial and hoop strain components across the mid-section of the bar *s27*, across radial line OB (Fig. 1a) and are compared with the corresponding FEA predicted strains. Figure 6 shows the measured and predicted residual radial and hoop strains along the longitudinal axis of the bar *s26* at positions A, B and C (Fig. 1b). In general, a good correlation existed between the measured and the predicted residual strain distributions in Figs. 5 and 6.

4 Concluding Remarks

The use of a purpose-built diffractometer ENGIN-X at ISIS, with the ability to accurately measure polycrystalline lattice parameters, made it possible to measure residual strains rapidly and accurately in 316H type stainless steel specimens. An
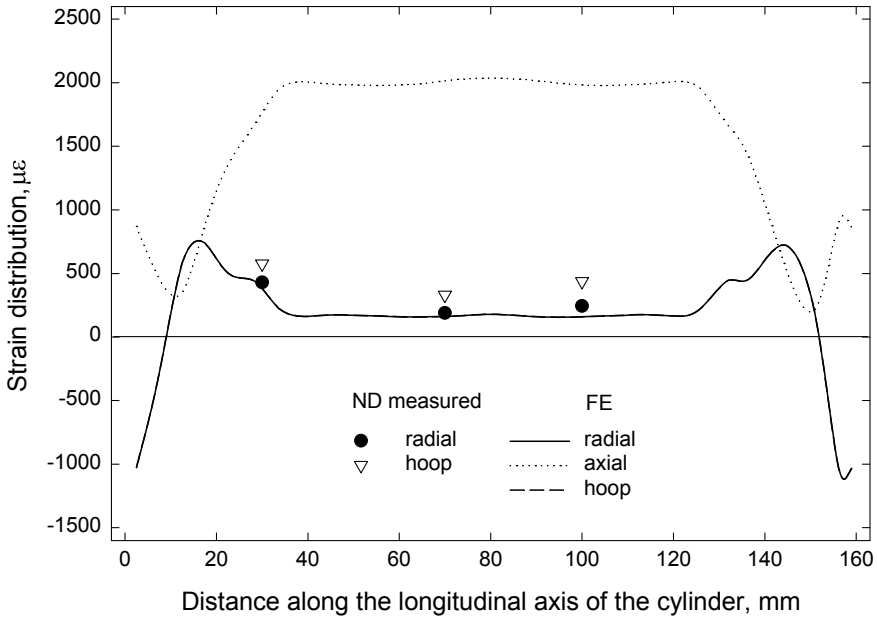
Fig. 6 Residual strains in s26 at positions A, B, C (Fig. 1a)

extensive 3D FEA simulation demonstrated the use of holes in ND measurement of residual strains in large quenched section to considerably reduce the counting time, without much distortion to the original residual stress state. The holes drilled into the quenched cylinder *s26* shortened only the incoming (and not outgoing) path length during the ND measurement since the outgoing path consisted of diverging beam. The constant diameter hole drilled "for the outgoing beam" did not completely facilitate in reducing the total path length. Nevertheless, the counting time was essentially reduced during measurement of the radial and hoop residual strains at positions A, B and C in *s26*. The close correlation between the measured and the FEA predicted residual strains validated the present finite element study to predict the generation of residual stresses following water quenching.

References

1. Sedeghi M, McMahon CA (2000) The influence of quenchant agitation on the heat transfer coefficient and residual stress development in the quenching of steels. Proc Inst Mech Eng Part B J Eng Manuf 214(7):555–567. https://doi.org/10.1243/0954405001518251

2. Landau HG, Weiner JH (1958) Transient and residual stresses in heat-treated plates. J Appl Mech 25(4):450–465

3. Withers PJ, Bhadeshia HKDH (2001) Residual stress: part 1-mesurement techniques. Mater Sci Technol 17(4):355–365. https://doi.org/10.1179/026708301101509980

4. Hossain S, Truman CE, Smith DJ, Daymond MR (2004) Prediction and measurement of residual stresses in quenched stainless-steel spheres. Mater Sci Eng, A 373:339–349. https://doi.org/10.1016/j.msea.2004.02.014

5. Hossain S, Truman CE, Smith DJ, Daymond MR (2004) Creating highly triaxial residual stresses and relaxation of the stress field due to thermal ageing. J Neutron Res 12(1–3):111–115. https://doi.org/10.1080/10238160410001734540

6. Mckenzie AC, Moakler M (1973) On the relaxation of residual stress fields by thermal relief. In: Proceeding of 2nd international conference of pressure vessel technology, San Antonio, pp 1167–1178

7. Sen S, Aksakal B, Ozel A (2000) Transient and residual thermal stresses in quenched cylindrical bodies. Int J Mech Sci 42(10):2013–2029. https://doi.org/10.1016/S0020-7403(99)00063-6

8. Aksel B, Arthur WR, Mukherjee S (1992) A study of quenching: experiment and modeling. J Eng Ind 114(3):309–316. https://doi.org/10.1115/1.2899797

9. Hossain S, Truman CE, Smith DJ, Daymond MR (2003) Creating highly triaxial stresses in stainless steel. In: The abstracts of ATEM international conference on advanced technology in experimental mechanics asian conference on experimental mechanics 2003, 170. https://doi.org/10.1299/jsmeatem.2003.170

10. Hibbit, Karlsson and Sorenson Inc. (1998) HKS Inc., 1080 Main Street, Pawtucket, RI 02680–4847, USA

11. Gür CH, Tekkaya AE (1998) Numerical and experimental analysis of quench induced stresses and microstructures. J Mech Behav Mater 9(4):237–256. https://doi.org/10.1515/JMBM.1998.9.4.237

12. Johnson MW, Daymond MR (2002) An optimum design for a time-of-flight neutron diffractometer for measuring engineering stresses. J Appl Crystallogr 35(1):49–57. https://doi.org/10.1107/S002188980101891X

13. Daymond MR, Bourke MAM, Von Dreele R, Clausen B, Lorentzen T (1997) Use of Rietveld refinement for elastic macrostrain determination and for evaluation of plastic strain history from diffraction spectra. J Appl Phys 82(4):1554–1562. https://doi.org/10.1063/1.365956

Evolution of Deformation Modes, Microstructure, and Texture of Zircaloy-4 During High Strain Rate Deformation

G. Bharat Reddy, Rajeev Kapoor, and Apu Sarkar

Abstract Specimens of recrystallized Zircaloy-4 were deformed in compression at ~1200 s^{-1} and 25 °C using the split-Hopkinson pressure bar. The deformation was carried along the specimen orientation that favored tensile twinning. Zircaloy-4 showed sigmoidal stress-strain behavior with three stages of work hardening. Specimens were deformed to different strains to determine the evolution of microstructure, texture, and deformation modes. Microstructure and texture characterization were carried out using EBSD. Microstructure revealed the formation of tensile twins of types I (TT1) and II (TT2) with primary twinning mode being TT1. The strength of basal poles along the compression direction increased with strain.

1 Introduction

Hcp metals deform by both slip and twinning to accommodate any arbitrary strain [1, 2]. The choice of the deformation modes depends on the texture and loading direction. In hcp materials the primary mode of deformation is either basal <a> (Mg, Zn) or prismatic <a> slip (Ti, Zr) [1, 3–6]. Pyramidal <c + a> slip which accommodates the deformation along <c> direction has a critical resolved shear stress greater than or comparable to those of twinning systems at low and ambient temperatures. Tensile twins are formed when <c>-axis experiences tensile force whereas compressive twins form under <c>-axis compression [1, 2]. The activation of the above deformation modes depends on microstructural factors such as texture, grain size, dislocation density, stacking fault energy, and deformation conditions such as temperature and strain rate [1, 4–13].

G. Bharat Reddy (✉) · R. Kapoor · A. Sarkar
Division of Engineering Sciences, Homi Bhabha National Institute, Mumbai 400094, India
e-mail: gbharat@barc.gov.in

Mechanical Metallurgy Division, Bhabha Atomic Research Centre, Mumbai 400085, India

Zr and its alloys primarily deform via prismatic <a> slip at near ambient temperatures. At low temperatures (25 °C or below), both tensile and compressive twins can form depending on the texture and loading direction [4, 6, 14]. One study on Zr-1Nb [5], deformed at both quasi-static and high strain rates showed that tensile twin of type-I formed at both the strain rates. Further, the three stage work hardening behavior typically observed in hcp metals deforming via twinning was characterized based on evolution of boundary spacing, dislocation density, and Taylor factor for prismatic <a> slip. In our previous study [6], Zircaloy-4 (a Zr-Sn alloy) deformed at quasi-static strain rate of 0.001 s^{-1} resulted in the formation of TT1 at 25 °C. The present work focuses on understanding the deformation behavior of Zircaloy-4 at high strain rates. Split-Hopkinson pressure bar setup has been used for compression of Zircaloy-4 specimens. The microstructure was characterized using SEM-EBSD to determine the deformation modes and texture evolution with strain.

2   Material and Experiments

A rolled plate of Zircaloy-4 was annealed at 800 °C for 1 h. The initial recrystallized microstructure is shown in Fig. 1. The inverse pole figure (IPF) map and IPF parallel to rolling direction (RD) in Fig. 1 show that basal poles are perpendicular to RD. The compression axis was chosen as RD so that basal poles (along <c>-axis) experience
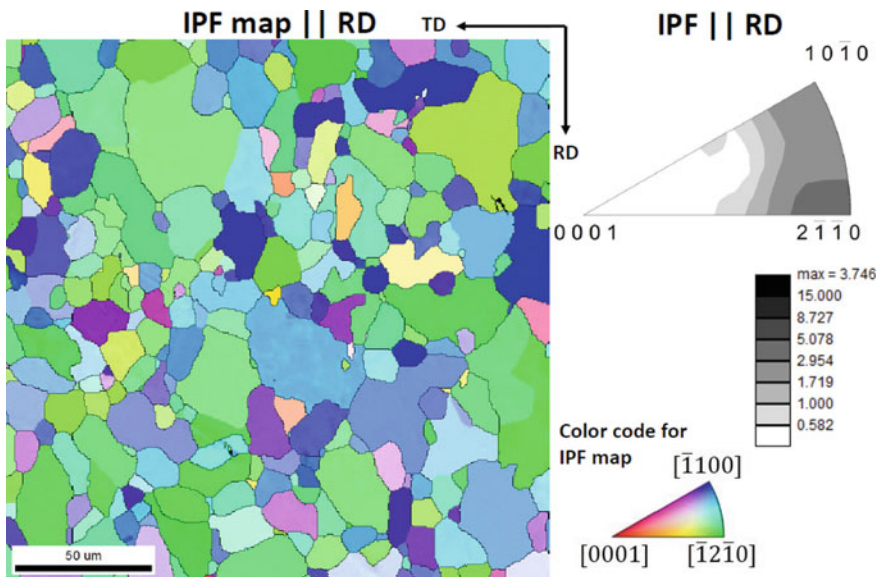
Fig. 1   (Left) IPF map parallel to RD and (Right) IPF shows the distribution of crystal axes parallel to RD of annealed Ziraloy-4

Fig. 2 A raw signal obtained upon compression of Zircaloy-4 using SHPB setup
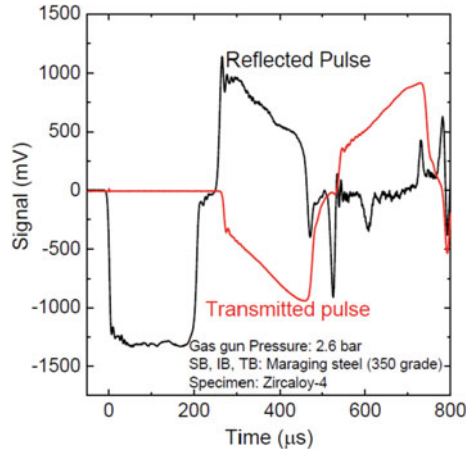
tensile forces leading to the possible formation of tensile twins. High strain rate deformation experiments at 25 °C were carried out using split-Hopkinson pressure bar (SHPB) setup (for details of testing using SHPB see Refs. [15–19]). The striker, incident, and transmission bars used in the current study are made of 13 mm diameter maraging steel grade 350. The length of incident and transmission bars is 1.3 m each, and the striker bar used is 0.5 m. Specimens with dimensions of 6 mm height and 4 mm × 4 mm cross-section were used for the current study. The specimens were deformed to different true strains of 0.05, 0.13, and 0.19 using different lengths of hollow rings encapsulating the specimen. This method ensures same strain rate evolution for all the deformation experiments. A raw signal obtained for the deformation of Zircaloy-4 is shown in Fig. 2.

The wave reflected from the specimen measures the strain rate whereas the wave transmitted through the specimen measures the stress response as a function of time. The details of the determination of strain rate, strain, and stress from reflected and transmitted signals can be found in Refs. [15, 19]. The deformed specimens were sectioned parallel to the deformation axis, mechanically grinded and polished to 1 µm surface finish and subsequently electropolished in a solution of 20:80 perchloric acid to methanol at −25 °C and 20 V. SEM-EBSD measurements were performed on a ZEISS FEG SEM using an accelerating voltage of 20 kV.

3   Results and Discussion

3.1   Mechanical Response of Zircaloy-4

The evolution of flow stress, strain rate and work hardening rate for Zircaloy-4 deformed using SHPB setup is shown in Fig. 3. The average strain rate determined
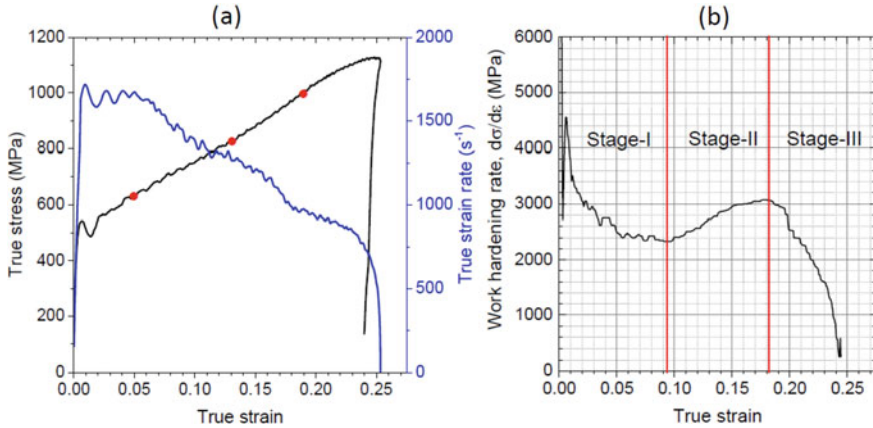
Fig. 3 **a** Flow stress and strain rate evolution with strain, and **b** evolution of work hardening rate with strain showing three stage work hardening behavior

from Fig. 3a is about 1200 s^{-1}. The flow curve shows a sigmoidal stress–strain response with a three stage work hardening behavior (Fig. 3) typically associated with the formation of twins during deformation [5, 20]. Under the same deformations conditions (gun pressure and striker bar length) three samples were deformed to different true strains of 0.05, 0.13, and 0.19 to study the microstructural evolution during deformation.

3.2 Evolution of Microstructure and Deformation Modes

The IPF maps and IPFs parallel to the compression axis shown on the left side of Fig. 4 suggest the increase in basal pole intensity with strain (at the start of deformation basal pole intensity along compression axis was nearly zero, see Fig. 1) indicating the abrupt reorientation due to twinning and growth of twins. The IPF and the IQ maps corresponding to a specimen deformed to strain of 0.05 clearly show the abrupt reorientation of the grains within the sharp interfaces or boundaries. Two such special sharp interfaces were found as shown in image quality (IQ) maps (Fig. 4). These interfaces were identified to be that of tensile twins of type-I (TT1) and type-II (TT2). Boundaries marked in red color were found to have misorientation angle-axis pair of 85° $\langle 11\bar{2}0 \rangle$ between the parent and the twinned grain which correspond to TT1 and the boundaries marked in blue color had misorientation angle-axis pair of 34° $\langle 10\bar{1}0 \rangle$ corresponds to TT2. In our previous study [6], deformation of Zircaloy-4 at quasi-static strain rate of 0.001 s^{-1} along RD resulted in only TT1. It is understood that in contrast to slip systems, the CRSS of twin systems is largely unaffected by the change in strain rate and temperature. Usually TT2 twin possesses a higher CRSS value in comparison to TT1 and pyramidal <c + a> due to its large characteristic
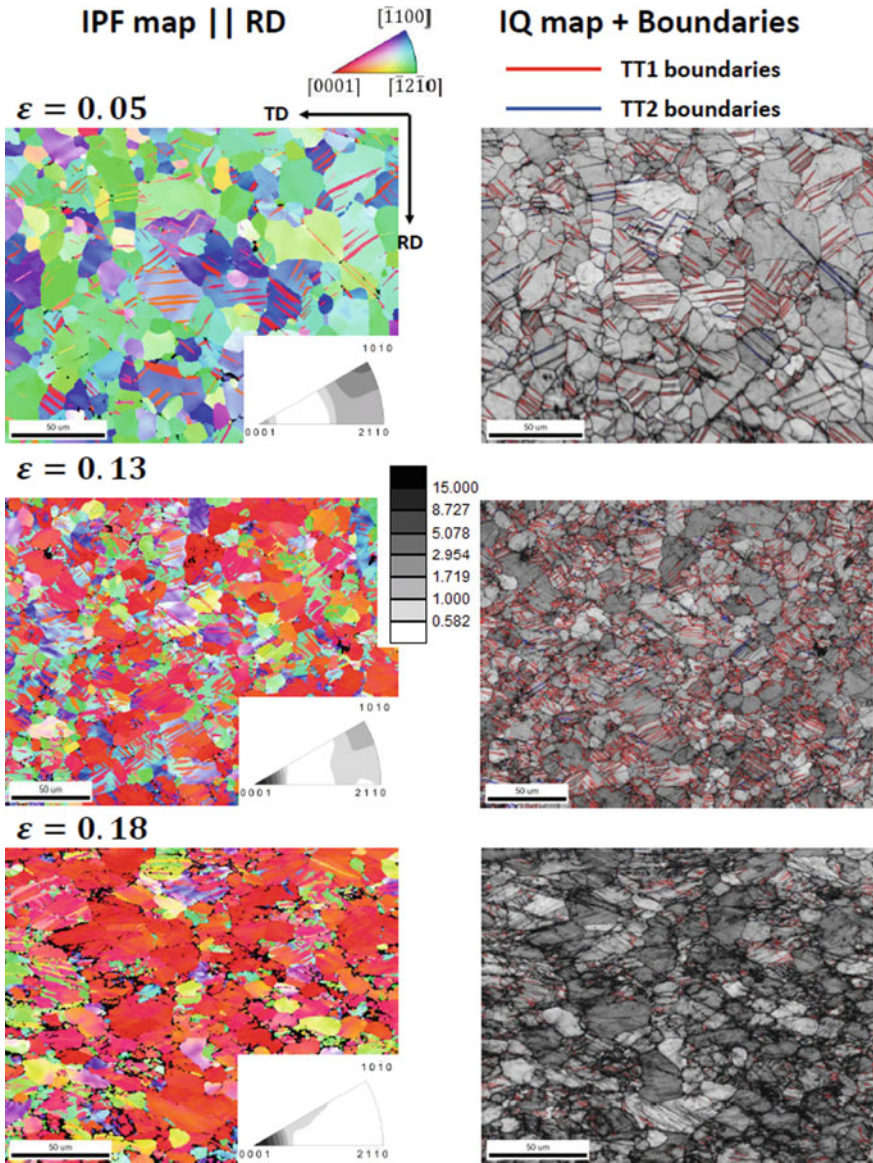
Fig. 4 (Left) IPF maps and (right bottom of IPF maps) IPFs parallel to compression axis for the specimens deformed to strain levels of 0.05, 0.13, and 0.19, as labeled. (Right) The corresponding image quality maps with twin boundaries marked in red for TT1 and blue (see arrows) for TT2

shear. However, due to the increase in strain rate the CRSS of pyramidal <c + a> slip system could have increased to a value comparable to that of TT2 leading to the formation of TT2 twins.

The misorientation angle distribution (MAD) plots for the specimens deformed to different strain levels are shown in Fig. 5. For the undeformed specimens the distribution of boundaries appears uniform. For the subsequent deformation of the specimen to a strain of 0.05, a peak is visible at 85° in the MAD plot, these boundaries correspond to TT1. A small peak is also observed at an angle of about 34° corresponding to TT2. The twin boundary fraction showed a decreasing trend after a strain of 0.05. The boundary fraction of TT2 was found to be negligible in comparison to TT1 at all strain values. With increasing strain, the fraction of low angle boundaries (Fig. 5) increased which is typically associated with interactions among dislocations
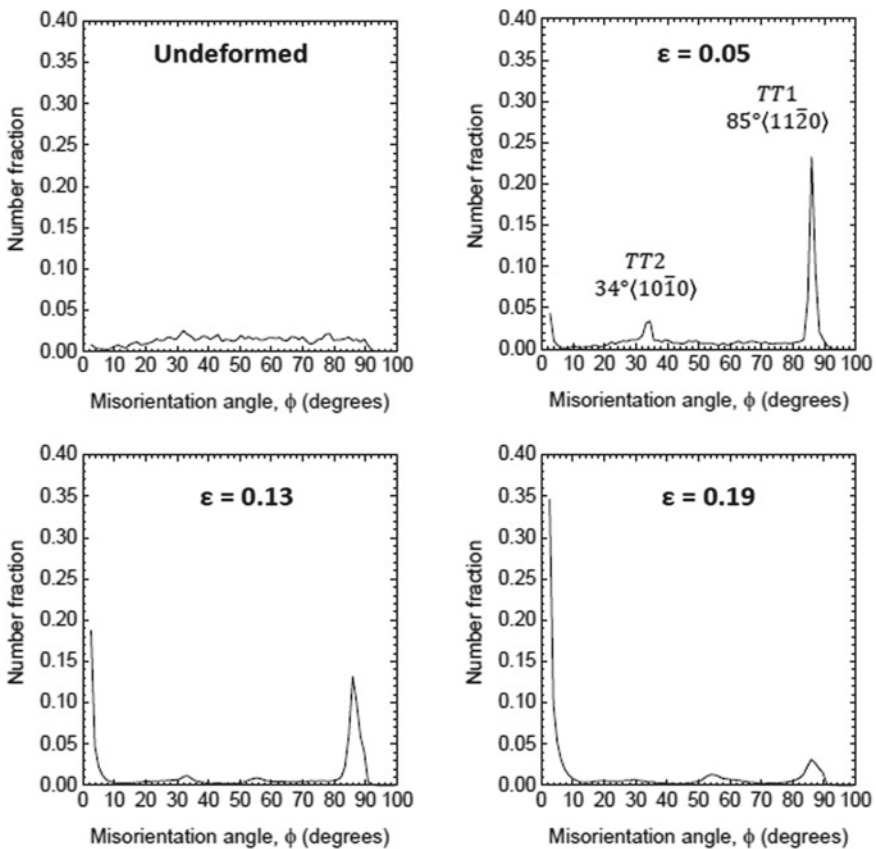
Fig. 5 Misorientation angle distribution plots for Zircaloy-4—undeformed specimen and specimens deformed to strain levels of 0.05, 0.13, 0.19

of various slip systems. The evolution of twin boundary fraction[1] with strain calcu-
lated from the MAD plots in Fig. 5 has been shown in Fig. 6. It can be seen that a
maximum twin boundary fraction of ~0.50 is attained at strain of 0.05 which reduces
to less than 0.1 at strain of 0.19. The initial increase in twin boundary fraction can be
attributed to the formation of twins within the parent grains. The subsequent decrease
in twin boundary fraction could be due to the following reasons.

i.   Growth of twins, which ultimately grow to reach prior grain boundaries,
ii.   Increase in some high angle boundaries (shallow peak between 50 and 60° in
       Fig. 5 for strain of 0.19) corresponding to twin-twin (the interaction of a twin
       with another twin results in boundaries having misorientation angle different
       from that of original parent-twin misorientation relationship) and slip-twin
       interactions (slip, which is a consequence of motion of dislocations, when
       interact with twin causes damage to the original parent-twin interface resulting
       in a boundary misorientation angle that is slightly higher or lower than that of
       original parent-twin interface) and
iii.   Increase in low angle boundaries due to slip-slip interactions (interactions
       among dislocations results in formation of dislocation junctions and networks
       that lead to formation of low angle boundaries, LABs. The fraction of these
       boundaries increase with strain. Considering a same amount twin boundaries
       with and without LABs, it can be said that with increase in LABs the number
       of fraction of twin boundaries decrease).

With increasing strain, the boundaries of existing twins get damaged by the inter-
acting dislocations, other twins, and prior grain boundaries. Due to such damage,

---

[1] Twin boundary fraction = $\frac{\text{length of twin boundaries}}{\text{length of all boundaries}}$ = $\frac{\text{number of twin misorientations}}{\text{number of total misorientations} > 2°}$ = $\sum\limits_{\varphi_1}^{\varphi_2} f(\varphi)$

where φ_1 and φ_2 are 80 and 90° for TT1 and 33 and 37° for TT2, and f is the number fraction in
MAD plot.

identification of twin boundaries or the reflection plane of the twin system becomes difficult. Using the textural information from the initial undeformed specimen (Fig. 1), the area fraction of twins for the deformed specimens was calculated using image analysis. In the undeformed specimen, most of the grains have <c>-axis or basal poles perpendicular to the compression axis (red color, in IPF map color code, referring to basal poles is not visible in the IPF map ∥ RD of the undeformed specimen). With straining, the formation of TT1 twins resulted in an abrupt reorientation of the lattice by 85° about ⟨11$\bar{2}$0⟩ axis which ultimately led to the alignment of basal poles parallel to the compression axis (red color, in IPF map color code, referring to basal poles increased with strain). A color threshold was used to identify areas with red color (basal poles) in the IPF maps shown in Fig. 4 to determine the twin area fraction. The evolution of the twin area fraction is shown in Fig. 6. The area fraction of twins increased monotonically with strain in contrast to twin boundary fraction which initially increased to reach a maximum and reduce thereafter.

The observed three stage work hardening behavior (Fig. 3b) was suggested to occur as a consequence of competition among different hardening mechanisms [5, 20]: (i) reduction in boundary spacing and the formation of twins results in a decrease in the effective grain size, (ii) increase in sessile dislocation density, referred to as Basinski hardening, and (iii) abrupt change in grain orientation due to twinning causes either softening or hardening of the grain by directly affecting the resolved shear stresses on the slip/twin systems. The initial low work hardening rate (stage-I) could be due to interactions among soft prismatic <a> dislocations which is the primary slip system for α-Zr alloys. The increasing work hardening rates (stage-II) could be primarily attributed to the reduction in boundary spacing due to the formation of twins (interactions of dislocations with twin boundaries). The decreasing work hardening rate in stage-III could be attributed to the reduction in twin boundary fraction (increased boundary spacing as a consequence of twin growth.

In order to determine the evolution of grain hardness due to grain reorientation by twinning, Schmid factor evolution for prismatic <a> slip was mapped as shown in Fig. 7. The Schmid factor values were calculated for all three prismatic <a> slip systems at each indexed point in the EBSD map and the maximum among the three is mapped in Fig. 7. It can be seen that for the undeformed sample, almost all grains are likely to deform by prismatic <a> slip. The deformation along the <c> axis of the lattice is found to be accommodated majorly by the formation of TT1 twins. The grain reorientation caused by TT1 twins resulted in very low Schmid factor values for the prismatic <a> slip systems within the twinned regions. This would lead to possible activation of secondary slip system, pyramidal <c + a> slip, within the twinned region. The interaction of hard pyramidal <c + a> slip with twin boundaries could lead to an increased work hardening rate observed in stage-II of work hardening response.
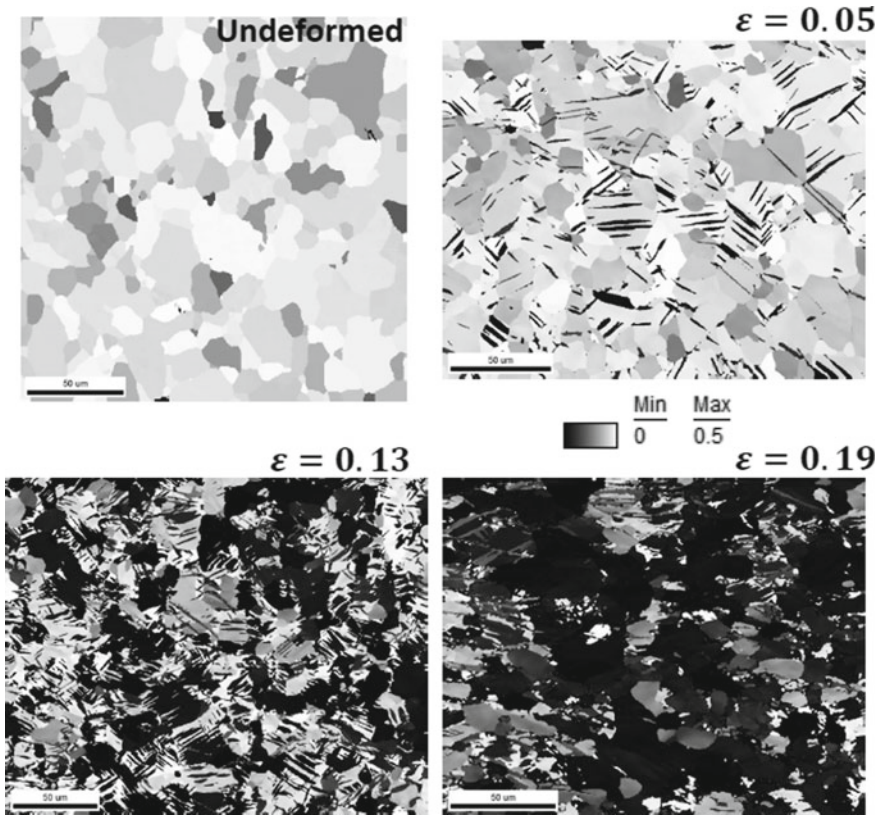
Fig. 7 Schmid factor maps for the prismatic <a> slip system for the undeformed specimen and subsequent deformed specimens to strain levels of 0.05, 0.13 and 0.19

4 Summary and Conclusions

- Specimens of Zircaloy-4 were deformed at high strain rate of about 1200 s^{-1} and at 25 °C using the SHPB setup.
- The flow curve showed a sigmoidal stress-strain response with three stages of work hardening behavior typically associated with the formation of twins during deformation.
- Microstructural analysis using EBSD revealed the formation of TT1 and TT2 twins at high strain rate in contrast to only TT1 at quasi-static strain rate. The formation of TT2 could be due to a possible increase in the CRSS of pyramidal <c + a> slip system at high strain rate.
- The evolution of work hardening rate was correlated with twin boundary and area fraction.
- The high and increasing work hardening rates in stage-II deformation could be attributed to (1) reduced average boundary spacing due to the formation of twins

and (2) decrease in the Schmid factor of soft prismatic <a> slip within the twinned volume which leads to an increase in the possibility of the activation of hard pyramidal <c + a> slip within the twinned regions. The interaction of hard (slip system with high CRSS) pyramidal <c + a> slip with twin boundaries leads to high work hardening rates as were observed during stage-II deformation of Zircaloy-4.

References

1. Britton T, Dunne F, Wilkinson A (2015) Proc R Soc A Math Phys Eng Sci 471:20140881
2. Tenckhoff E (2005) J ASTM Int 2:1–26
3. Akhtar A, Teghtsoonian A (1971) Acta Metall 19:655–663
4. Beyerlein I, Tomé C (2008) Int J Plast 24:867–895
5. Kapoor R, Sarkar A, Singh J, Samajdar I, Raabe D (2014) Scripta Mater 74:72–75
6. Reddy GB, Sarkar A, Kapoor R, Kanjarla AK (2018) Mater Sci Eng A 734:210–223
7. Barnett M, Ghaderi A, Da Fonseca JQ, Robson J (2014) Acta Mater 80:380–391
8. Beyerlein I, McCabe R, Tomé C (2011) J Mech Phys Solids 59:988–1003
9. Fundenberger J, Philippe M, Esling C (1990) Scr Metall Mater 24:1215–1220
10. Khosravani A, Fullwood D, Adams B, Rampton T, Miles M, Mishra R (2015) Acta Mater 100:202–214
11. Knezevic M, Zecevic M, Beyerlein IJ, Bingert JF, McCabe RJ (2015) Acta Mater 88:55–73
12. McCabe R, Cerreta E, Misra A, Kaschner G, Tomé C (2006) Phil Mag 86:3595–3611
13. McCabe RJ, Proust G, Cerreta EK, Misra A (2009) Int J Plast 25:454–472
14. Reddy GB, Kapoor R, Sarkar A (2019) Int J Plast 122:164–187
15. M.A. Meyers, Dynamic behavior of materials, John wiley & sons, 1994.
16. Nemat-Nasser S, Kapoor R (2001) Int J Plast 17:1351–1366
17. Kuhn H, Medlin D (2000) ASM International, Member/Customer Service Center, Materials Park, OH 44073-0002, USA, 998
18. Chen WW, Song B (2010) Split Hopkinson (Kolsky) bar: design, testing and applications. Springer Science & Business Media
19. Sharma S, Chavan V, Agrawal R, Patel R, Kapoor R, Chakravartty J (2011) Bhabha Atomic Research Centre
20. Salem AA, Kalidindi SR, Doherty RD (2003) Acta Mater 51:4225–4237

Use of Compression-Bending Fracture Geometry to Study the Effects of Stoichiometry on Fracture Toughness of β-NiAl

Devi Lal, Ananya Tripathi, Abhijit Ghosh, Ravi Bathe, Praveen Kumar, and Vikram Jayaram

Abstract Compression-bending fracture geometry is a stable fracture geometry, which can enable the study of crack propagation and associated processes, such as crack bridging and microstructural and compositional inhomogeneity induced variation of fracture toughness and R-curve behavior. It was observed that surface friction strongly influences the fracture behavior of this geometry. The existing equation of Mode I stress intensity factor, K_I, has been found to be accurate for the case of very low platen-sample surface friction and a narrow range of crack length. The fracture toughness of bulk polycrystalline β-NiAl of two compositions was measured using this geometry. The measured values of fracture toughness of Ni-50Al and Ni-40Al are 1.7 ± 0.6 and 4.3 ± 1 MPa m$^{0.5}$, respectively.

Keywords Compression-bending fracture geometry · FEM · NiAl · Fracture toughness

1 Introduction

Brittle materials show wide variations in compressive strength, depending on sample dimension, surface roughness, platen alignment, etc. Kendall [1] studied this phenomenon and proposed that uneven distribution of compressive stresses on the surfaces leads to bending of the structure, which produces tensile stresses near pre-existing cracks, thereby leading to failure. Since the magnitude of these stresses depends on sample dimensions, platen alignment, etc., the compressive strength of the material also varies. Kendall [1] exploited the bending stresses to study Mode I

D. Lal (✉) · A. Tripathi · A. Ghosh · P. Kumar · V. Jayaram
Department of Materials Engineering, Indian Institute of Science, Bengaluru 560012, India

A. Ghosh
Department of Metallurgy Engineering and Materials Science, Indian Institute of Technology Indore, Indore 453552, India

R. Bathe
Centre for Laser Processing of Materials, International Advanced Research Centre for Powder Metallurgy and New Materials (ARCI), Hyderabad 500005, India

fracture using a sample with a vertical pre-crack by loading it using a loading punch. This is remarkable as it brings the convenience of compressive loads in studying the fracture behavior of brittle materials, which are often difficult to grip. He studied axial splitting of pre-cracked glassy material in compression and discussed the effects of sample dimensions, platen dimensions, and the lateral pressure, which restricts the outward bending, on the crack propagation. Later, Karihaloo [2] showed that the platen-sample surface friction also affects the outward bending and therefore influences the stress distribution near the pre-crack.

Liu et al. [3] revisited the above-mentioned approach of compression-bending and proposed a modified new geometry (see Fig. 1) to study the fracture toughness of hard thin coatings, such as SiC, CrN, GaAs, etc. They also provided the mechanistic details of this geometry, including the following relationship to determine applied K_I:

$$KI = \sqrt{3}\frac{P}{bd^{3/2}}\left(\frac{d-w}{2} - \mu h\right) \tag{1}$$

where P is the applied load, 2d is the width of the sample, w and h are width and height of the pillar, respectively, μ is the coefficient of friction between punch and pillar, c is crack length, as shown in Fig. 1. In Eq. (1), the first term in the parenthesis on the right-hand side represents the moment opening the crack in Mode I, whereas the second term denotes the moment arising due to the friction opposing the crack opening. Hence, the applicability of Eq. (1) is limited to the condition wherein the pillar slides outward relative to the punch. Furthermore, the geometry is shown in
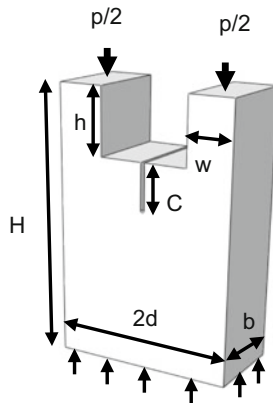
Fig. 1 Schematic illustrating the compression-bending fracture sample. In this geometry, both compression and bending occur together; however, outward bending relative to the crack tip is responsible for opening the crack in Mode I. The crack plane is assumed to be the neutral axis. All-important parameters required to define the geometry are also defined. An ideal sample, for which Eq. (1) is valid, satisfies the following conditions: H >> h, w ~ d/2, c << h, and friction between the base of sample and sample platform is zero

Fig. 1 and Eq. (1) work only if fracture precedes yielding in the loaded pillars, and hence it is ideally suited to estimate fracture toughness of hard and brittle materials. Furthermore, later, we will show that Eq. (1) provides reasonably acceptable values of Mode I fracture toughness when friction is very low (i.e., close to zero) and over a limited range of crack length; however, significant error may arise as the friction coefficient and the crack length increase. Nevertheless, the geometry shown in Fig. 1 has gained popularity due to the relative ease of specimen fabrication and performing the test.

In this study, the above-mentioned compression-bending fracture geometry (CBFG) was further developed for a sample with c ~ h and subsequently used to study the fracture behavior of a couple of cast β-NiAl alloys. β-NiAl constitutes the principal component of the bond coat, which is used to protect superalloys from oxidation. NiAl in the bond coat acts as a reservoir for Al, which forms a very thin protective layer of alumina, known as thermally grown oxide (TGO). The formation of TGO protects the superalloy from oxidation by acting as a barrier to oxygen diffusion from the environment [4]. Therefore, the structural integrity of the bond-coats is critical for the acceptable functioning of the superalloy structure. Now, the structural integrity of NiAl, which is the material of choice for the bond coat because of its high melting point and thermal stability along with good oxidation resistance [5], is affected by various parameters, such as high-temperature creep, cracking at a lower temperature, phase transformation, etc. [6]. Therefore, studying the room temperature fracture behavior of NiAl will impart an improved understanding of the mechanisms of coating failure. To our best knowledge, the fracture behavior of β-NiAl, which is brittle at room temperature, has never been studied using the compression-bending geometry shown in Fig. 1.

2 Details of Experiments and Numerical Analysis

High Purity Al (99.9%) and Ni (99.9%) pellets were arc-melted to produce two compositions of β-NiAl, namely Ni-49 Al and Ni-40 Al. The buttons produced after arc melting were homogenized at 1000 °C for 100 h. Post heat treatment microstructure and composition were analyzed using optical microscopy and energy dispersive spectroscopy (EDS), respectively. The microstructure of the cast-homogenized β-NiAl alloys is shown in Fig. 2, revealing that the grain size was of the order of 1 mm.

The compression-bending fracture geometry was machined from homogenized buttons of NiAl using electric discharge machining (EDM). The pre-notch was fabricated using the femtosecond laser ablation technique. The associated parameters of laser power, wavelength (λ), pulse width, repetition rate, and cutting speed were 200–300 mW, 800 nm, 100 fs, 10^4 Hz and 1.5 mm/min, respectively. The notches were V-shaped, with a notch-tip radius of <1 μm. The important dimensions of the compression-bending fracture samples are as follows: pillar height, h = 1 mm, pillar
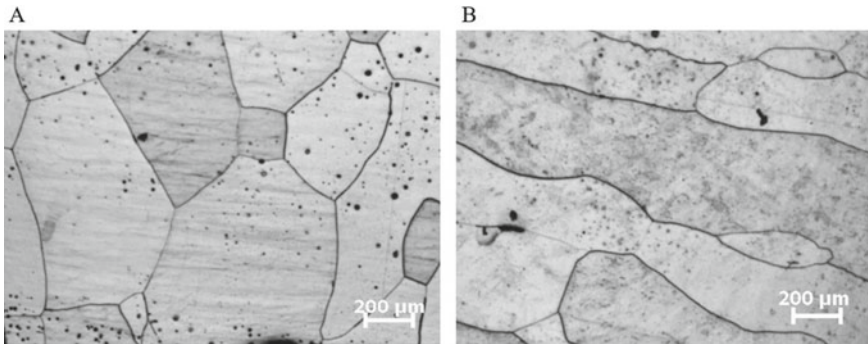
Fig. 2 Optical micrographs showing the microstructure of (A) Ni-40Al and (B) Ni-49Al alloys after homogenization

width, w = 1.2 mm, sample width, 2d = 6 mm, sample thickness, b = 2 mm, and crack length, c = 0.5 ± 0.1 mm.

The pre-notched samples were loaded in compression in a universal testing machine (UTM) using a punch made up of WC in the displacement control mode. A graphite sheet placed in between the loading punch and the pillar was used as the lubricant to reduce the friction coefficient. The lubricated sample-platen friction coefficient was taken as 0.1 for the calculation of the fracture toughness. Three measurements were carried out for each alloy, and the average was taken as the value of fracture toughness.

Extended finite element analysis (XFEA) was performed using ABAQUS, a commercial FEA software, to estimate the stress intensity factor for the selected sample geometry and test condition. Since Eq. (1) assumes that the frictional moment is $\mu Ph/2$, which is a reasonable approximation when the μ is close to 0, c << h and the outward deflection is insignificant, a parametric study was performed here using FEA to examine the case when c is not negligible as compared to h. For this purpose, c was varied from 0.2 to 2 mm, and other dimensions of the FEA model were kept constant as follows: h = 2 mm, 2d = 4 mm, w = 1 mm, b = 2 mm, H = 6 mm. FEA was performed assuming material to be elastic, with Young's modulus, E, of 200 GPa and Poisson's ratio, ν, of 0.25[7]. Finite friction, with a sliding contact option, was applied between the loading platen and the pillar, whereas the base of the sample was affixed completely to the sample platform.

3 Results and Discussion

As mentioned earlier and shown clearly in Fig. 3, the friction between the loading punch and the pillars prevents the outward bending of the sample. A comparison between Fig. 3a, b, which shows the outward bending at a fixed load for friction coefficient, μ, of 0.2 and 0.0002, respectively, reveals that the maximum deflection
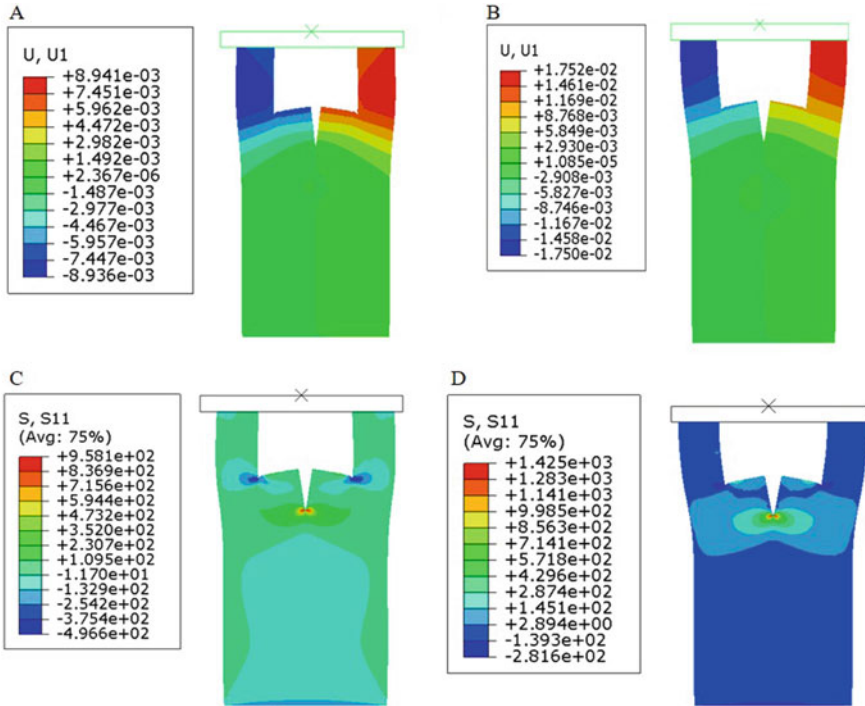
Fig. 3 FEA results showing the effect of the friction coefficient between the loading platen and the pillars on the deformation-field (in x-direction) in the compression-bending fracture sample: $\mu =$ **a** 0.2 and **b** 0.0002, and corresponding stresses are shown in (**c**) and (**d**), respectively. All degrees of freedom of the base were fully constrained (i.e., at the base, $U_1 = U_2 = 0$). Deformation scale factors in (**a–d**) are 20, 20, 24, and 24, respectively. The x-axis and y-axis are horizontal and vertical, respectively. The S11 shown in (**c**) and (**d**) is x-direction normal stresses

increases by a factor of ≈ 2 if the corresponding surface friction is reduced by three orders. Furthermore, Fig. 3 also shows that the tendency of the top surface to stick to the loading punch and the bulging of the sample at the center would increase with the friction coefficient. Consistent with displacement contours, Fig. 3c, d, which show the stress distribution for μ of 0.2 and 0.0002, respectively, reveal that the friction coefficient also affects the stress distribution, such that the stress near the crack tip increases with a decrease in the friction coefficient. Therefore, friction plays a significant role in outward bending as well as stress field ahead of the crack tip, and hence the stress intensity factor.

Figure 4 shows the variation of K_I as a function of c for various values of μ, as obtained from FEA and Eq. (1). Since Eq. (1) is not sensitive to the crack length (i.e., it assumes c << h), it could only capture the effect of μ, revealing a decrease in K_I with μ. Nevertheless, there is a significant difference between the FEA results and Eq. (1), even for the smallest crack lengths. As a matter of fact, the closest match between Eq. (1) and FEA over a noticeable range of c was observed only when the
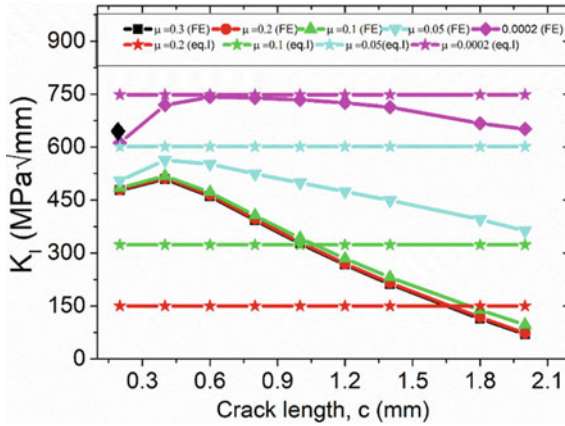
Fig. 4 Variation of stress intensity factor in Mode I, K_I, as a function of the crack length, c, for various friction coefficient, μ, as obtained using FEA (various symbols) and Eq. (1) (shown by the star symbol). The datum point shown by the black diamond symbol represents the value of K_I calculated for the model, with c = 0.2 mm (i.e., the smallest crack length) and μ = 0.0002, using a mesh size 4 times smaller than the corresponding model shown by a pink diamond. A similar match was observed for other models also. A close match between these two sets of values indicates the attainment of mesh insensitivity in the FEA in this study

μ was extremely small (e.g., μ = 0.0002). Interestingly, FEA also revealed that for μ = 0.0002, K_I did not vary significantly with c. This is reasonable as the moment due to the friction, given as $M_f \approx 0.5\mu P(h + c)$, remains negligible for all value of c due to a very small value of μ. Figure 4 shows that the values of K_I, calculated using FEA, increased with c when the latter is very small, reaching a maximum, and then started to decrease with further increase in c. As the stress field of the long crack starts interacting with the compressive stress field near the bottom surfaces, K_I is expected to decrease for large c. However, the major differences between FEA and Eq. (1) appear when μ increases to the values encountered in real tests (e.g., $\mu \sim$ 0.1): K_I becomes insensitive to μ once μ becomes $\geq$0.1. It is reasonable as beyond a certain high value of μ, the sliding between the pillar and the loading platen will cease, and the tensile stress near crack tip and hence K_I will be mainly determined by bulging of the sample. It can be inferred from Fig. 4 that FEA, rather than Eq. (1), should be used to estimate K_I, as performed in this study.

A few example load-deflection curves and the corresponding SEM micrographs showing the crack propagation are shown in Fig. 5. The fracture toughness was calculated corresponding to the load at the pop-ins using FEA, following the approach proposed by Jaya et al. [6]. Despite local deviations, the average direction of movement in the first pop-in is approximately perpendicular to the original crack front, though the second kink in Fig. 5d has a significant mode II component and may be associated with propagation along a grain boundary. The surface friction coefficient between two hard surfaces lubricated with a graphite sheet has been reported to be in the range of 0.1–0.15, depending on the surface and the ambient conditions [8].
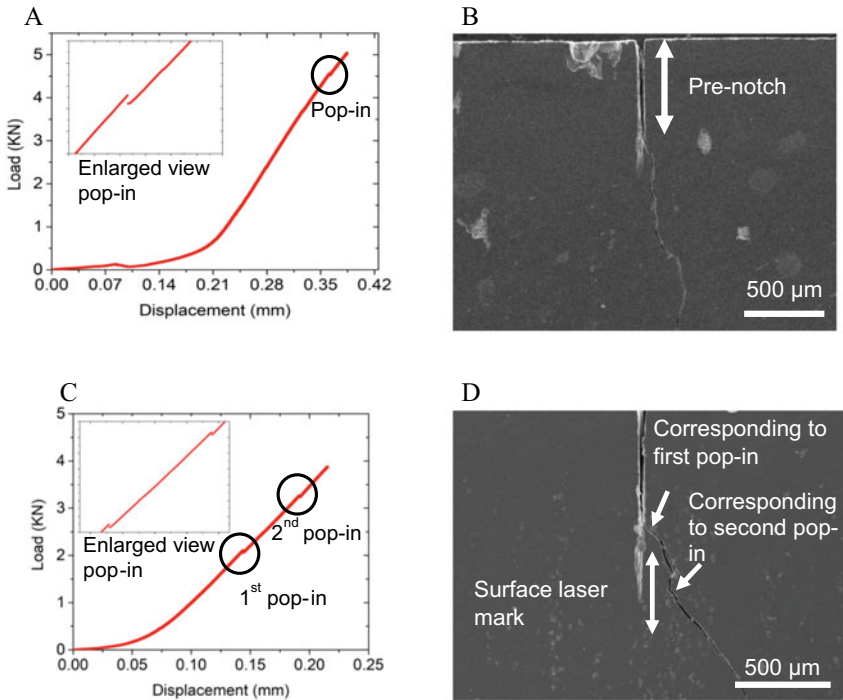
Fig. 5 Load-displacement plot of compression-bending fracture geometry and SEM micrograph showing corresponding crack extension: **a** Load-displacement plot showing a single pop-in and **b** SEM micrograph showing crack propagation corresponding to (**a**), **c** load-displacement plot showing double pop-in events, and **d** SEM micrograph showing crack propagation corresponding to (**c**). The inset in (**a**) and (**c**) show an enlarged view of the pop-in events

Now, as shown in Fig. 4, K_I does not depend significantly on the friction coefficient once μ becomes greater than 0.1. Hence, a reasonable value of $\mu = 0.1$ was used here for the calculations of fracture toughness. The average values of the fracture toughness, in terms of K_{IC}, for Ni-49Al and Ni-40Al were estimated to be 1.7 ± 0.6 and 4.3 ± 1 MPa $m^{0.5}$, respectively. The fracture toughness of NiAl reported in the literature has wide variations, ranging from 1.8 MPa $m^{0.5}$ to 6 MPa $m^{0.5}$ [9–11], and the values measured in this study fall within the reported range.

The higher fracture toughness in Ni-rich β-NiAl is believed to be due to the segregation of the Ni_3Al phases near the grain boundary [11]. Occasionally, it was also observed that crack propagation occurs with two pop-ins, as shown in Fig. 5c, d. In this work, it has been observed that in a few tests, the crack deflected from its original path, possibly due to the presence of a grain boundary and the crystallographic anisotropy of cleavage energy [8] in these coarse-grained samples (see Fig. 2), where there are only a few grains across the section of the test samples. In line with the above statement, K_{IC} measured corresponding to the first pop-in was observed to be lower than that at the second pop-in (Fig. 5c). The lower resistance direction might be the

weaker grain boundaries or crystallographic planes having lower fracture toughness, such as {110}.

4   Conclusions

The compression-bending fracture geometry is attractive for studying fracture behavior of brittle and small samples. However, the currently used analytical expressions are only applicable in the limit of vanishing friction coefficient and small crack lengths. FEA reveals that the stress intensity factors deviate substantially when the friction coefficient is increased up to ~0.1 and the crack length is increased. The measured values of room temperature fracture toughness of Ni-50Al and Ni-40Al are 1.7 ± 0.6 and 4.3 ± 1 MPa m$^{0.5}$, respectively, which are within the previously reported values for these alloys.

References

1. Kendall K (1978) Complexities of compression failure. Proc R Soc London Ser A 361(1705):245–263. https://doi.org/10.1098/rspa.1978.0101
2. Karihaloo BL (1979) Note on complexities of compression failure. Proc R Soc Lond Ser A Math Phys Sci 368(1735):483–493. https://doi.org/10.1098/rspa.1979.0142
3. Liu S, Wheeler JM, Howie PR, Zeng XT, Michler J, Clegg WJ (2013) Measuring the fracture resistance of hard coatings. Appl Phys Lett 102(17):1–5. https://doi.org/10.1063/1.4803928
4. Feuerstein A, Knapp J, Taylor T, Ashary A, Bolcavage A, Hitchman N (2008) Technical and economical aspects of current thermal barrier coating systems for gas turbine engines by thermal spray and EBPVD: a review. J Therm Spray Technol 17(2):199–213. https://doi.org/10.1007/s11666-007-9148-y
5. Tobergte DR, Curtis S (2013) Physical and mechanical properties of the polymer. J Chem Inf Model 53(9):1689–1699
6. Jaya NB, Jayaram V, Biswas SK (2012) A new method for fracture toughness determination of graded (Pt,Ni)Al bond coats by microbeam bend tests. Philos Mag 92(25–27):3326–3345. https://doi.org/10.1080/14786435.2012.669068
7. Deng YH (2014) Study of the mechanical and thermodynamic properties on NiAl and Ni3Al. Appl Mech Mater 584–586:1256–1263. https://doi.org/10.4028/www.scientific.net/AMM.584-586.1256
8. Bill RC (1978) Friction and wear of carbon-graphite materials for high-energy brakes
9. Iqbal F, Ast J, Göken M, Durst K (2012) In situ micro-cantilever tests to study fracture properties of NiAl single crystals. Acta Mater 60(3):1193–1200. https://doi.org/10.1016/j.actamat.2011.10.060
10. Ast J, Przybilla T, Maier V, Durst K, Göken M (2014) Microcantilever bending experiments in NiAl—evaluation, size effects, and crack tip plasticity. J Mater Res 29(18):2129–2140. https://doi.org/10.1557/jmr.2014.240
11. Kumar KS, Mannan SK, Viswanadham RK (1992) Fracture toughness of NiAl and NiAl-based composites. Acta Metall Mater 40(6):1201–1222. https://doi.org/10.1016/0956-7151(92)90419-F

Numerical Slosh Studies of Multiple Ring Baffles in a Semi-Cryogenic Fuel Tank

**Aleena Seban, Kodati Srinivas, M. Satyakumar,
and S. Sarath Chandran Nair**

Abstract One of the heavy lift launch vehicles being developed by ISRO uses semi-cryogenic stage. Semi-cryogenic stage uses Isrosene as a fuel and liquid oxygen (LOX) as the oxidizer. These propellants will be supplied at a specific flow rates to the rocket engine to develop the required thrust. Sloshing is an important phenomenon to be considered for liquid/cryogenic/semi-cryogenic stages in order to design control system for the launch vehicle. For modeling slosh for control system studies, mathematical parameters such as slosh frequency, slosh mass and its location are required to be evaluated. In addition to these parameters, damping also play a major role in containing the vehicle response due to slosh. In the present study the parameters required for mathematical modeling of slosh for control stability analysis are evaluated using two different FE codes. The requirement of damping and duration envisaged from control stability analysis is met by designing multiple ring baffles using semi-empirical relations. In addition to the above, the achievable damping values for the designed baffle and its effect on slosh parameters are also studied.

Keywords Semi-cryogenic stage · Sloshing · Slosh frequency · Slosh mass

1 Introduction

Slosh is termed as the periodic oscillations of the free surface of a liquid in a partially filled tank when subjected to external disturbance. Liquid carrying trucks have to face different road conditions and the unavoidable motion of the vehicle may cause

A. Seban (✉)
Mar Baselios College of Engineering and Technology, Thiruvananthapuram 695015, India

K. Srinivas · S. Sarath Chandran Nair
Structural Dynamics Division, Mechanical Design and Analysis Entity, LPSC/ISRO, Valiamala, Thiruvananthapuram 695547, India

M. Satyakumar
Department of Civil Engineering, Mar Baselios College of Engineering and Technology, Thiruvananthapuram 695015, India

sloshing of the liquid. The forces associated with the sloshing can cause violent movement of the interface [1]. Slosh suppression devices are employed to damp unwanted liquid motions and avert any kind of subsequent instabilities. Tank geometry influences the natural sloshing frequencies and sloshing modes, forced response and resultant pressure forces and moments acting on the tank. The obstructions in the fluid path, generally as baffles, increase the effective fluid damping and thereby reduce the magnitude of forced oscillations (i.e., there by suppressing the liquid motions) by dissipation of energy. Thus, the anti-sloshing baffles are designed to provide damping to the system so that the high amplitudes of slosh oscillations are reduced. Configuration and number of baffles are determined primarily by the damping and its duration requirement. The structural requirements of the baffle are determined after consideration of many factors such as strength and rigidity needed during manufacturing and handling. Based on the damping requirement, different types of baffles are used. They are generally vertical, annular ring, staggered, perforated [2].

The semi-cryogenic engine replaces liquid hydrogen with refined kerosene (Isrosene as ISRO calls it) which will be liquid at room temperature and LOX will be retained as oxidizer which will be liquid at around 80 K temperature compared to cryogenic stage. Development of semi-cryogenic engine is envisaged for launching heavier satellites into space using GSLV Mk-III vehicle. It is eco-friendly and cost-effective stage in place of existing earth storable booster stage.

In the last few decades researches have investigated sloshing of liquid numerically, analytically as well as experimentally. The special NASA monograph edited by Abramson addressed the sloshing problems encountered in aerospace vehicles. The monograph contained the analytical and experimental studies of linear, nonlinear sloshing, damping of liquid motions, vertical excitations of tanks, interaction of liquid propellants and elastic structures, vehicle stability and control, liquid propellant behavior at low and zero gravity, longitudinal oscillation of flight vehicles, etc., Yu et al. [1] conducted experimental studies of suppressing effectiveness on sloshing with two perforated floating plates. It was observed that perforated plate with the median solidity ratio was most optimal in slosh suppression. Yu et al. [3] conducted experimental study of vertical slat screens effects on reducing shallow water sloshing in a tank under horizontal excitation with a wide frequency range. Xue et al. [4] conducted experimental study on vertical baffle of different configurations in slosh suppression. Kumar and Sinhamahapatra [5] studied the dynamics of rectangular tank with perforated vertical baffle. Suyal and Sathapathy [6] conducted CFD analysis of fuel in a cylindrical tank with and without baffles. Kamitkar et al. [7] conducted CFD analysis of spacecraft vehicle fuel tank to reduce sloshing by using ANSYS Fluent. In this study it was studied damping produced by single flexible ring baffle. Baffles were of different thickness and material. Brar and Singh [8] conducted experimental and CFD analysis of sloshing in a tanker. Singal et al. [9] conducted CFD analysis of kerosene fuel tank to reduce liquid sloshing. CFD analysis was carried out using ANSYS FLUENT 12.0. VOF model was designed to capture the position of interface of air and kerosene. Jin et al. [10] conducted experimental study on sloshing in a tank with an inner horizontal perforated plate. Wang et al. [11] conducted sloshing of liquid in rigid cylindrical container with multiple rigid annular baffles.

The focus on the present study is to design anti-slosh baffles for the required specification of damping and duration by multiple ring baffle concept for a semi-cryogenic stage. And also, to evaluate the slosh parameters in fuel tank with and without anti-slosh baffles thereby study the effect of baffles on slosh parameters. Slosh parameters for clean tank will be initially evaluated numerically for arriving at damping specification by control team. Multiple ring baffles are designed using closed form solutions based on the specified damping requirements.

2 Design of Multiple Ring Baffles

The ring baffles provide a substantial amount of damping when the free surface is near its location. The spacing between the baffles is to be optimally chosen so that the minimum damping provided by one of the baffle exceeds the damping requirements. Baffle damping is determined by using semi-empirical relation called Miles equation[1].

$$\gamma = 2.83 e^{\left(-4.6 \times \frac{hs}{R}\right)} a^{\left(\frac{3}{2}\right)} \frac{\delta^{\left(\frac{1}{2}\right)}}{R} \tag{1}$$

The exponential term in equation implies that γ decreases with the liquid depth of immersion hs above the baffle. In contrast to viscous damping, the damping provided by a ring baffle is nonlinear and depends on amplitude of the sloshing (pendulum angle). 'a' is the area ratio given by $a = \frac{Ro^2 - Ri^2}{R^2}$, where Ro is the outer radius and Ri is the inner radius of baffle and R is the total tank radius, $\frac{\delta}{R}$ is the pendulum angle in radian. γ is the damping ratio [2]. Damping specifications are worked based on control stability analysis studies. Damping requirements were concluded as 1% damping ratio for an effectiveness period of 55 s based on these studies. Design factor considered for damping ratio is 1.25. Design effectiveness period is considered as 60 s by proving a margin on duration. Propellant density and kinematic viscosity of Isrosene is 796.14 kg/m^3 and 1.81E-6m^2/s, respectively. Based on the propellant loading and propellant depletion mass flow rate, initial fill height and height corresponds to 60 s are evaluated. Tank geometry of fuel tank is a cylindrical tank with tori-spherical end domes. The ratio of the total height of tank-to-tank radius is 2.5. Tank is made of aluminum alloy and considered as rigid for slosh studies.

Two ring baffles optimally spaced are designed to meet the damping specification. Width to radius of tank (w/R) of both baffles works out to be 0.1375. First baffle is located at h/R ratio of 1.325 and second baffle is located at h/R ratio of 1.037.

From Fig. 1 it can be concluded that total damping meets the damping requirement of 1.25% for required duration of 55 s. Thus, the designed baffle configuration and location of baffle are meeting the given requirements of damping.
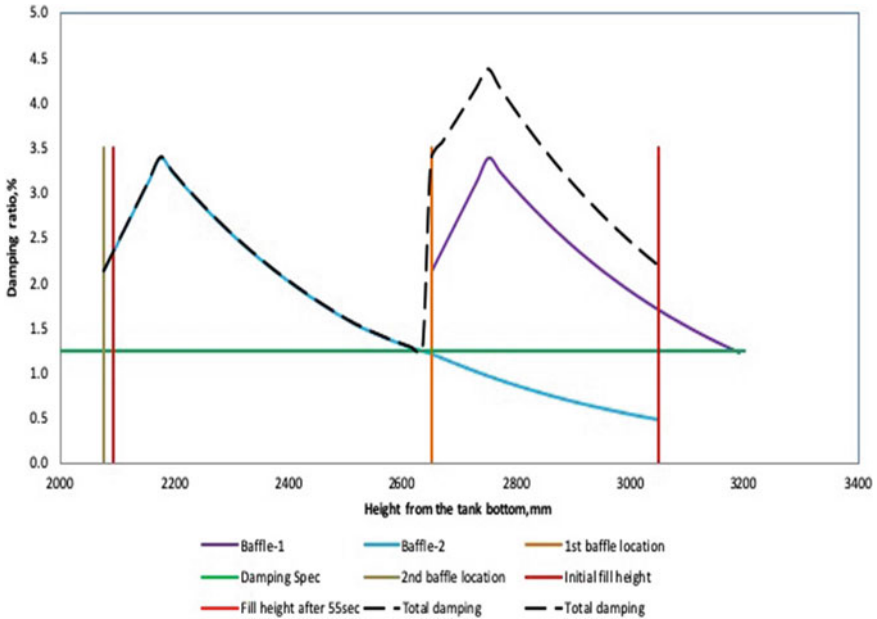
Fig. 1 Achievable damping in tank with designed baffle configuration

3 Numerical Analysis

Two different FE codes are used for carrying out slosh analysis. Both codes use linear velocity potential flow equation in frequency domain with appropriate boundary conditions to obtain solution. Difference in both codes is limitation in problem size and operating system used. Analysis is done for different fill ratios vary from 1.037 to 1.325. The geometry of the tank shown in Fig. 2 and baffle geometry are the input data.

3.1 Slosh Parameter Evaluation Using FE Code 1

It is a user-friendly code written in FORTAN. This code can run in any 32 bit or 64 bit based windows software. This code provides more converged solution. It uses QUAD4 elements. It has the ability to handle very fine meshes as well since the mesh generation is done in pre-processor of ANSYS Mechanical FE commercial software.

Fig. 2 Tank geometry
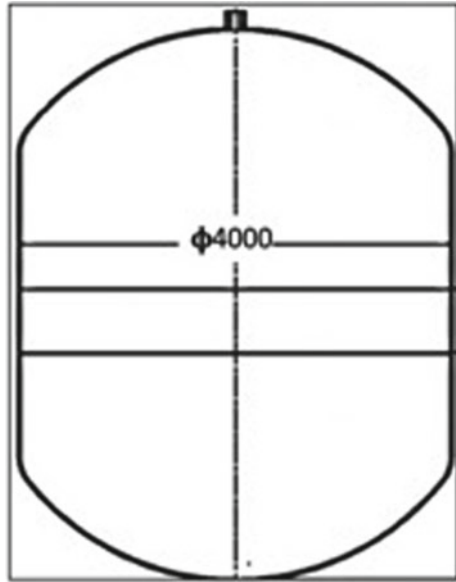
3.2 Slosh Parameter Evaluation Using FE Code 2

FE code for slosh analysis was a commercial software. The software is in-house ISRO codes. It used mid node triangular elements. Initial mesh is generated manually by identifying sides, elements, boundaries, and nodes. It employs adaptive meshing till convergence is achieved by generating 4 elements in place of one element using mid nodes. It works only on MSDOS operating system and handles limited problem size. It is required to define x and r the coordinates of nodes in cylindrical coordinates system.

4 Comparison Study

Initially slosh parameters are evaluated for clean tank (without baffle) using both FE codes and used for control stability studies for finalizing the damping specification. Non dimensional slosh parameters M_1/M_t, h_1/R, w^2R/a are evaluated with respect to h/R from both FE codes and compared them.

Figure 3 shows that the mass ratio M_1/M_t decreases as the h/R increases. Slosh mass reaches saturation value beyond h/R = 1.0. Hence ratio of slosh mass (M_1) to total mass (M_t) decreases as the mass of the liquid increases due to increase in h/R. Figure 4 shows that with the increase of h/R, h_1/R also increases constantly. It is because as h/R increases, the fill height (h1) also increases and thus the location mass also increases accordingly.

Fig. 3 Variation of mass ratio (M_1/M_t) with h/R obtained for both FE codes
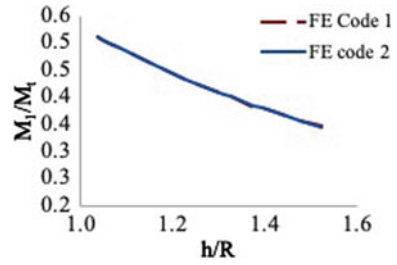
Fig. 4 Variation of slosh mass location (h_1/R) with h/R obtained for both FE codes
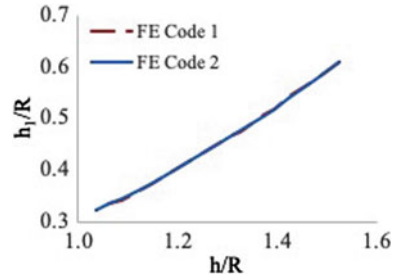
Fig. 5 h/R versus w^2R/a plot for clean tank
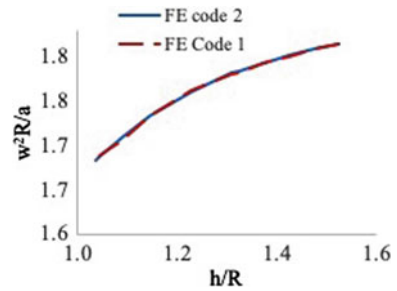
Figure 5 hows slosh frequency is proportional to h/R thus increase in frequency parameter is observed as h/R increases.

5 Slosh Parameter Evaluation for Multiple Baffles

Slosh parameters are evaluated for cylindrical tank with two tori-spherical end domes. Since slosh parameters from both FE codes are in close agreement for clean tank, FE code 2 is used for further studies. Multiple ring baffles consisting of two ring baffles designed to meet damping requirement and located at required heights from tank bottom. Due to the presence of baffle, slosh parameters get altered. Slosh mass for tank with baffle is lesser compared to unbaffled tank and also reduction is higher when

the fill height matches with baffle location. This is due to reduction in free surface radius at baffle location. h1/R is the non-dimensional parameter that represents the slosh mass location. At and near the position of baffles the slosh mass (oscillating mass) will be lesser. Presence of multiple baffle increases mass location except the locate on of baffles.

Figure 6 shows that as h/R increases with M_1/M_t decreases. Sudden decrease in M_1/M_t occurs due to the presence of baffles at that locations. Due to the presence of baffle the radius at that position may also decrease. Then the space available for liquid slosh will again decrease at that particular point. Thus, the amount of slosh mass for tank with baffle will be lesser than that of a clean tank. Figure 7 shows that with the increase of h/R, h_1/R also increases constantly. Sudden decrease in location mass is observed due to the presence of baffles. At and near the position of baffles the slosh mass (M_1) will be lesser, thus the mass location (h_1) will also decrease at and near baffles. Figure 8 shows that as expected increase in slosh frequency parameter is observed at baffle locations due to the reduction in liquid free surface radius. Baffle

Fig. 6 h/R versus M_1/M_t plot
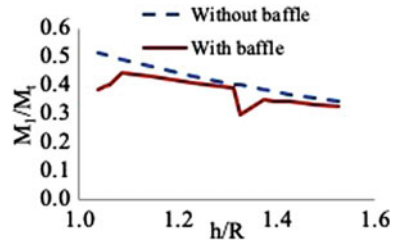
Fig. 7 h/R versus h_1/R plot
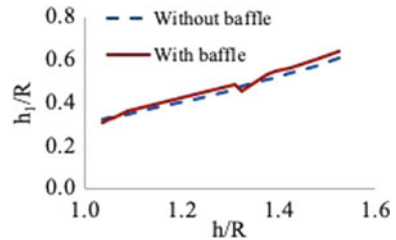
Fig. 8 h/R versus w^2R/a plot
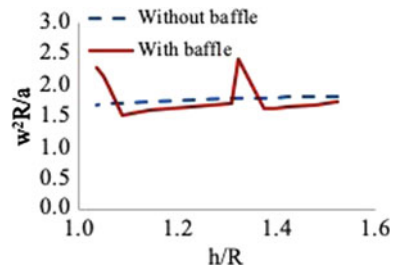
actually behaved like a rigid wall. All other locations, frequency parameter is less compared to unbaffled slosh frequency.

6 Conclusions

Parameters required for slosh modeling in order to carryout control stability studies to finalize the damping requirements for stability of slosh are evaluated using two different FE codes. Damping requirement is met by designing a multiple ring baffle configuration (two ring baffles) which are optimally sized and located. In addition to the above, influence of designed baffle on slosh parameters is also studied using finite element slosh code. Effect of baffle on slosh parameters especially slosh frequency, slosh mass and its location are near in the vicinity of baffle and its effect diminishes as the fill ratio above the baffle is far from the baffle as expected. Control stability studies have been revisited with the revised slosh parameters due to presence of baffle including achievable damping and ensured the slosh stability.

References

1. Yu MY, Ma N, Fan MS, Gu CX (2019) Experimental studies of suppressing effectiveness on sloshing with two perforated floating plates. Int J Naval Arch Ocean Eng 11:285–293
2. Dodge FT (1966) The new dynamic behaviour of liquids in moving containers. Southwest Research Institute, Sab Antonio, Texas
3. Yu L, Xue AM, Zheng J (2019) Experimental study of vertical slat screens effects on reducing shallow water sloshing in a tank under horizontal excitation with a wide frequency range. Ocean Eng 173:131–141
4. Kim PS, Chung MS, Shin JW, Cho SD, Park CJ (2018) Experimental study on sloshing reduction effects of baffles linked to a spring system. Ocean Eng 170:136–147
5. Hosseini M, Goudarzi AM, Soroor A (2017) Reduction of seismic sloshing in floating roof liquid storage tanks by using a suspended annular baffle (SAB). J Fluids Struct 71:40–55
6. Joshi YA, Bansal A, Rakshit D (2017) Effects of baffles on sloshing impact pressure of a chamfered tank. Proc Eng 173:940–947
7. Xue AM, Zheng J, Lin P, Yuan X (2017) Experimental study on vertical baffles of different configurations in suppressing sloshing pressure. Ocean Eng 136:178–189
8. Kumar A, Sinhamahapatra PK (2016) Dynamics of rectangular tank with perforated vertical baffle. Ocean Eng 126:384–401
9. Suyal R, Sathapathy KA (2016) CFD analysis of fuel in a cylindrical tank with and without baffles. Proc Eng 134:152–176
10. Jin H, Liu Y, Li JH (2014) Experimental study on sloshing in a tank with an inner horizontal perforated plate. Ocean Eng 82:75–84
11. Wang DJ, Lo HS, Zhou D (2013) Sloshing of liquid in rigid cylindrical container with multiple rigid annular baffles: lateral excitation. J Fluids Struct 42:421–436

Multiaxial Cyclic Test Response of Low C-Mn Steel Under Proportional/Non-proportional Conditions and Constitutive Material Equations Aspects

Punit Arora, Suneel K. Gupta, M. K. Samal, and J. Chattopadhyay

Abstract The present study is aimed at understanding the saturated cyclic stress-strain material behaviour of low C-Mn steel under pure axial, pure torsion, proportional axial-torsion and non-proportional axial-torsion test conditions. The axial/shear stress-strain hysteresis loops have been investigated vis-à-vis classical cyclic material modelling rules/criteria available at continuum length scale. It has been observed that non-linear loading arms of pure axial, pure torsion and proportional axial-torsion loops are comparable on von-Mises equivalent stress and strain axes for corresponding equivalent strain amplitude. This indicates the need of von-Mises yield criterion for uniaxial and proportional conditions. The nature of axial and torsion loops under proportional conditions closely resembles with associative flow rule. Therefore, von-Mises yield criterion, Prandtl–Reuss flow rule, Armstrong–Frederick family of non-linear kinematic hardening rules are required to simulate uniaxial and proportional conditions. However, axial and shear test hysteresis loops under non-proportional conditions indicated non-associative nature of plastic flow. This test observation under non-proportional cyclic condition is scarcely reported. Most of the advanced cyclic plasticity material models use associative flow rule as it is simple to apply computationally on evolving yield function. This study is an attempt to highlight the key issues related to material constitutive equations under non-proportional loading conditions.

Keywords Associative/non-associative flow rule · Cyclic plasticity · Multiaxial fatigue · Proportional/non-proportional · Kinematic hardening

P. Arora (✉) · S. K. Gupta · M. K. Samal · J. Chattopadhyay
Reactor Safety Division, Bhabha Atomic Research Centre, Mumbai 400 085, India
e-mail: punit.barc@gmail.com; punit@barc.gov.in

Homi Bhabha National Institute, Mumbai 400 094, India

329

1   Introduction

The piping/vessel components having structural discontinuities are subjected to multiaxial cyclic loading conditions under various service induced transients. The multiaxial loading can be broadly categorized as proportional and non-proportional, in general. Generally, fatigue life curve is determined under uniaxial strain controlled conditions [1]. The proportional loading is defined based on constant (or time independent) ratio of any two stress (or strain) time histories. For generalized state of stress with six stress components, proportional loading results in fixed principal stress axes, however, non-proportional loading conditions lead to rotation of principal stress axes. This rotation of principal stress axes under non-proportional conditions results in additional material hardening as reported for various material [2–5]. The effect of this additional hardening has been investigated on fatigue life [2–5] in comparison with corresponding uniaxial and proportional conditions.

For assessment of fatigue life of realistic piping/vessel components, generally critical plane theory based models [2–5] are used. These critical plane models require multiaxial stress-strain hysteresis loop information as input. Therefore, simulation of cyclic elastic-plastic response of a component is pre-requisite for fatigue life assessments. For accurate simulations of multiaxial stress-strain response of material, a suitable combination of yield criterion, flow rule, hardening rules need to be chosen. The material parameters in these rules are generally calibrated from uniaxial conditions. These material parameters are subsequently extended for simulation of multiaxial stress-strain response of material. The use of von-Mises (vM) yield criterion with Prandtl–Reuss (P–R) flow rule and non-linear kinematic hardening rule of Chaboche [6] resulted in under-prediction of axial and shear stresses for non-proportional conditions [7, 8]. However, reasonable assessments have been reported for pure axial, pure torsion and proportional axial-torsion conditions with same set of material equations [7, 8]. The advanced material models have been reported in literature which account for additional non-proportional material hardening using isotropic hardening rule [9, 10]. These advanced models are also based on vM yield criterion and P-R flow rule.

In view of above, pure Axial (A), pure Torsion (T), Proportional Axial-Torsion (P-AT) and Non-Proportional Axial-Torsion (NP-AT) tests have been recently conducted on primary piping material of Indian Pressurized Heavy Water Reactor (IPHWR) [2]. These NP-AT tests have been conducted under various phase shift angles between axial and torsion strain waveforms [2]. The present study systematically investigates the uniaxial (A, T) and proportional (P-AT) hysteresis loops on vM equivalent stress-strain curve to idealize material behaviour w.r.t. Masing characteristics. The present study also correlates the observed incremental plastic flow with associative/non-associative nature of flow rules under different loading scenarios, as tested [2]. The overall objective of this study is to investigate observed cyclic stress-strain behaviour of material under various loading conditions vis-à-vis applicability of vM yield criterion, P-R flow rule and Armstrong–Frederick (A–F) family of hardening rules. The

Table 1 Chemical composition in weight percentage [2]

C	Mn	Si	P	S	Cr	Ni	N	Balance
0.14	0.9	0.25	0.016	0.018	0.08	0.05	0.01	Fe

Table 2 Tensile properties of SA 333 Gr. 6 material at room temperature [2]

E (GPa)	ν	σ_y (MPa)	σ_u (MPa)	Total elongation (%)
203	0.3	307	463	39.1

σ_y: yield strength, σ_u: ultimate tensile strength

key finding on non-associative flow rule under non-proportional conditions has been highlighted in present study.

2 Material and Test Details

The SA 333 Gr. 6 grade of low C-Mn steel is used as primary piping material of IPHWR. Typical chemical composition of this grade is given in Table 1. The tensile properties of this material at room temperature are listed in Table 2 [2].

Pure axial (A), pure torsion (T), proportional (P-AT) and non-proportional (NP-AT) tests with different phase shift angles such as 45°, 90° and 180° have been performed on tube specimens of 22 mm as inner diameter and 1.7 mm/2.4 mm as thickness [2]. Typical test set up is shown in Fig. 1. These tests have been carried out following standard test procedures of ASTM E2207 [1]. All the tests have been conducted with total axial strain and total shear strain controls using biaxial extensometer as shown in Fig. 1. The axial load and torque reactions are the measured responses of material from load and torque cells [2].

3 Axial (A), Torsion (T) and Proportional Axial-Torsion (P-AT) Conditions

The saturated hysteresis loops are plotted in Fig. 2 (a), (b) and (c) for A, T and P-AT test conditions, respectively. These loops have been plotted for different equivalent strain amplitudes $\left(\overline{\varepsilon}^a = \sqrt{\left(\varepsilon_x^a\right)^2 + \frac{\left(\gamma_{xy}^a\right)^2}{3}}\right)$, on shifted von-Mises equivalent stress and strain time history space $(\overline{\sigma}^t - \overline{\varepsilon}^t)$. The shifting of individual axial and shear loops is performed in two steps. The first step is required to bring the minima of both axial and shear loops at origin (0, 0) point for a given $\overline{\varepsilon}^a$ case. Now, equivalent stress (or strain) is evaluated from shifted axial and shifted shear stress (or strain) using
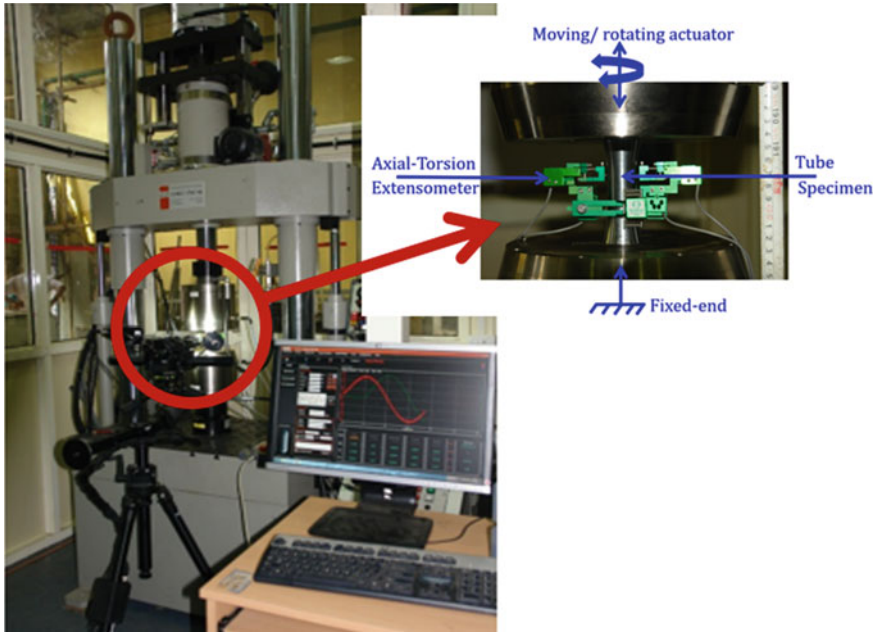
Fig. 1 Typical test set up for axial/torsion tests

$$\overline{\sigma}^t = \sqrt{\left(\sigma_x^t - \sigma_x^{min}\right)^2 + 3 \bullet \left(\tau_{xy}^t - \tau_{xy}^{min}\right)^2} \left(or\, \overline{\varepsilon}^t = \sqrt{\left(\varepsilon_x^t - \varepsilon_x^{min}\right)^2 + \frac{\left(\gamma_{xy}^t - \gamma_{xy}^{min}\right)^2}{3}}\right).$$

The second step is required to move the individual shifted equivalent stress-versus-equivalent strain loops along elastic line to an extent such that loading arms of each hysteresis loop for different $\overline{\varepsilon}^a$ overlap each other (refer Fig. 2 (a), (b) and (c for A, T and P-AT conditions, respectively). It is observed that shifted hysteresis loops for A, T and P-AT conditions are nearly identical on von-Mises equivalent stress and strain space, therefore, von-Mises yield criterion (Eqs. (1) and (2)) is suitable for pure axial, pure torsion and proportional axial-torsion conditions.

Further, the loading arms corresponding to different $\overline{\varepsilon}^a$ overlap one another, indicating a single set of non-linear kinematic hardening parameters are adequate for all strain amplitudes under A, T and P-AT scenarios. However, the material deviates from Masing idealization due to linear shift along elastic line. This signifies the need of strain amplitude dependent cyclic yield strength is required to be input in material constitutive relations. The variation of cyclic yield strength with equivalent strain amplitude has been shown in Fig. 2d. The cyclic yield strength corresponds to equivalent plastic strain offset line of 0.005%. The offset line in Fig. 2a, b, c have been drawn for representation purpose only and is not to the scale of 0.005%.

The von-Mises (vM) yield equation is given as,
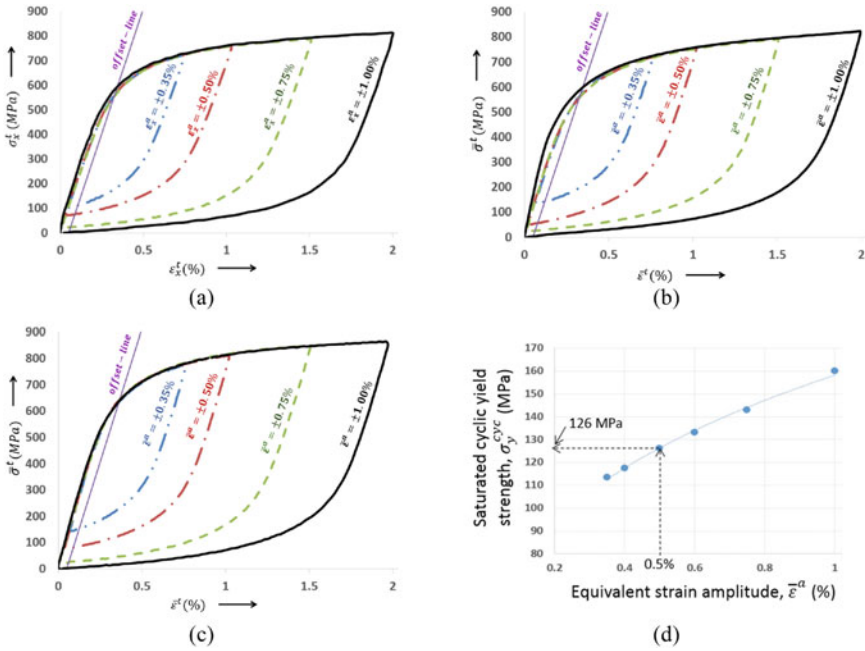
Fig. 2 Shifted saturated vM equivalent stress-versus-equivalent strain hysteresis loops under **a** A, **b** T, **c** P-AT conditions and **d** variation of saturated cyclic yield strength with equivalent strain amplitudes [7, 8]

$$f = \left(\frac{3}{2}\left(\boldsymbol{\sigma}' - \boldsymbol{\alpha}'\right) : \left(\boldsymbol{\sigma}' - \boldsymbol{\alpha}'\right)\right)^{1/2} - \sigma_y^{cyc} = 0 \tag{1}$$

where, $\boldsymbol{\sigma}'$: deviator stress tensor, $\boldsymbol{\alpha}'$: deviator back stress tensor, σ_y^{cyc} : saturated cyclic yield strength corresponding to equivalent plastic strain offset of 0.005%.

For P-AT condition, Eq. (1) becomes,

$$f = \sqrt{(\sigma_x - \alpha_x)^2 + \left\{\sqrt{3}.(\tau_{xy} - \alpha_{xy})\right\}^2} - \sigma_y^{cyc} = 0 \tag{2}$$

where, α_x, α_{xy}: back stress components in normal (x) and shear (xy) directions.

Equivalent plastic strain (or increment) is as,

$$\bar{\varepsilon}^{pl} = \left(\frac{2}{3}\boldsymbol{\varepsilon}^{pl} : \boldsymbol{\varepsilon}^{pl}\right)^{1/2} ; dp = \left(\frac{2}{3}d\boldsymbol{\varepsilon}^{pl} : d\boldsymbol{\varepsilon}^{pl}\right)^{1/2} \tag{3}$$

where, $\boldsymbol{\varepsilon}^{pl}$: plastic strain tensor, $d\boldsymbol{\varepsilon}^{pl}$: plastic strain increment tensor, $\bar{\varepsilon}^{pl}, dp$: equivalent plastic strain and increment

$$\varepsilon_x^{pl,t} = \varepsilon_x^{tot,t} - \frac{\sigma_x^t}{E}; \gamma_{xy}^{pl,t} = \gamma_{xy}^{tot,t} - \frac{\tau_{xy}^t}{G} \tag{4}$$

In Eq. (4), $\varepsilon_x^{tot,t}$, $\gamma_{xy}^{tot,t}$ are the time histories of total axial and shear strains, as controlled and σ_x^t, τ_{xy}^t are the time histories of axial and shear stresses calculated from measured values of load and torque cell reactions, respectively.

The von-Mises equivalent back stress is as,

$$\overline{\alpha} = \sqrt{\alpha_x^2 + 3.\alpha_{xy}^2} \tag{5}$$

Three decomposed Chaboche model [6] for deviator back stress increment tensor, $d\alpha_i^{'}$,

$$d\alpha_i^{'} = \frac{2}{3} C_i.d\varepsilon^{pl} - \gamma_i.dp.\alpha_i^{'} \tag{6}$$

where, C_i, γ_i are the material parameters which are generally calibrated from uniaxial conditions and i denotes i^{th} segment of common post-yield loading arm of cyclic stress-strain curve (refer Fig. 2 a, b, c).

$$d\alpha^{'} = \sum_{i=1}^{i=3} d\alpha_i^{'} \tag{7}$$

Now, a typical test case of P-AT with axial and shear strain amplitudes as 0.35% and 0.61% (equivalent strain amplitude of 0.5% with cyclic yield strength of 126 MPa (Fig. 2d)), respectively has been considered to verify if proportional loading follows associative flow rule. For this purpose, stress states 'a' and 'b' have been chosen randomly from test axial and shear loops as indicated in Fig. 3a. The stress state 'a' is evaluated from load/torque reactions during the test. The stress point 'a' must lie on yield locus to satisfy consistency condition (Eqs. (1) and (2)). From the von-Mises equivalent stress value at 'a', cyclic yield strength (σ_y^{cyc}) is subtracted to obtain the von-Mises equivalent back stress (i.e., magnitude of back stress position vector in α_x and $\sqrt{3}.\alpha_{xy}$ space), as given by Eq. (5). This treatment considers that stress origin, centre of current yield locus and current stress state lie on single line for proportional strain path. The centre coordinate (α_x, $\sqrt{3}.\alpha_{xy}$) of yield locus (see Fig. 3b) are calculated from non-linear set of equations (Eqns. (2) and (5)) for stress state 'a' viz. the calculated values of (α_x, $\sqrt{3}.\alpha_{xy}$) satisfy Eqns. (2) and (5) simultaneously. The coordinates of yield locus centre 'o' have been evaluated for the stress state at 'a' and radial direction ($\overrightarrow{oa}$, normal for yield locus in $\sigma_x - \sqrt{3}\tau_{xy}$ space) is inclined at 46.1° w.r.t. σ_x.

Subsequently, this normal direction ($\overrightarrow{oa}$) has been compared with the directions of plastic strain increments, $\left(d\varepsilon_x^{pl}, d\varepsilon_{xy}^{pl}(= 0.5d\gamma_{xy}^{pl})\right)$ which are calculated from the measured strains test data using Eq. (4) for state 'a' to state 'b'. The vector, $\overrightarrow{ab}$ has
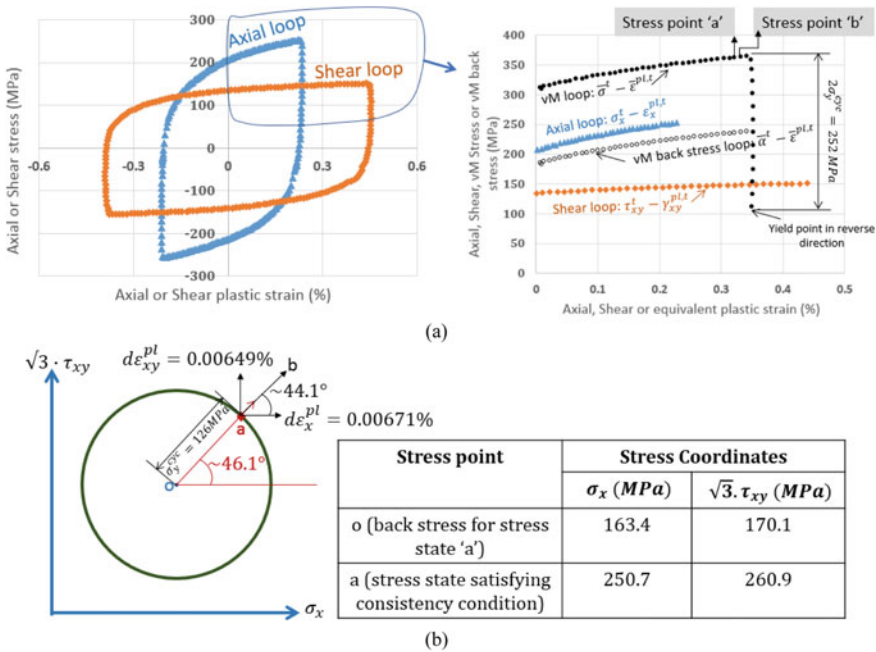
Fig. 3 **a** Axial stress-plastic axial strain and shear stress-plastic shear strain loops [2] used to calculate vM stress and vM back stress variations with corresponding plastic strains and **b** yield locus centred at 'o' back stress and stress point 'a' lying on it for P-AT test conducted with 0.35% as axial strain amplitude and 0.61% as shear strain amplitude

been evaluated to be inclined at 44.1° w.r.t. σ_x, indicating that proportional axial-torsion conditions nearly follow normality condition. Therefore, associative flow rule such as Prandtl–Reuss flow rule can be applied for proportional load cases. The yield locus as plotted in Fig. 3b is for representation purposes and is not to the scale.

Therefore, von-Mises yield criterion, 3 decomposed Chaboche's non-linear kinematic hardening rule (Eqs. (6) and (7)) with cyclic yield as a function of equivalent strain amplitude (Fig. 2d) and Prandtl–Reuss flow rule can be used to accurately model A, T and P-AT conditions. This combination has been used for predicting the axial/shear stress-strain response of SA 333 Gr. 6 under various proportional conditions [7, 8]. The predicted pure axial, pure torsion and proportional axial-torsion stress-strain response of material compares well with test response. The typical comparisons of predicted and test axial and shear loops has been shown in Fig. 4 for P-AT conditions.
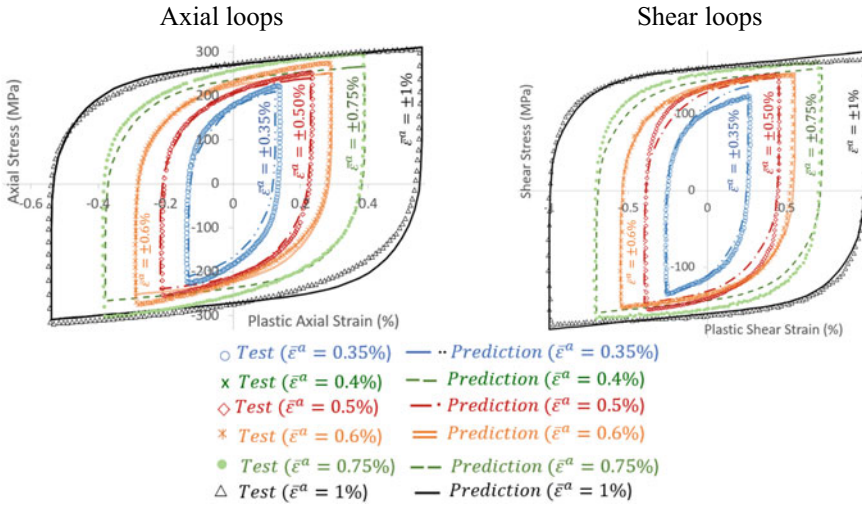
Fig. 4 Comparison between predicted and test material response under P-AT conditions with $\varepsilon_x^a = \pm 0.25\%, \gamma_{xy}^a = \pm 0.43\%(\overline{\varepsilon}^a = 0.35\%), \varepsilon_x^a = \pm 0.35\%, \gamma_{xy}^a = \pm 0.61\%(\overline{\varepsilon}^a = 0.50\%), \varepsilon_x^a = \pm 0.42\%, \gamma_{xy}^a = \pm 0.74\%(\overline{\varepsilon}^a = 0.60\%), \varepsilon_x^a = \pm 0.53\%, \gamma_{xy}^a = \pm 0.92\%(\overline{\varepsilon}^a = 0.75\%), \varepsilon_x^a = \pm 0.70\%, \gamma_{xy}^a = \pm 1.21\%(\overline{\varepsilon}^a = 1.00\%)$ [8]

4   Non-proportional Axial-Torsion (NP-AT) Conditions

This section outlines the typical saturated test behaviour as observed under non-proportional axial-torsion conditions and discusses the aspects related to material constitutive equations vis-à-vis test observations.

A typical time variation of axial and shear strains (controlled parameters) having amplitudes as 0.53% and 0.92%, respectively, with triangular waveforms and phase shift angle of 90° is shown in Fig. 5a. Time instants from t_0 to t_4 are marked on these waveforms. The corresponding saturated material response in the form of axial and shear loops is shown in Fig. 5b with time instant tags (t_0 to t_4) as labelled in Fig. 5a. For time $t = t_1^+, (t_1^+$ being infinitesimal higher than t_1) unloading takes place in axial loop, whereas plastic loading continues in negative shear direction as shown in Fig. 5b. The slope of axial loop at $t = t_1^+$ has been calculated from test data and found nearly equal to Young's modulus (E). However, the slope of shear loop at this time is significantly lesser than modulus of rigidity (G). This indicates that from time t_1 to t_1^+, plastic axial strain increment $\left(d\varepsilon_x^{pl,t}\right)$ is zero and plastic shear strain increment $\left(d\gamma_{xy}^{pl,t}\right)$ is non-zero. The time variations of plastic axial and shear strains, as evaluated from Eq. (4), can be seen in Fig. 5c. This figure also indicates non-zero plastic shear strain increment and nearly zero plastic axial strain increment for $t = t_1^+$. For other time instants, plastic axial and shear strain increments have been given in Table 3. This table shows that during the elastic unloading in one direction, the plastic straining occurs in the other direction. Therefore, the equivalent plastic
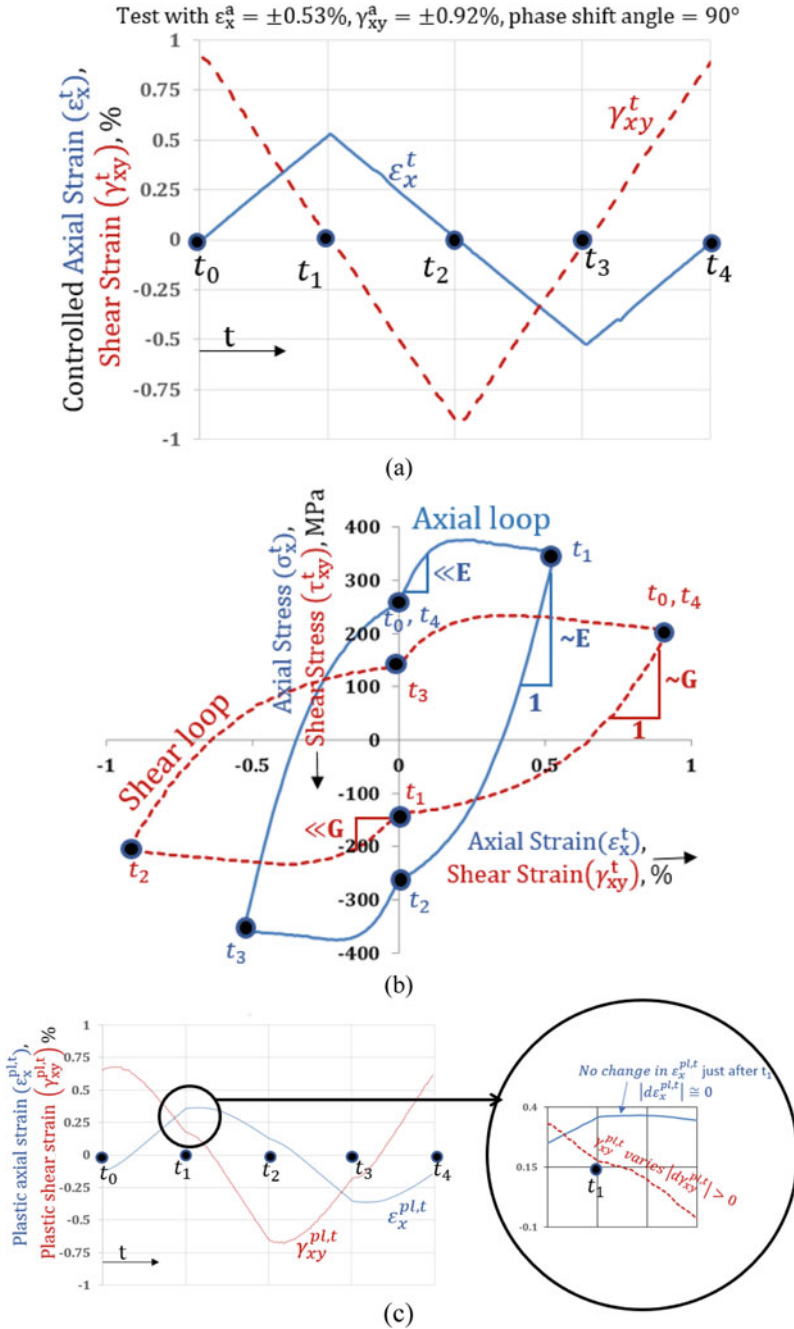
Fig. 5 **a** Time variation of axial and shear strain waveforms under NP conditions with 90° phase shift angle, **b** axial and shear hysteresis loops and **c** time variation of plastic axial and shear strains

Table 3 Slope of axial and shear hysteresis loops and plastic axial and shear strain increments for different time ranges in one complete NP cycle

Time interval	Slope of axial loop	Axial plastic strain increment	Slope of shear loop	Shear plastic strain increment
$t > t_0$ and $t \ll t_1$	$\ll E$	$\left\| d\varepsilon_x^{pl,t} \right\| > 0$	$\sim G$	$\left\| d\gamma_{xy}^{pl,t} \right\| \cong 0$
$t > t_1$ and $t \ll t_2$	$\sim E$	$\left\| d\varepsilon_x^{pl,t} \right\| \cong 0$	$\ll G$	$\left\| d\gamma_{xy}^{pl,t} \right\| > 0$
$t > t_2$ and $t \ll t_3$	$\ll E$	$\left\| d\varepsilon_x^{pl,t} \right\| > 0$	$\sim G$	$\left\| d\gamma_{xy}^{pl,t} \right\| \cong 0$
$t > t_3$ and $t \ll t_4$	$\sim E$	$\left\| d\varepsilon_x^{pl,t} \right\| \cong 0$	$\ll G$	$\left\| d\gamma_{xy}^{pl,t} \right\| > 0$

strain increment (Eq. (3)) is non-zero for any time t between t_0 and t_4. This indicates that material does not return back to elastic regime even if one of the directions experiences elastic unloading.

The material modelling should account for these test observations for accurately simulating multiaxial stress-strain response. For material modelling purpose, the von-Mises yield criterion (as given by Eq. (1)) is considered applicable under non-proportional conditions also. It may be noted that additional hardening under NP condition in the form of higher yield strength $\left(\sigma_y^{NP}\right)$ should be used in place of calibrated cyclic yield strength $\left(\sigma_y^{cyc}\right)$ under uniaxial conditions, as given in Eq. (1). Similar formulation has been undertaken by Meggiolaro et al. [10] to address additional hardening under NP conditions. The vM yield criterion consideration makes a circular yield locus in $\sigma_x - \sqrt{3}.\tau_{xy}$ space with its centre coordinate as $\left(\alpha_x, \sqrt{3}.\alpha_{xy}\right)$ and radius as σ_y^{NP}. Now, a yield locus is qualitatively drawn for time instant $t = t_1$ in Fig. 6. As discussed earlier, the material remains in elastic-plastic regime despite the fact elastic unloading in one of the directions. Therefore, the stress point lies on yield locus to satisfy consistency condition. For yield locus at $t = t_1$, the stress coordinate (point "A") is having coordinate $\left(\sigma_x^{t1}, \sqrt{3}.\tau_{xy}^{t1}\right)$ and the centre is located at point 'a' with coordinates $\left(\alpha_x^{t1}, \sqrt{3}.\alpha_{xy}^{t1}\right)$. Now, in order to obey the perpendicularity condition of plastic strain increment and test observation of non-zero plastic shear strain increment $\left(d\gamma_{xy}^{pl,t_1-t_1^+} < 0\right)$ and zero plastic axial strain $\left(d\varepsilon_x^{pl,t_1-t_1^+} \cong 0\right)$, stress point 'A' must lie on '*south pole*' of yield locus at $t = t_1$.

This increment in plastic strain $\left(d\gamma_{xy}^{pl,t_1-t_1^+}\right)$ and previous centre information $\left(\alpha_x^{t1}, \sqrt{3}.\alpha_{xy}^{t1}\right)$ is used to update the centre of new yield locus at $t = t_1^+$ typically using A-F family of kinematic hardening rule. For simulation of NP material behaviour, higher saturated cyclic yield strength $\left(\sigma_y^{NP}\right)$ is used in place of uniaxial saturated cyclic yield strength $\left(\sigma_y^{cyc}\right)$ [8, 10]. After the cyclic saturation (or stabilization) has been achieved under NP condition, the yield locus size would not change its size. Therefore, pure kinematic hardening can be considered after attainment of cyclic saturation. A yield locus with same radius σ_y^{NP}, is plotted at $t = t_1^+$ with its centre at point 'b' having coordinates as $\left(\alpha_x^{t1+}, \sqrt{3}.\alpha_{xy}^{t1+}\right)$ in Fig. 6. In order to

Fig. 6 The von-Mises yield loci at $t = t_1$ and $t = t_1^+$
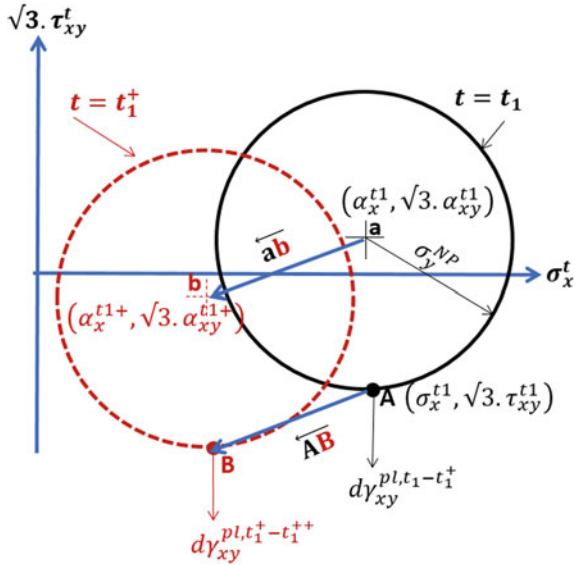
satisfy the perpendicularity condition and non-zero plastic shear strain increment $\left(d\gamma_{xy}^{pl,t_1^+-t_1^{++}} < 0\right)$ and nearly zero plastic axial strain increment $\left(d\varepsilon_x^{pl,t_1^+-t_1^{++}} \cong 0\right)$, the stress point 'B' must lie again on 'south pole' of yield locus at $t = t_1^+$ as indicated in Fig. 6.

Hence, in order to simulate the test behaviour exactly, the shift in centre $\left(\overleftarrow{ab}\right)$ should be equal in magnitude and direction as that of change in stress coordinate $\left(\overleftarrow{AB}\right)$. This represents $d\alpha_x = d\sigma_x \, and \, d\alpha_{xy} = d\tau_{xy}$. If $\overleftarrow{ab} \neq \overleftarrow{AB}$ (the general condition), then, stress point 'B' does not lie on 'south pole' of yield locus at $t = t_1^+$ and there would be non-zero plastic axial strain increment as per perpendicularity condition (or associative nature of plastic flow rule) which does not follow the test observation of zero plastic axial strain increment. In computational plasticity, the change in back stress tensor (or shift in center of yield loci) is governed by plastic flow and previous history of back stress (see Eq. (6)). However, the simulated stress tensor (such as point "A" and "B") is obtained after satisfying additional conditions/fulfilling additional criteria such as yield criterion (or consistency condition), global convergence criterion for force balance. Hence, yield criterion, flow rule, hardening rule and global convergence are embedded in estimation of simulated converged stress state. Therefore, it is not necessary that the condition of $\overleftarrow{ab} = \overleftarrow{AB}$ is satisfied always. As a result of this, point 'B' would not lie on 'south-pole'. However, the test requirement needs that only non-zero plastic shear strain increment should occur. Therefore, irrespective of the stress point lies anywhere along the yield boundary, the strain increment tensor must point in $-\sqrt{3}.\tau_{xy}$ direction. With these conditions, non-associative nature of plastic flow needs to be applied for

correct assessment of under non-proportional loading conditions. It may be noted that the above discussions on flow behaviour under proportional and non-proportional conditions, have considered plastic strain increments $\left(d\varepsilon_x^{pl}, d\gamma_{xy}^{pl}\right)$ lying in the same direction of corresponding stress components.

This aspect of plastic flow vis-à-vis non-proportional cyclic loading conditions has been scarcely discussed in literature. The advanced material models [8–10] use associative flow rule as it is simpler to apply it in computational mechanics for evolving yield surface. For realistic assessment of non-associative material behaviour, it is required to formulate a plastic potential function and its subsequent evolutions. The formulation of such potential function requires systematic and extensive test efforts with precise measurements of plastic strain increments for various NP conditions. It may be noted that the maximum percentage difference between simulated and test response on peak stress has been reported ~12% [8], which can be acceptable for engineering calculations on fatigue life assessments using critical plane models [3–5]. The difference between simulated and test cyclic response may further reduce, if adequate non-associative flow rule is included in material constitutive equations.

5   Conclusions

Based on the uniaxial/multiaxial fatigue test studies on SA 333 Gr. 6 steel [2], the saturated stress-strain test response under pure axial (A), pure torsion (T), proportional axial-torsion (P-AT) and non-proportional axial-torsion (NP-AT) conditions has been investigated with respect to implications in material modelling. The observed cyclic behaviour vis-à-vis material model considerations is summarized below,

1. The test behaviour under A, T and P-AT conditions showed material exhibiting deviation from Masing idealization with a linear shift along elastic line. This indicates the need of Armstrong–Frederick family of kinematic hardening rules and equivalent strain amplitude dependent cyclic yield strength in material constitutive equations.
2. Test response under A, T and P-AT conditions showed associative nature of plastic flow. Therefore, Prandtl–Reuss flow rule can be used to model such conditions.
3. For NP-AT conditions, the material mostly remains in elastic-plastic regime despite the fact of elastic unloading in one of the directions for 90° out-of-phase condition.
4. The material indicated the need of non-associative flow rule for NP-AT condition with 90° phase shift angle between axial and shear strains.

References

1. Standard practice for strain-controlled axial-torsional fatigue testing with thin walled tubular specimens (Designation: E2207 – 08). American Society of Testing Materials (ASTM)
2. Arora P, Gupta SK, Bhasin V, Singh RK, Sivaprasad S, Tarafder S (2016) Testing and assessment of fatigue life prediction models for Indian PHWRs piping material under multi-axial load cycling. Int J Fatigue 85:98–113
3. Chu CC (1995) Fatigue damage calculations using the critical plane approach. J Eng Mater Technol 117:41–49
4. Jiang Y, Hertel O, Vormwald M (2007) An experimental evaluation of three critical plane multiaxial fatigue criteria. Int J Fatigue 29:1490–1502
5. Arora P, Gupta SK, Samal MK, Chattopadhyay J (2019) Development of new critical plane model for assessment of fatigue life under multi-axial loading conditions. Int J Fatigue 129. Article 105209
6. Chaboche JL (1991) On some modifications of kinematic hardening to improve the description of ratchetting effects. Int J Plast 7:661–678
7. Arora P, Samal MK, Gupta SK, Chattopadhyay J (2019) Assessment of cyclic plasticity behavior of primary piping material of Indian PHWRs under multiaxial loading scenario. In: 3rd international conference & exhibition on fatigue, durability and fracture mechanics, August 2019 at Visvesvaraya Technological University, Belagavi, Karnataka, India, pp 29–31
8. Arora P, Samal MK, Gupta SK, Chattopadhyay J (2021) Proposing an improved cyclic plasticity model for assessment of multi-axial response of low C-Mn steel. Int J Fatigue 142. Article 105888
9. Tanaka E (1994) A non-proportionality parameter and a viscoplastic constitutive model taking into account amplitude dependences and memory effects of isotropic hardening. Eur J Mech A/Solids 13:155
10. Meggiolaro MA, Wu H, de Castro JTP (2016) Non-proportional hardening models for predicting mean and peak stress evolution in multiaxial fatigue using Tanaka's incremental plasticity concepts. Int J Fatigue 82:146–157

Extracting Strain Rate Sensitivity of Metals from a Single Cantilever Under Bending

Priya Goel, Praveen Kumar, and Vikram Jayaram

Abstract The accuracy and reliability of material parameters obtained through small scale testing are a challenge as testing is limited by the difficulty in sample preparation, its mounting, and alignment. Thus, there is great interest in the development of high throughput testing methodologies, to generate a large amount of data using fewer tests. In a cantilever, in addition to ease of gripping and alignment, the strain gradient along thickness (as well as length) enables the generation of a large volume of data from a single specimen, thereby improving accuracy and reliability. However, the non-linear stress-strain relationship in plasticity leads to redistribution of stress across the cantilever to maintain section planarity. The extraction of flow parameters using a cantilever relies upon the estimation of stress during the deformation. In the present work, a framework is developed to extract strain rate sensitivity from a single cantilever during a deflection rate-controlled test. This demonstrates the effectiveness of bending in reducing the number of tests required to obtain strain rate sensitivity.

Keywords Bending · Strain rate sensitivity · High throughput

Symbols and Notations

E	Young's modulus
ε_t	Total strain
ε_{el}	Elastic strain
ε_{pl}	Plastic strain
$\varepsilon_{t,h}$	Total strain at distance 'h' from the neutral axis
σ_h	Stress at distance 'h' from the neutral axis
σ_y	Stress at distance 'y' from the neutral axis
M_x	Moment acting at a distance 'x' from the free end
κ	Curvature of the neutral axis of the beam at any section

P. Goel (✉) · P. Kumar · V. Jayaram
Indian Institute of Science, Bengaluru, India
e-mail: priyagoel@iisc.ac.in

F	Force
L	Length of the cantilever
b	Width of the cantilever
h	Half-height of the cantilever
l_i	Length of ith element
θ_i	Slope of ith element
δ_i	Deflection of ith element

1   Introduction

The most-commonly measured mechanical properties representing the time-independent plasticity of material are yield strength, strain hardening exponent, and strain rate sensitivity. There is a demand for extensive testing to achieve acceptable reliability of measured properties which may not be practical in all cases. Conventional uniaxial testing is time consuming owing to the number of tests needed and the laborious sample preparation involved. The geometry prescribed by ASTM standards for tension tests is difficult to prepare for materials with limited ductility. The mounting of such specimens in the grips is also a challenge due to the risk of damage during alignment. Misalignment, barreling, and buckling of samples lead to unreliable results from compression tests as well. These issues are resolved under indentation technique, but its complex interpretation is the major obstruction in making it the preferred choice. Bending offers a convenient alternative because in addition to easy sample preparation and mounting, the strain gradient throughout the beam makes every point deform under a different load history. The response at these points can be captured to generate high throughput data from a single specimen. Strain gradients in small volumes also make bending stress states closer to in-service conditions. Bending also allows optimization of sample volume required for material testing by choosing the material of interest in the high strain region only. Therefore, it becomes important to study the local response of a beam and relate it to the bulk behavior to exploit the advantages offered by bending. Under elastic deformation, stress along the thickness is linear and can be calculated from the strain profile using the Euler–Bernoulli beam theory. When the beam starts to deform plastically, the dependence of stress on strain becomes non-linear. However, it has been observed experimentally [1] that the beam cross-section continues to remain plane during plastic deformation. It implies that the total strain remains linear. Therefore, the non-linear relationship between strain and stress forces stress at any cross-section to redistribute in a non-linear fashion to maintain strain linearity across the thickness.

This stress evolution is dictated by the magnitude of the stress exponent, which changes from 1 for Hookean behavior to the strain hardening exponent seen in plasticity. Thus, the stress distribution depends on the ratio of elastic to plastic strain and is therefore transient in nature. The estimation of stress distribution during plastic deformation is the major challenge in measuring the flow properties using

cantilevers. A model that accounts for stress evolution has been developed to obtain localized response of the entire beam which allows calculation of rate sensitivity from a single cantilever. It has been proposed, based on the findings of the model, that flow parameters can also be estimated without knowing the stress distribution if the experimental data is extracted from specific locations. Therefore, the model plays an instrumental role in developing insight into various aspects of plastic deformation under bending load and paves the way for the formulation of methodologies to extract flow parameters like yield strength, hardening exponent and rate sensitivity directly from experiments without knowing the full stress profile.

2 Background

The phenomenon of plasticity is known since nineteenth century, but the theory of plasticity was given for the first time by Tresca [2] in 1868, which was further developed by Saint-Venant [3] and Levy [4] in 1870. It was only in the early 1920s when the plasticity theories were taken up again by Richard von-Mises [5]. However, these theories did not find much application due to the mathematical difficulties associated with solving the partial differential equations. The simplifications of ideal plastic and elastic-plastic behavior were suggested by Prandtl [6], and focus was limited to axisymmetric structures such as those with only three unknowns to solve the system of equations. The constitutive relations based on the incremental form of the Saint-Venant and Levy's approach proposed independently by Prandtl [6] and Reuss [7] enabled simplifications required for the application on modern structures and great developments followed thereafter. At the same time, there were attempts by Schmidt [8] and Odqvist [9] to account for hardening, which were later revised by Reuss and Prager [10] to consider the Bauschinger effect in the form of kinematic hardening models. The development of these theories was responsible for the design of highly reliable structures primarily made of metals.

Later, it was realized that the flow properties depend on strain rate at high temperature and high strain rate. There were some preliminary studies on iron and steel at high temperature over a limited range of strain rate [11] when the susceptibility of steel to loading rate at elevated temperature was of interest for the design of power plants. The understanding of deformation rate effects also has implications in the forming operations like rolling, drawing, and cold bending where power consumed to generate desired force can be reduced tremendously. Extensive experiments on a variety of materials were conducted by Nadai and Manjoine [12], who did pioneer work by developing customized machines that allowed extreme strain rates (10^{-6}–10^3 s^{-1}) to be achieved over a wide range of temperature. However, strain rate sensitivity was formally defined in terms of strain rate and stress by Zener and Hollomon [13] based on their experiments.

Strain rate sensitivity is conventionally calculated from a set of tests at different strain rates by taking the ratio of difference in stress to difference in strain rate at any given strain. An alternative method was proposed by Carreker et al. [14] where

strain rate in a single test can be abruptly increased/decreased at a constant strain. This method has benefits that the rate sensitivity is obtained from a single test and microstructure remains practically unchanged during the jump. In addition, stress relaxation tests were also used to measure rate sensitivity by Hayden et al. [15] but were limited to low strain rates and difficult to operate. There were also numerous parallel efforts to find equivalence between the inverse of the creep exponent and the rate sensitivity, the physical foundation for which was laid by Kocks [16]. However, this equivalence holds only for materials having negligible strain hardening as it corresponds to steady state in creep, which limits its application as well. There were studies which employed torsion tests to evaluate rate sensitivity due to its ability to avoid instability due to necking and any error in shear strain due to dimensional variation of sample and testing setup at high temperature [17]. In bending, in addition to the advantages offered by torsion, the strain gradient throughout the beam offers the feature of high throughput. However, there was limited understanding of the relationship between stress distribution and the applied moment in a beam.

Robertson and Cook [18] conducted bending tests on mild steel to show that the phenomenon of upper yield point is real by demonstrating that stress reduction at yield is not an artifact due to unavoidable eccentricity in uniaxial loading. Although their interest was specific to mild steel, it was one of the first attempts to relate plastic response from uniaxial and bending tests. Nadai [1] experimentally verified the section planarity of beams during plastic deformation and supported the approach of stress redistribution in mild steel beams though it was based on the lower yield point. It was assumed by previous researchers that as soon as the stress at any point of the beam reaches the yield strength, yielding occurs at that point. It was contradicted by Prager [19] whose statement was based on the experiments on I-section beams by Thum and Wunderlich [20]. According to him, yielding can occur at any section only if stress at all the points of a section have reached yield strength. It was counteracted by Volterra [21], who did extensive work on metallic beams having a wide variety of cross-sections under various loading conditions. He studied the effect of beam cross-section on the stress distribution and attributed the observation of higher bending moment corresponding to yield to the higher resistance of I-section beams to the plastic deformation. He also emphasized the importance of strain hardening and justified the discrepancy between experimental and calculated moment-curvature curves on hardening. The formal mathematical treatment of linear strain hardening was given by Roderick and Phillipps [22] for simply supported beams of mild steel. There were parallel efforts by Trifan [23], who proposed the solution for the plastic response of a circular plate under bending for a hardening material using partial differential equations. Later, with the advent of finite element tools, Popov et al. [24] developed the formulation to solve these problems using computer codes. The studies that followed were primarily aimed at obtaining the load-deflection curve under a range of loading, boundary conditions, and hardening criteria, and there were no further attempts to better understand the nature of stress evolution during non-linear hardening. There was interest in studying the stress distribution diagrams for reinforced concrete beams, which are generally non-linear and asymmetric in tension and compression. Most of these studies focused on obtaining the equivalent

rectangular stress blocks for non-linear stress blocks using a set of coefficients. However, there has not been an attempt to study the localized response of these beams and to obtain the material parameters directly from the bending based upon these localized responses. The aim of the present work is to develop the equations governing the stress redistribution in a beam and subsequently obtain the material parameters, such as strain rate sensitivity, using load-deflection curve of the beam.

3 Model

3.1 Formulation

A rectangular prismatic cantilever beam is considered which is subjected to a line load at its free end (see Fig. 1). The plastic flow properties of a material are assumed to be symmetric in tension and compression. The assumption of a large aspect ratio allows the shear strain at any section of the beam to be neglected. The assumption of section planarity under the Euler–Bernoulli beam theory is experimentally verified even beyond the yield point and for materials which do not follow the Hooke's law [1]. Section planarity is the foundation for the procedure adopted in the proposed model. However, the choice of the specific non-linear relationship for the constitutive law is immaterial.

The material is assumed to follow the Hooke's law in the elastic regime. Stress at any point can be expressed in terms of curvature and distance from the neutral axis using Hooke's law and planarity condition as follows:

Hooke's law:

$$\sigma = -E\kappa y \tag{1a}$$

Planarity condition:
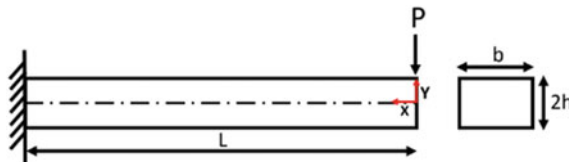
$$\varepsilon_{t,y} \propto y \tag{1b}$$

Fig. 1 A schematic illustration of a prismatic rectangular cantilever. The left-end of the cantilever is fixed, while a point-load, P, is applied in -y-direction at the right-end. Important dimensions of the cantilever are shown

The equations of static equilibrium, as given below, are satisfied at every section throughout the deformation:

$$\int_{-h}^{h} \sigma b \, dy = 0 \tag{2a}$$

$$\int_{-h}^{h} \sigma b y \, dy = M_x \tag{2b}$$

For a doubly symmetric cross-section, the equation of force balance makes the neutral axis to pass through its centroid. The equation of moment balance relates the stress at any point on a section with the moment acting on that section, as follows:

$$\sigma = \frac{M_x y}{I} \tag{3}$$

In the elastic regime, stress and strain are linear along the thickness, as shown by solid lines AB and DE in Fig. 2(a), (b), respectively. As load continues to increase, the beam starts to deform plastically at the locations where stress reaches the yield limit. Any non-linear constitutive law can be used to describe the plastic strain in terms of stress and strain rate. Here, the following power-law relation is assumed where 'n' and 'm' denote strain hardening and strain rate sensitivity index, respectively:

$$\sigma = C \varepsilon_{pl}^{n} \dot{\varepsilon}^{m} \tag{4a}$$

$$\varepsilon_{pl} = K \sigma^{1/n} \dot{\varepsilon}^{-m/n} \tag{4b}$$

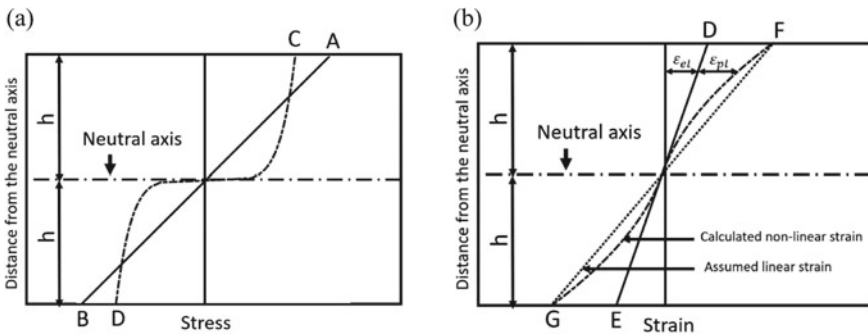**Fig. 2** Evolution of (**a**) stress and (**b**) strain along the thickness of a cantilever sample. Lines AB in (**a**) and DE in (**b**) represent the stress and strain distributions under elastic condition, respectively. CD in (**a**) is the non-linear stress profile that is established to satisfy the linear strain profile, FG in (**b**), along with a non-linear constitutive relationship (e.g., Eq. 5)

Hence, the total strain is given as the sum of elastic and plastic strain as follows:

$$\varepsilon_t = \frac{\sigma}{E} + K\sigma^{1/n}\dot{\varepsilon}^{-m/n} \tag{5}$$

The non-linear dependence of plastic strain on stress will result in non-linear strain along the thickness for linear stress distribution, as shown by dashed line FG (see Fig. 2(b)). However, the experimental observation of planarity during plastic deformation contradicts this statement. In this model, it is proposed that it is the stress which redistributes itself at any section to maintain strain linearity.

Stress redistribution at any section is driven by the amount of non-linearity. The non-linearity at any point is given by the difference between the assumed linear strain and the calculated non-linear strain (see Fig. 2(b)). A hypothesis is made that the linearity is restored by an additional elastic strain which is equal to the non-linearity at that point.

$$\Delta\varepsilon_{additional} = \left(\varepsilon_{t,assumed} - \varepsilon_{t,calculated}\right) \tag{6}$$

This additional elastic strain gives rise to additional stress as follows:

$$\Delta\sigma = E\Delta\varepsilon_{additional} = E\left(\varepsilon_{t,assumed} - \varepsilon_{t,calculated}\right) \tag{7}$$

However, any additional stress disturbs the moment balance established previously. Therefore, moment in Eq. (3) is updated such that moment remains conserved after accounting for additional stress $\Delta\sigma$. Moment at any section is reduced by an amount equivalent to moment generated by $\Delta\sigma$.

$$M_x^{updated} = M_x - \Delta M \tag{8}$$

where,

$$\Delta M = \int_{-h}^{h} \Delta\sigma\, b y\, dy \tag{9}$$

The updated moment is used to calculate new stress using Eq. (3) and combined with $\Delta\sigma$ to update stress as follows:

$$\sigma^{updated} = \frac{M_x^{updated} y}{I} + \Delta\sigma \tag{10}$$

The expression for updated stress clearly indicates that stress becomes non-linear due to $\Delta\sigma$, which in turn is a measure of the non-linearity. It is shown by the dashed

line CD (see Fig. 2(a)). It is to note that stress converges to a non-linear profile for which elastic and plastic strain are non-linear in such a way that their summation, i.e., total strain, is linear.

The analytical expressions for deflection and slope defined for a beam subjected to constant moment are manipulated in terms of strain. The slope and deflection are first calculated for the element closest to the fixed end followed by its superposition on the adjacent element toward loading end as follows:

$$\theta_i = \theta_{i-1} - \frac{2\varepsilon_{t,h}l_i}{h} \tag{11a}$$

$$\delta_i = \delta_{i-1} - \frac{\varepsilon_{t,h}l_i^2}{h} + \theta_{i-1}l_i \tag{11b}$$

The deflection of all the elements is superimposed to obtain the free end deflection. The above-mentioned steps can be repeated until deflection converges to the imposed value. Therefore, the evolution of stress, strain, and strain rate at any location of the beam can be solved by the model as a function of deflection. It can be used to obtain yield strength and strain hardening exponent for a strain rate-insensitive material. However, the high throughput feature is exploited when the strain rate sensitivity is calculated by plotting stress and strain rate from locations having a specified strain at any instant, on a logarithmic scale. In the next section, it is shown that at large deformation, stress and strain rate practically remain invariant within a specific range of location which enables experimentalists to extract flow properties without solving for stress redistribution.

3.2 Invariant Stress Point

At sufficiently large deflection, most of the region near the fixed end is subjected to high strain such that total strain is almost equal to plastic strain as elastic strain is negligible. If the elastic strain is negligible in comparison to plastic strain, then the total strain can be written as (see Eq. 5):

$$\varepsilon_t = K\sigma^{1/n}\dot{\varepsilon}^{-m/n} \tag{12}$$

Using the condition of section planarity (which includes both linearity in strain and strain rate along thickness at a cross-section),

$$\sigma_y = \sigma_h\left(\frac{y}{h}\right)^{m+n} \tag{13}$$

The equation of moment equilibrium can be used to express stress at any point in terms of moment acting at the plane passing through this point.

$$2\int_0^h \sigma_y by dy = M_x \tag{14}$$

Substituting for σ_y from Eq. (13),

$$2\int_0^h \sigma_h \left(\frac{y}{h}\right)^{m+n} by dy = M_x \tag{15}$$

$$\sigma_h = \frac{M_x}{bh^2}\left(\frac{m+n+2}{2}\right) \tag{16}$$

The analytical expression for stress distribution along thickness is obtained in terms of moment 'M_x', hardening exponent 'n' and rate sensitivity 'p' by substituting for σ_h from Eq. (16) in Eq. (13). It is rearranged in terms of area moment of inertia, I, to give:

$$\sigma_y = \frac{M_x h}{I}\left(\frac{m+n+2}{3}\right)\left(\frac{y}{h}\right)^{m+n} \tag{17}$$

where $I = \frac{2bh^3}{3}$.

The evolution of the stress profile indicates that there may exist a unique point in any cross-section where stress is same as given by linear elasticity. It can be obtained by the intersection of the redistributed stress profile given by Eq. (17) and the linear stress profile for any moment M_x.

$$\frac{M_x h}{I}\left(\frac{m+n+2}{3}\right)\left(\frac{y}{h}\right)^{m+n} = \frac{M_x y}{I} \tag{18}$$

$$\frac{y}{h} = \left(\frac{m+n+2}{3}\right)^{\frac{1}{1-m-n}} \tag{19}$$

It is clear from Eq. (19) that the position of such a point is independent of the load (as well as moment) and depends only on the materials parameters, m and n. Hence, this location is termed as 'invariant point'. It can be defined as the location at any cross-section where stress under flow is same as given by elasticity at the given load, and it holds under the assumption of negligible elastic strain. In general, the location of the invariant point is transient as it is governed by the ratio of plastic to elastic strain. However, when the elastic strain becomes negligible (for which Eq. 17 is derived), it saturates to a location dictated by 'm' and 'n'. The strain hardening

Fig. 3 Effect of '*m*' and '*n*' on the location of the invariant point, as predicted by Eq. 19
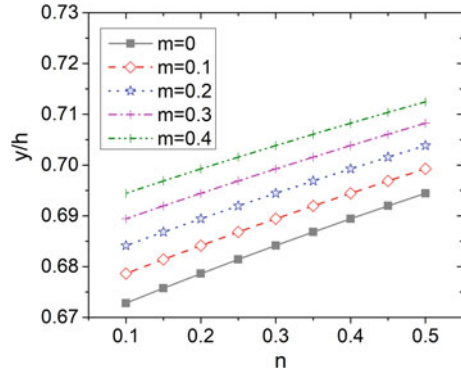
exponent '*n*' generally varies from 0.1–0.5 for metals. The rate sensitivity index '*m*' can be assumed to lie between 0–0.4 for metals having micron sized grains at temperature < 0.5 T$_\mathrm{m}$ and $10^{-5}s^{-1} \leq \dot{\varepsilon} \leq 10^{-2}s^{-1}$. The invariant point lies within a narrow range of 0.67 *h*–0.71 *h* (see Fig. 3).

The strain data from locations within this range at different lengths can be extracted using digital image correlation (DIC). The invariant strain can be obtained by averaging the response in this range which covers a maximum of 3–4 points in a high-resolution image. The corresponding stress can be calculated using elasticity as given by Eq. (3). The stress-strain curves, thus, obtained from multiple invariant points give the plasticity-governing properties with better statistics. Equation (12) can be rearranged as:

$$\sigma_{invariant} = \left(\frac{\varepsilon_{invariant}}{K}\right)^n (\dot{\varepsilon}_{invariant})^m \tag{20}$$

The stress at different invariant points for a particular strain value can be plotted against the strain rate on a logarithmic scale and the slope can be used to obtain strain rate sensitivity *m*. This finding plays a significant role as it allows the extraction of strain rate sensitivity from a single test using DIC without solving for stress distribution.

4　Simulated Results

The bending behavior of doubly symmetric cantilever deformed under deflection rate-controlled test at a rate of 1×10^{-5}mm/s is simulated (see Fig. 4). The dimension of the beam is $3 \times 3 \times 21$ mm^3. The material parameters are given in Table 1. A mesh size of 100×350 elements is used.

A better representation of the experiments is obtained by averaging the behavior in a region around the invariant point as the displacement field in DIC is obtained by

Fig. 4 The simulated load-deflection curve of the cantilever (of size 3 × 3 × 21 mm^3) with the properties shown in Table 1 and the free end moving downward at a constant displacement rate of 10^{-5} mm/s

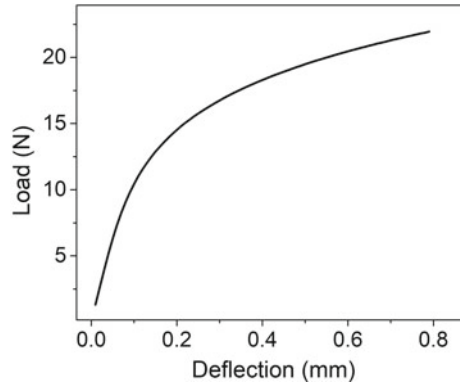**Table 1** Material parameters

Parameter	E (GPa)	σ_y (MPa)	K	n	m
Value	60	50	3×10^{-12}	0.2	0.01

tracking a finite region rather than a point. The values of strain, stress, and strain rate at any deformation are obtained by taking the mean of points in a region of 0.12×0.12 mm^2 around the invariant points. The stress-strain curves from the invariant point at different lengths along the beam are plotted (see Fig. 5) and stress corresponding to a fixed plastic strain of 0.547% is noted down. The strain rate at these locations is plotted against the stress on a logarithmic scale (see Fig. 6). The slope of the linear fit gives strain rate sensitivity as 0.0092 which matches well with the imposed value of 0.01.

The good agreement of the back-calculated values with the input values validates the approach proposed in this work. The estimates can be improved if the data is extracted at the higher strains. The accuracy in determination of strain rate sensitivity
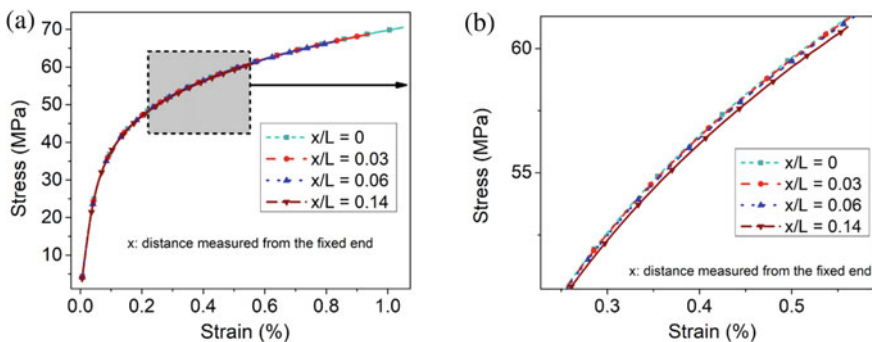

Fig. 5 **(a)** Stress-strain curves from the invariant point at multiple cross-sections **(b)** Magnified view of the inset

Fig. 6 Simulation results: Variation of stress at a strain of 0.547% as a function of the strain rate, as observed at the invariant points. The black squares show the mean value of simulated datum points and error bars give the standard deviation in a region of $0.12 \times 0.12 \ mm^2$ around the invariant points, whereas the blue dashed line shows the best-fit curve, whose equation is given in the legend
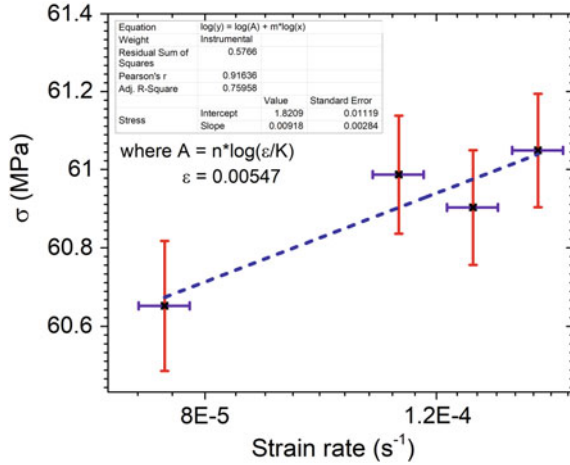
depends on the accuracy by which strain can be measured. Therefore, in addition to high strains, better strain resolution is also a key parameter in calculating the strain rate sensitivity from a single bending test.

5 Conclusion

The concept of 'invariant point' is proposed for the non-linearly deforming beam and it is used to obtain strain rate sensitivity within reasonable accuracy from a single cantilever. The influence of material parameters on the invariant location is shown and the importance of strain resolution in calculating the material parameters is highlighted. It is observed that the methodology proposed in this work is general and it is suitable for a wide range of material parameters. This work can serve as a guide for conducting experiments and measuring rate sensitivity from high throughput data generated by deflection rate-controlled test on a beam using techniques like DIC.

References

1. Nadai A (1931) Plasticity, 2nd edn. McGraw-Hill Book Company, New York
2. Tresca HE (1868) Mémoire sur l'écoulement des corps solides. M´em Pres Par Div Sav 18:733–799
3. de Saint-Venant B (1870) Sur l'etablissement des equations des mouvements interieurs operes dans les corps solides ductiles au-dela des limites ou l'elasticite pourrait les ramener a leur premier etat. Comptes Rendus 70:473–480
4. Levy M (1870) Mémoire sur les équations générales des mouvements intérieurs des corps solides ductiles au delà des limites où l'élasticité pourrait les ramener à leur premier état. CR Acad Sci Paris 70:1323–1325

5. Mises RV (1913) Mechanik der festen Körper im plastisch-deformablen Zustand. Nachr Ges Wiss Göttingen Math-Phys Kl 1913:582–592
6. Prandtl, L.: Spannungsverteilung in plastischen Körpern. In: Proceedings of the 1st international congress on applied mechanics, Delft, pp 43–46 (1924)
7. Reuss A (1930) Berücksichtigung der elastischen Formänderung in der Plastizitätstheorie. ZAMM-J Appl Math Mech/Z Angew Math Mech 10(3):266–274
8. Schmidt R (1932) Über den zusammenhang von spannungen und formänderungen im verfestigungsgebiet. Ingenieur-archiv 3(3):215–235
9. Odqvist FKG (1933) Die verfestigung von flusseisenähnlichen körpern. ein beitrag zur plastizitätstheorie. ZAMM-Journal Appl Math Mech/Z Angew Math Mech 13(5):360–363
10. Prager W (1935) Der Einfluß der Verformung auf die Fließbedingung zähplastischer Körper. ZAMM-J Appl Math Mech/Z Angew Math Mech 15(1–2):76–80
11. Howard JE (1890) Physical properties of iron and steel at high temperature. Iron Age 585
12. Nadai A, Manjoine MJ (1941) High-speed tension tests at elevated temperatures—parts II and III. J Appl Mech 8:A77
13. Zener C, Hollomon JH (1944) Effect of strain rate upon plastic flow of steel. J Appl Phys 15(1):22–32
14. Carreker RP, Hibbard WR (1953) Tensile deformation of high-purity copper as a function of temperature, strain rate, and grain size. Acta Metall 1(6):654–663
15. Hayden HW, Brophy JH (1968) The interrelation of grain size and superplastic deformation in Ni-Cr-Fe alloys. ASM Trans Q 61(3):542–549 (1968)
16. Kocks UF (1976) Laws for work-hardening and low-temperature creep. J Eng Mater Technol 98(1):76–85
17. Johnson AE (1950) A high-sensitivity torsion creep unit. J Sci Instrum 27(3):74–75
18. Robertson A, Cook G (1913) The transition from the elastic to the plastic state in mild steel. Proc R Soc Lond 88(605):462–471
19. Prager W (1937) Mécanique des solides isotropes au delà du domaine élastique, vol 87. Gauthier-Villar, Paris
20. Thum A, Wunderlich F (1932) Die Fließgrenze bei behinderter Formänderung. Forsch Geb Ing A 3(6):261–270
21. Volterra E, Danusso A, Colonnetti G (1943) Results of experiments on metallic beams bent beyond the elastic limit. J Inst Civ Eng 20(5):1–19
22. Roderick JW, Phillipps IH (1950) The carrying capacity of simply supported mild steel beams. BWRA
23. Trifan D (1949) On the plastic bending of circular plates under uniform transverse loads. Q Appl Math 6(4):417–427
24. Popov EP, Khojasteh-Bakht M, Yaghmai S (1967) Bending of circular plates of hardening material. Int J Solids Struct 3(6):975–988

Modelling the Strengthening and Softening Mechanisms in Maraging Steel 250

Kevin Jacob, Saurabh Dixit, and B. Nagamani Jaya

Abstract Plastic flow of materials is dependent on the ability of dislocations to move along specific crystallographic planes under the application of an external stress. Hindrances encountered to this flow will result in a higher stress required to facilitate this movement, leading to the overall hardening of the material. In certain situations, however dislocations prefer to move along a single plane in a condition called as planar slip, the occurrence of which leads to an overall softening of the material. Maraging steels are one such class of materials that exhibit primarily planar slip on solutionising. Upon ageing, they acquire a diverse microstructure with the presence of lath boundaries, precipitates and reverted austenite each of which have a different effect on the overall hardening behaviour of the material. In the current study, the extent of different strengthening or softening mechanisms was quantified as a function of ageing parameters in maraging steel 250. The effect of precipitation in changing the mechanism from softening to hardening is studied through finite element modelling to understand the distribution of stresses, strain partitioning and eventually on the composite stress–strain behaviour. This will help explain the differences in structural integrity of these steels under different ageing conditions.

Keywords Maraging steel 250 · Strain hardening · Softening mechanism

1 Introduction

The microstructure of maraging steel is one with many hierarchies from the point of view of obstacles present in the path of dislocations. The obstacles encountered start from the basic martensitic lath microstructure which includes the lath boundaries (100–150 nm width) separated by block boundaries (1–2 µm block width) with a small degree of misorientation, in turn separated by packet boundaries with different

K. Jacob (✉) · B. Nagamani Jaya
Department of Metallurgical Engineering and Materials Science, Indian Institute of Technology Bombay, Mumbai, Maharashtra 400076, India

S. Dixit
Mishra Dhatu Nigam Ltd. (MIDHANI), Hyderabad, Telangana 500058, India

habit planes nucleating from the colony boundary (prior austenitic grain boundaries) (10–15 μm diameter). These steels have a precipitate free microstructure in the solutionised condition strengthened primarily by the solutes and dislocations but on ageing they initially start to form precipitates of $Ni_3[Ti,Mo]$ and Ni_3Ti [1, 2]. These nanometre-sized ordered intermetallic precipitates are coherent and share an orientation relationship with the matrix but are hard to shear, which increases the strength of the material [3]. Incoherent precipitates of Fe_2Mo type form on ageing above 480 °C, 3 h [4] and lead to looping/bowing of dislocations around them. The peak strength achieved during ageing is observed when the precipitate fraction due to the combined effect of Ni_3Ti and Fe_2Mo are at its maximum.

The objective of the current work is to model the effect of the ageing parameters on the overall strengthening of maraging steel 250. The stress–strain response of maraging steels under different ageing conditions are measured and the stages of the hardening are identified and quantified through the Kocks–Mecking [5] relationship. The same is used as input in an elastic–plastic finite element model (FEM) to identify the strain partitioning between the matrix and precipitates, and predict the composite behaviour and initiation of its failure.

2   Experimental Methods

As received (AR) as solutionised plates of MDN250 were subjected to ageing at 440 °C, 480 °C and 540 °C for 3 h to achieve cases of under-ageing (AR + UA), peak ageing (AR + PA) and over-ageing (AR + OA). Flat tensile samples were cut out of these plates using electrical discharge machining (EDM) with gauge dimensions of 5 mm length and (2×2) mm^2 cross-sectional area. Tensile tests were carried out at room temperature (25 °C) at a strain rate 2×10^{-3} s^{-1}. Optical digital image correction (DIC) was used to obtain the full field strain map. Compliance corrected stress–strain data was used to plot the strain hardening and softening exponents.

2.1   Finite Element Modelling

Finite element simulations were carried out on dog bone-shaped samples using ABAQUS CAE v6.144 ®. The experimental data obtained by performing uniaxial tensile testing at room temperature on sub-sized miniature tensile samples has been used as input to simulate the elastic–plastic micromechanical response of the maraging steels in FEM. The model was first validated using the tensile data for the AR condition and other factors such as precipitates and slip plane to aid planar slip were added to understand the effects of these on the overall deformation. The simulation was carried out in a 300 nm gauge length specimen with a (120×120) nm cross-sectional area. These dimensions amount to the size of few individual laths as seen in maraging steel 250. The precipitate fraction was maintained at 5% and

Table 1 Input properties for different materials

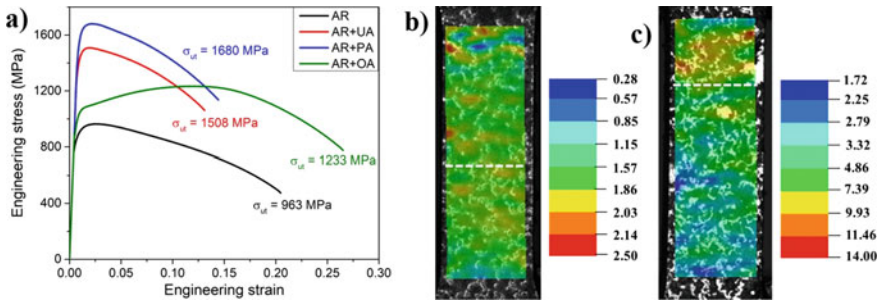| Material properties	Maraging steel matrix	Ni₃Ti [8]	Fe₂Mo [9]
Young's modulus	190 GPa	250 GPa	230 GPa
Poisson's ratio	0.3	0.29	0.28
Yield strength	843 MPa (AR) 1582 MPa (AR + PA) 983 MPa (AR + OA)	4.3 GPa	NA
Strain hardening	Refer Fig. 1a	0	NA

Fig. 1 a) Engineering stress–strain curves for different ageing conditions **b)** and **c)** Equivalent plastic strain maps obtained through DIC corresponding to UTS in case of AR and AR + OA, respectively. The white dotted line represents the final plane of fracture, and the red regions correspond to the points of strain localisations

the morphologies and size are taken from a previous work [6, 7] for the differently aged conditions. Table 1 gives the detailed input parameters for the same. C3D10 type mesh elements were used for meshing. The boundary conditions applied were such that the bottom face of the sample was encastered and the top face was allowed displacement in the Y-direction. Failure was not explicitly modelled, but the stresses at particular values of strain were used to predict initiation of cavities/microcracks.

3 Results and Discussion

3.1 Strain Hardening and Softening Behaviour

Figure 1a shows the engineering stress–strain response of all the specimen represented as: as solutionised, as received (AR) and aged to different extents. From Fig. 1b, c. it can be seen that the point of UTS corresponds to the necking in case of AR + OA but not in the other ageing conditions. The AR sample shows regions

of localisation at several locations at strain corresponding to UTS, while the AR + OA shows severe localisation at a single region where it necks down. As expected, the peak aged condition has the highest strength, the same was observed in case of the hardness plot as well [7], wherein the peak hardness obtained was 620 ± 17 HV along with a hardness of 319 ± 10 HV in case of the unaged sample. While the AR, AR + UA and AR + PA showed a macroscopic softening with very little strain hardening, the AR + OA showed a conventional strain hardening before necking. Figure 2 shows the strain hardening and softening exponents obtained from fitting the data into Eq. 1.

$$\sigma = H\varepsilon^{n}; \varepsilon_y \to \varepsilon_{ut} \qquad (1)$$

$$\sigma = S\varepsilon^{-m}; \varepsilon_{ut} \to \varepsilon_{neck} \qquad (2)$$

where n and m represent the strain hardening and softening exponents, respectively.

Karnthaler et al, have reported the formation of planar slip mechanism in Fe–Ni alloys [10], wherein the plastic deformation is localised to a single plane along with an increase in the slip velocity. The occurrence of planar slip is mainly due to short range ordering (SRO) observed in these steels which has been well established in Fe–Ni alloys [11]. Due to the presence of SRO the first dislocation passing through the lattice experiences a high resistance to the motion as it would destroy the SRO, with the piled up dislocations following it unable to restore this order. When a high enough stress is present to activate the dislocation sources all the surrounding dislocations help the first dislocation push against the forthcoming barrier. Once this barrier is broken there is a sudden flow of dislocations along this particular plane leading to a glide plane softening mechanism. This is the reason why maraging steels show the peculiar behaviour of a low ultimate to yield strength value (1.13 for AR, 1.06 for AR + UA and AR + PA) followed by a sudden drop in stress and an increased slip velocity. The above mechanism is observed in these steels up to the AR + PA
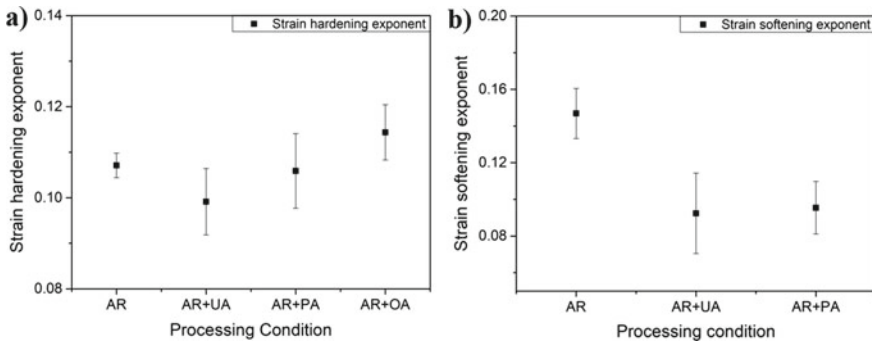

Fig. 2 **a)** Hardening **b)** Softening exponents with respect to ageing

condition, albeit with a decreasing softening exponent, as the precipitates formed are coherent in nature in this ageing condition. The dislocations are able to cut through these rod shaped precipitates rather easily due to the large number of dislocations that are traversing through a single plane. This also results in the low uniform strains of the order of 2–3% observed in case of the AR, AR + UA and AR + PA conditions and the point of necking does not coincide with that of UTS (Fig. 1b). This behaviour is in agreement with the stress–strain curves observed in similarly heat treated Ti containing alloys [12]. This behaviour would lead to problems in conditions of plastic overload as the material would start undergoing localised deformation once the yield stress is reached due to lack of hardening mechanisms in the material.

However, in the AR + OA condition the SRO is broken due to two new additions to the existing system in the form of the FCC austenite phase and the incoherent Fe_2Mo phase, which promote looping of the dislocation around the precipitates. Hence, a larger uniform strain of 12% is reached (Fig. 1a). This specimen shows significant strain hardening, which proves that planar slip is no more the dominant deformation mechanism here. Overaging of maraging steels leads to the formation of second phase austenite in the structure which is a softer, precipitate free phase in comparison to the BCC martensite and does not promote planar slip. The fraction of austenite measured using XRD measurements was $38 \pm 2\%$ [7]. The presence of incoherent Fe_2Mo promotes Orowan looping of the dislocations. These also prevent the occurrence of planar slip as it is more difficult to bow dislocation around particles where there are loops of like dislocations repelling the same.

3.2 Strain Partitioning and Onset of Failure

The above data from Figs. 1 and 2 were used as inputs in the FE model to explain the role of precipitates in the onset of failure through precipitate fracture and interface decohesion. The planar slip mechanism in AR which leads to the softening mechanism in these steels was modelled using a thin strip emulating the slip plane with a 30% lower yield stress of 600 MPa as compared to that of macroscopic yield. The volume modelled corresponds to only a couple of laths across which a single planar slip event will occur while the experimentally tested sample is macroscopic and contains a number of laths, blocks and colonies within the tested volume. The experimental and simulated stress–strain response overlap (Fig. 3a), serving as a calibration of the input properties and the choice of the representative volume element (RVE). From the equivalent plastic strain (PEEQ) contour maps (Fig. 3b), the delayed onset of necking becomes obvious. Plastic strain is uniform throughout the sample up to strains corresponding to UTS, much like what was seen in the DIC maps of Fig. 1b. At the UTS, points of strain localisation begin to appear over a number of regions. Eventually, at the macroscopic strain corresponding to (iii), it is seen that there is a concentration of the overall deformation along a particular plane replicating planar slip, leading to the softening of the material along that specific plane and eventual failure at that location. The model is representative of the deformation mechanism
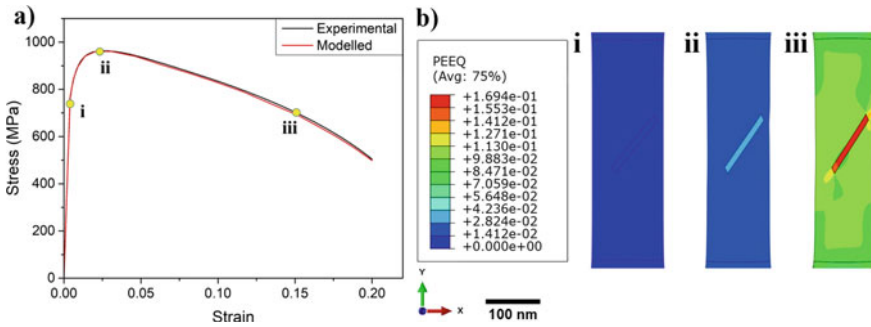
Fig. 3 a) Stress strain curve from simulations versus experiment **b)** PEEQ maps showing effect of planar slip at strains corresponding to (i) yield (ii) ultimate and (iii) necking point in AR specimen

when an easier path for deformation exists and shows how strain concentrates along that plane. It gives a semi-quantitative picture of how strain localises along specific planes leading to initiation of failure there.

The AR + PA condition has rod-shaped Ni_3Ti precipitates. The effect of precipitate orientation (parallel, perpendicular and inclined to the tensile axis) on the stress distribution and strain partitioning was modelled while maintaining both matrix and precipitates as elastic–plastic. The contours shown in Fig. 4 correspond to the macroscopic strain at UTS of the AR + PA sample. Based on a comparison of von Mises stress to yield stress (4.3 GPa) and maximum principal stress (MAXPS) to fracture stress (assumed ~2 GPa [13]), it is clear that precipitate fracture or interface decohesion will precede their yielding for all orientations. It is also seen that the mechanism
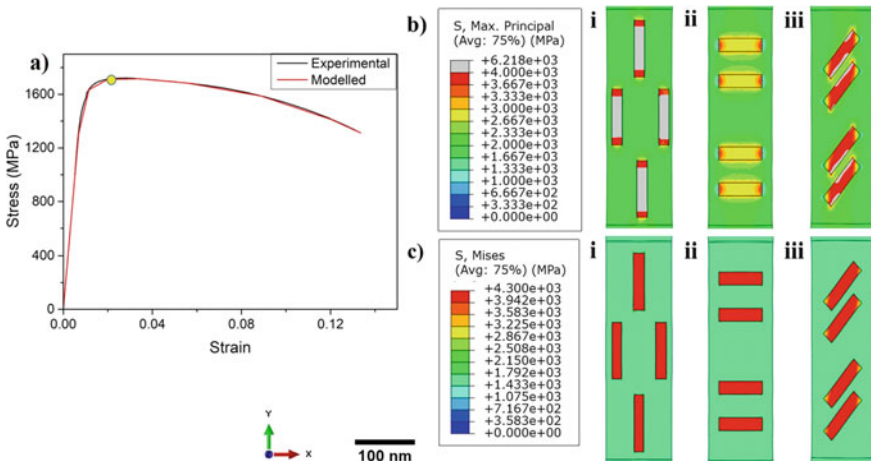

Fig. 4 a) Stress–strain curve for simulation versus experiment for AR + PA condition **b)** MAXPS contours **c)** von Mises contours for rod-shaped precipitates at the UTS with orientations (i) parallel (ii) perpendicular and (iii) inclined at 45° to the tensile loading direction

of void nucleation will be through precipitate fracture when precipitates are parallel to the tensile axis and through interface decohesion between the precipitate and the matrix in case of those aligned perpendicular to the loading axis. Microcracks so nucleated will undergo blunting due to the plasticity of the matrix that it encounters, but their formation will nevertheless lead to decrease in load carrying capacity and softening that is observed. In addition, at a given strain, the MAXPS in precipitates oriented parallel is significantly higher than those oriented perpendicular to the tensile axis. Hence, the latter will be able to accommodate larger strains before initiating failure. Assuming that both fracture and interface decohesion occurs at the same critical stress of ~2GPa, the overall strain at which micro-fracture events initiate can be calculated from PEEQ maps to be 0.6%, 1.1% and 1.3%, respectively, for the precipitates aligned parallel, inclined and perpendicular to the tensile axis. In a macroscopic sample, the orientation of precipitates will change based on the lath orientation and will require a micro-DIC to determine the initiation of failure.

In case of the AR + OA condition, hard, brittle Fe-Mo precipitates are spherical and are non-shearing. Hence only elastic properties were assigned to the precipitates while the matrix was elastic–plastic. Failure is assumed to initiate by fracture of precipitates. Figure 5 shows the strain and MAXPS contours around them. A strong strain partitioning is seen to occur between the matrix and precipitate, at the strain corresponding to the point shown. The MAXPS stress exceeds the fracture strength at this point, leading to precipitate fracture. Beyond this point though, most of the stress is being taken up by the precipitate while the matrix is relaxed due to plasticity. The AR + OA matrix being softer than the AR + PA condition, blunting of the microcracks is expected to be more. This coupled with the ability of the precipitates to promote looping of the dislocations around them results in the higher work hardening and improved ductility observed in the AR + OA condition.

An improved micromechanical model requires precise determination of yield and fracture properties of precipitates, but the model presented here helps understand both the mechanism and a semi-empirical quantification of strain hardening and softening in maraging steels with a complex microstructure.
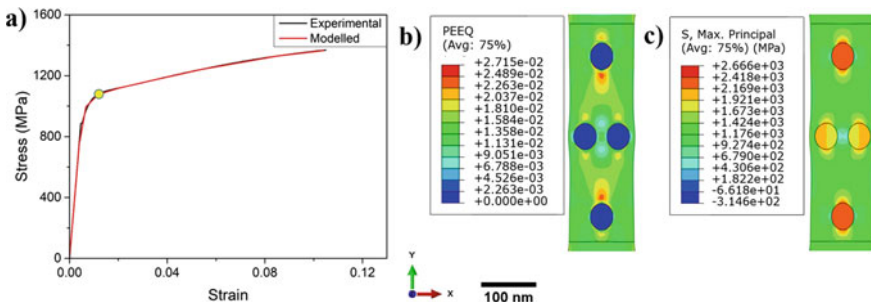

Fig. 5 **a)** Stress–strain curve for simulation vs experiment for AR + OA condition **b)** PEEQ map representing strain partitioning in case of Fe-Mo precipitates **c)** MAXPS contour indicating initiation of fracture at the precipitates

4 Conclusion

Softening and hardening mechanisms in maraging steel have been studied through tensile tests combined with FEM. Mechanistic explanation of softening and hardening as well as semi-empirical predictions of onset of failure through void nucleation/microcracks for different precipitate orientations and morphologies have been made.

References

1. Li K et al (2018) On the origin and contribution of extended kinks and jogs and stacking fault ribbons to deformation behavior in an ultrahigh strength cobalt-free maraging steel with high density of low lattice misfit precipitates. Mater Sci Eng A 728(April):208–217
2. Viswanathan UK, Dey GK, Asundi MK (1993) Precipitation hardening in 350 grade maraging steel. Metall Trans A 24(11):2429–2442
3. Mukhopadhyay CK, Rajkumar KV, Jayakumar T, Raj B (2010) Study of tensile deformation behaviour of M250 grade maraging steel using acoustic emission. J Mater Sci 45(5):1371–1384
4. Vasudevan VK, Kim SJ, Wayman CM (1990) Precipitation reactions and strengthening behavior in 18 Wt Pct nickel maraging steels. Metall Trans A 21(10):2655–2668
5. Bambach M, Sizova I, Bolz S, Weiß S (2016) Devising strain hardening models using kocks-mecking plots-a comparison of model development for titanium aluminides and case hardening steel. Metals (Basel) 6(9)
6. Guo Z, Sha W (2004) Quantification of precipitate fraction in maraging steels by X-ray diffraction analysis. Mater Sci Technol 20(1):126–130
7. Jacob K, Yadav D, Dixit S, Hohenwarter A, Nagamani B (2021) High pressure torsion processing of maraging steel 250 : microstructure and mechanical behaviour evolution. Mater Sci Eng A 802(December 2020):140665
8. Miller C, Dellacorte C, Zou M (2021) Nanomechanical properties of hardened 60NiTi. Mater Sci Eng A 800(September 2020):140284
9. Vasilyev DA, Udovsky AL (2020) Quantum-mechanical calculations of the difference of structural energies C14 and bcc phases C14 Fe and Mo and formation energy of ferromagnetic C14 Fe 2 Mo Laves phase Quantum-mechanical calculations of the difference of structural energies C14 and bcc ph. J Phys Conf Ser 1431(1):012059
10. Gerold V, Karanthaler HP (1989) On the origin of planar slip in FCC alloys. Acta Metall 37(8):2177–2183
11. Lomova NV, Shabanova IN, Chirkov AG, Ponomaryov AG (2007) On short-range ordering in Fe-Ni alloys. J Electron Spectros Relat Phenomena 156–158:401–404
12. Leitner H, Schober M, Schnitzer R, Zinner S (2011) Strengthening behavior of Fe-Cr-Ni-Al-(Ti) maraging steels. Mater Sci Eng A 528(15):5264–5270
13. Korte-Kerzel S (2017) Microcompression of brittle and anisotropic crystals: recent advances and current challenges in studying plasticity in hard materials. MRS Commun 7(2):109–120

A Numerical Study of Void Interactions in Elastic–Plastic Solids Containing Two-Scale Voids

A. K. Dwivedi, I. A. Khan, and J. Chattopadhyay

Abstract Ductile fracture in metals occurs due to the nucleation, growth and coalescence of microscopic voids, resulting in a macroscopic crack. These voids often originate at different length scales due to cracking of large-sized inclusions or decohesion at second-phase particles. In several structural materials like low-alloy steels, secondary voids accelerate the ductile damage process, thus, resulting in a severe reduction in ductility. A systematic study analyzing the effect of spatial distribution of secondary voids on the growth and coalescence of primary voids has yet not been reported. In the present work, finite element-based cell model studies are carried out to understand the void interactions in elastic–plastic solids containing voids at two distinct length scales. A double periodic array of primary and secondary voids subjected to uniaxial loading under plane strain condition is analyzed. The effect of secondary void location and its orientation on the mesoscale response and evolution of porosity is studied numerically. Our numerical results suggest that the interactions between the two-scale voids accelerate the growth and coalescence of primary voids.

Keywords Ductile fracture · Voids · Elastic-plastic solids · Finite element analysis

Nomenclature

$2A_0$	Intervoid distance of primary voids in X_1 direction in undeformed state
$2B_0$	Intervoid distance of primary voids in X_2 direction in undeformed state
D_{P0}	Initial diameter of primary void
D_{S0}	Initial diameter of secondary void
a_0	Undeformed radius of primary void in X_1 direction
c_0	Undeformed radius of primary void in X_2 direction

A. K. Dwivedi (✉) · I. A. Khan · J. Chattopadhyay
Homi Bhabha National Institute, Mumbai 400094, India
e-mail: akdwivedi@barc.gov.in

I. A. Khan · J. Chattopadhyay
Reactor Safety Division, Bhabha Atomic Research Center, Mumbai 400085, India

P	Distance between primary and secondary void
θ_o	Angle between secondary void and X_1 direction in the undeformed state
σ_y	Yield strength
E	Young's modulus
ν	Poisson's ratio
n	Hardening exponent
σ_e	Equivalent stress
σ_h	Hydrostatic stress
T	Stress triaxiality ratio
E_e	Equivalent strain
VVF	Void Volume Fraction
F_p	Primary void volume fraction
F_S	Secondary void volume fraction
F_T	Total void volume fraction
Fp_0	Initial volume fraction of primary void
Fs_0	Initial volume fraction of secondary void
V_0, V	Initial and current volume of the cell, respectively

1 Introduction

Ductile fracture in metals comprises a three-stage process namely; void nucleation, growth and coalescence [1]. In structural metals like low-alloy steels, voids typically nucleate at different length scales due to cracking of large-sized inclusions or decohesion at second-phase particles. The larger-sized (primary) voids nucleate relatively early and enlarge due to plastic deformation of the surrounding matrix up to a point where plasticity localizes in the ligament between neighbouring voids [2, 3]. This stage is often referred to as the onset of void coalescence. Beyond this stage, primary voids typically link up to each other or to a main crack due to new surfaces created by nucleation, growth and coalescence of much smaller (secondary) voids that nucleate at relatively large strains [2]. Typically, secondary voids are defined as being one order of magnitude smaller than primary voids. The volume fraction of these secondary voids can be of the order of 1%. Experimental evaluation of the effect of secondary voids on the growth and coalescence of primary voids and, hence, on macroscopic ductility poses several challenges [2].

It is generally agreed that the mechanism of fracture in ductile materials is a manifestation of the role played by void population attributes, namely porosity, shape of voids and their spatial distribution (location and orientation), and the matrix hardening attributes in the mechanism of plastic flow and localization. The existing models of ductile fracture, however, have mainly focussed on the role of primary voids in the macroscopic fracture process. The development of these models is motivated by the seminal work of McClintock [4] and Rice and Tracey [5], who analyzed the growth of an isolated void in an infinite medium. Later, Gurson [6, 7] performed

a limit-analysis of a hollow sphere of finite radius, thus, incorporating the effect of arbitrary non-zero porosities on the macroscopic response of a rigid-plastic solid. The model was extended to include the effect of matrix hardening in a heuristic manner. Since the Gurson model accounted only for the void growth, heuristic corrections were incorporated to account for the mechanism of void nucleation and coalescence, notably based on micromechanical cell model studies. In recent years, an increasing attention has been paid to improved characterization of ductile fracture at low stress triaxiality [8]. Various generalizations of the Gurson model have been proposed to account for the anisotropies associated with plastic deformation of the matrix and the evolution of void shapes at arbitrary finite strains [10]. The existing ductile fracture models (including the recent ones which account for the anisotropic effects of matrix deformations and void shapes, as well as those based on rigorous nonlinear bounds), were developed on the basis that the void growth is driven by some diffuse plastic flow in the matrix. Consequently, predictions based on these models overestimate measured ductilities [2, 3]. Experimental observations suggest strong evidence for a termination to stable void growth by various mechanisms of flow localization in the intervoid matrix. An important contribution to the modelling of internal necking was made by Koplik and Needleman [11]. Void coalescence can also occur due to formation of a micro shear band between the neighbouring voids. Material instability inside this band is described by the localization condition proposed by Rice [12] and Needleman and Rice [13]. These studies, however, were focused on modelling the flow localization in a matrix containing only one population of void nucleating particles.

Although the role played by secondary voids in the macroscopic fracture process is well-recognized, till date only limited studies have focussed on modelling their effects on the fracture ductility. Perrin and Leblond [14] analyzed a hollow sphere containing one large primary void surrounded by a porous plastic matrix containing the secondary voids. Brocks et al. [15] and Fabregue and Pardoen [16] numerically modelled the effect of second population of voids using a Gurson-type model. Gao and Kim [17] proposed to account for the secondary voids through calibration of a critical porosity for the coalescence of primary voids. Faleskog and Shih [18], and Tvergaard [19, 20] carried out numerical studies with an explicit representation of both primary and secondary voids. These studies were focused on analyzing the role of increased local stresses resulting from the growth of larger voids in a cavitation type instability at the smaller void. The effect of void volume fraction on the void growth rate was studied numerically. While the former authors performed plane strain analysis of cylindrical voids, the later author carried out axi-symmetric studies on a special void configuration where each larger void was surrounded by a smaller void and vice-versa. More recent research in this area has focused on bringing the size effects of the secondary voids, [21–25] for a fixed volume fraction, on ductile fracture. While Zybell et al. [25] performed cell model studies, Hutter et al. [24] focused on modelling the process zone near the crack tip. In both these studies, the primary voids were modelled discretely, and the size of the secondary voids was incorporated indirectly in terms of an intrinsic length that was introduced in the non-local formulation of the GTN model.

Most of the above-mentioned studies, employing a homogenized representation of the secondary voids, suggest that the nucleation and growth of secondary voids mainly accelerate the void coalescence process, the primary void growth is largely uninfluenced [16]. Based on an explicit representation of primary and secondary voids, Khan and Bhasin [26] have shown that the secondary voids can enhance the growth of primary voids and the mesoscopic ductility depends on the spatial distribution of secondary voids. In the present work, the effect of location and orientation of a secondary void, in the intervoid ligament between the primary voids, on the mesoscopic response and evolution of porosity is studied numerically. In particular, focus is laid on understanding how the voids originating at two distinct length scales interact with each other. Both the primary and secondary voids are assumed to be present from right from the beginning of the deformation history. Plane strain condition is assumed, and a uniaxial tensile load is applied. Our numerical results suggest that the interactions between the two-scale voids accelerate the growth and, hence, the coalescence of primary voids.

2 Problem Formulation

An elastic–plastic solid containing pre-existing voids of two different sizes is analyzed numerically. 2D double periodic arrays containing cylindrical primary and secondary voids are shown in Fig. 1. The diameters of primary and secondary voids, in the undeformed state, are denoted as D_{po} and D_{so}, respectively. The initial spacing
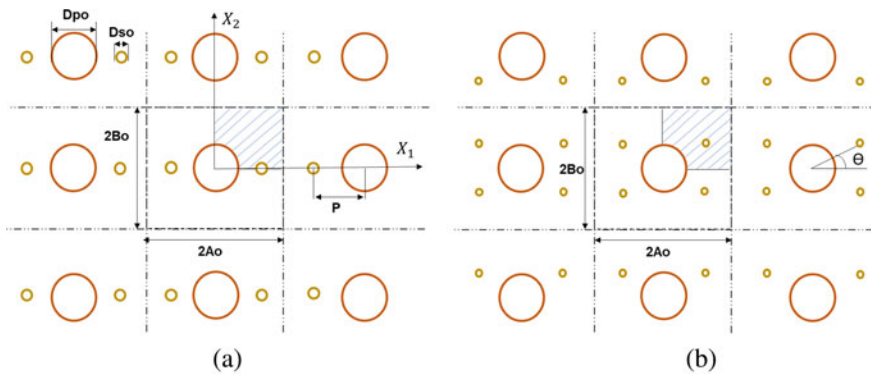

Fig. 1 2D double periodic arrays of primary and secondary voids analyzed in this study **a** two secondary voids are located in the intervoid ligament between the two primary voids **b** four secondary voids surround each primary void. Dashed square is showing a unit cell and the hatched portions are analyzed due to symmetry conditions. The initial volume fraction of primary and secondary voids is kept the same in (a) and (b)

between the two primary (large sized) voids is $2A_o$ and $2B_o$ in the X_1 and X_2 directions, respectively. Two different spatial distributions of secondary voids are considered. In Fig. 1a, two secondary voids are located in the intervoid ligament between the two primary voids. In the undeformed state, the distance of a secondary void from the neighbouring primary void is denoted by P. Figure 1b depicts an arrangement where four secondary voids surround each primary void and are lying at a fixed distance P from the neighbouring primary void. The initial orientation of a secondary void with respect to the intervoid ligament is described by the angle θ. A uniaxial tensile load is applied at $X_2 = B_o$. The initial volume fraction of the secondary voids is kept the same for the two different voids arrangements, shown in Fig. 1.

2.1 Governing Equations

A Lagrangian finite strain formulation of the field equations is used. The initial unstressed state is taken as the reference configuration and the position of a material point, relative to a fixed Cartesian frame, in the reference configuration is denoted as x. The material point, initially at x, is at $\overline{x}$ in the current configuration. The displacement vector u and the deformation gradient F are defined as

$$u = \overline{x}\text{- x, } F = \frac{\partial \overline{x}}{\partial x} \tag{1}$$

The finite element formulation is based on the principle of virtual work written as

$$\int_v s : \delta F dV = \int_s T \cdot \delta u \ dS \tag{2}$$

where s is the (nonsymmetric) nomial stress, T is the traction, u is the displacement, V and S are, respectively, the volume and surface of the body in the reference configuration. The traction and the reference configuration normal are related by $T = n.s$ and $s = F^{-1} \tau$ with $\tau = \det(F)\sigma$ and σ the Cauchy stress.

Due to symmetry considerations only 1/4th models, shown by hatched lines in Fig. 1, are analyzed numerically. Symmetry conditions are incorporated using the following boundary conditions,

$$u_1 = 0 \text{ at } x_1 = 0 \tag{3}$$

$$u_2 = 0 \text{ at } x_2 = 0 \tag{4}$$

The boundary of the cell model at $x_1 = A_o$ is constrained to remain plane throughout the loading history to simulate periodic boundary condition. Plane strain condition is simulated by constraining the nodal displacements, that is,

$$u_3 = 0 \text{ at } x_3 = 0 \text{ and } x_3 = 1 \tag{5}$$

2.2 Constitutive Relations

Most of the numerical calculations reported in this study are carried out using a rate-independent J_2 isotropic hardening response for the elastic–plastic matrix between the two populations of voids. The matrix response is characterized by the following representation in uniaxial tension,

$$\varepsilon = \begin{cases} \frac{\sigma}{E}, \text{ for } \sigma \leq \sigma_y \\ \frac{\sigma_y}{E}\left(\frac{\sigma}{\sigma_y}\right)^n \text{ for } \sigma > \sigma_y \end{cases} \tag{6}$$

Here, E is Young's modulus, σ_y is the initial yield stress, and n is the strain-hardening exponent. In all our studies, $\sigma_y/E = 0.004$, $\nu = 0.333$ and $n = 0.1$ are used.

And the modified Gurson model is used for the homogenized representation of secondary voids volume fraction (0.036%) over the matrix. The following constitutive equation describes the matrix behaviour

$$\left(\frac{\sigma e}{\sigma o}\right)^2 + 2q_1 F_s \cosh\left(q_2 \frac{3\sigma h}{2\sigma o}\right) - 1 - q_3 F_s^2 = 0 \tag{7}$$

where q parameters values are taken $q_1 = 1.5$, $q_2 = 1$ and $q_3 = q_1{}^2$. F_s is the current volume fraction of secondary voids and σ_0 is the equivalent tensile flow stress in the matrix.

The mesoscopic response of the unit cell is described by the following variables,

$$\text{Equivalent stress}: \quad \sigma_e = \sqrt{\frac{1}{2}\left[(\sigma_1 - \sigma_2)^2 + (\sigma_2 - \sigma_3)^2 + (\sigma_3 - \sigma_1)^2\right]} \tag{8}$$

$$\text{Hydrostatic stress}: \quad \sigma_h \frac{(\sigma_1 + \sigma_2 + \sigma_3)}{3} \tag{9}$$

$$\text{Stress Triaxiality}: \quad T = \frac{\sigma_h}{\sigma_e} \tag{10}$$

$$\text{Equivalent strain}: \quad E_e = \left(\frac{\sqrt{2}}{3}\right)\sqrt{(E_1 - E_2)^2 + (E_2 - E_3)^2 + (E_3 - E_1)^2} \tag{11}$$

Here, σ_1, σ_2 and σ_3 are the Cauchy stresses and E_1, E_2 and E_3 are the logarithmic strains in X_1, X_2 and X_3 direction, respectively. Numerical analyses are performed at fixed triaxiality, $T = 1/3$.

3 Results and Discussion

In this section, the numerical results obtained from finite element analysis of a unit cell containing two-scale voids are presented. As mentioned earlier, both primary and secondary voids are assumed to be present right from the beginning of the deformation history. IN all our numerical analyses, the initial volume fraction of the primary voids (F_{po}) and secondary voids (F_{so}) is taken as 2.4% and 0.036%, respectively. The two populations of voids are modelled explicitly and an assumption of plane strain deformation is made. Twenty noded hexahedral brick elements are used to discretize the quarter symmetric models. A unit thickness is assumed in the X_3 direction and only one element is modelled across the thickness. Typical finite element meshes used to model the two different spatial arrangements of secondary voids, shown in Fig. 1, are presented in Fig. 2. We first present the results for the case where only primary voids exist and then analyze the influence of small secondary voids on interactions between the two-scale voids and plastic flow localization.
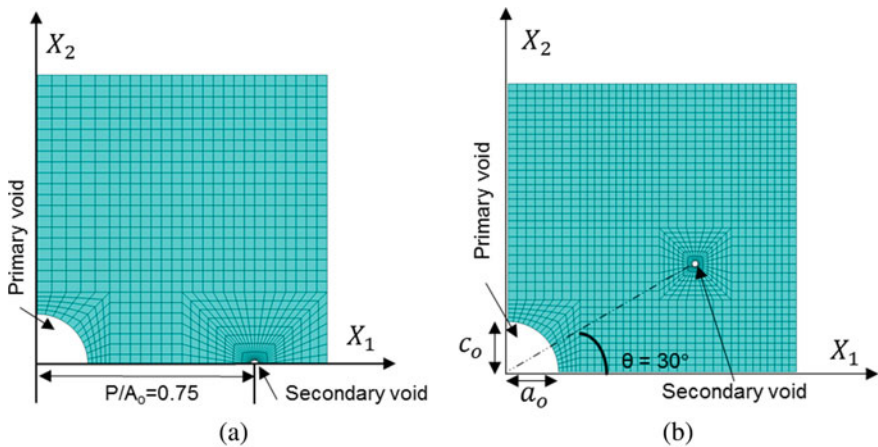

Fig. 2 Typical finite element meshes used to discretize a quarter symmetric unit cell containing primary and secondary voids **a** Secondary void lying in the ligament between the two primary voids **b** Secondary void at an orientation of 30° with respect to the intervoid ligament (a_o and c_o are the undeformed radii of the primary void in X_1 and X_2 directions, respectively)

3.1 Mesoscopic Response of an Elastic–Plastic Solid Containing Only Primary Voids

The mesoscopic equivalent stress s equivalent strain response of a unit cell containing only primary void is shown in Fig. 3a. A competition between matrix material strain hardening and the porosity-induced softening can be clearly observed. Towards the later stages of the deformation history ($E_e > 0.4$), the stress carrying capacity reduces abruptly. For an elastic–plastic solid containing only primary voids, the evolution of porosity is rather straightforward. Based on matrix incompressibility condition, Koplik and Needleman [11] have proposed the following relation to compute the void volume fraction F,

$$F = 1 - (1 - F_0)\left(\frac{V_0}{V}\right) - \frac{\Delta V_e}{V} \tag{12}$$

Here, V_0 and V are the initial and current volume of the unit cell, respectively, and F_0 is the initial void volume fraction. ΔV_e is the elastic dilation of the matrix resulting from the hydrostatic stress and can be obtained as

$$\Delta V_e = V_0(1 - F_0)\frac{3(1 - 2\nu)}{E}\sigma_h \tag{13}$$

The evolution of porosity obtained from the Koplik and Needleman scheme is presented in Fig. 3b. Initially, the void growth is slow, and the porosity evolution curve is varying almost linearly with the equivalent strain. As the deformation progresses, the deformation mode shifts to a uniaxial mode of straining that corresponds to flow localization in the ligament between the two adjacent voids. At this stage, the void volume fraction increases rapidly, often referred to as the onset of void coalescence, and the event is associated with a rapid drop in the load carrying capacity. An interested reader can find further details elsewhere [11]. Apart from porosity the evolution of void aspect ratio W, defined as the ratio of axial to transverse semi-axes (W = c/a), with the equivalent strain is also analyzed, see Fig. 3c. Under uniaxial tension, the void first evolves into a prolate shape. With the onset of plastic flow localization, the void starts growing rapidly in the transverse direction with internal necking as the mode of coalescence.

3.2 Effect of Secondary Voids Location on Void Interactions and Plastic Flow Localization

The spatial arrangement of secondary voids shown in Fig. 1a is analyzed in this subsection. The position of primary void is kept fixed and the location of secondary void, in the intervoid ligament between the two primary voids, is varied to understand the
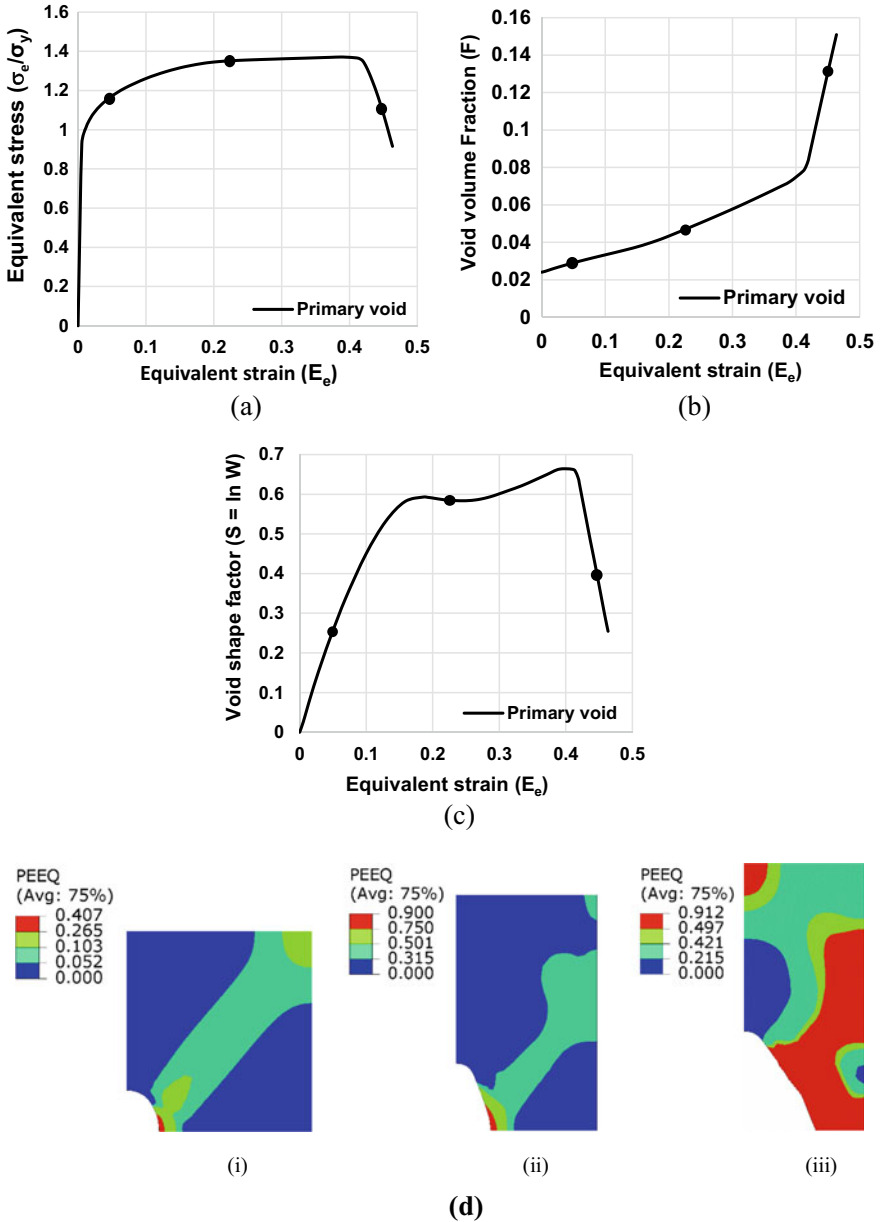
Fig. 3 Plane strain response of a unit cell containing only primary voids ($F_p = 0.024$) under a uniaxial tensile load (**a**) Normalized equivalent stress versus equivalent strain (**b**) Void volume fraction versus equivalent strain (**c**) Void shape versus equivalent strain (**d**) Contours of equivalent plastic strain at different stages in the deformation history (shown by open circle in figure a,b and c)

influence of secondary voids distribution on the interactions between the two-scale voids and plastic flow localization. The mesoscopic equivalent stress Vs equivalent strain response of the unit cell for the three different arrangements of secondary voids ($P/A_o = 0.25, 0.50$ and 0.75) is shown in Fig. 4a. For comparison purpose, the results for the case where only primary voids exist, presented in Sect. 3.1, are also included. For an initial void volume fraction of 0.036%, a homogenized representation of the secondary voids, using the Gurson model, lead to a very small additional constitutive softening and the mesoscopic response is almost the same as observed for the case where only primary voids exist. In contrast, the discrete representation of secondary voids has shown an interesting effect of voids distribution on the mesoscopic response. When a secondary void is located close to a primary void ($P/A_o = 0.25$), the intervoid ligament is quite small. As the voids grow, the ligament reduces, leading to the coalescence of the secondary void during the early stage of the deformation history.

Beyond this stage, the two coalesced voids start behaving like a single primary void but with a larger void volume fraction. As a result, the mesoscopic stress–strain curve deviates from that of primary voids almost right from the beginning. When $P/A_o = 0.5$, initially, both the voids grow almost independent of each other. As deformation progresses, the von-mises stress around the secondary void distorts its shape. This leads to magnification of the hydrostatic stress around the primary void causing it to grow at a faster rate. The accelerated growth of the primary void generates sufficient hydrostatic stress around the secondary void, thus, enhancing the growth of the latter. This complex interaction between the two-scale voids results in a rapid evolution of total porosity. As a result, the mesoscopic response becomes soft and starts falling below that of the primary voids. With further deformations, the localization of plastic flow sets in with a consequent rapid drop in the load carrying capacity. When the distance of the secondary void from the neighbouring primary void is large ($P/A_o = 0.75$), it is basically the two secondary voids that interact with each other, and the growth of primary voids is largely uninfluenced. The mesoscopic response, therefore, is almost like that of primary voids till the localization of plastic flow starts. A plot of mesoscopic transverse strain E_1 Versus equivalent strain for the three different arrangements of secondary voids is presented in Fig. 4b. Near the onset of flow localization, the deformation mode abruptly shifts to a uniaxial mode of straining and the cell transverse deformation stops. The maximum reduction in the mesoscopic ductility is observed when the secondary voids are located at the distance of $P/A_o = 0.5$. Figure 4d, f shows the influence of secondary voids locations on the evolution of porosity. A numerical integration scheme was used to evaluate the primary and secondary void volume fractions separately. The accuracy of the numerical scheme was assessed by comparing the total void volume fraction ($F_p + F_s$) with that obtained from the Koplik and Needleman scheme [11]. For $P/A_o = 0.25$, the coalescence between primary and secondary void occurs during the early stage of the deformation process. The porosity evolution curves of the two voids are terminated at the stage of void collapse and subsequently, only the evolution of total porosity is shown. When $P/A_o = 0.5$, the void collapse occurs after significant plastic deformation, and the total porosity at this stage is more than three times the
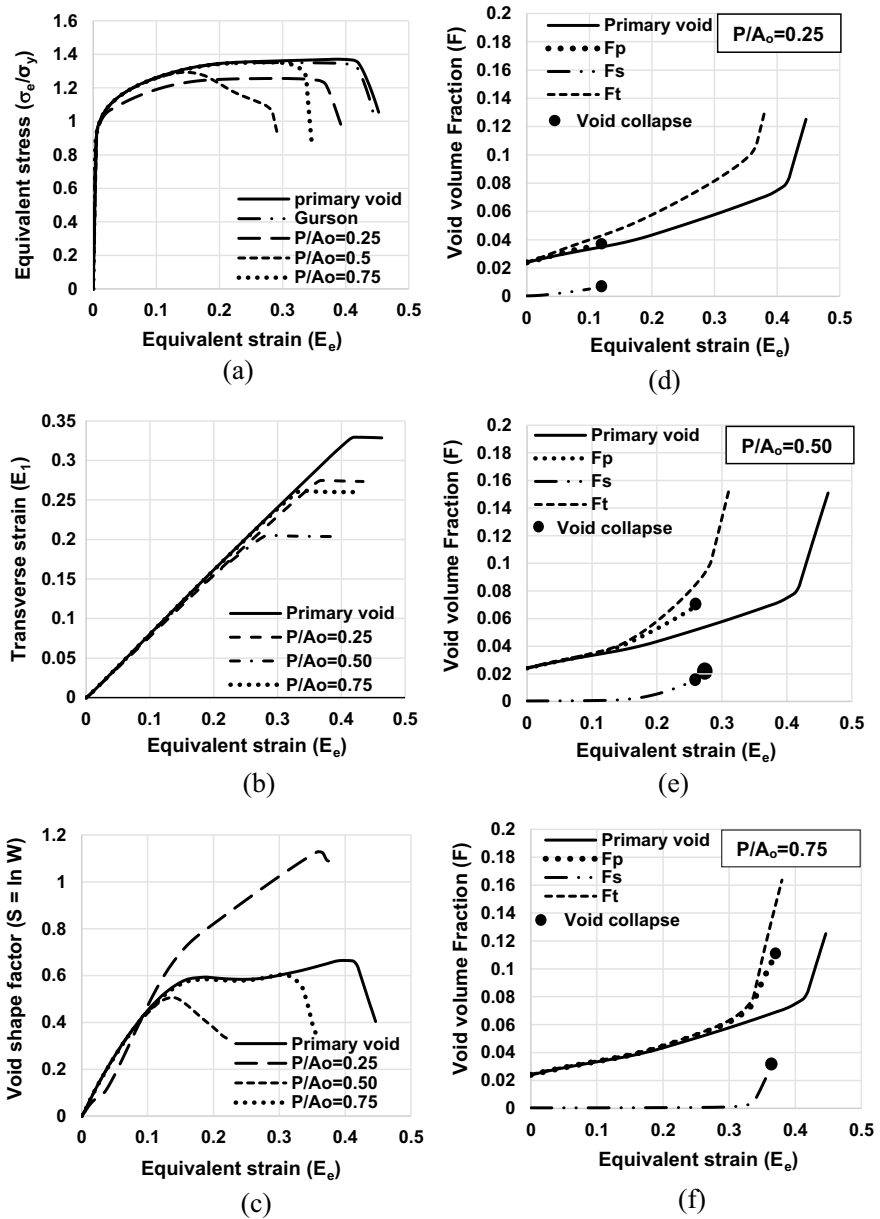
Fig. 4 Effect of secondary voids location on **a** equivalent stress Versus equivalent strain **b** Transverse strain versus equivalent strain **c** evolution of primary void shape. The evolution of void volume fraction for $P/A_o = 0.25$, 0.5 and 0.75 is shown in **d**, **e** and **f**, respectively. Notations F_p and F_s denote the void volume fraction of primary and secondary voids, respectively. The total void volume fraction is denoted as F_t

initial porosity. When secondary void is located at a large distance $P/A_o = 0.75$, the localization of plastic flow arising due to growth of the primary void accelerates the growth of the secondary void. As a result, the collapse between primary and secondary void is observed at a strain level that is higher than that required for localization of plastic flow.

The effect of secondary voids distribution on the evolution of primary void shape was also analyzed, see Fig. 4c. For $P/A_o = 0.25$, the presence of a secondary void and its early coalescence results in some changes in the shape of primary voids particularly in the initial stage of deformations. Subsequently, the primary void continues to evolve into a prolate shape till the localization of plastic flow starts. When $P/A_o = 0.5$, the strong interactions between the two-scale voids arrest the axial stretching of primary void and void flattening starts resulting in collapse between the primary and secondary void. For the case, where secondary voids are located at a large distance from the primary void $P/A_o = 0.75$, the shape of the latter, until the commencement of flow localization, remains almost the same as observed for the case where only primary voids exist.

The effect of secondary voids distribution, in the ligament between the two primary voids, on the two-scale voids interactions is shown pictorially in Fig. 5. The plots of equivalent plastic strain for the case where only primary voids exist and the other three cases where secondary voids are at different locations in the intervoid ligament are extracted at a fixed imposed strain ($E_2 = 0.2$).

3.3 Effect of Secondary Voids Orientation on Void Interactions and Plastic Flow Localization

We now examine the effect of secondary voids orientation with respect to the ligament between the two primary voids, see Fig. 1b, on the two-scale voids interaction and plastic flow localization. Since the boundary conditions imposed on the cell model exclude the possibility of bifurcation, internal necking is the only mode of void coalescence that can be simulated in our numerical studies. Nevertheless, some useful insights can still be gained by analyzing the effect of the spatial distribution of secondary voids on mesoscale plastic flow. In all the results presented in this subsection, the secondary voids are located at a fixed distance $P/A_o = 0.5$ and the orientation angle θ is varied. Numerical results of mesoscopic stress–strain response, the evolution of porosity and primary void shape is presented for $\theta = 0$, 15 and 30°, see Fig. 6. Results for the case $\theta = 0°$ have already been presented in the previous sub-Sect. 3.2 and are included here just for comparison's sake. As expected, the case $\theta = 0°$ leads to a maximum reduction in the mesoscopic ductility. As the angle θ increases, the effect of secondary voids on the mesoscopic stress–strain response and porosity evolution diminishes and for $\theta \geq 30°$ it becomes almost insignificant.

It is recognized that typically the secondary voids nucleate in the regions of strain concentration arising due to flow localization in the ligament between the two
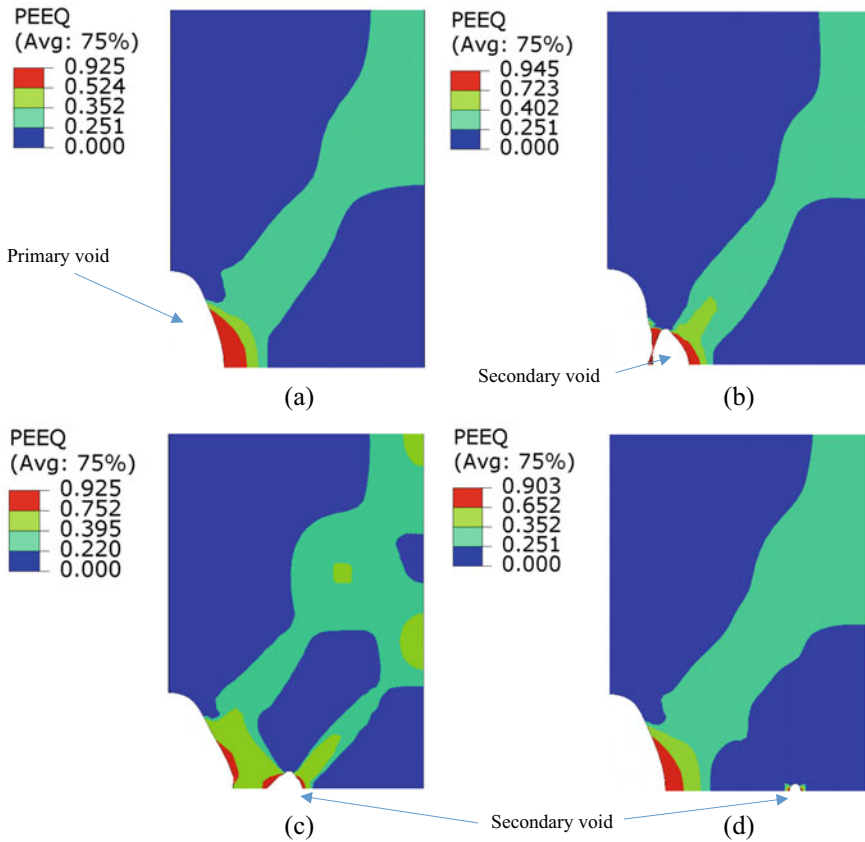
Fig. 5 Contours of equivalent plastic strain for the case where only primary voids exist is shown in (**a**). The distance of the secondary void from the neighbouring primary void P/A_o is 0.25, 0.5 and 0.75 in (**b**), (**c**) and (**d**), respectively. The contours are extracted at a fixed value of axial strain $E_2 = 0.2$

neighbouring primary voids. If due to local heterogeneity in the matrix or some other reason the secondary void has nucleated at an arbitrary location, then to what extent its growth may affect the macroscopic response is examined numerically.

The configuration of voids shown in Fig. 1, especially under the uniaxial loading condition, is favourable to internal necking as the mode of coalescence between the neighbouring primary voids. Initially, as the deformation increases, the tendency for shear band formation is observed. Since the kinematic constraint in our cell model analysis excludes the possibility of bifurcation, the developed stress fields around the secondary voids oriented at an angle of 15° and 30° are not strong enough to trigger the growth of voids. With further deformation, internal necking occurs between the ligament of primary voids. As a result, the secondary voids located at 0-degree
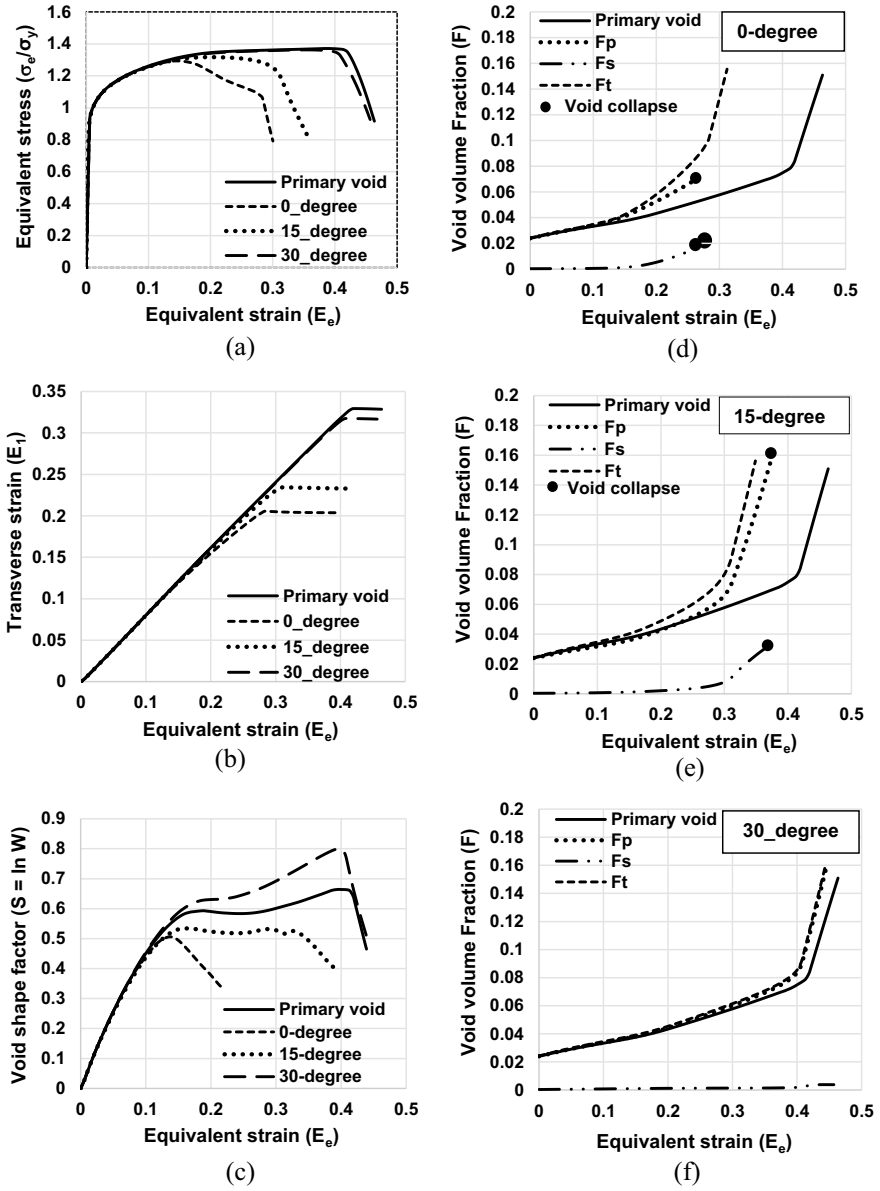
Fig. 6 Effect of orientation of secondary voids on (**a**) equivalent stress versus equivalent strain (**b**) Transverse strain versus equivalent strain (**c**) evolution of primary void shape. The evolution of void volume fraction for $P/A_o = 0.25$, 0.5 and 0.75 is shown in (**d**), (**e**) and (**f**), respectively. Notations F_p and F_s denote the void volume fraction of primary and secondary voids, respectively. The total void volume fraction is denoted as F_t

exhibits an accelerated growth, see Fig. 6d, resulting in a significant loss of stress carrying capacity and an earlier localization of plastic flow.

At $\theta = 0°$, the secondary void is lying in the relatively higher stress triaxiality regime and, therefore, exhibits a much faster lateral growth. In fact, a physical collapse (void impingement) between primary and secondary void occurs slightly before the mesoscopic flow localization. For $\theta = 15°$, the growth of secondary voids is comparatively slow, see Fig. 6e, and the mesoscopic flow localization occurs earlier before their physical collapse. For $\theta = 30°$, a collapse between primary and secondary voids is not observed. It is perhaps worth discussing the influence of secondary voids orientation on their shape evolution. In general, a high stress triaxiality promotes void growth whereas void shape changes and void rotations are more prominent at low stress triaxiality. The contours of equivalent plastic strain, shown in Fig. 7, clearly show this tendency. As the orientation angle θ increases, shear stress field around
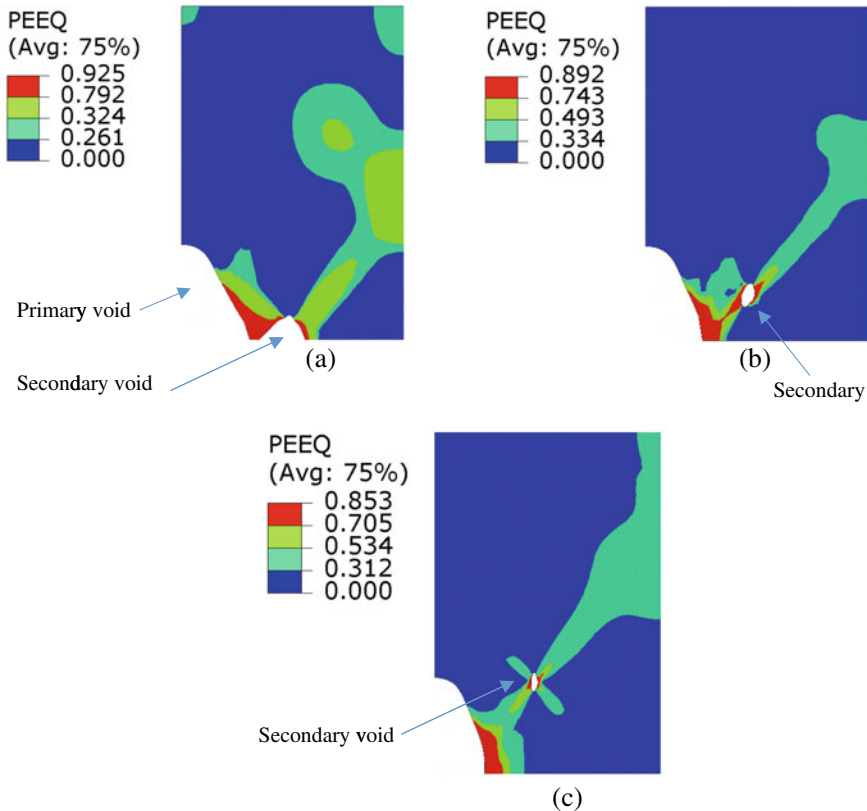

Fig. 7 Contours of equivalent plastic strain for three different orientations of secondary voids. The secondary void is at a fixed distance ($P/A_o = 0.5$) from the primary void. The orientation angle θ is 0, 15 and 30° in (**a**), (**b**) and (**c**), respectively. The contours are extracted at a fixed value of axial strain $E_2 = 0.25$

the secondary void becomes significant, thus, leading to noticeable changes in shape and orientation of secondary voids.

4 Conclusions

The numerical results reported in this study have led to the following conclusions:

1. Secondary voids even of small initial volume fraction ($fs_o/fp_o \approx 0.015$) may exhibit a significant influence on the evolution of porosity and, hence, on the mesoscopic ductility.
2. Depending upon the location of secondary voids in the intervoid ligament between the primary voids, a complex interaction between the two-scale voids sets in which results in a faster evolution of total porosity. In such cases, a physical collapse between the primary and secondary void is observed slightly before the onset of plastic flow localization. If the secondary voids are too near or too far from the primary voids, then it is the localization of plastic flow that accelerates the evolution of porosity.
3. For the mode of internal necking analyzed in this study, a secondary void lying in the intervoid ligament between the primary voids ($\theta = 0°$) leads to a maximum reduction in mesoscopic ductility.

References

1. Tipper CF (1949) The fracture of metals 39:133–137
2. Benzerga AA, Leblond JB (2010) Ductile fracture by void growth to coalescence. Adv Appl Mech 44:169–305. https://doi.org/10.1016/S0065-2156(10)44003-X
3. Benzerga AA, Leblond JB, Needleman A, Tvergaard V (2016) Ductile failure modeling. Int J Fract 201:29–80. https://doi.org/10.1007/s10704-016-0142-6
4. McClintock (1968) A criterion for ductile fracture by the growth of holes. J Appl Mech 35:363–373
5. Rice JR, Tracey DM (1969) On the ductile enlargement of voids in triaxial stress fields*. J Mech Phys Solids 17:201–217. https://doi.org/10.1016/0022-5096(69)90033-7
6. Gurson AL (1975) Plastic flow and fracture behavior of ductile materials incorporating void nucleation
7. Gurson AL (1977) Continuum theory of ductile rupture by void nucleation and growth : Part 1—Yield criteria and flow rules for porous ductile media. J Eng Mat Tech 2–15
8. Bao Y, Wierzbicki T (2004) On fracture locus in the equivalent strain and stress triaxiality space 46:81–98. https://doi.org/10.1016/j.ijmecsci.2004.02.006
9. Benzerga AA, Leblond JB, Needleman A, Tvergaard V (2016). Ductile failure modeling. https://doi.org/10.1007/s10704-016-0142-6
10. Morin L, Leblond JB, Tvergaard V (2016) Application of a model of plastic porous materials including void shape effects to the prediction of ductile failure under shear-dominated loadings. J Mech Phys Solids 94:148–166. https://doi.org/10.1016/j.jmps.2016.04.032
11. Koplik J, Needleman A (1988) Void growth and coalescence in porous. Int J Solids Struct 24:835–853. https://doi.org/10.0020-7683(88)90051-0

12. Rice JR (1976) The localization of plastic deformation. 14th international congress on theoretical applied mechanics. 207–220. https://doi.org/10.1.1.160.6740
13. Needleman A, Rice JR (1978) Limits to ductility set by plastic flow localization 44:262–270
14. Perrin G, Leblond JB (2000) Accelerated void growth in porous ductile solids containing two populations of cavities. Int J Plast 16:91–120. https://doi.org/10.1016/S0749-6419(99)00049-2
15. Brocks W, Sun DZ, Hönig A (1995) Verification of the transferability of micromechanical parameters by cell model calculations with visco-plastic materials. Int J Plast 11:971–989. https://doi.org/10.1016/S0749-6419(95)00039-9
16. Fabrègue D, Pardoen T (2008) A constitutive model for elastoplastic solids containing primary and secondary voids. J Mech Phys Solids 56:719–741. https://doi.org/10.1016/j.jmps.2007.07.008
17. Gao X, Kim J (2006) Modeling of ductile fracture: significance of void coalescence. Int J Solids Struct 43:6277–6293. https://doi.org/10.1016/j.ijsolstr.2005.08.008
18. Faleskog J, Shih CF (1996) Micromechanics of coalescence: Synergism between elasticity, plastic yielding and multi-size scale voids. J Phys IV JP. 6. https://doi.org/10.1051/jp4:1996609.
19. Tvergaard V (1996) Effect of void size difference on growth and cavitation instabilities. J Mech Phys Solids 44:1237–1253. https://doi.org/10.1016/0022-5096(96)00032-4
20. Tvergaard V (1998) Interaction of very small voids with larger voids. Int J Solids Struct 35:3989–4000
21. Wen J, Huang Y, Hwang KC, Liu C, Li M (2005) The modified Gurson model accounting for the void size effect. Int J Plast 21:381–395. https://doi.org/10.1016/j.ijplas.2004.01.004
22. Peerlings RHJ, Poh LH, Geers MGD (2012) An implicit gradient plasticity-damage theory for predicting size effects in hardening and softening. Eng Fract Mech 95:2–12. https://doi.org/10.1016/j.engfracmech.2011.12.016
23. Monchiet V, Bonnet G (2013) A Gurson-type model accounting for void size effects. Int J Solids Struct 50:320–327. https://doi.org/10.1016/j.ijsolstr.2012.09.005
24. Hütter G, Zybell L, Kuna M (2014) Size effects due to secondary voids during ductile crack propagation. Int J Solids Struct 51:839–847. https://doi.org/10.1016/j.ijsolstr.2013.11.012
25. Zybell L, Hütter G, Linse T, Mühlich U, Kuna M (2014) Size effects in ductile failure of porous materials containing two populations of voids. Eur J Mech A/Solids 45:8–19. https://doi.org/10.1016/j.euromechsol.2013.11.006
26. Khan IA, Bhasin V (2017) On the role of secondary voids and their distribution in the mechanism of void growth and coalescence in porous plastic solids. Int J Solids Struct 108:203–215. https://doi.org/10.1016/j.ijsolstr.2016.12.016
27. Tvergaard V (2009) Behaviour of voids in a shear field. Int J Fract 158:41–49. https://doi.org/10.1007/s10704-009-9364-1

Al/GFRP Interface Strength Under Quasi-Static and Dynamic Loading Conditions

S. Sooriyan, U. Madhusudhanan, and R. Kitey

Abstract   Metal/composite adhesively bonded joints are quite common in aerospace applications since several aircraft components are smaller in size and/or have complex shapes which make it challenging to use riveting, bolting, or welding techniques. Apparently, the interfacial properties in such cases govern the reliability of components. In this investigation, the experiments are conducted to assess the influence of surface roughness and fiber orientation on aluminum/GFRP (glass fiber reinforced polymer) interface strength. Pull test fixtures are designed to conduct the experiments under quasi-static loading condition. To prepare the test samples first the circular surface of Al6063-T6 aluminum alloy cylinders is polished and a surface roughness, ranging from 35 to 175 nm, is developed. The prepared surface is bonded to a 3 mm thick GFRP laminate. Two different sets of laminates, unidirectional (UD) and bidirectional (BD), of the same volume fraction, are considered in the study. The results suggest that the Al/GFRP interface strength increases with decreasing interface roughness. The results also indicate that the bidirectional laminates provide better adhesion when compared to the unidirectional case. The adhesion strength between Al and composite is also measured under ultra-high strain rate loading conditions by employing laser spallation technique. Test samples are prepared by bonding aluminum and GFRP plates of thickness, 1 mm and 0.4 mm, respectively. Failure is instigated at the interface by using high-amplitude short-duration laser-induced stress waves. The failure initiation is identified through optical microscopy. The associated stress wave characteristics, obtained from calibration experiments, are used in computational wave propagation analysis to assess the interface stress. Similar to the quasi-static loading case, the dynamic adhesion strength between aluminum and composite is observed to increase with decreasing interface roughness. The bidirectional laminates again exhibit higher adhesion strength when compared to the unidirectional ones.

S. Sooriyan
TCS Research (TRDDC), Pune, India

U. Madhusudhanan (✉) · R. Kitey
Department of Aerospace Engineering, IIT Kanpur, Kanpur, India
e-mail: madhusud@iitk.ac.in

1 Introduction

Metal/composite adhesively bonded joints are quite common in aerospace applications since several aircraft components are smaller in size and/or have complex shapes which make it challenging to use riveting, bolting, or welding techniques. Apparently, the interfacial properties in such cases govern the reliability of components. The performance of dissimilar material joints depends upon various parameters such as constituent material properties, interface geometry and profile, surface processing. Often the constituent surfaces are mechanically and/or chemically pretreated to improve the adhesion strength. While designing bonded structures or to improve the strength of bonded joints, it is imperative to quantify the influence of various parameters affecting the adhesion. In this study, the effect of bonded layer roughness and fiber orientation on aluminum/glass fiber reinforced polymer (GFRP) interface strength under quasi-static and dynamic loading conditions is evaluated.

Uehara and Sakurai [1] measured the bonding strength of adhesives (epoxy resin, cyanoacrylate, vinyl chloride, synthetic rubber, and cellulose type) by systematically varying the surface roughness of the mating surfaces. They suggested that an optimum surface roughness exists to achieve the maximum normal strength of adhesion. Critchow and Brewis [2] employed various surface treatments on the titanium substrate and studied the influence of adherend surface roughness on the durability of adhesive bonds. They concluded that the variations in surface macro-roughness as observed by scanning electron microscopy and measured by profilometry had a small but consistent effect on the durability of the adhesive joints. Zhang et al. [3] experimentally investigated the influence of surface morphology on the fracture behavior of Al/epoxy interface. They used steel wedge to peel off the double cantilever beam specimens. They established a correlation between the surface roughness of aluminum substrate and the fracture resistance of the bimaterial interface. Dayss et al. [4] used mechanical grinding and low-pressure plasma treatment for modifying the surface properties of polymer adherend and evaluated the bonding strength between polypropylene and copper by employing pull-off test. They suggested that mechanical roughening had positive effect on the bimaterial adhesion strength.

Wang et al. [5] conducted parametric study by employing laser spallation technique and reported the spallation strength of Al films as a function of substrate thickness, film thickness, and incident laser energy. They suggested that the maximum stress in the substrate and at the substrate/film interface increased with increasing laser fluence. Moreover, the maximum interface stress was observed to increase with increasing film thickness but decrease with increasing substrate thickness due to geometric attenuation. Rahul and Kitey [6] applied hybrid experimental/numerical approach to assess the dynamic interface strength of epoxy film, deposited on fused

quartz substrate. Interfacial failure was initiated by subjecting substrate/film interface to laser-induced high-amplitude short-duration stress wave. They used experimentally obtained substrate stress histories for performing one-dimensional computational wave propagation analysis. They suggested that naturally bonded epoxy provide better adhesion when compared to the case when a release agent was introduced at the interface. Singh and Kitey [7] investigated the effect of interface profile on aluminum/epoxy adhesion strength under extreme dynamic loading condition. Test samples were prepared by depositing an epoxy film onto polished aluminum substrates of roughness less than 200 nm. They instigated failure at the interface by using laser-induced stress waves and evaluated the adhesion strength of the film by employing hybrid experimental/numerical approach. They observed that the adhesion strength increased with decreasing interface roughness.

2 Materials and Methods

For preparing metal/composite bonded specimens, Al6063-T6 aluminum alloy and glass fiber reinforced polymer (GFRP) composites are used. The GFRP laminates are fabricated by using unidirectional (UD) and bidirectional (BD) fiber cloth of areal density 450 GSM. An epoxy system, prepared by mixing diglycidyl ether of bisphenol-A (DGEBA) and Methyl Tetra Hydrophthalic Anhydride (MTHPA) in 10:8 ratio by weight, is used as the matrix material. The fiber clothes smeared with the matrix are stacked together by hand layup technique, and cured in a temperature and pressure controlled hot press. For rapid curing, a small amount of 2,4,5-tris (dimethylamino)methyl -Phenol (DMP-30) accelerator is used. For measuring fiber volume fractions, representative 15 mm × 15 mm square samples are cut from a few locations and their cross sections are polished. The polished surface images are captured and the fiber volume fractions are calculated from the proportion of visible fibers and/or fiber cross sections in the micrographs. For unidirectional and bidirectional laminate cases, the fiber volume fractions are measured to be 54.3% and 58.4%, respectively.

The test specimens to conduct dynamic experiments are prepared by bonding a single ply of GFRP with the aluminum substrate. First the Al surface is prepared by polishing a rectangular plate of dimension 25 mm × 25 mm × 0.75 mm. The substrate with three different roughness values, 35 nm, 57 nm, and 175 nm, is considered in this investigation (see, Fig. 1a). The substrate is then placed on the top of an epoxy smeared GFRP layer. The assembly is kept in a hot press at 1 bar pressure. The temperature cycles, 85 °C for 2 h followed by 140 °C for 12 h, are used to cure the GFRP in the Al/GFRP assembly. Prior to conducting laser spallation experiments, the back surface of the aluminum is spin-coated by using a 10 μm thick sodium silicate solution. The sample configuration is shown in Fig. 1b. As shown in Fig. 1c, the specimen to conduct pull test under quasi-static loading is prepared by bonding a 30 mm × 30 mm GFRP plate to an 11 mm diameter Al cylinder. The cross section
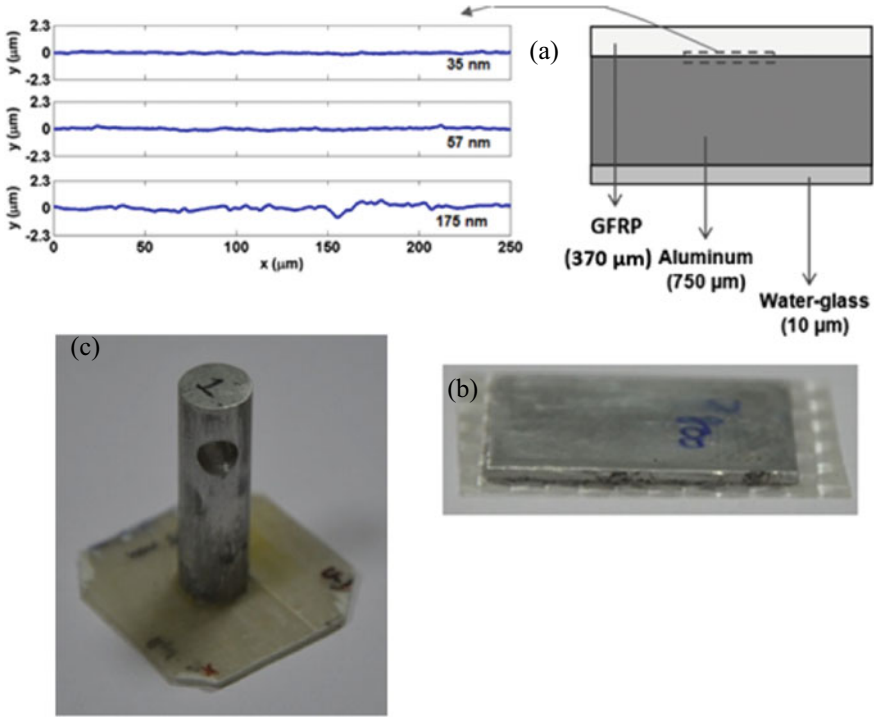
Fig. 1 **a** The polished Al surface profiles, **b** specimen configuration to conduct laser spallation experiments, **c** specimen to conduct pull test under quasi-static loading condition

of the cylinder was polished prior to bonding. The GFRP laminates were prepared by using 8 layers.

For conducting experimental and computational analyses, the physical and acoustic properties of constituent layers are measured in their bulk form. The density (ρ) of UD and BD GFRP laminates and Al are calculated by weighing 10 mm × 10 mm × 10 mm cubic samples. Ultrasonic thickness gauge OLYMPUS—Parametrics 35DL, in combination with 10 MHz longitudinal (M112-RM) and 5 MHz shear (V154-RM) wave transducers, respectively, are employed to measure the wave speeds. The density and the longitudinal (Cd) and shear (Cs) wave speeds of constituent layers are presented in Table 1. The dynamic elastic modulus (Ed) and

Table 1 The measured mechanical (dynamic) and acoustic properties of Al and GFRP

Material	Density [Kg/m^3]	C_d [m/s]	C_s [m/s]	E_d [GPa]	ϑ_d
Aluminum	2700	6420	3100	69.95	0.348
UD GFRP	1550	3593	1966	15.42	0.286
BD GFRP	1635	3250	1947	15.13	0.22

Poisson's ratio (νd), determined by applying the following plane strain equations, are also included in the table.

$$C_d = \sqrt{\frac{E_d(1 - \vartheta_d)}{\rho(1 + \vartheta_d)(1 - 2\vartheta_d)}} \tag{1}$$

$$C_s = \sqrt{\frac{E_d}{2\rho(1 + \vartheta_d)}} \tag{2}$$

3 Experimental Details

Pullout tests under quasi-static loading condition are conducted by using INSTRON 3345 uniaxial tensile testing machine. The GFRP plates are fixed at the bottom fixture while the bonded cylinder is pulled from the top at a crosshead speed of 0.5 mm/min. The load corresponds to the interfacial failure, and the area of the cross section, at which the failure occurs, is used to calculate the (quasi-static) adhesion strength.

For evaluating Al/GFRP adhesion strength under dynamic loading conditions, the test samples are loaded at a strain rate of 107/s by employing laser spallation technique in combination with Michelson interferometry. A schematic representation of the experimental setup is shown in Fig. 2. The substrate and the film are marked by S and F, respectively, in the figure. A 5 ns Gaussian pulse of variable energy content (0–300 mJ) from Q-switched Nd: YAG laser ($\lambda = 1064$ nm) is focused at the back surface of the substrate. The instantaneous absorption of irradiated YAG energy by the constrained substrate results in the formation and expansion of the plasma, which develops a high-amplitude short-duration compressive pulse. The stress pulse
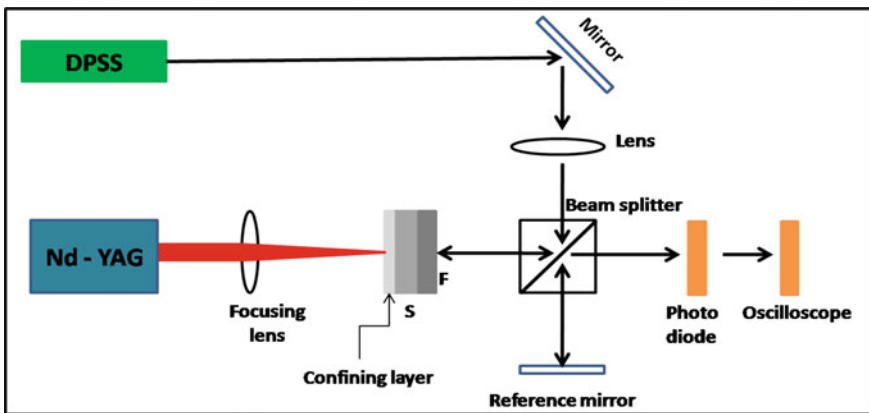

Fig. 2 Laser spallation technique with Michelson interferometric setup

propagates through the thickness and reflects back as a tensile wave upon reaching the free surface of the film. The reflected pulse loads the substrate/film interface in tension and for sufficiently high interface stress, the spallation in the film is observed.

Out-of-plane displacement is measured at the free surface of film by employing Michelson interferometer (see, Fig. 2). The probe beam is aligned with the incident Nd:YAG laser, and the variation of fringe intensity $I(t)$ is recorded by using a photo-diode EOT-ET4000 and Tektronix 7254C, 2.5 GHz ultra-high frequency oscilloscope. The fringe order $N(t)$ is calculated from the intensity data by

$$I(t) = \frac{\mathrm{I}max + \mathrm{I}min}{2} + \frac{\mathrm{I}max - \mathrm{I}min}{2} \sin 2\pi N(t) \tag{3}$$

The I_{max} and I_{min} are the maximum and minimum intensities of the interference fringes, respectively. The out-of-plane displacement history $u(t)$ is calculated by applying the Doppler shift [8],

$$u(t) = \frac{\lambda}{2} N(t) \tag{4}$$

In the above equation, λ represents the wavelength of the probe beam (514 nm). The substrate stress history $\sigma_{sub}(t)$ is then evaluated by

$$\sigma_{sub}(t) = -\frac{1}{2}(\rho c_d)_{sub} \frac{\partial u}{\partial t} \tag{5}$$

where ρ and C_d represent the density and the longitudinal wave speed of the substrate.

Due to non-reflective surface of GFRP, in situ interferometric measurements cannot be performed, therefore, experimental/numerical approach is adopted to assess Al/GFRP interface strength. First, the laser spallation experiments are performed on a calibration sample, which is prepared with the substrate with no film on the top. A range of laser fluences is impinged and corresponding substrate stress histories are evaluated by performing in situ interferometric measurements. Next, the Al/GFRP specimen is computationally modeled and the elastic properties tabulated in Table 1 are assigned to the Al and GFRP layers. A plane strain four noded element CPE4R is used to mesh the model geometry. Based on a convergence study, the smallest size of the element is used as 0.3 μm. Nd:YAG laser beam is 1 mm, which is larger than the film thickness, therefore, planar wave propagation is considered in the analysis. The substrate stress history ($\sigma_{sub}(t)$) is applied at the back surface of the aluminum substrate and wave propagation analysis is performed. The maximum stress developed at the Al/GFRP interface is noted for each of the considered laser fluences. Once the laser fluence versus interface stress calibration chart is prepared, the laser spallation experiments are conducted on actual test samples, and critical laser fluences associated with the failure initiations are noted. The interface strength is then inferred from the calibration chart.

4 Results and Discussion

4.1 Adhesion Strength Under Dynamic Loading Condition

The representative interfacial failure micrographs in the cases of UD and BD GFRP specimens are illustrated in Fig. 3a, b, respectively. The associated laser fluences are labeled in the micrograph. It is evident from the images that the failure region is comparatively smaller in the case of Al/BD GFRP, even if the incident laser energy was much larger.

The values of laser fluence at failure initiation, tabulated in Table 2, correspond to the UD and BD laminates bonded to the Al substrate with three different roughness profiles. The table suggests that for a given GFRP (UD or BD) laminate, the critical laser fluence increases with decreasing interface roughness. The data also show that higher laser energy is required to initiate failure et al./BD GFRP interface when compared to the UD GFRP case. Representative interferometric fringes, out-of-plane
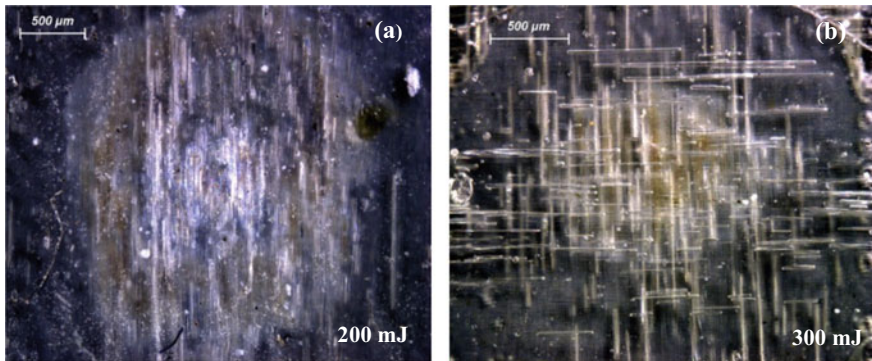
Fig. 3 Laser-induced interfacial failure in **a** UD GFRP and **b** BD GFRP laminates

Table 2 Aluminum/epoxy interface characteristics and the associated dynamic and quasi-static interface strength

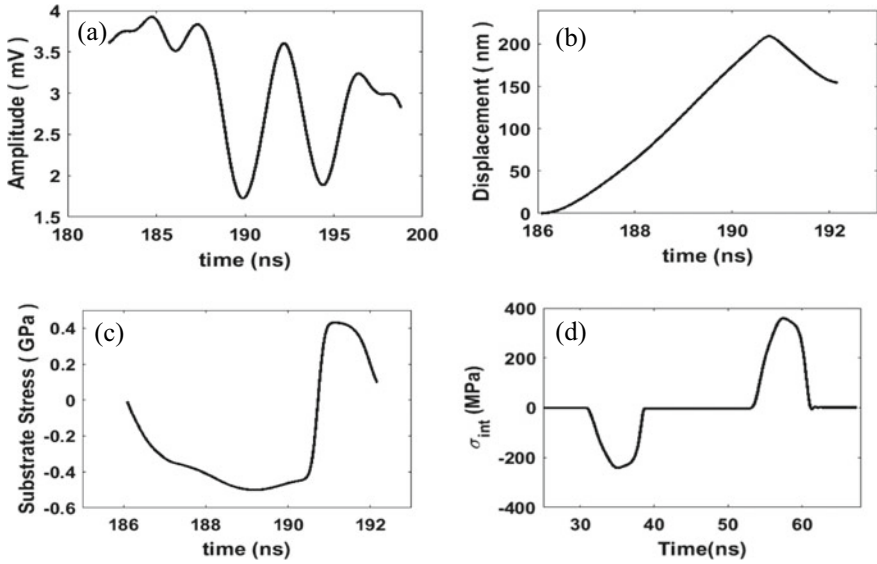| Polished substrate roughness R_q (nm)	Fiber orientation of the lamina (UD / BD)	Laser fluence at failure initiation (mJ/mm^2)	Substrate stress at failure initiation σ_{sub} (MPa)	Al/GFRP interface strength σ_{int} (MPa)	
				Dynamic	Quasi-Static
175 ± 24	UD	107	435	318	3.02
	BD	151	461	330	4.17
57 ± 6	UD	151	461	336	3.45
	BD	166	479	342	5.02
35 ± 5	UD	188	496	355	4.32
	BD	210	513	365	5.26

Fig. 4 **a** Representative fringe intensity obtained from interferometric measurements performed on (aluminum) calibration sample at 188 mJ/mm² laser fluence. **b** and **c** present the corresponding out-of-plane free surface displacement and substrate stress history, respectively. **d** The associated interface stress history obtained from computational wave propagation analysis

displacement and substrate stress history correspond the 188 mJ/mm² laser fluence, are plotted in Fig. 4a–c. These data are obtained from the calibration experiments. The substrate stress histories evaluated by using Eq. (5) show a characteristic linear ramp until a peak compressive stress is attained (see, Fig. 4c). The associated interface stress histories are illustrated in Fig. 4d. The tabulated data and the figure suggest that for a given GFRP (UD or BD) laminate Al/GFRP interface strength increases with decreasing interface roughness. The data also show that the adhesion strength of BD GFRP with Al is consistently higher when compared to the UD GFRP case.

4.2 Adhesion Strength Under Quasi-Static Loading Condition

Following Al/GFRP interfacial failure, the aluminum surface is observed under microscope. Micrographs illustrated in Fig. 5a, b correspond to the UD and BD composites, bonded to the Al cylinder with 35 nm cross section roughness. Figure 5a indicates that the failure in UD case has mostly remained at the interface. The micrograph shows that the failure marks have followed the path along the unidirectional fibers. The figure also shows that the interfacial cracks get into the laminate material at a few locations, indicating cohesive failure in GFRP. The failure image in Fig. 5b
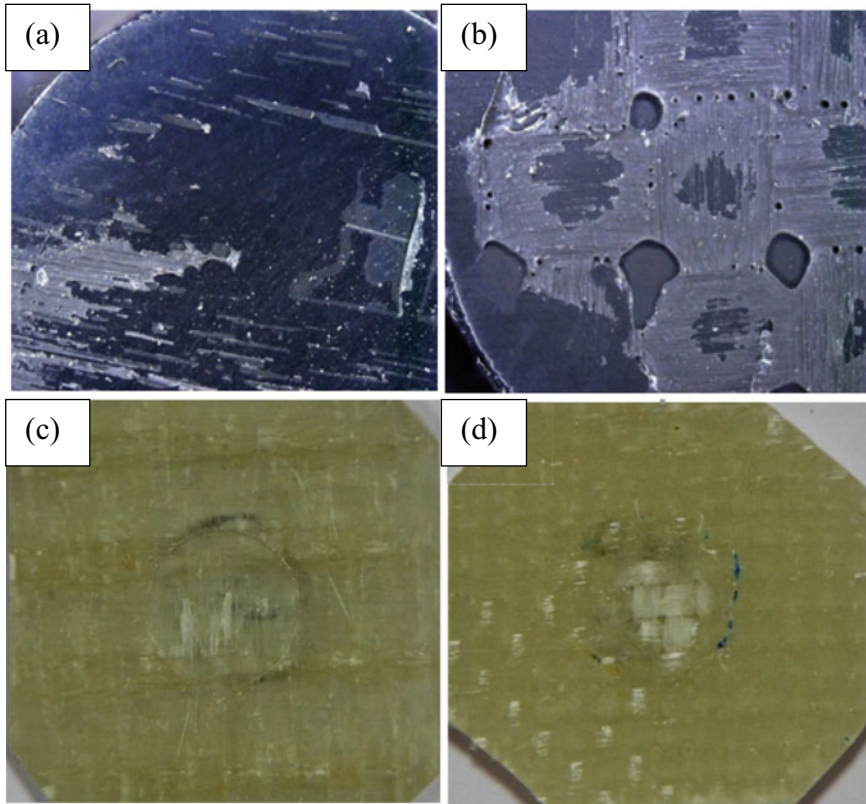
Fig. 5 Failed interface after conducting pull tests in Al/GFRP specimens. Al **a** and GFRP **c** surfaces from Al/UD GFRP specimen. Al **b** and GFRP **d** surfaces from Al/BD GFRP specimen

suggests that the failure at the Al/BD GFRP interface has initiated from the circular edge. It appears that the interface crack propagating inside towards the center of the sample got diverted into the GFRP, causing a cohesive failure. Away from the edge a nearly uniform epoxy layer with intermittent interfacial failure pockets can be seen on the Al surface. Post-failure GFRP surfaces in UD and BD bonded joint cases are shown in Fig. 5c, d, respectively. The failure images complement the trends observed on the opposite Al surfaces. The figures show that the top epoxy layer from near the bonded interface edge has failed and fibers are visible in the case of UD joint, whereas in the case of Al/BD GFRP, the middle of the circular interface region shows that the delamination has gone into the GFRP laminate. The load vs. crosshead displacement data (not included here for brevity) suggest that the interfacial failure was not instantaneous. Even after failure initiation, the laminate interface could still take up the load during gradual propagation of delamination. The strength of Al/GFRP interfaces is tabulated in Table 2 and plotted in Fig. 6. The data suggest that the adhesion strength between Al and GFRP materials increases with decreasing
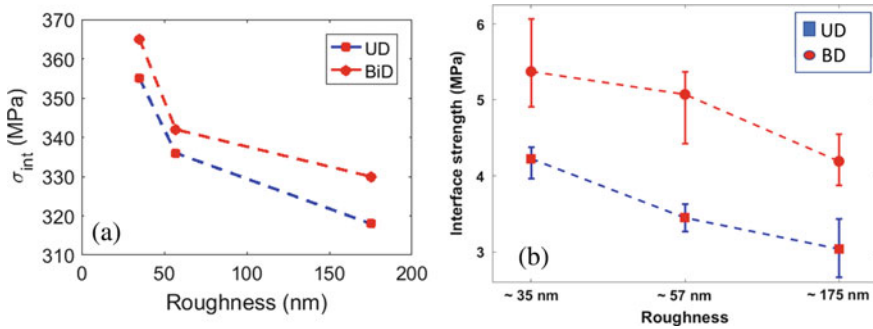
Fig. 6 Effect of interface roughness and fiber orientation on Al/GFRP interface strength **a** dynamic case & **b** Quasi-static case

interface roughness. Also, the strengths are consistently higher when BD layers are used in Al/GFRP assembly.

5 Concluding Remarks

Laser spallation technique is extended to evaluate metal/composite interface strength under extreme dynamic loading conditions. While the adhesion between Al substrate and GFRP film layer increases with decreasing interface roughness, the interface strength was consistently higher in the cases when the BD fiber cloth was used to prepare the GFRP laminates. To measure the adhesion strength under quasi-static loading condition, a pull test method is evolved with in-house designed test fixtures. The measured Al/GFRP interface strength values complement the observations made under dynamic loading conditions. Nearly 2 order of difference was noted between the adhesion strength values under quasi-static and dynamic loading conditions.

References

1. Uehara K, Sakurai M (2002) Bonding strength of adhesives and surface roughness of joined parts. J Mater Process Technol 127:178–181
2. Critchlow GW, Brewis DM (1995) Review of surface pretreatments for titanium alloys. Int J Adhes Adhesiv 15(3):161–172
3. Sulin Z, Rahul P, Jimmy K (2003) Hsia.: Influence of surface morphology on the adhesion strength of epoxy–aluminium interfaces. J Adhes Sci Technol 17(12):1685–1711

4. Dayss E, Leps G, Meinhardt J (1999) Surface modification for improved adhesion of a polymer-metal compound. Surf Coat 116–119:986–990
5. Wang J, Richard L, Weaver, Nancy R, Sottos (2002) A parametric study of laser induced thin film spallation. Exp Mech 42(1):74–83
6. Rahul R, Kitey R (2015) Measuring thin film Interface strength by LASER induced Stress waves. J Aerosp Sci Technol 67(2B), 335–340
7. Sarthak S Singh, R Kitey (2017) Effect of interface profile and incident wave characteristics on aluminum/epoxy dynamic adhesion strength. Int J Adhes Adhesiv 8–17
8. Barker LM (1972) Laser interferometry in shock-wave research. Exp Mech 12(5):209–215

Tensile Properties and Statistical Analysis of Freestanding YSZ Thin Films with and Without Stress Concentrations

Supriya Patibanda, Ralph Abrahams, and Krishna N. Jonnalagadda

Abstract Yttria-stabilized zirconia (YSZ) is used as a top coat in the thermal barrier coating system on superalloy components of aircraft engines, for its low thermal conductivity and superior thermal insulation properties. To avoid premature failure due to excessive operating temperatures, turbine blades and some engine components are provided with holes for cooling purposes. Therefore, in this study, the effect of stress concentrations on the tensile properties of freestanding YSZ thin films of ~300 μm was studied using samples with an inherent circular hole of Ø1 mm at the centre of the tensile sample, devoid of any machining. The effect of the presence of a circular hole on the tensile strength was studied and compared to that of continuous YSZ films using a custom-built uniaxial microtensile setup in conjunction with digital image correlation. A drop in fracture strength from 16 ± 4 MPa in continuous samples to ~11 ± 3 MPa in samples with a circular hole was observed. The cracks initiated at the circumference of the hole and perpendicular to the loading direction. Weibull statistical analysis was performed on tensile strength of continuous and hole containing samples. It was observed that the three-parameter method is more accurate for YSZ films than for two-parameter analysis. The properties reported in this current study could contribute to the design database for modelling the mechanical behaviour of YSZ.

Keywords Freestanding yttria-stabilized zirconia · Tensile properties · Digital image correlation · Weibull statistical analysis

S. Patibanda (✉)
Department of Mechanical Engineering, IITB-Monash Research Academy, Mumbai, India

R. Abrahams
Department of Mechanical and Aerospace Engineering, Monash University, Clayton, VIC, Australia

K. N. Jonnalagadda
Department of Mechanical Engineering, Indian Institute of Technology Bombay, Mumbai, India

1 Introduction

The outstanding properties of ceramic materials, such as high load-bearing capacity at high temperatures, fatigue and thermal shock resistance, low thermal conductivity, etc., enable them to be used as protection for gas turbine components. To avoid premature failure due to excessive operating temperatures, turbine blades and some engine components are provided with holes for passing a portion of air through them. A few holes are drilled on the surface of blades as outlets to the inflow of air. The diameter and spacing between these holes throughout the blade are carefully worked out by the designers. As TBCs are coated onto these blades, it is important to understand the effect of these holes on the fracture behaviour of TBC. Therefore, fracture properties of YSZ with holes need to be investigated. To address the basic problem of data scatter in fracture strength in these materials, designers have proposed a probabilistic approach to the design of ceramic materials based on Weibull's weakest link theory [1]. As the microstructural defects play a major role in determining the strength in these materials, fracture in these materials is often expressed statistically.

It is also observed that the film cooling hole could be one of the crucial factors for TBC failure as a huge local stress concentration is developed around the hole [2]. Hence, a better understanding of the failure stress with a hole inside the coating is essential to estimate the failure strength of TBCs. In this context, thermomechanical fatigue damage evolution at the circular hole was investigated by Tanaka et al. [3] and observed surface cracks near the hole. The residual stress distribution in the TGO layer around the hole was studied by Peng et al. [4] and reported the development of mode I and mode II edge cracks. Jiang et al. [2] have studied the stress and failure around the hole in TBCs under thermal cycling and observed surface and interfacial cracks in the top coat and top coat/bond coat interface, respectively. As the present work involves experimental investigation of fracture properties of YSZ, keeping in view the literature reported above, the effect of stress concentration developed due to a circular hole on fracture strength of YSZ has been measured via uniaxial tensile tests. Testing of YSZ coatings with circular holes also aids in determining whether the most detrimental flaws reside on a particular specimen surface, edge, or uniformly distributed in the entire volume of the component.

In general, the critical parameters for predicting the fracture behaviour are the specific component dimensions, characteristic strength, Weibull modulus, and threshold strength [5–7]. Often, failure of large-scale ceramic specimens is described with two-parameter Weibull statistics comprising characteristic strength and Weibull modulus [6]. The introduction of threshold stress appears to be especially reasonable for thin ceramic components, where the maximum defect size is limited by the specimen dimensions. Three-parameter (3-P) Weibull distribution not only models the actual distribution of strength but also allows us to predict and assess the strength of the weakest specimen of the entire population. The threshold value can be used to determine the minimum value of properties of any material. It also helps in using the obtained results from experiments for the design of structural elements, where the stress distribution is much more complicated. A two-parameter (2-P) distribution is a

particular case of a 3-P Weibull distribution, which implicitly defines zero-threshold stress for fracture. Consequently, stresses vanishingly small compared to the fracture stress yield a non-zero (although small) probability for fracture. In general, in quasi-brittle materials, threshold stress is greater than zero, so it is advisable in most cases to use the 3-P Weibull distribution [6]. Most of the research is done using two-parameter Weibull analysis and very few reports on YSZ are mentioned on three-parameter distribution. Hence, the present study is aimed at estimating the fracture strength of YSZ with and without a circular hole and fitting both two- and three-parameter Weibull distribution to the data. The one with the low error was chosen to be the best fit for the data.

2 Experimental Details

To obtain the fracture strength of YSZ with circular holes, stainless steel substrates with a diameter of 4 mm width and a hole of Ø1 mm were machined. After coating YSZ onto the templates and obtaining freestanding YSZ, the templates were immersed in an HCl solution. The schematic of sample design and surface of the sample with hole after the release is shown in Fig. 1. The freestanding YSZ samples with holes are loaded in a custom-built uni-axial tensile setup and displaced with a velocity of 1 μm s^{-1}. The setup was built in such a way that the samples can be mounted horizontally onto the grips. This kind of setup aids in imaging the sample under any optical microscope. The setup majorly comprises a load cell, a linear actuator, and specimen gripping fixtures. The entire unit was placed under an optical lens (Qioptiq®) of magnification 2.4× to capture images with a resolution of 2048 × 1536 pixels using a PointGrey® monochrome CMOS camera. To obtain the full-field deformation of the sample through DIC, a random speckle pattern is necessary. Carbon powder particles (~12 μm) were gently spread onto the YSZ surface with a paintbrush yielded the best pattern. More details of the experimental setup and the
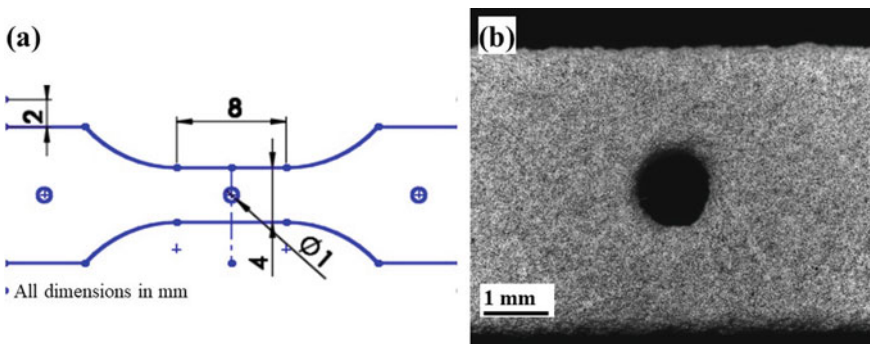

Fig. 1 **a** Schematic of the sample indicating the location of the hole and other dimensions, and **b** Optical micrograph of the hole in YSZ freestanding film

speckle pattern for DIC are described in [8]. To obtain the statistical distribution, uniaxial tensile tests were done on 11 ~300 μm freestanding YSZ films.

In order to exemplify the failure characterization potential of the two (2-P) and three-parameter (3-P) Weibull relationships, fracture test results of thin YSZ specimens with and without a circular hole are considered in the present study. The fracture strength values of the material without the hole are considered from the tensile strength data of YSZ mentioned in [8]. In this study, the maximum likelihood method (MLE) was used to estimate the Weibull parameters. While using MLE to estimate the parameters of the distribution model, the likelihood value can be used to assess the fit of the distribution. The goodness of fit of the distribution is checked for both two-parameter and three-parameter analyses. The distribution which has the higher likelihood value displays better goodness of fit. From this method, the Weibull parameters were estimated and the distribution which gives a better fit out of 2-P and 3-P is verified.

3   Results and Discussion

3.1   Effect of Stress Concentration (Circular Hole) on Fracture Strength

The freestanding YSZ samples with holes as shown in Fig. 2a were loaded in the uniaxial tensile setup described in [8] and a velocity of 1 μm/s was applied to the specimen for deformation. The load curves were as shown in Fig. 2b. The top view of the fractured sample showing crack propagation is shown in Fig. 2c. All the samples indicated that the failure has initiated from the top edge of the hole indicating that the flaws are distributed around that vicinity. The strain contour of the image just before the fracture indicates the increase in strain around the top and bottom points of the hole as shown in Fig. 2d. The fracture strength taken by the samples without hole [8] was ~16 ± 4 MPa (average of 20 samples), whereas the fracture strength of YSZ with holes is ~11 ± 3 MPa (average of 11 samples). It is obvious that the introduction of the hole in the specimen led to a decrease in fracture strength. The strength values of both the samples with and without a hole are further used for Weibull 2-P and 3-P statistical analysis.

3.2   Calculation of Weibull Statistical Parameters

Weibull two-parameter and three-parameter studies were done on the obtained strength values from samples with holes. Two-parameter and three-parameter Weibull distribution can be mathematically written as [6]
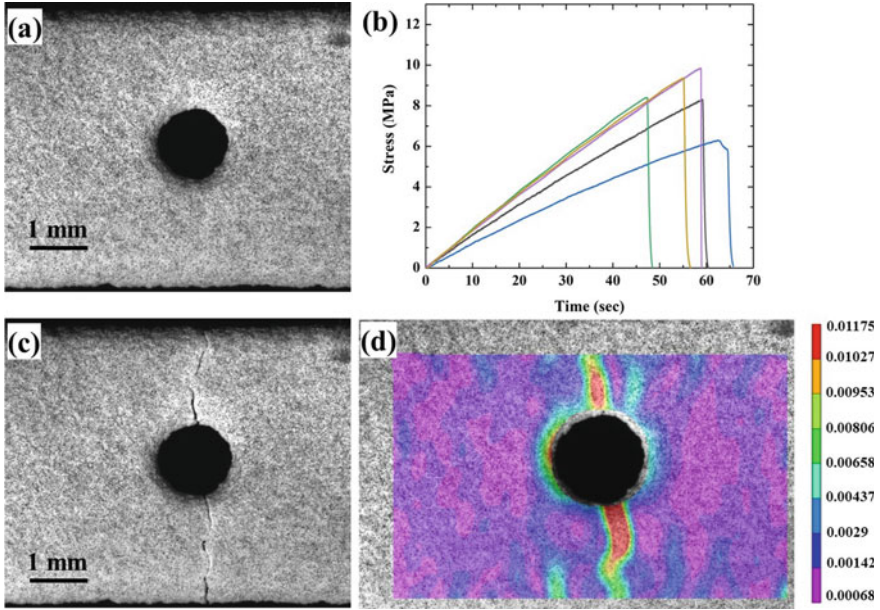
Fig. 2 **a** Optical micrograph of YSZ with a circular hole, **b** Stress vs time graphs of different samples consisting of a hole, **c** optical image showing crack postfracture from the top view, and **d** strain contour map along x-direction (ε_{xx}) near the hole, just before the fracture

$$P(\sigma) = 1 - \exp\left[-\left(\frac{\sigma - \sigma_u}{\sigma_0}\right)^3\right] \qquad (2.1)$$

where P is the failure probability of specimens subjected to stress σ; σ_o is a normalization factor known as the characteristic fracture strength or scale parameter, σ_u the threshold stress or location parameter, below which no failure will occur, and m is the Weibull modulus or shape parameter of the distribution, being a measure of strength diversity. The maximum likelihood method (MLE) was used to estimate the Weibull parameters. When the two-parameter Weibull analysis is done, m was obtained to be 7.4 and the characteristic strength to be 12.5 MPa. The same data when analyzed with three-parameter analysis, m was obtained to be 3.32. The threshold strength (σ_u) was obtained as 5.8 MPa and the characteristic strength to be 6.6 MPa. As reported in [6], the three-parameter distribution leads to a lower Weibull modulus if fitted to the same set of experimental data. The Weibull plots of both two-parameter and three-parameter distributions for samples with holes are plotted as shown in Fig. 3(a and b), respectively. The threshold strength (σ_u) was obtained as 10.3 MPa and the Weibull modulus was calculated to be 3.5; the characteristic strength was found to be 5.4 MPa. However, the Weibull modulus from two-parameter distribution was 5.5 and the characteristic strength was obtained to be 15.9 MPa. The Weibull fits for two
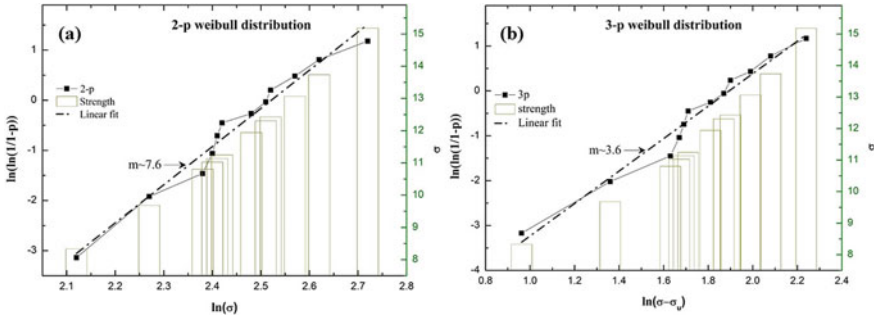
Fig. 3 Weibull distribution plots of **a** two-parameter and **b** three-parameter distribution of samples with holes
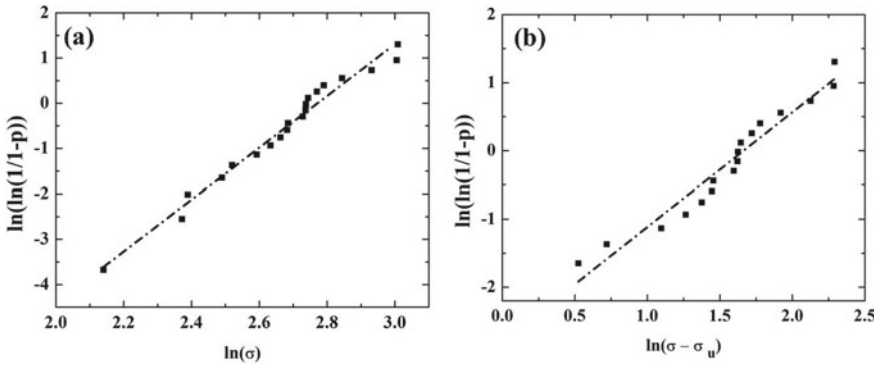

Fig. 4 Weibull distribution plots of **a** two-parameter and **b** three-parameter distribution of uniform samples

and three-parameter distribution for uniform samples are shown in Fig. 4 (a) and (b), respectively.

When using MLE to estimate the parameters of the distribution model, the likelihood value can be used to assess the fit of the distribution. The goodness of fit of the distribution is checked for both two-parameter and three-parameter analyses. The distribution which has the higher likelihood value displays better goodness of fit. The likelihood value for the two-parameter distribution is obtained to be 50.14 and for the three-parameter distribution as 86.97. Hence, it may be inferred that three-parameter is better than two-parameter Weibull distribution. The estimation of the threshold value of stress value can be extremely useful in finding the minimum value of the material that can be used for design purposes. Hence, three-parameter Weibull distribution always provides a better estimate of fracture strength values.

4   Conclusions

In this paper, the effect of stress concentration on the fracture behaviour of free-standing YSZ thin films of ~300 μm was studied. The effect of the presence of a circular hole of Ø1 mm, at the centre of the gauge, on the fracture behaviour was compared with the data of YSZ without a hole. The probability of failure was estimated using a statistical approach for the data obtained using samples with a hole. The key conclusions from these studies are summarized as follows:

- The fracture strength drops to ~11 ± 3 MPa in samples with a circular hole, from 16 ± 4 MPa in continuous samples. The cracks initiated at the circumference of the hole and perpendicular to the loading direction. This observation emphasizes the importance of considering the loss of fracture strength based on the stress-concentration geometry while designing components for turbine engines.
- Statistical analysis of continuous and stress concentrated (hole) samples indicated that the three-parameter Weibull analysis is a more accurate method for reporting the probability of failure than two-parameter Weibull analysis. The threshold strength (σ_u) was obtained as 10.3 MPa and 5.7 MPa, and the characteristic strength was found to be 5.4 MPa and 6.5 MPa for continuous and hole containing samples, respectively.

References

1. Weibull W (1951) A statistical distribution function of wide applicability. J Appl Mech 18:293–305
2. Jiang J, Wu D, Wang W, Zhao X, Ma X, Wang B, Shi H (2020) Fracture behavior of TBCs with cooling hole structure under cyclic thermal loadings. Ceram Int 46:3644–3654
3. Tanaka M, Mercer C, Kagawa Y, Evans A (2011) Thermomechanical fatigue damage evolution in a superalloy/thermal barrier system containing a circular through hole. J Am Ceram Soc 94:128–135
4. Peng X, Sridhar N, Clarke DR (2004) The stress distribution around holes in thermal barrier coatings. Mater Sci Eng 380:208–214 (2004)
5. Teimouri M, Gupta AK (2013) On the three-parameter Weibull distribution shape parameter estimation. J Data Sci 11:403–414
6. Fiał C, Ciaś A, Czarski A, Sułowski M (2016) Fracture statistics using three-parameter and two-parameter Weibull distributions for Fe-0.4C-1.5Cr-1.5Ni-0.8Mn-0.2Mo structural sintered steel. Arch Metall Mater 61:1547–1554
7. Cousineau D (2009) Fitting the three-parameter weibull distribution: review and evaluation of existing and new methods. IEEE Trans Dielectr Electr Insul 16:281–288
8. Patibanda S, Nagda V, Karla J, Sivakumar G, Abrahams R, Jonnalagadda KN (2020) Mechanical behavior of freestanding 8YSZ thin films under tensile and bending loads. Surf Coatings Technol 393:125771

Fracture Toughness of Nafion-212 Polymer Electrolyte Membrane

Kartheek Pilla, Akash Tanwar, and Krishna N. Jonnalagadda

Abstract Polymer electrolyte membrane-based (PEM) fuel cells have numerous advantages over conventional power generation sources owing to their low operating noise, higher efficiency (compared to diesel or gas engines), and negligible pollution. These favourable factors have contributed to the demand for PEM-based fuel cells. PEM membrane is a crucial component of a fuel cell, whose reliability limits the life of the fuel cell. Formation of pinholes/cracks results in fuel crossover, which can lead to catastrophic failure of fuel cell/stack. Therefore, it is important to understand the fracture toughness of the PEM membranes. In the present work, the fracture toughness of the most widely used PEM membrane, Nafion-212, was investigated at room temperature under *in situ* tensile loading condition. Essential work of fracture (EWF) method on DDENT (deeply double-edge notch tension) and SENT (single-edge notch tension) specimens were employed to calculate the fracture toughness of Nafion-212 thin films. The Digital image correlation (DIC) technique was employed for validation of EWF as well as for computation of J-integral. The equivalence between EWF and J-integral calculation methods was established. It was observed that the crack tip root radius had a significant effect on the essential work of fracture. For laser-cut DDENT specimens with blunt crack, the EWF was 6.9 kJm^{-2}, whereas the razor blade-cut DDENT specimens with sharp crack tip have an EWF of 0.93 kJm^{-2}.

Keywords Polymer electrolyte membrane (PEM) · Essential work of fracture (EWF) · Fracture of thin films · Digital image correlation

K. Pilla (✉) · A. Tanwar · K. N. Jonnalagadda
Department of Mechanical Engineering, Indian Institute of Technology Bombay, Mumbai, India
e-mail: 154100019@iitb.ac.in

1 Introduction

A fuel cell converts the chemical energy from a hydrogen-based fuel into electricity. Fuel cells consist of an anode, a cathode, and an electrolyte (membrane electrode assembly (MEA)), as shown in Fig. 1. A proton exchange membrane (PEM) is an electrolyte, which allows positively charged hydrogen ions (protons) to move between the anode and cathode of the fuel cell. A fuel cell will have a continuous supply of fuel and oxygen (in the form of gas) to catalyze layer from gas diffusion layers (GDL). At the anode, a catalyst causes the oxidation of fuel containing hydrogen. This reaction generates protons (positively charged hydrogen ions) and electrons. The protons flow from the anode to the cathode through the PEM membrane. Electric potential is developed across cathode and anode resulting in DC electricity flow. At the cathode, another catalyst combines hydrogen ions, electrons, and oxygen to form water as the by-product. A proton exchange membrane, also called polymer electrolyte membrane (PEM), is a semipermeable membrane generally made from ionomers. These membranes are made by doping specific groups into their basic structure. They are designed to conduct protons while acting as an electron insulator. They do not allow the passage of reactants like oxygen and hydrogen gas from either side of the membrane. Nafion is a widely used proton exchange
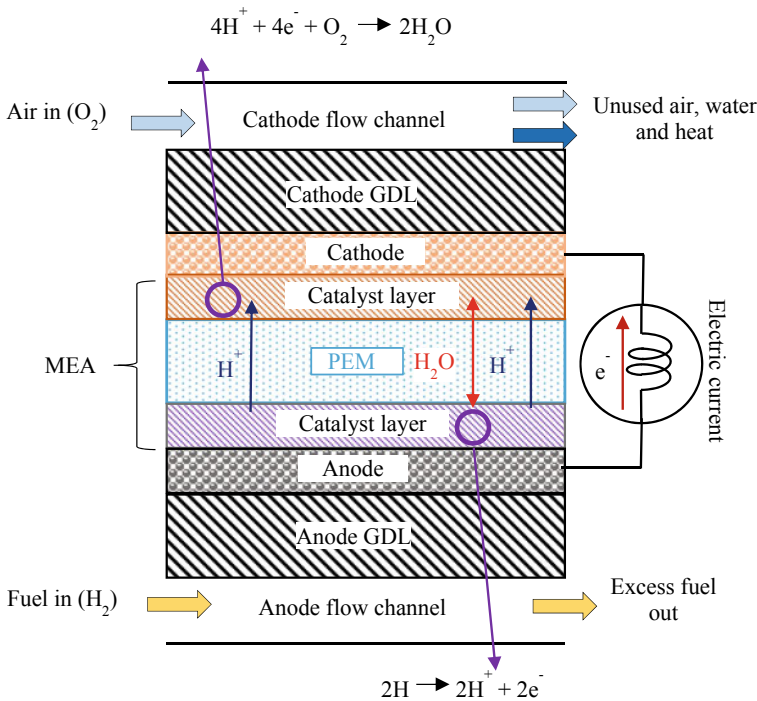

Fig. 1 Schematic of a fuel cell [3]

membrane due to its chemical and mechanical stability and high proton conductivity at low temperature and high performance [1]. In Nafion, specific functional groups facilitate proton exchange in the presence of water. The absorption of water causes significant swelling in Nafion membranes. This volumetric expansion in the fuel cell is constrained by the electrodes and fuel cell packaging. In addition, to increase ionic conductivity and efficiency, the fuel cells are operated at elevated temperatures of 50–80 °C. Therefore, the PEM is subjected to hygro-thermal stresses in addition to mechanical stresses due to constrained expansion. These along with chemical effects can lead to reducing the structural integrity of the PEM membrane [1, 2] and thereby its durability.

Among many factors that limit the lifetime of the fuel cell, the formation of pinholes/cracks in the membrane is a major concern. This results in fuel crossover, an exothermic reaction, and catastrophic failure of the fuel cell/stack due to short-circuit inside the cell as the electron movement is unrestricted [1, 4]. If there is a void in the membrane, either inside or on the surface, it can nucleate a crack. Propagation of this crack through the thickness can lead to fuel cell failure. Genrally stress concentration due to mud cracks in the anode/cathode catalyst layer can initiate the crack in the membrane [5, 6]. Whereas Repeated hygro-thermal loading, constrained expansion, and decomposing of the membrane through chemical degradation may cause thinning of the membrane leading to the formation of pinhole [7, 8]. Therefore, it is important to study and understand the pinhole formation and resistance to crack propagation. This can be done by studying the mechanical behavior of the PEM membrane. Fracture toughness is one such property that can be used for characterizing mechanical failure of the membrane. The toughness of PEM membranes depends on the polymer structure, doping level (e.g., water or acid), and operating temperature [9]. Fracture toughness is an intrinsic property, a material constant, which may be determined in different ways. Brittle materials fracture toughness is assessed by either critical stress intensity factor K_C or the critical strain energy release rate G_C using linear elastic fracture mechanics (LEFM) [10]. LEFM is not applicable when the crack propagation occurs through a highly deformed and yielded material, typically ductile polymers. In that case, the post-yield fracture mechanics (PYFM, also called elasto-plastic or nonlinear fracture mechanics) approach is preferred. The EWF method is reported to be appropriate for polymers exhibiting large deformation. The greatest advantage of the EWF method is that a clear distinction between surface (essential part) and volume-related (non-essential part) works is made [11–14]. To characterize fracture toughness of PEM different techniques like double-edge notch tension (DENT) [15, 16], knife slit [9, 15], trouser tear test [15, 17–19], and double cantilever beam test [20] have been employed in the past. Although the method of essential work of fracture is used for fracture toughness measurement of Nafion polymer, in the present study J-integral [21] method for fracture toughness estimation was also used to establish an equivalence between the J-integral and the EWF by using DDENT and SENT specimens. Digital image correlation (DIC), a whole field deformation measurement technique, to measure the strain distribution and ligament yielding during tensile loading was employed.

2 Experimental Details

In this work, experiments were performed on Nafion-212 polymer with a thickness of
50 μm, purchased from Sigma Aldrich. Fracture experiments were performed using
in situ uniaxial tensile stage with displacement control mode on the film at a strain
rate of 0.001 s^{-1}. The Details about the testing stage and speckle pattern generation
for DIC are described in [22, 23]. DDENT and SENT Nafion polymer films were cut
using CO_2 laser (rated power = 30 W, λ = 10.6 μm, Aditi Laser Tech) (Fig. 2a and b)
and razor blade cut (Fig. 2c). Gauge length of 4 mm and gauge width of 2.2 mm with
ligament lengths, viz., 450, 500, 550, 600, and 650 μm both in the case of DDENT
and SENT are chosen for fracture experiment. Ligament lengths are chosen to ensure
plane stress and avoid edge effects by maintaining the sample dimensions: in the limit
3t < ligament length < W/3, where t is the thickness and W is the gauge width of the
film [12].
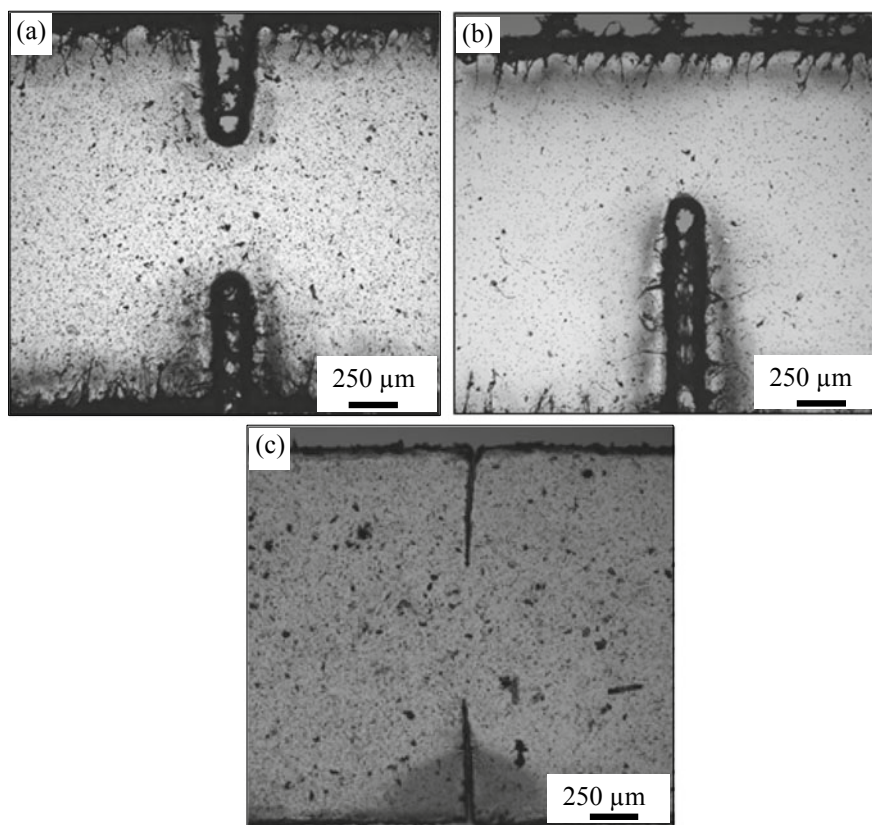
Fig. 2 Laser cut (**a**) DDENT, (**b**) SENT, and (**c**) razor blade cut DDENT specimens, with speckle
pattern of CuO nanoparticles

3 Results and Discussion

Yield Parameter Calculation

DIC analysis of the images of tensile test gives strain versus time data. Stress Vs. time data is calculated using load cell data. Concurrent stress versus strain data is then plotted (Fig. 3a) and the yield point is calculated. Nafion undergoes yielding and subsequent large elongation before fracture is observed in the samples. From the u-pixel data from DIC shown in Fig. 3b ensure that sample is aligned with the loading. From stress versus strain curve following properties of Nafion film were obtained Young's modulus E ~ 236 ± 6 MPa, yield stress ~12.15 ± 0.9 MPa, (Note that the Yield strength is taken as the point of intersection of slope of elastic part and post yield of the stress–strain curve (See Fig. 3a) yield strain ~0.052 and elongation at break ~207 ± 6.3 (%) are comparable with the existing literature [24].

Essential Work of Fracture Calculation

DDENT and SENT specimens of different ligament lengths are uniaxially loaded up to fracture. The load–displacement curves for DDENT and SENT specimens obtained are shown in Fig. 4a and b. Self-similar curves are obtained which confirms that the crack is advancing in one direction only for all the ligament lengths. This is an important point for the validity of the EWF technique [13].

Complete yielding of the ligament before fracture was identified from DIC data. Equivalent von Mises strain at every point for every image is calculated using DIC data. All the points where the equivalent von Mises strain is more than the yield strain is confirmed to be yielded. As seen in Fig. 5a, we can comment that the ligament has yielded completely before crack initiation. Complete ligament yielding before crack initiation is another condition required for the validity of EWF technique [12]. Area under the load–displacement curve (Fig. 4a and b) divided by the product of corresponding ligament length and film thickness (50 µm) gets the specific work of fracture. Specific work of fracture is plotted against ligament length as shown in

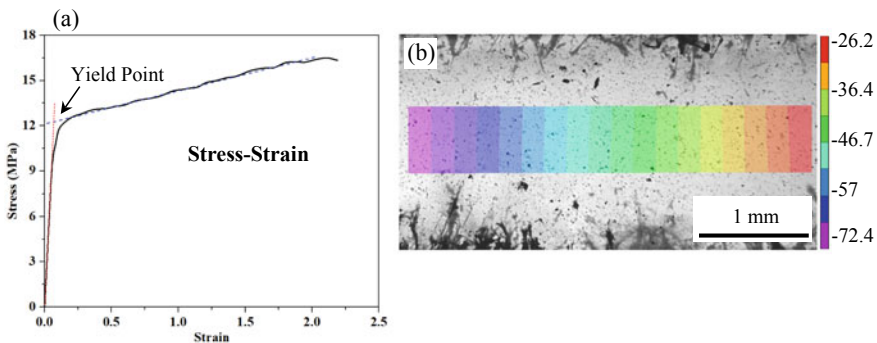**Fig. 3** (**a**) Engineering stress Vs. strain response of Nafion-212 polymer, and (**b**) u-pixel contour plot obtained from DIC analysis
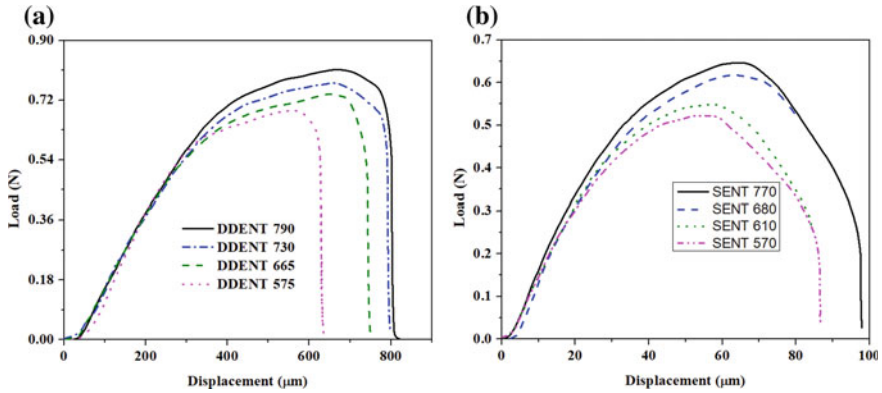
Fig. 4 Load versus displacement curves for (**a**) DDENT and (**b**) SENT specimens, at different ligament lengths (ligament length in μm is indicated in the legend
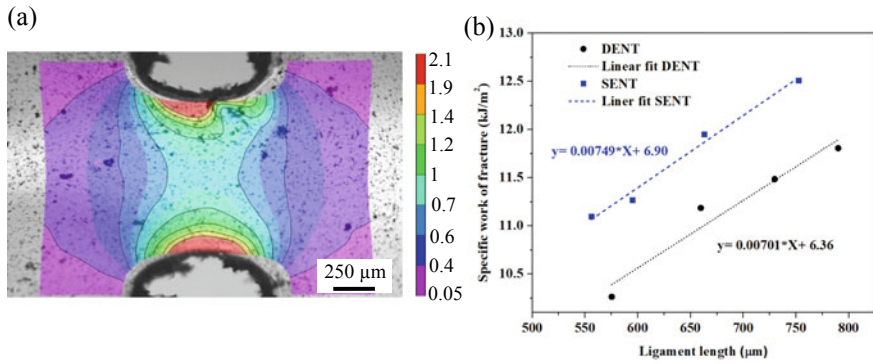

Fig. 5 (**a**) Contour plot of equivalent von Mises strain(~0.06) for the image captured at crack initiation for DENT specimen, and (**b**) specific work of fracture versus ligament length for DDENT and SENT specimens

Fig. 5b. Data points are linearly fitted and the specific work of fracture corresponding to zero ligament length is the essential work of fracture. From the plots, it is found that the essential work of fracture for DDENT and SENT specimen is 6.36 kJm^{-2} and 6.9 kJm^{-2} respectively.

J Integral Calculation

Begley-Landes [25] multiple specimen method along with the procedure proposed by Hodgkinson and Williams [26] is used for J-integral computation. In the Begley-Landes method, specimens having different crack lengths are loaded till fracture. Diagrams of the input energy U as a function of crack length a are obtained by integrating each load–displacement curve up to various displacements. Hodgkinson and Williams involve the construction of virtual constant crack length curves from experimental load versus displacement curves, as shown in Fig. 6a. The crack length is known for a given instant of time from the captured images. Subsequent points can be plotted for each ligament length curve having that constant virtual crack length. Using the integration of the curves shown in Fig. 6a up to various displacement value, the energy versus constant crack length curve is obtained. The slope of the curves shown in Fig. 7a gives the value of J for a given displacement. Using the images captured during the experiment, a crack length advancement is plotted against displacement as shown in Fig. 7b. Using plots of Fig. 7a and b, J-integral is plotted against crack length advancement. J-integral has a linear relation with crack advancement length. The intercept of this curve corresponding to zero crack length advancement is the critical J-integral. As seen in Fig. 7c, critical J-integral is calculated to be 6.2 kJm^{-2} which is almost equivalent to the essential work of fracture.

Effect of Notch on EWF

The blade cut DDENT specimens are loaded in micro tensile stage up to fracture. Load displacement curves are plotted as shown in Fig. 8a. Integration of load–displacement curves gives work of fracture, and dividing the work of fracture by the product of ligament length and film thickness gives specific work of fracture. Essential work of fracture is equal to the specific work of fracture corresponding to
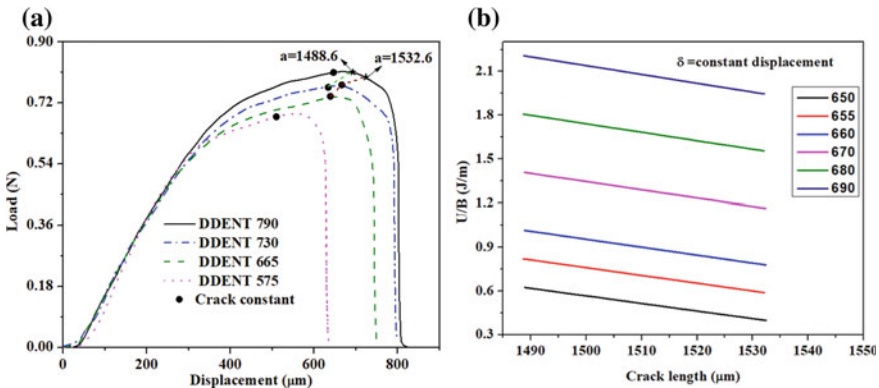

Fig. 6 (**a**) Load versus displacement curve for DDENT specimen with constant virtual crack length curves and (**b**) energy per thickness (U/B) versus crack length curves at constant displacement (δ in μm)
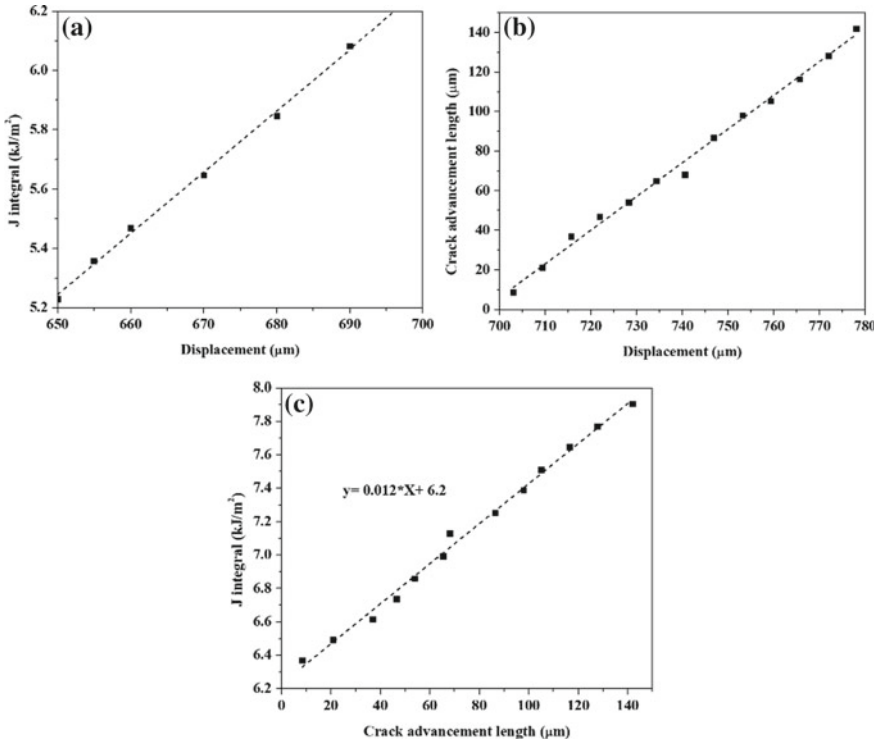
Fig. 7 (**a**) J-integral versus displacement, (**b**) crack advancement length versus displacement, and (**c**) J-integral versus crack advancement length plots of DDENT specimens
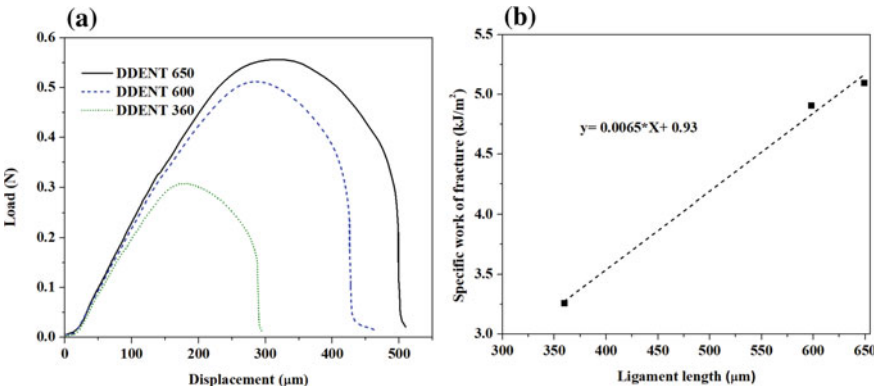

Fig. 8 (**a**) Load Vs. displacement curves, and (**b**) specific work of fracture versus ligament length, for different ligament lengths of blade cut DDENT specimens (ligament length in μm is indicated in legend)

zero ligament length (Fig. 8b). The EWF value for blade cut DDENT specimen is found to be 0.93 kJm^{-2}.

Essential work of fracture value of blade cut specimens is very less compared to the laser cut specimens. This is because the sharper blade cut notches exhibit less blunting compared to laser cut notches. The blade cut notches initiate crack at lower loads and hence absorb less energy till fracture. Because of this large variation in EWF value, the imaging of fractured surface was done using SEM (scanning electron microscope). The cross-sectional image of blade cut un-yielded region and fractured surface created due to crack propagation is shown in Fig. 9. The thickness of the yielded region of the film has reduced due to plastic deformation in the outer process zone. The value of the shape factor (β) is a material-dependent factor. Product of shape factor and w_p (specific energy absorption per unit volume) yields the total energy consumed in the outer process zone. From the fractured specimen image shown in Fig. 9c, it is seen that the process zone is elliptical. The elliptical process zone is confirmed from the contour plots drawn using the DIC-generated data. For an elliptical shape factor, $\beta = \Pi h / 4 \, l$ from Fig. 9c, β is calculated to be equal to 0.196.

It can be noted that DDENT specimens show rather sudden fracture compared to SENT specimens. In Fig. 3(a) stress Vs. strain curve sample has undergone displacement up to ~12.5 mm ($\varepsilon=2.5$) at maximum load of ~3 N ($\sigma = 15$ MPa), with a hardening behavior beyond yield point and sudden failure at maximum load. Similar
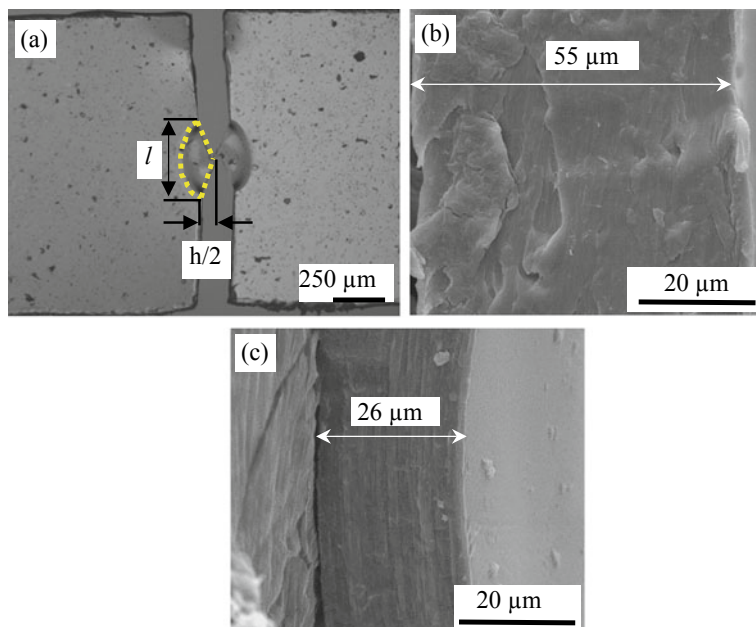

Fig. 9 Optical micrograph of (**a**) fractured region showing elliptical shape outer process zone; and cross-sectional SEM micrographs of (**b**) blade cut region, and (**c**) fractured region of DDENT specimens

load-displacement curve (although with lower magnitudes of load and extension) is exhibited by DDENT specimen cut with laser (resulting in ~250 μm notch radius). It can be interpreted that, as notches are introduced, the stress localization is maximized causing easy propagation of crack, resulting in less load and displacement. Even with notches, while the crack is propagating perpendicular to loading direction, a displacement of ~800 μm is observed, which is accommodated by the region in between the notches, leading to sudden failure after maximum load. However, DDENT specimen cut with razor blade (resulting in ~50 μm notch radius) show a considerable softening post maximum load (0.5 N), which is much lesser than that of DDENT laser cut specimen. It is expected that as the radius of notch is decreased, crack propagation is accelerated due to higher stress concentration at the notch. But since the displacement is quite less, implying very limited deformation (thickness reduction) during loading, softening is observed post maximum load, in DDENT razor blade cut samples. Similar behavior is observed in SENT laser cut samples where presence of single notch caused quick propagation of crack with less displacement, implying less deformation and thereby softening regime after maximum load. Hence it can be said that if considerable deformation (~800 μm) at maximum load has occurred, sudden failure takes place. But if the extension is quite less (~ 80μm) at maximum load, owing to local stress concentration, softening is observed due to accommodation of deformation of the remaining sample thickness.

4   Conclusions

Uniaxial tensile tests were conducted on tensile specimens to find out the yield parameters of Nafion-212 film. Nafion-212 is found to undergo yielding at ~0.052 strain and ~12.15 MPa stress. The polymer underwent an average elongation of ~207% and had an elastic modulus of ~236 MPa. High elongation of Nafion-212 confirms its highly ductile behavior which is a prerequisite of this work. Fracture experiments were performed on DDENT (laser cut and razor blade cut) and SENT samples (laser cut only) and the method of essential work of fracture is employed to compute the fracture toughness of the polymer. The value of essential work of fracture is 6.9 kJm^{-2} and 6.36 kJm^{-2}, respectively, for laser cut, DDENT, and SENT specimen geometries. It can be concluded that the value of essential work of fracture is independent of the specimen geometry. Full-field deformation data obtained from the DIC analysis is used to validate the conditions of ligament yielding before crack initiation and plane stress condition. Equivalence between the essential work of fracture and critical J-integral (JIC) is established. Multiple specimen Bagley-Landes method was used to compute the critical J-integral value, which is found to be 6.2 kJm^{-2}. This is almost equivalent to the essential work of fracture values obtained for DDENT and SENT specimens. For laser cut DDENT specimens with blunt crack EWF was 6.9 kJm^{-2}, whereas the razor blade cut DDENT specimens with sharp crack tip has EWF of 0.93 kJm^{-2}. Sharper crack produces higher stress intensity at crack tip and thereby leads to lower EWF.

References

1. Borup R (2007) Scientific aspects of polymer electrolyte fuel cell durability and degradation. Chem Rev 107(10):3904–3951
2. Kusoglu A (2017) New Insights into Perfluorinated Sulfonic-Acid Ionomers. Chem Rev 117(3):987–1104
3. Mauritz K (2017) State of understanding of Nafion. Chem Rev 104(10):4535–4586
4. Zhang H (2012) Recent development of polymer electrolyte membranes for fuel cells. Chem Rev 112(2)
5. Kundu S (2006) Morphological features (defects) in fuel cell membrane electrode assemblies. J Power Sources 157(2):650–656
6. Pestrak M (2010) The effect of mechanical fatigue on the lifetimes of membrane electrode assemblies. J Fuel Cell Sci Technol-ASME 7(4):041009–041010
7. Kusoglu A (2015) Electrochemical/mechanical coupling in ion-conducting soft matter. J Phys Chem Lett 6(22):4547–4552
8. Venkatesan S (2016) Progression in the morphology of fuel cell membranes upon conjoint chemical and mechanical degradation. J Electrochem Soc 163(7):F637–F643
9. Patankar K (2010) Characterizing fracture energy of proton exchange membranes using a knife slit test. J Polym Sci Part B: Polym Phys 48(3):333–343
10. Jin Z, Sun CT (2012) Fracture mechanics. Academic Press, Waltham
11. Broberg KB (1971) Crack-growth criteria and non-linear fracture mechanics. J Mech Phys Solids 19(6):407–418
12. Bárány T (2010) Application of the essential work of fracture (EWF) concept for polymers, related blends and composites: a review. Prog Polym Sci 35(10):1257–1287
13. Hashemi S (2003) Effect of temperature on fracture toughness of an amorphous poly(ether-ether ketone) film using essential work of fracture analysis. Polym Testing 22(5):589–599
14. Lee JM (2009) Determination of the tear properties of thermoplastic polyester elastomers (TPEEs) using essential work of fracture (EWF) test method. Polym Testing 28(8):854–865
15. Li Y (2008) Characterizing the fracture resistance of proton exchange membranes. J Power Sources 185(1):374–380
16. Moukheiber E (2014) Understanding the formation of pinholes in PFSA membranes with the essential work of fracture (EWF). Int J Hydrogen Energy 39(6):2717–2723
17. Jia R (2011) Mechanical durability of proton exchange membranes with catalyst platinum dispersion. J Power Sources 196(20):8234–8240
18. Jia R (2011) Effect of cation contamination and hydrated pressure loading on the mechanical properties of proton exchange membranes. J Power Sources 196(8):3803–3809
19. Yuen PY (2016) Effect of mechanical constraint on tearing energy of polymer membranes. Macromol Mater Eng 301(9):1096–1103
20. Jia R (2012) Contamination and moisture absorption effects on the mechanical properties of catalyst coated membranes in PEM fuel cells. Int J Hydrogen Energy 37(8):6790–6797
21. Rice JR (1968) A path independent integral and the approximate analysis of strain concentration by notches and cracks. J Appl Mech ASME 35(2):379–386
22. Das A (2017) Fracture in microscale SU-8 polymer thin films. Exp Mech 57(5):687–701
23. Robin CJ (2014) Mechanical behavior and anisotropy of spin-coated SU-8 thin films for MEMS. J Microelectromech Syst 23(1):168–180
24. Shi S (2013) Mechanical properties of Nafion 212 proton exchange membrane subjected to hygrothermal aging. J Power Sources 238(15):318–323
25. Begley JA (1972) J integral as a fracture criterion. Fract Toughness ASTM Int 514:1–23
26. Chan MKV (1993) J-integral studies of crack initiation of a tough high density polyethylene. Int J Fract 23:145–159

Structural Integrity Assessment of Calandria End-Shield Assembly for In-Vessel Corium Retention Under Severe Accident Condition

Nirmal Kumar, Varun Mishra, D. Faisal, R. K. Chaudhary, V. Chaudhry, and S. M. Ingole

Abstract Safety demonstration of nuclear power plant for beyond design basis accident (BDBA) conditions, called design extension conditions, has become an important requirement in pressurized heavy water reactors (PHWRs). One of the conditions resulting in severe core damage has been postulated due to loss of coolant accident (LOCA) along with the failure of the emergency core cooling system and loss of moderator circulation. Under such conditions, the reactor core geometry progressively degrades and results in core collapse. Calandria end-shield assembly of PHWRs acts as an important barrier in limiting the accident progression. Structural integrity assessment of Calandria end-shield assembly has been carried out for in-vessel retention (IVR) of collapsed core/corium under postulated BDBA scenario with provisions made as per Severe Accident Management Guidelines (SAMGs). Coupled thermo-mechanical analysis of the assembly has been carried out to simulate the accident scenario with SAMG provisions. The thermal analysis accounts for the decay heat, melt solidification and also corium (core melt) latent heat. The analysis gives a distribution of temperature with accident progression at various locations in the assembly. Sensitivity analysis has also been carried out to account for the uncertainties associated with input parameters, viz., heat transfer coefficient and radiation heat transfer. Subsequent to thermal analysis, structural analysis of the assembly has been carried out accounting for the temperature-dependent material properties. Based on the analysis, the failure modes provided in IAEA TECDOC-1549 for IVR, viz., failure due to creep, failure due to molten metal and failure of drain lines have been assessed. Based on the analytical evaluation, the structural integrity of Calandria end-shield assembly for in-vessel corium retention under severe accident condition for Indian PHWR has been demonstrated.

Keywords Safety · Structural integrity · In-vessel retention · Thermo-mechanical analysis

N. Kumar · V. Mishra · D. Faisal · R. K. Chaudhary · V. Chaudhry (✉) · S. M. Ingole
Nuclear Power Corporation of India Limited, Mumbai 400094, India
e-mail: vchaudhry@npcil.co.in

1   Introduction

Safety features both inherent and engineered are provided to ensure a balance between prevention and mitigation measures during accident condition in pressurized heavy water reactors (PHWRs) [1]. Inherent safety features are central to the design of PHWR and consist of multiple heat sinks, viz., removal of fission heat from the fuel bundle via heavy water primary coolant flowing through pressure tube, heavy water moderator inside the Calandria surrounding the pressure tube and light water surrounding the Calandria in Calandria vault [1]. These large water inventories available in the form of moderator and Calandria vault water provide a heat sink for varying lengths of time to remove core decay heat during accident condition [2].

After an accident at Fukushima nuclear power plant in Japan (2011), safety demonstration of the nuclear power plant under severe accident condition has become an important requirement in the nuclear industry [2]. Severe accident is beyond design basis plant damage state, which has significant consequences due to nuclear fuel degradation resulting in loss of reactor core geometry and/or core melting. Under such an accident, the reactor core geometry progressively degrades and results in core collapse. In-vessel retention (IVR) of corium (core melt) is considered as an accident termination point. In IPHWRs, Calandria end-shield assembly acts as an important barrier in limiting the accident progression by retaining the corium, subject to the availability of Calandria vault water and end-shield cooling water as heat sinks. IVR of corium in Calandria end-shield assembly not only depends on the structural integrity of the assembly but also on the integrity of penetrations/piping provided at the bottom of the Calandria vessel.

This paper brings out details of thermo-mechanical analysis carried out for the Calandria end-shield assembly and its components to demonstrate the effectiveness of heat sinks and IVR for standard 220MWe PHWRs under severe accident condition. Based on the observed heat flux, temperature and stress/strain distribution, assessment has been carried considering various failure modes provided in IAEA TECDOC-1549 [2], viz., failure due to creep, failure due to molten metal and failure of the drain line.

2   Accident Scenario

The PHWR reactor consists of a horizontal reactor vessel (Calandria) made of austenitic stainless steel (SS 304L) filled with heavy water moderator at low pressure and low temperature [1]. The Calandria vessel houses all the reactivity and reactor shut down devices. The main shell of Calandria is stepped down in diameter at each end. The stepped-down ends called small shells are joined to the main shell through flexible annulus plates. Either end of the Calandria vessel is welded to stainless steel end-shields for radiation shielding. The Calandria end-shield assembly is pierced through horizontal coolant channel assemblies which contain fuel bundles.

Through these coolant channels, pressurized heavy water coolant is circulated which removes the nuclear heat from the fuel bundles. The Calandria vessel always remains immersed in water which is filled in the Calandria vault [3]. The heat generated in the end-shields is cooled by an end-shield cooling system. The general arrangement of Calandria end-shield assembly is shown in Fig. 1.

One of the conditions resulting in severe core damage has been postulated due to loss of coolant accident (LOCA) along with the failure of the emergency core cooling system and loss of moderator circulation. In the case of LOCA (coincident with failure of the emergency core cooling system), fuel cooling would be provided initially by coolant blowdown and eventually by subcooled nucleate boiling heat transfer to a moderator. Heat transfer to the moderator will lead to a rise in moderator
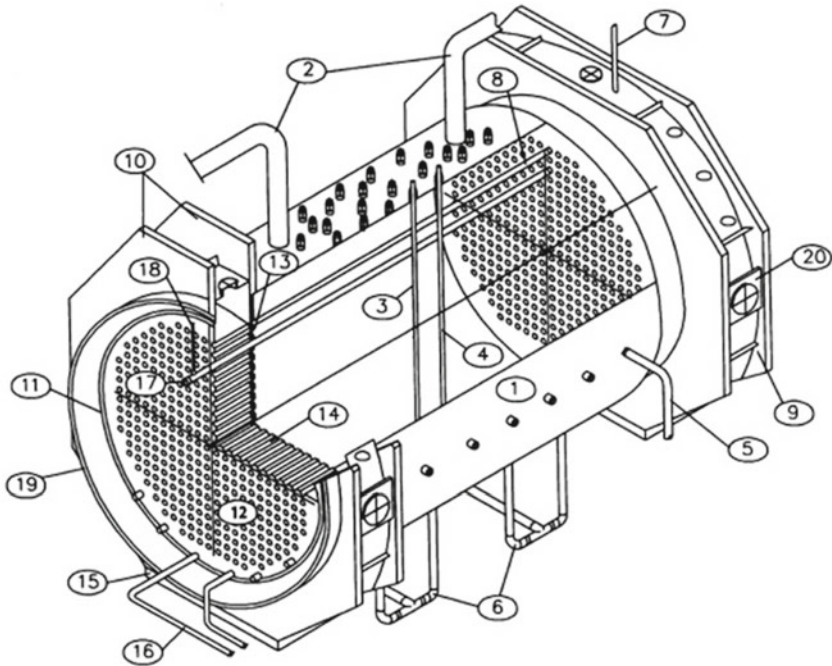
1.	CALANDRIA SHELL	2.	OVER PRESSURE RELIEF DEVICE
3.	SHUT DOWN SYSTEM #1	4.	SHUT DOWN SYSTEM #1
5.	MODERATOR INLET	6.	MODERATOR OUTLET
7.	VENT PIPE	8.	COOLANT CHANNEL ASSEMBLY
9.	END SHIELD	10.	END SHIELD SUPPORT STRUCTURE ASS'Y
11.	MAIN SHELL ASS'Y	12.	TUBE SHEET F/M SIDE
13.	TUBE SHEET CAL SIDE	14.	LATTICE TUBE
15.	END SHIELD SUPPORT PLATE	16.	END SHIELD COOLING INLET PIPES
17.	END FITTING ASS'Y	18.	FEEDER PIPES
19.	OUTER SHELL	20.	SUPPORT LUG

Fig. 1 Integral assembly of Calandria end-shields [1]

temperature and as soon as it reaches its saturation temperature, the moderator begins to boil and escape from the Calandria vessel through an overpressure relief device (OPRD), thereby exposing/uncovering the top rows of channels. Due to core decay heat, the channel heat up continues and reaches the channel failure criteria. The failed channel dislodges and sits on an adjoining lower channel. Further loss of moderator inventory leads to uncovering of the subsequent core. This results in sudden core collapse and moderator boil-off condition. This condition is referred to as late phase of severe accident condition [2]. The average temperature of core debris at the time of complete moderator boil-off is around 423 K, which is arrived at based on thermal-hydraulics analysis of accident progression. With the progression of an accident, heat will get transferred from debris to the Calandria shell, which in turn transfers it to Calandria vault water. The bottom part of Calandria filled with debris will cause nucleate boiling in Calandria vault water which will make the temperature of Calandria vault water rise. By implementing SAMG action, water is injected into the Calandria vault before the Calandria vault water level starts falling below the debris level. By this action, IVR of corium is considered as an accident termination point.

3 Analysis Methodology

In order to demonstrate the structural integrity of Calandria end-shield assembly for IVR, thermo-mechanical analysis is performed to simulate the late phase of severe accident condition (after moderator boil-off), wherein the molten core debris/corium is located at the bottom of the Calandria vessel and surrounded by Calandria vault water.

Thermal transient analysis is performed using the finite element method to estimate the temperature distribution in the assembly. In the analysis, it is presumed that the moderator water is completely boiled off; the disintegrated fuel channels and the quenched debris are accumulated at the bottom of Calandria and are uncovered completely. Thereafter, the debris will start to melt due to decay heat and will form a molten pool (corium) in the Calandria vessel.

From the various numerical and experimental studies [4–6], it is observed that a natural convection flow in an internally heated pool consists of a region where intense turbulence and mixing takes place that keeps a uniform temperature in the pool. Based on this, it is assumed that the core melt/corium is homogenous and uniformly distributed. The thermal analysis accounts for the decay heat, melt solidification and also corium (core melt) latent heat. The analysis accounts for the heat transfer from the disintegrated channels and debris to the heat sinks through conduction and convection mode. Heat transfer from the core melts to the outside surface of the Calandria shell simulated through conduction. Thereafter, the heat is dissipated through convection to the heat sinks, i.e., Calandria vault water and end-shield cooling water. Further, radiation heat transfer from the top surface of the corium to the Calandria end-shield internal surface (above the debris bed) is accounted for in the analysis.

Subsequent to thermal analysis, structural analysis has been carried out to evaluate the thermal stresses in the assembly based on the temperature distribution. These thermal stresses are then superimposed over the stresses induced due to sustained loads (dead weight). Material properties as a function of temperature have been accounted for in the analysis.

The structural integrity of the assembly has been assessed based on the following criteria:

(i)   Heat flux to be less than critical heat flux so as to demonstrate the effectiveness of heat sink.
(ii)   Creep assessment of the assembly in case the temperature is greater than 740 K (1/3 of the melting point).
(iii) Centre line temperature at penetration location to be less than solidus temperature to form freezing plug at the nozzle/penetration openings. This will retain the corium within the Calandria.
(iv)   Equivalent inelastic strain to be limited to 5% or else will result in excessive local plastic deformation.
(v)   Plastic instability or collapse of the assembly or connected piping based on a large or steep rise in displacement or strain.

4   Finite Element Analysis

As brought out above, in order to demonstrate the structural integrity of Calandria end-shield assembly under severe accident condition, thermo-mechanical analysis is performed using the finite element method. Finite element analysis has been carried out in ANSYS software [7].

4.1   Finite Element Model

The Calandria end-shield assembly has been approximated by a half-quarter symmetry finite element model based on its geometry and loading conditions. SOLID 90 and SOLID 186 elements have been used in the thermal and structural analysis, respectively. These elements are 20 nodded brick elements compatible with model curved boundaries and provide a more accurate solution accounting for the nonlinearity [7]. The finite element (FE) model of the assembly and the components are shown in Fig. 2. The FE model consists of Calandria main shell, annulus plate, small shell, Calandria side tube sheet (CSTS), fuelling machine side tube sheet (FSTS), end-shield inner and outer shell, diaphragm plates, octagonal flange, lattice tubes and corium. In the model, the axial stiffness of lattice tubes has been accounted for using an equivalent area method. Corium is considered homogenous and isotropic. Core debris and corium are assumed to be uniformly deposited at the bottom of the Calandria and its various bottom penetrations/nozzles.
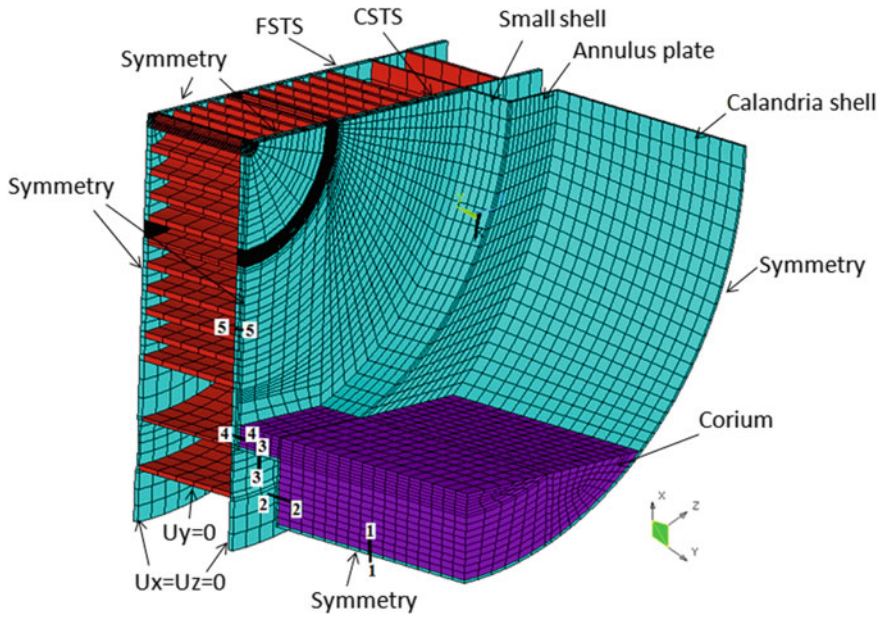
Fig. 2 Half-quarter symmetry finite element model of Calandria end-shield assembly

In addition to Calandria end-shield assembly, moderator outlet nozzle and moderator outlet piping are also analysed. Moderator outlet nozzle is modelled using axisymmetric element (Fig. 3), whereas moderator piping is modelled using pipe
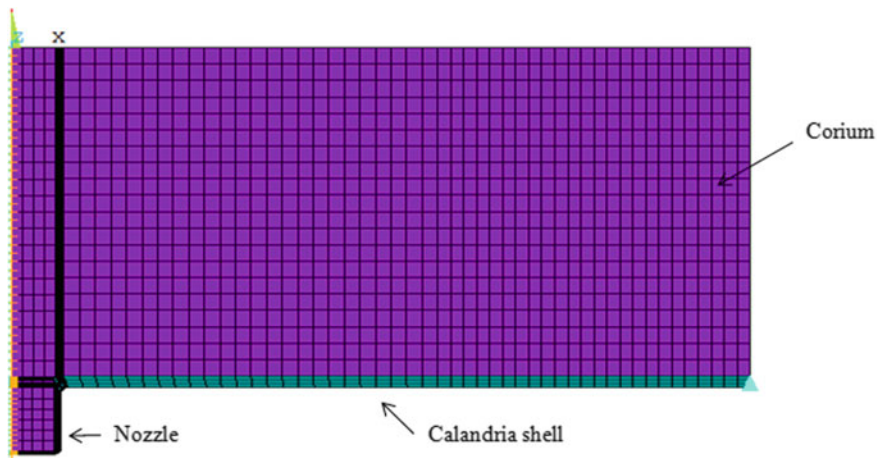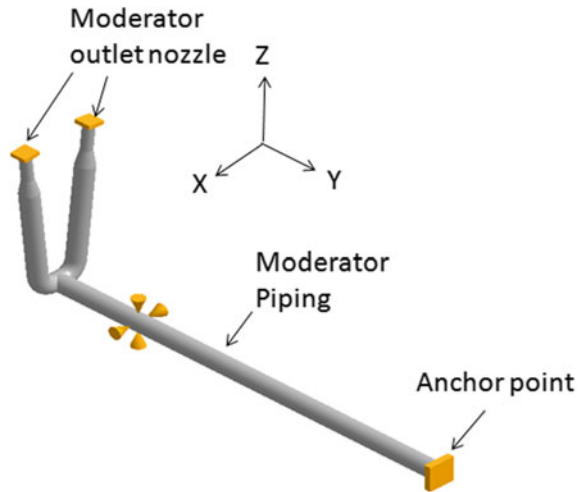

Fig. 3 Axisymmetric finite element model of moderator outlet nozzle

Fig. 4 Finite element model for moderator outlet piping

element (Fig. 4). The moderator outlet piping is considered from Calandria outlet bottom nozzles up to the anchor point in the Calandria vault.

4.2 Material Properties

The material of construction of Calandria end-shield assembly is stainless steel SS 304L. Temperature-dependent material properties are used in the analysis. Variation of thermal conductivity, density, specific heat, coefficient of thermal expansion, Young's modulus, Poisson's ratio and yield strength with temperature are shown in Fig. 5 [8, 9]. Figure 6 provides the details of true stress–strain values of SS as a function of temperature [10].

In the case of corium, due to uncertainties associated with its thermal properties, properties of pure uranium oxide have been used [11]. The specific heat capacity as a function of temperature is considered to be varying linearly from 266 J/(kg-K) to 700 J/(kg-K) for a temperature range between 400 and 3000 K. In the temperature range, between 3000 and 3200 K, the heat capacity of uranium oxide is accounted by latent heat of 289 kJ/kg. The specific heat and latent heat are specified in terms of enthalpy as a function of temperature. The variation in enthalpy and thermal conductivity of corium with temperature is brought out in Table 1. The density of the corium has been estimated as equivalent density accounting for the fraction of the fuel and structural material present in core debris. Equivalent density has been evaluated as 9350 kg/m^3.
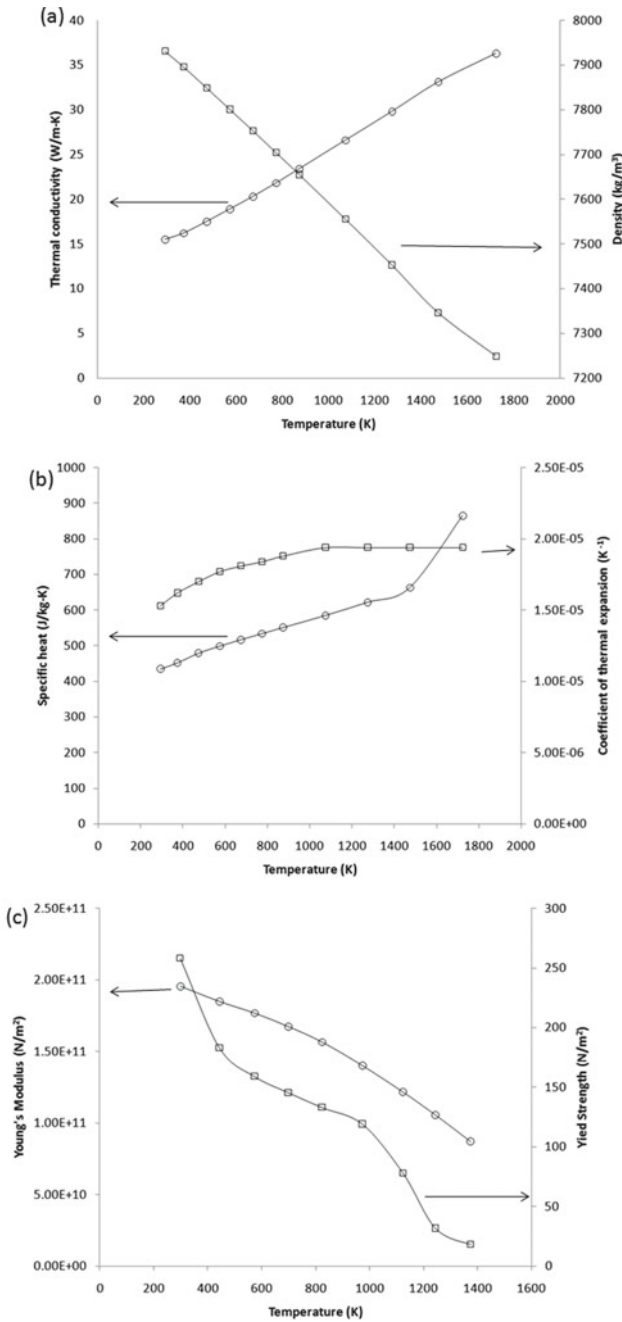
Fig. 5 Variation of **a** thermal conductivity and density **b** specific heat and coefficient of thermal expansion **c** Young's modulus and yield strength with temperature
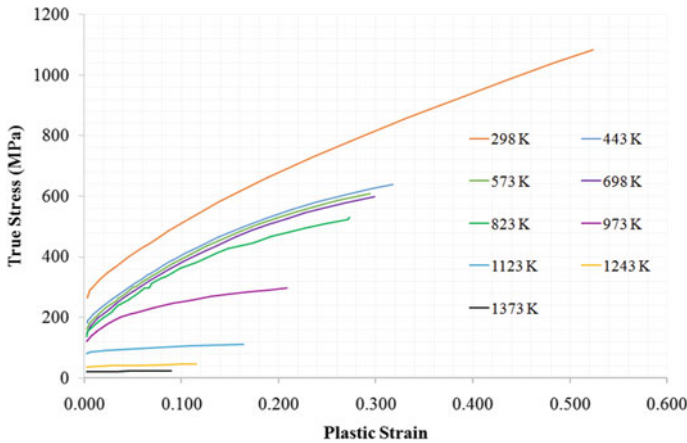
Fig. 6 Plastic strain–stress curve at various temperatures [10]

Table 1 Thermal properties of corium [11]

Properties	Temperature (K)		
	400	3000	3200
Thermal conductivity (W/m-K)	5.73	4.09	4.55
Enthalpy (J/kg-K)	2.50E + 8	17.25E + 9	20.00E + 9

4.3 Boundary Conditions

4.3.1 Thermal Boundary Conditions

Thermal analysis has been performed considering moderator boil-off condition, as an initial condition. At this instant, the average temperature of corium is considered as 423 K. Initial temperature of the structural components is considered as 353 K and the fluid bulk temperature is considered as 338 K [12]. Figure 7 provides the details of variation of internal heat generation with time which simulates the decay heat in the corium.

Verma et al. [13] carried out experimental studies to find the heat transfer coefficient on the outer surface of the Calandria vessel and moderator drain nozzle, accounting for the actual curvature of the assembly. From the studies, the heat transfer coefficient has been deduced at different curvature angles. Studies revealed that at a heat flux of 100 kW/m^2, nucleate boiling starts and the heat transfer coefficient is observed to be more than 5000 W/m^2-K. At high heat flux (>120 kW/m^2), the heat transfer coefficient increases rapidly up to 20000 W/m^2-K. Similar observations have also been observed in the experiments carried out on a scaled-down model of the Calandria vessel by pouring the corium from the top [14]. Further, minimum heat
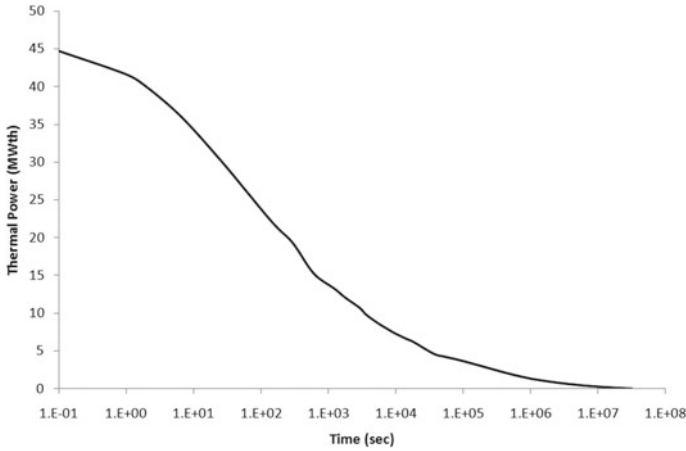
Fig. 7 Variation of internal heat generation with time

transfer coefficient is observed at the bottom-most position of the assembly which increases with the curvature angle due to an increase in the buoyancy-induced flow.

In order to study the sensitivity of the heat transfer coefficient on temperature distribution in the assembly, a parametric study has been carried out considering the heat transfer coefficient of 2000 W/m^2-K and 3000 W/m^2-K as lower bound values observed from the experimental studies, irrespective of heat flux [13, 14].

For nozzles and other penetrations with vertical configuration, the heat transfer coefficient has been evaluated using the following correlation [15]:

$$\overline{Nu} = 0.6\left[\frac{RaD}{L}\right]^{0.25} for \frac{RaD}{L} \geq 10^4 \tag{1}$$

Heat transfer coefficients inside end-shield assembly have been evaluated using the following correlation:

$$\overline{Nu} = C(Gr \times PR)^m \tag{2}$$

where C and m values are considered based on Ra (Gr x Pr) and also on the plate configuration [14].

Analysis has been performed with and without consideration of radiation heat transfer from corium top to the internal surface of the assembly. Radiation analysis has been performed using the radiosity solver method. The Stefan-Boltzmann constant value is taken as 5.67e-8 W/m^2-K^4. The emissivity of the Calandria end-shield surface is considered 0.6, whereas the emissivity of the debris bed is considered 0.7 [8].

4.3.2 Structural Boundary Conditions

Subsequent to thermal analysis, the same finite element models have been used for structural analysis with structural compatible finite elements. Symmetry boundary condition has been applied on the plane of symmetry. In addition to this, displacement boundary condition has been applied at support locations.

5 Results

Thermal analysis has been performed considering moderator boil-off condition as an initial condition and analysed till steady state is achieved. Steady-state is defined as the state when the heat flux on the outer surface of the Calandria vessel becomes asymptotic, i.e., remains constant.

5.1 Calandria End-Shield Assembly

Analyses have been carried out for three cases, i.e., considering heat transfer coefficient (HTC) of 3000 W/m^2-K (with radiation), HTC of 2000 W/m^2-K (with radiation) and HTC of 2000 W/m^2-K (without radiation) on the outer surface of the Calandria shell.

Comparing the temperature distribution in the assembly for these cases, it is seen that the maximum surface temperature is observed for the condition where the heat transfer coefficient on the outer surface of the Calandria shell is 2000 W/m^2-K. Based on this, the results for this case will be discussed.

Under the steady-state condition, the temperature distribution in the assembly for HTC of 2000 W/m^2-K (with and without radiation heat transfer) is shown in Fig. 8. Maximum corium temperature is observed as 3319 K, irrespective of the thermal boundary conditions. Figure 9 shows the variation of the outer and inner surface temperature of Calandria main shell for the conditions: with and without radiation. Maximum average wall temperature in the assembly is observed as 507.3 K. The maximum heat flux at various sections (Fig. 2) of the outer surface of the Calandria shell (sec 1–1), annulus plate (sec 2–2), small shell (sec 3–3) and CSTS (sec 4–4) are observed to be 100.5 kW/m^2, 82.6 kW/m^2, 42.5 kW/m^2 and 32.2 kW/m^2, respectively. The observed heat fluxes are found to be less than the critical heat flux of 425 kW/m^2 [14]. This has demonstrated the availability of an effective heat sink for providing the cooling of the corium in the vessel.

Subsequent to the thermal analysis, nonlinear structural analysis is performed considering the corium weight and self-weight of the assembly. Figure 10 shows the distribution of maximum stress intensity and von Mises plastic strain intensity in the assembly. The maximum stress intensity is observed as 404 MPa in the outer shell of
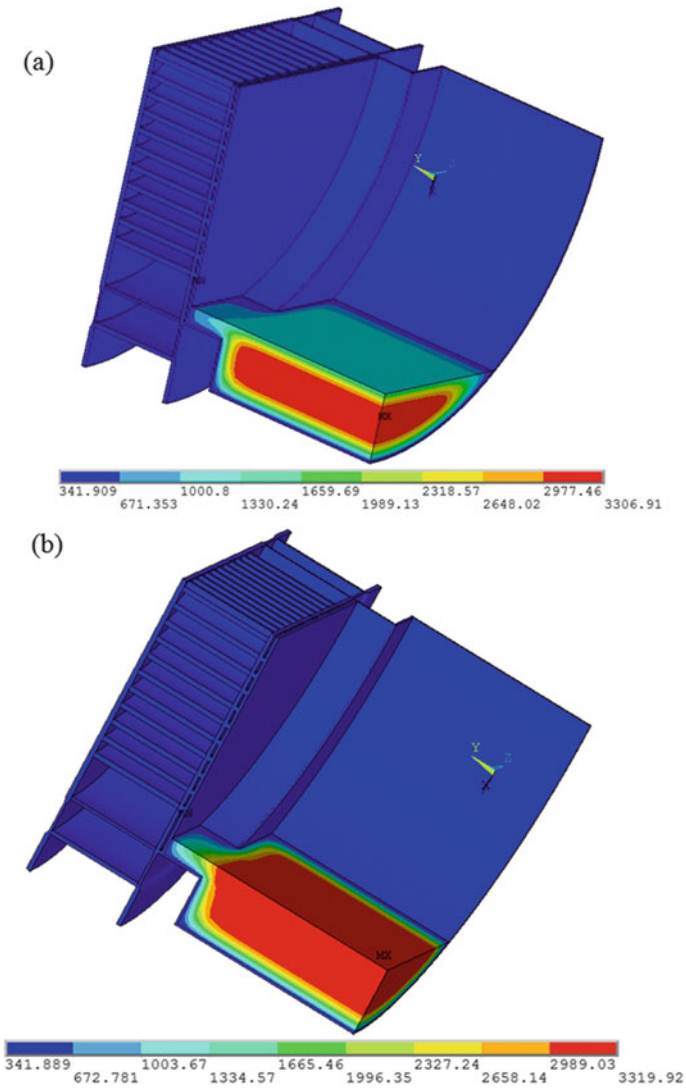
(a)

341.909   1000.8   1659.69   2318.57   2977.46
         671.353   1330.24   1989.13   2648.02   3306.91

(b)

341.889   1003.67   1665.46   2327.24   2989.03
         672.781   1334.57   1996.35   2658.14   3319.92

Fig. 8 Temperature contour at the steady-state condition for **a** HTC $= 2000$ W/m^2-K, with radiation **b** HTC $= 2000$ W/m^2-K, without radiation

the assembly. The maximum von Mises plastic strain intensity is observed as 0.48% at the main shell and the annulus plate junction.
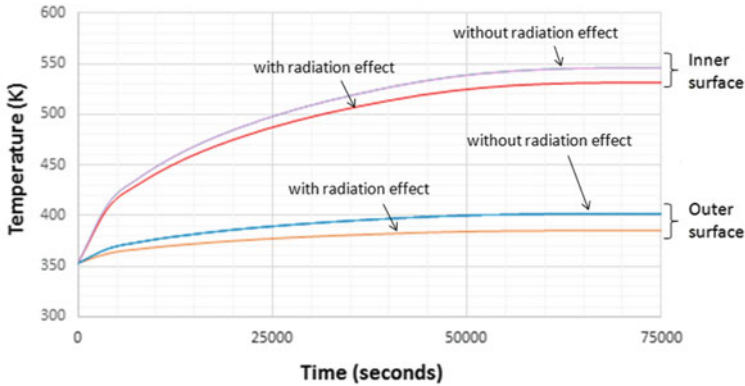
Fig. 9 Variation in the outer and inner surface temperature of Calandria main shell

5.2 Moderator Outlet Nozzle

Moderator nozzle-shell junction along with corium has been analysed using the axisymmetric finite element model. For thermal and structural analysis, PLANE 77 and PLANE 183 elements are used. These elements are eight nodded and are well suited to model curved boundaries [7]. Modelling of the Calandria shell portion and corium has been carried out in such a way that sufficient length of Calandria in the axial direction (~2.5 times the diameter of nozzle opening) is considered to take into account the local effect. Corium has been modelled up to a height of 704 mm which was arrived at based on the equivalent density of core debris. Structural stiffness offered by the Calandria end-shield assembly is considered as per the design.

Here also, the thermal analysis has been performed from the initial moderator boil-off condition till the steady-state is reached. Figure 11 shows the temperature contours under steady-state for the conditions, with and without radiation heat transfer. Figure 12 shows the variation of temperature along the centre line of the nozzle from the corium top to the nozzle location. The minimum centre line temperature in the nozzle is observed as 519.4 K which is less than the corium solidus temperature of 2773 K. This means that the corium will solidify in the nozzle, resulting in the formation of a freezing plug and will assist in retaining the corium within the Calandria vessel. The maximum heat flux on the outer surface of the Calandria vessel at steady-state condition is observed as 108.5 kW/m^2, which is less than the critical heat flux of 425 kW/m^2 [14].

Structural nonlinear analysis has been performed considering the corium weight, self-weight of the assembly and thermal loads. The thermal loads obtained from thermal analysis at steady-state condition have been applied at nodal temperature. The structural stiffness of the corium is not accounted for in the analysis. The maximum stress intensity observed in the Calandria shell is 245 MPa. The maximum plastic strain is observed as 0.45% and occurs at the Calandria shell-nozzle junction.
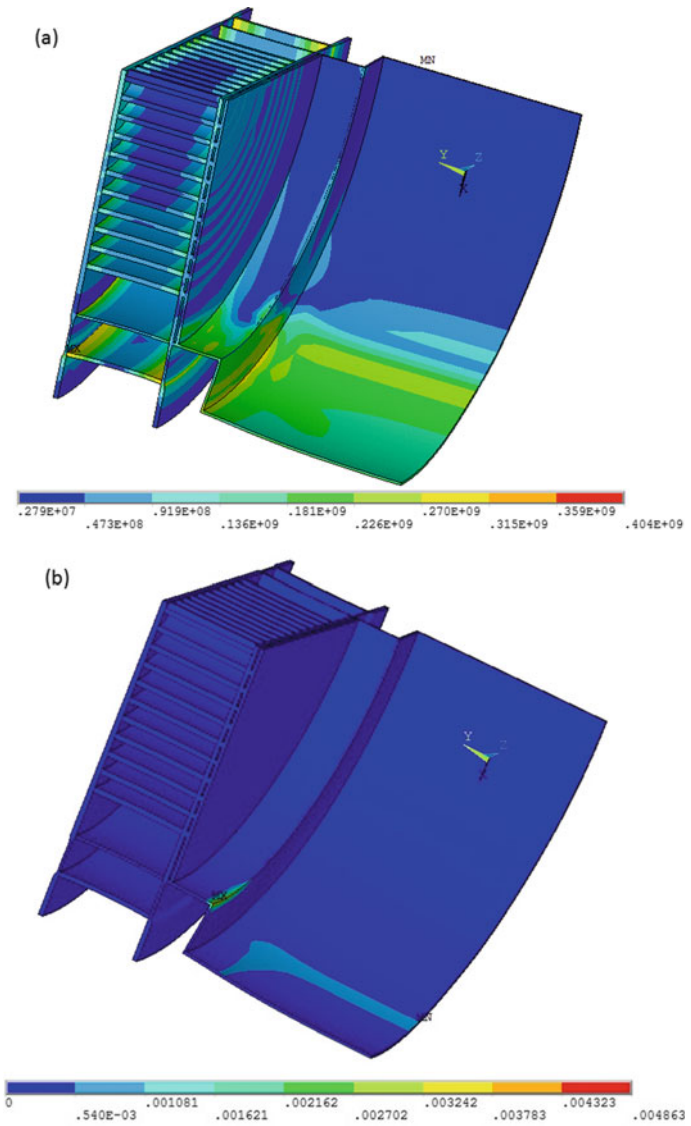
Fig. 10 **a** Maximum stress intensity distribution **b** von Mises plastic strain intensity distribution in Calandria end-shield assembly

5.3 Moderator Piping Analysis

Analysis of moderator piping has been carried out for the thermal loads and the sustained loads. For the sustained load, it has been assumed that corium is filled in the pipe up to the first bend connected to the moderator outlet nozzles and the
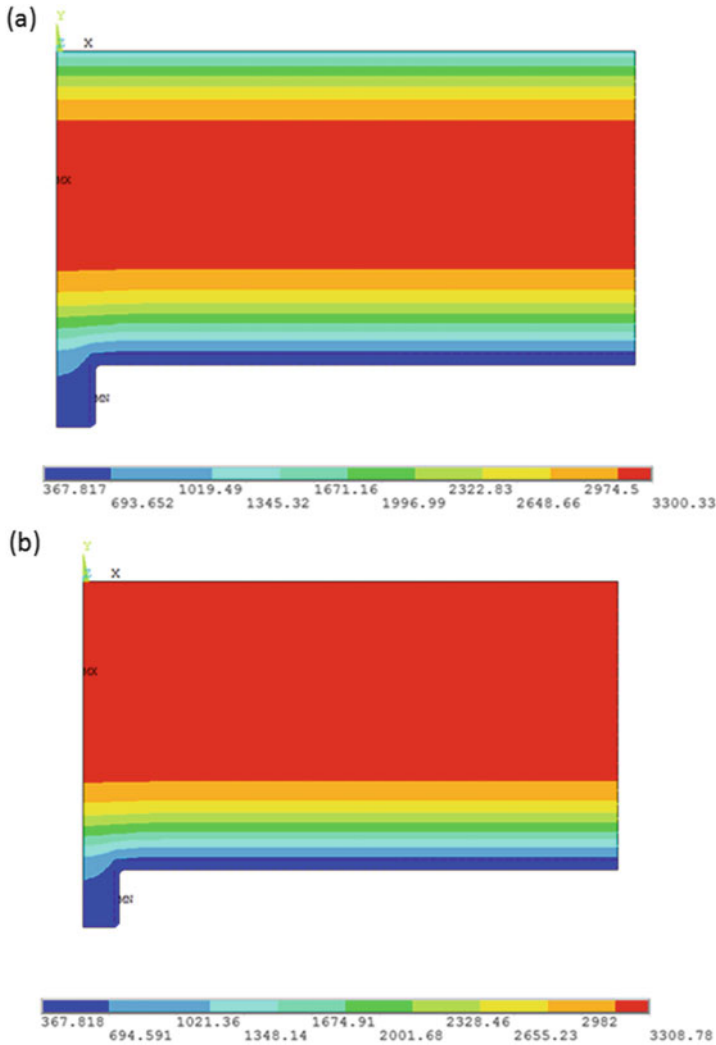
Fig. 11 Temperature contour at steady-state condition considering **a** HTC = 2000 W/m²-K, with radiation **b** HTC = 2000 W/m²-K, without radiation

remaining portion is filled with water. In the analysis, the average temperature of the Calandria shell is taken as 390 K. The thermal anchor movement at the moderator outlet nozzle is calculated from the thermal displacement of Calandria end-shield assembly. Figure 13 provides stress intensity distribution in the piping. The maximum stress intensity in the piping is observed as 351.8 MPa which is less than the allowable stress intensity limit of 420.8 MPa (2Sy) as per ASME Section III, NB. Thus, moderator outlet piping will retain its structural integrity and hold the molten corium within the Calandria vessel under severe accident scenario.

Fig. 12 Temperature
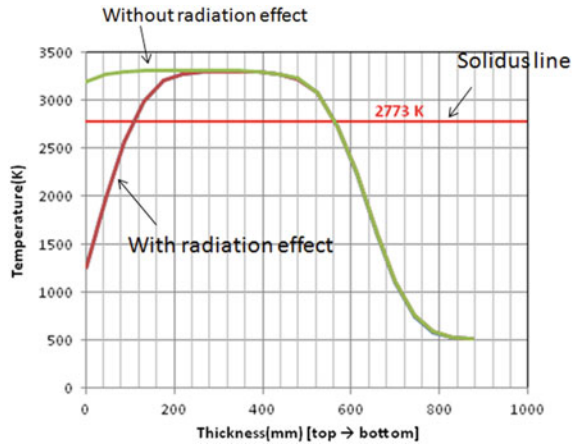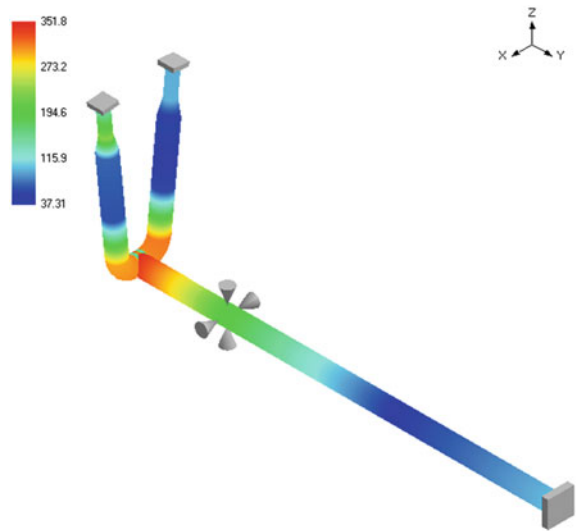distribution along the centre
line of the moderator outlet
nozzle

Fig. 13 Stress intensity
distribution in the moderator
piping

6 Discussion

Thermo-mechanical analysis of Calandria end-shield assembly has been carried out
for in-vessel retention of the corium in the Calandria. Assessment has also been
carried out for the moderator outlet nozzle and connected piping. Thermal transient
analysis has been carried out considering the decay heat simulating the late phase
of severe accident condition. Figure 14 shows the schematic of the geometrical
configuration along with the heat transfer path of corium in the Calandria. The heat
generated in the corium is transferred to the Calandria vault water via the Calandria
vessel through conduction in the downward direction and through radiation in the

Fig. 14 Schematic of heat transfer phenomenon under in-vessel retention of corium
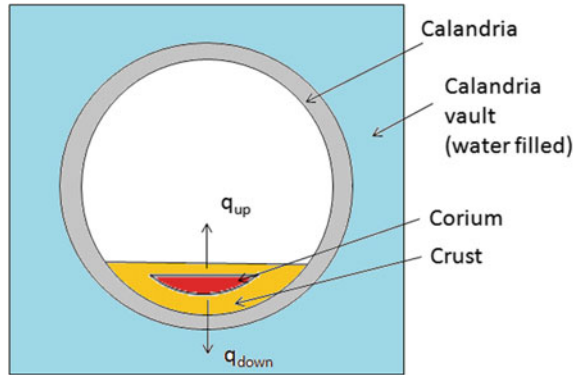
upward direction. The maximum heat flux from the Calandria vessel wall to the Calandria vault water is observed as 100.5 kW/m^2(downward direction), which is less than the critical heat flux of 425 kW/m^2. This has demonstrated the availability of an effective heat sink. The overall heat transfer in the downward direction from the corium to the Calandria vault water is given by

$$Q = U \times A \times (T_{corium} T_{pool})$$ (3)

where U is the overall heat transfer coefficient, A is the surface area, T_{corium} is the corium temperature and T_{pool} is the Calandria vault temperature.

Overall heat transfer coefficient depends on the thermal conductivity of the corium and Calandria vessel and the convective heat transfer coefficient. The analysis revealed that the thermal conductivity of the corium plays a vital role in limiting the inside surface temperature of the Calandria vessel. Solidified corium in contact with the vessel is referred to as the crust which acts as a heat insulator [14]. Due to the formation of the crust, a steep gradient is observed within the corium and the maximum temperature at the inside surface of the Calandria is limited to 550 K (Fig. 9). Similar observations are made in the analysis of the moderator outlet nozzle. The analysis revealed that the maximum average temperature in the assembly is 507 K which is well below the temperature at which creep initiates and also lower than the temperature (1173 K) required for material ablation [16]. Further, the centerline temperature of the nozzle is observed as 519.4 K which is less than the solidus temperature of 2773 K and confirms the possibility of forming of freezing plug at nozzle/penetration opening.

Stress analysis of the assembly has been carried out considering sustained loads and thermal loads. Thermal anchor movements have also been accounted for in the analysis. It has been observed that by virtue of the flexibility provided in the design of the assembly, thermal strains (0.48%) are observed to be less than the limiting value of 5%. Further, maximum stress intensity in the piping is observed as 351.8 MPa, which is less than the allowable stress limit of 420.8 MPa (twice the yield strength).

Further, no plastic instability or collapse of the assembly or connected piping is observed.

7 Conclusion

Structural integrity assessment of Calandria end-shield assembly, moderator outlet nozzles and connected piping has been carried out. The assessment has been made based on the following criteria:

(a) Heat flux is observed less than critical heat flux which demonstrates the effectiveness of heat sink.

(b) Maximum average temperature is observed less than the temperature at which creep initiates.

(c) Centreline temperature at penetration location is found less than solidus temperature. Thus, corium will form a freezing plug at the nozzle/penetration openings.

(d) Equivalent inelastic strain is observed less than the limiting value of 5%. Thus, assembly will not be subjected to excessive local plastic deformation.

(e) No plastic instability or collapse of the assembly or connected piping is observed.

Based on the above observations, the structural integrity of Calandria end-shield assemblies for in-vessel corium retention of standard 220 MWe IPHWR has been demonstrated with SAMG provisions.

References

1. Muktibodh UC, Dixit KB, Ingole SM, Parkash B (2016) In: Rao KR (ed) Design of Indian pressurized heavy water reactors, global application of the ASME boiler & pressure vessel code. ASME Press
2. IAEA-TECDOC-1594 (2008) Analysis of severe accident in pressurized heavy water reactors
3. Design manual on End shield (1999)
4. Luxat Dl, Luxat JC (2007) Calandria vessel integrity under severe accident loads, paper # J07/2, SMiRT 19, Toronto
5. Nicolici S, Dupleac D, Prisecaru I (2013) Numerical analysis of debris melting phenomenon during late phase CANDU 6 severe accident. Nucl Eng Des 254:272–279
6. Luxat J (2009) Thermal hydraulic aspects of progression of severe accidents in CANDU reactors. Nuclear technology, vol 167
7. ANSYS Software User Manual
8. Lee HT, Chen CT (2011) Numerical and experimental investigation in to effect of temperature field on sensitization of AISI 304 in butt welds fabricated by Gas Tungsten Arc welding. Mater Trans 52(7):1506–1514
9. ASME Section III, Division I, (2017)
10. Mohta K, Gupta SK, Mukhopadhayay D, Chattopadhyay J, Soupramanien C, Swaminathan J (2019) High temperature tensile and creep properties of calandria material SS 304L, report no. BARC/2019/E/011

11. Dombrovskii LA, Zaichik LI, Zeigarnik YA (1998) Numerical simulation of the stratified-corium temperature field and melting of the reactor vessel for a severe accident in a nuclear power station. Therm Eng 45(9):755–765
12. Internal Design Report (2001).
13. Verma PK, Kulkarni PP, Pandey P, Prasad SV, Nayak AK (2021) Critical heat flux on curved calandria vessel of Indian PHWRs during severe accident condition. J Heat Transf 143
14. Prasad SV, Nayak AK (2016) Experimental investigation of heat transfer during severe accident ofa Pressurized Heavy Water Reactor with simulated decay heat generation in molten pool inside calandria vessel. Nucl Eng Des 303:75–87
15. Janna WS (2000) Engineering heat transfer
16. Nitheanandan T (2015) Emerging trends in PHWR safety-post fukushima measures, CANSAS-NRTHS

Finite Element Simulation of Residual Stresses in Friction Stir Welding of AA2219 Plates

Krishnajith Jayamani, K. Abhishekaran, R. Vasudevan, H. M. Umer, and A. K. Asraff

Abstract Friction stir welding (FSW) is a solid-state welding process in which the temperatures never exceed the melting point of the work-piece material. The process is widely used in the aerospace industry for welding aluminum alloys, and aluminum–lithium alloys are used in the fabrication of propellant tanks. Knowledge of the residual stresses developed due to the welding process is an important parameter used in the design of propellant tanks. The present work details the finite element simulation of friction stir welding of two flat plates made of AA2219 material, a material used for fabrication of the propellant tanks used in the launch vehicles of ISRO. The simulation is performed using a nonlinear, fully coupled thermal-structural finite element analysis using ANSYS (version 18.1) code. The computational model involves two work-plates and the FSW tool modeled using three-dimensional solid elements and the effect of the fixtures supporting the work-piece is brought in using appropriate structural and thermal boundary conditions. The constitutive models used for the analysis are capable of simulating the frictional heat generation and the associated temperature-dependent mechanical response of the material. The entire sequence of operations involved in the welding process from the initial plunge of the tool to the final removal of clamps after cooling is simulated.

It is seen that the predicted temperatures on the work-piece fall with 70–90% of the melting temperature of this particular alloy. The predicted residual stress pattern shows a characteristic M-shaped distribution along the width of the work-piece which agrees well with results reported in the literature.

Keywords Friction stir welding · Residual stress · Finite element analysis

---

K. Jayamani (✉) · K. Abhishekaran · R. Vasudevan · H. M. Umer · A. K. Asraff
Mechanical Design & Analysis Entity, Liquid Propulsion Systems Centre, Valiamama,
Thiruvanathapuram, India
e-mail: krishnajith@lpsc.gov.in

1 Introduction

Friction stir welding (FSW), a solid-state welding process, is developed by The Welding Institute (TWI), the UK in 1991. FSW is an attractive option in welding materials like aluminum that are difficult to weld using conventional welding processes [1, 4]. The FSW process, in general, involves the following steps:

(1) Plunge: A specially shaped tool is positioned on the butting faces of work-pieces (where joint is to be established). The tool is then pressed down onto the work-piece with a pre-defined load.
(2) Dwell: The tool is rotated while being pressed against the work-piece for a specified amount of time. This generates heat due to friction between the tool and the work-pieces as well as due to plastic deformation of the work-pieces.
(3) Traverse: The rotating tool is moved along the indented weld line. This causes the softened material ahead of the tool to flow backward. This softened material on cooling forms a continuous joint along the length of the traverse [1, 2]. Figure 1 shows the schematic of the process.

Unlike in the case of conventional welding processes like gas welding, there is no melting of the workpiece in FSW. The temperatures are generally within 70–90% of the melting point of the material [3]. The local heating up of the work-piece material and subsequent cooling down while being rigidly clamped generates welding residual stress. These stresses are inimical to the structural integrity, fatigue life and corrosion resistance of the weld. Hence prior knowledge of the distribution and magnitude of residual stress in the weld is an important input for the design of pressure vessels, especially thin-walled ones used in the aerospace industry. The present study aims at the evaluation of residual stress developed in a weld between two sheets of aluminum alloy by means of finite element simulations.
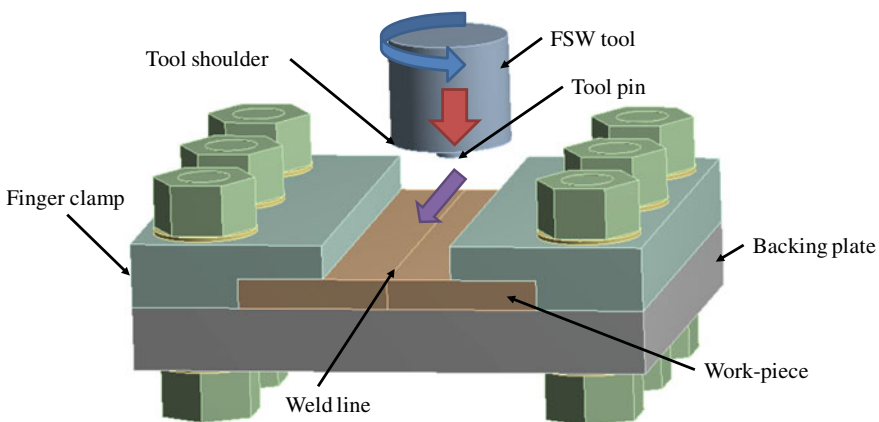

Fig. 1 Friction stir welding process

2 Simulation of FSW Using ANSYS

The behavior of the system while being friction stir welded is nonlinear and involves significant interaction between mechanical and thermal fields. A numerical simulation of this process is beneficial as it enables the study of different aspects of the process and the sensitivity of process parameters without elaborate welding trials [2].

There are several methods presented in the literature that detail the numerical modeling of FSW [2]. Depending on the focus of study, they can be either numerical simulations on a global level or at a local level wherein the aim is at studying the variation of stress at the vicinity of the weld line. The present study uses the finite element analysis-based (FEA) method proposed by Chen and Kovacevic [3]. Simulation of the welding process is done by means of a nonlinear coupled analysis using the ANSYS APDL finite element package. Both tool and the work-pieces are modeled using a three-dimensional 20-noded coupled-field solid element named SOLID226 used for analysis that has four degrees of freedom at each node: three translations along orthogonal axes and a temperature DOF. Contact elements are defined between the tool and the work-pieces. Heat is generated by the frictional resistance at the contact locations when the tool is pressed against and rotated against the work-piece [3, 4].

2.1 Problem Definition

The residual stresses are studied by simulating the friction stir welding of two plates of AA2219 alloy. This alloy is widely used in the aerospace industry as a structural material and is used to fabricate launch vehicle propellant tanks of ISRO.

Each work-piece is 100 mm long, 35 mm wide and 7 mm thick. While being welded, the work-pieces would be supported at the base using a thick metallic plate and would be clamped down using rigid fixtures called finger clamps. The distance between such finger clamps is 30 mm. The tool made of high-strength steel has a shoulder diameter of 29.8 mm while the tool pin is 9 mm in diameter and has a height of 6.8 mm.

2.2 Finite Element Model

The computational domain is represented by a three-dimensional finite element model created using 3039 number of SOLID226 elements. Only the tool and the work-pieces are modeled and the effect of the backing plate and clamps are represented by appropriate boundary conditions given to this model. The finite element model is shown in Fig. 2.

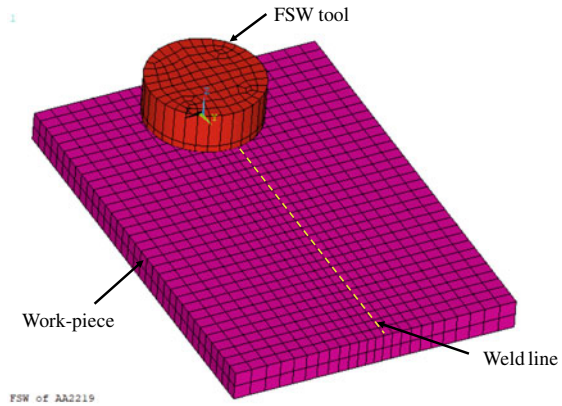**Fig. 2** SOLID226 element
used for simulation

Table 1 Mechanical
properties of tool material

Elastic modulus (N/mm^2)	680,000
Poisson's ratio	0.22
Thermal conductivity (W/m^{o}C)	100
Specific heat (J/kg^{o}C)	750

The tool pin is responsible only for about 2–3% of the total heat generated [5].
Hence the effect of tool pin is neglected [3] and the tool is modeled as a cylinder
having a uniform diameter of 29.8 mm. The tool is assumed to exhibit rigid, linear
behavior, and the material properties used are enumerated in Table 1.

The elasto-plastic behavior of work-piece material is simulated by using a bilinear
isotropic (BISO) hardening plasticity model. Temperature-dependent values of yield
strength of AA2219 used for the analysis are shown in Fig. 3. Variation of thermal
properties and coefficient of friction are shown in Figs. 4 and 5, respectively [6, 7].

Fig. 3 Variation of yield
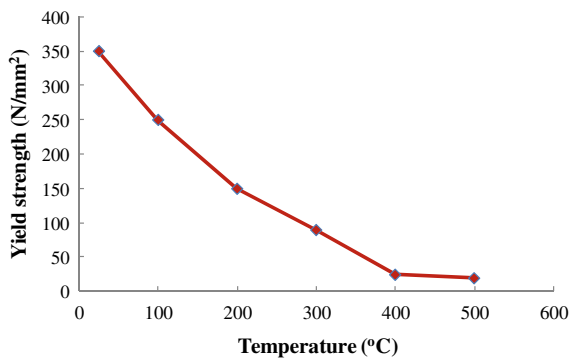strength with temperature

Fig. 4 Variation of thermal properties with temperature
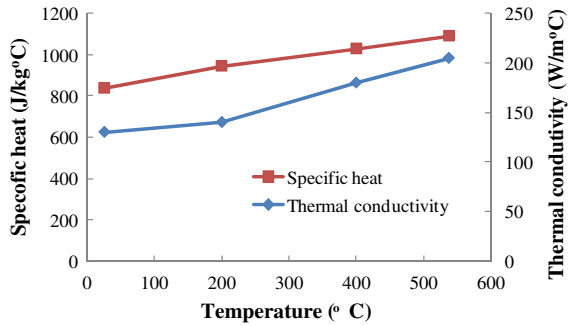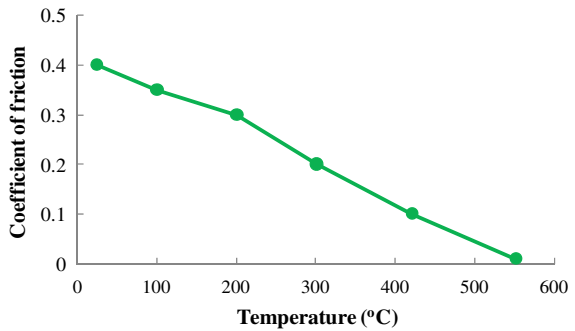

Fig. 5 Variation of coefficient of friction with temperature


2.3 Sequence of Loading

The different steps involved in the FSW process are simulated in the finite element analysis through different load steps. The details of such load steps are given in Table 2.

The tool is pressed against the work-pieces by a force of 31 kN. The rotational velocity of the tool is 400 rpm and the translational speed along the weld line is 250 mm/min.

Table 2 Sequence of loading simulated using ANSYS

Step no	End time (s)	Description
1	1	Tool plunges into the work-pieces
2	13	Rotation of tool on work-pieces (Dwell)
3	30.83	Tool Rotation + translation along weld-line (Traverse)
4	31.83	Tool retracted up at end of weld
5	427.83	Set-up allowed to cool down to ambient temperature
7	428.83	Clamp restraints removed

Fig. 6 Mechanical
boundary conditions
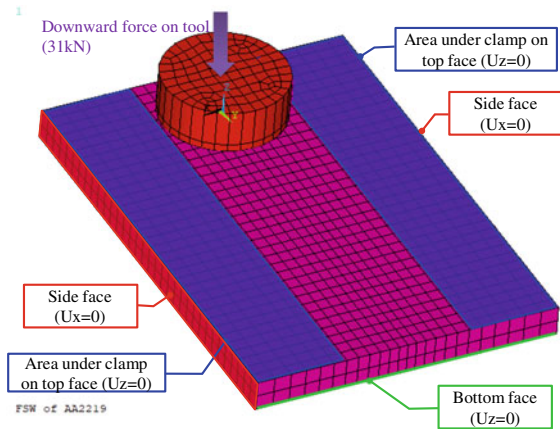
2.4 Mechanical Boundary Conditions

Mechanical boundary conditions are so imposed on the finite element model that they match conditions during the actual welding process. The nodes of the model where the backing plate would have supported it are restrained in the normal direction. Structural degrees of freedom of nodes falling within the width of finger clamps are arrested to replicate the rigid clamping. The tool is constrained such that only rotation about its longitudinal axis and translation along the weld direction are permitted. The mechanical boundary conditions are shown in Fig. 6.

2.5 Thermal Boundary Conditions

Convection from the free surfaces is the main reason for heat loss from the work-piece. Additionally, backing plate and finger clamps are significant thermal masses and act as heat sinks. Hence, a heat transfer coefficient of 100 W/m^2 is assigned for the top surfaces under the finger clamps and a value of 300 W/m^2 is used for the bottom surface. A heat transfer coefficient of 30 W/m^2 which corresponds to the value for free convection from aluminum to air is specified on all other surfaces [4].

2.6 Contacts

Contact elements are defined between tool and work-pieces using TARGET170 elements and CONTACT174 elements. This frictional contact is responsible for bulk of the heat generation that occurs when the rotating tool is pressed against work-pieces and travels along their butting faces. It is assumed that the entire energy

dissipated by friction is converted to heat. It is further assumed that the majority (95%) of frictional heat generated goes into the work-piece and only 5% is absorbed by the tool.

Contact between the work-pieces is also defined using TARGET170 elements and CONTACT174 elements. A relatively high value of contact conductance is defined between the surfaces to ensure proper thermal contact between the plates. Welding is assumed to occur at contact locations where the temperature exceeds 350 °C (roughly 70% of melting temperature). Hence for this contact pair, the contact definition is changed to "bonded" for temperatures beyond 350 °C. Once bonding occurs, the status of the contact pair remains unchanged even if temperature decreases subsequently.

Additionally, a rigid contact pair is defined between nodes at the top surface of the tool and a pilot node at the center of the surface. This effort ensures that the boundary conditions need to be applied only on the pilot node alone.

3   Results of Finite Element Simulations

The temperature distribution on the work-piece at the end of dwell is shown in Fig. 7. The heating is localized around the portion under the tool and the maximum temperature is 427 °C. This agrees very well with the expected temperature range of 70–90% of the melting temperature.

As the tool traverses along the intended weld line, the peak temperature moves with it. The maximum temperature after the end of the traverse is 449 °C. When the tool is retracted after reaching the end of the weld, the temperature starts to fall and finally reaches the ambient temperature after 400 s. The time-history of the peak temperature on the top and bottom surfaces of work-piece is shown in Fig. 8, which agrees well with is expected pattern [8, 10].

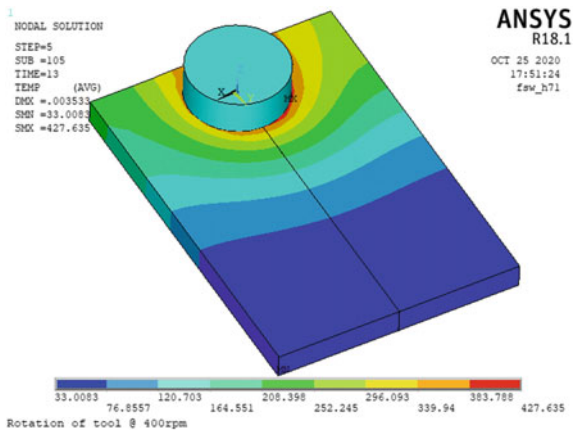**Fig. 7** Temperature contours at the end of dwell step

Fig. 8 Time-history of peak
temperature at top and
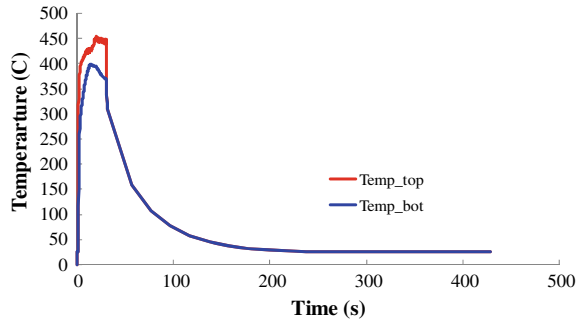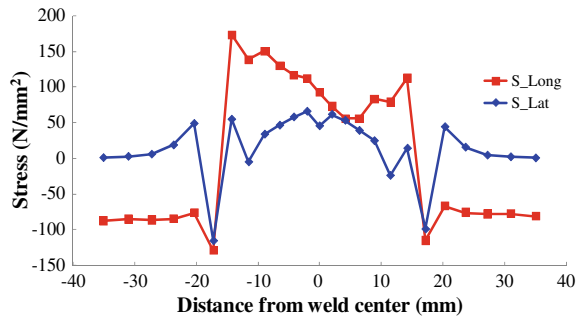bottom of work-piece

Fig. 9 Longitudinal and
lateral residual stress

After it has reached the ambient temperature, all boundary conditions on the finite element model are removed. This simulates the release of clamps after the welding process is complete, and stresses remaining on the model at this instant would be the residual stress. The variation of residual stress along the weld (S_long) and normal to it (S_lat) is plotted as a function of distance from weld center in Fig. 9.

The residual stresses pattern shows a characteristic M-shaped variation. Tensile residual stress along the weld line is the predominant one near the weld. The peak longitudinal stress of 174 N/mm^2 occurs at a region that roughly corresponds to the shoulder width of the tool. The peak values of longitudinal and lateral tensile stresses at the weld nugget are 93 N/mm^2 and 46 N/mm^2, respectively. In regions away from the weld region, both longitudinal and lateral residual stresses are of a compressive nature. These observations are consistent with the expected behavior of residual stress for aluminum alloys [9, 10].

4   Discussions and Conclusions

Friction stir welding of two plates made of AA2219 alloy is simulated using coupled thermo-mechanical finite element model in ANSYS. Thermal results, as well as residual stress distribution from finite element simulations, show a good match with

their expected patterns and values and those reported in the literature. The approach shows great promise in studying the behavior of joints made using FSW.

References

1. Mubiayi PM, Akinlabi E, Mamookho M (2018) Current trends in Friction Stir Welding (FSW) and Friction Stir Spot Welding (FSSW): an overview and case studies. Springer, Switzerland
2. Dialami N, Chiumenti M, Cervera M et al (2017) Challenges in thermo-mechanical analysis of friction stir welding processes. Arch Comput Methods 24(1):189–225
3. Chen C, Kovacevic R (2004) Thermo mechanical modelling and force analysis of friction stir welding by the finite element method. Proc Inst Mech Eng C J Mech Eng Sci 218:509
4. Aziz SB, Dewan MW, Huggett DJ (2016) Impact of Friction Stir Welding (FSW) process parameters on thermal modeling and heat generation of aluminum alloy joints. Acta Metall Sin 29:869–883
5. Kaid M, Zemri M, Brahami A, Zahaf S (2019) Effect of friction stir welding (FSW) parameters on the peak temperature and the residual stresses of aluminum alloy 6061–T6: numerical modelisation. Int J Interact Des Manuf (IJIDeM) 13:797–807
6. Kang S, Jang B, Song H (2015) Residual stresses analysis of friction stir welding using one-way FSI simulation. J Mech Sci Technol 29:1111–1121
7. Metallic Materials Properties Development and Standardization (MMPDS-09). FAA, Battelle Memorial Institute, Atlantic City, NJ, 2005
8. Farajkhah V, Liu Y (2017) Effect of clamping area and welding speed on the friction stir welding-induced residual stresses. Int J Adv Manuf Technol 90:339–348
9. Kumar N, Mishra RS, Baumann JA (2014) Residual stresses in friction stir welding. Butterworth-Heinemann USA
10. Zhang Z, Zhang H (2007) The simulation of residual stresses in friction stir welds. J Mech Mater Struct 2(5)

An FEA-Based Study on the Damage Behavior of CFRP Hybrid Joint Under Tensile Loading

Isha Paliwal and M. Ramji

Abstract A 3D finite element analysis has been carried out to estimate the damage evolution in the CFRP adherend joined using hybrid joint under tensile loading. The load versus displacement behavior of bonded, bolted, and the hybrid joint is compared. Further, damage growth in the CFRP laminate joined using the bolted and the hybrid joint has been compared. From the results, it has been observed that the hybrid joint exhibits significantly higher strength. The failure mechanism of the bolted and the hybrid joint was observed to be different even though the damaged area accumulated before the final failure is approximately the same.

Keywords Hybrid joint · FEA · Bolt load transfer · CFRP · Progressive damage

1 Introduction

The extensive use of composite materials in aircraft primary structures led to the increasing interest of many researchers to improve the joint efficiency of existing joint techniques as well as develop a newer approach for composite material. The conventional joints used in composite structures are bolted, bonded, and hybrid (bonded/bolted) joints. The hybrid joint exhibits the advantages of both adhesively bonded and bolted. Hence, they have the potential to meet the requirements for primary aircraft structures joint requirements.

To understand the significance of the hybrid joint subjected to static and fatigue loading and the effect of various parameters on joint strength, many studies have been carried out in the previous two decades. Hart Smith [1] has performed a detailed analysis and found that the hybrid joint could be used as a safe-fail mechanism as it prevents sudden failure. Kelly et al. [2] observed that the hybrid joint has shown higher strength than the bonded joint with low modulus adhesive. Franco et al. [3] have observed that with minimum overlap length the hybrid joint exhibits significantly greater static strength, energy absorption, and damage tolerance. Bodjona

I. Paliwal · M. Ramji (✉)
Engineering Optics Lab, Department of Mechanical and Aerospace Engineering, IIT Hyderabad, Hyderabad, India
e-mail: ramji_mano@mae.iith.ac.in

et al. [4] have carried out a detailed study to understand the effect of various joint parameters on the load transfer through the bolt in the hybrid joint and found that the adhesive yield strength, adhesive hardening slope, and edge to bolt diameter has got a major influence on the load transfer. Li et al. [5] have also performed a parametric study to understand the effect of various design parameters on hybrid joint strength, joint stiffness and they observed that adhesive strength, bolt strength, width to bolt diameter ratio, and edge to bolt diameter ratio have got a positive influence on the joint behavior. Nabil et al. [6, 7] have done static and fatigue analysis with multiple bolts in the hybrid joint and found fatigue life of hybrid joint is higher for hybrid joint even with weak bond-line than the bonded joint, and with more bolts, fatigue life has increased unlike the static strength of the hybrid joint.

The hybrid joint has a complex failure mechanism due to multiple design factors. Hence, it is important to understand the failure behavior under the influence of those selected parameters. A very few studies focus on the damage analysis of the hybrid joint. In this investigation, the damage assessment of the hybrid joint subjected to tensile loading is presented. A progressive damage model (PDM) has been developed using a finite element framework to capture the damage evolution and prediction of the ultimate strength of the hybrid composite joint specimen.

2 Finite Element Model

Two laminates that are partially overlapped, when they are bonded using adhesive material and fasten by the bolt are called a hybrid joint. The details about the joint configuration along with the dimensions are shown in Fig. 1 realized as per the ASTM D5791 standard. Material characterization of the carbon-epoxy unidirectional prepreg tape (Bhor Preg UC 202-A45-38) laminates was carried out experimentally
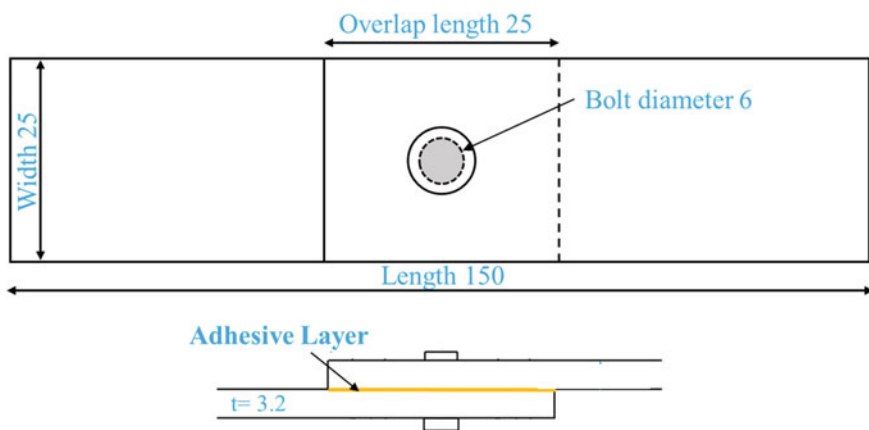

Fig. 1 The dimensions of the hybrid joint specimen (*Note:* All dimensions are in mm)

Table 1 Mechanical material properties of CFRP

Material properties of the CFRP prepreg	Values
Longitudinal modulus, E_{11} (GPa)	141.40
Transverse modulus, E_{22} (GPa)	9.6
In-plane Poisson's ratio, $(\upsilon_{12},\ \upsilon_{13})$	0.31
In-plane Poisson's ratio, υ_{23}	0.44
In-plane shear modulus $(G_{12},\ G_{13})$ (GPa)	5.6
In-plane shear modulus G_{23} (GPa)	3.04
In-plane shear strength, S_{12} (MPa)	81.34
In-plane shear strength, S_{23} (MPa)	69.7
Longitudinal tensile strength, X_T (MPa)	1777.1
Transverse tensile strength, Y_T (MPa)	26.33
Longitudinal compressive strength, X_C (MPa)	830.2
Transverse compressive strength, Y_C (MPa)	105.5

using an in-house DIC technique. The coupons were cut from the CFRP laminates and tests were carried out on it as per the recommendations given in the ASTM standards. The average values of the three test coupons were considered and they are summarized in Table 1. The CFRP adherend has a stacking sequence $[0/45/90/\text{-}45]_{2S}$ and the nominal thickness of each ply is measured to be 0.2 mm. The commercial finite element tool ABAQUS/Standard (Version 2017) is used for the study. An eight-noded brick element (C3D8R) with reduced integration is used to develop the 3D finite element model.

The solid brick element C3D8 and C3D20 with reduced or full integration can be used. The C3D8R element is preferred in the bolted joint subjected to tensile/compressive loading as it has a low computational cost without compromising the accuracy significantly. But for bending load, the shear locking occurs with C3D8 elements, hence for that loading the C3D20 elements are the preferable choice. The mesh size is chosen based upon the convergence study. As illustrated in Fig. 2 the finer mesh around the hole is assigned to get accurate and coarse mesh away from the hole boundary to reduce the computational cost. One element per ply is assigned along with the thickness of the laminate.

The cohesive contact approach (zero adhesive thickness) is used to model the adhesive layer with material properties given in Table 2. The damage in the adhesive layer is modeled using traction–separation law followed by the quadratic stress criteria for damage initiation and mixed-mode damage evolution based on the energy by Benzeggagh-Kenane (BK) [8] with power 2.07. The bolt with material properties (Table 2) is modeled as a single unit including the nut, to reduce the complexity of the model. Bolt surfaces that are in contact with the laminate are modeled using contact pairs with 0.2 friction. On the left face of the specimen, all the DOFs of nodes are arrested and on the right face, a finite displacement along the u_x direction is given with $u_y = 0$ and $u_z = 0$. It is iteratively solved and the FEM-based solution allows computing the increment of the laminate's homogenized strain field. By involving the
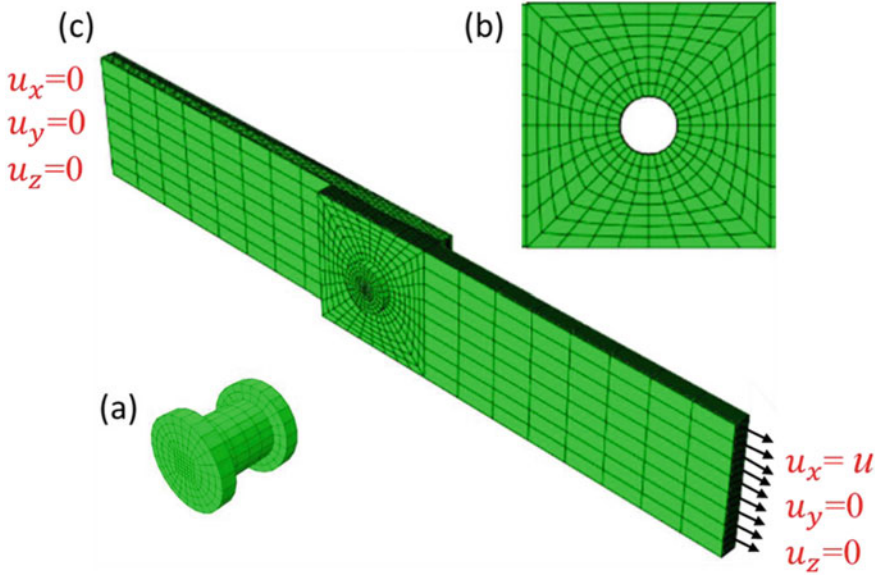
Fig. 2 Mesh modeling of the assembly and its parts bolt (**a**), around the hole (**b**), and the joined laminate (**c**) with boundary conditions

Table 2 Adhesives (Ref. [9]) and bolt material properties (Ref. [5])

Adhesive (Araldite 2015) material properties	
Young's modulus, E (MPa)	1860
Shear modulus, G (MPa)	560
Normal strength, σ_n (MPa)	32.7
Shear strength, τ_n (MPa)	14.6
Fracture toughness Mode I, G_{IC} (N/mm)	0.534
Fracture toughness Mode II, G_{IIC} (N/mm)	2.97
Bolt Material Properties	
Young's modulus, E (GPa)	194
Poisson's ratio	0.33

constitutive relationships with the stiffness matrix, the strain field is used to compute the increment of the stress field in each layer.

2.1 Progressive Damage Model and Its Validation

Three-dimensional stress-based Hashin failure criteria [10] are used to predict the failure modes, including fiber failure, matrix failure under tension, and compression.

Table 3 Composite laminate failure initiation criteria

Mode of the failure	Failure criteria
Fiber tensile failure ($\sigma_{11} > 0$)	$\left(\frac{\sigma_{11}}{X_T}\right)^2 + \left(\frac{\sigma_{12}}{S_{12}}\right)^2 + \left(\frac{\sigma_{13}}{S_{13}}\right)^2 \geq 1$
Fiber compression failure ($\sigma_{11} < 0$)	$\left(\frac{\sigma_{11}}{X_C}\right)^2 \geq 1$
Matrix tensile failure ($\sigma_{22} > 0$)	$\left(\frac{\sigma_{22}}{Y_T}\right)^2 + \left(\frac{\sigma_{12}}{S_{12}}\right)^2 + \left(\frac{\sigma_{23}}{S_{23}}\right)^2 \geq 1$
Matrix compression failure ($\sigma_{22} < 0$)	$\left(\frac{\sigma_{22}}{Y_C}\right)^2 + \left(\frac{\sigma_{12}}{S_{12}}\right)^2 + \left(\frac{\sigma_{23}}{S_{23}}\right)^2 \geq 1$
Delamination under tension ($\sigma_{33} > 0$)	$\left(\frac{\sigma_{33}}{Z_T}\right)^2 + \left(\frac{\sigma_{13}}{S_{13}}\right)^2 + \left(\frac{\sigma_{23}}{S_{23}}\right)^2 \geq 1$
Delamination under compression ($\sigma_{33} < 0$)	$\left(\frac{\sigma_{33}}{Z_C}\right)^2 + \left(\frac{\sigma_{13}}{S_{13}}\right)^2 + \left(\frac{\sigma_{23}}{S_{23}}\right)^2 \geq 1$
Fiber matrix shear failure ($\sigma_{11} < 0$)	$\left(\frac{\sigma_{11}}{X_C}\right)^2 + \left(\frac{\sigma_{12}}{S_{12}}\right)^2 + \left(\frac{\sigma_{13}}{S_{13}}\right)^2 \geq 1$

The fiber shear failure mode is predicted using Chang's fiber shear criteria [11]. Ye's delamination criteria are used to model delamination failure [12] (see Table 3).

The material degradation rules proposed by the Camanho [13] and Tserpes [14] are used for damage propagation. According to the material degradation rule when the failure occurs in any element, then the material properties of that particular element are modified as $E_{ijmodified} = D \times E_{ijold}$ and $v_{ijmodified} = D \times v_{ijold}$, where E is Young's modulus and v is Poisson's ratio, and D is the degradation factor. The value of the degradation depends upon the type of failure, as illustrated in Table 4. The progressive damage model is validated with the experimental results presented by X. Li et al. [5]. The load versus displacement curves for the hybrid joint from the presented model and experimental results [5] as shown in Fig. 3 are in good agreement with each other. The FEM results have shown slightly higher strength than the experimental results. This can be due to variations in the material properties of the samples.

Table 4 Material property degradation rule for the CFRP laminate

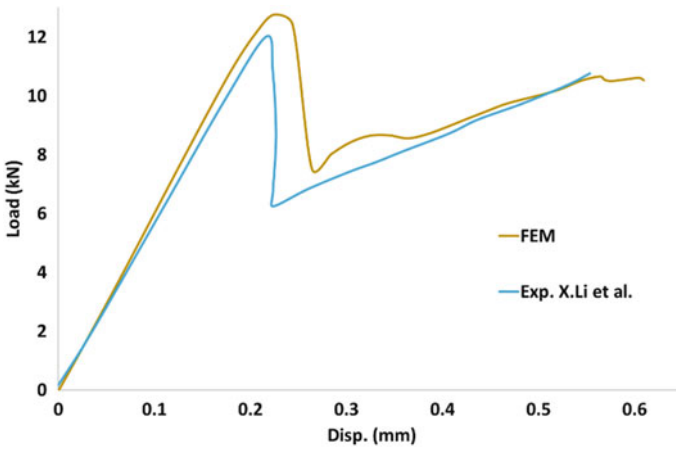| Failure mode	Degradation value (D)	Affected properties
Fiber failure	$D = 0.07$	All material properties constant
Fiber matrix shear failure	$D = 0.2$	G_{12}, ϑ_{12}
Delamination	$D = 0.01$	$E_{33}, \vartheta_{23}, \vartheta_{13}, G_{13}, G_{23}$
Matrix failure	$D = 0.2$	$E_{22}, \vartheta_{12}, \vartheta_{13}, G_{13}, G_{12}$

Fig. 3 Presented model and Experimental [5] load-displacement curve for the hybrid joint

3 Results and Discussion

Load versus displacement, load transfer through the bolt of the hybrid joint, and damage evolution are examined using the 3D FEM method and compared with the bonded and bolted joint explicitly. As illustrated in Fig. 4, the hybrid joint has higher strength than the bolted and bonded joints. They exhibit complex load versus displacement behavior and are ideally classified into three stages. In stage I and stage III the hybrid joint behaves like bonded and bolted joints, respectively. Stage II depicts the transition, where the adhesive layer begins to fail, and simultaneously bolt assembly starts to carry the load. The understating of the failure mechanism over the
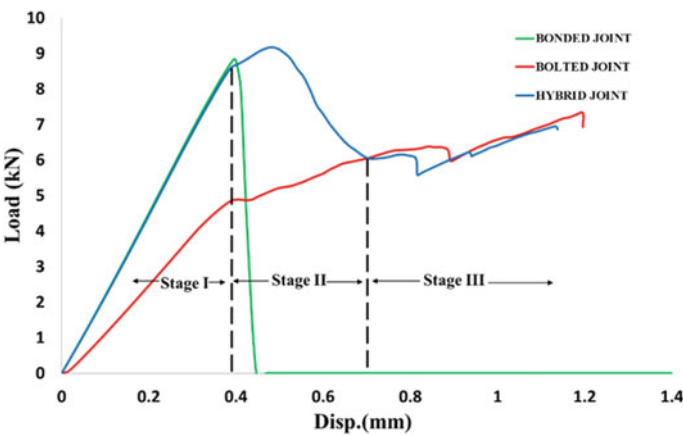

Fig. 4 Load versus displacement behavior of hybrid joint bonded joint and bolted joint
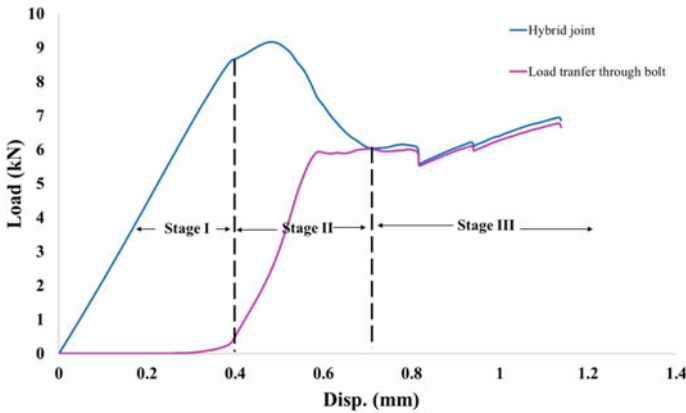
Fig. 5 Load transfer through the bolt versus displacement of the hybrid joint

transition stage is critical and important for its practical application. To further understand the in-depth damage mechanism and the significance of the bolt with bonded joint, the load transfer through the bolt is estimated (Fig. 5). It has been observed that the bolt starts carrying the load when the damage initiates in the adhesive layer and the percentage of load sharing increases gradually till the complete bond failure. Once the adhesive layer fails, the total load transfer happens only through the bolt. The adhesive failure mechanism of the hybrid joint including damage initiation and evolution has been compared with the bonded joint to appreciate the hybrid joint. The damage is initiated almost at the same load in both the joints; however, damage evolution in the adhesive at the peak load and afterward has been delayed in an appreciable amount in the hybrid joint, as illustrated in Fig. 6. A sudden failure of the adhesive layer has been noticed in the bonded joint. However, the adhesive layer of the hybrid joint has been failed gradually in Stage II.

From the above results, one can conclude that the load-sharing feature before the complete failure of the bond is responsible for the significant increase in strength capacity of the hybrid joint than the bonded joint. Hybrid joint exhibiting bearing failure due to fastening with the bolt is a safe-fail damage mode and is preferred over the sudden failure of bonded joint configuration. A detailed evaluation of the damage evolution has been carried out. The $0°$ plies are responsible for the load-carrying capacity; hence, the damage growth in the $0°$ plies results in the final failure of the CFRP joint specimen.

Damage evolution in the hybrid joint is compared with the bolted joint only in the $0°$ plies. Comparison of fiber and matrix failure under compression and tension in the $0°$ plies has been carried out between the hybrid and bolted joints (see Fig. 7). Fiber and matrix failure under compression demonstrate the bearing failure due to the bolt. Bearing failure in the hybrid joint gets initiated after the damage initiation of the fiber under tension in the $0°$ plies, unlike the bolted joint where the bearing failure is the first damage mode that occurred in the plies. Hence, a delay in the bearing failure
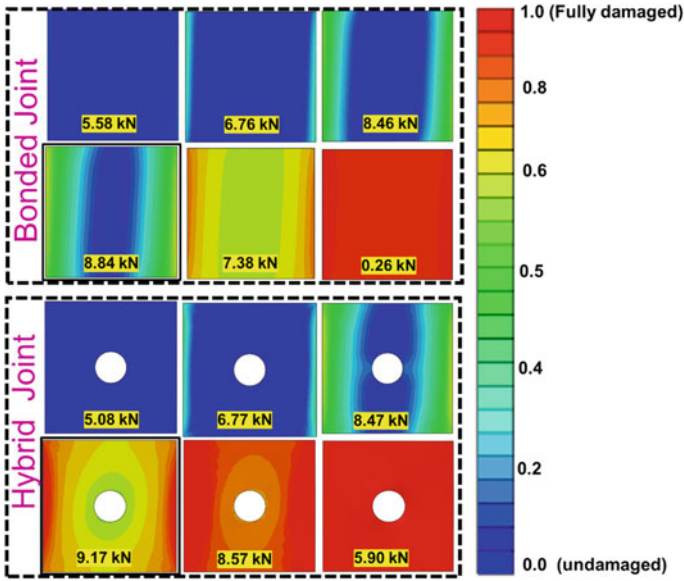
Fig. 6 The comparison of adhesive layer failure of the hybrid joint with the bonded joint
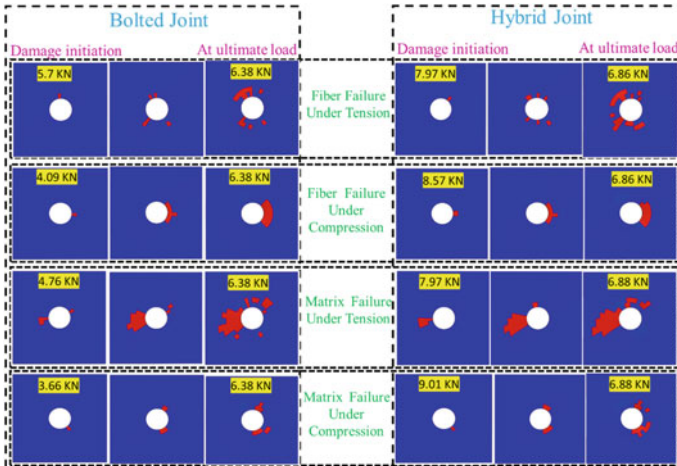

Fig. 7 Damage initiation and progression in the 0° plies of the bolted and the hybrid joint

initiation has been observed in the hybrid joint. In the hybrid joint case, the laminate starts failing from the beginning of the load sharing. The damaged area in both the joints is found to be almost the same but the rate of damage progression is more in the hybrid case as the load capacity values are higher than the bolted joint.

4 Conclusion

Detailed progressive damage analysis of the hybrid joint is performed using a 3D FEM model. The hybrid joint is modeled with Araldite 2015 adhesive layer and fastened by a steel bolt. It exhibits higher tensile strength than bonded and bolted joint with a safe-fail failure mechanism as stated in the literature. The load sharing begins when the adhesive layer starts to debond and at the end of the complete debond, the entire load is carried by the bolts.

- The bolted joint starts failing due to bearing failure, i.e., matrix failure followed by fiber failing under compression, but the joint stiffness has changed when laminate starts to fail under tension (i.e., at 4.76 kN).
- In the hybrid joint case, the damage gets initiated in the laminate under tension both fiber and matrix failure followed by bearing failure, i.e., matrix and fiber failure under compression.
- By correlating the load transfer through the bolt curve and damage evolution results of the hybrid, one can conclude that the damage in the laminate began from the moment when the bolt starts sharing load (i.e., at 7.97 kN).
- Unlike the bolted joint, the stiffness of the hybrid joint got changed when fiber failure under compression gets initiated and reached the peak value till matrix failure under compression (i.e., at 9.17 kN)
- Damage evolution of the adhesive layer is gradual in the case of the hybrid joint, unlike the bonded joint where the bond failed suddenly.

Hence, the damage evolution in the hybrid joint is quite different from the bolted joint. Although, the area accumulated by the damages before the ultimate failure is approximately the same. The load-sharing mechanism has a major contribution towards increased joint strength. To further improve the joint strength, greater load sharing by the bolt is a must before the adhesive layer starts to debond.

References

1. Hart-Smith LJ (1980) Bonded-bolted composite joints. J Aircr 22(11):993–1000
2. Kelly G (2006) Load transfer in hybrid (Bonded/Bolted) composite single-lap joints. Compos Struct 69:35–43
3. Di Franco G, Zuccarello B (2014) Analysis and optimization of hybrid double lap aluminum-GFRP joints. Compos Struct 93:116–131
4. Bodjona K, Lessard L (2016) Hybrid bonded-fastened joints and their application in composite structures: a general review. J Reinf Plast 35:764–781
5. Li X, Cheng X, Guo X, Liu S, Wang Z (2020) Tensile properties of a hybrid bonded/bolted joint: parameter study. Compos Struct 245:112–329
6. Chowdhury NM, Chiu WK, Wang J, Chang P (2015) Static and fatigue testing thin riveted, bonded and hybrid carbon fiber double lap joints used in aircraft structures. Compos Part B 121:315–327

7. Chowdhury NM, Chiu WK, Wang J, Chang P (2016) Experimental and finite element studies of bolted, bonded, and hybrid step lap joints of thick carbon fiber/epoxy panels used in aircraft structures. Compos Part B 100:68–77
8. Benzeggagh ML, Kenane M (1996) Measurement of mixed-mode delamination fracture toughness of unidirectional glass/epoxy composites with mixed-mode bending apparatus. Compos Sci Technol 56:439–449
9. Carvalho UTF, Campilho RDSG (2017) Validation of pure tensile and shear cohesive laws obtained by the direct method with single-lap joints. Int J Adhes Adhes 77:41–50
10. Hashin Z (1980) Failure criteria for unidirectional fiber composites. J Appl Mech 47:329–334
11. Chang FK, Chang KY (1987) A progressive damage model for laminated composites. Compos Mater 21:834–855
12. Ye L (1988) Role of matrix resin in delamination onset and growth in composite laminates. Compos Sci Technol 33:257–277
13. Camanho PP, Matthews FL (1999) A progressive damage model for mechanically fastened joints in composite laminates. J Compos Mater 33:2248–2280
14. Tserpes KI, Labeas G, Papanikos P, Kermanidis T (2002) Strength prediction of bolted joints in graphite/epoxy composite laminates. Compos Part B 33:521–529